

KfK 4710
August 1990

LIBRA — A Light Ion Beam Fusion Conceptual Reactor Design

**B. Badger, G. A. Moses, R. L. Engelstad, G. L. Kulcinski,
E. Lovell, J. MacFarlane, R. R. Peterson, M. E. Sawan,
I. N. Sviatoslavsky, L. J. Wittenberg, I. Smith, R. Altes,
P. Corcoran, R. Kuenning, D. Pellow, D. Wake,**

J. Ehrhardt, G. Kessler, E. Stein,

D. L. Cook, R. E. Olson, R. W. Stinnett

Institut für Neutronenphysik und Reaktortechnik

Kernforschungszentrum Karlsruhe

KERNFORSCHUNGSZENTRUM KARLSRUHE
Institut für Neutronenphysik und Reaktortechnik

KfK 4710
UWFDM 800
FPA 90-3

LIBRA - A Light Ion Beam Fusion Conceptual Reactor Design

B. Badger, G.A. Moses, R.L. Engelstad, G.L. Kulcinski, E. Lovell, J. MacFarlane,
R.R. Peterson, M.E. Sawan, I.N. Sviatoslavsky, L.J. Wittenberg
I. Smith, R. Altes, P. Corcoran, R. Kuenning, D. Pellow, D. Wake
J. Ehrhardt, G. Kessler, E. Stein
D.L. Cook, R.E. Olson, R.W. Stinnett

Kernforschungszentrum Karlsruhe GmbH, Karlsruhe

Als Manuskript gedruckt
Für diesen Bericht behalten wir uns alle Rechte vor

Kernforschungszentrum Karlsruhe GmbH
Postfach 3640, 7500 Karlsruhe 1

ISSN 0303-4003

B. Badger, G.A. Moses, R.L. Engelstad, G.L. Kulcinski, E. Lovell, J. MacFarlane,
R.R. Peterson, M.E. Sawan, I.N. Sviatoslavsky, L.J. Wittenberg

Fusion Technology Institute
University of Wisconsin
1500 Johnson Drive
Madison, WI 53 706

I. Smith, R. Altes, P. Corcoran, R. Kuenning, D. Pellow, D. Wake

Pulse Sciences Inc.
600 McCormick Street
San Leondro, CA 94 577

J. Ehrhardt, G. Kessler, E. Stein

Kernforschungszentrum Karlsruhe
Institut für Neutronenphysik
und Reaktortechnik
Postfach 3640
D-7500 Karlsruhe 1

D.L. Cook, R.E. Olson, R.W. Stinnett

Sandia National Laboratories
Albuquerque, NM 87 185

ABSTRACT

The LIBRA light ion beam fusion commercial reactor study is a self-consistent conceptual design of a 330 MWe power plant with an accompanying economic analysis. Fusion targets are imploded by 4 MJ shaped pulses of 30 MeV Li ions at a rate of 3 Hz. The target gain is 80, leading to a yield of 320 MJ. The high intensity part of the ion pulse is delivered by 16 diodes through 16 separate z-pinch plasma channels formed in 100 torr of helium with trace amounts of lithium. The blanket is an array of porous flexible silicon carbide tubes with $\text{Li}_{17}\text{Pb}_{83}$ flowing downward through them. These tubes (INPORT units) shield the target chamber wall from both neutron damage and the shock overpressure of the target explosion. The target chamber is "self-pumped" by the target explosion generated overpressure into a surge tank partially filled with $\text{Li}_{17}\text{Pb}_{83}$ that surrounds the target chamber. This scheme refreshes the chamber at the desired 3 Hz frequency without excessive pumping demands. The blanket multiplication is 1.2 and the tritium breeding ratio is 1.4. The direct capital cost of a 331 MWe LIBRA design is estimated to be \$2843 \$/kWe while a 1200 MWe LIBRA design will cost approximately 1300 \$/kWe.

LIBRA - Eine Konzeptstudie für einen Trägheitsfusionsreaktor mit Leichtenstrahl-Treiber

Kurzfassung

Die LIBRA-Studie für einen Leichtenstrahl-Fusionsreaktor ist ein Konzeptentwurf, einschließlich einer Wirtschaftlichkeits-Analyse, für ein Kraftwerk mit einer Leistung von 330 MWe. Die Implosion der Fusionstargets erfolgt durch Lithium-Ionen-Pulse mit 30 MV Beschleunigungsspannung und 4 MJ Pulsenergie bei einer Frequenz von 3 Hz. Der Target-Gain beträgt 80, was einem Energieausstoß von 320 MJ entspricht. Der Treiberpuls höchster Strahlintensität wird von 16 Ionen-Dioden durch 16 getrennte z-Pinch-Plasmakanäle geliefert. Diese Plasmakanäle werden in einer Atmosphäre aus 100 Torr Helium mit Spuren von Lithium erzeugt. Das Blanket besteht aus einer Anordnung poröser elastischer Siliziumkarbidröhren, die von einem nach unten gerichteten $\text{Li}_{17}\text{Pb}_{83}$ -Strom durchflossen werden. Durch diese Röhren (INPORT-Units) wird die Wand der Targetkammer vor Neutronenschäden und dem durch die Targetexplosion entstehenden plötzlichen Überdruck geschützt. Durch Ausnutzung des bei der Targetexplosion erzeugten Überdrucks wird die Targetkammer "selbst-entleert". Der Inhalt wird in einen Kondensationsstank gepumpt, der teilweise mit dem die Targetkammer umgebenden $\text{Li}_{17}\text{Pb}_{83}$ gefüllt ist. Auf diese Weise ist ein Austausch der Kammeratmosphäre bei der gewünschten Frequenz von 3 Hz ohne übermäßig hohen Pumpaufwand möglich. Der Multiplikationsfaktor des Blankets liegt bei 1, 2. Die Tritiumbrutrate beträgt 1, 4. Die Anlagenkosten für den LIBRA-Reaktor mit der Leistung von 331 MWe werden auf 2843 \$/kWe geschätzt. Für den LIBRA-Reaktor mit der Leistung 1200 MWe reduzieren sich die Kosten auf etwa 1300 \$/kWe.

PREFACE

The LIBRA (Light Ion Beam ReActor) project began as a small, scoping study project in 1982. It was then intermittently funded by the Kernforschungszentrum Karlsruhe (KfK) over the time period 1982-1988 to study critical issues. During that time, the technical work was performed by Fusion Power Associates (FPA), Pulse Sciences Incorporated (PSI), as well as by scientists at KfK. In 1989, the scoping studies were elevated to a preconceptual design phase by a combination of Sandia National Laboratories (SNL) and KfK. The main effort was then directed through the University of Wisconsin (UW) along with FPA, PSI and SNL scientists.

The idea of this project is to carry through a preconceptual DT fusion reactor study to the point that one could make a technical, environmental, as well as economic comparison of LIBRA to previous magnetic fusion and inertial confinement fusion commercial reactor designs. This has been accomplished here with reference to the current state of the art in physics and technology and one will find that the LIBRA reactor has a large number of attractive features. It also has some drawbacks which we point out in this report.

TABLE OF CONTENTS

Page

PREFACE

ABSTRACT

1. EXECUTIVE SUMMARY

1.1. Target Performance.....	1-1
1.2. Pulsed Power Driver	1-9
1.3. Diode Performance	1-10
1.4. Channel Formation	1-10
1.5. Beam Transport	1-11
1.6. Channel Insulation.....	1-13
1.7. Cavity Analysis	1-13
1.8. INPORT Response	1-19
1.9. Target Chamber Design	1-19
1.10. Blanket Response.....	1-21
1.11. Tritium Fueling, Breeding and Inventory.....	1-23
1.12. LIBRA Economics.....	1-23
1.13. Conclusions	1-26
References for Chapter 1	1-29

2. PULSED POWER DRIVER

2.1. Introduction.....	2-1
2.2. Driver Parameters and Design Sequence.....	2-2
2.3. Cell Design	2-3
2.4. Pulseline Design	2-5
2.5. Circuit Calculations.....	2-8
2.6. Cell and Pulseline Electric Stresses.....	2-10
2.7. Voltage Adder Calculations.....	2-15
2.7.1. MIVA Design	2-15
2.7.2. NEVA Design.....	2-18
2.8. Ion Bunching.....	2-21
2.9. Charging System Design.....	2-21
2.9.1. Introduction	2-21
2.9.1.1. Driver and Charging System Configuration.....	2-21
2.9.1.2. Number of Cells Per Driver Module and Charge System Module.....	2-28
2.9.1.3. Electrical Specifications.....	2-30
2.9.2. Approach	2-30
2.9.3. 1.35 - 2.7 MV Transformer	2-33
2.9.4. 5 μ s Stage Reactor.....	2-38
2.9.5. 5 μ s Water Capacitor.....	2-38
2.9.6. Inductance Summary.....	2-40
2.9.7. Charging Transformer	2-40
2.9.8. Switches	2-42
2.9.9. Transfer Capacitor.....	2-45

2. PULSED POWER DRIVER (Cont.)

2.10. Configuration.....	2-45
2.11. Cost Estimate.....	2-45
2.11.1. Introduction and Basis of Estimates.....	2-45
Power Supply.....	2-49
Charging System.....	2-49
Magnetic Pulse Compression.....	2-51
Accelerator Modules.....	2-53
Mag and Accelerator Cell Fabrication Tooling and Fixtures.....	2-56
2.11.2. Conclusions.....	2-56
References for Chapter 2.....	2-57
Appendix 2.A - Trade-Off Study.....	
2.A.1. Method.....	2-58
2.A.2. Results.....	2-62

3. LIGHT ION DIODE

3.1. Introduction.....	3-1
3.1.1. Choice of Configuration for LIBRA Diodes.....	3-1
3.1.2. Choice of Ion for LIBRA.....	3-1
3.1.3. Repetitive Operation of LIBRA Diodes.....	3-2
3.1.4. Developments Pushing Technologies for Application in LIBRA.....	3-2
3.1.5. Summary of Diode Design for LIBRA.....	3-2
3.1.6. Organization of the Remainder of Chapter III.....	3-3
3.2. Basic Ion Diode Requirements.....	3-3
3.2.1. Summary of Basic Requirements for LIBRA Diodes.....	3-3
3.2.2. Ion Range in the Target.....	3-3
3.2.3. Transit-Time Ion Bunching.....	3-5
3.2.4. Pulse Shape at the Target.....	3-5
3.2.5. Adequate Total Energy.....	3-5
3.2.6. Adequate Spatial Symmetry and Temporal Synchrony.....	3-5
3.2.7. Ion Source Purity.....	3-5
3.2.8. Diode Repetition Rate.....	3-7
3.3. Ion Diode Design.....	3-7
3.3.1. Ion Beam Focusing Limitations.....	3-7
3.3.2. Ion Current Density Level Desired.....	3-7
3.3.3. Virtual Cathode Dynamics in the Diode.....	3-8
3.3.4. Adequate Level of Magnetic Field Uniformity, Including Edge Effects.....	3-8
3.3.5. Level of Critical Magnetic Field for Insulation of Electrons.....	3-9
3.4. Ion Diode Parameters.....	3-10
3.5. Electrohydrodynamic Ion Source.....	3-10
3.5.1. Physics of Electrohydrodynamic Source Operation.....	3-10
3.5.2. Growth Rates and Wavelengths for EHD Sources.....	3-10
3.5.3. Scale Tests of EHD.....	3-10
3.5.4. EHD Ion Source Divergence.....	3-13
3.5.5. EHD Anode Substrate.....	3-13
3.5.6. Inherent EHD Ion Source Repetitive Capability.....	3-13

3. LIGHT ION DIODE (Cont.)

3.6.	Physics of Ion Diode Operation.....	3-13
3.6.1.	Principal Stages of Diode Behavior	3-13
3.6.2.	Analytic Theory of Applied-B Ion Diodes.....	3-14
3.6.3.	Analytic Theory of Extraction Diodes.....	3-14
3.6.4.	Uniform Insulation of Extraction Diodes.....	3-14
3.6.5.	Coaxial vs. Triaxial Diodes.....	3-14
3.6.6.	Summary of Optimal Diode Features.....	3-15
3.7.	Repetitive Diode Behavior	3-15
3.7.1.	Liquid Anodes for EHD Ion Sources	3-15
3.7.2.	Electron Deposition at Anode	3-15
3.7.3.	Liquid-Cooled Anode	3-15
3.7.4.	Liquid-Cooled Cathode	3-16
3.7.5.	Diode Cleanliness at High Temperature.....	3-16
3.7.6.	Diode Average Power Levels	3-16
3.7.7.	Pulsed Magnetic Field Coils.....	3-16
3.7.8.	Isolation of Diode from Cavity.....	3-16
3.8.	Level of Technology Extrapolation	3-17
3.8.1.	Extrapolation from Diodes on PBFA II.....	3-17
3.8.2.	Extrapolation from Diodes on MITE, HELIA, SABRE, and Hermes III.....	3-17
3.8.3.	Extrapolation in Voltage	3-18
3.8.4.	Extrapolation in Current and Current Density.....	3-18
3.8.5.	Extrapolation in Power per Diode	3-18
3.8.6.	Extrapolation in Energy per Diode.....	3-18
3.8.7.	Extrapolation in Diode Impedance.....	3-18
3.8.8.	Extrapolation in Power Brightness	3-18
3.8.9.	Extrapolation in Power Intensity at Focus.....	3-19
3.8.10.	Extrapolation in Ion Divergence	3-19
3.8.11.	Extrapolation in Diode Repetition Rate.....	3-19
3.A.	Appendix: Repetitive Diode Workshop.....	3-20
3.A.1.	Some Comments From the Workshop on Repetitive Ion Diodes.....	3-20
	References for Chapter 3	3-24

4. LIGHT ION BEAM TRANSPORT

4.1.	Introduction.....	4-1
4.2.	Channel Formation	4-4
4.3.	Ion Beam Propagation in Plasma Channels.....	4-18
4.4.	Electrical Insulation of Plasma Channels.....	4-23
4.5.	Future Considerations.....	4-29
	References for Chapter 4	4-32

5. TARGET

5.1.	Target Design.....	5-1
5.2.	Target Microexplosion	5-6
5.3.	Target Heating During Injection.....	5-9
5.4.	Optional Hybrid Target Design.....	5-17
	References for Chapter 5	5-19

6. TARGET CHAMBER DESIGN AND MAINTENANCE

6.1. General Discussion	6-1
6.2. Target Chamber Description.....	6-2
6.3. Target Chamber Evacuation	6-5
6.4. Beamline Magnetic Protection.....	6-7
6.5. Target Chamber Thermal Hydraulics.....	6-12
6.6. Reactor Target Chamber Maintenance.....	6-13
References for Chapter 6	6-16

7. CAVITY RESPONSE

7.1. Overview.....	7-1
7.2. Radiation-Hydrodynamic Calculations for the LIBRA Target Chamber Cavity	7-3
7.2.1. Overview of the Radiation-Hydrodynamic Simulations	7-3
7.2.2. Equation of State and Opacity Data.....	7-8
7.2.3. Target X-ray Energy Deposition and Rapid Vaporization	7-17
7.2.4. Debris Ion Energy Deposition.....	7-24
7.2.5. Results of Radiation-Hydrodynamic Simulations	7-27
7.2.6. Summary of Radiation-Hydrodynamic Calculations.....	7-38
7.3. INPORT Mechanical Response	7-38
7.3.1. Dynamic Modelling Background	7-38
7.3.2. Analytical Outline.....	7-39
7.3.3. Response Characteristics	7-41
References for Chapter 7	7-50

8. CHAMBER NEUTRONICS ANALYSIS

8.1. One-Dimensional Scoping Analysis	8-1
8.2. Three-Dimensional Neutronics Analysis.....	8-4
8.2.1. Reactor Geometrical Model.....	8-5
8.2.2. Material Compositions	8-8
8.2.3. Determination of the Volumes.....	8-8
8.2.4. Neutronic and Photonic Source.....	8-13
8.2.5. Volumes and Masses.....	8-13
8.2.6. Neutron and Photon Flux Densities	8-13
8.2.7. Tritium Breeding Rates	8-18
8.2.8. Neutron and Photon Nuclear Heating.....	8-21
8.3. Activation Analysis	8-26
8.3.1. Calculational Procedure.....	8-26
8.3.2. Activity, Biological Hazard Potential (BHP) and Decay Heat in the LIBRA Chamber Structure.....	8-32
8.3.3. Waste Disposal Rating (WDR) of LIBRA Chamber Structure.....	8-38
8.3.4. Coolant Activity.....	8-42
8.3.5. Dose After Shutdown.....	8-42
References for Chapter 8	8-46

9. TRITIUM SYSTEMS

9.1. Tritium Fuel Preparation	9-1
9.2. Tritium Breeding and Recovery	9-6
9.3. Environmental and Safety Concerns.....	9-10
9.3.1. Tritium Inventory and Pathways.....	9-10
9.3.2. Additional Radioactive Products in the Liquid Breeder Alloy.....	9-15
9.4. Environmental Analysis.....	9-17
9.4.1. Tritium Release During Normal Operation	9-17
9.4.2. Accidental Releases of Radioactivity	9-17

References for Chapter 9	9-21
--------------------------------	------

10. POWER CONVERSION AND BALANCE OF PLANT

10.1. LIBRA Power Cycle	10-1
-------------------------------	------

11. COST ESTIMATE

11.1. Scaling Laws	11-1
11.2. Unit Costs	11-2
11.3. Target Costs	11-3
11.4. Economic Model	11-3
11.5. Capital Costs and Cost of Electricity	11-3
11.6. Economic Implications of Scaling LIBRA from 330-1200 MWe.....	11-8
11.6.1. Reactor Chamber Modifications	11-8
11.6.2. Scaleup Scenarios	11-9
11.6.3. Scaling Laws.....	11-9
11.6.4. Results and Conclusions.....	11-9

References for Chapter 11	11-14
---------------------------------	-------

APPENDIX - PARAMETER LIST

1. General Parameters	A-1
2. Target Parameters	A-2
3. Target Manufacture and Delivery Parameters.....	A-4
4. Driver Parameters	A-6
5. Diode Parameters.....	A-9
6. Preformed Plasma Channel Parameters	A-12
7. Ion Beam Parameters	A-14
8. Cavity and Blanket Parameters	A-16
9. Chamber, Reflector and Shield Parameters	A-20
A. Reflector	A-20
B. Shield	A-22
10. Power Conversion and Balance of Plant	A-23
11. System Parameters.....	A-24
12. Tritium Parameters (for 29% Burnup).....	A-25
13. LIBRA Costing.....	A-27

1. EXECUTIVE SUMMARY

The LIBRA study is a self-consistent conceptual design of a light ion driven commercial fusion power reactor.⁽¹⁾ Other previous LIB reactor designs include UTLIF,⁽²⁾ ADLIB,⁽³⁾ and EAGLE.⁽⁴⁾ A point design for LIBRA was completed and a cost estimate was based on a 331 MWe plant. A cost scaling study was then done to examine the effect of redesigning to different power levels. Specific design parameters are given in Table 1.1 and schematic of the design is given in Fig. 1.1. A cross section of the reactor chamber is shown in Fig. 1.2.

This executive summary covers the major features of the LIBRA design. More detailed discussions of each aspect of the design are given in Chapters 2-12 of the LIBRA report. Specific aspects of the LIBRA design have also been reported in a number of published papers.⁽⁵⁻⁷⁾

1.1 Target Performance

The target for LIBRA is a generic single shell design similar to that used in the HIBALL study.⁽⁸⁾ The initial target configuration is shown in Fig. 1.3. The configuration at the instant of ignition is also shown. No implosion calculations were done for this specific design, but calculations done for similar target⁽⁹⁾ give us confidence that the energetics of our design (i.e., input energy per unit mass accelerated) is roughly correct. While other designs, unavailable to us for this study, may in fact be required to reach ignition conditions, we feel that this generic design adequately serves our purposes.

The target gain was chosen to be 80 for 4 MJ of ion input energy. This is consistent with published gain estimates⁽¹⁰⁾ as shown in Fig. 1.4 for a Li ion range of 0.025 g/cm² and for various target radii. The power on target of 400 TW is within 20% of the published requirements⁽¹⁰⁾ (Fig. 1.5).

Coupled thermonuclear burn-radiation hydrodynamic simulations predict that a fuel mass compressed to a ρR -value of 2 g/cm² and surrounded by a low-Z pusher with a ρR -value of 1 g/cm² burns with a 30% burn-up fraction. For 3.2 mg of DT fuel this results in a thermonuclear yield of 320 MJ.

The x-ray spectrum used for the cavity response calculations is given in Fig. 1.6. The ion spectrum was assumed to consist of the following components: 1.93 keV D, 2.89 keV T, 3.8 keV He, 11.1 keV C, and 198 keV Pb. The x-ray spectrum has both a hard and soft component. The hard part is due to bremsstrahlung x-rays generated by the burning DT escaping through the high-Z tamper material. The soft part is due to radiation from the target once its temperature equilibrates during the expansion phase following burn. The neutron spectrum is softened by collisions in the target with the average energy per escaping neutron being 11.93 MeV.

Table 1.1 LIBRA Parameters

<u>General</u>		<u>Lithium Ion Beams</u>	
Net electric power	331 MW	Energy	25-35 MeV
Gross electric power	441 MW	Number high power	16
Thermal power	1161 MW	low power	2
Recirc. power fraction	0.25	Peak power on target	400 TW
Driver efficiency	0.235	Pulse compression ratio	5
Target gain	80	Pulse length on target	9 ns
η_G	18.8	Current/channel	0.3 MA
Direct capital cost (1989\$)	\$2200/kW	Entering on target	1.1 MA
		Ion energy transport eff.	0.63
<u>Target Performance</u>		<u>Laser-Guided, Free Standing Channels</u>	
DT mass	3.2 mg	Length	5.4 m
Input energy	4 MJ	Radius	0.5 cm
Yield	320 MJ	Peak B-field	27 kG
X-ray yield	67 MJ	Peak current	100 kA
Neutron yield	217 MJ	Rise time	1 μ s
Charged particle yield	28.5 MJ	Voltage drop	1 MV
Endoergic loss	7 MJ		
Neutron mult.	1.02		
<u>Applied-B Diode</u>		<u>Cavity</u>	
Anode source	Liquid Li	Gas pressure	100 torr He
Anode current density	5 kA/cm ²	Radius to first surface	3 meters
Anode radius	8.4 cm	Pumping time	300 ms
Focal length	70 cm	Impulse on INPORTs	125 Pa-s
Microdivergence	5 mrad	Vaporized LiPb mass/shot	8 kg
Macrodivergence	120 mrad		
Conversion efficiency	0.80	<u>INPORT Tube Blanket</u>	
		Tube material	SiC
<u>Helia Pulsed Power</u>		Packing fraction	0.33
Waterline energy	11.1 MJ	Coolant/breeder	Li ₁₇ Pb ₈₃
No. of cells/module	26	Li-6 enrichment	90%
Voltage/cell	1.15 MV	Thickness	1.35 m
Cell diameter	2.9 meters	Energy mult.	1.28
Module diameter	5.15 meters	Tritium breeding ratio	1.4
Module length	14.4 meters		
PFL output voltage	1.15 MV	<u>Tritium</u>	
Impedance	3 Ω	Inventory: target prep.	680 g
Dielectric	water	Reactor hall	174 g
Switch type	metglas	Effluent release	32 Ci/day
	saturable reactor		

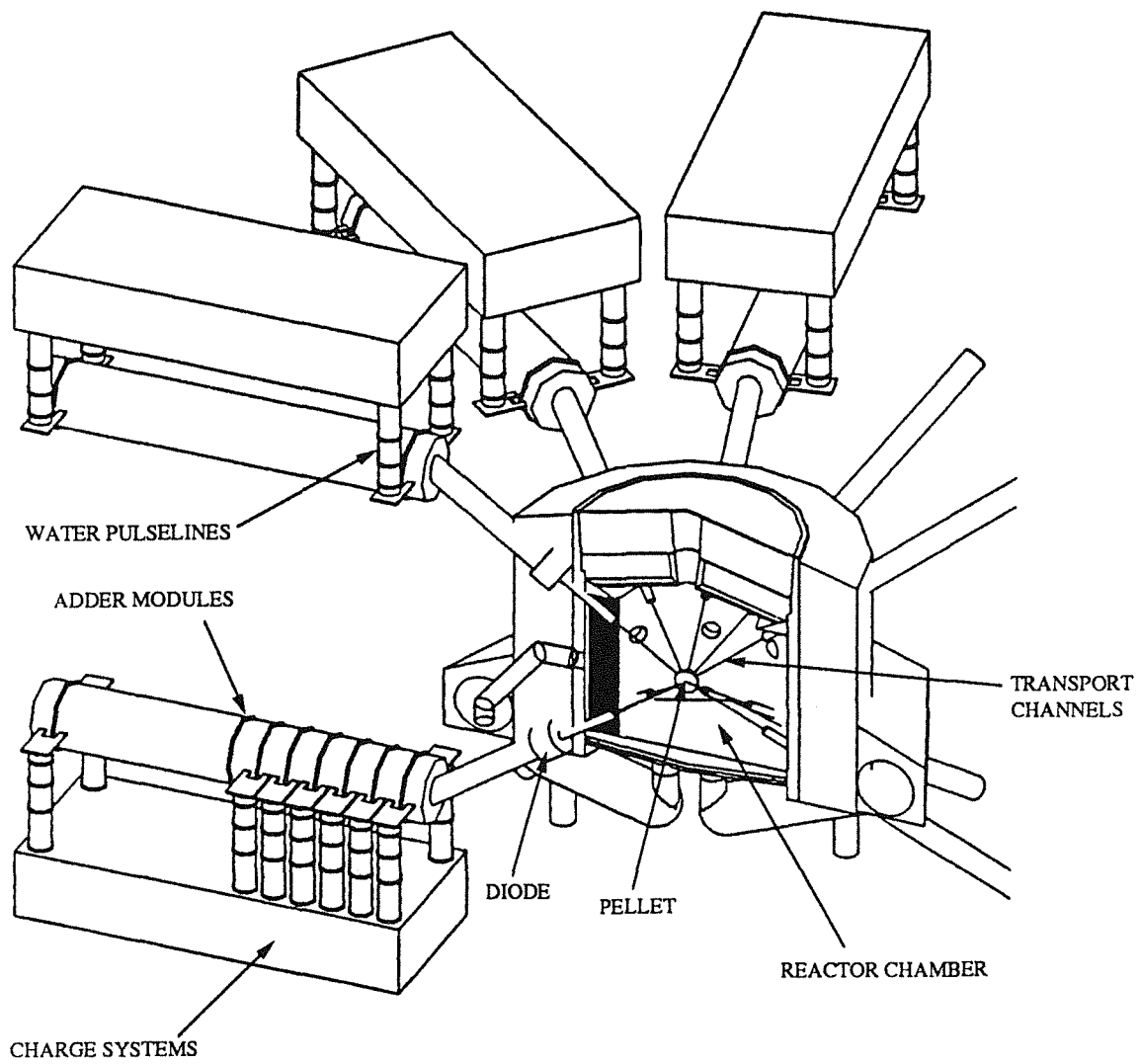


Figure 1.1. LIBRA reactor design.

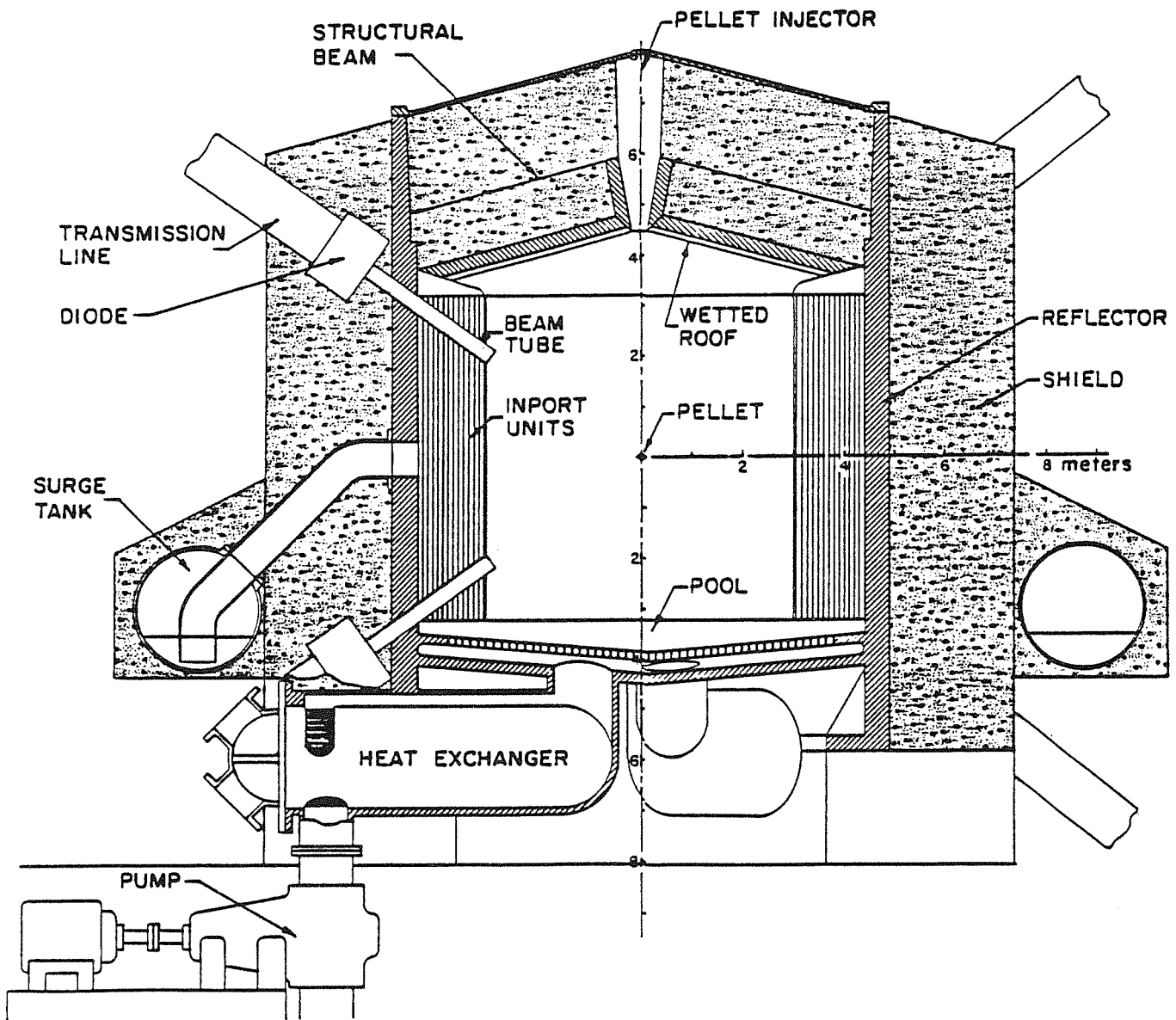


Fig. 1.2. Cross section of target chamber.

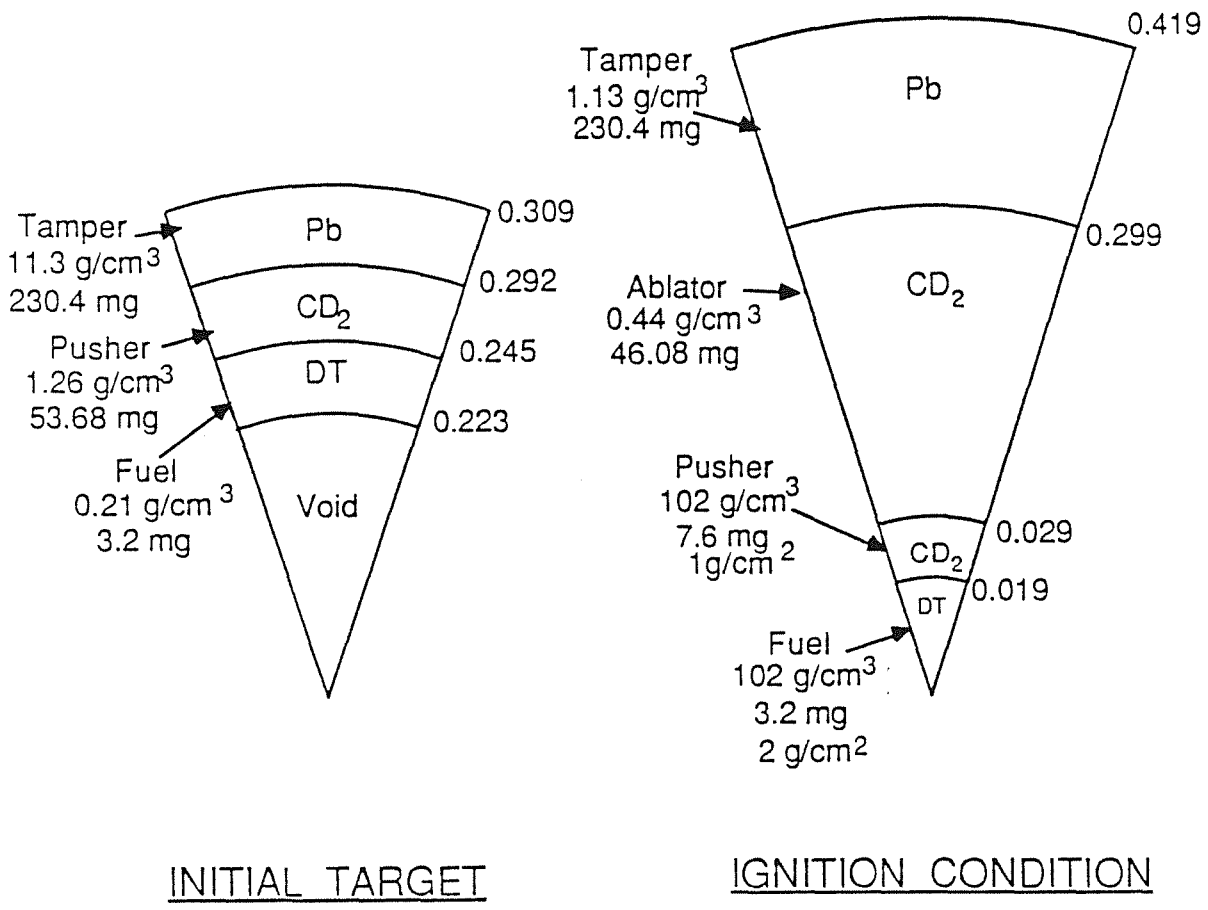


Fig. 1.3. Generic single shell target design for LIBRA analysis.

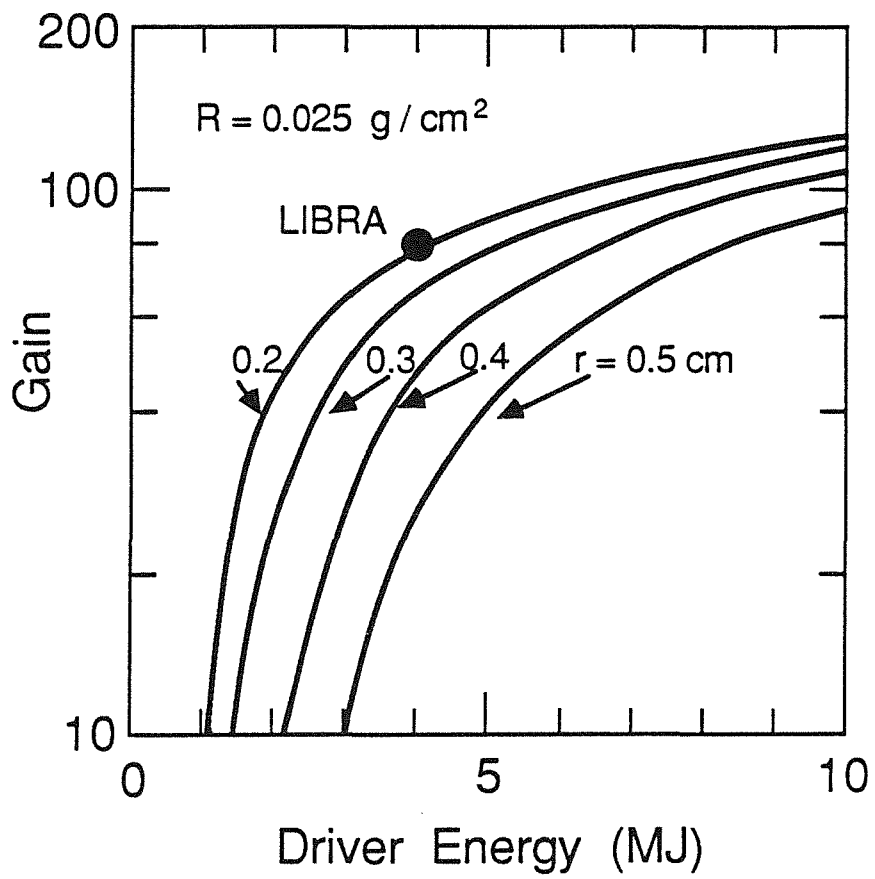


Fig. 1.4. Comparison of LIBRA gain to LLNL gain estimates [R. Bangerter, Fusion Tech. 13, 348 (1988)].

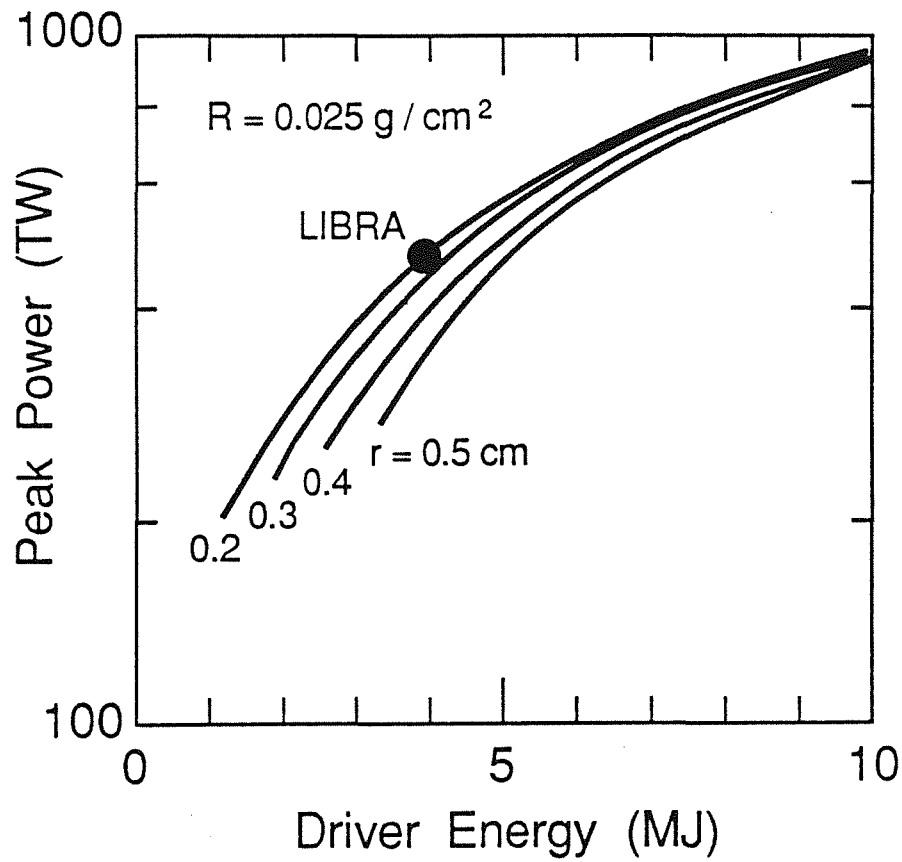


Fig. 1.5. Comparison of LIBRA power on target to LLNL requirements [R. Bangerter, Fusion Tech. 13, 348 (1988)].

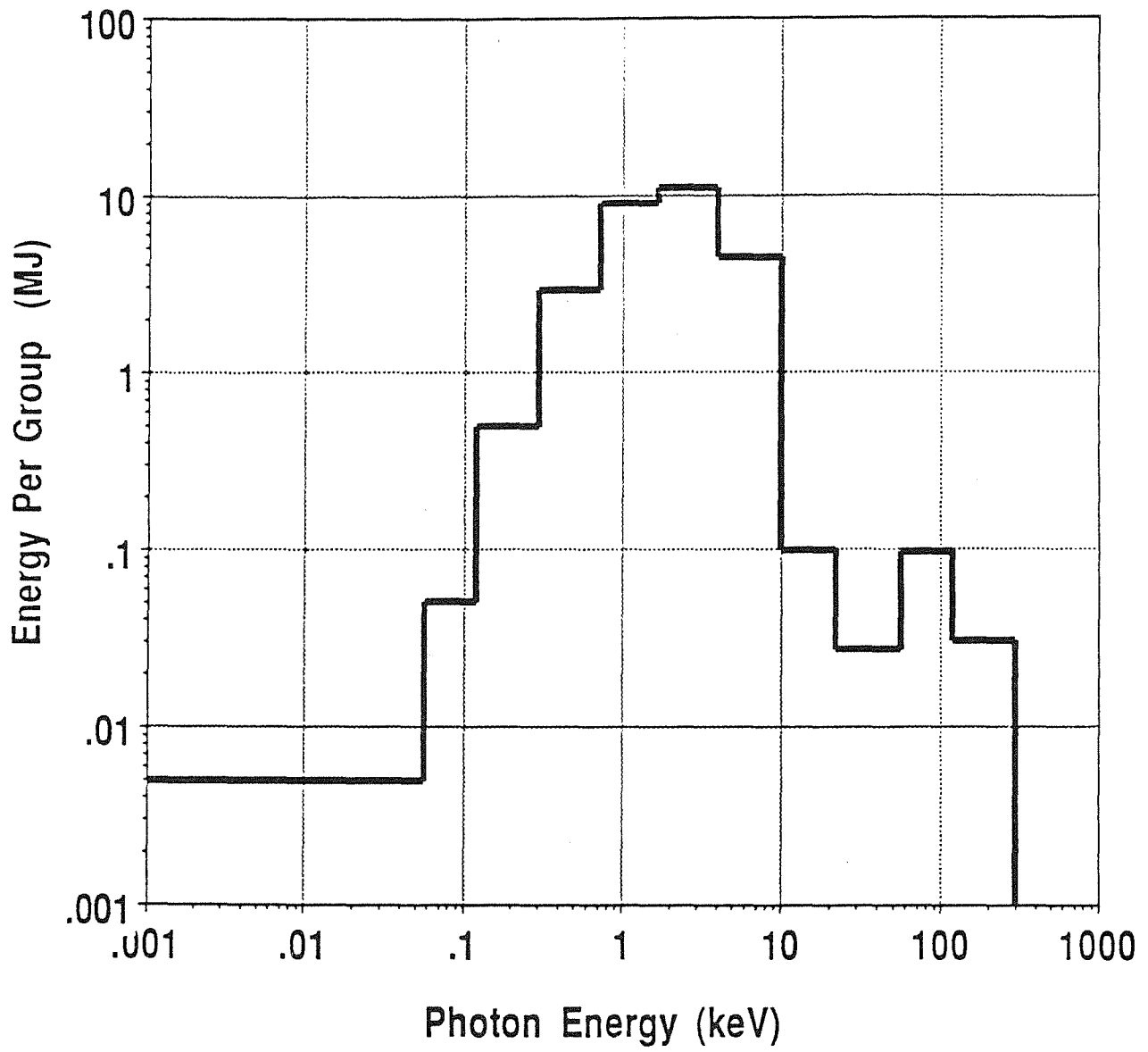


Fig. 1.6. X-ray spectrum from LIBRA target.

1.2. Pulsed Power Driver

A 30 MV lithium ion driver has been designed for LIBRA. This effort follows earlier studies made by PSI of drivers for different particle species and energies. After an early examination of design options, these studies assumed the use of the Helia design approach, first formulated by PSI in which induction cells driven at about 1 MV by water dielectric pulselines are assembled in series to drive the full voltage ion diode via a magnetically insulated vacuum voltage adder (MIVA). The most detailed of the previous work was on a 20 MV deuterium driver. Initially, a design was developed for the induction cells, MIVA, and pulselines. Subsequently, calculations addressed the performance of the MIVA and the bunching of the ions.

In the present 30 MV driver study, the design of the pulse lines, cells, and MIVA, the performance of all circuits including the MIVA and the bunching of the ions were addressed. This culminated in calculated power and energy waveforms at the pellet that more than satisfied specifications. In a subsequent task, the design of the charging system from wall plug to pulse lines was developed, and a cost estimate was made for the whole driver.

At the outset of the LIBRA studies, the Helia approach had not been tested. An initial four-stage, 4 MV proof-of-principle test was completed in 1985 by PSI and Sandia National Laboratory (SNL) under DNA and DOE funding. During the course of the 30 MV driver study, the 20 MV, 750 kA Hermes-III electron accelerator has been successfully operated at full power at Sandia. Hermes-III has also been successfully tested for a short period at ≥ 22 MV in the positive polarity required to accelerate ions. The scalability of the driver to 30 MV now seems fairly well assured, at least up to the diode; some questions remain about the efficiency of the positive polarity voltage adder, but there are a number of promising ways to design this successfully.

No accelerator of the Helia type has yet operated repetitively. However, the technology of repetitive magnetic (i.e. saturable reactor) pulse compressors developed at Lawrence Livermore National Laboratory has achieved > 1 kHz operation, and by incorporating magnetic switches into the pulse lines of machines like Helia and Hermes-III it seems probable that reliable long life repetitive operation can be realized.

The result of this design effort is a 30 MeV Li ion driver that provides 4 MJ onto an ICF target. This driver contains 18 independent modules; 16 to provide 3.6 MJ on the driver in a 9 ns wide main pulse, 2 to provide 0.4 MJ in a 45 ns wide pre-pulse. The 16 main modules provide pulses on the ion diodes that are ramped in voltage from 25 to 35 MV over a time of 45 ns so that the pulse of ions is time-of-flight bunched during its propagation to the target into a 9 ns pulse. The pre-pulse modules do not have this voltage ramp so there is no bunching. The driver components and their relationship to the target chamber are schematically shown in Fig. 1.1.

1.3 Diode Performance

The 30 MeV Li+1 ion beams in LIBRA are generated with applied magnetic field extraction diodes. The design of the ion diodes is determined by several factors. These include ion beam focussing limitations, required ion current density, virtual cathode dynamics, magnetic field uniformity, and critical magnetic field for insulation of electrons. Consistent with trapping the ions in plasma channels, we have chosen a focal length of 70 cm, a microdivergence of 5 milliradians, and an outer anode radius of 5.2 cm. We have also chosen an anode current density of 5 kA/cm², consistent with best experimental focussing on PBFA II and Proto I. Based on the Desjarlais theory, a 30 MV operating voltage was picked which is one half of the critical voltage and leads to a physical anode-cathode gap of 2.4 cm and a dynamic gap of 1.94 cm. To insure good magnetic field uniformity, the difference between the outer and inner anode radii is taken to be twice the dynamic gap, or 3.88 cm. Combining this with the current density and the total required current per diode of 317 kA, the inner and outer anode radii of 1.31 cm and 5.19 cm is obtained. For a dynamic gap of 1.94 cm and an operating voltage of 30 MV, a critical magnetic field for insulation of the electrons of 4.3 Tesla has been calculated. The applied field of twice the critical field, or 8.6 Tesla is used.

The diode has been designed to operate at a rate of 3 Hz. The anode surface is of fritted steel, through which flows liquid lithium. Lithium ions are ejected from the liquid at cusps formed by an electrohydrodynamic instability. Most of the energy loss in the diode is in the form of 30 MeV electrons that deposit in the liquid lithium when the magnetic insulation in the diode breaks down. This heat cleans the anode surface for the next shot and the heat is carried away by the flowing lithium. The lithium beam ions are stripped from charge state 1 to charge state 3 by a jet of argon gas that is puffed into the exit region of the diode at a 3 Hz rate.

The diodes are designed to provide a proper pulse shape for driving an ICF target. There are sixteen main pulse diodes that provide a 25-35 MV ramped pulse that compress the pulse by time-of flight bunching from 45 ns to 9 ns and provide 90% of the 4 MJ of total beam energy on target. There are 2 pre-pulse diodes that are not ramped and provide a much longer pre-pulse.

1.4 Channel Formation

The ion beams must be transported from the ion diodes to the target in plasma channels. The channels enter the target chamber in two cones, 35° above and below the horizontal plane containing the target. For each channel, there is a 4.5 meter channel to return the discharge current that leaves the target chamber through the top. The channel parameters are listed in Table 1.1.

The electrical resistivity must be high away from the channel and low on the axis to confine the discharge current to a small radius channel. Since resistivity decreases rapidly with increasing temperature, the radial temperature profile in the channels must be peaked along the channel axis

and low in the region just outside the channel. A small diameter pre-ionizing laser beam and a fast rising discharge current should be advantageous for this channel formation.

A two stage discharge current history where a large main pulse follows a smaller prepulse was first proposed several years ago⁽¹²⁾ and this was parameterized by a delay time Δt . Simulations of channel formation in helium gas at a mass density of $2.37 \times 10^{-5} \text{ g/cm}^3$ were performed using the ZPINCH radiation magnetohydrodynamics computer code.⁽¹³⁾ A $1 \mu\text{s}$ delay time in the discharge current and a laser beam half-width of 2 mm was used. For these values the simulations predict that the magnetic field at 0.5 cm from the channel axis reaches 27 kG and that the average mass density in the channel is approximately $5 \times 10^{-6} \text{ g/cm}^3$ (Fig. 1.7). These results are acceptable for LIBRA.

1.5 Beam Transport

The efficiency of individual ion transport from diode to target is determined by two mechanisms. First, the ions must enter the channel within an angular and radial constraint.⁽¹⁴⁾ Ions that have larger angles of incidence and are at relatively large distances from the channel axis are either not trapped by the channel's magnetic field and pass through the background gas never turning back toward the channel axis, or are turned back by the magnetic field at such a large radius that they have a small chance of striking the target. Second, the ions must enter the overlap region near the target within an angular constraint that will allow them to hit the target while travelling on a ballistic path.

These two mechanisms were studied by following the trajectories of a random selection of ions in initial angle and radial position as they propagate down the channel using the ION computer code.⁽¹⁵⁾ The magnetic field is assumed to be only in the azimuthal direction and rises linearly from zero on the channel axis to 27 kG at 0.5 cm and falls as $1/r$ beyond 0.5 cm in the main part of the channel. Within the overlap region, the azimuthal fields fall linearly to zero over an axial distance of 1 cm from the entrance to the region. The ions enter the channels with radial positions distributed in a Gaussian with a half-width of 0.35 cm and with angles of incidence distributed uniformly out to 0.12 radians. In LIBRA there are 18 channels with 9 in each of 2 cones. The channels are 0.5 cm in radius and the target is 0.5 cm in radius, so the distance between the point where the channels begin to overlap and the target surface is 0.43 cm. Calculations predict that about 80% of the ions reach the target.

Each of the plasma channels in LIBRA must carry several hundred kiloamperes of beam ion current, which can perturb the channels and possibly inhibit the transport of the beam ions. The limits on the ion beam power imposed by the onset of electrostatic instabilities, filamentation of the ion beam and the plasma channel, and beam ion energy loss have been analyzed. The expansion of the channels due to the ion beam has also been analyzed, and does not pose an important

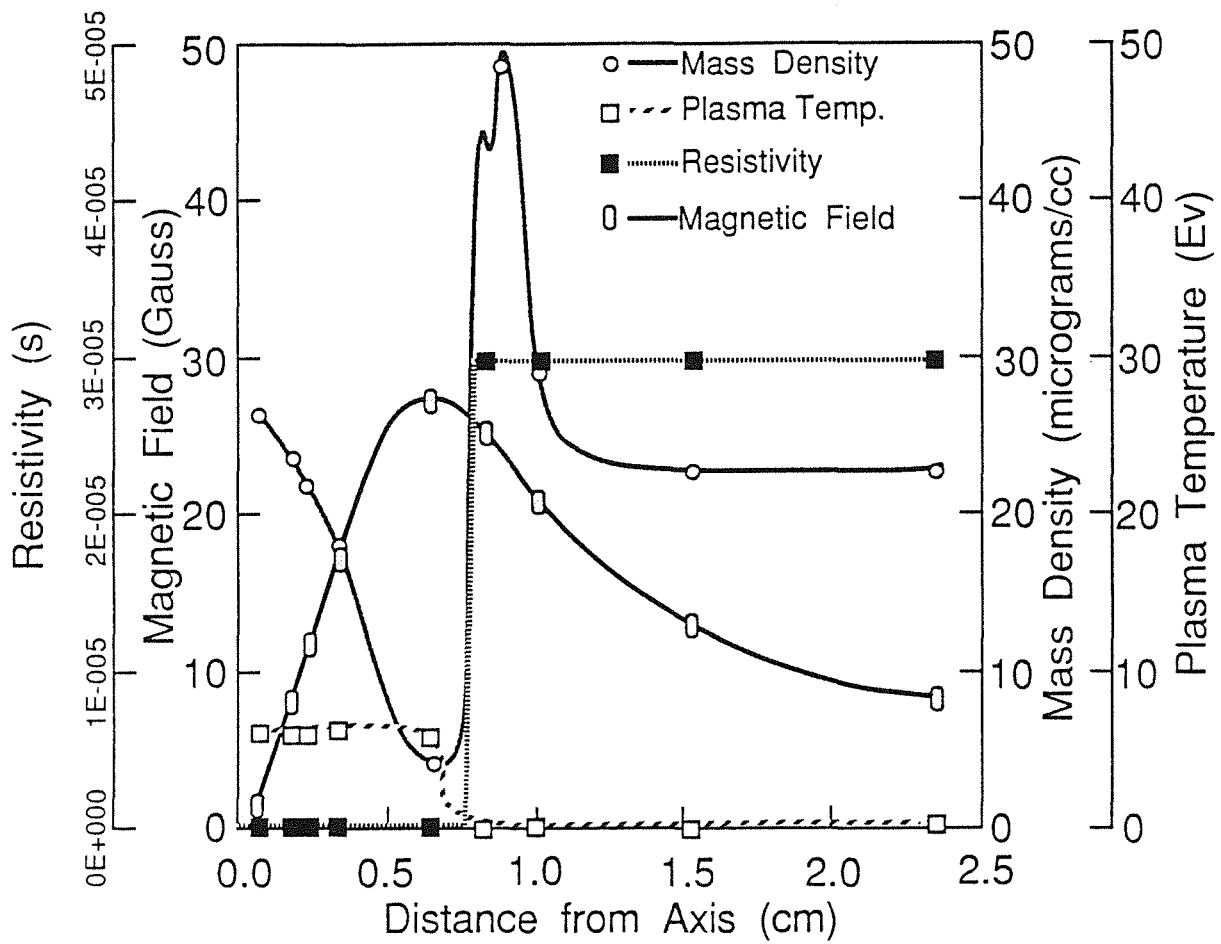


Fig. 1.7. Plasma channel conditions for ion transport.

constraint. The analysis has followed the formalism developed a number of years ago at the Naval Research Laboratory⁽¹⁶⁾ and involves the use of the WINDOW computer code.⁽¹⁷⁾

The results are shown for LIBRA parameters in Fig. 1.8. One sees that the input ion beam power per channel is limited to 9 TW at a diode R/F (Radius of Diode/Focal Length) of 0.12, the LIBRA value.

1.6 Channel Insulation

The long channels in LIBRA (or any light ion beam reactor) have a large inductance. Thus, the microsecond rise-time of the current necessary for channel formation requires very large discharge voltages. The potential drop between the channel and the target chamber structure (assumed to be at ground) is 500 kV for LIBRA. To prevent breakdown between the channel and the chamber wall would require a prohibitively large gap. Thus the channel is surrounded by solenoids between the diode structure and the inside row of INPORT units. An axial magnetic field of 32 kG is expected to slow the flow of electrons in the breakdown to a time scale greater than the 1 μ s channel formation time.⁽¹⁸⁾ This allows the diameter of the penetrations for the channels and beams to be 20 cm.

1.7 Cavity Analysis

The response of the He gas and liquid LiPb coating on the INPORT tubes to a LIBRA target explosion was studied using a 1-D radiation-hydrodynamics code, CONRAD.⁽¹⁹⁾ CONRAD calculates the target x-ray and debris ion energy deposition in a background gas and surrounding first surface material using time-dependent point source models. Conservation of mass, momentum, and energy equations are solved in Lagrangian form in a spherical coordinate system. Because CONRAD is a one-dimensional code and the INPORT tubes basically pose a cylindrical boundary, the LiPb first surface is modeled by a thin spherical region at a radius of 3 meters; i.e., the minimum distance from the target to the INPORT tubes.

Target energy absorbed by the background gas is transported throughout the cavity by fluid motion, radiation, and electron thermal conduction. We use a multigroup flux-limited diffusion model to transport radiation. Equations of state and frequency-dependent radiative properties of the chamber gases are tabulated prior to the simulation using a collisional-radiative equilibrium computer code -- IONMIX.⁽²⁰⁾ IONMIX calculates steady-state ionization populations by balancing collisional ionization rates with the sum of collisional, radiative, and dielectronic recombination rates. The extinction coefficients and emissivities include contributions from bound-bound, bound-free, and free-free transitions, as well as electron scattering.

In addition, CONRAD simulates the vaporization, hydrodynamic motion, and recondensation of the LiPb. Ablation due to the target x-rays is calculated using a volumetric energy deposition

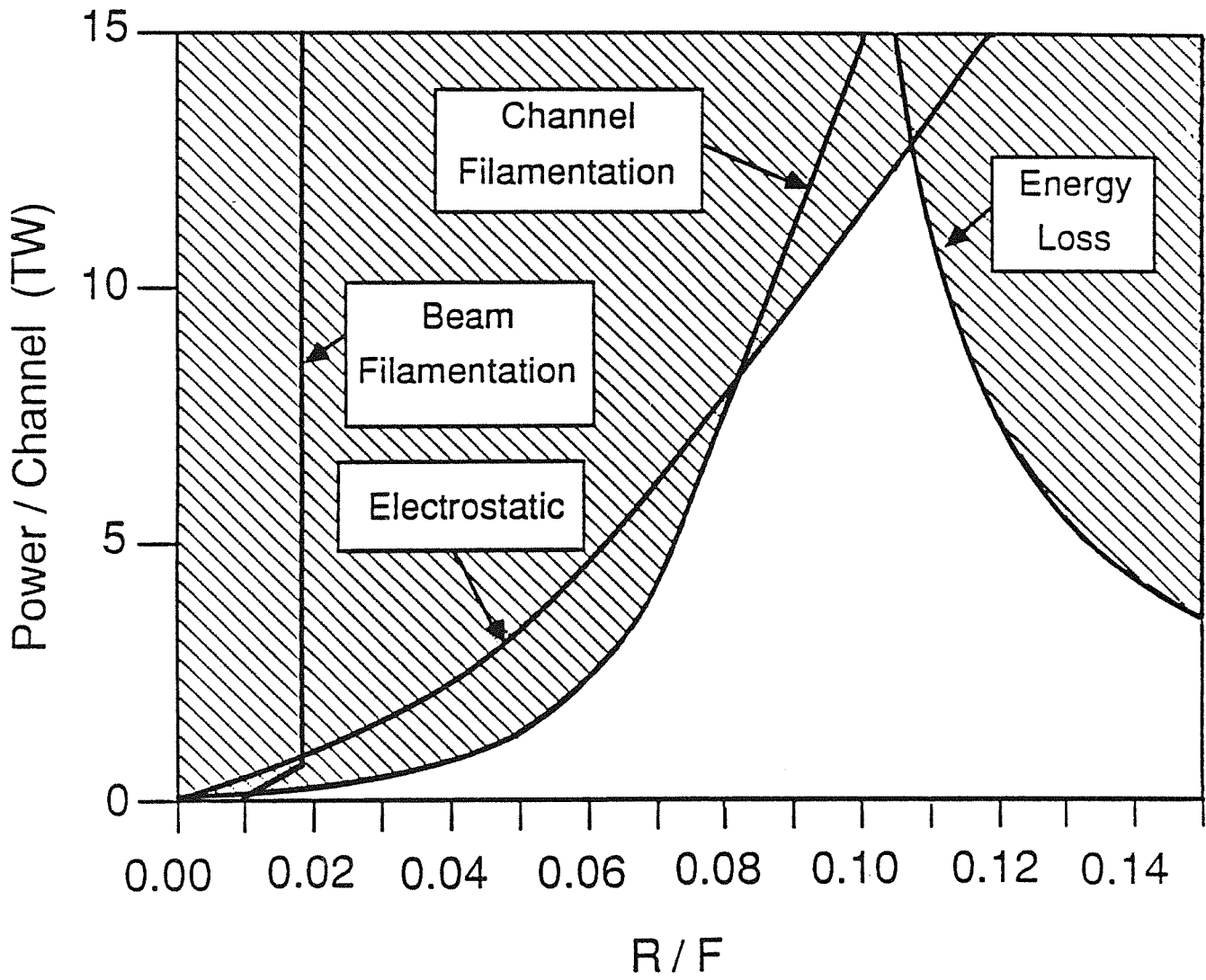


Fig. 1.8. Propagation "window" for LIBRA ion beams.

model. Energy, reradiated by the cavity gas and the debris ions kinetic energy is assumed to be deposited at the vapor/first surface interface because of their relatively short mean free paths. Heat transfer through the first surface material is computed by solving a 1-D thermal conduction equation. A detailed description of the CONRAD vaporization/condensation model is presented elsewhere.⁽²¹⁾

A schematic representation of the physical processes occurring in the LIBRA target chamber is shown in Fig. 1.9. After the target explodes, x-ray and debris ion energy is absorbed by the background gas, creating a high-temperature (~several eV) microfireball at the center of the chamber. The resulting high pressures cause the gas to expand rapidly outward and form a strong shock front ahead of the microfireball. Some of the target x-rays penetrate through the He gas and deposit their energy in a thin layer (~ several microns) of LiPb at the INPORT tubes. Some LiPb is immediately vaporized and, due to the high pressures in the vapor, is hydrodynamically accelerated toward the center of the chamber.

The LIBRA target performance and cavity parameters are listed in Table 1.1. The He gas absorbs approximately 20% of the target x-ray energy and all of the debris ion energy. The remaining 80% of the x-ray energy is absorbed in the LiPb, and immediately vaporizes about 6.7 kg. The LiPb mass vaporized from the INPORT tubes is shown in Fig. 1.10 as a function of time. The LiPb vaporization front moves away from the tubes and collides with the outward moving shock front at about 0.1 ms. The high pressures in the LiPb vapor produce a recoil impulse of 125 Pa-s on the tubes. The shock originating from the high-temperature microfireball contributes little to the total impulse on the tubes because it is overwhelmed by the inward moving vaporization front.

Between 10^{-6} and 10^{-4} seconds, an additional 1.3 kg of LiPb is vaporized as energy radiated by the He gas and LiPb vapor is absorbed at the tubes. Figure 1.11 shows the radiative flux (solid curve) and radiative energy deposited (dashed curve) at the INPORT tubes as a function of time. The vapor/liquid interface absorbs roughly 4 MJ (i.e., 4 J/cm^2) by 100 μs . When the radiative energy flux into the liquid exceeds the conductive energy flux through the liquid, the temperature at the surface rises. This produces an increase in the equilibrium (saturation) vapor pressure, and hence the vaporization flux.

At times ≥ 1 ms, the LiPb recondenses back onto the tubes or side-walls. By 10 ms, only 0.8 kg of LiPb remains in the vapor phase, corresponding to a LiPb/He number ratio of 0.007. According to these calculations, the LiPb condensation time would not be expected to limit the shot rate. However, the effects of the noncondensable He gas on the condensation rate have not been considered in our calculations. Preliminary calculations⁽²¹⁾ indicate that the He may dramatically slow the LiPb condensation rates. Because of the uncertainties associated with the

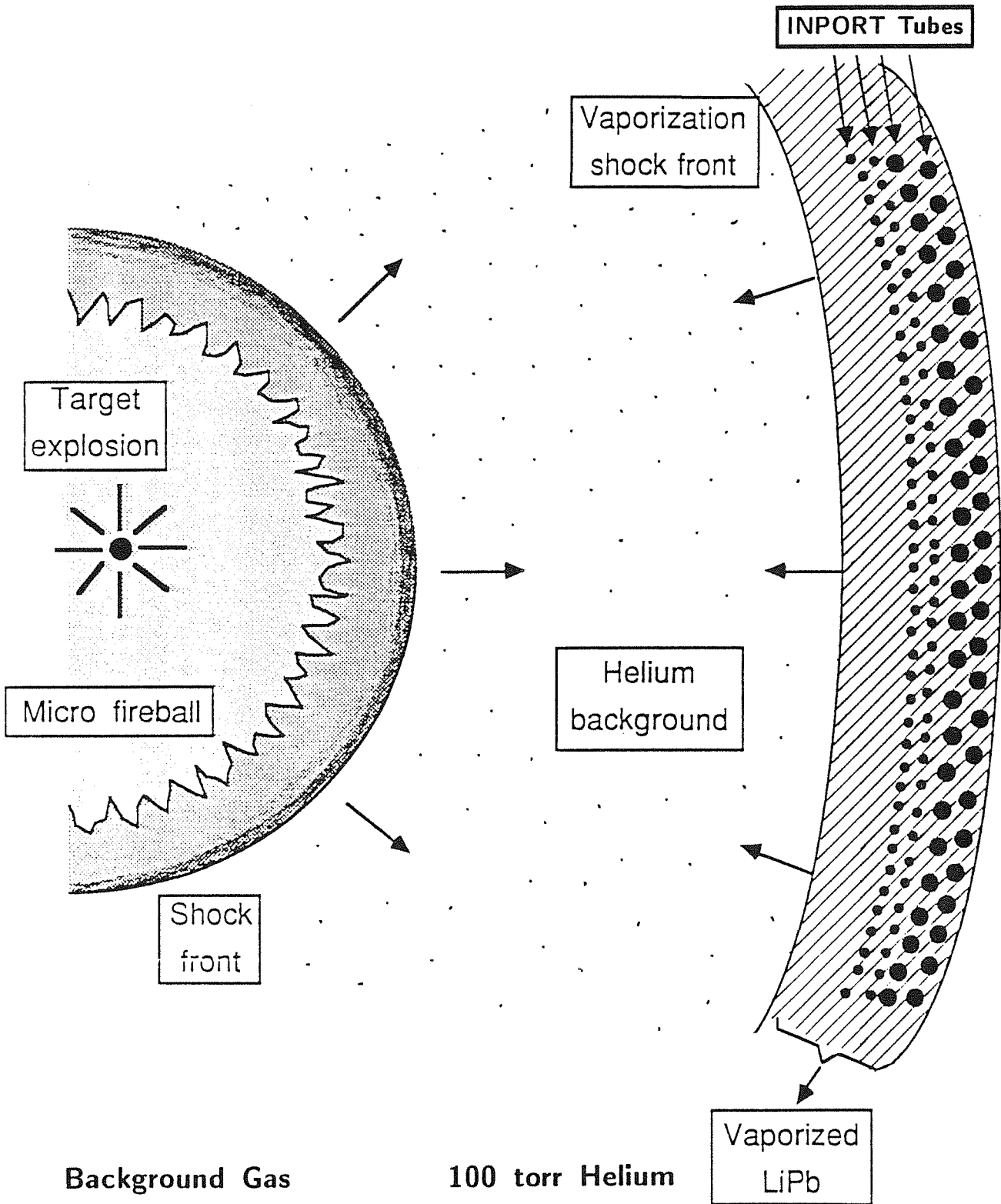


Fig. 1.9. Schematic of physical processes in target chamber following microexplosion.

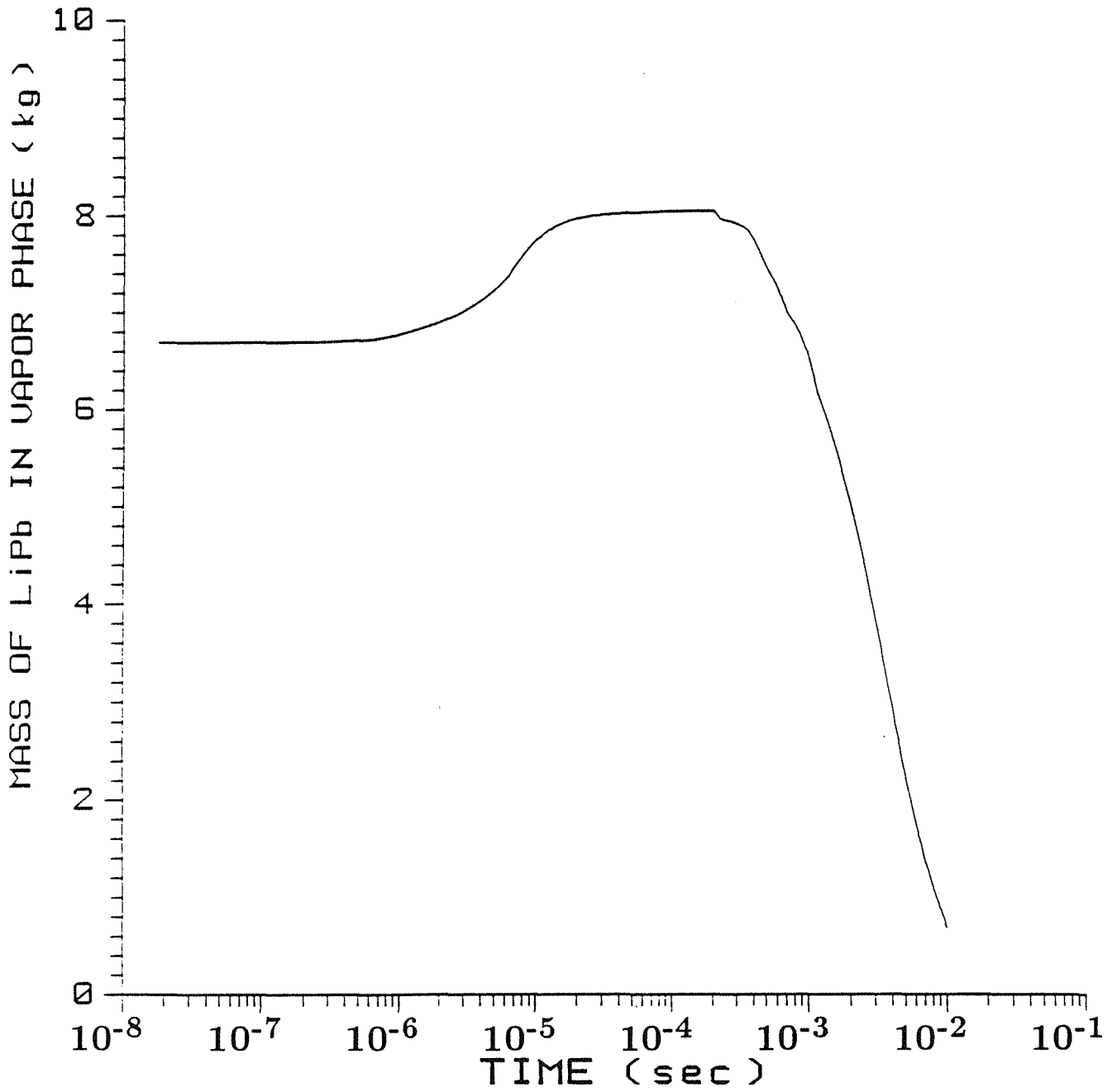


Fig. 1.10. Lithium-lead mass vaporized vs. time.

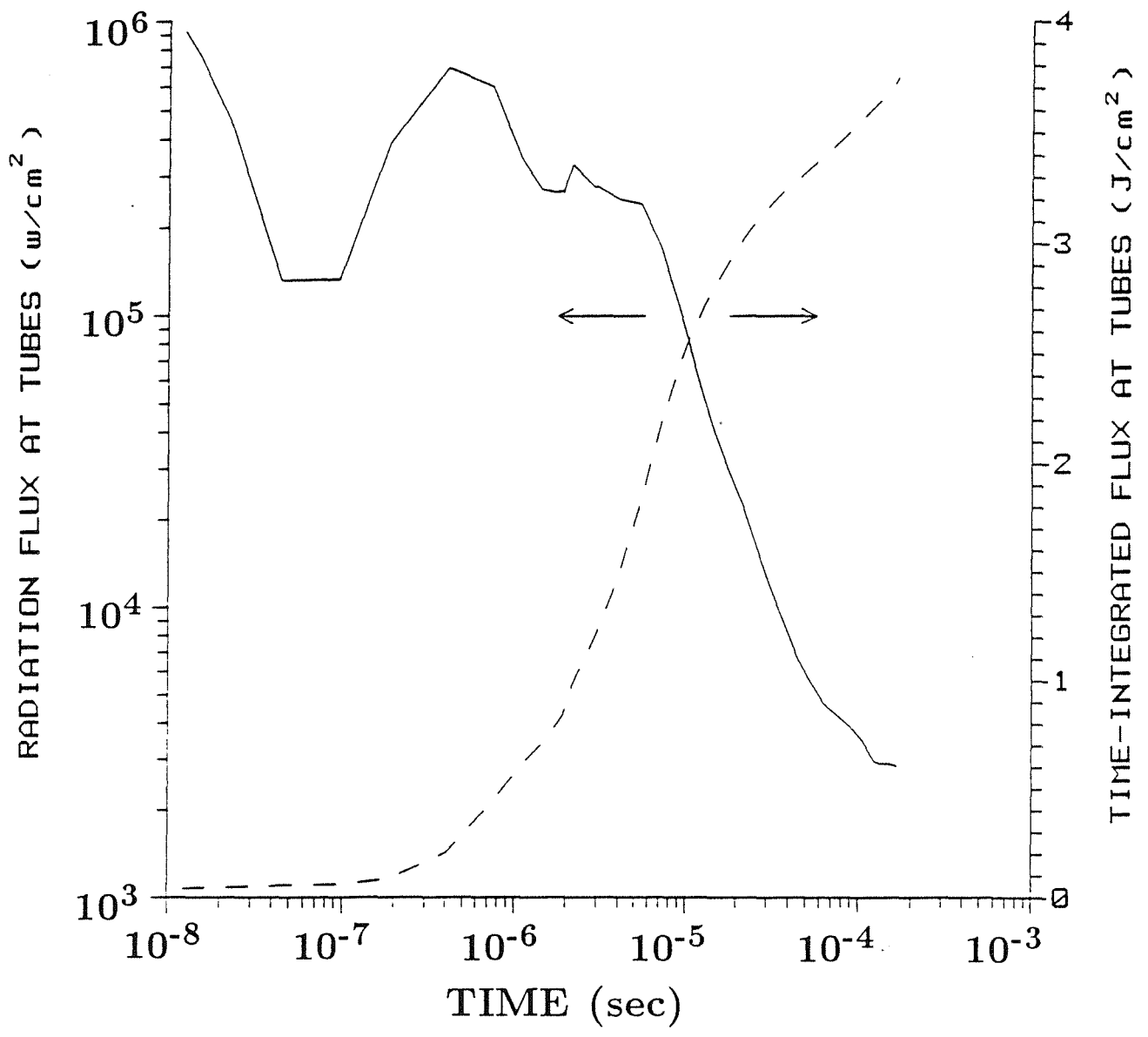


Fig. 1.11. Radiative flux and deposited energy vs. time.

condensation times, a pumping system has been devised to evacuate the post shot gases from the target chamber.(6)

1.8 INPORT Response

The impulse given to the INPORT tubes is approximately 125 Pa-s/shot. This is almost entirely due to the vaporization-induced recoil impulse. The shock ahead of the microfireball contributes little because it is overwhelmed by the vaporization front. The repetitive impulsive loading will produce dynamic motion of the first row of INPORTs. The determination of this mechanical response is necessary for radial placement of the tubes as well as identifying potential interference problems from circumferential movement. A comprehensive numerical simulation program has been developed which includes effects such as axial preload, tension gradient, flow velocity, length, diameter, dissipation, rep-rate and nonlinear displacement effects which are essential for modelling three dimensional motion. For all cases, the sequential impulses are applied radially, i.e., planar for each INPORT. It has been found that persistent radial and circumferential (orbital) motion is possible for some designs. However, for particular choices of physical parameters (e.g., flow velocity and pretension) the steady-state motion will be strictly planar, the preferred response. Figure 1.12 shows such results. The planar impulses of 125 Pa-s at 3 Hz produce radial displacements with a maximum startup value of 6 cm and a steady-state peak of 4 cm. The circumferential displacement has an initial perturbation which quickly dissipates. The INPORT length, diameter, and wall thickness are 6.4 m, 3 cm and 2 mm, respectively, and with a mean tension of 3000 N, the wall stresses are well below current strength levels of silicon carbide fiber.

1.9 Target Chamber Design

The target chamber is a vertical cylinder with a slanting roof. The roof and sides of the chamber are covered with SiC fabric passages through which LiPb coolant/breeder flows collecting in a pool at the bottom of the chamber. Coolant seeping through the porous SiC fabric on the roof and the sides, and the bottom pool provide liquid protection against the surface heat emanating from the target. The deep penetrating neutrons deposit their energy within the bulk of the blanket and reflector components of the chamber.

Figure 1.2 is a cross section of the LIBRA chamber. The INPORT units are at a radius of 3 m from the target and occupy a zone up to a radius of 4.35 m at a 33% volumetric fraction. The front two rows are 3 cm and the remaining 9 rows are 10 cm in diameter, respectively. They are followed by a 50 cm thick LiPb cooled steel reflector which is the primary structural component of the chamber. It is followed by a 2.5 m thick concrete shield cooled by He gas.

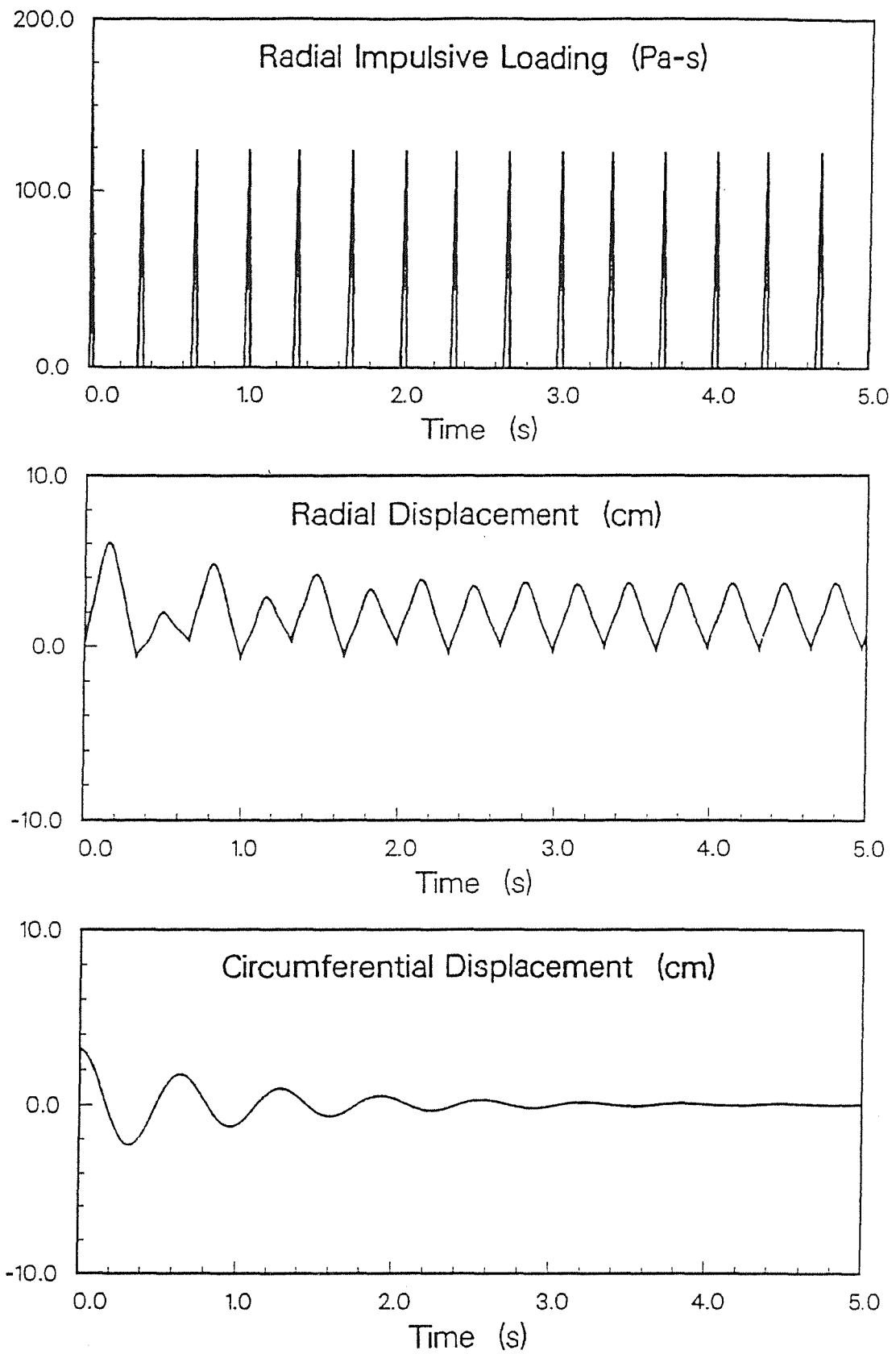


Fig. 1.12. INPORT unit response.

There are nine equally spaced beam tubes on the top and an equal number on the bottom penetrating between the INPORT units at a 35° angle to the horizontal. The beam tubes are made of TZM coils which provide magnetic insulation for the plasma channels by generating a 3.2 T field within the tubes. At the reflector midplane, there are nine equally spaced 0.75 m diameter exhaust ducts leading to a toroidal suppression tank attached to the outer perimeter of the chamber. The post shot plasma in the chamber expands into the suppression tank where vacuum pumps evacuate it to maintain the needed operating conditions.

The bottom pool drains through a perforated plate which also acts as a shock absorber. The LiPb then goes to three heat exchangers built into the base of the chamber and then exits to be recycled through again. Helium gas circulating through the tubes of the heat exchanger then carries the energy to a conventional steam power cycle.

The chamber roof is 7.7 m at its highest point above the pool and slants at 15°. It is designed to be taken apart for providing access to the inside of the chamber for maintenance purposes. The SiC fabric passages are attached to a 0.25 m thick LiPb cooled steel conical reflector which is welded to six equally spaced structural beams. This structure provides the support for the roof shield segments. At its center is a hub which holds the pellet injector. The last element in the roof is a flange which is the vacuum boundary for the chamber. When this flange is removed, the roof can be dismantled by removing the shield in six separate segments, then the reflector as a single unit. A 100 tonne crane is needed to accomplish this task.

1.10 Blanket Response

A one-dimensional (1-D) scoping analysis was performed to determine the blanket design options that satisfy the tritium breeding and wall protection requirements. A point source emitting neutrons and gamma photons with the spectra calculated for the LIBRA target was used at the center of the 3 m radius cavity. A minimum tritium breeding ratio (TBR) of 1.1 is required to achieve tritium self-sufficiency. The peak end-of-life atomic displacements (dpa) in HT-9 is required to not exceed 200 dpa implying that for 30 full power year (FPY) reactor life the peak dpa rate should not exceed 6.6 dpa/FPY. In addition, the blanket thickness needs to be minimized to minimize the length of the channels used for beam propagation.

Calculations were performed for different blanket thicknesses and ${}^6\text{Li}$ enrichments. The TBR and dpa rate values are mapped in Fig. 1.13. The design point should be in the box indicated in the upper left corner. In order to satisfy the other design goals of minimizing the blanket thickness and maximizing M, it is clear that the design point should be at the right or lower boundaries of the box. The intersection of the boundaries of the box with the curves that correspond to different enrichments gives the options that satisfy the design requirements. To minimize the length of the beam propagation channel, a 1.35 m thick blanket with 90% ${}^6\text{Li}$ enrichment is used in LIBRA,

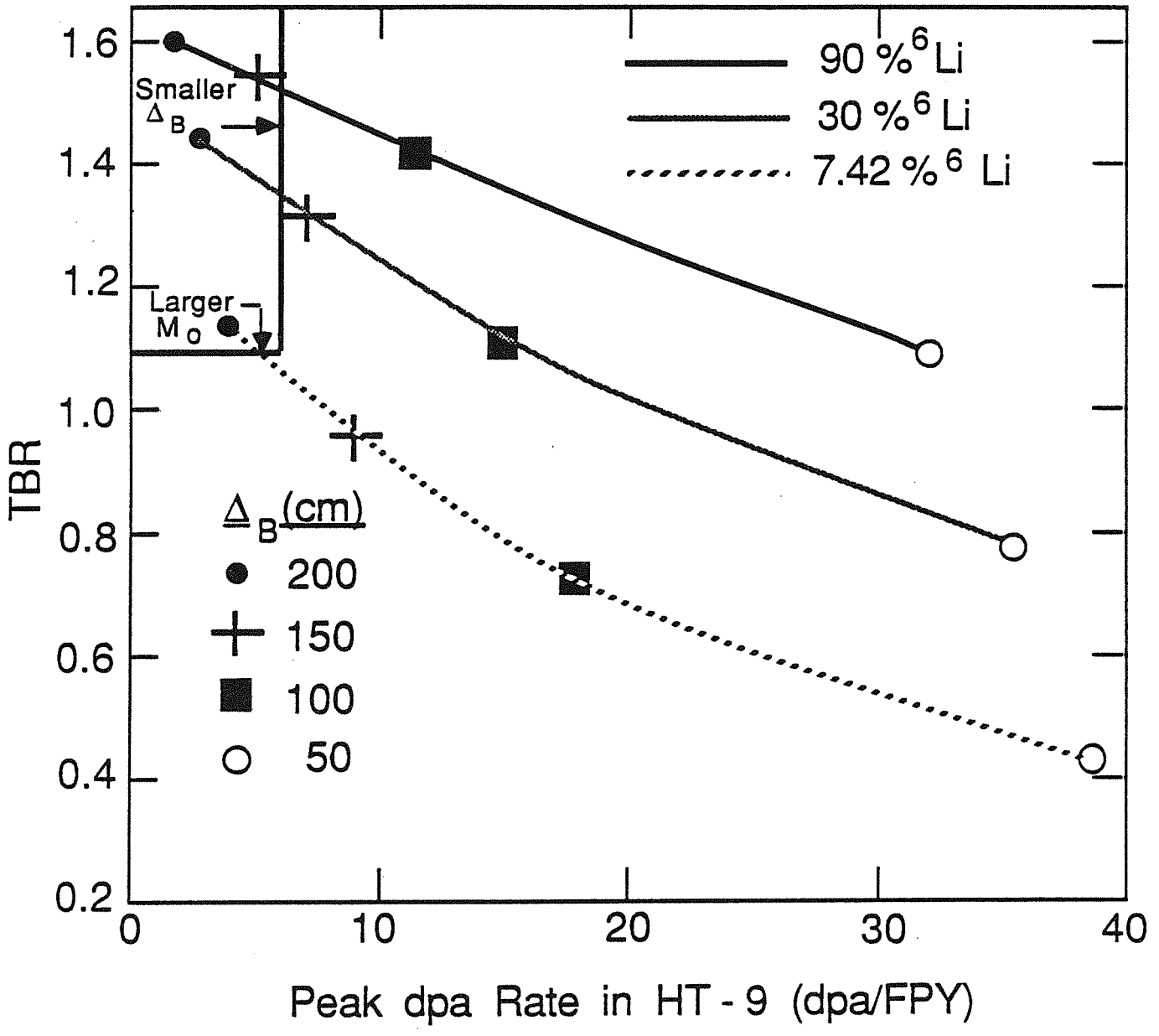


Fig. 1.13. Tritium breeding ratio and damage rate.

leading to local (1-D) TBR and M of 1.5 and 1.18, respectively. Since this results in a relatively large TBR in the chamber sides, a smaller local TBR is allowed in the reactor roof. A scoping analysis for the roof leads to a 10 cm thick $\text{Li}_{17}\text{Pb}_{83}$ protective layer followed by a 25 cm thick $\text{Li}_{17}\text{Pb}_{83}$ cooled HT-9 reflector. The local TBR in this zone is 0.8 and the peak dpa rate in HT-9 is 50 dpa/FPY implying that the roof structure needs to be replaced every 4 FPY. Since only ~ 14% of the source neutrons go to the roof, this design will yield an overall TBR that exceeds the minimum requirement by an adequate margin. In fact, detailed three-dimensional neutronics calculations have shown that the overall TBR is equal to 1.36.

1.11 Tritium Fueling, Breeding and Inventory

Hollow organic polymer shells are filled remotely in a pressure chamber with molecular DT and are subsequently overcoated mechanically with Pb foil. Batches of targets are stored at 19.8 K for 2 hours while a uniform thickness of solid DT forms on the interior surface of the polymer shell.⁽²³⁾ The uniformity of the fuel coating is caused by the radioactive induced sublimation of the DT.⁽²³⁾ A one-day's supply of fuel targets is maintained.

In order to limit the loss of tritium to < 20 Ci/d at the steam generator, tritium removal is accomplished from both the liquid metal and the helium circuits. Tritium in the helium circuit is converted to the oxide and is adsorbed on a desiccant.

The liquid breeder alloy within the reactor cavity contains the tritium formed during breeding plus the unburned DT from each target explosion. The tritium concentration in this liquid alloy is controlled by the diversion of 6.3 m³/s of the alloy to a Tritium Removal System (TRS).⁽²⁴⁾ By this technique the average tritium partial pressure in the alloy is maintained at 1.3×10^{-2} Pa and a concentration of 1.4×10^{-4} wt.ppm.

Tritium solubility in the SiC fibers of the INPORT tubes is estimated to yield an inventory of 150 g of tritium.

1.12 LIBRA Economics

A costing analysis for the LIBRA reactor was performed using the FUSCOST code⁽²⁵⁾ with input from both MFE and other ICF costing sources.⁽²⁶⁻²⁹⁾ The main costing algorithms come from the SAFIRE code⁽²⁹⁾ except the driver costs which resulted from a detailed Pulse Sciences Incorporated (PSI) analysis based on HERMES-III technology. Target costs were based on a 20 Hz production facility that would supply several plants. Base target costs started at 18¢/target. All cost numbers are quoted in 1988\$ but can be easily escalated to present values at ~ 5% per year.

The total direct costs are shown in Fig. 1.14 where it is obvious that the driver costs dominate (roughly 50% of the total cost). This results in a specific direct capital cost of 2843 \$/kWe.

The total overnight costs (Table 1.2), including direct and indirect capital costs, amounts to 1270 \$M (1988\$). When the cost of money is included, the total capital costs (in constant 1988\$) is 1654 \$M.

Table 1.2. Summary of Cost Parameters for LIBRA (331 MWe)

	(1988\$)	
	<u>\$M</u>	<u>\$/kWe</u>
Total Direct Capital Cost	941	2843
Total Indirect Capital Cost	329	-
Total Overnight Costs	1270	3837
Time Related Costs	384	-
Total Capital Cost	1654	4997
	<u>\$M/y</u>	<u>mills/kWh</u>
Annualized Fuel Costs	13	-
Annualized O&M Costs	39	-
Annualized Cost of Capital	141	-
Total Annualized Costs	193	-
Total Cost of Electricity	-	88.7

A more meaningful number is the levelized cost of electricity (COE) in mills/kWh. The COE is made up of three main components:

- Cost of capital
- O&M costs
- Fuel costs.

The levelized annual operating costs amount to 193 \$M/year in constant 1988\$. This number is largely dependent on the cost of capital (74%) with a smaller dependence on O&M costs (20%) and only 6% comes from the fuel costs at 18¢/target. Doubling the target cost has less than a 10% impact on the COE. The total levelized COE is 88.7 mills/kWh for a 331 MWe plant.

The question of how to compare LIBRA to previous large (1000-4000 MWe) MCF or ICF reactors was addressed by scaling the 331 MWe costs to approximately 1200 MWe. This was accomplished by increasing the driver energy from 4 to 6 MJ, allowing an increase in gain from 80 to 100, and an increase in the rep rate from 3 to 6 Hz. This larger LIBRA reactor benefited

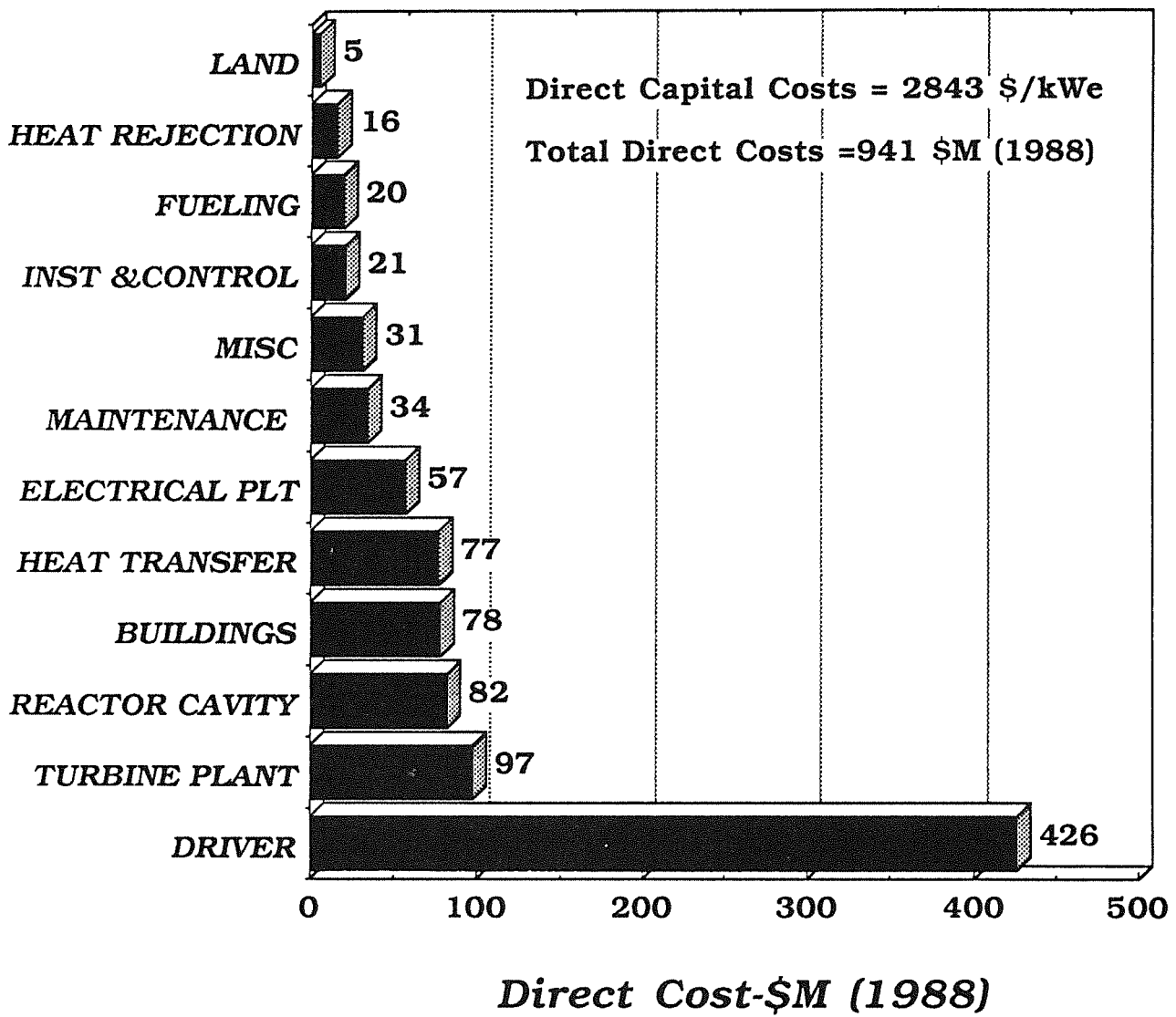


Figure 1.14. Direct capital costs of LIBRA.

from the economy of scale and the total cost per kWe dropped almost 50% (Fig. 1.15). A comparison of the 331 and 1200 MWe LIBRA designs to recent tokamak and heavy ion beam reactor studies is shown in Fig. 1.16. Clearly, when LIBRA is compared to other reactor designs at the 1000 MWe level and above, it is quite competitive. More importantly, LIBRA is also competitive at the lower size level which reduces the capital investment required by utilities. Such an advantage makes light ion beams very attractive from the investor standpoint.

1.13 Conclusions

The LIBRA conceptual design indicates that light ion beam driven fusion is an excellent candidate for small, economical power plants of ~ 500 MW electrical. Technical uncertainties associated with diode design and ion transport to the target remain the major issues associated with light ion fusion. Additional uncertainties exist regarding target performance and manufacturing which are generic ICF issues. It is concluded that the light ion beam method of producing commercial fusion power can be competitive with the more established laser driver approach and with the more traditional heavy ion driver approach.

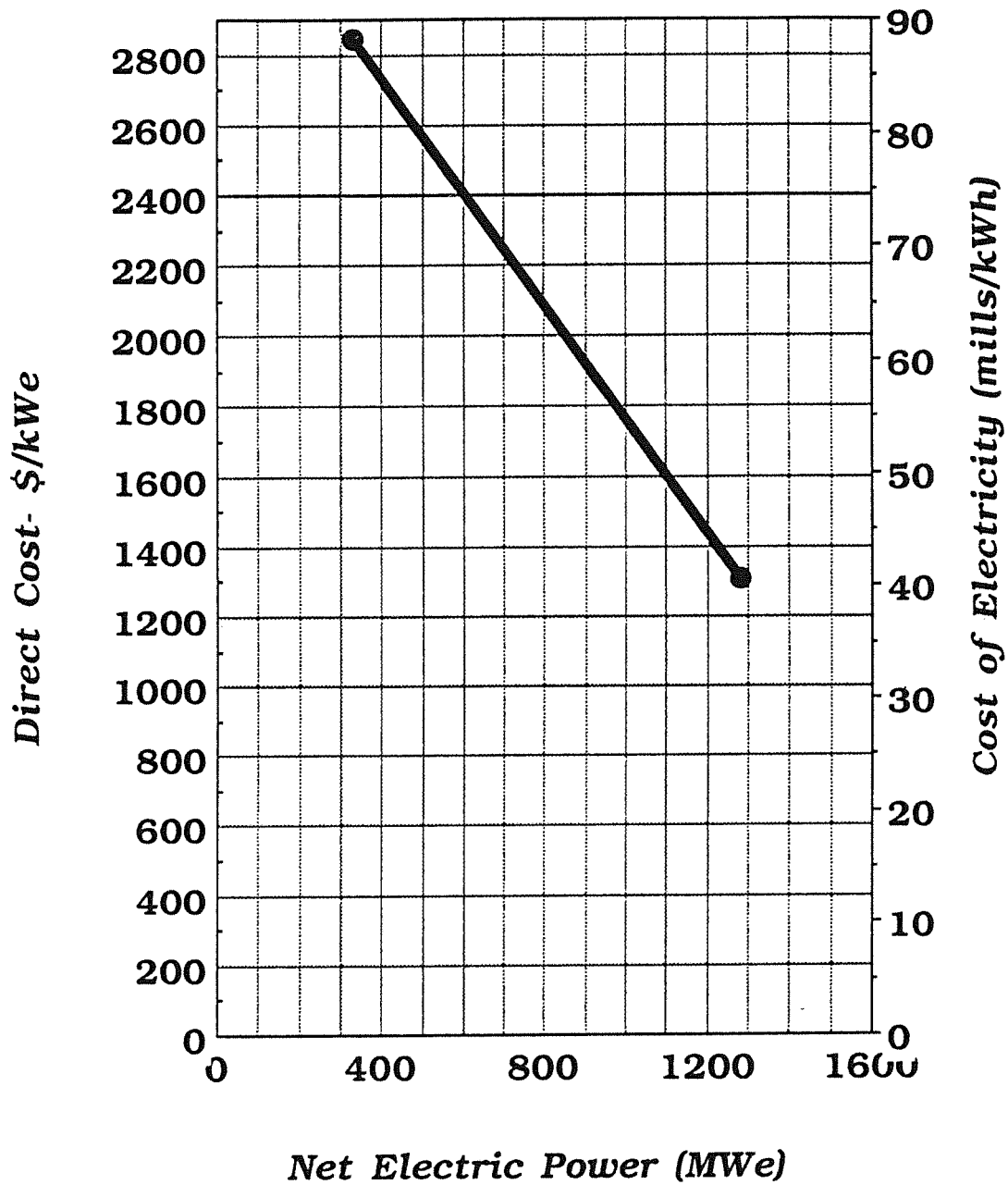


Figure 1.15. Comparison of direct capital costs for LIBRA as the power level is increased.

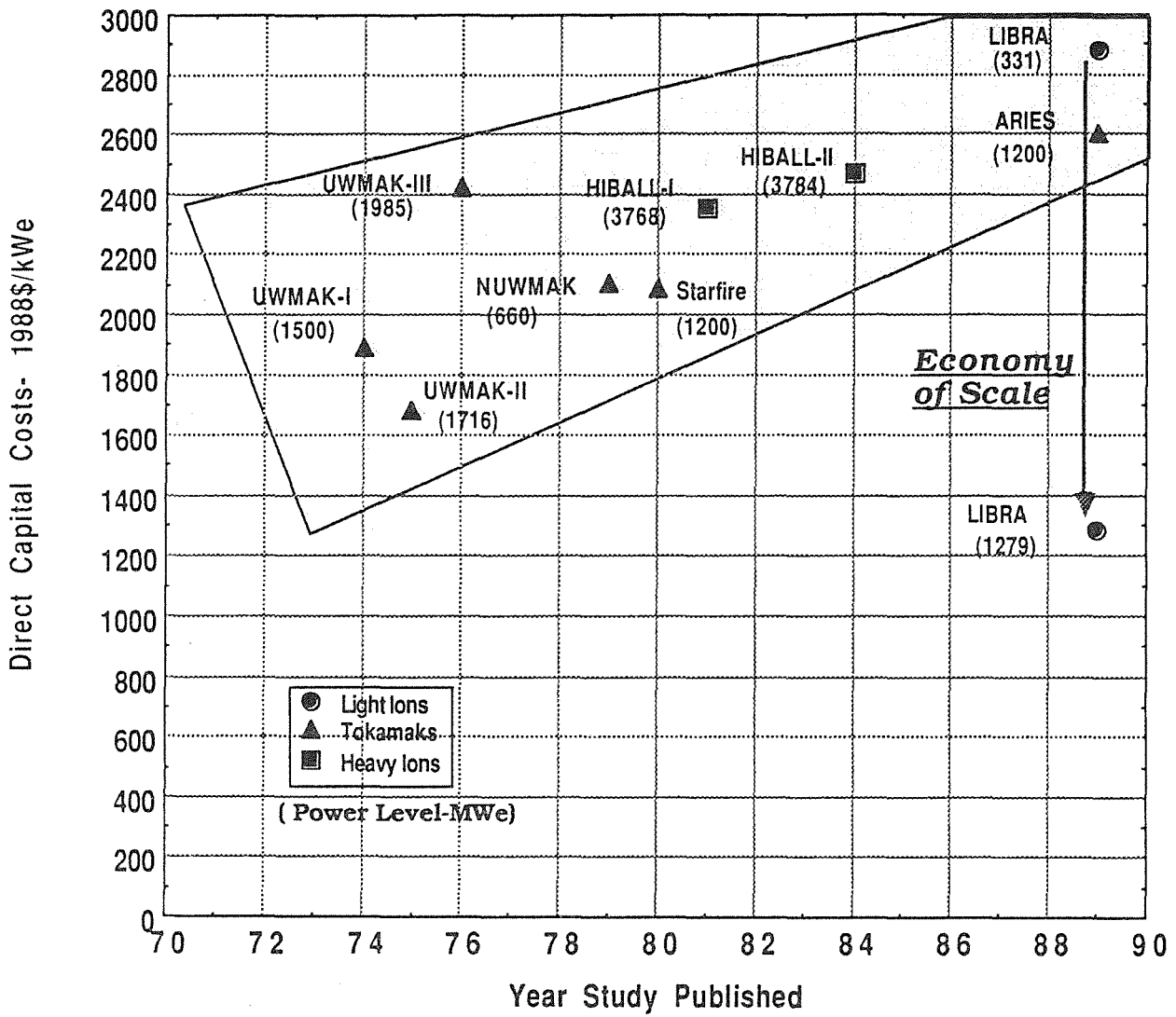


Figure 1.16. Comparison of LIBRA to other tokamak and heavy ion beam fusion designs.

References for Chapter 1

1. G.A. Moses, et al., "LIBRA - A Light Ion Beam Fusion Reactor Conceptual Design", BEAMS '88, Proceedings of the 7th International Conference on High-Power Particle Beams, Volume 1, Karlsruhe, Fed.Rep.Germany, July 4-8, 1988, pp. 113-126 and Laser and Particle Beams (1989), Vol.7, Part 4, pp.721-731.
2. "Preliminary Design of Light Ion Beam Fusion Reactors, UTLIF (1) & ADLIB-1," University of Tokyo Nuclear Engineering Research Laboratory UTNL-R-0135 (1982).
3. K. Niu and S. Kawata, "Proposal of Power Plant by Light Ion Beam Fusion," Fusion Technology, 11, 365 (1987).
4. "Light Ion System Analysis and Design-Phase I: Engineering Test Reactor Goal Specification," Research Project 1527, Electric Power Research Institute (April 1982), no author.
5. G.A. Moses, et al., "Overview of the LIBRA Light Ion Beam Fusion Conceptual Design," Fusion Technology 15(2), 756 (March 1989).
6. M. Sawan, I. Sviatoslavsky, L. Wittenberg, E. Lovell, and R. Engelstad, "Chamber Design for the LIBRA Light Ion Beam Fusion Reactor," Fusion Technology 15(2), 766 (March 1989).
7. G.L. Kulcinski, "Advances in Commercial ICF Technology Since 1986," Fusion Technology 15(2), 749 (March 1989).
8. D. Böhne, et al., "HIBALL - A Conceptual Design Study of a Heavy-Ion Driven Inertial Confinement Fusion Power Plant," Nucl. Engr. and Design, 73, 195 (1982).
9. N.A. Tahir and K.A. Long, "A Study of Ignition and Burn Propagation in Reactor-Size Inertial Fusion Targets Using a Three-Temperature Plasma Simulation Model," Phys. Fluids, 30, 1820 (1987).
10. R.O. Bangerter, "Targets for Heavy Ion Fusion," Fusion Tech., 13, 348 (1988).
11. I. Smith, P. Corcoran, H. Nishimoto, and D. Wake, "Conceptual Design of a 30 MV Driver for LIBRA", BEAMS '88, Proceedings of the 7th International Conference on High-Power Particle Beams, Volume 1, Karlsruhe, Fed.Rep.Germany, July 4-8, 1988, pp.127-136.
12. J.R. Freeman, L. Baker, and D.L. Cook, "Plasma Channels for Intense-Light-Ion-Beam Reactors," Nucl. Fusion, 22, 383 (1982).
13. J.J. Watrous, G.A. Moses, and R.R. Peterson, "Z-PINCH -- A Multifrequency Radiative Transfer Magnetohydrodynamics Computer Code," University of Wisconsin Fusion Technology Institute Report UWFD-584 (June 1984).
14. P.F. Ottinger, D. Mosher, S.A. Goldstein, "Propagation of Intense Ion Beams in Straight and Taper Z-Discharge Plasma Channels," Phys. Fluids, 23, 909 (1980).
15. G.A. Moses, "ION -- A Code to Compute Ion Trajectories in Z-Pinch Plasma Channels," University of Wisconsin Fusion Technology Institute Report UWFD-712 (January 1986).
16. P.F. Ottinger, S.A. Goldstein, and D. Mosher, "Constraints on Transportable Ion Beam Power," Naval Research Laboratory Memorandum Report 4948 (November 1982).

17. R.R. Peterson, "WINDOW -- A Code to Compute Ion Beam Power Constraints," Fusion Power Associates Report FPA-84-6 (December 1984).
18. A.E.D. Heylen, "Electrical Ionization and Breakdown of Gases in a Crossed Magnetic Field," IEEE Proc., Vol. 127, Pt. A., No. 4, May 1980.
19. R.R. Peterson, J.J. MacFarlane, and G.A. Moses, "CONRAD -- A Combined Hydrodynamics-Condensation/Vaporization Computer Code," UWFDM-670, University of Wisconsin Fusion Technology Institute Report (1988).
20. J.J. MacFarlane, "IONMIX -- A Code for Computing the Equation of State and Radiative Properties of LTE and Non-LTE Plasmas," University of Wisconsin Fusion Technology Institute Report UWFDM-750, (1987), submitted to Comput. Phys. Commun.
21. J.J. MacFarlane, R.R. Peterson, and G.A. Moses, "Analysis of Physical Processes in ICF Target Chambers: Application to the Laboratory Microfusion Facility," Fusion Technology 15(2), 557 (March 1989).
22. M. El-Afify and M. Corradini, "Transient Condensation of Vapor Using a Direct Simulation Monte Carlo Method," Fusion Technology 15(2), 783 (March 1989).
23. J.K. Hoffer and L.R. Foreman, "Radioactively Induced Sublimation in Solid Tritium," Phys. Rev. Letters, 60, 1310 (1988).
24. K.E. Plute, E.M. Larsen and L.J. Wittenberg, "Tritium Recovery from Liquid Lithium-Lead by Vacuum Degassing," Nuclear Tech./Fusion 4, 407 (1983).
25. Zoran Musicki, "FUSCOST: A PC-Based Menu Driven Program for Economic Analysis of Fusion Facilities," 12th Symposium on Fusion Engineering, Monterey, CA, Oct. 1987, University of Wisconsin Fusion Technology Institute Report UWFDM-743.
26. Scott Thompson, "Reference Cost Data for Fusion Studies," Fusion Engineering Design Center, Sept. 1986.
27. Z. Musicki, "The Economic Analysis of SIRIUS-M, A Symmetrically Illuminated, ICF Engineering Test Reactor," University of Wisconsin Fusion Technology Institute Report UWFDM-708, Sept. 1986.
28. Z. Musicki, "Continuation of Economic Analysis of SIRIUS-M," University of Wisconsin Fusion Technology Institute Report UWFDM-746, Sept. 1987.
29. T.J. McCarville, W.R. Meier, C.F. Carson, B.B. Glasgow, "SAFIRE - A Systems Analysis Code for ICF Reactor Economics," LLNL UCRL-15872, Vol. 1, January 12, 1987.
30. E.K. Cleveland et al., "Preliminary Scoping Study for the Target Development Facility," Los Alamos Technical Associates Inc. Report SAND 83-7005.
31. J.H. Pendergrass, et al., "Heavy-Ion Fusion Target Cost Model", Fusion Technology, Vol.13, No.2, February 1988, pp. 375-395.

2. PULSED POWER DRIVER

2.1 Introduction

The objective of this work is to generate a conceptual design for a 30 MV lithium ion driver for the light ion beam fusion reactor concept known as LIBRA.

The present effort follows earlier studies made by PSI of drivers for different particle species and energies. After an early examination of design options,⁽¹⁾ these studies assumed the use of the Helia design approach, first formulated by PSI⁽²⁾ in which induction cells driven at about 1 MV by water dielectric pulselines are assembled in series to drive the full voltage ion diode via a magnetically insulated vacuum voltage adder (MIVA). The most detailed of the previous work was on a 20 MV deuterium driver. Initially,⁽³⁾ a design was developed for the induction cells, MIVA, and pulselines. Subsequently, calculations addressed the performance of the MIVA⁽⁴⁾ and the bunching of the ions.⁽⁵⁾

In the present 30 MV driver study, the design of the pulse lines, cells, and MIVA, the performance of all circuits including the MIVA and the bunching of the ions were addressed. This culminated in calculated power and energy waveforms at the pellet that more than satisfied specifications. In a subsequent task, the design of the charging system from wall plug to pulse lines was developed, and a cost estimate was made for the whole driver.

At the outset of the LIBRA studies, the Helia approach had not been tested. An initial four-stage, 4 MV proof-of-principle test was completed in 1985 by PSI and Sandia National Laboratory (SNL) under DNA and DOE funding.⁽⁶⁾ During the course of the 30 MV driver study, the 20 MV, 750 kA Hermes-III electron accelerator has been successfully operated at full power at SNL.⁽⁷⁾ Hermes-III has also been successfully tested for a short period at ≥ 22 MV in the positive polarity required to accelerate ions. The scalability of the driver to 30 MV now seems fairly well assured, at least up to the diode; some questions remain about the efficiency of the positive polarity voltage adder, but there are a number of promising ways to design this successfully.

No accelerator of the Helia type has yet operated repetitively. However, the technology of repetitive magnetic (i.e. saturable reactor) pulse compressors developed at Lawrence Livermore National Laboratory⁽⁸⁾ has achieved > 1 kHz operation, and by incorporating magnetic switches into the pulse lines of machines like Helia and Hermes-III it seems probable that reliable long life repetitive operation can be realized.

The design parameters of the 30 MV driver are discussed in Section 2.2. Sections 2.3 - 2.8 present the design of the pulselines, cells, and MIVA, and the calculations of performance up to the pellet. Section 2.9 discusses considerations of overall driver layout and presents the design of the charging system. Section 2.10 presents the final proposed driver layout with respect to the reactor, and includes a number of conceptual engineering layout drawings. Section 2.11 summarizes the cost estimate.

2.2. Driver Parameters and Design Sequence

For the 30 MV lithium ion driver, as with the 20 MV deuterium driver, the goal is 4 MJ delivered to the pellet. The beam transport distance is 6-7 meters. The pulse duration specification was revised from the 16.7 ns duration of the 20 MV driver to require 3.6 MJ delivered in 9 ns. The remaining 0.4 MJ are to be delivered in a longer pulse immediately preceding the 3.6 MJ, by a few smaller driver modules whose design was not considered in the present work.

The number of driver modules and the parameters of each module were chosen after a tradeoff of difficulties of driver design and beam transport with the University of Wisconsin and SNL. The driver tradeoffs, presented in Appendix 2.A, showed that the total driver volume and complexity increased with the number of modules. The driver chosen, represented by the left column of Table 2.A-2, has 16 modules for the 3.6 MJ pulse. Each module is made up of 26 cells, with a mean voltage of $30/26 = 1.15$ MV per cell. The current in each module is $1.15 \text{ MV}/3 \Omega = 385$ kA. The pulse duration required at the diode in order to deliver the necessary $3.6/16 = 0.225$ MJ at the pellet, or 450 kJ at the diode, is $450/30 \times 0.385 = 39.0$ ns. Because it is assumed that 9 ns of useful pulse duration is lost in the MIVA, the drive pulse from the water pulselines must be 48 ns long. In the previous 20 MV driver study, the duration of the pulse top at the diode that delivered ions to the pellet in the required time interval was 48 ns neglecting MIVA losses, and this was obtained from water pulselines designed to produce a nominal 60 ns pulse; finite risetime reduced the useful pulse top duration to 48 ns. Therefore the nominal pulseline duration was made 60 ns again in the 30 MV driver design.

The driver design proper began with the design of the cell. Using the approximate cell dimensions generated in the tradeoff study as a guide, the cell design was developed in enough detail to calculate circuit element values. These values were then used to design the pulselines (Section 2.4) and in pulseline and cell circuit calculations (Section 2.5) that resulted in a pulseline design that delivered to the vacuum bore a pulse with the

desired voltage, ramp shape, and pulse duration. The calculations and the physical design gave electrical stresses (Section 2.6) that were shown to be adequately low. Calculations were next made of the vacuum bore performance (Section 2.7) treating it both as a MIVA (unbiased) and as a non-emitting voltage adder (NEVA). In each case, a diode voltage waveform was calculated. The ion power pulse shape after transport was then determined for both the MIVA and the NEVA (Section 2.8). The voltage adder and transport calculations used programs developed in the previous study of the 20 MV driver.

The design of the charging system was performed after completion of the above design effort for the cells through transport to the pellet. It was found that the charging system design was much better suited to a number of cells per module divisible by four, and a 28 cell module was assumed for the charge system design. It was not possible to go back in detail and make the module design consistent, but the changes would not be major; the cell, pulseline voltage and pulseline impedance would be reduced by about 10%.

The charging system specifications are discussed in Section 2.8. The design study dealt with (1) a magnetic pulse compressor to link the previously designed pulselines to (2) a capacitor bank and switching system charged by (3) a dc power supply. The conceptual electrical design and mechanical design for the major elements were determined (Section 2.9).

An overall driver layout was then developed in a series of engineering layout drawings (Section 2.10). The design formed the basis for a cost estimate (Section 2.10).

2.3. Cell Design

A side view of the 1.15 MV cell is shown in Figure 2.1. The outside diameter is 2.8 meters, excluding flanges. At the outside are a set of 15 Ω azimuthal oil transmission lines that conduct the negative input pulse azimuthally in both directions from each of the diametrically opposite points where the water pulselines drive the cell. A cross-section of the azimuthal oil line, which has a 6 cm spacing, is shown at the bottom of Figure 2.1, and at the top is shown how the line feeds at four points, each 45° from a cell drive point, to the vacuum insulator rim. The rim is another azimuthal transmission line that conducts the pulse in both directions away from the rim feed point. The width of the rim conductor tapers with increasing distance from the rim feed point, so that the impedance of the rim line increases from 24 Ω (chosen so that the eight parallel sections of this line match the 3 Ω load) as current flows from the rim radially in to the vacuum region. The rim width becomes zero midway between feed points.

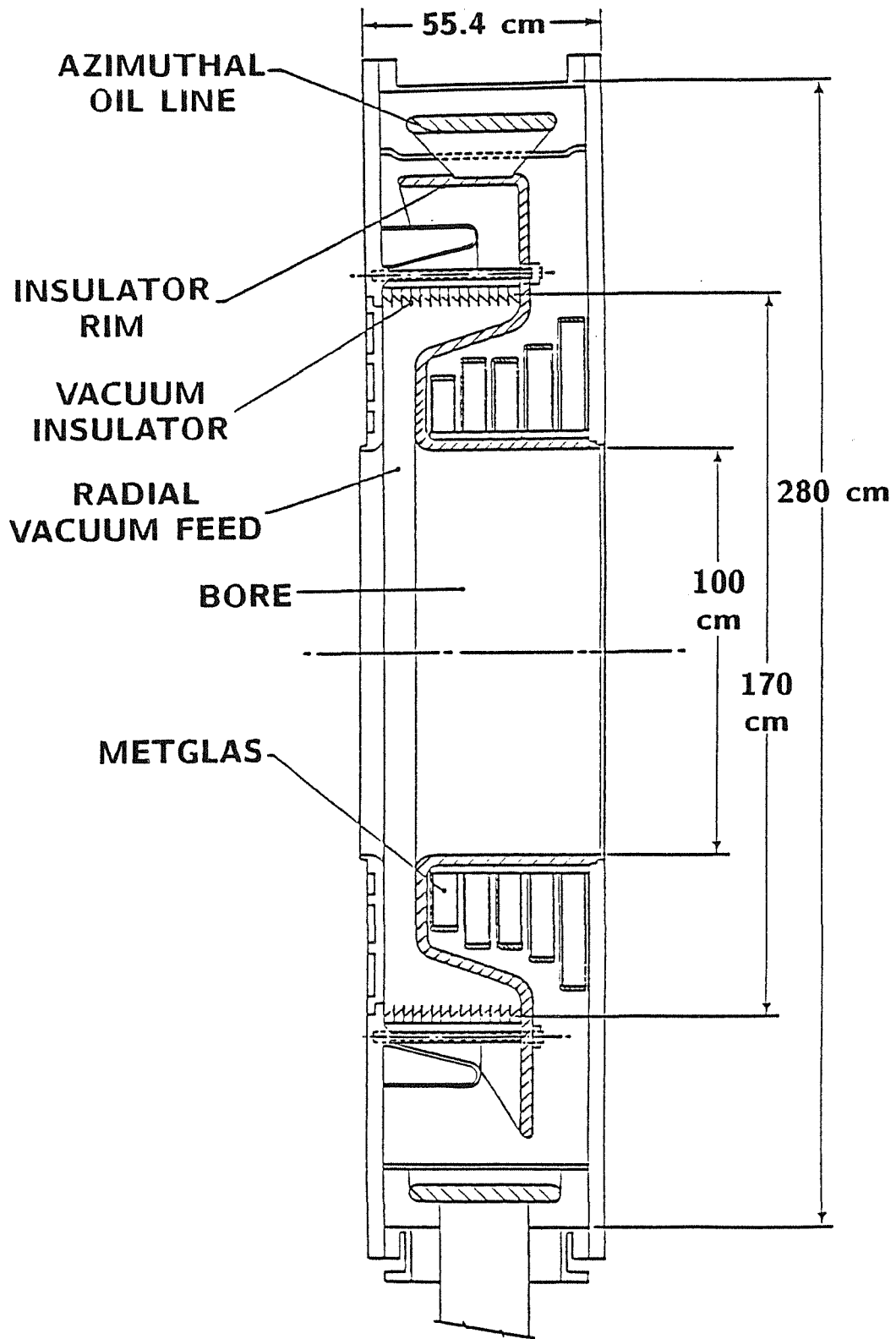


Fig. 2.1. Side view of the 1.15 MV cell.

The tapered rim helps equalize the transit times from the four feed points to all points on the vacuum insulator, since at the feed points the distance around the wide rim conductor is equivalent to about 3 ns while the transit time around to the insulator midway between feed points is about 4 ns.

The vacuum interface is a 1.7 meter diameter stack of 14 insulators, each 2 cm thick, with 45° angled surfaces on the inside, separated by 3 mm thick metal "gradient rings". Inside the interface, the spacing in the vacuum closes to 7.7 cm in the parallel disc feed to the 50 cm radius vacuum bore.

The Metglas isolation inductance is provided by five cores wound on 1.11 meter diameter mandrels, to four different outer radii. Each core is terminated at the outside by a 1 cm thick metal shroud with full radius to avoid large edge fields. The total radial build of the five cores is 0.86 meter, and each core is made from 2 inch (5.1 cm) wide Metglas. The radial packing fraction is assumed to be 60%; using Metglas available now, this is consistent with 1 mil Metglas and 0.5 mil insulation, or 0.6 mil Metglas and 0.33 mil insulation. Using active bias to obtain the manufacturer's published flux density swing of 3.2 T from reverse to forward saturation, the five cores provide a total flux swing of

$$0.86 \text{ m} \times 0.051 \text{ m} \times 0.60 \times 3.2 \text{ T} = 0.084 \text{ V-s} . \quad (2.1)$$

The total length of the cell over its end plates is 55.4 cm, so that the length of the 30 MV module comprising 26 cells is 14.4 meters.

The electrical stresses in the various cell regions are discussed in Section 2.6, following presentation of the pulseline design and pulseline cell circuit calculations.

2.4. Pulseline Design

The pulseline system is shown in Figure 2.2. A first approximation to the design of the pulse line system was made by scaling from the 20 MV design obtained earlier. It consists of two water coaxes operating in "triple-bounce" mode. Since the pulse duration (60 ns nominal) and load impedance (3 Ω) are the same in the 30 MV driver, the first stage or charging pulseline (CPL) is again a 54 ns long, 5.4 Ω coax, and the pulse charging switch (PCS) has an inductance of 334. The pulseforming line (PFL) has a length of 30 ns; its average impedance is 3 Ω , but the impedance varies along its length in a way that provides the voltage ramping needed to bunch the ions. The PCS is negatively charged to provide a negative pulse to the cell.

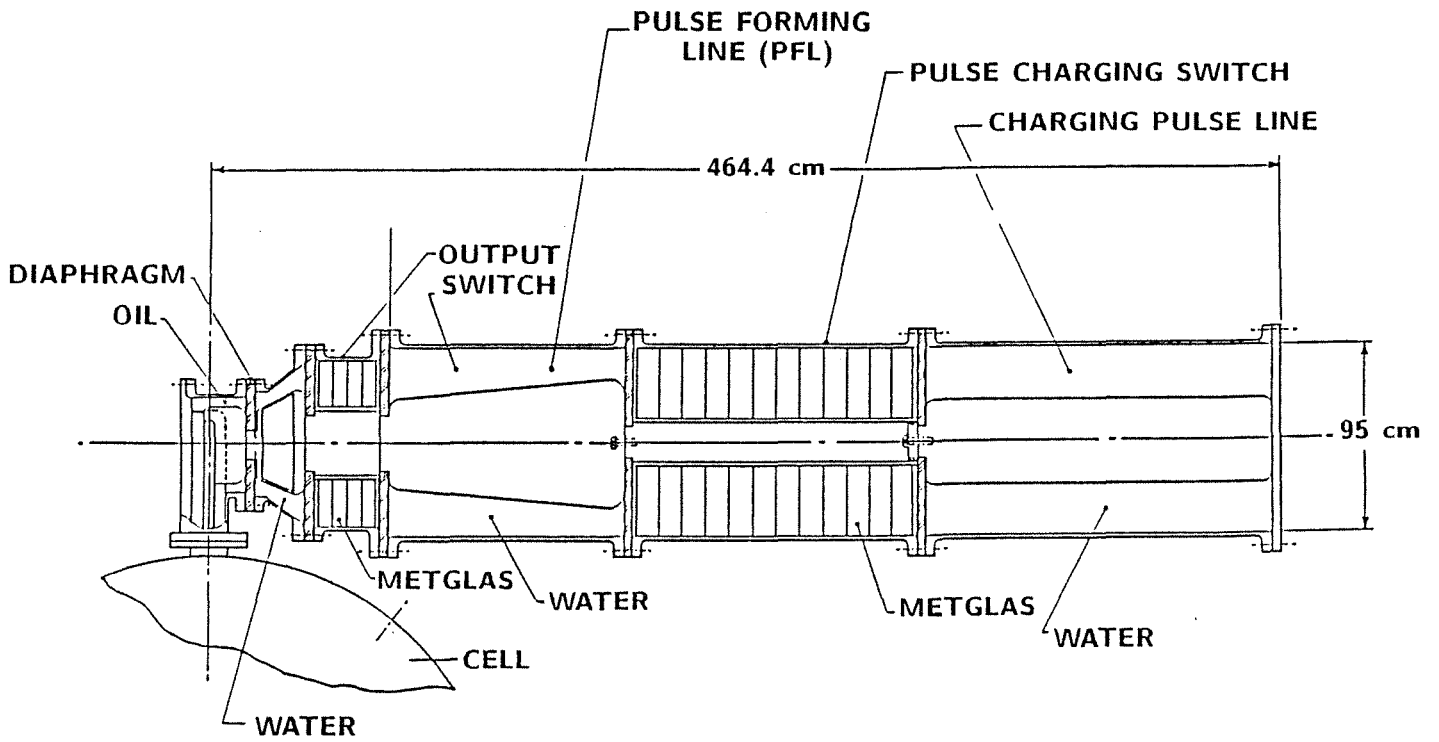


Fig. 2.2. Water pulseline and connection to cell.

The PCS and the output switch are both formed from Metglas cores designed to saturate at the correct times. Following the 20 MV design, the PCS is designed for a charge time of 0.75 μ s to peak. At peak voltage, the volt-seconds on the CPL switch are

$$1/2 \times 2.7 \text{ MV} \times 0.75 \text{ MV} = 1.01 \text{ V-s} \quad (2.2)$$

where the 1/2 term arises because the average voltage during charge is half the peak. However, the optimum closure time for the CPL switch is before peak by half the time to charge the PFL, or 75 ns, and the volt-seconds on the CPL switch at this time is less by $0.075 \times 2.7 = 0.2 \text{ V-s}$, and is thus 0.8 V-s (80% of the value at peak). The output switch closes 75-80 ns after the arrival of the voltage from the PCS. Both switches are biased to use the Metglas at the full flux density swing of 3.2 T.

The output switch consists of four 2-inch-wide (5.1 cm) cores with 1/18 inch (0.16 cm) margins, with 18 cm radial build (outer radius 40 cm, inner radius 22 cm). The thinnest available Metglas (0.6 mil) is used because of the fast charge time. With a packing fraction of about 60%, the flux swing is 0.07 V-s. The length of the switch including 2.5 cm diaphragms is 27 cm, and its saturated inductance is

$$2 \times 27 \text{ cm} \ln 40/31 = 32 \text{ nH} . \quad (2.3)$$

The PCS consists of 12 cores with outer radius 45 cm and inner radius 12.5 cm, each 4 inches (10.2 cm) long with 1/10 in 16 (0.16 cm) margins. With a radial packing fraction of about 65%, the flux swing is 0.8 V-s. The length, including two 2.5 cm diaphragms, is 130 cm, and the estimated inductance is given by

$$2 \times 130 \ln (45/12.5) = 334 \text{ nH}, \quad (2.4)$$

the required value.

Losses in the Metglas cores have not been included in the modelling, and the charge voltages on the CPL and PFL will actually need to be slightly larger to compensate for these losses. Estimates of the losses and the thermal properties of the cores indicate that the cores can be cooled adequately with modest velocity flow of oil in spaces between individual cores.

Between the output switch and the cell is a short length of water transmission line that tapers from the 80 cm output switch diameter to the 30 inch diameter of the water-oil diaphragms at the connection to the cell. This line section has an impedance approximately equal to that of the system of azimuthal oil transmission lines it drives. Its length is somewhat arbitrary and was chosen in the process of circuit calculations to optimize the pulse shape delivered to the cell.

2.5. Circuit Calculations

Computer calculations were performed to simulate a circuit extending from the CPL to the vacuum bore of the cell. The calculations used the PSI transmission line code previously used in the 20 MV driver design.

The circuit is shown schematically in Figure 2.3. The line section lengths are specified as multiples of 0.1 ns, making the effective time-step of the calculations 0.2 ns. The CPL was treated as if dc charged, to a voltage initially estimated as 2.6 MV, then adjusted to give the required load voltage. The PCS was represented as a single inductive line section of the shortest possible length (0.1 ns) in series with a perfect switch. The impedance profile of the PFL was varied to obtain the described load waveform. In the output switch, the capacitance and transit time were approximated by representing it as two equal line sections with an ideal switch between them; the impedance and transit times of the line sections were chosen so that their total capacitance and inductance equalled those of the switch region with the Metglas saturated. The closing time of the output switch was varied to optimize the load voltage waveform while minimizing the CPL charge voltage. The lengths of the water line between the output switch and the oil-water diaphragm were also varied to help optimize the load waveform.

From the oil-water diaphragm on, the line sections were chosen by calculating the properties of each region of the cell design described above. The low impedance line section in parallel with the insulator rim is a capacitance that provides an RC time equal to the time required for the pulse to spread around the rim. The cell Metglas was treated as an open circuit. The vacuum bore of the module is simply represented by a 3Ω load.

The objective of the circuit optimization was to provide a ramped shaped load waveform, having a mean voltage of 1.15 MV and rising from about 1 MV to about 1.33 MV, with some concave upward curvature that approximated the ideal waveform needed to bunch ions. As a result of varying the PFL impedance profile, the output

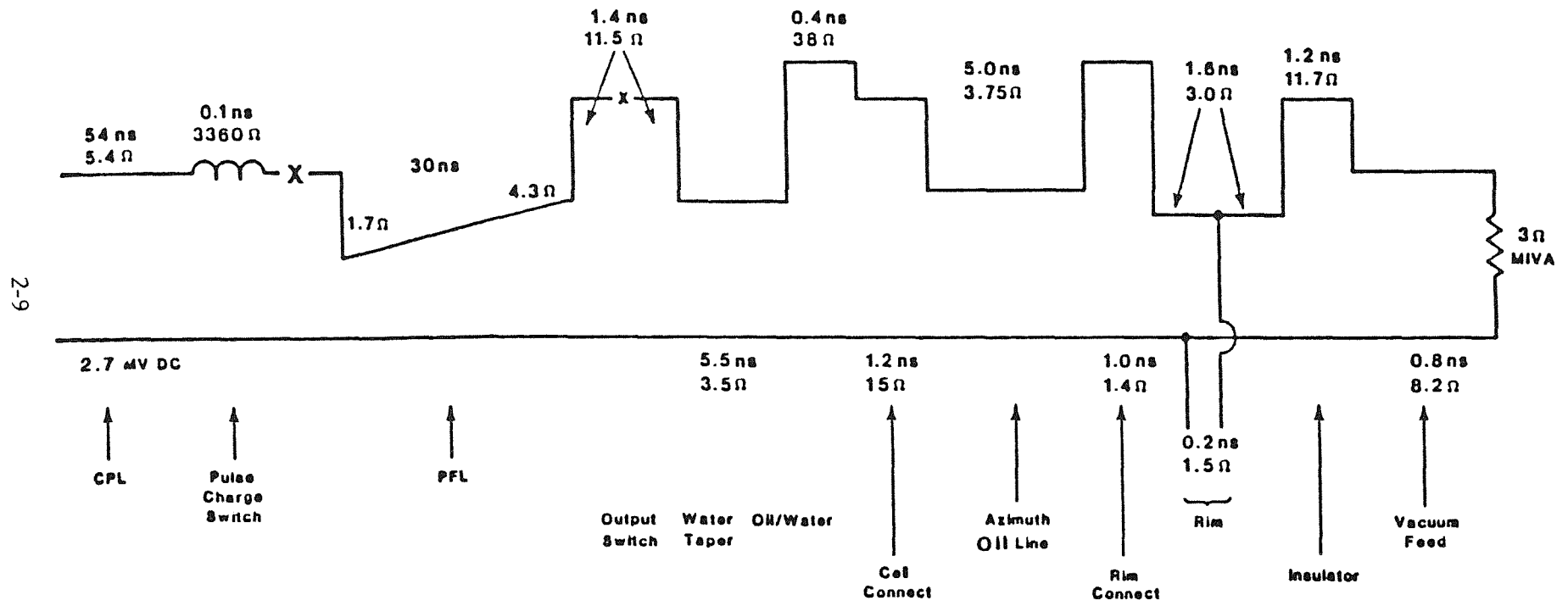


Fig. 2.3. Pulseline and cell circuit.

switch closure time, and the length of the line between the output switch and the water-oil diaphragm, the load waveform shown in Figure 2.4 was obtained. Note that the duration of the ramped pulse top when the voltage rises from 1 MV to 1.33 MV is approximately the 48 ns estimated to be necessary to deliver the correct ion energy and pulse duration at the pellet. The circuit parameters that produce the waveform in Figure 2.4 are those shown in Figure 2.3. The output switch was closed 77 ns after arrival of the leading edge of the charging wave from the PCS.

The exact charge voltage on the CPL was chosen after the waveform in Figure 2.4 had been applied to the MIVA and the NEVA, when it could be adjusted to provide the correct diode voltages. The CPL voltage for the calculation in Figure 2.4 was 2.7 MV, chosen for the MIVA-driven diode. The corresponding voltage waveforms at other points in the pulseline and cell are shown in Figure 2.5. For the NEVA-driven diode, the CPL voltage had to be increased by about 7%, and all the voltages in Figure 2.5 would increase by a similar factor.

2.6. Cell and Pulseline Electric Stresses

The breakdown fractions in the water and oil dielectrics are assessed using the formula

$$Ft^{1/3} A^X = K \quad (2.5)$$

derived by I. Smith at Aldermaston^(8,9) with values for X and K for the two liquids refined by additional data obtained in the USA.

At 2.7 MV charge, the field on the positive outer conductor of the CPL is 70.5 kV/cm. The effective stress time for a 0.75 μs charge is 0.75 μs. At the breakdown condition:

$$Ft_{eff}^{1/3} A^{.06} = 0.23 \quad (2.6)$$

and taking the area corresponding to the CPL of one module, the fraction of breakdown is about 45%.

The highest stressed region in the PFL is at the input, where the impedance is 1.7 Ω, the peak voltage 2.28 MV, and the effective stress time 53 ns. The field on the outer conductor is estimated to be 173 kV/cm (the geometry is not exactly coaxial

2-11

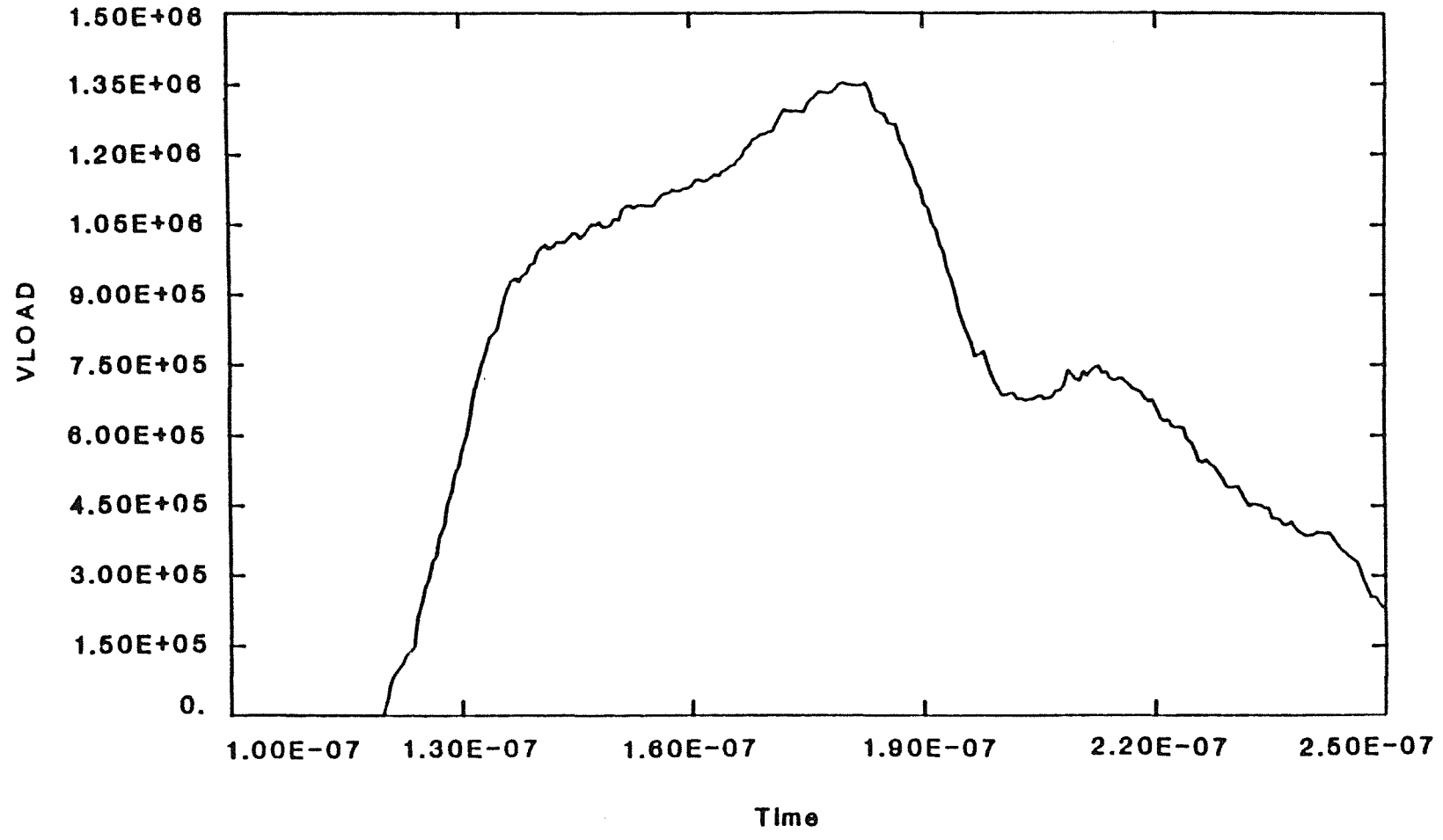


Fig. 2.4. Pulseline circuit load voltage.

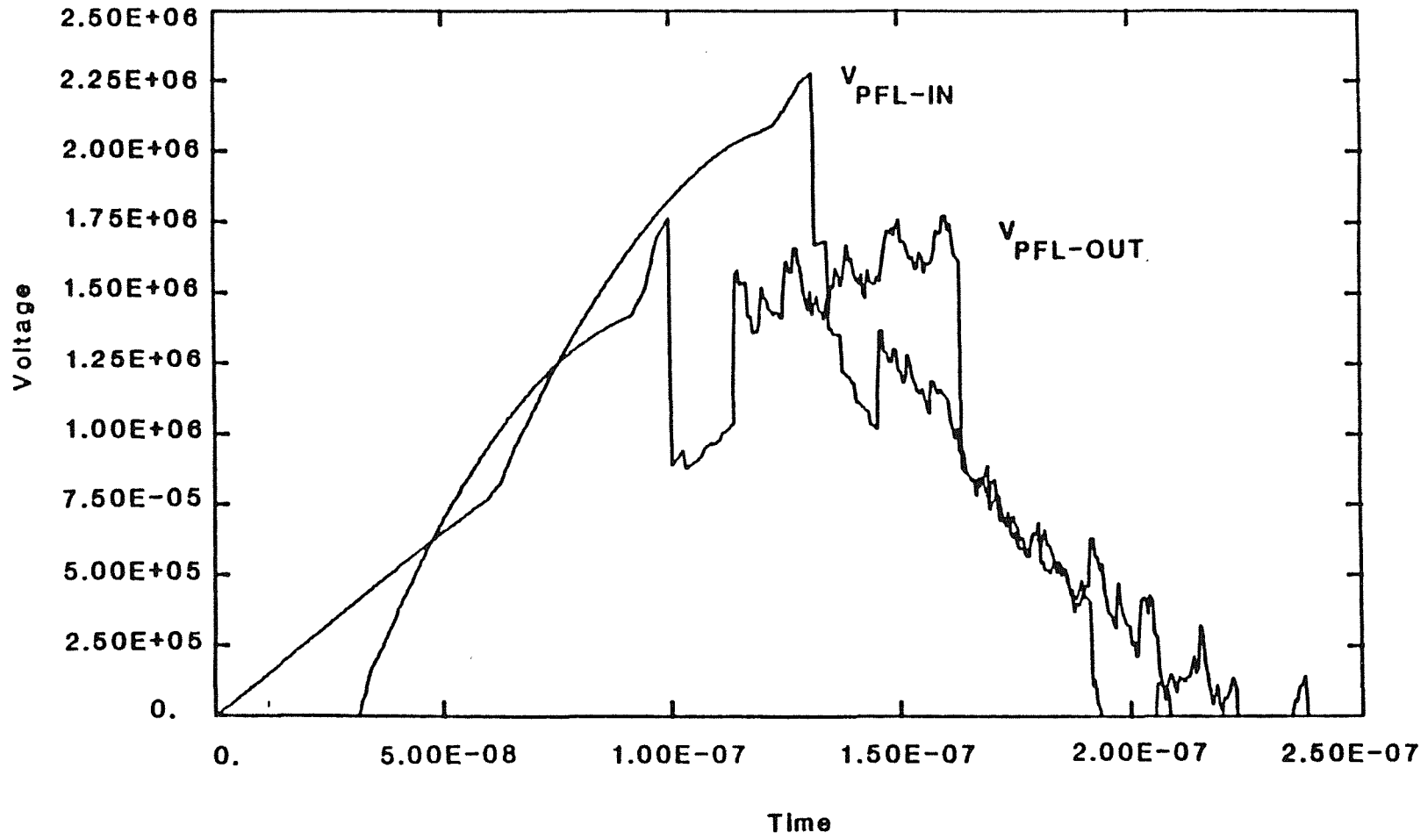


Fig. 2.5(a). Pulseline circuit PFL voltage.

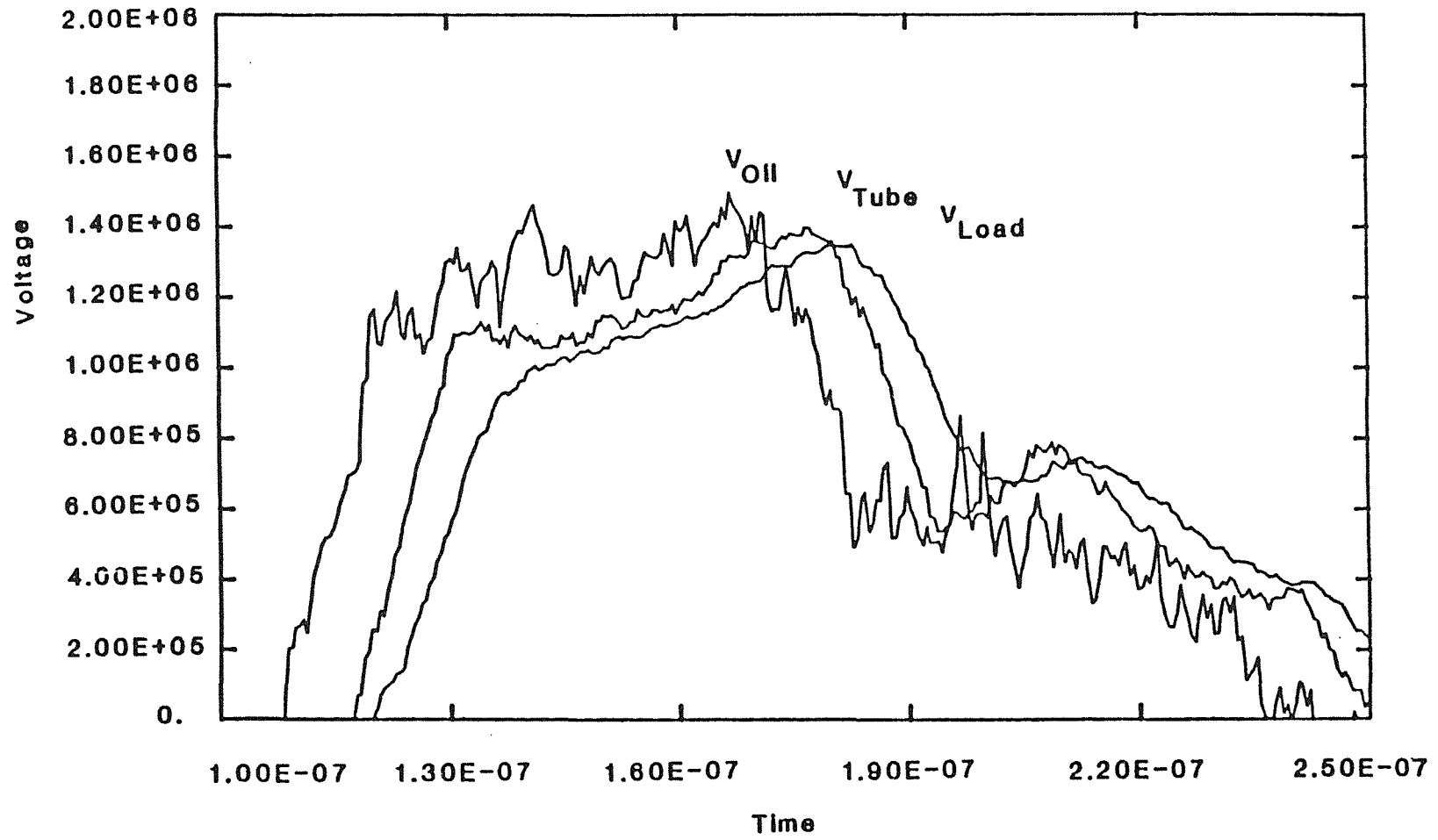


Fig. 2.5(b). Pulseline circuit oil, tube, and load voltage.

because of the impedance taper), and the stress calculates to be about 54% of breakdown for one module.

In the water line just upstream of the water oil diaphragm, the diameter is 50 cm, the peak voltage is 1.04 MV for 60 ns, and the breakdown fraction for the outer conductor is about 37%.

The polarity effect in water is large enough that the inner conductors of the pulseline system are all well below 50% of breakdown.

In the azimuthal oil transmission lines of the cell, the voltage waveform (see Figure 2.5) has the form of a ramped pulse with rapid fluctuations. The peak voltage is 1.5 MV at the input and 1.48 MV at the output, with a minimum of 1.44 MV in between. Averaging over the line length, the fluctuation, and the ramp, the voltage is at most 1.4 MV. The spacing is 6 cm, and the peak field on the outer conductor is 233 kV/cm. With a total area of about 10^6 cm^2 for one module, the breakdown fraction using

$$F_t^{1/3} A^{.075} = 0.48 \quad (2.7)$$

is about 54%. The field on the edges of the negative inner conductor has not been calculated, but can probably be kept below about 50% of breakdown, which according to a quasi-uniform field breakdown criterion assuming a 1.5:1 polarity effect would be about 425 kV/cm. Negative streamer transit times are in any case longer than the pulse duration, even assuming initiation from sharp points.

The peak voltage on the vacuum insulator is 1.40 MV, and the insulator field is 50 kV/cm. The voltage waveform (see Figure 2.5) is such that it is difficult to estimate an effective pulse duration, but a value of 30 ns is taken. According to J.C. Martin's formula for vacuum flashover:⁽¹⁰⁾

$$F_t^{1/6} A^{0.1} = 175 \quad (2.8)$$

the fields correspond to 60% of breakdown for one module. As in the 20 MV design, it is thought that this fraction is low enough, since the flashover of one of the fourteen insulators should not overvolt the remainder sufficiently that the whole stack fails.

The electric field in the radial vacuum feed is 150 kV/cm.

The voltage waveform on the cell Metglas was integrated, and it was shown that the saturation flux of 0.084 V-s was reached, but only late in the pulse when the voltage has fallen to about 40% of peak.

The volt-seconds on the PFL output switch was similarly integrated to obtain 0.068 V-s, close to the value of 0.07 calculated from the switch geometry.

The electric fields in the water, oil, vacuum and vacuum interface are within the ranges expected to be safe in long life repetitive operation, though the safe fields in such a large system need to be demonstrated by experiment. The fields in the cell Metglas cores are also much lower than those in Helia. However, the fields in the Metglas cores of the pulseline switches are relatively high. The field in the insulation between Metglas turns in the output switch is up to 700 V/mil, which is well above that used in existing repetitive switches. However, it is well below what is used in capacitors. The field in the PCS switch insulation is more than 1000 V/mil, but this can probably be reduced by redesign.

2.7. Voltage Adder Calculations

2.7.1 MIVA Design

The voltage adder was modelled as a MIVA (magnetically insulated) design using the code previously used in the 20 MV driver design.⁽⁴⁾ The MIVA section within in each cell was again represented as two sections of transmission line with a resistor in between to model the losses. The drive provided by each cell was represented by a source having an open circuit voltage equal to twice that in Figure 2.4, with the same waveshape; the source has an ideal impedance of 3 Ω .

The MIVA was designed on the principle that the load current of 385 kA should in each section be 1.2 times the minimum parapotential current at the voltage expected there. The wave impedance of each section is listed in Table 2.1, along with the diameter of the center conductor.

The diode was modelled as an ideal resistor of impedance $20 \times 3 = 78 \Omega$. The code calculations were first checked by making the MIVA section impedances 3, 6, 9 ... 78 Ω , turning the losses off, and showing that the diode waveform was exactly 26 times the matched voltage waveform of an individual source.

With the actual MIVA design, with losses present, and with an emission threshold of 150 kV/cm, the diode waveform of Figure 2.6 was obtained. Note that the useful part of the pulse is about 45 ns long, because the early losses are over at about the time that the ramped plateau is reached. The loss in pulse duration has in fact not increased from the 6 ns lost in the 20 MV driver design, although the MIVA is 50% longer. This result presumably stems from the fact that at very high voltages the loss front moves almost at the velocity of light, and is not much further delayed behind the vacuum signal.

Table 2.1. MIVA Voltage Adder Impedances

<u>Section</u>	<u>Z</u> <u>(ohms)</u>	<u>Inner Diameter*</u> <u>(cm)</u>
1	6.35	89
2	11.04	83
3	15.51	77
4	19.86	72
5	24.06	67
6	28.15	63
7	32.14	59
8	36.05	55
9	39.89	51
10	43.68	48
11	47.41	45
12	51.09	43
13	54.73	40
14	58.34	38
15	61.90	36
16	65.44	34
17	68.94	32
18	72.41	30
19	75.86	28
20	79.28	27
21	82.68	25
22	86.05	24
23	89.41	23
24	92.70	21
25	96.05	20
26	99.35	19

*outer diameter = 100 cm

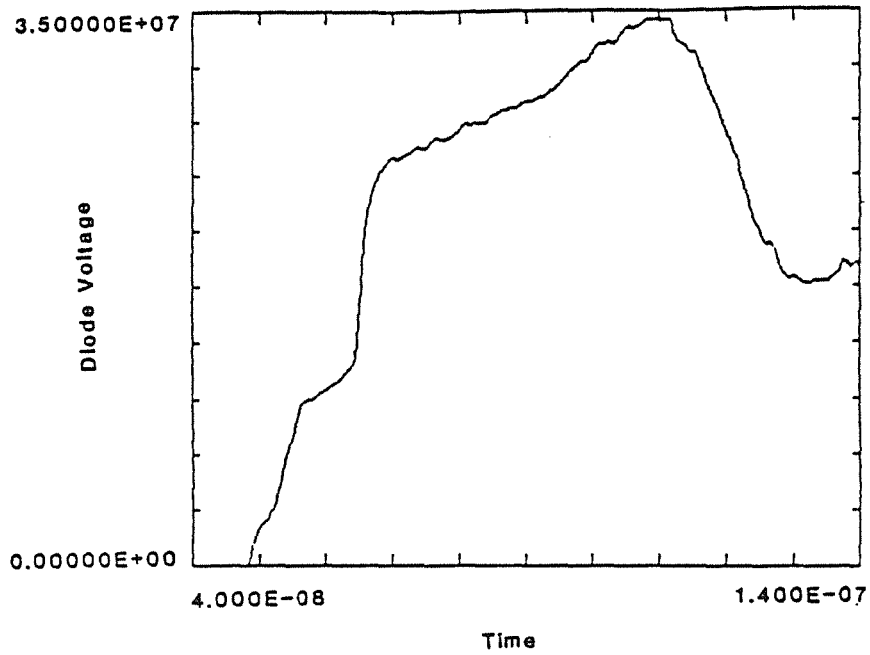


Fig. 2.6(a). MIVA-driven diode voltage, mean diode voltage = 30 MV; diode impedance = 78 Ω (constant); emission = 150 kV/cm.

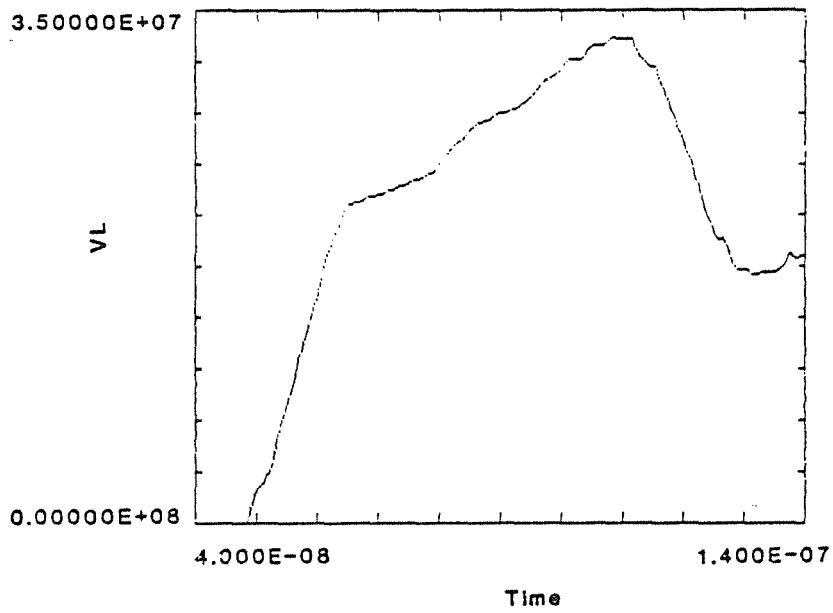


Fig. 2.6(b). MIVA-driven diode voltage, mean diode voltage = 30 MV; diode impedance = 78 Ω (constant); emission = 300 kV/cm.

The preservation of adequate pulse top duration depends on the relatively low emission threshold assumed in the calculation represented by Figure 2.6(a). With a 300 kV/cm threshold, the losses begin later and continue later, Figure 2.6(b). (Because the ratio of bore radius to current is larger than in the 20 MV design, the losses begin later than they did in that case at the same field.) Achieving emission at 150 kV/cm will require special treatment of the surface of the outer conductor; presumably coating with carbon would suffice.

The energy delivered by the useful part of the pulse in Figure 2.7 is 500 kJ, about 10% more than the 450 kJ needed to provide 3.6 MJ at the pellet with 50% transport efficiency.

2.7.2 NEVA Design

The design of a non-emitting voltage adder was also studied. The calculation assumed an operating field of 300 kV/cm on the outer conductor. The increase from 250 kV/cm assumed in the 20 MV design was made because in order to obtain only 10% energy loss from mismatches the 20 MV, 333 kA design required a 48 cm radius bore; the 30 MV, 385 kA adder would need a bore radius of more than $48 \times 385/333 \approx 55$ cm, because this value would achieve the same degree of mismatch, but in a longer bore. The bore in the 30 MV driver is only 50 cm in radius. The use of 300 - 400 kV/cm may well be possible using anodized aluminum for the material of the outer of the bore. If a lower field is necessary, this would mean an increase in the bore diameter. For example, the calculations and design solution below would apply equally with 250 kV/cm field at a bore radius of 60 cm, which would not represent a major increase in overall module dimensions.

The lossless circuit code was used iteratively to find an impedance profile for the NEVA that gave a field of 300 kV/cm on the outer of the bore in every cell at the actual peak voltage obtained there. The impedance profile and the inner conductor diameters (assuming a 50 cm outer radius) are listed in Table 2.2.

The diode waveform is shown in Figure 2.7. Because there are no losses, the useful pulse duration is still about 47 ns. The voltage ramp has been increased to about 1.40:1 by the effect of the mismatched or somewhat inductive NEVA. Note also that to obtain the same peak voltage the driver voltages needed to be increased about 7% from those used in the MIVA design. The energy delivered during the pulse top is 510 kJ.

Table 2.2. NEVA Voltage Adder Impedances

<u>Section</u>	Z (ohms)	Inner Diameter* (cm)
1	7.83	87
2	15.43	77
3	22.86	68
4	30.18	60
5	37.42	53
6	44.62	47
7	51.85	42
8	59.03	37
9	66.13	33
10	73.07	29
11	79.01	26
12	83.23	24
13	87.76	23
14	90.37	22
15	92.09	21
16	95.14	20
17	99.28	19
18	103.01	17
19	104.73	17
20	110.19	15
21	115.41	14
22	120.95	13
23	126.20	12
24	130.13	11
25	134.27	10
26	139.20	9.8

*outer diameter = 100 cm

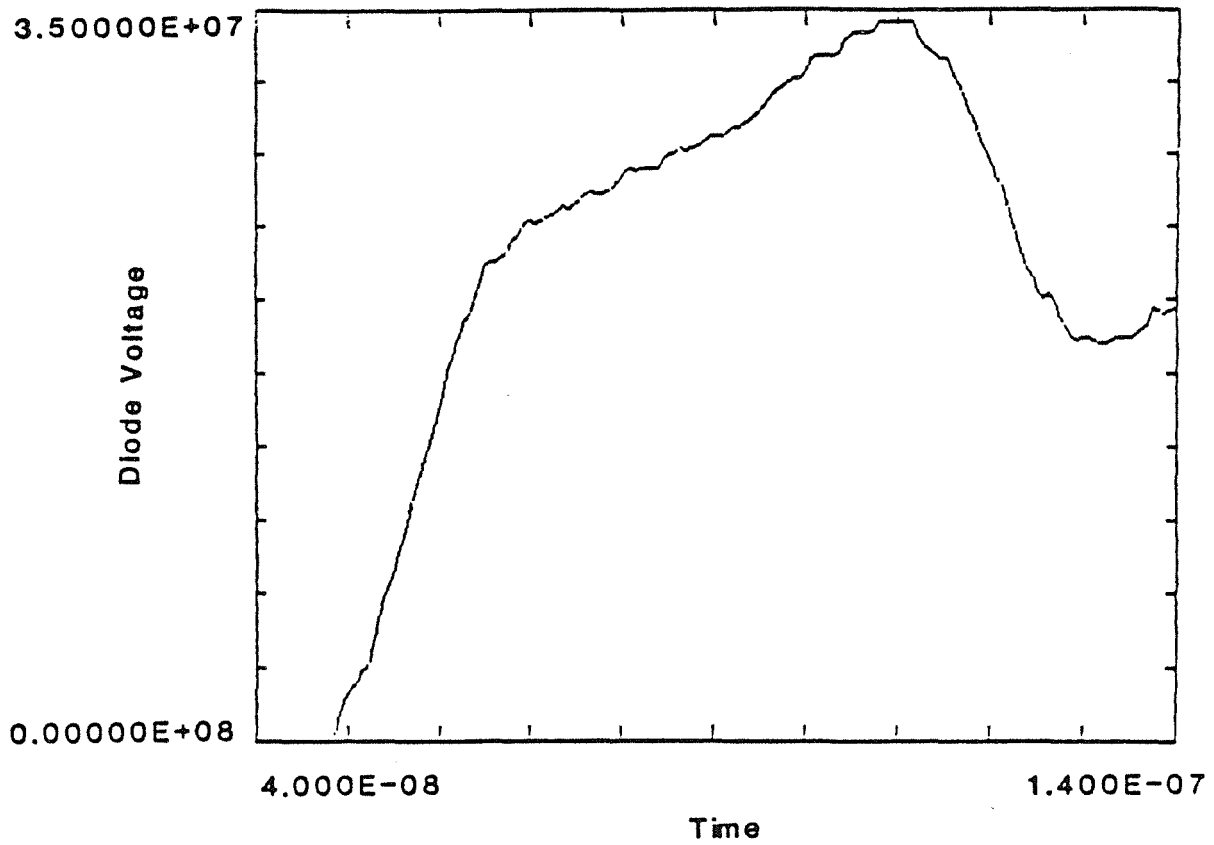


Fig. 2.7. NEVA-driven diode voltage, 30 MV mean voltage; diode impedance = 30Ω (constant).

2.8. Ion Bunching

The transport of ion beams to the target from both the MIVA-driven and NEVA-driven diodes was calculated as in the 20 MV driver design. The transport model neglects variations in axial velocity of ions due to finite injection angles and transverse velocity. The use of pure lithium-7 isotope was assumed, and 50% efficiency from diode power.

For the MIVA-driven diode, the time required for one module to deliver 225 kJ of ions to the target (3.6 MJ from 16 modules) is shown as a fraction of distance along the channel in Figure 2.8. The specified delivery time of 9 ns is reached after 6 meters, as required. The maximum degree of bunching occurs at about 7 meters, where less than 5 ns is needed to deliver 225 kJ; 250 kJ is delivered in 5 ns. Since the ions originate in an interval of about 45 ns in the diode, they have been bunched by a factor up to nine.

The target power pulses at 6 m and 6.5 m are shown in Figure 2.9. The ripples on the top of the diode voltage pulse have produced power spikes, but these are not as large as in the 20 MV driver, because the ripples are not so pronounced. Figure 2.10 shows the total energy arriving at the target from an individual channel as a fraction of time.

Figures 2.11, 2.12, and 2.13 show the corresponding results for the NEVA-driven diode. Although the useful output pulse duration at the diode is longer for the NEVA than for the MIVA, the extra voltage ramping provided by the NEVA causes the maximum bunching to occur at a slightly shorter distance, 6.5 meters. An energy of 225 kJ is delivered at 6.5 meters in less than 4 ns, a bunching factor of more than ten. In other respects, the results obtained with the NEVA are very similar to those with the MIVA.

2.9. Charging System Design

2.9.1 Introduction

This section covers the design of the charging system from the wall plug to the charging of the 0.75 μ s pulselines to 2.7 MV.

2.9.1.1 Driver and Charging System Configuration

The charging system design was performed some time after completion of the design of the modules, cells, and water pulselines, documented in previous sections. Thus the initial specifications for the charging system were those determined by the design with 16 modules, each comprising 26 cells and pulselines, in each of which the 10 nF charging pulseline (CPL) is to be charged to an effective peak voltage of 2.7 MV in 0.75 μ s. The configuration of the charging system was required to be compatible with

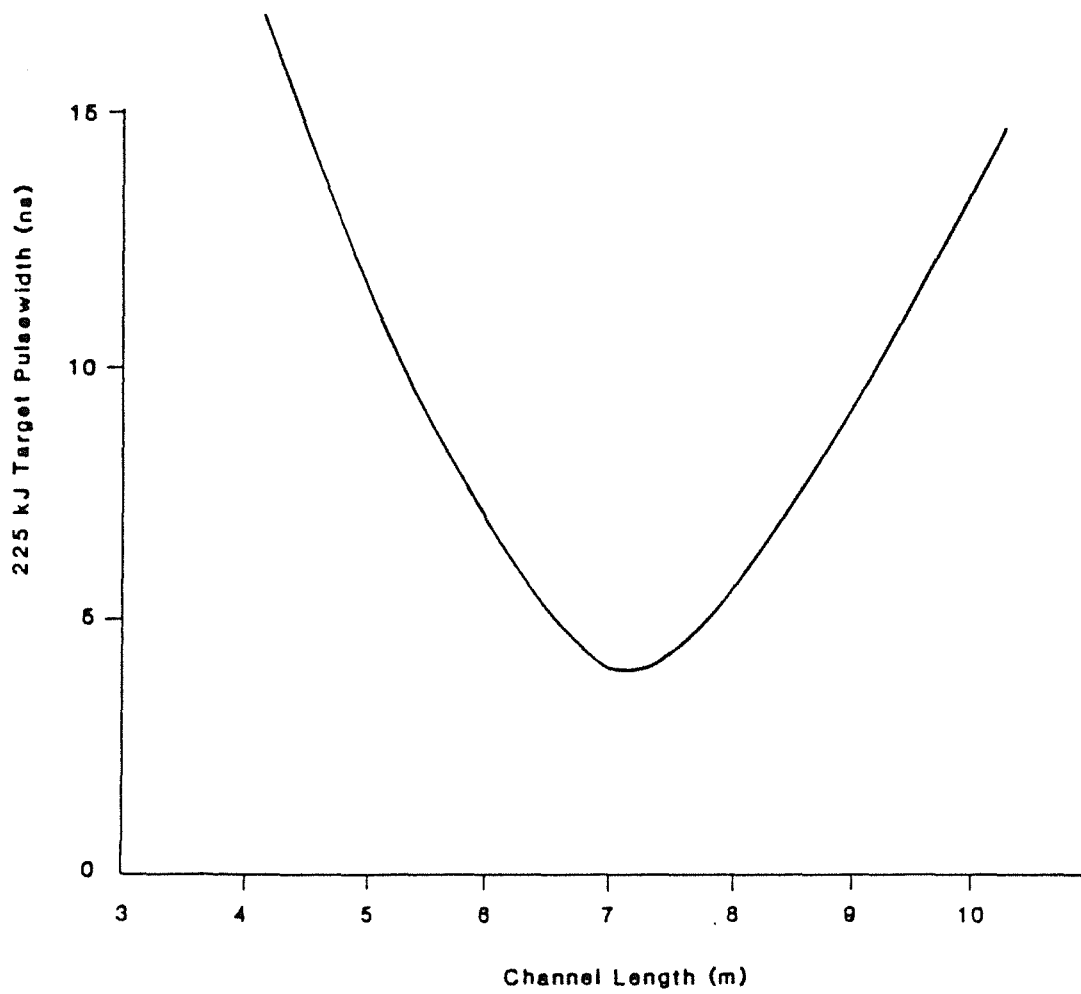


Fig. 2.8. MIVA target power bunching.

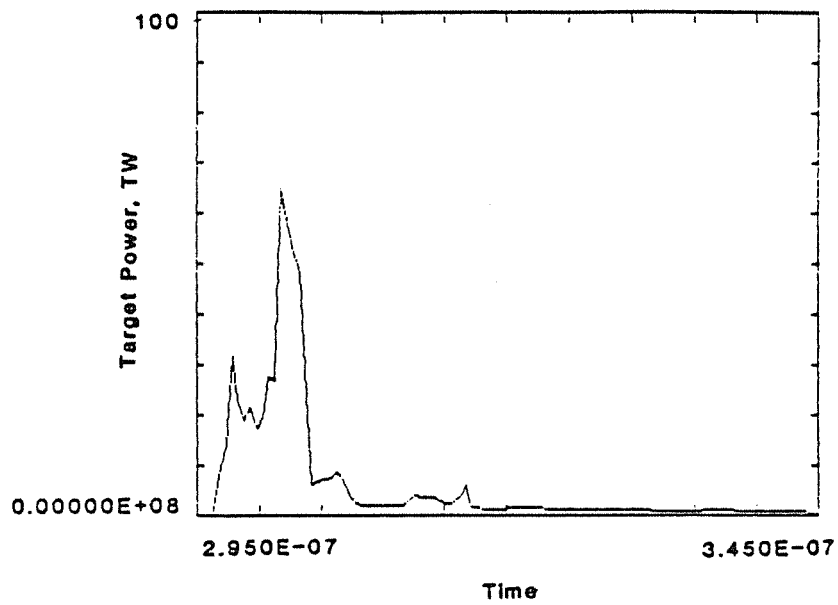


Fig. 2.9(a). Target power form MIVA single module output 6.0 meter beam channel.

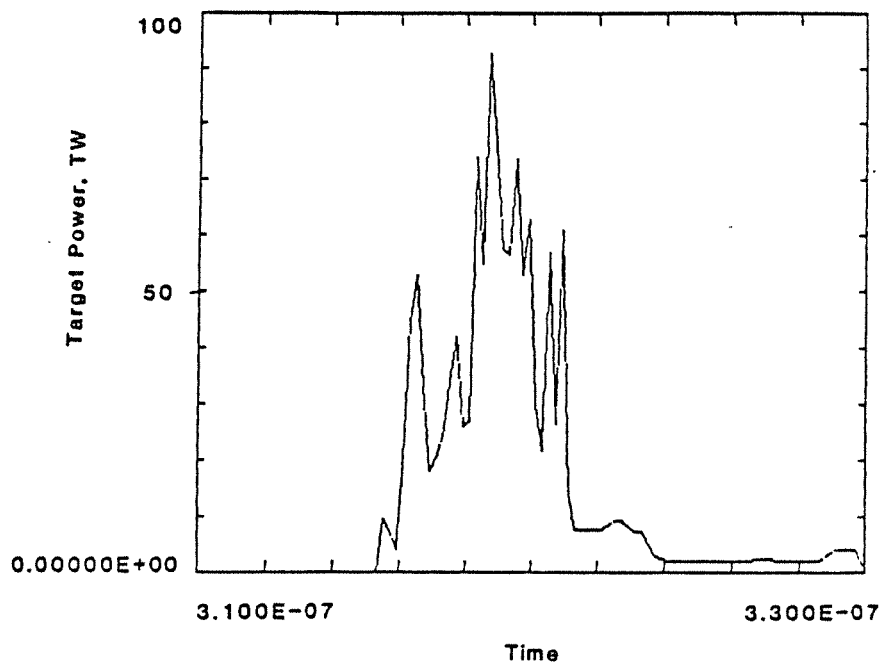


Fig. 2.9(b). Target power from MIVA single module output 6.5 meter beam channel.

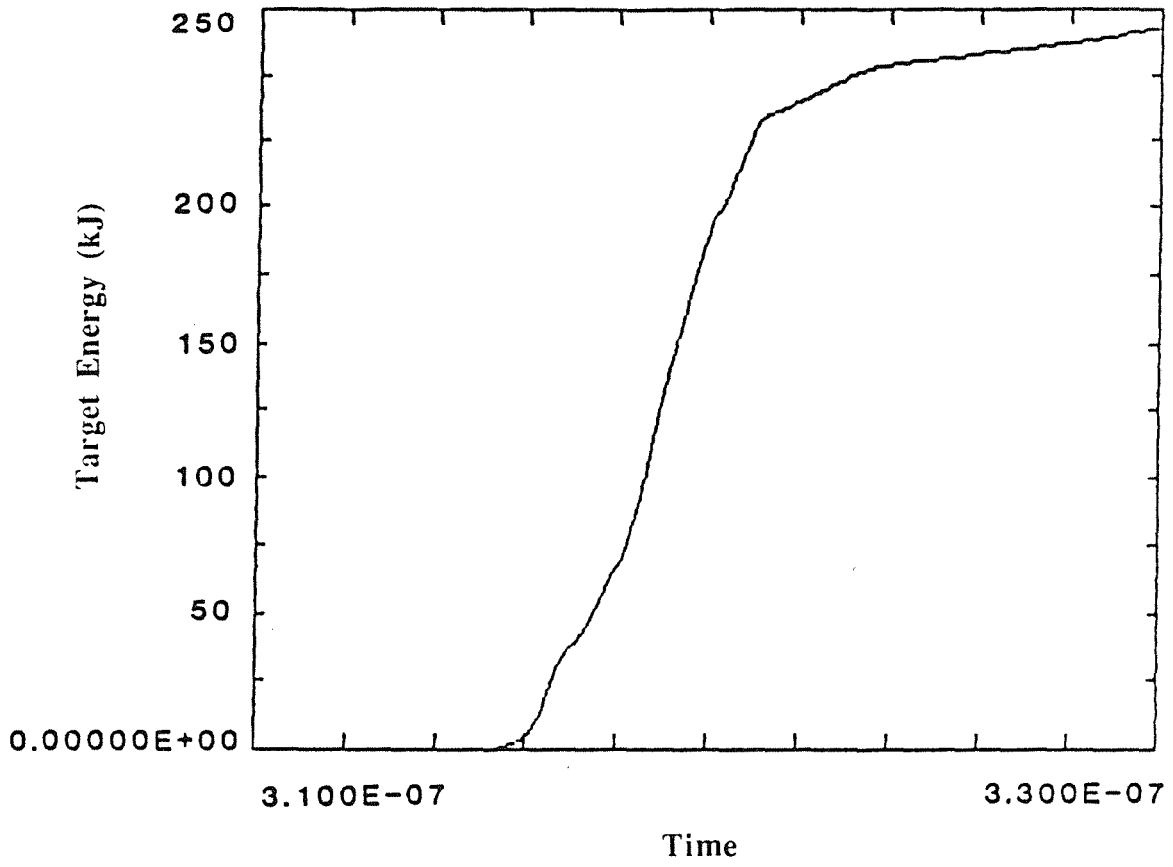


Fig. 2.10. Target energy for MIVA-driven diode single module 6.5 meter beam channel.

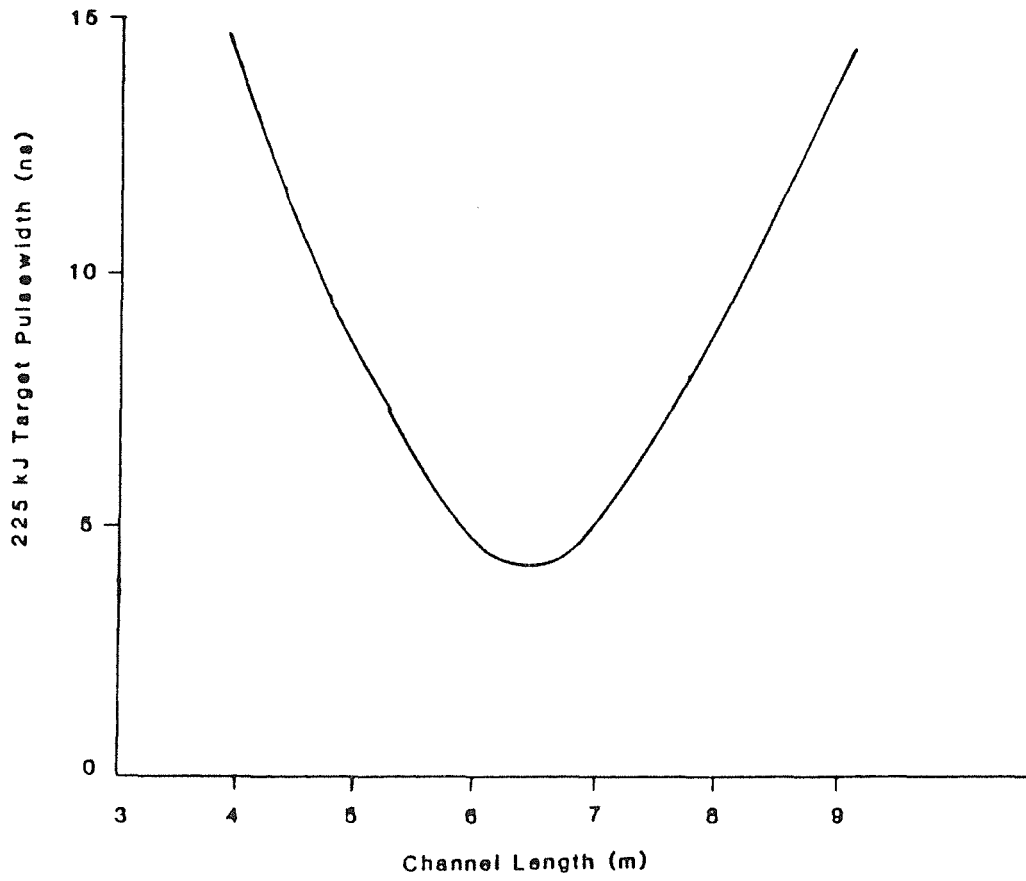


Fig. 2.11. NEVA target power bunching.

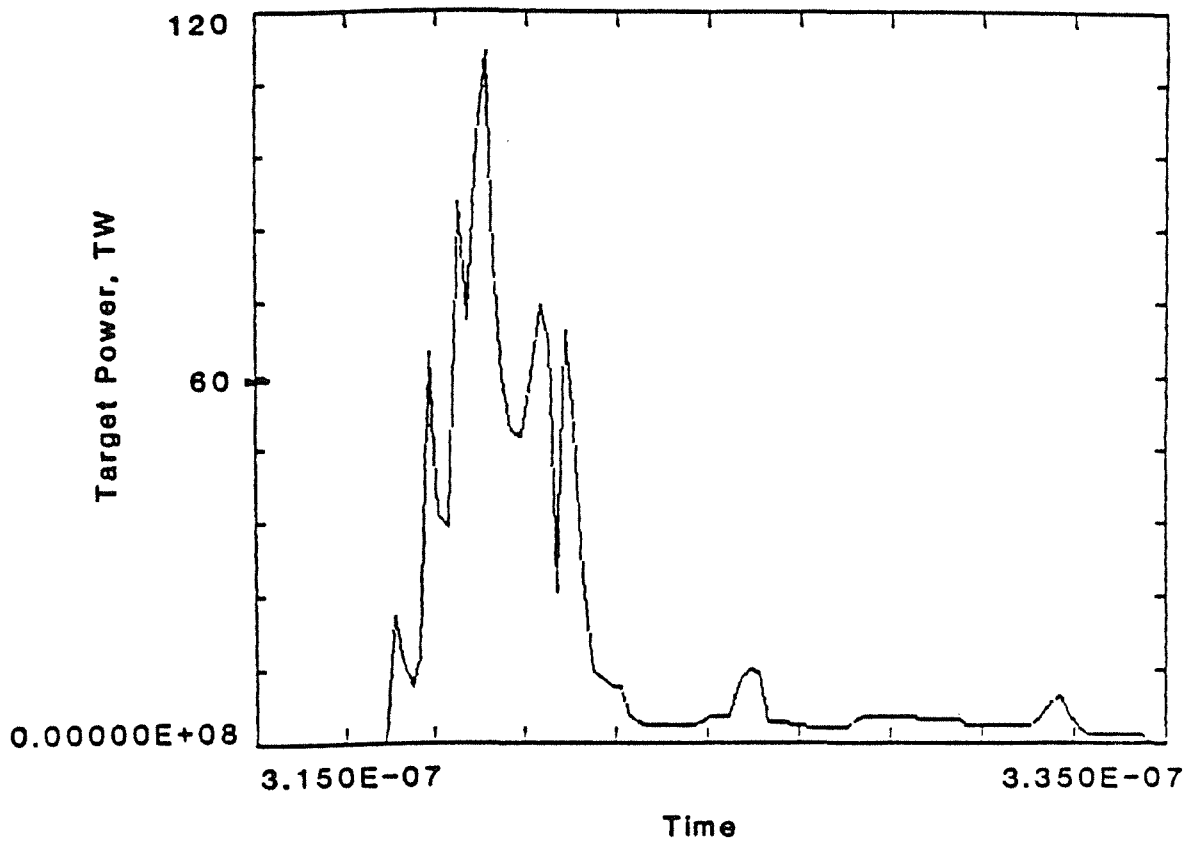


Fig. 2.12. Target power for NEVA-driven diode single module 6.5 meter beam channel.

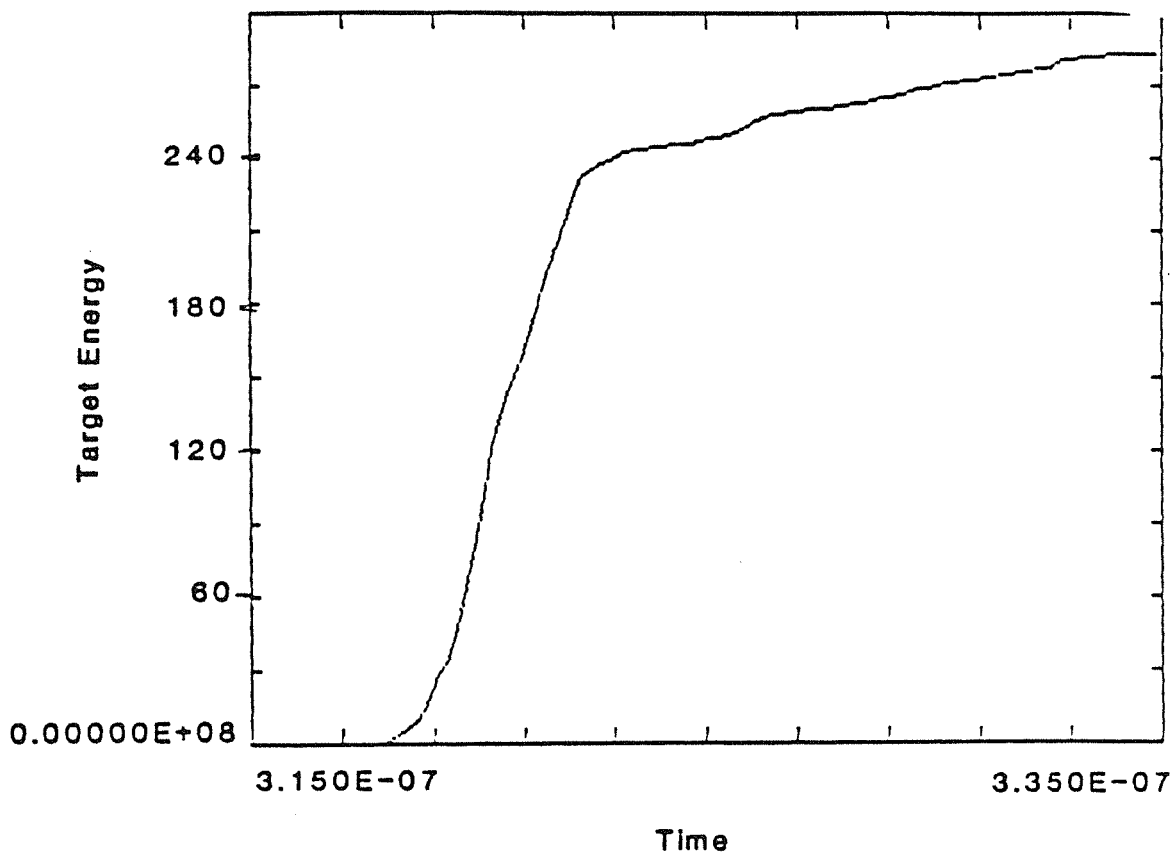


Fig. 2.13. Target energy for NEVA-driven diode single module 6.5 meter beam channel.

that of the modules. Since the modules have a width of about 4.8 meters over the pulse-lines, it is convenient to place them in two circles about the reactor chamber, one above the other, as in the conceptual layout shown in Figure 2.14. With the pulselines of adjacent modules almost touching, the face of each module is about 6.3 meters from the system axis, approximately the distance required to bunch the ions in the transport channel. A short extension of the MIVA can be used to penetrate part of the reactor chamber wall, or to make up any difference between the transport channel length and the minimum distance from the module to the pellet. (For example, if the transport channel length is less than 6 meters or if the circle of modules must be enlarged to allow for a small module providing the energy preceding the main 9 ns pulse.) In Figure 2.14 the pulselines are shown extending upwards from the top modules and downwards from the bottom modules. The location of the charging systems is then specified as above and below, represented (before the charging system was designed) by the rectangular regions shown in Figure 2.14.

A different configuration has been described by the University of Wisconsin elsewhere in the report (see Figure 2.14). In this, the driver modules are placed further from the reactor chamber, and are separated vertically. (Vertical separation might be required to achieve beam incidence angles that give more uniform irradiation of the pellet.) Long extensions of the MIVA are needed to connect to the ~ 6 meter long transport channels; it is not expected that these extensions will entail losses or other problems. In this configuration, there is a space of about 10 meters between the two layers of modules that could be used to accommodate the pulselines and charge systems of one layer, e.g. by extending the pulselines downward from the top layer of modules. However, the charge system study showed that the distance of about 10 meters is too small. Therefore the charge systems are designed to fit above and below the modules as in Figure 2.14.

2.9.1.2 Number of Cells Per Driver Module and Charge System Module

The choice of 26 cells and pulse lines per module was made without consideration of the charging system, which subsequently showed that it is very desirable that the number of pulselines be divisible by four, so that the pulselines on each side of a module can be charged in pairs. Therefore the charging system is designed to drive a 28 cell, 28 pulseline module, and layouts of the driver provided later in this section reflect this. The driver illustrated in this section is therefore actually a 32.3 MV, 4.3 MJ driver, since the cell and pulse line parameters have been maintained at the values discussed in the previous sections of the report.

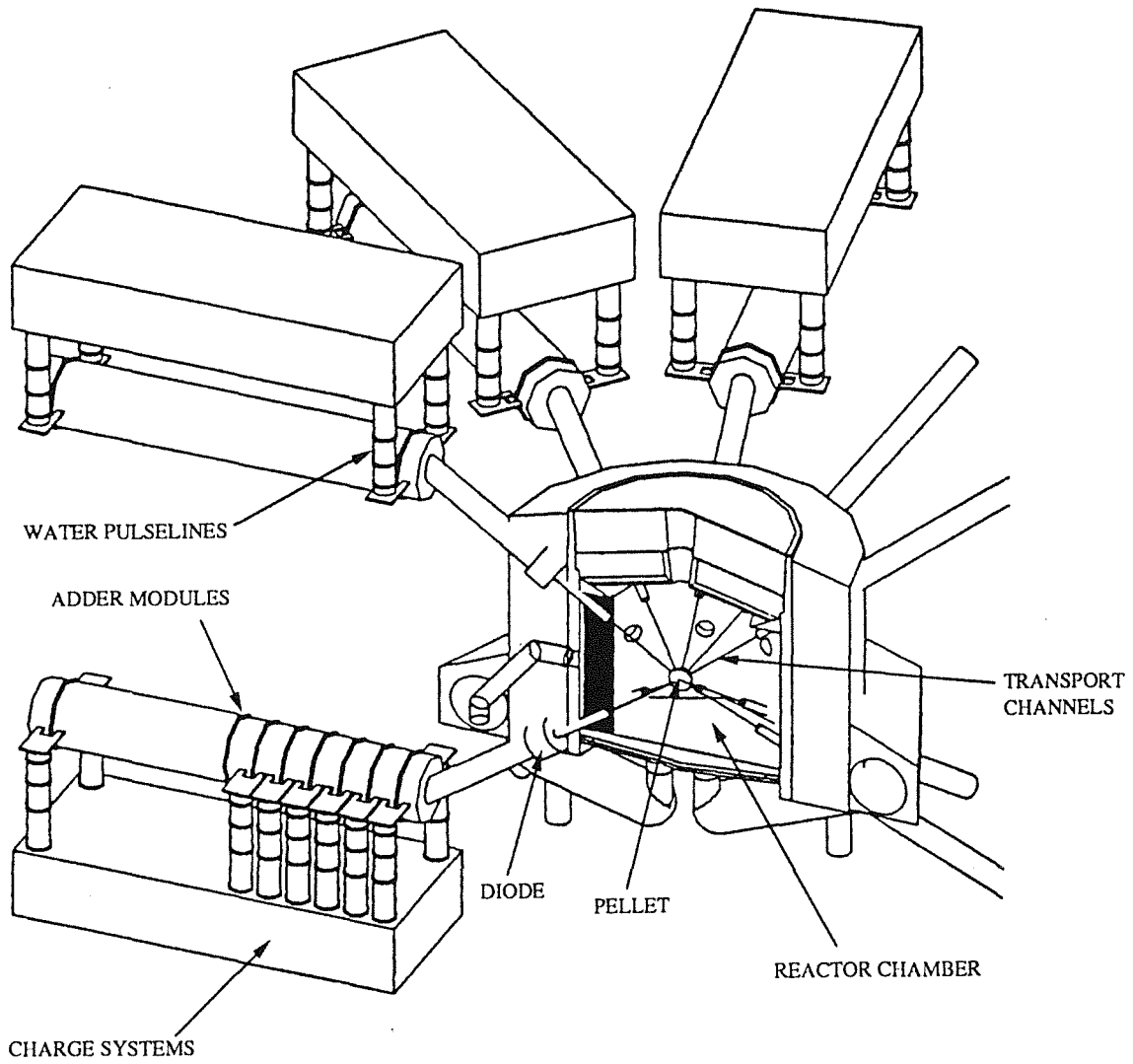


Fig. 2.14. Sixteen module LIBRA design.

2.9.1.3 Electrical Specifications

Each of the 10 nF CPLs stores 36.5 kJ at its effective peak charge voltage of 2.7 MV. The energy supplied per module is 1.02 MJ, or 16.33 MJ for the total driver. The operation is at 3 Hz, and the system lifetime is assumed to be at least 10 years, which is 10^9 pulses. Maintenance could be allowed to replace finite life components such as switches, but assuming this takes place once per year, lifetimes must be at least 10^8 pulses.

Jitter requirements for the driver are not specified, but it is assumed that with a 9 ns pulse duration at the pellet each module must start to deliver its energy within a total window of about ± 1 ns. The jitter of individual drive circuits within each module may be larger by the square root of the number of circuits or switches, since averaging of cell outputs will reduce the effective jitter at each diode.

It is of course desirable to minimize the driver cost. To this end, it has been considered permissible to assume improvements in technology and production techniques where, based on present plans and rate of development, these can be reasonably predicted to occur before the time frame of 2010 when a commercial reactor of this type might be built.

2.9.2 Approach

It was considered desirable that the charging system be based on technology with a proven capability for long life repetitive operation. In particular, switches such as thyratrons and solid state switches are attractive in this context.

Several options were considered and rejected, as follows:

- Megavolt triggered spark gaps;
- 100 kV triggered spark gaps;
- Rotating machine charging.

The triggered megavolt gas spark gaps previously considered for charging the 0.75 μ s pulse line were judged to have inadequate lifetime to meet the 10^8 - 10^9 pulse life goal. Spark gaps typically have a few thousand pulse lifetime.

Similarly, the 100 kV triggered gas spark gaps considered for charging the transfer capacitors had too short a lifetime and would have required excessive maintenance and would have required an excessive number of gaps.

Charging the transfer capacitors from a multipolar rotating machine does not work because the 3 Hz rep-rate is too low. Multicycle resonant voltage buildup only works

with about five cycles between pulses, whereas about 20 cycles would be required for 3 Hz.

The 0.75 μ s charge time is too short to be handled economically by non-spark gap switches, so it was necessary to add a 5 μ s magnetic compression stage including a water capacitor.

By using a 1.35 - 2.7 MV step-up transformer following the 5 μ s compression stage, the volt-seconds on the 5 μ s reactor were reduced by a factor of two, thus halving the Metglas required. (Two turns on the 5 μ s reactor gave too high a saturated inductance.) A 2.7 MV transformer of the conventional iron core type for charging the 5 μ s pulse line to 2.7 MV has not been built, whereas one with a 1.5 MV output has.

The switching level was chosen as 100 kV, since this fits hydrogen thyratrons well. Ignitrons and SCRs can be stacked to 100 kV reasonably well, with proper care and circuit design. 100 kV is also a reasonable level for the primary of the step-up transformer used to charge the 5 μ s stage water capacitor.

Solid dielectric capacitors were chosen for the transfer capacitor original energy store, since the charge time is much too long for a water capacitor.

An important constraint was to have compatibility with the previously chosen dimensions of the cells, pulselines, and overall reactor assembly. This influenced the choice of how many charging pulselines (CPL) to drive per 5 μ s stage. Driving only one line precluded the use of the 1.35 - 2.7 MV transformer. The diameter of the transformer is determined to a large extent by the voltage, and four transformers would not fit in the length of four cells. Driving two lines per 5 μ s/stage worked out, as two transformers side by side would fit into the length of four cells. The layout is straightforward and there is ample working room around the components, as shown in Figure 2.15. There are twice as many 5 μ s stage assemblies as for the four-line driver, but the 5 μ s reactor has a smaller diameter so that the total weight of Metglas is comparable.

Driving four lines per 5 μ s stage turned out to be marginal on saturated inductance. It was also about 7.6 m longer due to the extra stored energy and thus length of the 5 μ s water capacitor. One transformer will fit in the length of four cells, but bringing the four CPL's together by tilting them to connect to the end of one transformer does not leave enough working room for assembly and disassembly. Building a large rectangular transition box to go between the transformer and the four CPL's, leaving the CPL's vertical, may be workable. It could be filled with water to function as the CPL's, but the Z_0 's

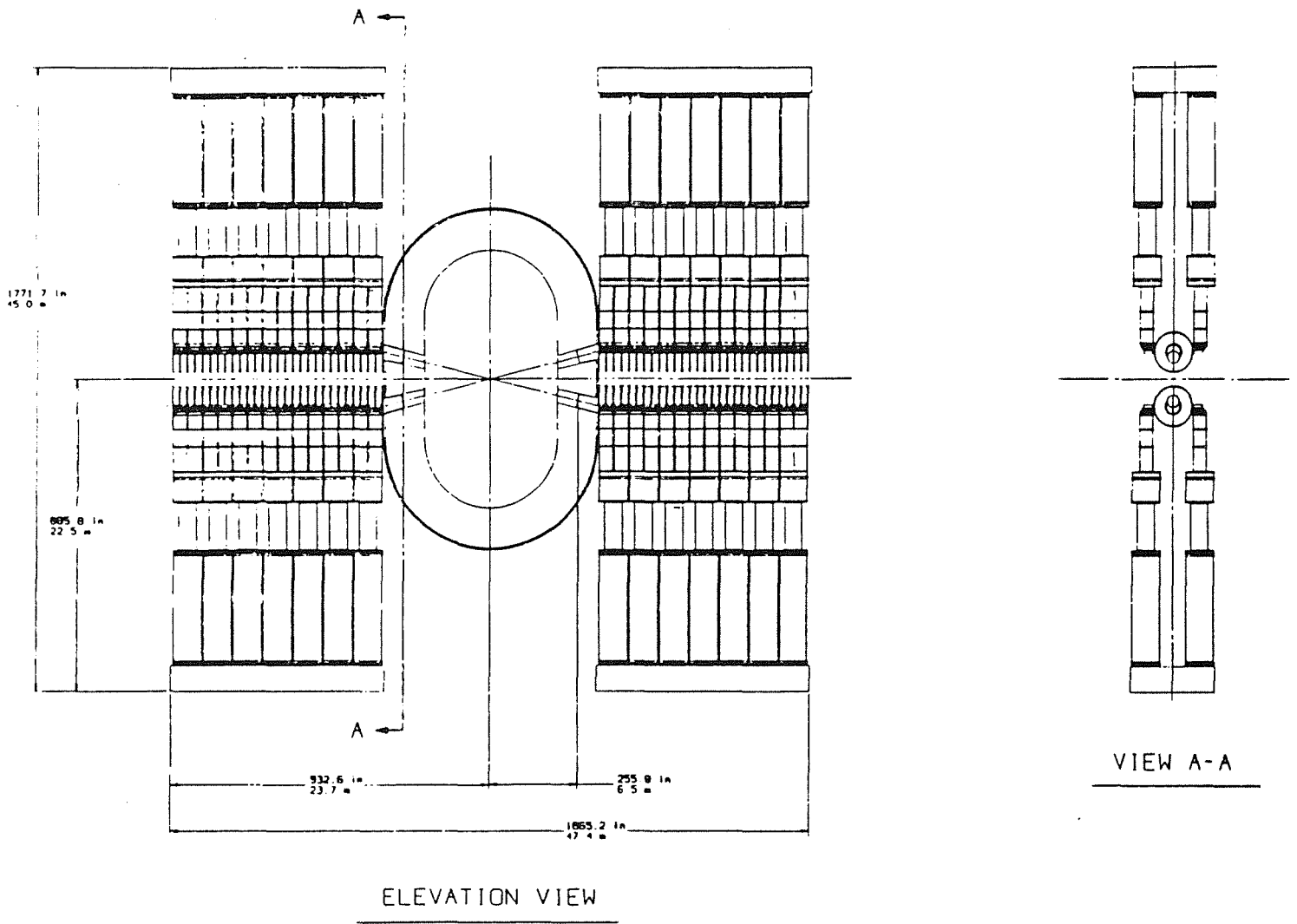


Fig. 2.15. LIBRA 16-module driver conceptual design.

would be very nonuniform due to the two right angle bends, which could adversely affect the output pulse shape.

There is no obvious large cost advantage to charging four CPLs in parallel, so this approach was not pursued any further. The two-line driver approach was chosen.

The two pulselines that are driven by one 5 μ s stage will require matched volt-seconds on the two sets of cores. For a 0.5 ns difference in timing, the volt-second match has to be within

$$\frac{0.5 \times 10^{-9} \times 2}{0.75 \times 10^{-6}} = 1.3 \times 10^{-3} . \quad (2.9)$$

This can be done by measuring the flux swing and then adjusting the number of Metglas layers.

2.9.3 1.35 - 2.7 MV Transformer

A 1:2 turn auto-transformer was chosen as the minimum leakage inductance approach to step-up from 1.35 to 2.7 MV. A schematic of the transformer is shown in Figure 2.16. The primary winding goes from the center conductor around the core to the outer conductor. The secondary is just the portion of the center conductor that passes through the core, so that the secondary voltage is the sum of the input voltage and the induced voltage of the center conductor linking the core. The cross-over of the two sections of the primary winding is accomplished by using two sectors for each section of the primary, interleaved as shown in Figure 2.17.

Early switchout of the CPL does not affect the transformer volt-seconds significantly, so the volt-second requirement at 1.35 MV is

$$V\text{-s} = \frac{1.35 \times 10^6 \text{ V} \times 0.75 \times 10^{-6} \text{ s}}{2} = 0.51 . \quad (2.10)$$

The gross length of Metglas required, with a stacking factor of 0.65, a flux change of 3.2 T, and a radial build of 0.35 meters, is

$$L = \frac{0.51}{3.2 \text{ T} \times 0.65 \times 0.35} = 0.7 \text{ m} . \quad (2.11)$$

Figure 2.18 shows the cross-section dimensions, which are determined primarily by electrical stress on the positive electrodes. There are two critical locations. The first is

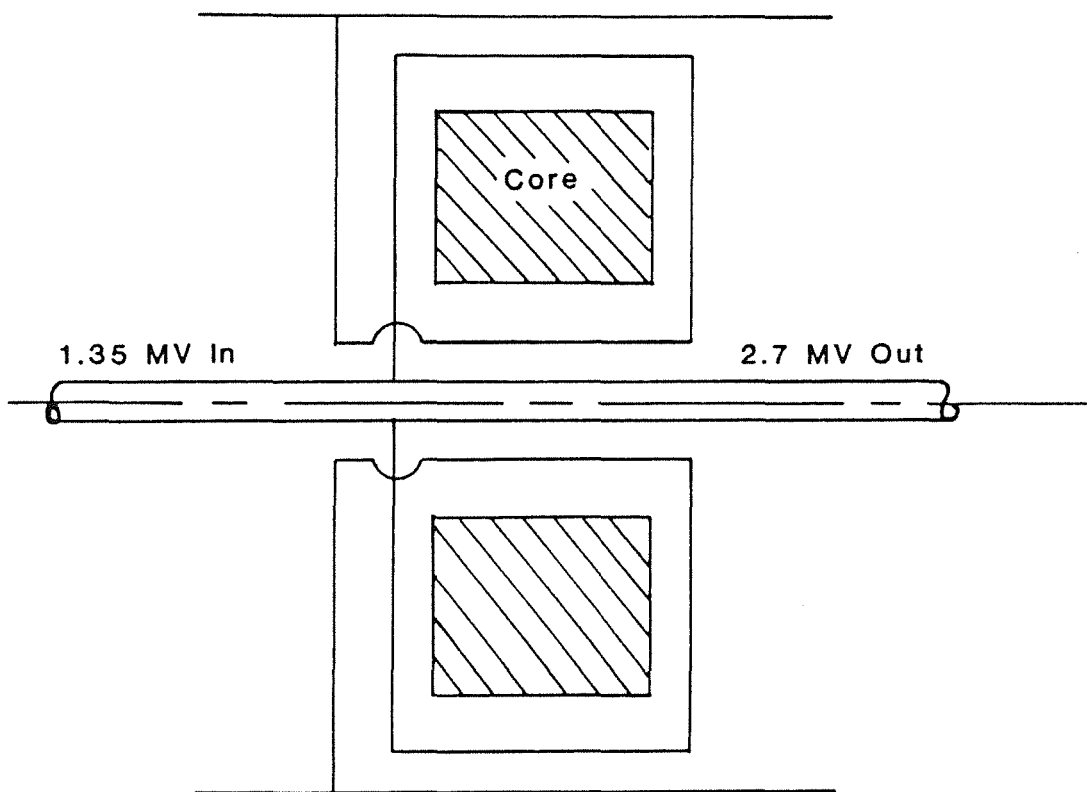


Fig. 2.16. Schematic of 1.35-2.7 MV transformer.

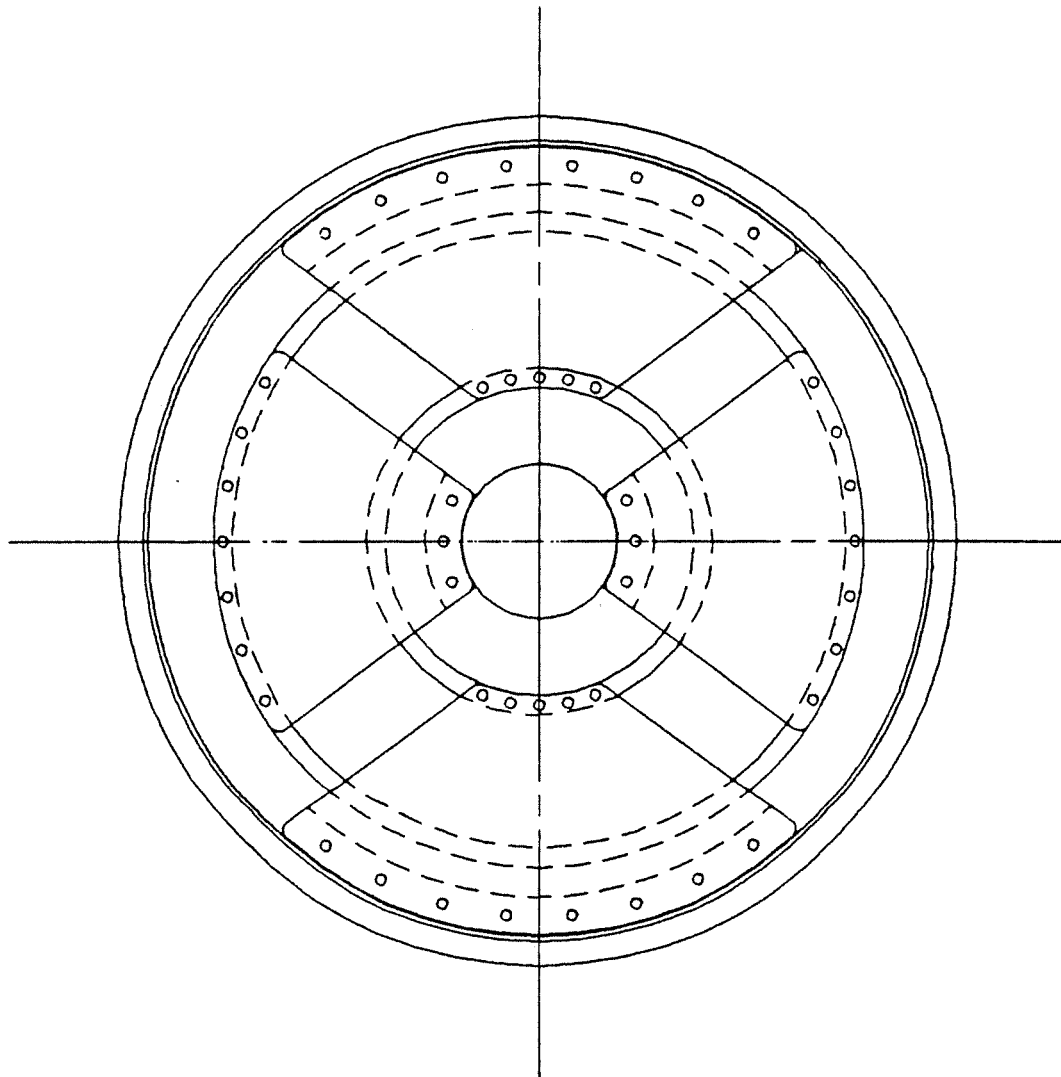


Fig. 2.17. Transformer primary sector connections.

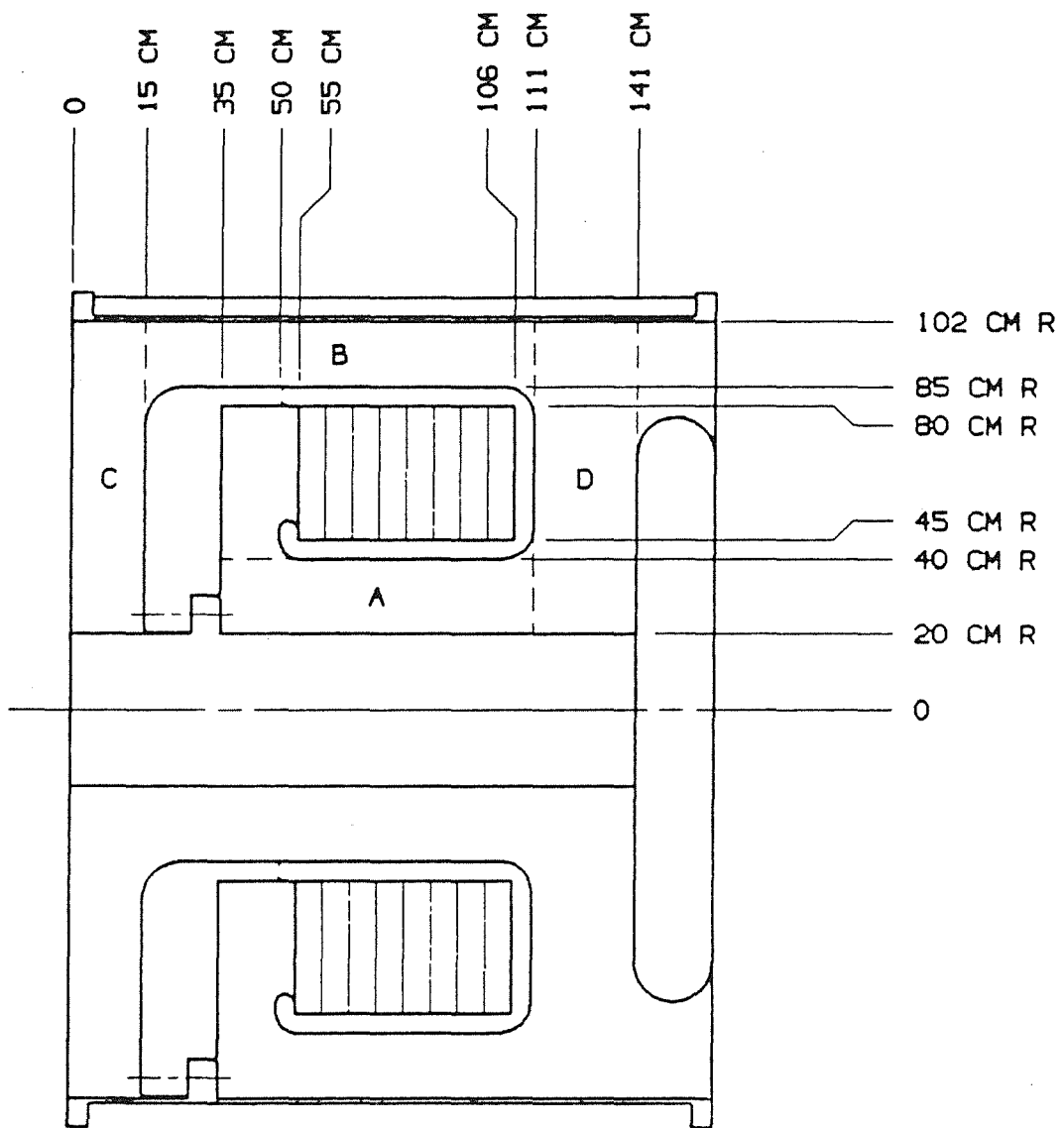


Fig. 2.18. 1.35-2.7 MV transformer dimensions.

the outer conductor. With a potential difference of 1.35 MV,

$$E = \frac{1300 \text{ kV}}{102 \text{ cm} \ln 102/85} = 73 \text{ kV/cm} . \quad (2.12)$$

The breakdown field is

$$F = \frac{0.24}{(0.31)^{0.2} (2\pi \cdot 102 \times 70)^{0.075}} = 134 \text{ kV/cm} . \quad (2.13)$$

The ratio is $73/134 = 0.55$.

The second is the inner corner of the primary winding nearest the CPL. The breakdown field is

$$F = \frac{0.24}{(0.31)^{0.2} (2\pi \cdot 45 \times 2\pi \cdot 10 \times 0.25)^{0.075}} = 162 \text{ kV/cm} . \quad (2.14)$$

With the use of field enhancement curves that apply approximately, the field is estimated at 90 kV, with a ratio of $90/162 = 0.56$.

The primary radial sector connections have to be 20 cm thick and rounded with a 20 cm spacing to have adequate margin against breakdown.

The leakage inductance is calculated from the leakage flux paths using mainly the coaxial inductance formula. Leakage flux is the flux that links only one winding when the primary and secondary have equal ampere turns. In Figure 2.9 the leakage flux paths are split into several regions for calculation:

A _{inner gap}	$L = 2 \times (15 + 70 + 5) \ln 40/20 = 125 \text{ nH}$
B _{outer gap}	$L = 2 \times (20 + 15 + 70 + 5) \ln 102/85 = 40 \text{ nH}$
C _{entrance}	$L = 2 \times 15 \ln 102/20 = 49 \text{ nH}$
D _{exit}	$L = 2 \times 30 \ln 102/20 = 98 \text{ nH}$.

The leakage inductance around the primary sectors is estimated by assuming approximate flux paths as 40 nH. Flux paths A, B, and D link the secondary and translate to the primary by the square of the turns ratio. The total leakage inductance referred to the primary is

$$L_{\text{tot}} = 40 + 49 + (125 + 40 + 98)/4 = 155 \text{ nH}. \quad (2.15)$$

As for the CPL and PFL cores, cooling of the transformer core can be effected by modest velocity oil flow in the region between windings. This also applies to the 5 μ s stage reactor core discussed below.

2.9.4 5 μ s Stage Reactor

A 5 μ s charging time was chosen as about the shortest switching time suitable for an economic primary switch. A shorter time would have been desirable, giving a smaller 5 μ s reactor.

The volt-second requirement at 1.35 MV and early switchout at 80% V-s (as in the case of the CPL switch, discussed in Section 2.3) is

$$V-s = \frac{1.35 \times 10^6 \text{ V} \times 5 \times 10^{-6} \text{ s} \times 0.8}{2} = 2.7 \text{ .} \quad (2.16)$$

The gross length of Metglas required with a stacking factor of 0.65, a flux change of 3.2 T, and a radial build of 0.4 meters is

$$l = \frac{2.7}{3.2 \text{ T} \times 0.65 \times 0.4} = 3.25 \text{ m .} \quad (2.17)$$

The radial field at the center conductor is

$$E = \frac{1350 \text{ kV}}{20 \text{ cm} \ln 60/20} = 61 \text{ kV/cm .} \quad (2.18)$$

This is substantially less than the fields in the Metglas/insulation for the PCS and the output switch. In the oil adjacent to the Metglas, it is only about one-third of the calculated breakdown value.

With an allowance of 20 cm insulation length at the input end, the saturated inductance is

$$L = 2 (325 + 20) \ln 60/20 = 760 \text{ nH.} \quad (2.19)$$

2.9.5 5 μ s Water Capacitor

A length of 102 cm was chosen as the radius of the outer conductor, and 74 cm as the inner conductor radius. The electric field at the positive outer conductor is

$$E = \frac{1350 \text{ kV}}{102 \text{ cm} \ln 102/74} = 41 \text{ kV/cm} . \quad (2.20)$$

The breakdown field is

$$F = \frac{0.23}{(2.1)^{0.333} (2\pi 102 \times 377)^{0.06}} = 82 \text{ kV/cm} . \quad (2.21)$$

The ratio is $41/82 = 0.5$. The impedance Z_o is

$$Z_o = \frac{60}{\sqrt{81}} \ln \frac{102}{74} = 2.14 \Omega . \quad (2.22)$$

Twenty percent additional capacitance was added as a margin for losses. The required transit time is

$$\tau = C Z_o = 9.6 \times 10^{-8} \times 2.14 = 205 \text{ ns} \quad (2.23)$$

$$L = \tau Z_o = 205 \text{ ns} \times 2.14 = 440 \text{ nH} .$$

Since this inductance is distributed, the equivalent for discharge is at most half this, or 220 nH.

The length is 7.6 m. Adding another center conductor inside to get two parallel coaxial lines (one inside the other) gives too high an electric field on the positive innermost conductor. Thus shortening the water capacitor is not possible.

The 5 μs coaxial water capacitor is quite long. It would be desirable to shorten it by adding an inner conductor to give a triaxial construction with two parallel capacitors. The inner conductor would then be positive, which has the lowest allowable electric field. It turns out that the field at the inner conductor cannot be kept low enough.

In a second attempt to shorten the 5 μs water capacitor, the 1.35 - 2.7 MV transformer was moved ahead of the water capacitors, so that the water capacitor ran at 2.7 MV. This saved 5.8 meters on water capacitor length. However, an additional 3.2 meters was required on the length of the 5 μs reactor since its volt-second requirement was doubled. An additional 3.2 meters was required on the 1.35 - 2.7 MV transformer since it now was operating at 5 μs rather than 0.75 μs ; so there was a net length increase plus substantially more Metglas required.

In a third attempt to reduce the 5 μ s water capacitor length, a 675 kV - 1.35 MV transformer was placed ahead of the 1.35 - 2.7 MV transformer. The lower voltage allowed a four conductor coaxial arrangement with three capacitors in parallel, but only saved 0.6 meters on the length of the water capacitor since the total capacitance required is quadrupled. The 5 μ s reactor length was reduced 1.6 meters but required an increase in core radii to meet the saturated inductance requirement, giving a net small increase in volume of Metglas. The additional transformer added 0.8 meters, for a net reduction in length of 1.4 meters. This approach did not appear to offer enough cost benefit to be chosen. Figure 2.19 shows the 5 μ s stage and its connection to the two water PFLs.

2.9.6 Inductance Summary

The allowed inductance for a 0.75 μ s discharge at the 1.35 MV level is

$$L = \frac{t^2}{\pi^2 C/2} = \frac{2 \times (0.75 \times 10^{-6} \text{ s})^2}{\pi^2 9.6 \times 10^{-8} \text{ F}} = 1190 \text{ nH} \quad . \quad (2.24)$$

Two CPL's are in the discharge circuit

$$L = \tau Z = 54 \times 10^{-9} \times 5.4 \Omega = 290 \text{ nH} \quad . \quad (2.25)$$

This has to be reduced by four to get to the 1.35 MV level, by two for two parallel lines, and by two because the inductance is distributed. This gives 18 nH. Adding all the components gives

18	CPL's
220	5 μ s Water Capacitor
760	5 μ s Reactor
<u>155</u>	1.35 - 2.7 MV Transformer
1153	nH

There is a small margin below the 1190 nH allowed.

2.9.7 Charging Transformer

The 100 kV - 1.35 MV step-up transformer will be a conventional iron core pulse transformer, such as are made by Stangenes Industries. They have built a large 1.5 MV,

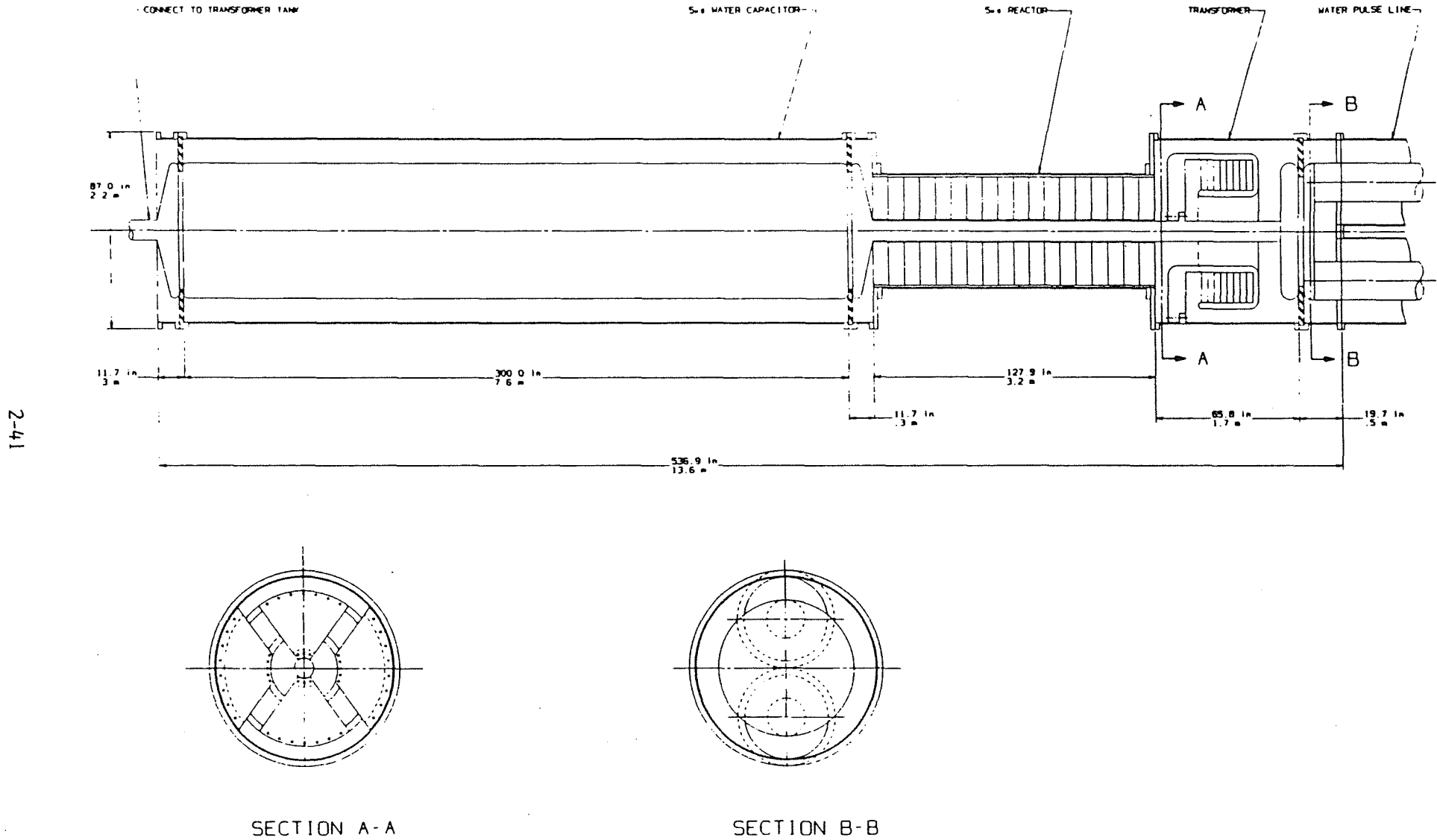


Fig. 2.19. 5 μs stage and its connection to the two water PFLs.

25 μs transformer. Higher voltages are considered developmental. It is expected, based on discussions with Stangenes, that a 30 μH leakage inductance, referred to the secondary, can be achieved. The allowable inductance for one 5 μs stage is

$$L = \frac{(5 \times 10^{-6} \text{ s})^2}{\pi^2 9.6 \times 10^{-8}} = 53 \mu\text{H} . \quad (2.26)$$

Thus 23 μH is available for the other components. The inductance of the 5 μs water capacitor is negligible. Referred to the primary,

$$23 \times 10^{-6} \times \left(\frac{10^5 \text{ V}}{1.5 \times 10^6 \text{ V}} \right) = 102 \text{ nH} \quad (2.27)$$

is allowed for the switch and transfer capacitor.

2.9.8 Switches

EEV CX1812 100 kV hydrogen thyratrons are a possible choice for the switch. Four are used in parallel per transformer, making the peak current 170 kA each. These thyratrons are undergoing development by EEV with a rating objective of 100 kV, 180 kA peak, 2 μs pulse length, di/dt of 4×10^{11} A/s, and 10 - 100 Hz rep-rate. They are currently being tested at Los Alamos National Laboratory. The 5 μs pulse length required for LIBRA is not a significant increase in duty as it is well within the capability of thyratrons, and the 3 Hz rep-rate is low enough that the average current is well within the thyatron's capability.

The thyratrons need to be put inside a coaxial return current housing, and connected with wide parallel plate buswork in order to keep the inductance down to the allowed value.

Thyatron firing jitter can be made less than 0.5 ns (1σ) including the firing circuit. This gets reduced by the square root of the number of thyratrons per module, $(56)^{1/2}$, which gives a negligible thyatron jitter.

The largest timing error will be that due to variations in the input voltage, given by

$$\Delta\tau = \frac{\Delta V}{V} \frac{\tau}{2} . \quad (2.28)$$

For a 0.5 ns timing error, the required regulation is

$$\frac{\Delta V}{V} = \frac{0.5 \times 10^{-9} \text{ s} \times 2}{5 \times 10^{-6} \text{ s}} = 0.02\% . \quad (2.29)$$

This may well be feasible. It is also possible to use compensation circuits that measure the voltage error and correct the timing on a pulse-to-pulse basis, with compensation circuits that measure the accelerator average output timing error over a number of pulses and correct the long-term timing drift. Use of these circuits can considerably reduce the required regulation accuracy.

A less expensive but more developmental switch might be made from 10 series, two parallel ignitrons. The geometry needs to be modified from the conventional ignitron. A small anode-cathode spacing is required, with a center hole in the anode for center firing. Ignitrons have too much variation in firing time, so spark gap firing is required, using a pointed tungsten rod as the pulsed electrode. Studies at Texas Tech have demonstrated several nanosecond 1σ jitter, which is satisfactory when the statistical averaging is taken into account. This geometry keeps the arc spots from getting on the walls, allows higher di/dt and gives faster deionization due to the short spacings.

A standard size E ignitron for capacitor discharge is rated 100 kA peak and 400 C. Ignitrons of size E diameter and special center fired design have been tested at over 500 kA and 200 C.⁽¹¹⁾ The circuit requirement is 680 kA peak and 2.2 C. Special design small size A ignitrons have been tested at 200 kA, 4 C, and di/dt of 10^{11} A/s with a several cycle ringing discharge.⁽¹²⁾ The ringing discharge represents much more severe duty, as there are spots on the anode during the second half-cycle and there is no control on where the arc spots start on the third half-cycle, so they almost certainly start on the walls rather than the mercury pool, where they melt and vaporize wall material. The circuit requirement is 4×10^{11} A/s. The requirements for peak current, coulombs per pulse, and di/dt all appear plausible, given some further development.

The only untested requirement is deionization time at 3 Hz, as all the other testing has been single pulse. Since ionization decay is exponential, there is a good chance it will be satisfactory.

Except for the uncertainty of deionization time, two parallel ignitron sets of center fired design and size E diameter should be adequate. The total of 28 chains of ignitrons used in each module will make the effective diode jitter less than that of an individual switch by a factor of $28^{1/2} \sim 5.3$.

Solid-state switching with thyristors was also considered. Turn-on losses due to slow conduction spread from the gate edge are normally quite high with short pulses and

high di/dt , and limit the allowable peak current. Substantially increasing the gate length and decreasing the gate spacing so the spreading distance is smaller reduces the losses, and using a MOS fired gate keeps the gate current low.⁽¹³⁾ Small devices of this type have been made. It is reasonable to expect that development of power size devices will be done in the next 10-15 years.

If complete elimination of turn-on losses is postulated, temperature cycling due to normal conduction losses determines the current limit.⁽¹⁴⁾ Continued temperature cycling fatigues the silicon until it cracks and fails. The lifetime in number of cycles is given by

$$N = \left(\frac{300}{\Delta T_j}\right)^9 . \quad (2.30)$$

For 10^9 cycles, $\Delta T_j = 30^\circ\text{C}$.

The Westcode R355C/A2W is a fast turn-on SCR with a 1200 volt rating that is commonly used in short pulse applications. Higher voltage devices have higher losses and slower turn-on. The transient thermal impedance⁽¹⁵⁾ of the R355C at $5 \mu\text{s}$ is 10^{-4}°C/W . This gives a peak allowed conduction loss of

$$P = \frac{30^\circ\text{C}}{10^{-4}^\circ\text{C/W}} = 3 \times 10^5 \text{ W} . \quad (2.31)$$

This is an energy per pulse of

$$U = 3 \times 10^5 \text{ W} \times 5 \times 10^{-6} \text{ s} = 1.5 \text{ J} . \quad (2.32)$$

With an estimated snubber and reverse recovery loss of approximately 0.7 J (due to reflected energy), 0.8 J conduction loss is allowed, and this is reached at a peak current of 40 kA. The total number of thyristors needed is then about

$$\frac{680 \text{ kA}}{40 \text{ kA}} \times \frac{10^5 \text{ V}}{10^3 \text{ V}} \times 13 \times 16 = 350,000 . \quad (2.33)$$

The estimated total cost of thyristor assemblies is at least \$500 M, which is clearly uneconomical.

The total current required in the driver switches can be reduced by using additional stages of pulse compression. However, for pulse durations in the range of $10 \mu\text{s}$ or

greater, the device loss is not characterized by a fixed device resistance but more by a fixed voltage drop, so that the energy loss does not decrease much with additional pulse duration. Moreover, the problem of maintaining adequately low module jitter in the presence of fluctuation in the charge voltage of each charger circuit becomes proportionately more severe as the input duration is increased. Thus even with additional stages of pulse compression the use of SCRs appears impossible on both economic and technical grounds.

2.9.9 Transfer Capacitor

Each transfer capacitor bank will consist of 72 polypropylene-foil units rated 50 kV, 1.2 μ F each, connected 2 series, 36 parallel. This assumes continued capacitor development to allow twice the voltage stress of today's commercially available long life, rep-rate capacitors. This assumption is consistent with development plans for capacitors in US military applications.

The bank will be split into four sections, each switched by one thyatron, with 5.5 μ F, 28 kJ per section. Low profile, low inductance bushings will be used.

Connections will be made with very wide, closely spaced parallel plate busbars in order to meet the inductance requirements.

2.10. Configuration

The overall width of the 5 μ s stage and transformer is 6.3 meters. The target chamber size defined by the University of Wisconsin⁽¹¹⁾ gives a minimum distance between the end module cells and the pellet of 8.5 meters which allows 6.5 meters of overall width of the 5 μ s stage and transformer.

No way was found to utilize the space between the pulse lines and still have a functional, accessible layout.

Figures 2.20, 2.21, and 2.22 are conceptual engineering layout drawings showing the configuration of the driver and the reactor chamber.

2.11. Cost Estimate

2.11.1 Introduction and Basis of Estimates

A cost estimate has been performed for the 30 MeV, 4 MJ LIBRA pulsed power reactor driver. Costs have been estimated for 3 and 12 Hz rep-rate systems with ignitron and thyatron switch options. The total costs (1989 dollars) for driver

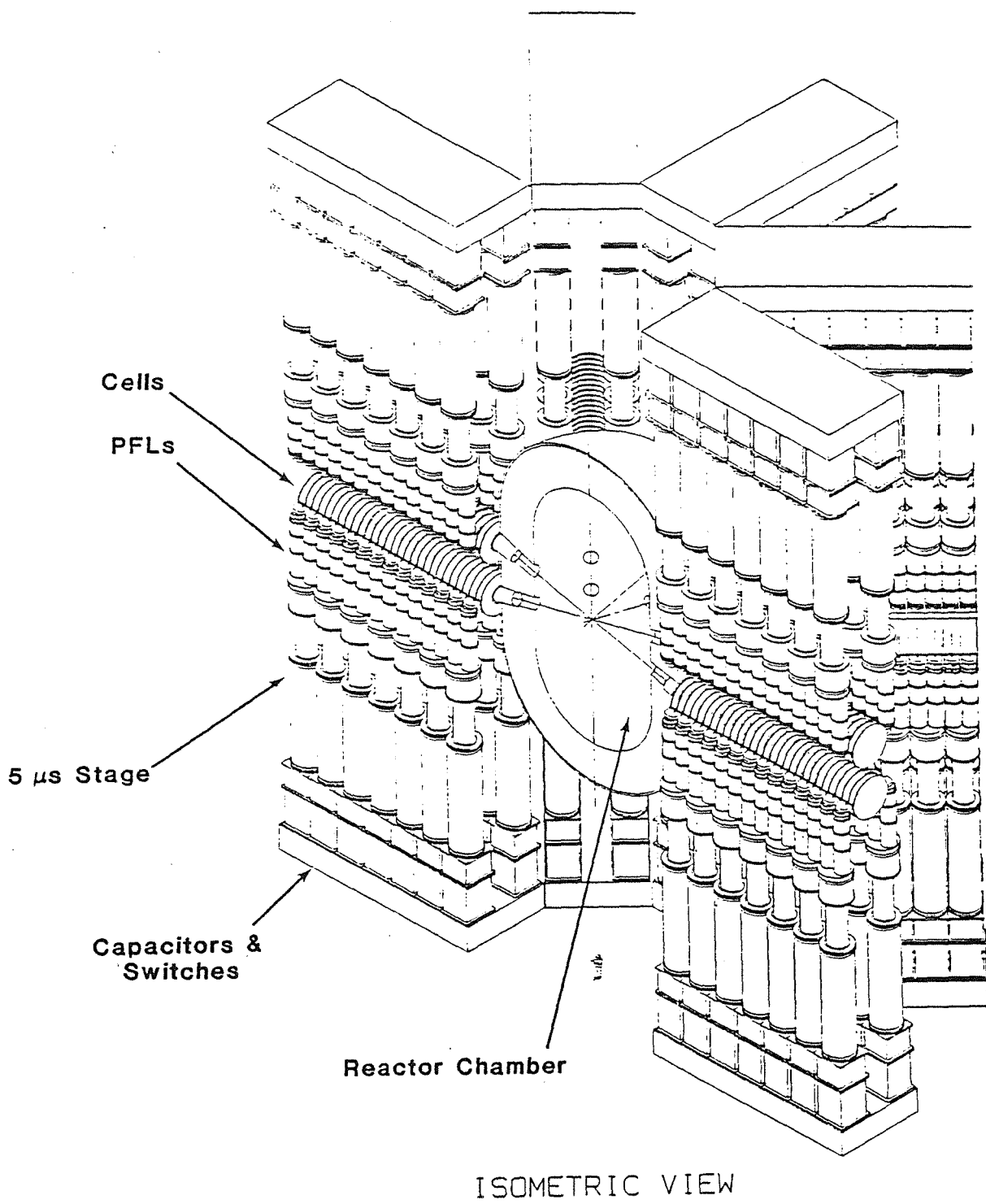


Fig. 2.20. LIBRA 16-module driver conceptual design.

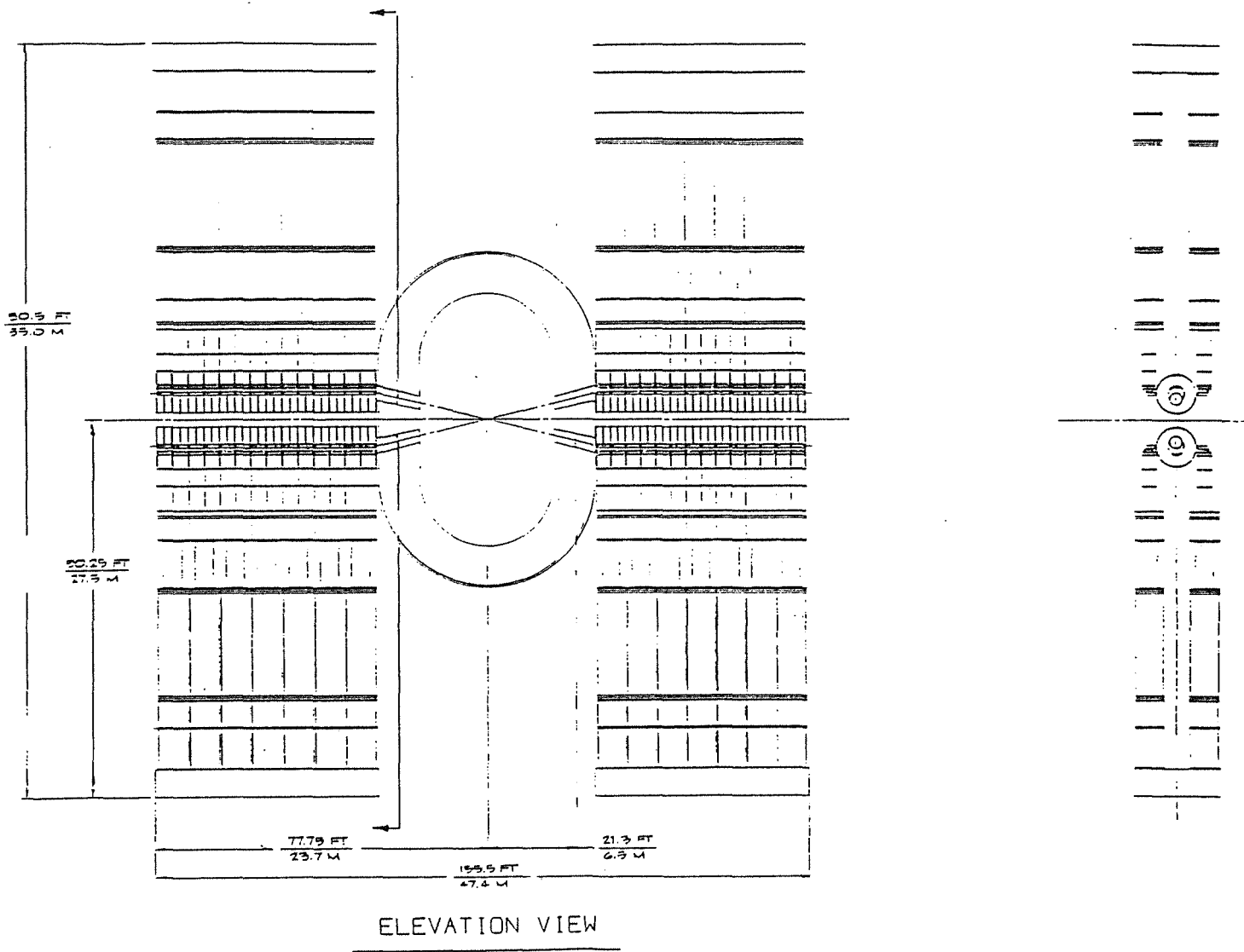


Fig. 2.21. LIBRA 16-module driver conceptual design--elevation view.

2-48

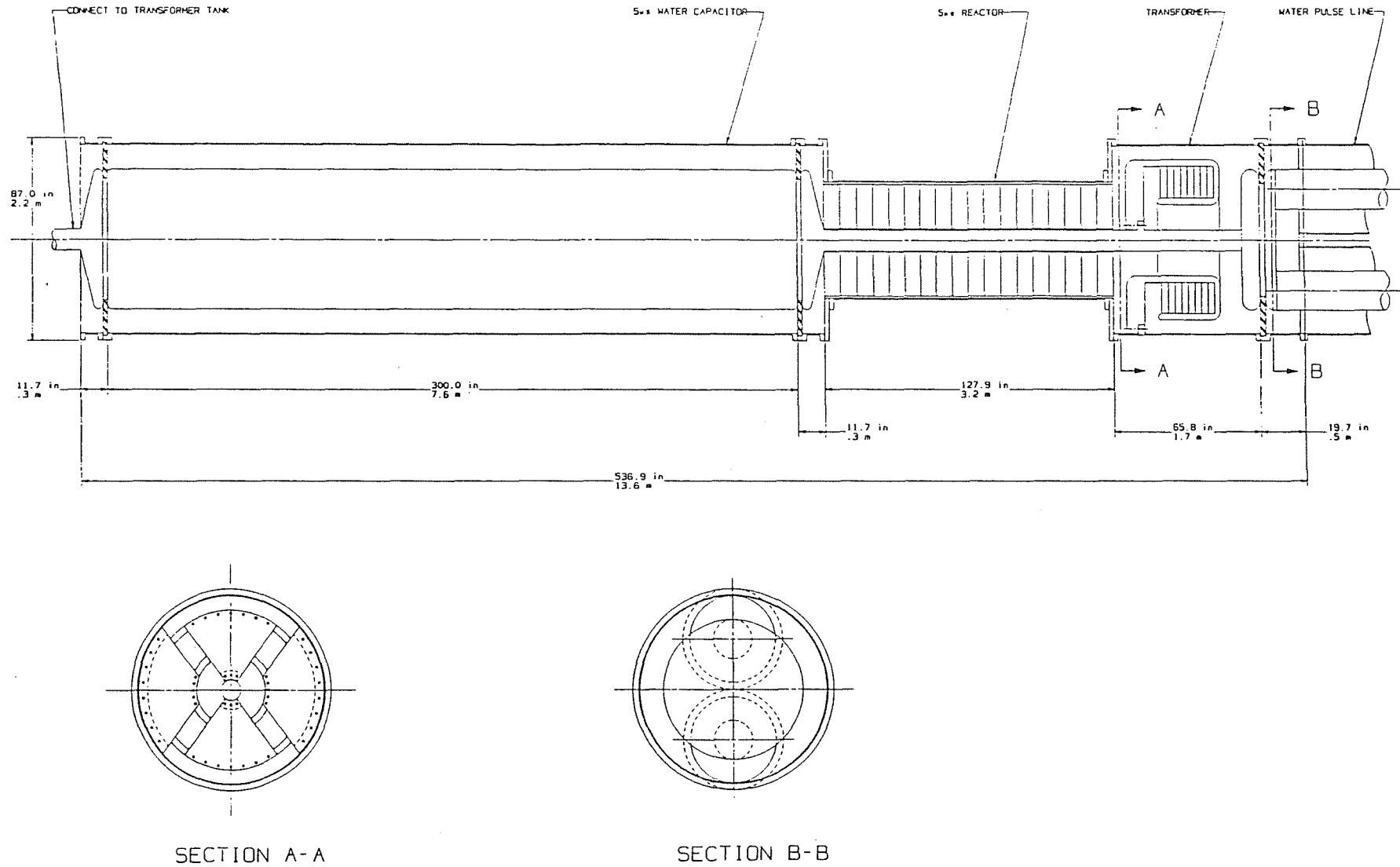


Fig. 2.22. LIBRA 16-module driver magnetic pulse compressor conceptual design.

components are summarized in Table 2.3 for each of the four rep-rate and switch options. On the summary sheet the costs are listed for:

- power supply
- charging system
- magnetic pulse compression (mag)
- accelerator modules
- mag and accelerator cell fabrication tooling and fixtures.

The costs listed include procurement, fabrication and assembly of the listed hardware items. Costs of electrical and mechanical engineering and design are not included. Costs of procurement activities and extensive quality assurance activities are also not included. Hardware items not estimated or included are as follows:

- Ancillary equipment including:
 - vacuum pumping equipment manifolds and piping;
 - oil handling equipment including pumps, manifolds, and piping.
- Structure for supporting driver module hardware, which is assumed to be part of the building.
- Diodes and beam transport hardware.

Unit costs and general assumptions used throughout the cost estimate are listed in Table 2.4. The most uncertain item is the cost of the Metglas cores, which is assumed to be about one-half of the present cost. The manufacturer indicates that the lower costs will be achieved by new and larger production facilities, well before the early twenty-first century date envisioned for LIBRA. Even further reduction may be possible if techniques are developed for coating Metglas with insulation; this would eliminate the Mylar insulation assumed in the present design, and reduce the volume of the magnetic compressor Metglas needed.

Power Supply

Costs for the dc power supplies were based on the cost per watt of recent quotations for large power supplies obtained in other programs.

Charging System

Capacitor costs for the 3 Hz designs are based on manufacturer's quotations for $> 10^9$ shot units, with an assumed increase of 100% in working electric stress that is assumed to be realized as a result of development programs occurring before LIBRA reactors are built.

Table 2.3 LIBRA Driver Module Costs.

		Total Cost k\$			
	<u>Required</u>	<u>3 Hz Thyratron Switches</u>	<u>3 Hz Ignitron Switches</u>	<u>12 Hz Thyratron Switches</u>	<u>12 Hz Ignitron Switches</u>
Power Supply	1	5,000	5,000	20,000	20,000
Charging System (14x16)					
Switch	224	107,900	60,300	107,900	60,300
Capacitors	224	8,064 ⁽¹⁾	same	9,632 ⁽²⁾	same
Capacitor Hardware	224	4,000	→	4,800	→
Transformer	224	21,300		21,300	
Oil Tank	16	1,400		1,600	
		<u>142,664</u>	<u>95,064</u>	<u>145,232</u>	<u>97,632</u>
Mags (14x16=224 total)					
Fabricated Parts	224	107,968	same	117,600	same
Cores (Total)	224	153,216		116,208	
.5 μs Stage		82,880		90,048	
Transformer		24,864	→	26,048	→
.75 μs Stage		40,096		43,456	
OP Switch		5,376		5,824	
Assembly Labor	224	4,480		4,480	
		<u>265,664</u>	<u>265,664</u>	<u>288,288</u>	<u>288,288</u>
Accelerator Modules					
Cell (28x16-448 total)					
Fabricated Parts	448	54,208	same	57,344	same
Cores	448	16,128		16,128	
Cell Supports	448	1,792		1,792	
Assembly Labor	448	2,240	→	2,240	→
Cathode Stalk	16	800		800	
Diagnostics	16	800		800	
Assembly Labor	16	720		720	
		<u>76,688</u>	<u>76,688</u>	<u>79,824</u>	<u>79,824</u>
Accelerator & Mag Fab.	Lot	927	927	927	927
Tooling & Fixtures					
TOTAL:		<u>490,943</u>	<u>443,343</u>	<u>533,731</u>	<u>486,671</u>

(1) 72/set; (2) 86/set

Table 2.4. LIBRA Driver Module Cost Estimate Unit Costs and Assumptions

Aluminum Alloy	\$5.5 \$/kg
Stainless Steel	\$4.4 \$/kg
Steel	\$1.6 \$/kg
Metglas (wound cores)	\$15/kg
Shop Labor Rate	\$60/hr

The thyatron cost of \$75 k/unit was supplied by the manufacturer, EEV. We use this price although for the quantity of 900 needed we would expect a larger reduction from the present price of \$100k in small quantities

The cost of the ignitrons, \$4.5k apiece, is an engineering estimate that the \$1.5k cost of a type E ignitron might be tripled by modifications to achieve nanosecond jitter and low inductance.

The cost of the remainder of the capacitor bank-switch systems was obtained by breaking each design into about ten items and estimating the cost of each.

A quantity cost estimate was obtained from a transformer supplier.

The prices of the oil tank and oil were estimated from the dimensions.

For the 12 Hz designs the capacitor stress was adjusted according to manufacturer guidance to obtain four times greater life. The switches are not limited by average duty and therefore switch costs are unchanged.

Magnetic Pulse Compression

The costs for magnetic pulse compression (mags) are based on a detailed cost estimate for each stage of the pulse compression system including fabricated hardware (parts), diagnostics, and assembly labor, as listed on the engineering estimate sheet for the 3 Hz mag, Table 2.5. The costs shown for each state listed in Table 2.5 are based on a detailed cost estimate of the component parts of the stage. This includes an estimate of raw materials and fabrication hours to produce the component parts of the stage. The costs were calculated using the unit costs shown in Table 2.4 and experience gained from estimating costs of similar equipment.

Costs of some components were minimized by using forgings and through reduction of stock material size and thicknesses. Labor costs were then reduced by having near net size for components compared with machining parts from thick plate or rings formed from bar stock.

Table 2.5. Engineering Cost Estimate - Magnetic Pulse Compressor, 3 Hz Option
Costs Including Learning (95% curve on fab labor)

Item Description	Qty.	Unit	MATERIAL		LABOR				Total Item Cost	Core Total Cost
			Unit Cost	Total \$	Unit Man Hours	Total Man Hours	\$/Hr	\$		
1.1.2 Mag Consisting of	1	ea								
1.1.2.1 5 μs Water Capacitor	1	ea	-	6,160				53,088	114,698	-
.2 5 μs Pulse Charging Switch	1	ea	-	379,424				10,822	390,246	370,260
.3 Transformer	1	ea	-	197,723				45,878	243,601	110,880
.4 .75 μs Water Capacitor	2	ea	4,988	9,976				11,761	21,737	-
.5 .75 μs PCS	2	ea	94,670	189,340				13,705	203,045	178,968
.6 PFL	2	ea	6,318	12,636				13,997	26,633	-
.7 Output Switch	2	ea	15,426	30,852				15,260	46,112	23,672
.8 Transition	2	ea	4,151	8,302				8,554	16,856	-
.9 Cell Feed (bus)	2	ea	4,840	9,680				12,377	22,057	-
.10 Reset Inductor	1	ea	-	13,550				17,026	30,576	-
.11 Reset Inductor	1	ea	-	13,550				17,026	30,576	-
.12 Fasteners, Seals, etc.	1	lot	-	10,000				-	10,000	-
.13 Assembly	1	ea	-	-				20,412	20,412	-
.14 Diagnostics	1	lot	-	<u>10,000</u>				-	<u>10,000</u>	-
TOTAL				946,643				239,906	1,186,549	683,780

2-52

Summary

Cores \$683,780
 Parts 482,357
 Assy. 20,412
 TOTAL \$1,186,549

Labor estimates considered the benefits of quantity production. Initially estimates were made that were appropriate for a single module. A 95% learning curve was applied to the labor for 16 modules, resulting in a 19% savings. This learning curve was selected after the meeting with Sandia and Titan discussed in the next section, Accelerator Modules. The learning curve is weaker than that applied to the cells, because the mag components, such as large cylinders, were considered to benefit less from quantity production. No learning curve was applied to material costs, which were obtained in quantities appropriate for 16 modules.

The cost for diagnostics is only for detector hardware that is an integral part of the mechanical assembly. The cost does not include the cost for data acquisition equipment and associated cables.

Costs for the 12 Hz mag were derived from the detailed estimates for the 3 Hz mag by applying the following factors, designed to reduce electric stresses to increase life by a factor of four.

- Water lines:
 - diameter of inner and outer conductors increased by 8.5%;
 - lengths of lines held constant.
- Metglas cores:
 - volume increased by 8.5% with corresponding increases in diameter of associated metal pieces.

Accelerator Modules

The costs for the accelerator modules are tabulated in the summary (Table 2.3) for cell component parts and assembly, cathode stalks, diagnostics and module assembly labor for the four driver options.

The costs shown for the cells are based on a detailed cost estimate of cell component parts as listed on the engineering estimate sheet for a 3 Hz cell, Table 2.6. The costs shown for each component part in the table are based on a detailed cost estimate of the part. This includes an estimate of raw materials and fabrication hours to produce the cell components. The costs were calculated using the unit costs shown in Table 2.4 and experience gained from estimating costs of similar equipment. The estimates took account of the large quantities of similar items to be fabricated, as discussed in the following two paragraphs.

An initial estimate for the accelerator modules was generated by PSI and subsequently reviewed at a meeting at Sandia Albuquerque with Sandia engineers familiar

with the Hermes III project and representatives of Titan Systems and Titan Spectron. Sam Gibson, Titan Systems, presented the methods widely used in industry whereby costs in large quantities are estimated from costs in smaller quantities by applying a learning curve. In a typical 85% learning curve, when the quantity is doubled the unit cost decreases to 85% because initial learning and tooling costs are amortized over a larger number of parts and because the fabrication process can be re-optimized for the larger number by using more elaborate tooling or a process more appropriate for larger quantities. The unit cost of n parts then decreases as $n^{-\ln.085/\ln2}$ or $n^{-0.234}$.

After comparison of the initial PSI estimate with hardware costs for Hermes-III induction cells, it was determined that the initial estimate was appropriate for the fabrication of a single driver module. In fabricating 16 modules cost savings were projected using the 85% learning curve. This reduction in unit costs was applied only to labor, since materials had already been costed in the quantities needed. This projection resulted in the costs shown in Table 2.6 and in Table 2.3, the total driver cost summaries.

The cost for cell supports shown in Table 2.3 is for brackets which fasten to the cell cavity housing. After the brackets are attached to the housings the cells can be installed on a facility structure, aligned and fastened together to form 28 cell modules.

The cathode stalk cost includes the stalk and mounting hardware to mount the stalk in a module.

The cost for diagnostics is only for detector hardware that is an integral part of the module assembly. The cost does not include the cost for data acquisition equipment and associated cables.

The costs for the 12 Hz accelerator cells were derived from the detailed estimates for the 3 Hz cells by applying the following factors, which are intended to reduce electric stress in order to increase life by a factor of four.

- Cells metal and plastic parts:
 - length increased by 8.5%
 - radius unchanged
 - insulator stack increased by two each insulators and grading rings.
- Metglas cores:
 - unchanged.

Table 2.6. Engineering Cost Estimate (One Cell Including Assembly) - Cell Component Parts, 3 Hz Option
Costs Including Learning (85% curve on fab labor)

Item Description	Qty.	Unit	MATERIAL		LABOR				Total Item Cost
			Unit Cost	Total \$	Unit Man Hours	Total Man Hours	\$/Hr	\$	
1.1.3.1 Cell Consisting of									
1.1.3.1 Cavity Housing	1	ea	-	4,068		207.1	60	12,430	16,498
.2 Front Cover Plate	1	ea	-	5,400		43.8		2,632	8,032
.3 Vacuum Insulator	14	ea	800	11,200		118.4		7,103	18,303
.4 Grading Rings	13	ea	425	5,525		137.4		8,245	13,770
.5 Tie Rods	24	ea	10	240		12.7		761	1,001
.6 Field Shaping Ring	1	ea	-	1,225		29.6		1,776	3,001
.7 Cathode	1	ea	-	19,963		169.6		10,179	30,142
.8 Ground Ring	1	ea	-	1,833		66.0		3,964	5,797
.9 Azimuthal Oil Line	2	ea	1,178	2,356		54.9		3,298	5,654
.10 Diode Rim Feeds	4	ea	100	400		33.8		2,029	2,429
.11 Cell Feeds			included in mag					-	
.12 Metglas Cores	1	set	-	36,232		-		-	36,232
.13 Rear Cover Plate	1	ea	-	5,400		36.4		2,188	7,588
.14 Current Contact Retainer	1	ea	-	280		25.3		1,522	1,802
.15 Anode Disk	1	ea	-	2,593		24.3		1,459	4,052
.16 Input Feed Base	2	ea	100	200		8.4		507	707
.17 Cell Assembly	1	ea	-	-		80.0	60	4,800	4,800
.18 Seals, Contacts, Fasteners	1	lot	-	2,000		-	-	-	2,000
.19 Support Brackets	1	set	-	<u>4,000</u>		-	-	-	<u>4,000</u>
TOTAL				102,915				62,893	165,808

Summary

Cores \$ 36,232
 Parts 124,776
 Assy. 4,800
 TOTAL \$165,808

Mag and Accelerator Cell Fabrication Tooling and Fixtures

The cost for tooling and fixtures includes the cost of fabrication tooling and lifting and handling fixtures required during driver module parts fabrication, assembly and installation. An itemized list of tooling and fixtures was developed in parallel with the cost estimating process for driver component parts. A budgetary cost was assigned to each item resulting in the \$927 k total cost.

2.11.2 Conclusions

The cost of the driver increases only weakly with prf in the 3-12 Hz range, so that the use of a prf closer to 12 Hz will greatly decrease the price per watt of driver power.

The ignitron switched design is substantially cheaper than the thyatron switched design. The use of ignitrons appears feasible, but some development is needed. While it is legitimate to assume that some technology improvement will occur before the reactor is built, the advantage gained here is not important.

The estimates assume the development of cheaper bulk fabrication methods for Metglas cores which make up over one third of the total cost. This assumption appears reasonable. Cost benefits of developing an insulation coated Metglas material have not been assumed. Improved capacitors have also been assumed, but these are a small portion of the cost.

In this estimate, cost reductions assumed from learning curves, or quantity production, amount to less than 10% of the total cost. This is a relatively small adjustment.

Finally, the electrical calculations of section 2.7 indicate that the 26 cell module delivers about 7% more energy at the target in 9 ns than specified. The design costed has 28 cells per module (because the pulse compression system is not consistent with the 26 cell module previously designed) and thus would deliver an additional 8% energy, or 15% more than specified. A design with 28 smaller cells and lower energy pulse lines (or 24 larger cells) would cost less. This cost difference could be considered to roughly cover the cost of one or two additional small modules needed to produce the additional 400 kJ precursor pulse at the pellet.

References for Chapter 2

1. J.J. Ramirez, et al., "The Four Stage Helia Experiment", Proceedings of 5th IEEE Pulsed Power Conference, Arlington, Virginia, June 10-12, 1985, pp. 143-146
2. J.J. Ramirez, et al., "HERMES III - A 16 TW, Short Pulse, Gamma Ray Simulator", BEAMS '88, Proceedings of the 7th International Conference on High-Power Particle Beams, Volume 1, Karlsruhe, Fed.Rep.Germany, July 4-8, 1988, pp. 148-157
3. K.R. Prestwich and M.T. Buttram, "Repetitive Pulsed Power Technology for Inertial Confinement Fusion", 5th Topical Meeting on the Technology of Fusion Energy, ANS, Knoxville, Tennessee, April 26-28, 1983.
4. L.L. Reginato and R.E. Hester, "Pulse Power for ETA/ATA", 16th Pulsed Power Modular Symposium, June 1980.
5. G.B. Frazier, et al., "Performance of Double-Eagle", Proceedings of 5th IEEE Pulsed Power Conference, Arlington, Virginia, June 10-12, 1985, pp. 151-154.
6. B.N. Turman, et al., "PBFA-II, A 100 TW Pulsed Power Driver for the Inertial Confinement Fusion Program", Proceedings of 5th IEEE Pulsed Power Conference, Arlington, Virginia, June 10-12, 1985, pp. 155-161.
7. I.D. Smith, "Breakdown of Transformer Oil", AWRE Note, 10 November 1966 and AFWL Dielectric Strength Note.
8. I. Smith, "Impulse Breakdown of Deionized Water", November 1985 (AWRE Notes; AFWL Dielectric Strength Notes).
9. J.C. Martin, "Fast Pulse Vacuum Flashover", AWRE Note SSWA, JCM/713/157, March 1971; and AFWL Dielectric Strength Note.
10. D.B. Cummings, R. Kihara and K.S. Leighton, "High Current Ignitron Development", 1988 Power Modulator Symposium, pp. 122-127.
11. R.A. Burden, J.W. Gray and A.P. Shulski, "High Current Ignitron Development", 1988 Eighteenth Power Modulator Symposium, pp. 128-132.
12. B.J. Baliga, "Enhancement and Depletion Mode Vertical Channel MOS Gated Thyristors", Electron. Lett., V15, 645-647 (1979).

13. I.L. Somos, L.O. Eriksson and W.H. Tobin, "Understanding di/dt Ratings and Life Expectancy for Thyristors", PCIM, February 1986, pp. 56-59.
14. Data sheet, Westcode TR355C/A2W.
15. D.L. Birx, et al., "Experiments in Magnetic Switching", Proceedings of 3th IEEE Pulsed Power Conference, Albuquerque, NM, 1981, pp. 262-268.

Appendix 2.A - Trade-Off Study

2.A.1 Method

Table 2.A-1 defines the module parameters considered in the 30 MV driver tradeoff study. Their significance can be understood by referring to Figure 2.A-1, which shows the cell design from the previous study of a 20 MV deuterium ion driver.

The 30 MV driver is to be designed to deliver 4 MJ of ions on target. Of these, 3.6 MJ are to be provided in a 9 ns FWHM pulse. This is to be preceded by the delivery of 0.4 MJ over a longer duration. The present tradeoff study considered only the driver modules for the main 3.6 MJ, 9 ns pulse.

The overall tradeoff process is a choice between the desire to keep the module current low to ease problems of diode focussing, channel formation, and beam transport, and the desire to use a large module current to minimize the number of modules and hence the size and cost of the driver. Consideration was given early on to resolving these opposing requirements by driving two diodes and beam transport channels per module, but this approach was rejected because of the difficulty of splitting the magnetically insulated transmission line of the module to feed two diodes.

Thus the energy to be delivered by each module is given by:

$$W = 3600/Nn \text{ (kJ)}. \quad (2.A.1)$$

The ion energy at the target is nominally 30 MV. The diode or module voltage, V_M , may need to be larger than this if the ions lose kinetic energy during transport. The diode voltage must also be ramped during the pulse to bunch the ions during transport.

For a particular set of possible overall driver specifications given by the transport efficiency and the module voltage, the design study examined various choices for the number of driver modules (N). In each case the number of cells per module (n) was varied under a set of well defined assumptions to determine an optimum design. The assumptions were partly based on scaling the 20 MV design. The optimum design was considered to be the smallest diameter module having an inner conductor in the vacuum bore that is a practical size.

The first assumption is that the axial lengths of the outer azimuthal oil line and of the vacuum interface are both the maximum consistent with the length of the cell. The insulator length is proportional to the cell voltage $V (= V_M/n)$. The azimuthal line length is proportional to the cell current I , since the line is designed at the maximum allowable

Table 2.A-1. Definition of parameters

Number of driver modules	=	N
Efficiency between module and target	=	η
Diode energy needed per module	=	W (kJ)
Module voltage	=	V_M (MV)
Number of cells/module	=	n
Cell voltage	=	V (MV)
Module current	=	I (MA)
Pulse duration	=	t (ns)
Insulator radius	=	R (cm)
Metglas core radial span	=	Δr (cm)
Bore outer radius	=	b (cm)
Bore inner radius	=	r_i (cm)
Diode impedance	=	Z (Ω)
Cell length	=	l (cm)

2-60

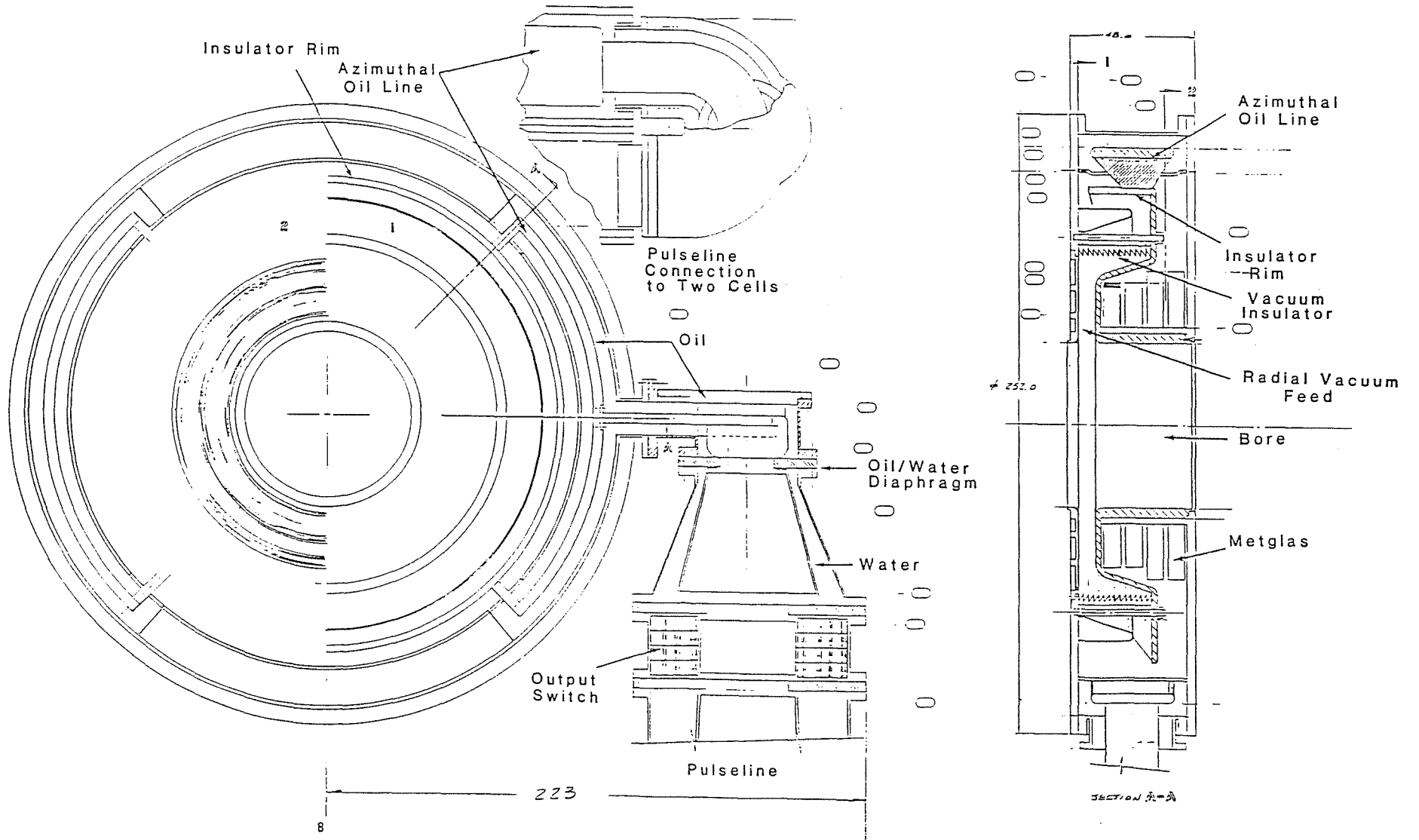


Figure 2.A-1. LIBRA 1 MV induction cell.

electric field and (hence) linear current density. Therefore the ratio of cell voltage to cell current is constant; it has the same 3Ω value used in the 20 MV design.

The second assumption is that magnetic insulation losses in the voltage adder result in the loss of an early portion of the pulse that is proportional to the module length. Since the module length is the sum of the lengths of each cell, which is determined by the insulator length and is thus proportional to voltage, the lost pulse duration is proportional to V_M . For the 20 MV module, the loss was 6 ns. The module energy requirement can therefore be written

$$V_M I (t - 0.3 V_M) = W . \quad (2.A.2)$$

The next assumption concerns vacuum insulator inductance. This is proportional to the cross-sectional area, which is proportional to V^2 , and inversely proportional to the mean insulator radius R . Since the drive impedance is fixed at 3Ω , the L/Z risetime of the insulator is proportional to L ; it is assumed that the risetime is allowed to be a fixed portion of the pulse duration t , so that $L \propto t$; hence $V^2/R \propto t$, or $R \propto V^2/t$. Reference to the cell of the 20 MV design gives

$$R = 3200 V^2/t \text{ (cm)} . \quad (2.A.3)$$

The Metglas isolation core area needed in each cell is proportional to Vt , and its axial length is proportional to V , so that the radial span of the Metglas is simply proportional to t . Referring to the 20 MV design,

$$\Delta r = 25 t/48 \text{ (cm)} . \quad (2.A.4)$$

The outer radius of the Metglas core is assumed to be 15 cm inside the mean insulator radius. Thus the inner core radius, which is the outer radius of the vacuum bore of the module, is given by

$$b = R - 15 - 25 t/48 \text{ (cm)} . \quad (2.A.5)$$

The magnetic insulation criterion for the voltage adder at the diode is assumed to be that the wave impedance of the coax is 1.25 times the diode impedance, so that the

diode current is about 1.2 times the minimum parapotential current of the coax. The diode impedance is

$$V_M/I = V_M/(V/3) = 3 V_M/V . \quad (2.A.6)$$

Hence the inner conductor radius of the voltage adder at the diode (r_i) is given by

$$60 \ln b/r_i = 3.75 V_M/V . \quad (2.A.7)$$

The optimum module design for a given N and n is found by an interactive process that starts with a trial number of cells per module and uses the sequence of equations (2.A.1-6) to determine r_i . If this is much less than 10 cm, the design is considered to be impractical. The number of cells is then decreased by one. This produces a relatively large increase in r_i , owing to a combination of several factors. First, increasing the cell voltage increases the cell current, and both factors require the insulator radius to increase. This increases the outer diameter of the vacuum bore, and simultaneously the increased module current and consequent decreased impedance allow a smaller ratio of b to r_i . Hence r_i increases rapidly as the number of cells is reduced.

The number of cells is reduced until r_i exceeds 10 cm. However, if a number of cells is found that makes r_i almost 10 cm, r_i is scaled up to 10 cm, b is scaled by the same factor, and R is increased by the same amount as b ; this design is adopted if it results in a smaller R (and hence a smaller cell radius) than a decrease in the integer n .

2.A.2 Results

Tables 2.A-2, 2.A-3, and 2.A-4 give the results obtained in the study. In Tables 2.A-1 and 2.A-2, the nominal voltage is 30 MV and the efficiency is assumed to be 50% and 62.5% respectively. In Table 2.A-3, the diode voltage is assumed to be 37.5 MV, anticipating 20% loss of kinetic energy per ion during transport as part of the assumed 50% total energy loss.

In each table, three different numbers of modules (8, 12, and 16) are considered. For the optimum design in each case, the number of cells, cell voltage, module current and pulse duration are stated. The physical parameters of the cells and voltage adder are then listed. Next, several derived quantities that reflect cost are shown. These include the total volumes of the modules, to which the cost of the modules is estimated to be

Table 2.A-2. Cell and module sizes for various numbers of modules
(30 MV diode, 50% efficient transport)

No. of modules	16	12	8
No. of cells/module	26	24	21
Current (kA)	385	416	476
Pulse length	48	57	72
Cell radius	138	138	141
Insulator radius	88	88	91
Bore radii:			
Outer	51	45	38
Inner	10.0	10.0	10.3
Module length (m)	14.4	14.4	14.4
Total volume (m ³)	1380	1035	720
Module efficiency (%)	81	84	87.5
Total no. of cells	416	288	168
Ramping factor (6 meter transport)	1.3	1.4	1.6

Table 2.A-3. Cell and module for various numbers of modules
(30 MV diode, 62.5% efficient transport)

No. of modules	16	12	8
No. of cells	27	25	22
Current	370	400	454
Pulse length	14.4	14.4	14.4
Cell radius	145	144	147
Insulator radius	95	94	97
Bore radii:			
Outer	59	53.5	49
Inner	10.9	11.2	12.4
Module length	14.4	14.4	14.4
Total volume (m3)	1530	1125	780
Total no. of cells	432	300	176
Module efficiency (%)	82	85	87
Ramp factor	1.25	1.35	1.5

Table 2.A-4. Cell and module sizes for various number of modules
(37.5 MV diode, 50% efficient transport)

No. of modules	16	12	8
No. of cells	25	23	21
Current	400	435	476
Pulse length	41.3	48.1	61.7
Cell radius	168	163	156
Insulator radius	118	113	106
Bore radii:			
Outer	75	73	59
Inner	10.7	12.1	11.4
Module length	18	18	18
Total volume (m ³)	2550	1800	1100
Total no. of cells	400	276	168
Module efficiency (%)	73	76.5	82
Ramp factor	1.3	1.4	1.5

roughly proportional; this cost may amount for one-third to one-half the total driver cost. The cost of the pulse line system that drives the modules increases with the number of pulse lines, which is proportional to the total number of cells. The cost of the pulse lines and charging system increases with total energy, which changes because the efficiency varies as the pulse duration varies, on account of the lost duration. The efficiency is listed in the tables. Finally, the tables give the voltage ramp factors needed to bunch the ions during 6 m transport.

By examining the tables, it is seen that as the number of modules increases, the size of each module either decreases very little or actually increases. The total volume and hence cost of the module system is thus roughly proportional to the number of modules. Further, the total number of cells and pulse lines always increases significantly more rapidly than in direct proportion to the number of modules, and the efficiency decreases as the module number increases, so that the cost and complexity of the pulse lines and charging system increases.

Thus to minimize cost (and complexity) it is highly desirable to choose the minimum number of modules consistent with transport considerations. The only limitation indicated in the tables from the driver standpoint is that as the module number decreases, the bunching factor and the magnitude of the voltage ramp needed to achieve it increase. In the results given, the bunching factor required to give a 9 ns pulse at the target never exceeds eight, and judging by the results obtained with the 20 MV driver this is achievable. However, voltage ramp factors greater than about 1.4 were not achieved in the 20 MV design, and may entail loss in pulse line efficiency. Thus it may not be desirable to reduce the number of modules below about twelve.

The tables also show that when a larger transport efficiency is assumed it is desirable to decrease the number of modules in proportion, otherwise module volumes increase. Also, increasing the diode voltage from 30 MV to 37.5 MV increases total module volume by 60-80% and reduces module efficiency by about 10%.

3. LIGHT ION DIODE

3.1 Introduction

3.1.1 Choice of Configuration for LIBRA Diodes

Ion beam diodes convert short-pulse, high-voltage electrical energy to ion beams. In the LIBRA design, there are a total of eighteen ion diodes. Sixteen of these provide the main pulse of energy to drive the target, while two provide the long, low "foot" of the power pulse.

The diodes for LIBRA use an externally applied magnetic field to insulate the flow of electrons from the cathode to the anode. This class of diode is referred to as "applied-B," and has demonstrated the highest beam brightness in experiments. Applied-B ion diodes were invented at Cornell University in the early 1970s.⁽¹⁾ They have been used extensively for ion generation experiments at Sandia since 1979 on the Proto-I, PBFA-I, and PBFA-II accelerators.

During the past two years, extraction ion diode efficiencies have been increased in experiments from 50 percent to 70 percent. Extraction ion diodes focus the ion beam outside the diode, unlike "barrel-shaped" ion diodes, such as those used in experiments on the Particle Beam Fusion Accelerator II (PBFA-II) at Sandia National Laboratories. The topology of the two diode types is similar. In the case of extraction diodes, however, providing uniform magnetic insulation requires the use of magnetic field coils in the anode structure. Development of the theory of uniform magnetic insulation for extraction diodes was the key to efficiency improvements.

3.1.2 Choice of Ion for LIBRA

The ion source, located on the anode of the diode, determines the type of ion accelerated by the diode. Singly-ionized lithium was chosen for this design for several reasons. (1) The optimal range in the target is about 40 mg/cm². In the range of a few tens of MV for the accelerator, singly ionized lithium provides the best coupling to the target (30 MeV). (2) Singly-ionized lithium has a closed shell electronic configuration. Ionizing lithium once is fairly easy (5.8 eV), but ionizing it again (75 eV) is very difficult. This property should permit a very pure Li⁺¹ beam to be generated. (3) Preheat of the target fuel by ions with greater penetrating power can be avoided through control of the lithium beam's canonical momentum. Preheat by protons, which could conceivably come from hydrogen contamination of the source, can be prevented by using a relatively high pressure (> few Torr) stripping region at the entrance to the gas-filled transport region to alter the canonical momentum of lithium by stripping it from the +1 ionization state to the +3 ionization state while leaving the proton canonical momentum unchanged. In this configuration, the lithium can be focused onto beam transport channels, while the protons miss it. (4) Liquid lithium metal is an excellent heat transport fluid, and offers the possibility of making a highly repetitive anode surface. The anode surface is the key element in a repetitive diode.

3.1.3 Repetitive Operation of LIBRA Diodes

Development of a repetitive ion diode for a power reactor has been a key issue in the light ion program, and is an important technical issue in the LIBRA design. The central problem is electron energy deposition at the anode. Electrons which cross the applied magnetic field can deposit approximately 20 percent of the diode average power on the anode. At low voltage, the electron energy deposition observed in experiments has caused anode surface ablation, due to the short electron range. At high voltage, however, the electron range increases greatly. At 30 MeV, for example, the electron range in lithium is 11 cm. The larger range makes it possible to design a porous anode containing liquid lithium used both as the ion source and the heat transfer fluid. The energy deposition by electrons can, in fact provide the heat necessary to maintain the diode at the high working temperature needed for lithium. Such a diode can be self-cleaning and repetitively operable.

3.1.4 Developments Pushing Technologies for Application in LIBRA

Recent developments in the light ion ICF program brighten the prospects for power generation using ion drivers: (1) On PBFA II, the focal intensity in a proton beam has been increased substantially. In March 1989, a proton beam was focused to an intensity exceeding 5 TW/cm² with more than 180 kJ in the focus. These values broke the 1984 record of 1.5 TW/cm² on Proto I with 5 kJ in the ion focus. (2) The linear induction voltage adder technology used in the LIBRA design has been demonstrated in the Hermes-III accelerator. The accelerator has exceeded 20 MV, will be used for development of extraction ion diodes and beam transport. (3) The emphasis provided by the Department of Energy on designs and preparation for a Laboratory Microfusion Facility (LMF) is encouraging the development of extraction ion diodes and beam transport techniques for propagation over distances of 1-2 meters. (4) The effort going into lithium ion source development and lithium beam experiments for PBFA II is providing a technology base for repetitive lithium diodes for power production.

3.1.5 Summary of Diode Design for LIBRA

The diode design chosen for LIBRA is a uniform-magnetic-insulation extraction applied-B ion diode. It uses a coaxial geometry for flow of electromagnetic power to the diode. It has externally driven magnetic field coils in both the cathode and anode housings. It uses a liquid lithium ion source to provide a singly ionized lithium beam. The lithium is contained in a stainless-steel fritted substrate. The source is an electrohydrodynamically driven (EHD) source, with ion emission occurring at field-enhanced cusps of lithium. Rarefied lithium plasma is injected into the diode prior to the diode power pulse to ensure rapid beam generation. A supersonic gas puff is used in the beam focal region to provide neutralized beam transport and charge stripping of Li⁺ to

Li^{+3} for canonical momentum separation of the lithium accelerated in the singly ionized state from protons and from lithium accelerated in doubly and triply ionized states. The diode is driven by a programmed voltage pulse ramped from 25 MV to 35 MV for a transit-time bunching factor of 4.4. A schematic drawing of the diode showing its important features is given in Fig. 3.1.

3.1.6 Organization of the Remainder of Chapter III

The remainder of this chapter presents the ion diode design for LIBRA in detail. The organization is as follows: In Section 3.2, we discuss the basic ion diode requirements. Section 3.3 covers the theoretical design of the diode, using results of analytic diode theory and general diode design principles. Section 3.4 includes a comprehensive list of the diode and ion beam parameters. In Section 3.5, we describe the electrohydrodynamic ion source chosen for LIBRA. Section 3.6 presents some of the important physics of ion diode operation. Section 3.7 covers issues important in repetitive operation of the diode. In Section 3.8, we summarize the level of technology extrapolation for the LIBRA diode by direct comparison with present experiments. In the Appendix, information on alternative repetitive diode concepts is discussed. The diode design chosen for LIBRA was an outgrowth of a workshop on repetitive ion diodes held at Sandia during the LIBRA study.

3.2 Basic Ion Diode Requirements

3.2.1 Summary of Basic Requirements for LIBRA Diodes

The set of ion diodes must provide very high power ion beams which have the correct ion range in the target, the correct power time history (pulse shape), adequate total energy, adequate spatial symmetry, adequate temporal synchrony. Additionally, they must not produce a significant level of preheat in the DT fuel of the target, or compression of the fuel on a higher adiabat will become more difficult.

3.2.2 Ion Range in the Target

From target design studies, the optimal ion range in the target is about 40 mg/cm^2 . This range determines the optimal lithium ion energy, which is about 30 MeV. Some variation of the ion range in the target is permissible. As the target heats up, the ion range at constant ion energy is decreased by a factor of about two. In order to compensate for the reduction in ion range, it is desirable to have the ion energy increase with time throughout the power pulse. An increasing ion energy can also provide transit-time ion bunching in the propagation channel. The range of lithium ion energies desired is about 25-35 MeV.

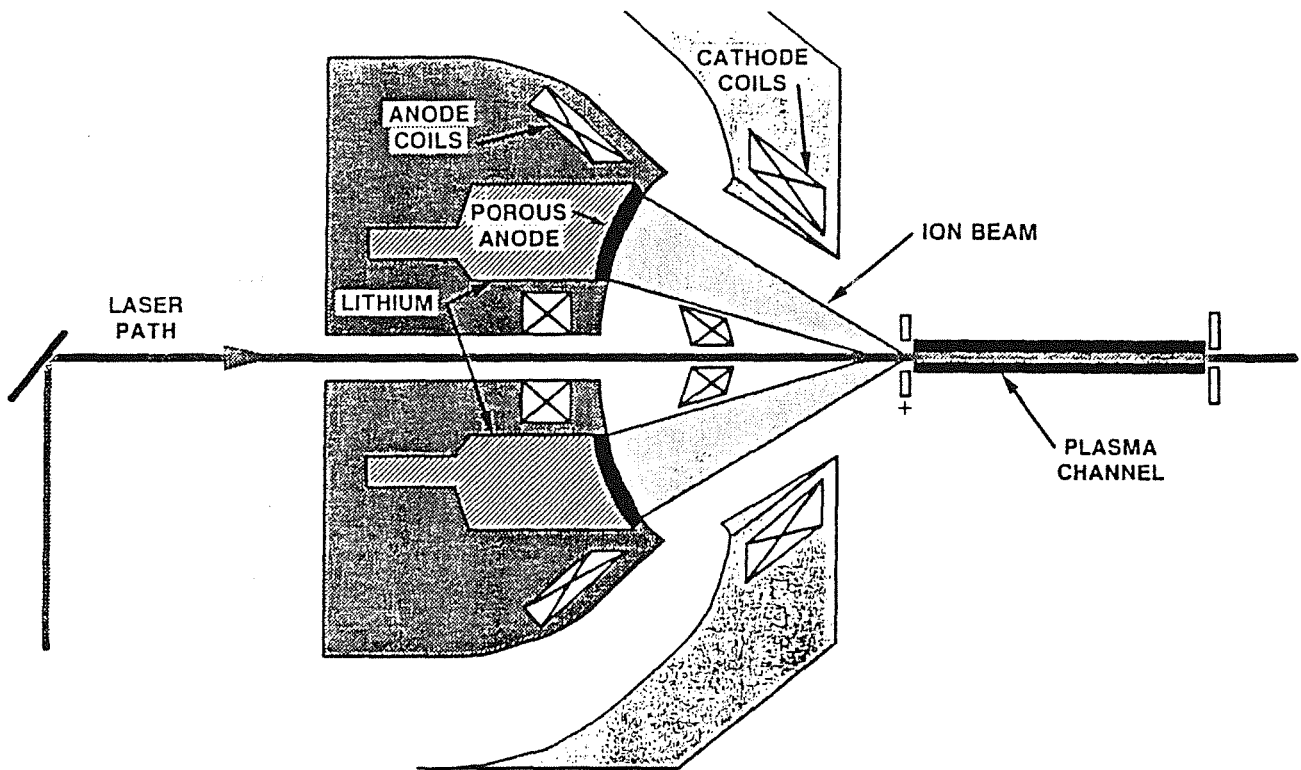


Figure 3.1. Schematic of Li ion diode.

3.2.3 Transit-Time Ion Bunching

The voltage ramp consistent with the span of ion energies through the pulse for acceptable range (25-35 MV) will compress the ion pulse during propagation in the plasma channels by a factor of 4.33. The 39 ns power pulse at the ion diode results in a 9 ns ion beam power pulse at the target. The shape of the ion pulse at the target is determined by the shape of the voltage pulse applied to the diode.

3.2.4 Pulse Shape at the Target

The pulse shape at the target has been prescribed by the target design. The features of the pulse shape are required to keep the DT fuel in the target on a low adiabat, enabling minimum energy to provide an adequate implosion for high gain. Approximately 10 percent of the energy delivered to the target is in a long, low "foot".

3.2.5 Adequate Total Energy

The total energy required by the target (4 MJ input for 320 MJ yield), in combination with the required pulse shape and propagation channel considerations, sets the number of ion diodes at 18 and the ion energy provided by each of the high-power diodes at about 360 kJ. Two low-power diodes provide the early part of the pulse shape, while sixteen high-power diodes provide the main pulse at the target.

3.2.6 Adequate Spatial Symmetry and Temporal Synchrony

Adequate spatial symmetry for the high-power portion of the power pulse is provided by sixteen beams. The synchrony required by the target is less than 1 ns side-to-side, so the diode turn-on time must be controlled to about this same level.

3.2.7 Ion Source Purity

With singly ionized lithium accelerated in the anode-cathode gap, the only ions which can act as a source of preheat for the DT fuel in the target are protons, or lithium accelerated in multiple charge states. The magnetic field configuration chosen for the diode shown schematically in Fig. 3.2, permits lithium to be stripped at a well-defined spatial location (shown as the gas puff). This field configuration results in zero canonical angular momentum in the transport region for the lithium which is accelerated as Li^+ , but non-zero canonical angular momentum for protons and lithium accelerated in +2 or +3 charge states. The Li^+ is therefore focused on the channel entrance, while the protons, Li^{+2} , and Li^{+3} miss the channel entrance and are not propagated to the target. In this way, preheat is avoided, and the only constraint put on lithium purity is an

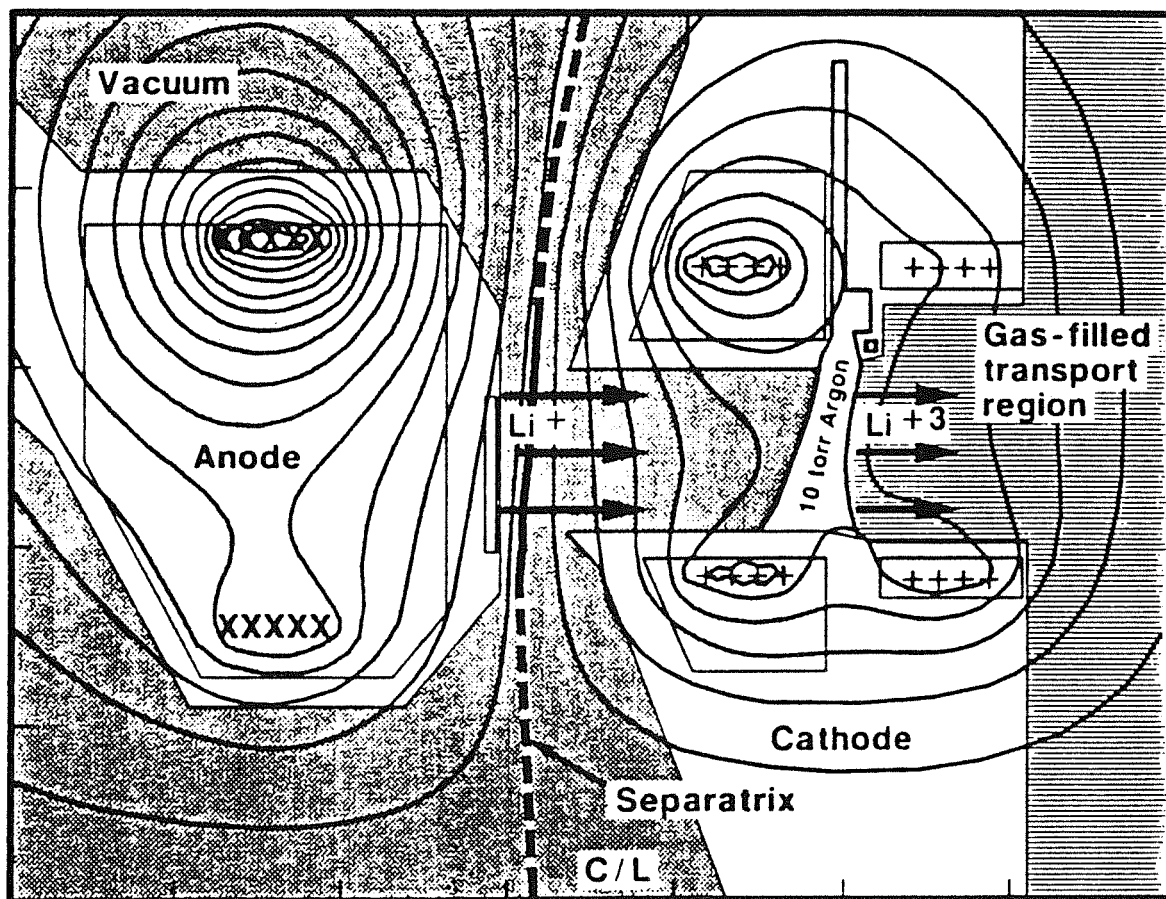


Figure 3.2. Magnetic field profiles for Li ion diode.

efficiency-based one. This was somewhat arbitrarily chosen to be 90 percent, so the basic requirement on lithium beam purity at the source is 90 percent.

3.2.8 Diode Repetition Rate

The diode repetition rate was chosen solely on the basis of the design target yield and the desirable reactor power. The rate of 3 Hz was selected.

3.3 Ion Diode Design

The design of the ion diode is determined by several factors. These include, in approximate order of importance, the following items:

- a. ion beam focusing limitations
- b. ion current density level desired
- c. virtual cathode dynamics in the diode
- d. adequate level of magnetic field uniformity, including edge effects
- e. level of critical magnetic field for insulation of electrons.

Each of these is discussed briefly below.

3.3.1 Ion Beam Focusing Limitations

The relation between diode outside radius (r_o), beam focal radius at the plasma channel entrance (r_c), ion microdivergence at the anode (θ), and the angle of incidence of the ions at the target (θ_{macro}), can be derived from Liouville's theorem:

$$r_o < r_c \cdot (\theta_{macro}/\theta_{micro}) .$$

With $\theta_{micro} = 5$ milliradians, a 51.9 cm diode focal length, and θ_{macro} set by propagation channel considerations to be 100 milliradians, the outside diode radius must be less than 8.4 cm. Since ion beam propagation in the plasma channels becomes more difficult as the injection angle increases, we have chosen to keep the diode radius smaller, at a value of 5.2 cm.

3.3.2 Ion Current Density Level Desired

The level of ion current density may have some effect on beam focusability, but the limitations are not known. As the current density increases, the level of power brightness in the diode (the product of voltage and current density divided by the square of the ion microdivergence) increases. Brighter beams should be more easily focusable. On the other hand, it is possible that instabilities in the virtual cathode contribute substantially to ion microdivergence, and electron density increases with ion current density. Experimental results on Proto I and PBFA II have, so

far, shown best focusing at an ion current density at the anode of about 5 kA/cm². For these reasons, this value was chosen as the design value for the LIBRA diodes. We adjusted this parameter slightly downward to keep the diode design consistent with the driver design. The effect of this was to increase the margin of safety.

3.3.3 Virtual Cathode Dynamics in the Diode

The space-charge-limited current density for a diode accelerating Li⁺ is given by

$$J_{\text{scl}} = 20.6 (V^{3/2}/d^2) \text{ A/cm}^2 \text{ for } V \text{ in MV, } d \text{ in cm.}$$

In the calculation of space-charge-limited flow, the electrons are confined to a thin region near the physical cathode. For a uniform density of electrons in the AK gap, the ion current density is 5.55 times higher than the value above. When motion of the virtual cathode closer to the anode is taken into account, the current density can be higher still, and it depends on the ratio of the operating diode voltage to V_c , the critical voltage for insulation of electrons. The value of V_c is calculable on the basis of an electron Larmor radius being about the size of the AK gap, given the applied magnetic field. For a diode operating at about one-half the critical insulation voltage,⁽²⁾

$$V_{\text{op}} = 0.5 V_c, \text{ and}$$

$$J_i = 8.5 J_{\text{scl}} = 175 (V_{\text{op}}^{3/2}/d^2) \text{ A/cm}^2 \text{ for } V \text{ in MV, } d \text{ in cm.}$$

The size of the physical anode-cathode gap, d , calculated using this equation, with $J_i = 5000 \text{ A/cm}^2$ and $V_{\text{op}} = 30 \text{ MV}$, is

$$d = 2.40 \text{ cm.}$$

The calculated size of the dynamic gap, g (the distance between the ion-emitting surface and the virtual cathode, where the potential is zero), is smaller than the physical AK gap by the square root of 5.55/8.5, or 0.81, so

$$g = 1.94 \text{ cm.}$$

3.3.4 Adequate Level of Magnetic Field Uniformity, Including Edge Effects

Since electrons are tied to magnetic field surfaces in the diode, the uniformity of ion current density is determined directly by the uniformity of the magnetic insulation field. Azimuthal

symmetry is generally quite good, but radial uniformity is more difficult to establish. With magnet coils in both the cathode structures and in the anode structures, there is great flexibility for tailoring an optimal field through the use of different numbers of windings, different current levels, and magnetic field shimming by selecting different materials and thicknesses. Good magnetic field uniformity can certainly be obtained if the radial extent of the diode is greater than the calculated dynamic gap. A good choice would be to have the radial extent of the diode twice the dynamic gap, or

$$r_o - r_i = 2 g .$$

Then

$$r_o - r_i = 3.88 \text{ cm} .$$

This value, taken with the total ion current per diode (317 kA, established during the LIBRA study by assuming the target energy requirement of 4.0 MJ was provided by sixteen main beams and two lower energy beams), and the ion current density of 5 kA/cm², provides the following outer and inner radii for the diode:

$$3.14 (r_o^2 - (r_o - 3.88 \text{ cm})^2) = I_i/J_i .$$

So

$$\begin{aligned} r_o &= 5.19 \text{ cm, and} \\ r_i &= 1.31 \text{ cm} . \end{aligned}$$

3.3.5 Level of Critical Magnetic Field for Insulation of Electrons

The mechanical structure of the diode must be able to support the magnetic forces associated with applied-B diode operation. The critical magnetic field for insulation of electrons in the diode is given by:

$$\begin{aligned} B_{\text{crit}} &= 0.34 (V_{\text{op}}^2 + V_{\text{op}})^{1/2}/d \text{ tesla,} \\ &\text{for } V_{\text{op}} \text{ in MV, } d \text{ in cm.} \end{aligned}$$

With $d = 1.94 \text{ cm}$, and $V_{\text{op}} = 30 \text{ MV}$,

$$B_{\text{crit}} = 4.3 \text{ tesla.}$$

The magnetic field which must be applied to the diode with $V_{\text{op}} = 0.5 V_{\text{crit}}$ is

$$B_{\text{app}} = B_{\text{crit}}/0.5 = 8.6 \text{ tesla.}$$

3.4 Ion Diode Parameters

A descriptive summary of ion diode and ion beam parameters elected for the primary diodes is given in Table 3.1. The key difference between the two low-level diodes used for the 39 ns precursor pulse in LIBRA is the lack of voltage programming at the diode for temporal compression of the pulse to 9 ns at the target. By retaining a reasonably flat voltage pulse at the diode for the two early beams, the early part of the required pulse shape is provided to the target. The LIBRA diode design is shown in Fig. 3.3.

3.5 Electrohydrodynamic Ion Source

3.5.1 Physics of Electrohydrodynamic Source Operation

Electrohydrodynamics (EHD) is the electrical analog of magnetohydrodynamics (MHD). For an EHD ion source, the electric field at the anode is sufficiently strong that the electric tension exceeds the restraining force of surface tension, resulting in instability growth, and eventually, cusp-like perturbations. As the surface perturbations grow in the direction of the electric field, the electric field at the tip of the perturbations increases, and the instability continues. Singular growth is observed in fluid simulations of EHD after about three growth times.⁽³⁾

3.5.2 Growth Rates and Wavelengths for EHD Sources

The growth rate for an EHD instability is proportional to the cube of the electric field, E , so that the time required for the surface to develop a two-dimensional array of cusp-shaped ion emitters goes as E^{-3} . The wavelength of the instability is proportional to E^{-2} , so the areal density of emitters goes as E^2 . For an electric field of 15 MV/cm, the time required for ion source formation and the beginning of ion emission (three growth periods) is one nanosecond. The wavelength of the dominant instability, or separation of ion emitters, is 0.2 microns. This provides 2.5×10^9 emitters/cm², so that a current density of 5 kA/cm² requires only 2 microamperes per emitter. This level is routinely provided by single-point steady-state EHD emitters at present in liquid metal capillary sources.

3.5.3 Scale Tests of EHD

Experiments of EHD growth have been performed with water and methanol in the presence of steady-state electric fields of 15-40 kV/cm. Unstable growth of surface perturbations with wavelengths in the 0.1 - 1 cm range, predicted by EHD theory, was observed in the experiments. The scaling from the level of 40 kV/cm to the level of 15 MV/cm is still a large extrapolation, but several basic aspects of the EHD theory including viscosity were confirmed.

Table 3.1. Ion Diode and Ion Beam Parameters

Ion Diode Parameters

Ion diode type	Externally applied-B
Ion diode configuration	Coaxial extractor
Acceleration method	Single gap
Anode-cathode gap, d	2.40 cm
Calculated dynamic gap	1.94 cm
Anode outside radius, r_o	5.19 cm
Anode inside radius, r_i	1.31 cm
Critical insulation voltage, V_c	50 MV
Operating voltage, V_{op}	25-35 MV (nom. 30 MV)
Critical B field at 30 MV, B_c	4.3 tesla
Applied-B field, B_{app}	8.6 tesla
Impedance, Z	76 ohms
Input diode current, I_d	385 kA
Input diode power, P_d	11.5 TW
Input diode energy per pulse, E_d	450 kJ
Electron energy per pulse, E_e	97 kJ
Pulse repetition rate	3 Hz
Average electron power loss, P_e	290 kW _{th}

Ion Beam Parameters

Ion type during acceleration	Li ⁺
Ion type during transport	Li ⁺³
Ion kinetic energy, E_i	25-35 MeV (nom. 30 MeV)
Voltage ramp magnitude	30%
Ion beam current at diode, I_i	308 kA
Design ion beam current density, J_i	5.0 kA/cm ²
Actual ion beam current density, J_i	3.9 kA/cm ²
Ion microdivergence, θ	5 mrad
Ion beam pulse width at diode, τ	39 ns
Ion beam power (per beam)	9.23 TW
Ion beam power (16 beams)	148 TW
Ion beam energy (per beam)	360 kJ
Ion beam energy (16 beams)	5.76 MJ
Design allowable ion beam power brightness, β	6000 TW/(cm-rad) ²
Actual ion beam power brightness, β	4670 TW/(cm-rad) ²
Ion beam focal power density	24.0 TW/cm ²

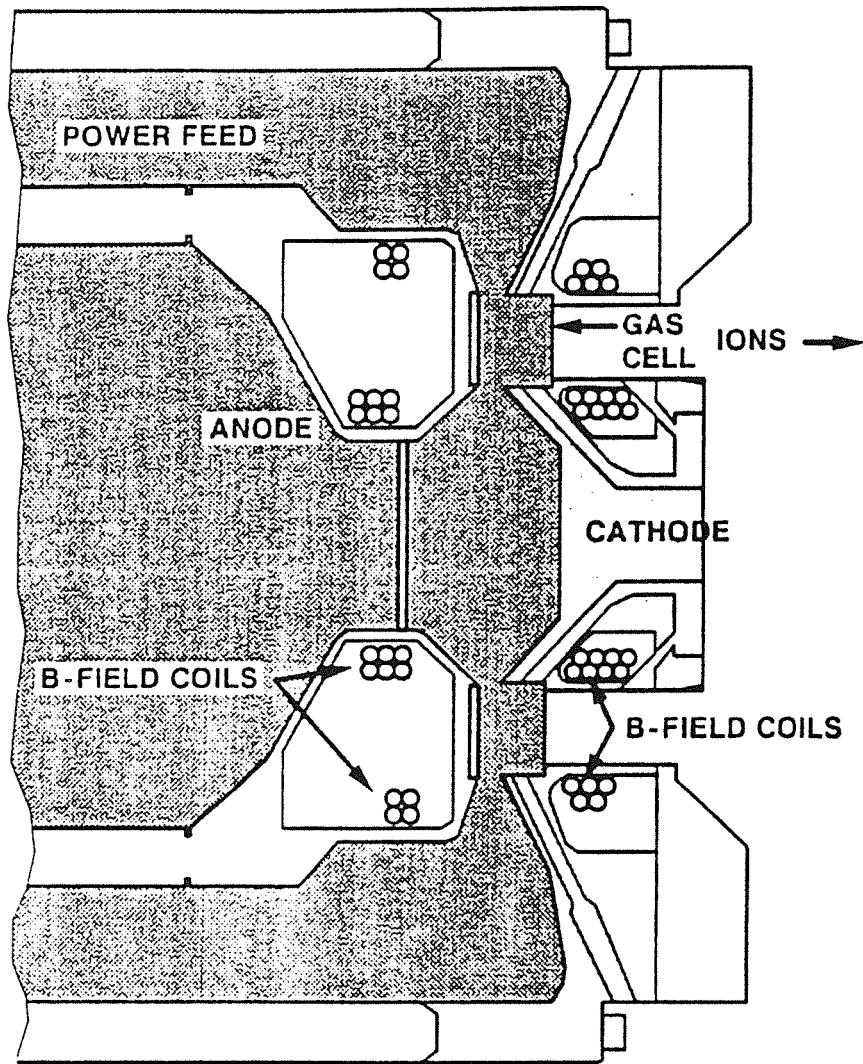


Fig. 3.3. LIBRA diode design.

3.5.4 EHD Ion Source Divergence

The divergence of the ion beam produced by an EHD ion source can be calculated from the electric field distribution in the region of the ion-emitting cusps. The calculated divergence depends on the spacing of emission sites. For a separation of 1.0 micron, the divergence calculated from geometric effects is about 3 milliradians. When small-angle scattering in the gas puff region is included, the divergence will increase by less than one milliradian.

3.5.5 EHD Anode Substrate

The anode substrate chosen is a fritted stainless steel or Inconel. The porosity of the substrate is about 50%. This material is saturated with liquid lithium, and allows the front surface to be replenished after each shot. As shown in Fig. 3.1, the lithium is contained in a reservoir behind the fritted anode. Circulation of the lithium allows the energy deposited in the lithium from diode electrons to be removed efficiently.

3.5.6 Inherent EHD Ion Source Repetitive Capability

The major source of energy loss in the diode is electrons. The range of electrons at 30 MeV in lithium is about 11 cm. With the porous anode substrate about 1 cm thick, nearly all of the electron energy is deposited in the lithium in an "in-depth" fashion. This feature allows volumetric (rather than surface-dominated) heating of the lithium, which is also used as the diode heat transfer fluid. Surface erosion takes place only in the liquid lithium front surface of the anode. This arrangement provides inherent repetitive capability for the diode.

3.6 Physics of Ion Diode Operation

3.6.1 Principal Stages of Diode Behavior

The important physics of ion diodes can be found in four temporal phases of the diode pulse. The initial conditions form the first state. Prior to arrival of the power pulse at the diode, the magnetic field geometry must be established with reasonable precision. The nonuniformity of the magnetic field in the diode acceleration gap must not exceed about 3-5%. The magnetic field separatrix must be controlled to within about 1 mm for high power density focusing of the ion beam. The second stage involves the formation of the electron sheath and movement of the virtual cathode closer to the anode for highly enhanced ion flow. The third stage occurs near peak power. In this stage, the ion current must rise to the appropriate level at the planned voltage so that bending of the ion beam in the externally applied and self magnetic fields of the ion beam during acceleration is counteracted by the vertical contour of the anode. The final phase occurs after peak power, but while the power is still being delivered to the beam by the diode. In this phase, the

impedance of the diode must be reasonably well controlled, or focusing will be decreased by time-dependent bending in the self-magnetic field.

3.6.2 Analytic Theory of Applied-B Ion Diodes

The analytic theory of applied-B ion diodes was developed by Desjarlais.⁽⁴⁾ The theory describes a limiting voltage, V_* , at which the current diverges. The limit is determined by diamagnetic compression of the virtual cathode up against the anode. The value of V_* is between 60% and 75% of the critical voltage for electron insulation, V_{crit} , depending on the electron density distribution in the electron sheath. A sheath which conforms closely to the virtual cathode is termed a "superinsulated" sheath. A sheath which has a uniform electron density is termed a "saturated" sheath. To date, the best theoretical agreement with experiment has been obtained by using a saturated sheath.

3.6.3 Analytic Theory of Extraction Diodes

The analytic diode theory of Desjarlais describes the operation of applied-B diodes in either barrel geometry (as on PBFA II) or in extraction geometry. The operating point analysis made possible by the theory allows determination of the voltage and current at peak power when driven by an accelerator with known impedance. The theory has been compared to extraction diode results on the MITE accelerator by Slutz.⁽⁵⁾ He found excellent agreement with the theory over more than a factor of ten variation in diode current density.

3.6.4 Uniform Insulation of Extraction Diodes

In extraction applied-B diodes, the insulating magnetic flux varies between anode and cathode directly with radius along the height of the anode emitting area. This is unlike the situation for barrel-geometry diodes, where the flux is constant along the anode height. In order to operate at highest efficiency, the magnetic insulation of the diode must be uniform. Otherwise, higher current density will be present where the insulation magnetic field is lower. In order to provide uniform insulation a diode must be used which allows magnetic field to diffuse into the anode.⁽⁶⁾

3.6.5 Coaxial vs. Triaxial Diodes

In simulating the behavior of extraction diode experiments on the MITE accelerator, Slutz used the 2.5 D electromagnetic particle-in-cell code MAGIC to study coaxial and triaxial diode geometries. In triaxial geometry, power flows into the diode from the inside (small radius) as well as the outside (large radius). In coaxial geometry, power flows into the diode from only one side (typically the outside). At the outset, it was believed that the triaxial geometry would be more efficient, since electrons leaving the diode gap would always see a magnetically insulated feed. Simulations, however, showed that the coaxial geometry gave highest efficiency. These results

were subsequently confirmed by experiment. The simulations showed that a properly designed coaxial diode has a better insulated feed configuration than a triaxial diode can have. In the triaxial diode, only one-half of the current is present in each feed, and the self-magnetic insulation, which is determined by current flow, is poorer. In addition, a triaxial diode has twice the length of total power feed, so the total losses are higher. These results were very encouraging, since coaxial diodes have the simpler geometry.

3.6.6 Summary of Optimal Diode Features

The analytic theory of applied-B diode behavior developed over the past two years has provided a quantitative design capability proven by experiment. The optimal features of the diode design for LIBRA determined using this understanding are the following:

Uniform insulation	for	Good beam quality and uniform current density
Coaxial geometry	for	Highest efficiency and greatest simplicity
Low-density plasma fill	for	Rapid diode transition to enhanced current flow
Liquid metal source	for	Long impedance lifetime

3.7 Repetitive Diode Behavior

3.7.1 Liquid Anodes for EHD Ion Sources

The anode for the LIBRA diode consists of a porous steel substrate which is saturated with liquid lithium. The lithium is contained in a reservoir behind the substrate. In laboratory experiments, liquid lithium is "wicked" into the porous substrate and forms a pure lithium layer at the surface. The substrate pore size of frits which have been tested with lithium ranges from 0.2 microns to 20 microns. For LIBRA, the pressure of the lithium in the reservoir and the pore size chosen will determine the rate of flow of lithium to the front surface of the anode.

3.7.2 Electron Deposition at Anode

Electron deposition at the anode was a persistent cause of anode "blow-off" and damage on low-voltage light ion machines. In particular, PBFA I diodes, which ran at 1 - 2 MV and 5 - 10 MA, showed substantial electron damage after each shot. However, the damage to PBFA II diodes, which run at 5 - 10 MV and 3 - 4 MA, is not as great as for PBFA I, even though the power and power densities are much higher. The key difference is in the electron range. Nearly all of the energy lost in an ion diode is carried by electrons. At low energy, the electron deposition is at the anode surface since the range is short. At high energy, the electron deposition can be through the bulk of the anode since the range is long.

3.7.3 Liquid-Cooled Anode

At the 30 MV voltage for the LIBRA diodes, the electron range is large, and deposition of the electron energy is "in-depth" in nature. The range of a 30 MeV electron is about 11 cm in lithium, allowing the electrons to pass through the anode substrate and deposit their energy in a lithium reservoir. The lithium in the reservoir is circulated to remove lost power from the diode.

3.7.4 Liquid-Cooled Cathode

A small portion of the total ion energy may be lost to the cathode. Since the range of lithium ions is about 40 mg/cm^2 at 30 MeV, ions can penetrate only 8 microns into the cathode surface. The front surface of the cathodes can be protected from the ion energy by being covered with liquid-lithium-saturated porous material. Cooling of the cathodes is then transpirational in nature. The power loss level at the cathodes is expected to be very small with suitable choice of anode shape, and no active pumping of coolant is anticipated to be necessary.

3.7.5 Diode Cleanliness at High Temperature

The 3 Hz shot rate, the anode temperature (above 300°C), and the bulk of lithium in the diode region are important to diode cleanliness. The lost electron power will maintain the lithium temperature at an adequately high level for EHD source operation. The amount of lithium available provides a sink for impurities, such as hydrogen, which could contaminate the beam if allowed to accumulate at the anode. Above 300°C , the solubility of hydrogen in liquid lithium is high. The geometry in the region of the channel entrance and the cavity wall precludes a direct line-of-sight from target debris to the diodes. Without a line-of-sight for debris, with differential pumping, and with the lithium source hotter than the surrounding area, condensation of target debris on the anodes should not be a problem, and diode cleanliness can be assured.

3.7.6 Diode Average Power Levels

At 3 Hz, with 484 kJ for each of the main diodes, the design power level is 1450 kW. The ion power produced is 1160 kW. The power lost in electrons is 290 kW, and is the power which must be removed by cooling the diode region. This is roughly the amount of power generated by a 400 horsepower engine, and it requires a similar level of cooling.

3.7.7 Pulsed Magnetic Field Coils

The diode magnetic fields must be pulsed on a time-scale of one-half to several milliseconds. It is unlikely that this pulse width can be provided by superconductors, but the energy which is invested in the insulation magnetic fields can be returned to a capacitor bank after each pulse by proper choice of circuit elements. Although a design has not been done for a repetitively pulsed magnetic system, the efficiency of such a system is anticipated to be fairly high for a "ring-in, ring-out" circuit.

3.7.8 Isolation of Diode from Cavity

Isolation of each diode from the cavity is necessary because of the different operating pressures. At shot time, the background density in the diode acceleration gap must be less than about 10^{12} cm^{-3} , while the density of helium in the cavity is $3.6 \times 10^{18} \text{ cm}^{-3}$. This can be achieved by a combination of rapidly rotating vanes and differential pumping. With one vane rotating at 3 Hz and another rotating at 60 Hz, the channel aperture will be open for the required duration at the correct repetition rate.

3.8 Level of Technology Extrapolation

The design levels of applied-B ion diodes for a number of light ion accelerators are shown in Table 3.2. The table shows the level of technology extrapolation in each of the key diode parameters.

Table 3.2

<u>Parameter</u>	<u>LIBRA</u>	<u>LMF</u>	<u>PBFA II</u>	<u>HERMES</u>	<u>SABRE</u>	<u>HELIA</u>	<u>MITE</u>
Voltage (MV)	30	30	30	20	10	3	1
Total Ion Current (kA)	317	1000	3500	580	200	200	170
Source Area (cm ²)	80	600	1000	290	100	100	80
Current Density (kA/cm ²)	5	2	3.5	2	2	2	2
Power (TW)	12	36	100	12	2	0.6	0.2
Impedance (ohms)	76	25	7	28	40	12	5
Energy (kJ)	387	1300	1500	350	80	20	8
Impedance Lifetime (ns)	80	80	40	40	40	40	40
Divergence (mrad)	5	6	12	8	12	20	20
Power Brightness (TW/(cm ² -rad ²))	6000	1700	730	630	135	15	5

3.8.1 Extrapolation from Diodes on PBFA II

The PBFA II diode is the most powerful diode tested to date. Its design level of voltage is 30 MV, and it has been operated at 10 MV in experiments so far. Total ion current at the level of 8 MV is typically 2000 kA. Current densities at the anode have exceeded 5 kA/cm², by using ion sources with smaller heights than 10 cm. Although the diode is still under development, it has provided more than 700 kJ in ions. The best ion divergence obtained so far has been 14 mrad. The extrapolation from PBFA II to the LIBRA diode is primarily in ion divergence, and consequently, power brightness.

3.8.2 Extrapolation from Diodes on MITE, HELIA, SABRE, and Hermes III

The diodes for MITE, HELIA, SABRE, and Hermes III form a progression of extraction diodes designed for increasing power and energy levels. The diodes have already been fielded on MITE and HELIA, and the parameters shown in the table were achieved. The SABRE diode will be tested during 1990-91, and the Hermes III diode will be tested beginning in 1991. Inspection of the parameters for Hermes III and LIBRA show a very close comparison. The Hermes III diode has comparable energy, power, and divergence, but has higher current, and lower voltage.

3.8.3 Extrapolation in Voltage

The LMF, PBFA II, and Hermes III diodes are closest to the level needed for LIBRA. The tests on PBFA II at 15-30 MV and on Hermes III at 15-20 MV will answer the most important questions of diode voltage scaling.

3.8.4 Extrapolation in Current and Current Density

Current densities higher than 5 kA/cm² have been used on PBFA II and MITE by decreasing the ion emitting area of the anode. In these experiments, ion beam uniformity was better than that seen at lower current density. The unresolved question in scaling of current density is the possibility of increased instability in the electron sheath which might increase divergence. Further experiments on PBFA II and particle simulations using the 3D electromagnetic particle-in-cell code QUICKSILVER⁽⁷⁾ are expected to resolve this question.

3.8.5 Extrapolation in Power per Diode

The power level delivered to an individual ion diode on PBFA II has already exceeded the level required for LIBRA.

3.8.6 Extrapolation in Energy per Diode

The energy level delivered to an individual ion diode on PBFA II has already exceeded the level required for LIBRA.

3.8.7 Extrapolation in Diode Impedance

The LIBRA diodes operate at an impedance higher than any tested to date. The key issue with high impedance diodes is the insulation of the power feeds to the diode. Since magnetic insulation is provided by the current carried by the line, the insulation of such lines becomes more difficult as impedance increases; i.e., as the voltage is increased and the current is decreased. While many of the most important questions will be answered by Hermes III experiments, an extrapolation in diode impedance by a factor of three from Hermes III to LIBRA will still be necessary since the LIBRA diodes operate at such a low current.

3.8.8 Extrapolation in Power Brightness

Diode power brightness is defined as the product of voltage and ion current density divided by the square of the ion divergence. Power brightness is the most important factor in ion beam focusing. PBFA II and Hermes III are expected to have comparable diode power brightness, but the scaling to LIBRA is still large. The high power brightness of PBFA II is obtained by having large voltage and current density, while that of Hermes III is obtained by having a smaller ion divergence. The combination of V and J from PBFA II with the lower divergence of Hermes III would provide a power brightness much closer to that needed for LIBRA. Experiments on PBFA II with much lower divergence will be possible if one of the three fully engineered lithium sources which will be tested on PBFA II can provide a reduced divergence beam.

3.8.9 Extrapolation in Power Intensity at Focus

The power intensity at the beam focus is proportional to the diode power brightness, the fraction of ions in a focusable species, and the fraction of total solid angle subtended by the ion emitting area. For separate beams, the amount of beam overlap also determines power intensity at the target. The power density at the diode focus required for LIBRA is 24 TW/cm². Experiments on PBFA II have demonstrated a power intensity of about 5.4 TW/cm² with protons, averaged over the surface of a 6 mm diameter target. The scaling with lithium beams to and beyond the level required for LIBRA will be demonstrated on PBFA II.

3.8.10 Extrapolation in Ion Divergence

A small ion divergence is one of the most important elements in achieving high brightness ion beams. The power brightness and focusability are inversely proportional to the square of beam divergence. A beam divergence of 14 milliradians has been obtained with proton beams on PBFA II. This level was achieved with an epoxy-in-groove surface flashover source. The lithium sources under development for PBFA II have much finer spatial scale and should provide lower divergence ion beams. Scaling to lower divergence lithium beams will be tested most thoroughly on PBFA II and SABRE.

3.8.11 Extrapolation in Diode Repetition Rate

Repetition rate is the area of the greatest extrapolation. Although diodes using liquid lithium for an EHD ion source are to be tested on PBFA II, and are being designed for SABRE, Hermes III, and LMF, they are all single-shot diodes. While repetitive capability may be there, it will not be tested on these accelerators.

References for Chapter 3

1. R. Dreike, C. Eichenberger, S. Humphries, and R.N. Sudan, J. Appl. Phys. 47, 85 (1976).
2. M.P. Desjarlais, "Theory of Applied-B Ion Diodes," Phys. Fluids B 1, 1709 (1989).
3. A.L. Pregonzer and B.M. Marder, J. Appl. Phys. 60, 3821 (1986).
4. M.P. Desjarlais, Phys. Rev. Lett. 59, 2295 (1987).
5. S.A. Slutz, submitted to J. Appl. Phys.
6. S.A. Slutz and D.B. Seidel, J. Appl. Phys. 59 (8) (1986).
7. D.B. Seidel, W.A. Johnson, R.S. Coats, T.D. Pointon, and J.P. Quintenz, in preparation.

4. LIGHT ION BEAM TRANSPORT

4.1 Introduction

Preformed plasma channels are used in the LIBRA concept to propagate the light ion beams over a distance of 6.6 meters. This propagation length of several meters allows the time-of-flight bunching and pulse shaping that is required for successful implosion of ICF targets. A stand-off distance has the added advantage of protecting the diode and target chamber first wall from the x-ray flux or the blast wave generated by the target explosion.⁽¹⁾ In the plasma channel concept, large electrical discharges, guided by laser preionization, rarify the channel and form ion confining azimuthal magnetic fields.

The target chamber design for LIBRA is shown in Fig. 4.1, where one can see the position of the ion diodes and the target. The channels enter the target chamber in two cones, 35° above and below the horizontal plane bisecting the target. For each channel, there is a 4.5 meter channel to return the discharge current that leaves the target chamber through the top. The channel parameters are listed in Table 4.1. The energy and power flow in the LIBRA beam propagation system is shown in Fig. 4.2.

Table 4.1 Parameters for LIBRA Channels

Number of beam channels	16+2
Number of return current channels	16+2
Channel length	6.6 m
Channel radius	0.5 cm
Beam ion	30 Mev Li ⁺³
Confining azimuthal magnetic field	27 kG
Average channel mass density	$< 5 \times 10^{-6} \text{ g/cm}^3$
Target chamber gas	$3.55 \times 10^{18} \text{ cm}^{-3}$ helium
Time delay between discharge current pulses	1 microsecond
Laser beam diameter	4 mm

The plasma discharge channels are guided through a background gas by laser beams. Lasers preionize paths in the gas that high voltage discharges then follow. In the LIBRA channel concept, laser-guided discharges form these plasma channels in a 3.55×10^{18} atoms/cm³ helium background gas. The discharges force the flow of electrons from an

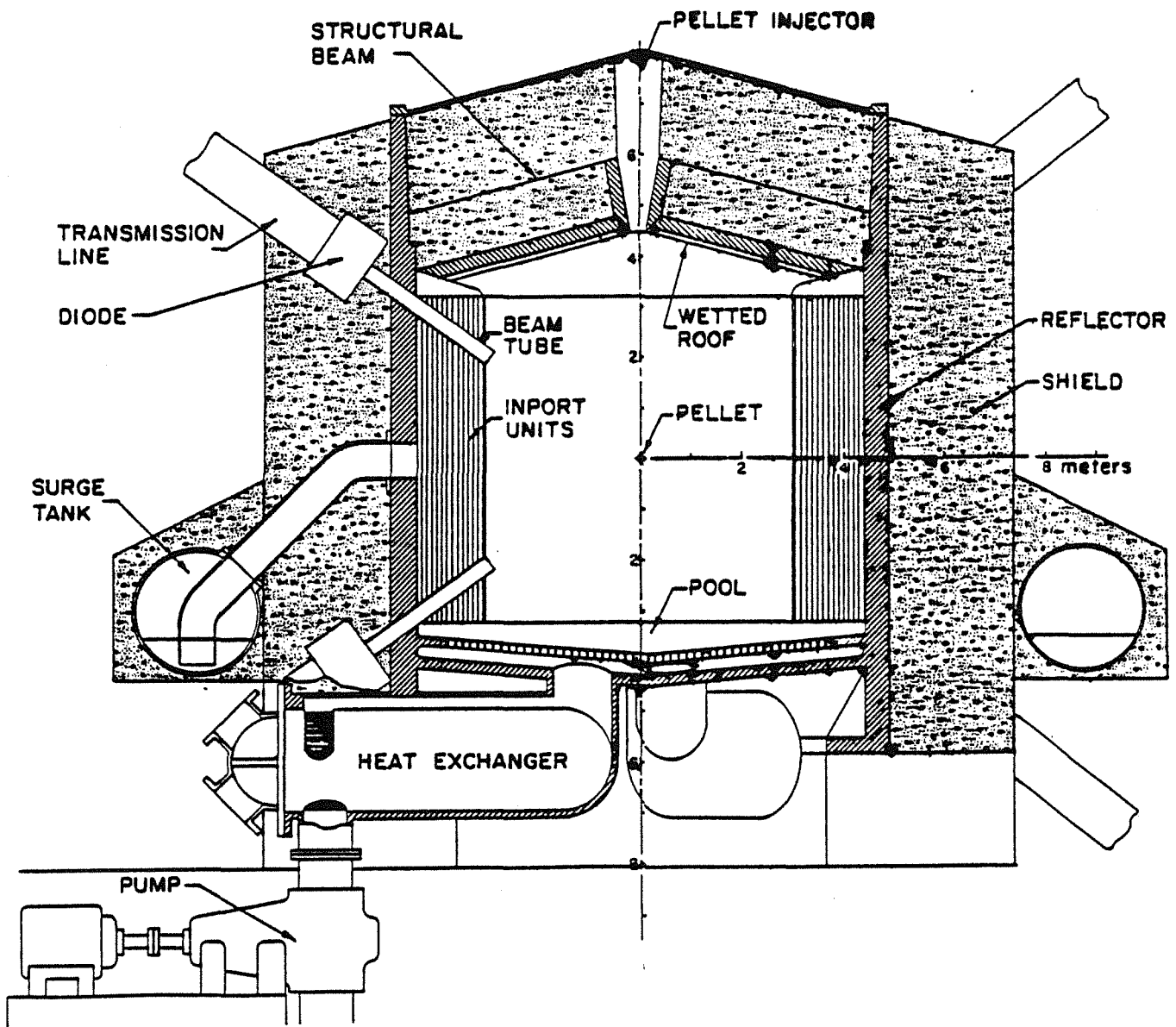


Fig. 4.1. LIBRA target chamber design

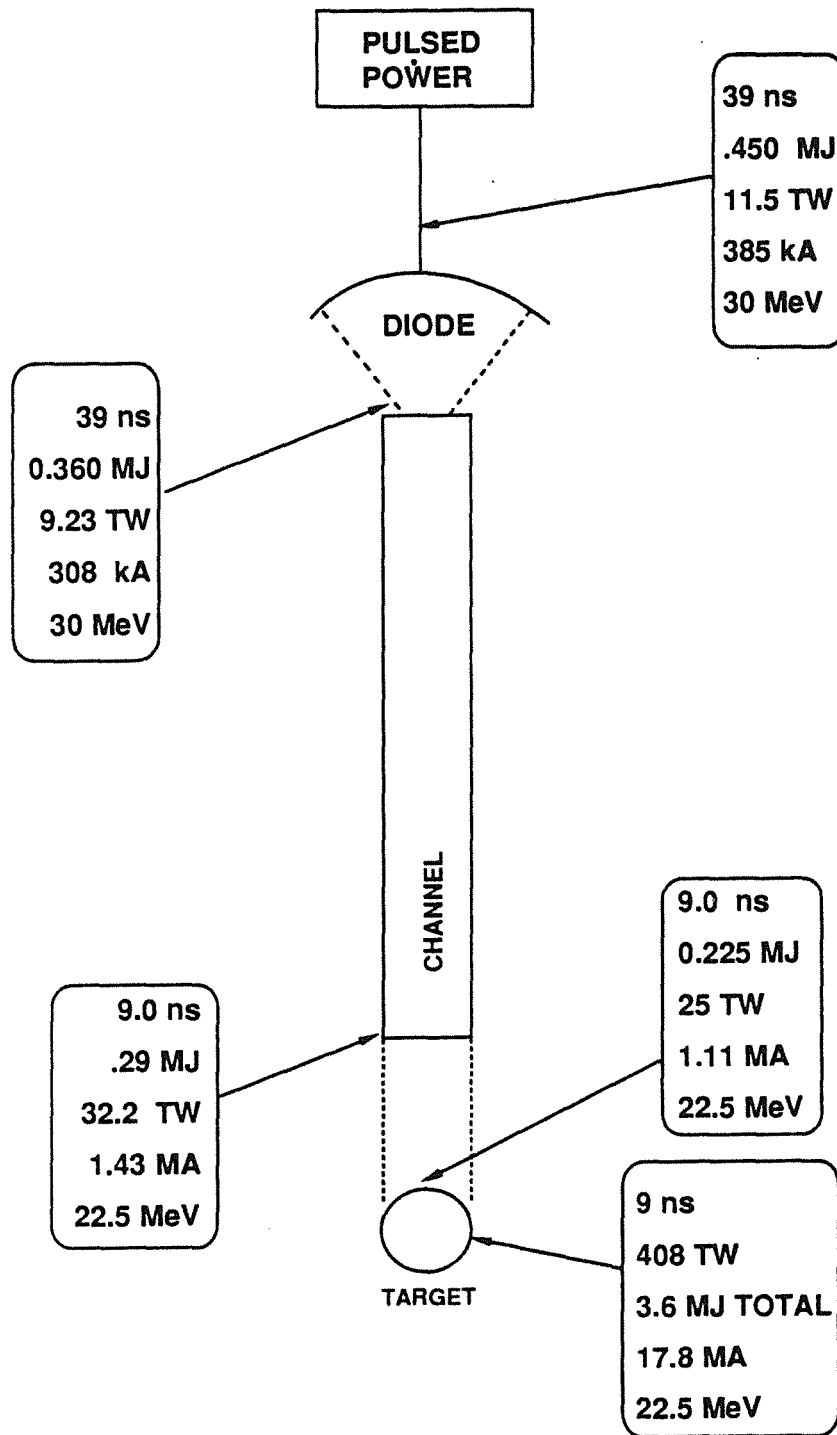


Fig. 4.2. Energy and power flow in LIBRA beam propagation system.

electrode at the top of the target chamber, to an overlap region near the target, and finally, to electrodes near the diodes. This electron current generates azimuthal magnetic fields that guide ion beams from the diodes to the target. The required magnetic fields are high enough that the electron discharge currents must be large. These high current densities could lead to magnetohydrodynamic instabilities that could disrupt the channels before the ion beams have reached the target. The avoidance of these instabilities and channel formation dynamics require a very rapidly rising discharge current, that calls for a high discharge voltage. This leads to electrical insulation problems; axial magnetic fields are used in an attempt to solve these problems. Also, the beam intensities are high enough to lead to plasma instabilities and induced ion energy loss that will lead to limitations on the ion beam power per channel. Issues of channel formation, ion transport in plasma channels, ion beam power limits imposed by stability and energy loss, and the use of applied magnetic fields to inhibit electrical breakdown between the channels and target chamber walls have been analyzed. Based on these analyses, a viable design for the LIBRA plasma channels has been obtained though there are still some issues that must yet be studied.

The final channel parameters in Table 4.1 were obtained through simulations of channel formation where the goal is to design channels that are acceptable for the propagation of 30 MeV lithium ions. The trajectories of beam ions in the designed plasma channels were followed to determine propagation efficiency. These calculations show that it is possible to carry a large fraction of the ions emitted by an ion diode through plasma channels to an ICF target. The results of analytic methods are used to study the stability of channels containing high current ion beams and to show the predicted limits on the power of ion beams that can be carried by channels. Finally, the problem of electrical breakdown between the plasma channels and the walls of the LIBRA target chamber is considered. Slowing the breakdown with the use of applied magnetic fields that are parallel to the channel axes has been investigated and the required magnetic fields are shown to be manageable.

4.2 Channel Formation

The formation of plasma channels for ion beam transport has been studied with computer simulation. First, a parametric study was done where several features of the channels were varied. On the basis of this parametric study, parameters for the LIBRA plasma channels were chosen. The chosen point design for the channels was then studied in detail.

Previous studies have determined the power of the lasers needed for preionization. The laser pulse energy required is related to the laser pulse width, the length of the channels, and the density of the gas species that is absorbing the laser radiation. Previous work considered absorption by a sodium vapor seed in a gas and 5 meter long channels.⁽²⁾ The method considered used a tuned laser to resonantly create a population of excited states that, through super-elastic collisions, then ionized the gas. For a sodium density of 10^{16} cm^{-3} , a 10 ns, 2 J laser could preionize a 2 mm radius path. A 500 ns, 2 J laser would be required for each channel if the sodium density were 10^{14} cm^{-3} . Sodium may not be an acceptable material to allow in the target chamber, so other schemes may need to be considered for LIBRA. Perhaps lasers could be tuned to a lithium atomic transition line since there will be some lithium vapor in the fill gas. If the process works the same as for sodium, a 2 J laser should be acceptable, if the pulse width is chosen consistent with the lithium vapor density.

Simulations of channel formation were performed with the ZPINCH computer code.⁽³⁾ ZPINCH is a one-dimensional Lagrangian hydrodynamics computer code with magnetic field generation and diffusion and magnetic force terms in the treatment of hydrodynamic motion. Both conductive and radiant heat transfer are considered, where the radiant heat transfer is done within a 20 energy group radiation diffusion model. Equations-of-state and opacities are interpolated from data tables created by the IONMIX computer code.⁽⁴⁾ ZPINCH uses experimental data for electrical conductivities for argon and molecular nitrogen.

Previous studies considered the formation of plasma channels for light ion beam propagation by predicting the ion beam confining azimuthal magnetic fields for various combinations of discharge current history, preionizing laser width and background gas.⁽²⁾ This parametric study assumed a molecular nitrogen gas at a mass density of $2.37 \times 10^{-5} \text{ g/cm}^3$, where for some calculations the radiation transport was artificially disabled and where laser and discharge current parameters were varied. Based on these calculations, lower atomic number gases that radiate less were studied for LIBRA. This hypothesis was tested by simulating the formation of a channel in helium gas and based on these calculations helium was chosen as the target chamber gas for the LIBRA study.

Channel formation for a discharge current history of the type shown in Fig. 4.3 was studied, where a large main pulse follows a smaller prepulse. A preionizing laser with a Gaussian radial intensity profile was assumed. The double pulsed current history was

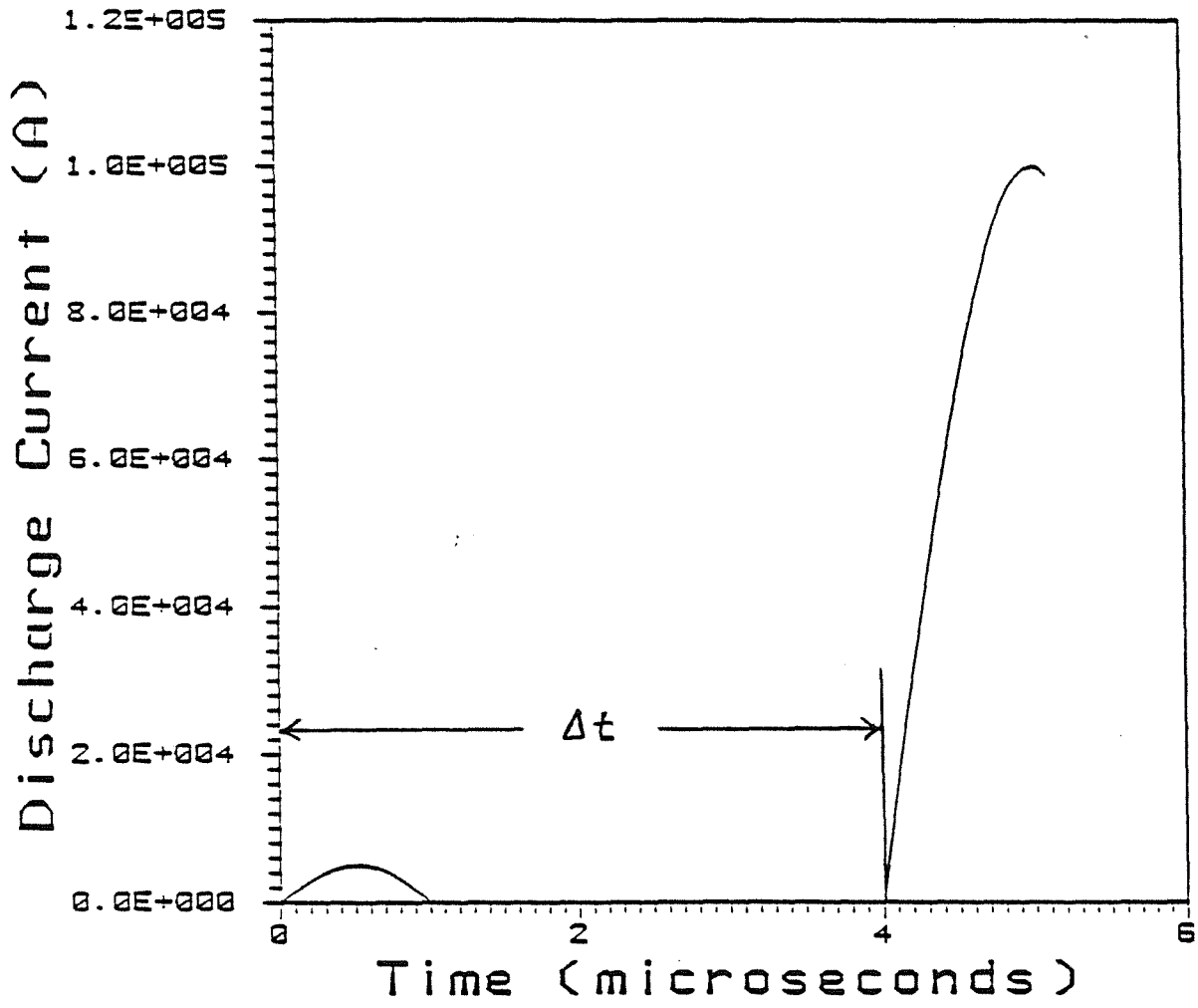


Fig. 4.3. Double pulse discharge current history for the formation of plasma channels for LIBRA.

first proposed several years ago.⁽⁵⁾ For this study it was parameterized by a delay time Δt . For these simulations a $2.37 \times 10^{-5} \text{ g/cm}^3$ nitrogen background gas was used. In Fig. 4.4 the maximum magnetic field and the peak field at 0.5 cm from the channel axis is shown to vary with Δt for a 5 mm Gaussian half-width laser beam. One readily sees that the maximum field and the field at 0.5 cm increase as the time delay is decreased, which is consistent with the hypothesis that radial heat transfer works to reduce the azimuthal magnetic fields. In Fig. 4.5 the fields change with laser width whether or not radiation transport is taken into account. Here one sees that the narrow initial discharges, implied by narrow laser beams, lead to higher azimuthal magnetic fields and that radiation transport reduces the fields.

These results show that, even for the optimum current history and laser profile, radiation transport prevents the formation in nitrogen of channels acceptable for the LIBRA reactor design. One should note that the required azimuthal field at 0.5 cm from the channel axis is 27 kG, while the best simulation result with nitrogen is 18 kG if radiant heat transfer is considered. Therefore, a low atomic number gas, such as helium, should radiate less and allow the formation of more acceptable channels.

Simulations of channel formation in helium gas at a mass density of $2.37 \times 10^{-5} \text{ g/cm}^3$ were performed. A $1 \mu\text{s}$ delay time in the discharge current and a laser half-width of 2 mm, values that seemed to be optimum in the nitrogen parameter study were used. For these values, ZPINCH simulations predict that the magnetic field at 0.5 cm from the channel axis reaches 27 kG and that the average mass density in the channel is approximately $5 \times 10^{-6} \text{ g/cm}^3$. Such a channel design would be able to focus 30 MeV lithium ions onto a light ion beam driven target, and is therefore acceptable for LIBRA.

Therefore, the point design for the LIBRA channels has the parameters outlined in Table 4.1. According to ZPINCH code simulations, this design is successful because helium gas does not radiate strongly when it is fully ionized, the initial channel radius is small, and the discharge current rises rapidly. The proposed discharge current is shown in Fig. 4.6, where one sees that the small first pulse is immediately followed by a large pulse that reaches a maximum of 100 kA at $2 \mu\text{s}$ after the start of the initial pulse. The hydrodynamic motion of the LIBRA channel, as simulated with the ZPINCH code, is shown in Fig. 4.7. Here, the positions of Lagrangian zone boundaries in the simulation are plotted against time. One can see that as the discharge current approaches its maximum value, the center of the discharge begins to pinch, while the edge of the discharge continues to expand as an outward moving cylindrical shock. The peak magnetic field

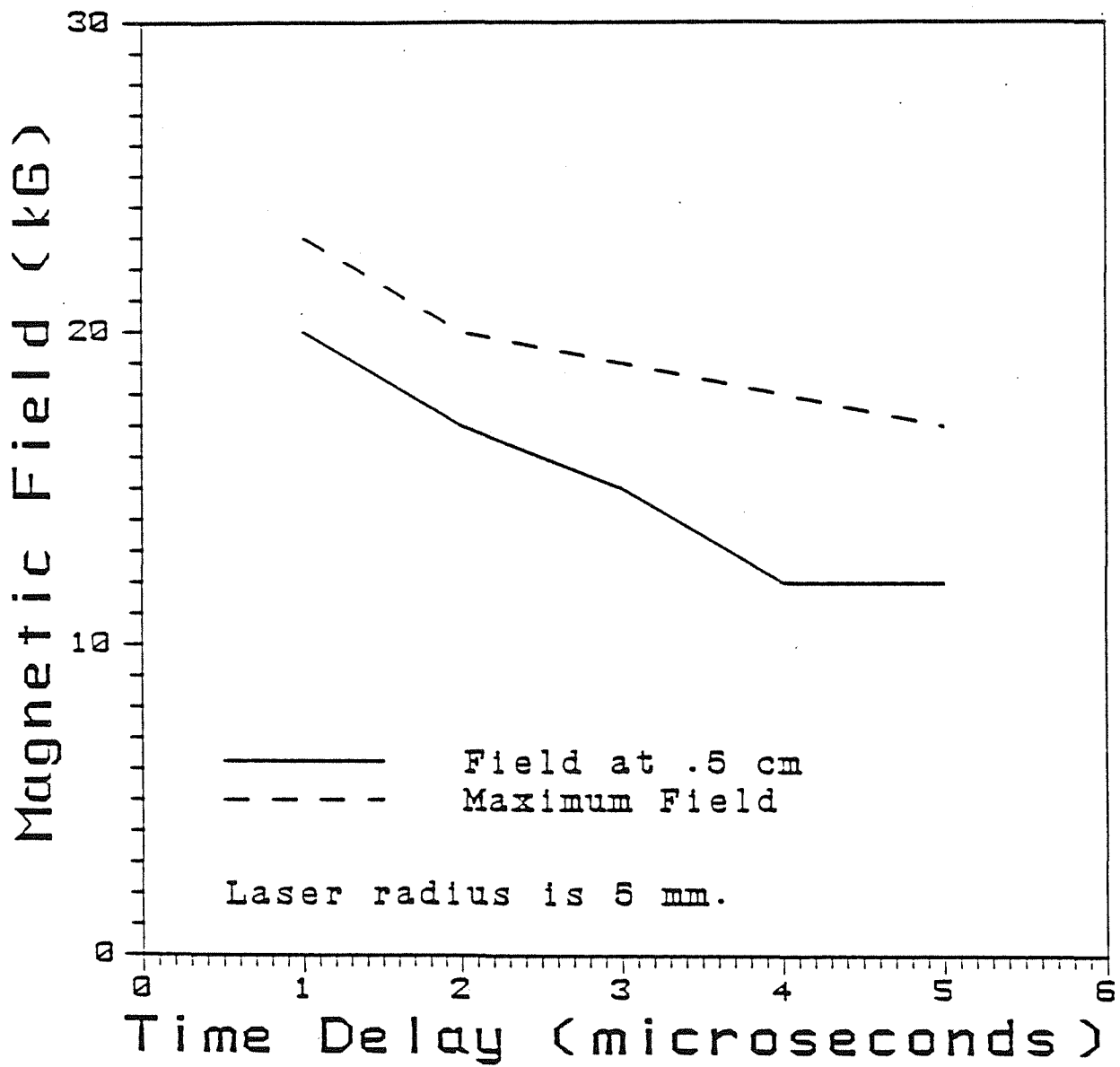


Fig. 4.4. Maximum and peak azimuthal magnetic fields @ 0.5 cm versus time delay for second discharge current pulse. These calculations are for laser-guided plasma channels created in 2.37×10^{-5} g/cm³ nitrogen with the discharge current shown in Fig 4.3. The laser Gaussian half-width was 5 mm.

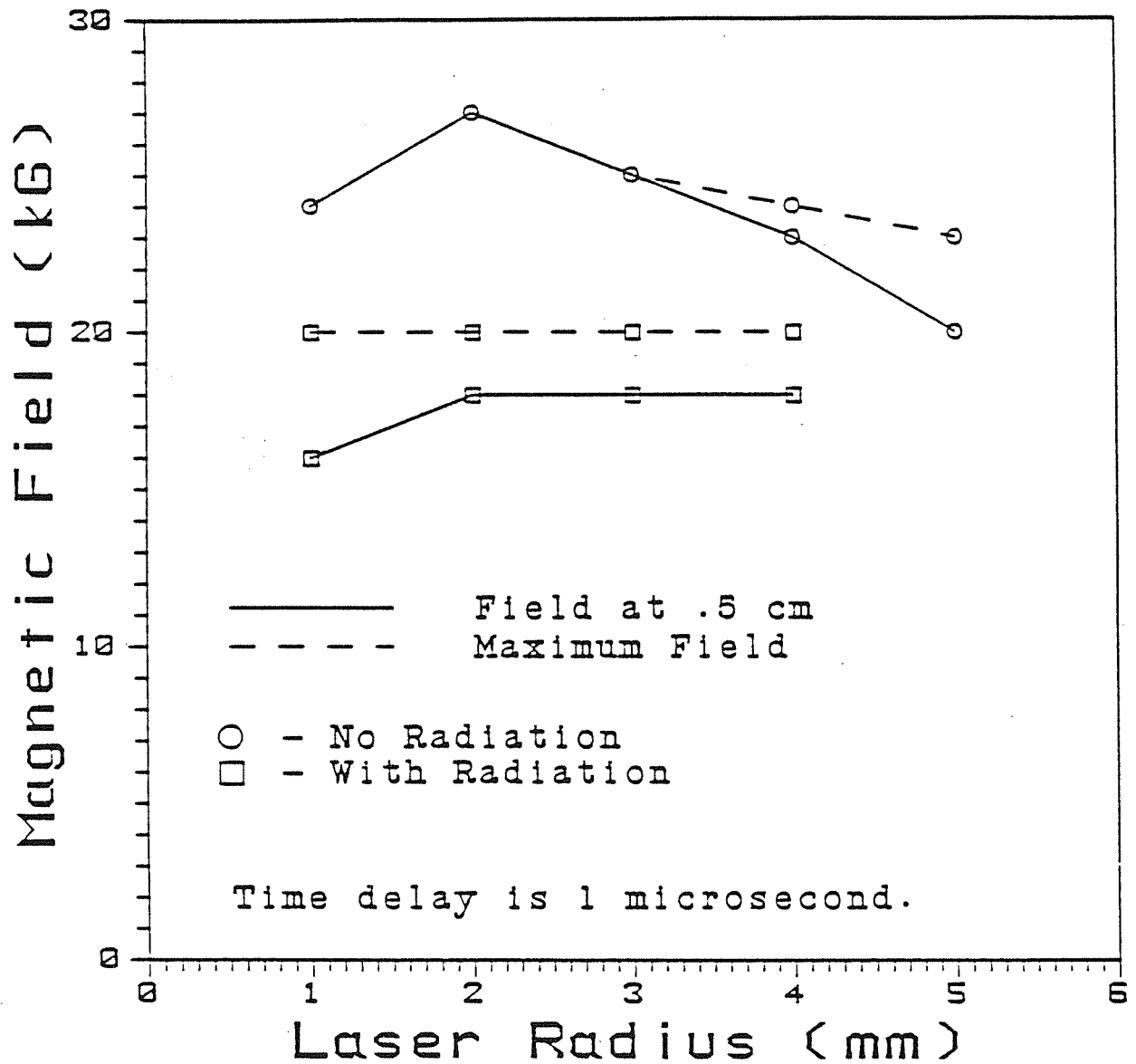


Fig. 4.5. Maximum and peak azimuthal magnetic fields @ 0.5 cm versus laser Gaussian half-width. These calculations are for laser-guided plasma channels created in 2.37×10^{-5} g/cm³ nitrogen with the discharge current shown in Fig. 4.3. The time delay for the second discharge current pulse was 1 μ s.

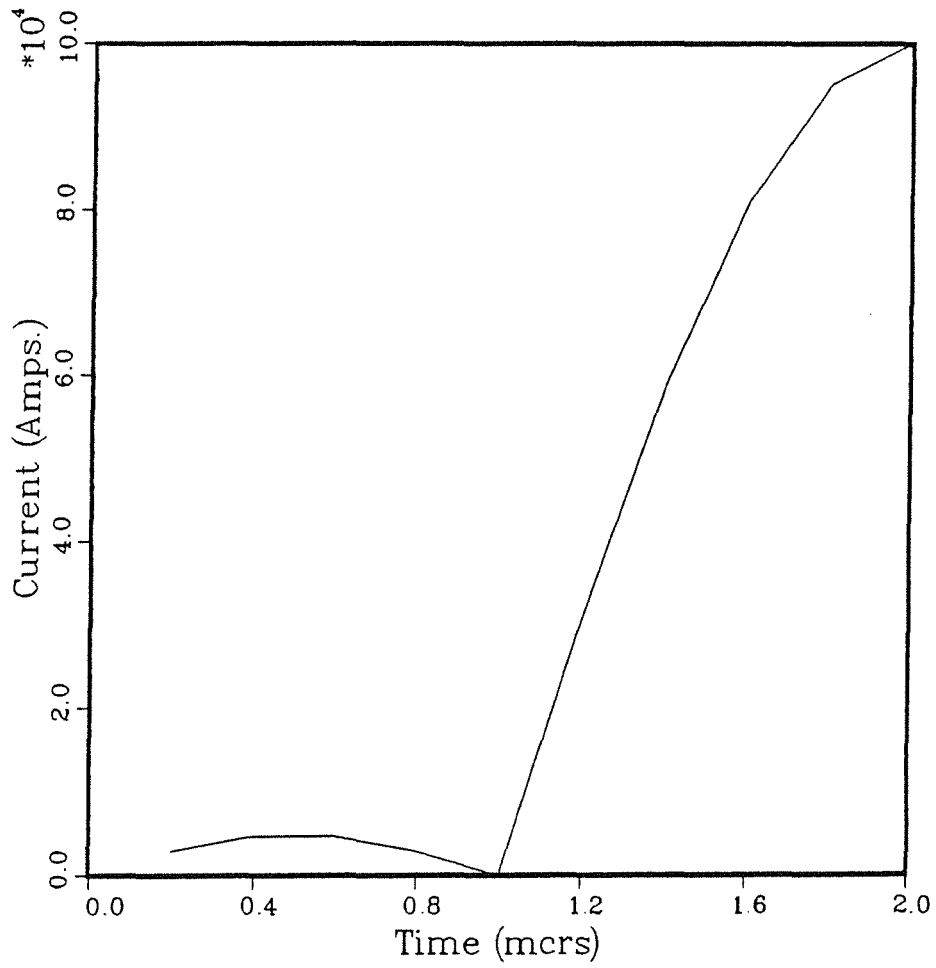


Fig. 4.6. Double pulse discharge current history for the formation of plasma channels for LIBRA.

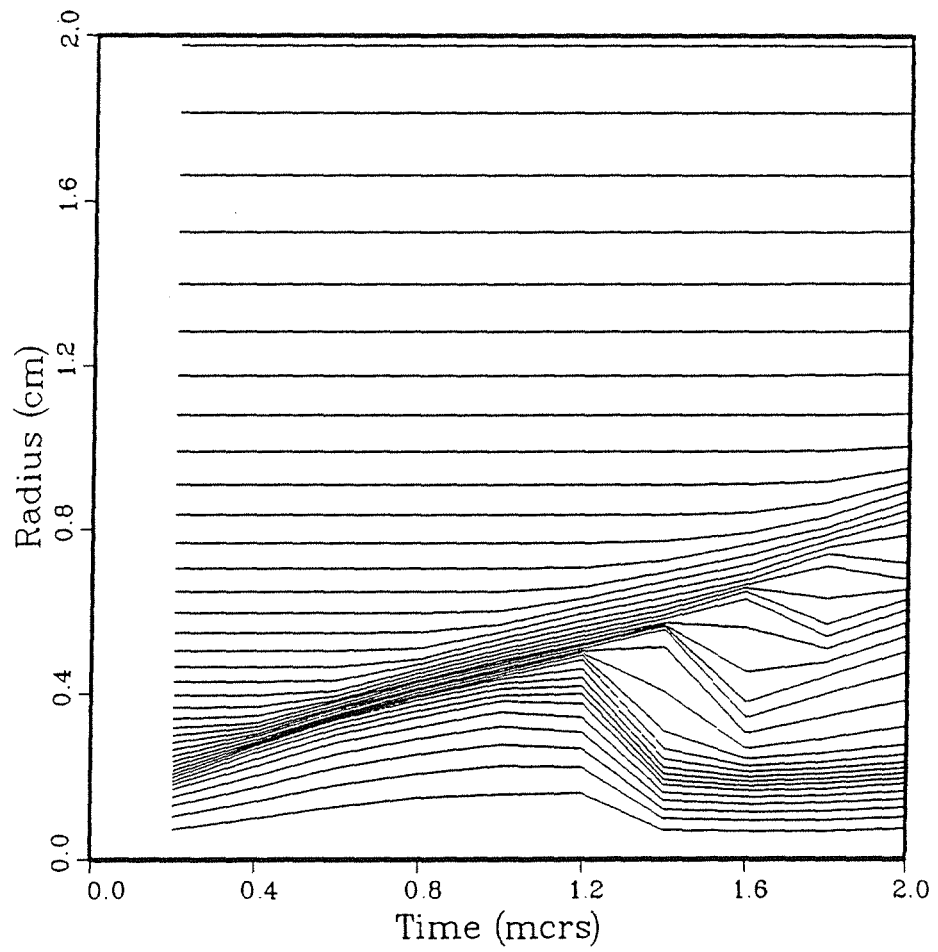


Fig. 4.7. Hydromotion during formation of LIBRA channels.

magnetic field and the edge of the discharge current remain just inside this shock front. One can see the plasma temperature profiles at various times in Fig. 4.8. The times at which the temperatures and other parameters are plotted are all within the main pulse of the discharge current. The temperatures are much higher than in a nitrogen discharge of the same mass density because helium radiates much less strongly. The low radiant power also means that there is little heating of the gas ahead of the shock. Fig. 4.8 clearly shows this. Therefore, the electrical resistivity is low in a region confined to a narrow radius. This is shown in Fig 4.9. The discharge current only flows in the regions where the resistivity is low. The discharge current profiles lead to the magnetic field profiles of Fig. 4.10. At a time around 1.7 μ s, ZPINCH predicts a magnetic field at 0.5 cm from the channel axis of 27 kG. The mass density profiles, plotted at the same times in Fig. 4.11, show the central pinching of the discharge. The density peak in the center of the discharge is roughly equal to the initial gas density, though the averaged density through the discharge is below the initial value by a factor of four.

One aspect of channel formation that is not considered in the ZPINCH code is the possible onset of magnetohydrodynamic instabilities that could disrupt the discharge before the required magnetic fields are reached. The standard stability criterion for MHD modes other than the sausage is based on an energy principle and is often reduced to an expression like

$$\frac{2}{B_z} \left(\frac{dP}{dr} \right) + \frac{1}{4r} \geq 0 . \quad (4.1)$$

The pressure profiles at various times as predicted by ZPINCH are shown in Fig. 4.12. One sees that $\frac{\partial P}{\partial r}$ is negative in most places, so that Eqn. 4.1 is not satisfied throughout unless B_z is large enough. In the standard plasma channel concept $B_z = 0$, so it is clear that the channels have the potential to be at least kink unstable. The important issue is the growth rates for the instabilities. Typically, one estimates the growth rate of MHD modes to be the ratio of the Alfvén speed to the channel radius:

$$\gamma = \frac{v_A}{r_c} = \sqrt{\frac{B_\theta^2}{4\pi e}} / r_c . \quad (4.2)$$

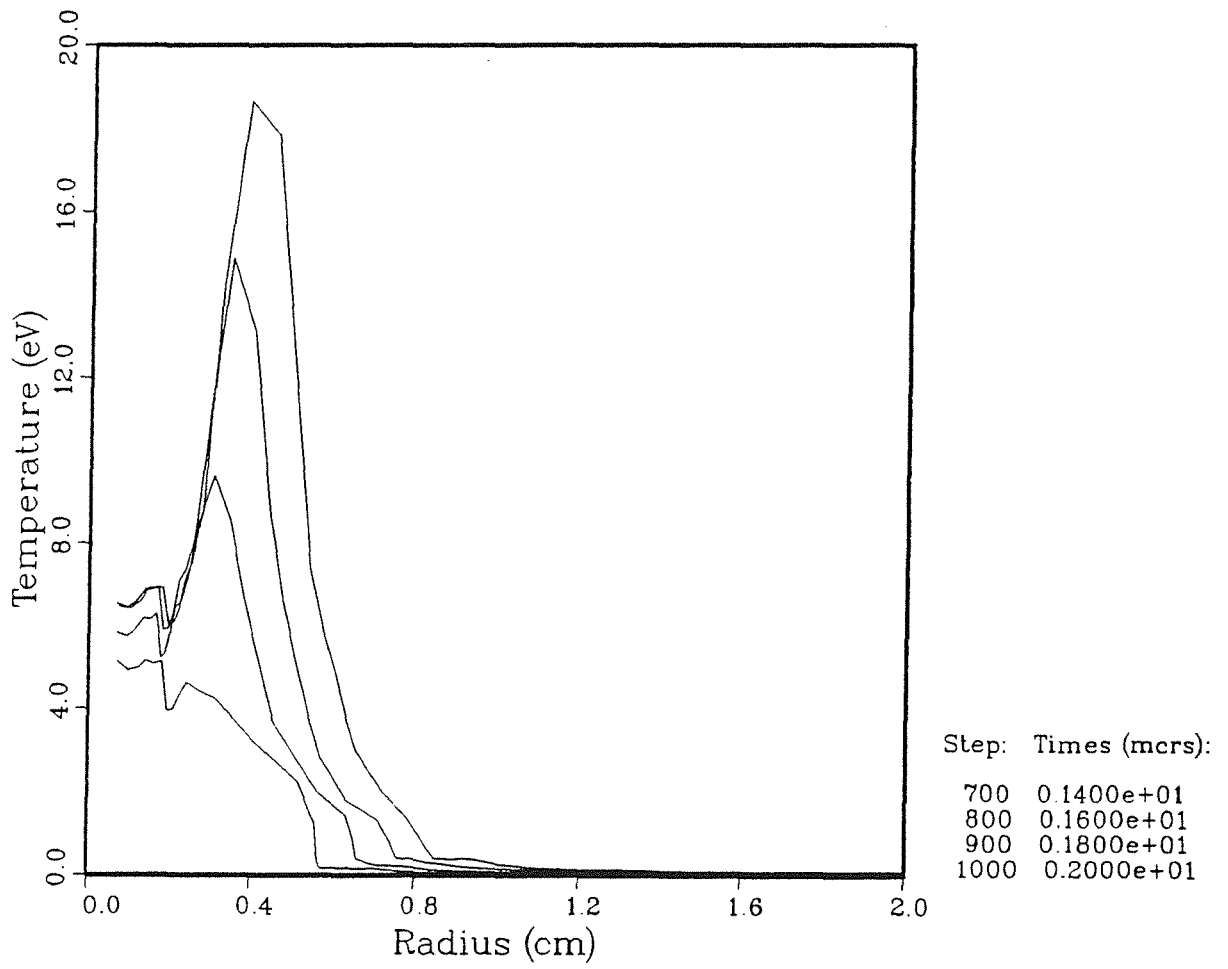


Fig. 4.8. Plasma temperature profiles during formation of LIBRA channels.

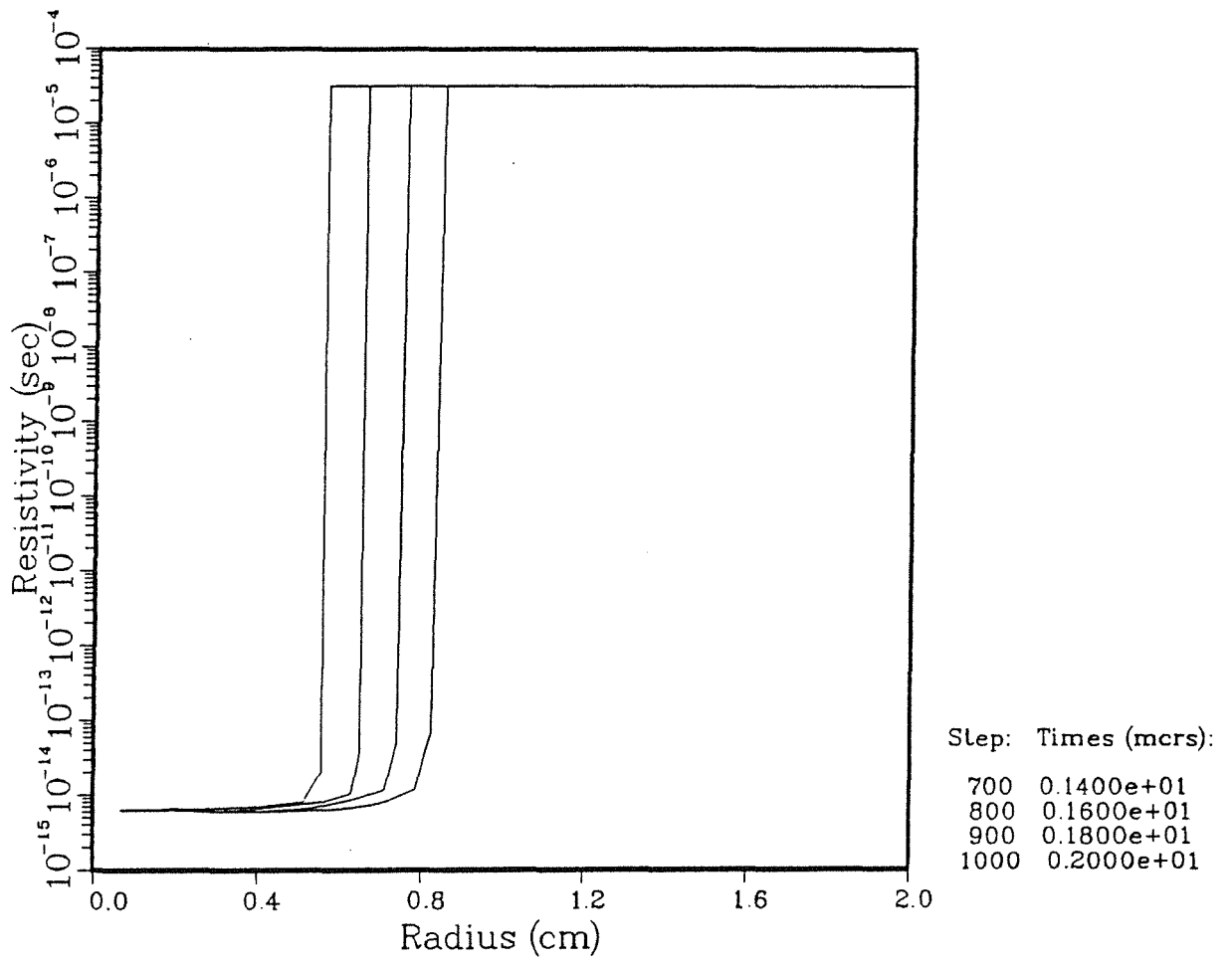


Fig. 4.9. Plasma resistivity profiles during formation of LIBRA channels.

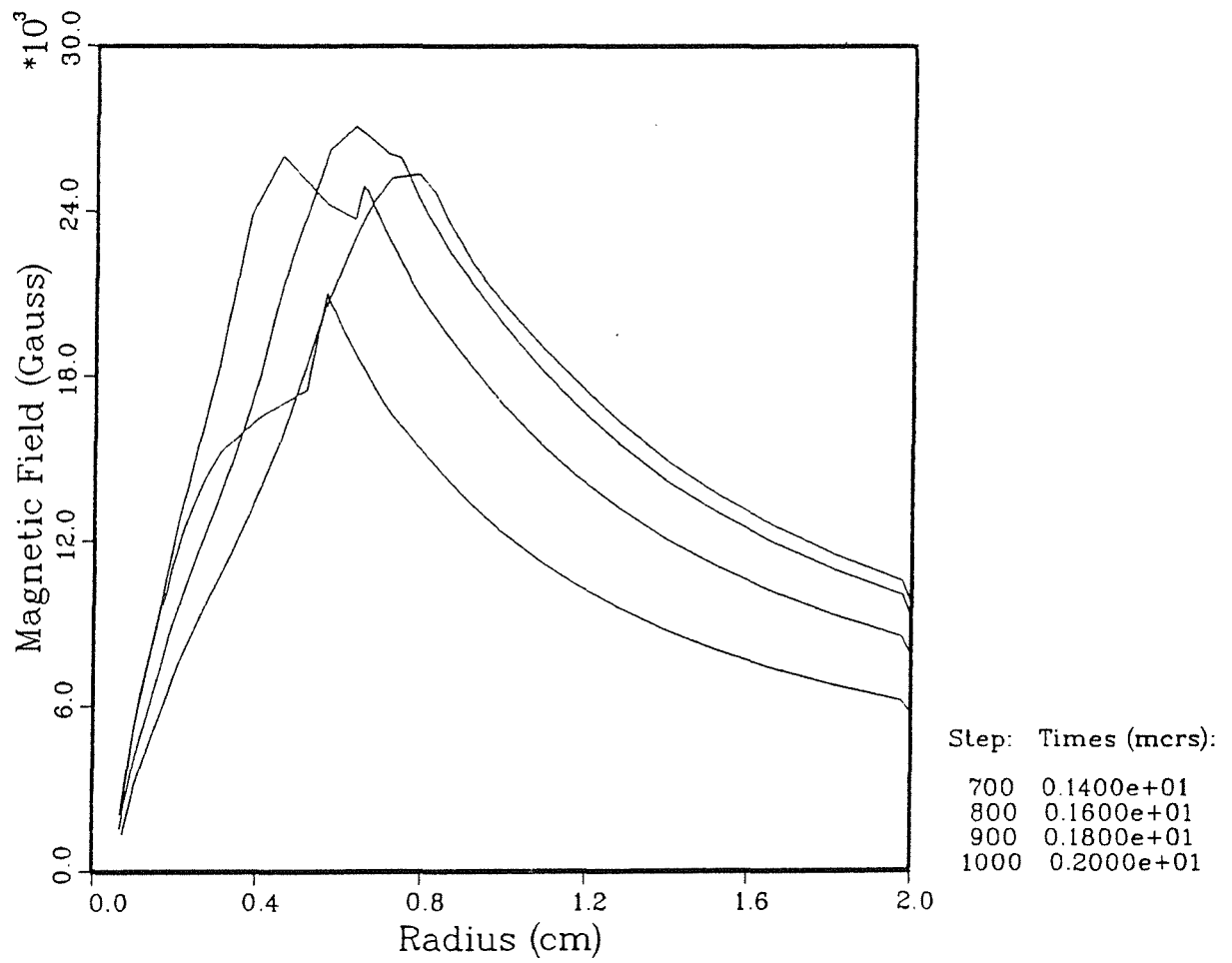


Fig. 4.10. Magnetic field profiles during formation of LIBRA channels.

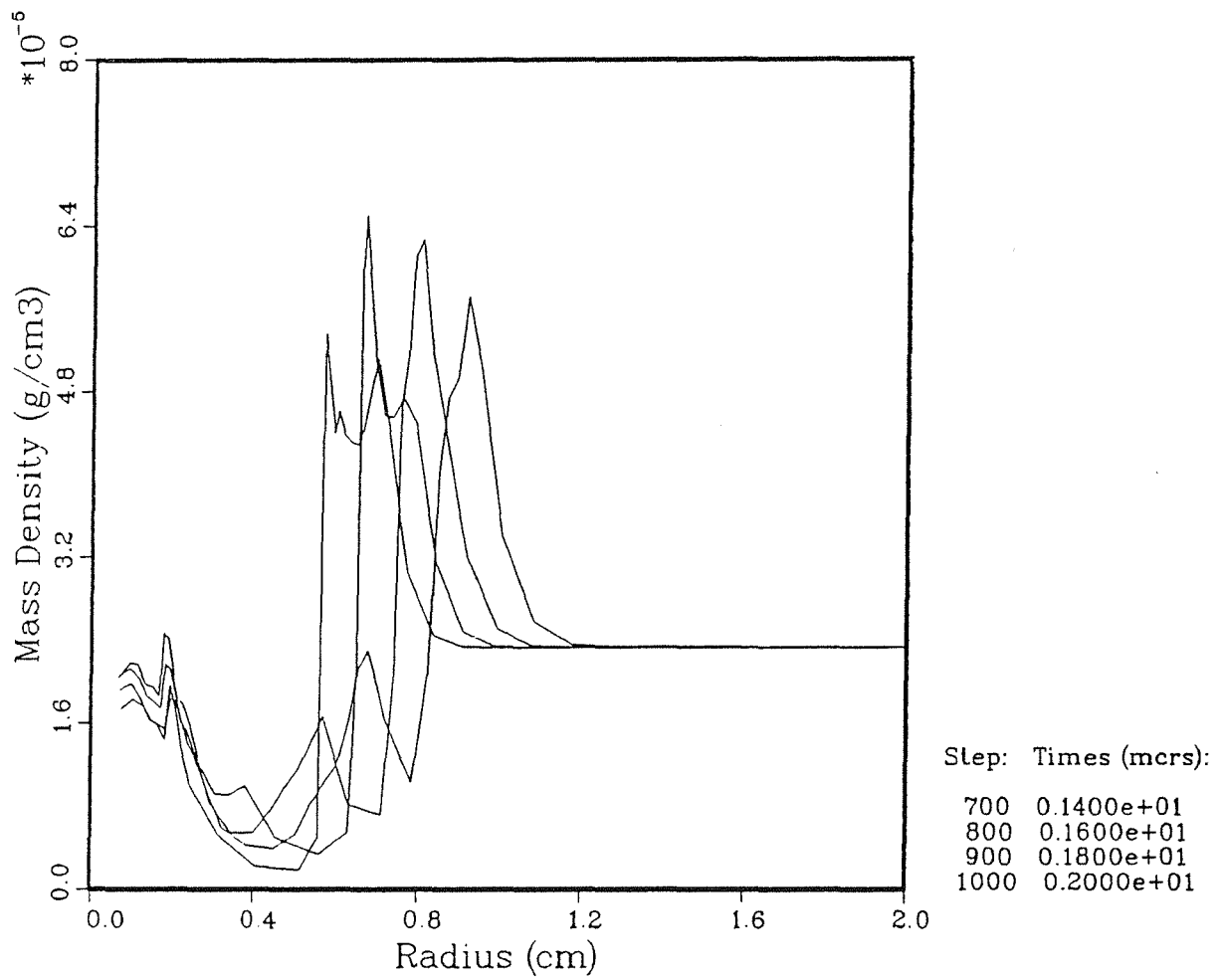


Fig. 4.11. Plasma mass density profiles during formation of LIBRA channels.

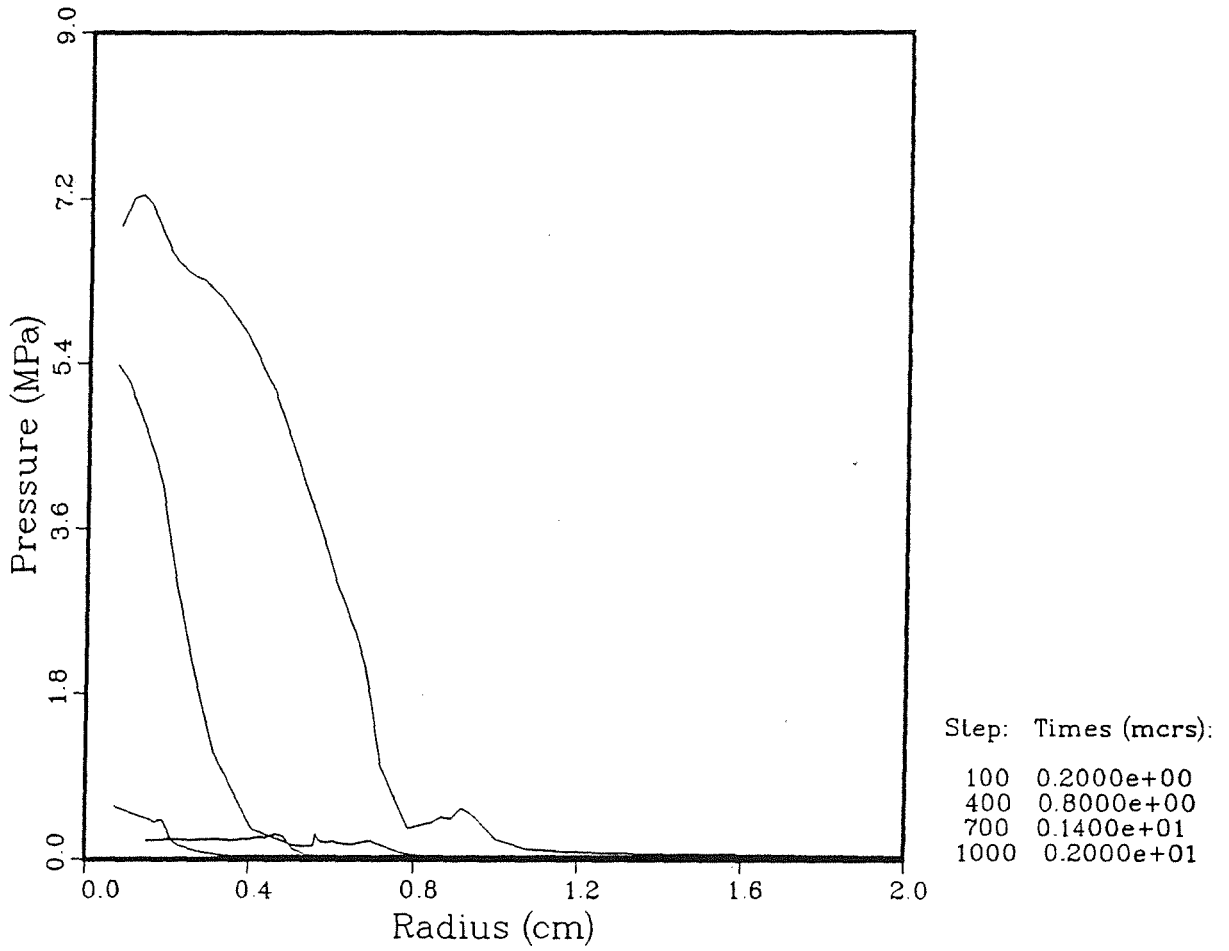


Fig. 4.12. Plasma pressure profiles during formation of LIBRA channels.

Due to recent experiments on solid pinches, there has been a reawakening of interest in the stability of pinches and this has led to improved calculations of the growth rates.⁽⁶⁾ This work shows that growth rates may be significantly less than the classical expression in Eqn. 4.2 at high density and plasma pressure. Conservatively using the classical expression, we estimate that the growth rate is about 10^7 s^{-1} . Therefore, the instability can grow for several e-folding times before the ion beam is injected at $0.7 \mu\text{s}$ after the beginning of the main pulse. Olsen⁽⁷⁾ has experimentally shown that the kink mode can severely limit the propagation of ion beams. In addition to high density and pressure effects, the channels may be additionally stabilized by the axial magnetic fields that are applied to impede breakdown between the channels and the target chamber wall. In summary, the classical estimates indicate that MHD instabilities will reduce ion transport in the channels, though there are mitigating effects. The MHD stability of plasma channels remains a critical issue.

4.3 Ion Beam Propagation in Plasma Channels

In addition to the MHD instabilities discussed in the preceding section, there are two other mechanisms that prohibit ions from reaching the target. First, the ions reach the channel entrance in a distribution in angle and radial position, so that some of them simultaneously have a large angle of incidence and are at a relatively large distance from the channel axis. These ions either are not trapped by the channel's magnetic fields and pass through the background gas never turning back toward the channel axis, or they are turned back by the magnetic fields but at a large enough radius that those ions have only a small chance of striking the target. Second, the ions are no longer confined by the channels when the magnetic fields cancel each other in the region near the target. The ions would just continue in the directions they were going when they entered this overlap region and the beam would spread, with some ions missing the target.

These two possibilities have been studied by following the trajectories of a random sampling of ions in initial angle and radial position as they move down the channel. It is assumed that the magnetic field is only in the azimuthal direction and that it rises linearly from zero on the channel axis to a maximum value at the channel radius and falls as the inverse of the radial position beyond the channel radius. This is the situation in the main part of the channel, between where it enters the target chamber at the inside edge of the channel insulation magnetic fields and the point near the target where azimuthal magnetic fields from adjacent channels begin to interfere significantly. For axial

positions within the overlap region, it is assumed that the azimuthal fields linearly fall to zero over a length of 1 cm from the edge of the region. The ions are assumed to enter the channels with radial positions distributed in a Gaussian distribution with a given half-width and with angles of incidence distributed uniformly out to a given value. The ION computer code⁽⁸⁾ was used to follow these ion trajectories. In the calculations presented here the trajectories of up to 5000 ions were followed. One obtains from these calculations the fraction of ions reaching a disk 0.5 cm in radius as a function of the distance from the end of the channel.

The trajectories of ions for a variety of maximum magnetic fields, focal spot sizes and maximum injection angles have been calculated. First, the sensitivity of the ion propagation to the maximum angle of injection that the ions make with the channel axis was computed. This angle is approximately equal to the ratio of the diode radius to the diode focal length, R/F . The peak magnetic field was assumed to be 28 kG, the diode microdivergence was 5 mrad, the channel radius was 0.5 cm, the diode focal spot radius was 0.35 cm, and the channel length was 540 cm. The fraction of ions leaving the diode that reach the target are plotted for these parameters versus the distance from the end of the channel for three different values of R/F in Fig. 4.13. One sees that the fraction is not greatly reduced by changes in R/F from 0.1 to 0.13. This spans the range of R/F that is expected for LIBRA diodes. In Fig. 4.14, the sensitivity to the focal spot size and the microdivergence is shown. This particular set of calculations used a peak field of 7 kG and an R/F of 0.08, corresponding to the case where a high field channel could not be formed, but where the source density on the anode of the diode was high enough so the required radius was small. The microdivergence is directly related to the spot size; the spot radius is equal to the product of the focal length and the microdivergence. One sees here that, for this set of parameters, the fraction gets much lower as the spot size is increased to 0.35 cm. This low magnetic field scenario will be acceptable for very low microdivergences.

The fraction of ions leaving the diode that strike the target in the LIBRA point design is shown in Fig. 4.15. For this calculation, the peak magnetic field was 28 kG, R/F was 0.12, the microdivergence was 5 mrad, the focal spot radius was 0.35 cm, and the channel radius was 0.5 cm. One sees that at the end of the channel, 83% of the ions are within 0.5 cm of the channel axis. The other 17% were not well confined by the channel. As the distance from the end of the channel increases, the fraction of ions within a 0.5 cm radius disk decreases, until at 9 cm from the channel the fraction has

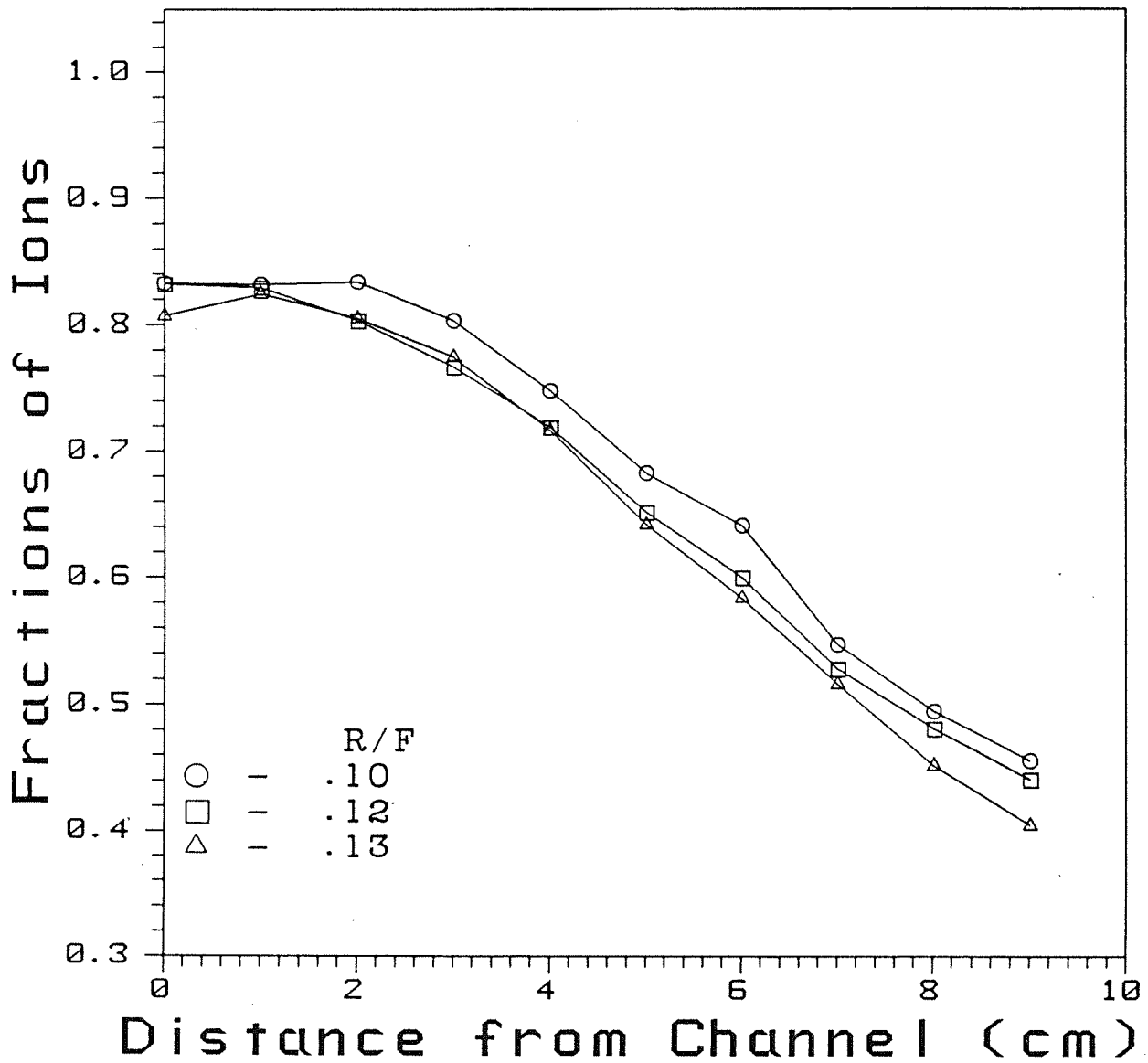


Fig. 4.13. The fraction of beam ions leaving the diode within a disk 0.5 cm in radius versus the distance from the target end of the channel. Calculations have been done for LIBRA channel parameters for three different values of R/F.

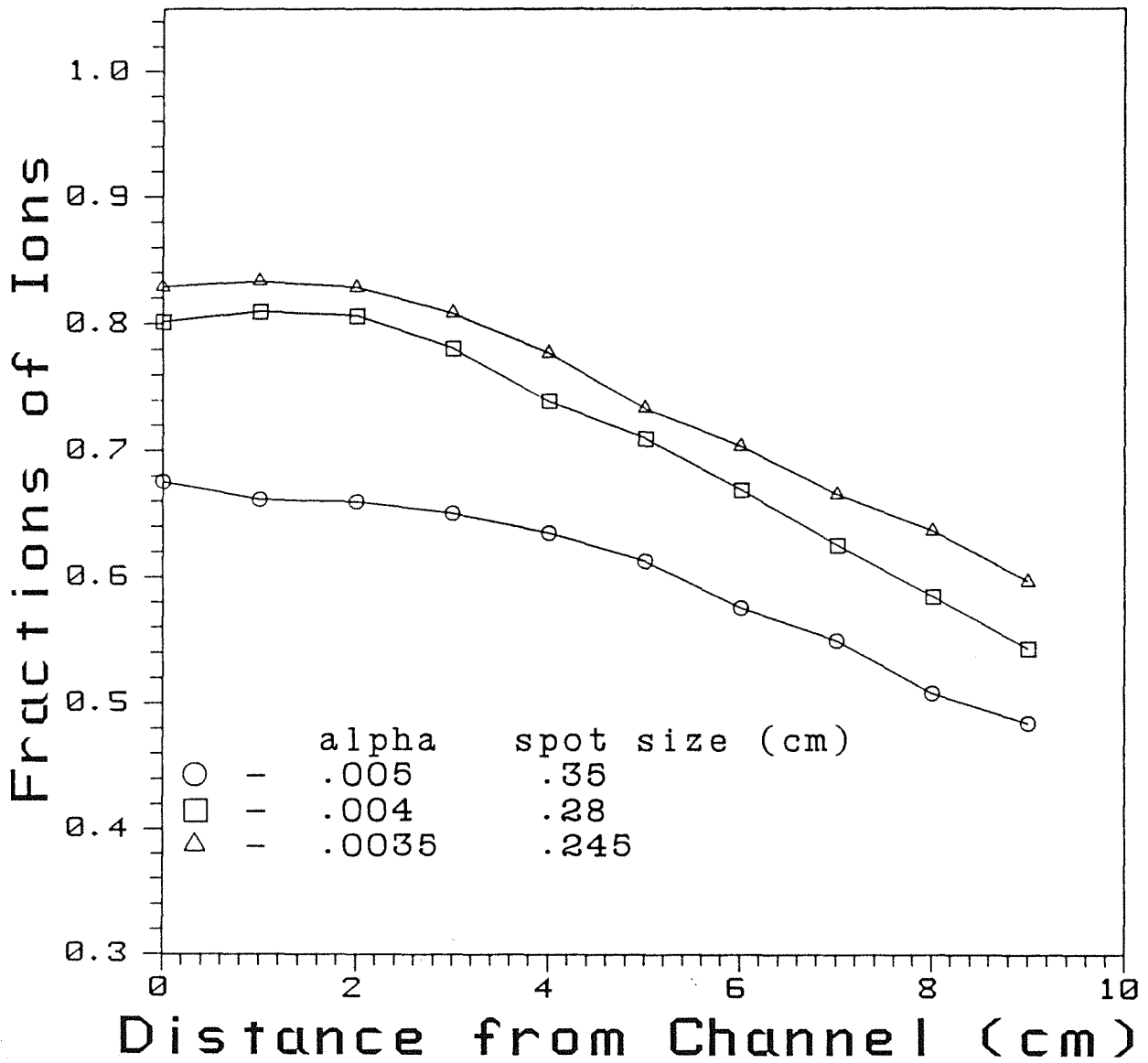


Fig. 4.14. The fraction of beam ions leaving the diode within a disk 0.5 cm in radius versus the distance from the target end of the channel. Calculations have been done for a low magnetic field channel at an R/F of .08 and for three values of the diode microdivergence.

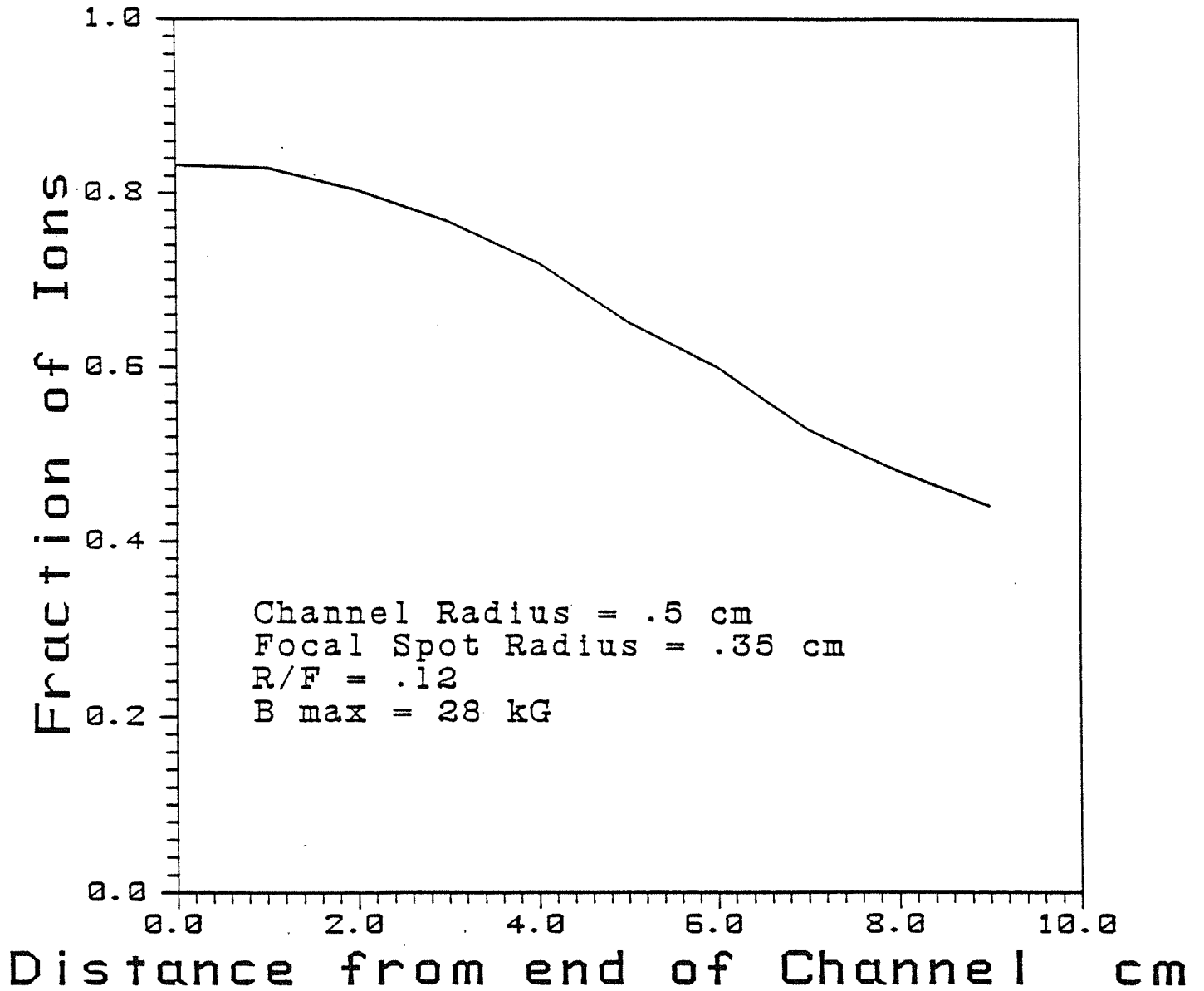


Fig. 4.15. The fraction of beam ions leaving the diode within a disk 0.5 cm in radius versus the distance from the target end of the channel. The calculation was done for LIBRA parameters.

fallen to 40%. In LIBRA, 18 channels converge on the target, with 9 in each of 2 cones. The channels are 0.5 cm in radius and the target is 0.5 cm in radius, so the distance between the point where the channels begin to overlap and the target surface is 0.43 cm. According to Fig. 4.15 about 80% of the ions reach the target. In Figs. 4.16, 4.17, and 4.18, the radial profiles of the LIBRA ion beams at the end of the channel, at 1 cm from the channel, and at 2 cm from the channel are shown. As one would expect, the beam begins to diverge as it moves out of the confining influence of the magnetic field.

Each of the plasma channels in LIBRA must carry several hundreds of kilo-amperes of beam ions, which can perturb the channels and possibly inhibit the transport of the beam ions. The limits on the ion beam power imposed by the onset of electrostatic instabilities, filamentation of the ion beam and the plasma channel, and beam ion energy loss were analyzed. Expansion of the channels due to the ion beam was also analyzed but it does not pose an important constraint. The analysis has followed the formalism developed a number of years ago at the Naval Research Laboratory⁽⁹⁾ and involves the use of the WINDOW computer code.⁽¹⁰⁾

The results are shown for LIBRA parameters in Fig. 4.19. One sees that the input ion beam power per channel is limited to 9 TW at a diode R/F value of 0.12.

4.4 Electrical Insulation of Plasma Channels

The LIBRA target chamber design requires that the channels pass through a neutron reflector, a structural wall, and a tritium breeding blanket. At least some of these will conduct electricity. The channel requires a discharge voltage of about 1 MV to produce the current history shown in Fig. 4.3 and 4.6. This voltage is applied across the channel at the points where it enters and leaves the target chamber. The electrical potential of the wall, blanket and reflector floats between the potentials of the two channel ends so that the maximum voltage between the channel and the structure surrounding the hole that it must pass through is about 500 kV. The holes in the target chamber must be as small as possible to minimize the leakage of neutrons from the target explosion, with a 10 cm radius as the goal. A method of preventing the breakdown of this gap in a 50 kV/cm electric field must be devised or the channels will not properly form.

Applied axial magnetic fields are proposed to slow the breakdown for a time long enough for the channels to form, that is, for about 1 μ s. The voltage across the gap between the channels and the wall is large enough that a very large gap would be

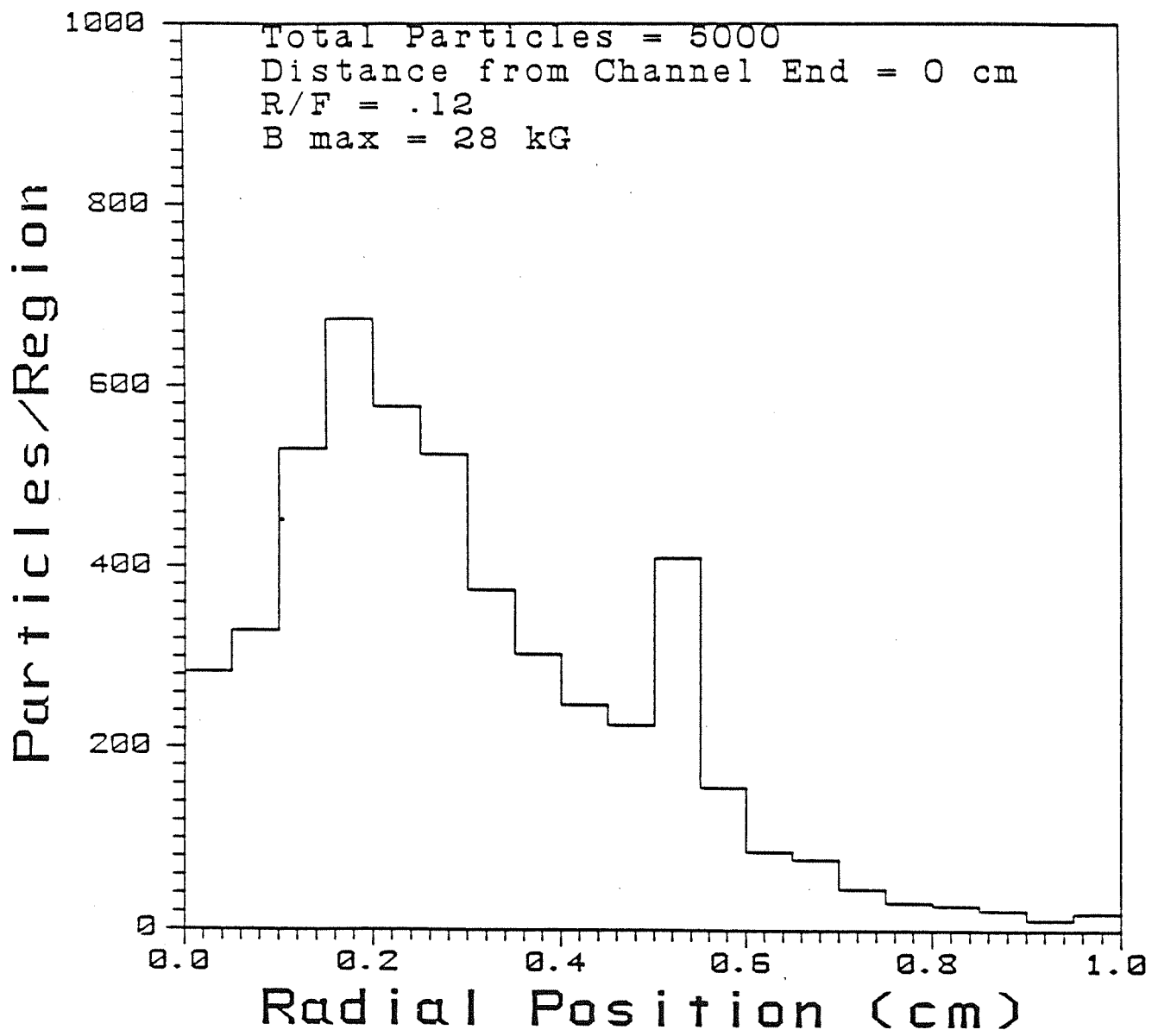


Fig. 4.16. Ion beam profile. The number of ions in each radial region of the simulation is shown at the end of the channel.

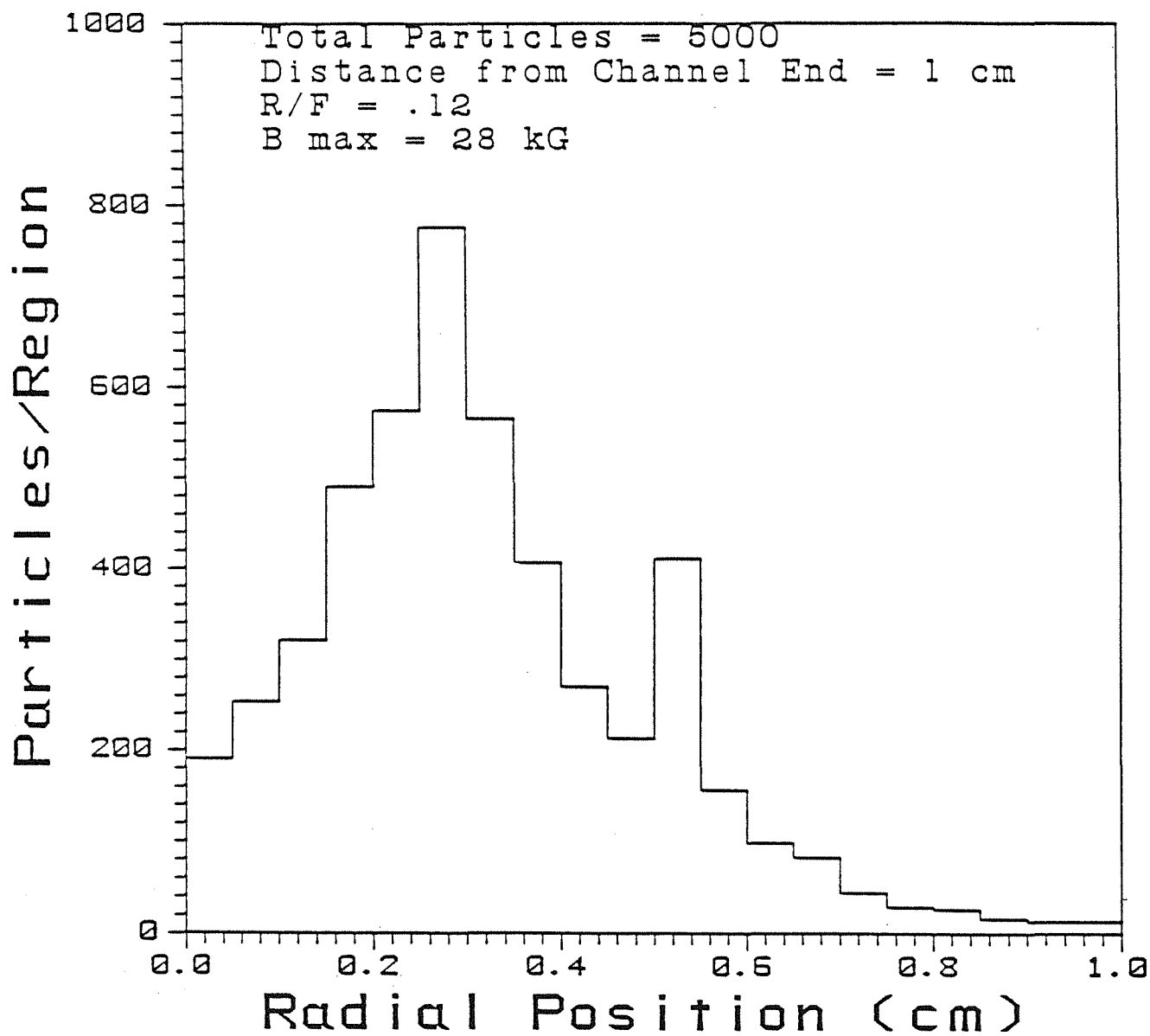


Fig. 4.17. Ion beam profile. The number of ions in each radial region of the simulation is shown 1 cm from the end of the channel.

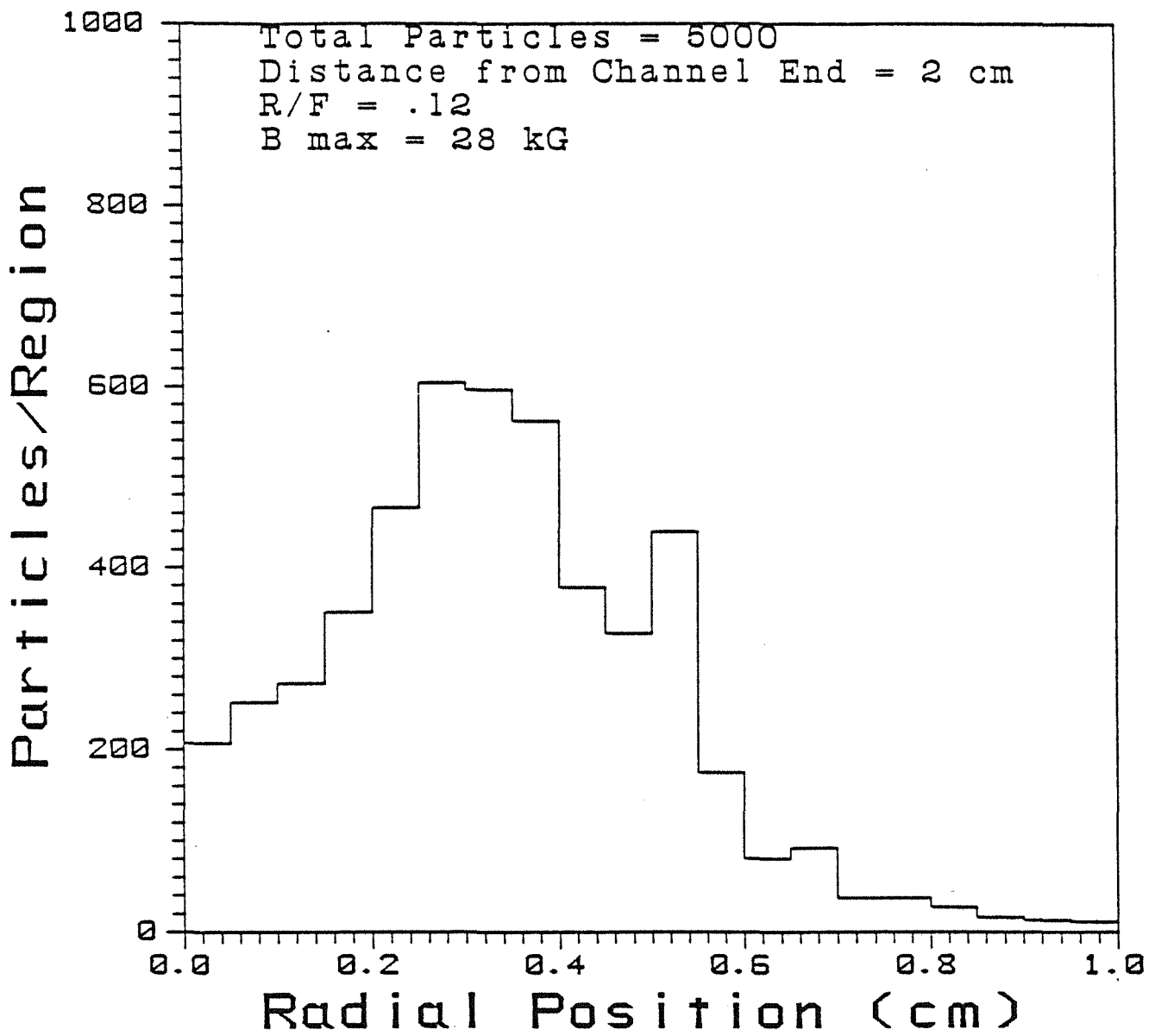


Fig. 4.18. Ion beam profile. The number of ions in each radial region of the simulation is shown 2 cm from the end of the channel.

BEAM POWER LIMITS FOR LIBRA

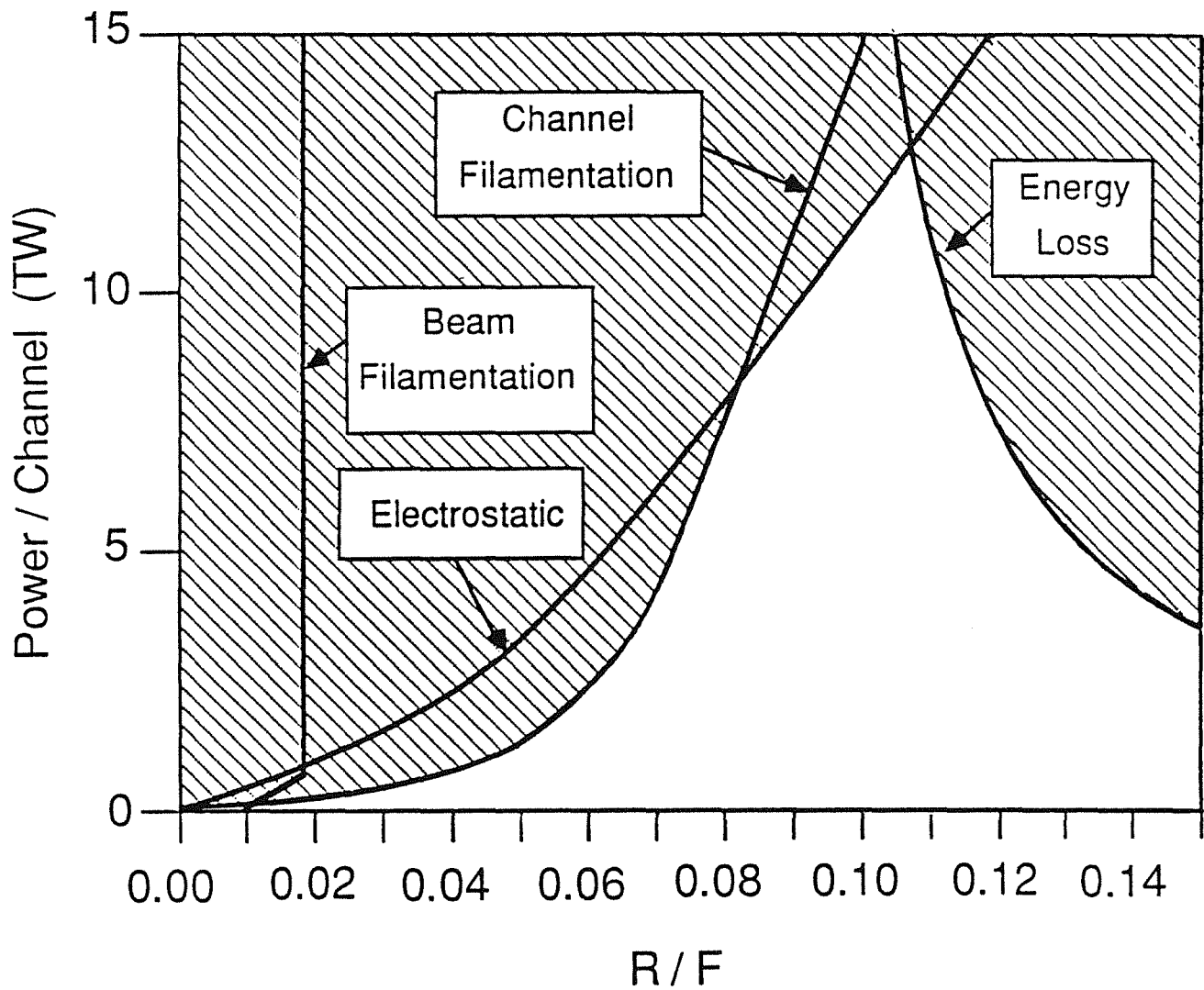


Fig. 4.19. Limits on ion beam power per channel imposed by stability and ion energy loss. R/F is the ratio of the ion diode anode radius to its focal length, and is roughly equal to the maximum angle of incidence of ions into the channels.

required to totally prevent breakdown, thus the hope is to slow the breakdown. Heylen⁽¹¹⁾ shows how magnetic fields can slow the flow of electrons in a breakdown and this analysis was used to predict that a 3.2 T axial magnetic field can slow the breakdown for a 10 cm gap by 1 μ s. A solenoidal magnet was designed to provide this field. Analysis shows that such magnets could survive in the LIBRA target chamber environment for an adequate length of time.

Heylen derives the following formula for the drift velocity v_T^B for electrons moving in a crossed electric field E and magnetic field B:

$$v_T^B = \frac{e}{m} \frac{E}{N} \frac{\sigma v}{(\sigma v)^2 + (\omega_c/N)^2} \quad (4.3)$$

Here, e/m is the charge to mass ratio for electrons, N is the number density of the gas, σv is the collision rate per gas atom for an electron, and ω_c is the electron cyclotron frequency. This formula is strictly valid for parallel plate geometries, where \vec{E} is directed from one plate to the other and \vec{B} is parallel to the plates. The geometry in plasma channels is, of course, coaxial, with \vec{B} parallel to the channel axis. This \vec{B} is an applied field and should not be confused with the fields created by the channel. Heylen states that coaxial geometries should have lower drift velocities than parallel plates, so using a parallel plate formulation is conservative.

The distance between the channel and the wall, D, divided by drift velocity in Eqn. 4.3 is the time that it takes for the breakdown to occur. This is dependent on the assumption that breakdown occurs through a Townsend process where the cascade begins at the inside of the opening in the wall and finishes at the channel edge. At the high-electric fields present in this system, breakdown may begin inside the gap which would render this analysis invalid. This time is required to be greater than or equal to the rise time for the channel discharge current, Δt . The electric field E can be written as the voltage drop between the channel and the wall, V_d , divided by D. These expressions can be rearranged in a formula for D,

$$D = (1.76 \times 10^{18} V_d \Delta t \sigma v) / (N((\sigma v)^2 + (\frac{\omega_c}{N})^2))^{1/2} \quad (4.4)$$

Here, D is in cm, V_d is in kV, Δt is in s, N is in cm^{-3} , and ω_c is in 1/s. ω_c can be written in terms of the magnetic field as 1.76×10^{11} B, if B is in tesla.

Using Eqn. 4.4, the minimum distance between the channel and the wall was calculated for some LIBRA parameters as a function of the applied magnetic field. In order to overcome the inductive impedance of the channels, $L \cdot di/dt = L(100 \text{ kA}/\mu\text{s})$, 1 MV must be applied across the length of the channels. It is assumed that one can bias the channel potential so that one end is 500 kV below the potential of the rest of the target chamber and the other end is 500 kV above it. Therefore, 500 kV must be held off for 1 μs , which is the rise time for the channel discharge current. The gas species is helium which has a σv of about $10^{-8} \text{ cm}^3/\text{s}$. Actually, σv is a function of electron energy, which depends on σv . Therefore, this value of σv is an estimate which is probably correct within a factor of 2.

The results are shown in Fig. 4.20, where D is plotted versus B for four different gas densities. Based on channel formulation simulations, the gas density was chosen as $3.55 \times 10^{18} \text{ cm}^{-3}$. If we wish to keep the distance from the channel to the wall down to 10 cm, we need a 3.2 T applied axial field. One can see the transition at the higher densities to the regime where the cyclotron frequency term is small compared to the collision term and the distance is no longer a function of magnetic field.

A preliminary design for a magnetic solenoid around the channels in the region of the blanket, reflector and wall has been done for LIBRA. This design, shown in Fig. 4.21, is discussed in Chapter 6.

One rather interesting thing to note in Eqn. 4.4 is that the required distance is not a function of the rise time. The maximum allowed V_d is proportional to $1/\Delta t$ so Eqn. 4.4 is independent of Δt . Obviously, other things may limit one from going to a very short Δt and a very high V_d .

4.5 Future Considerations

The development of plasma channels for ICF has reached a point where a set of self-consistent design parameters can be proposed, but there are still issues to be resolved. For example, in our proposal to use magnetic fields to inhibit breakdown, there are radial magnetic fields applied to the regions at the ends of the solenoidal magnets which will add angular momentum to the beam ions. This rotation of the beam may reduce the ion confinement. Another issue is accuracy of the ZPINCH computer code. The multigroup diffusion method currently used for radiation transport in ZPINCH is suspect because the channels are optically thin and because line radiation is important. New radiation transport schemes are under study.

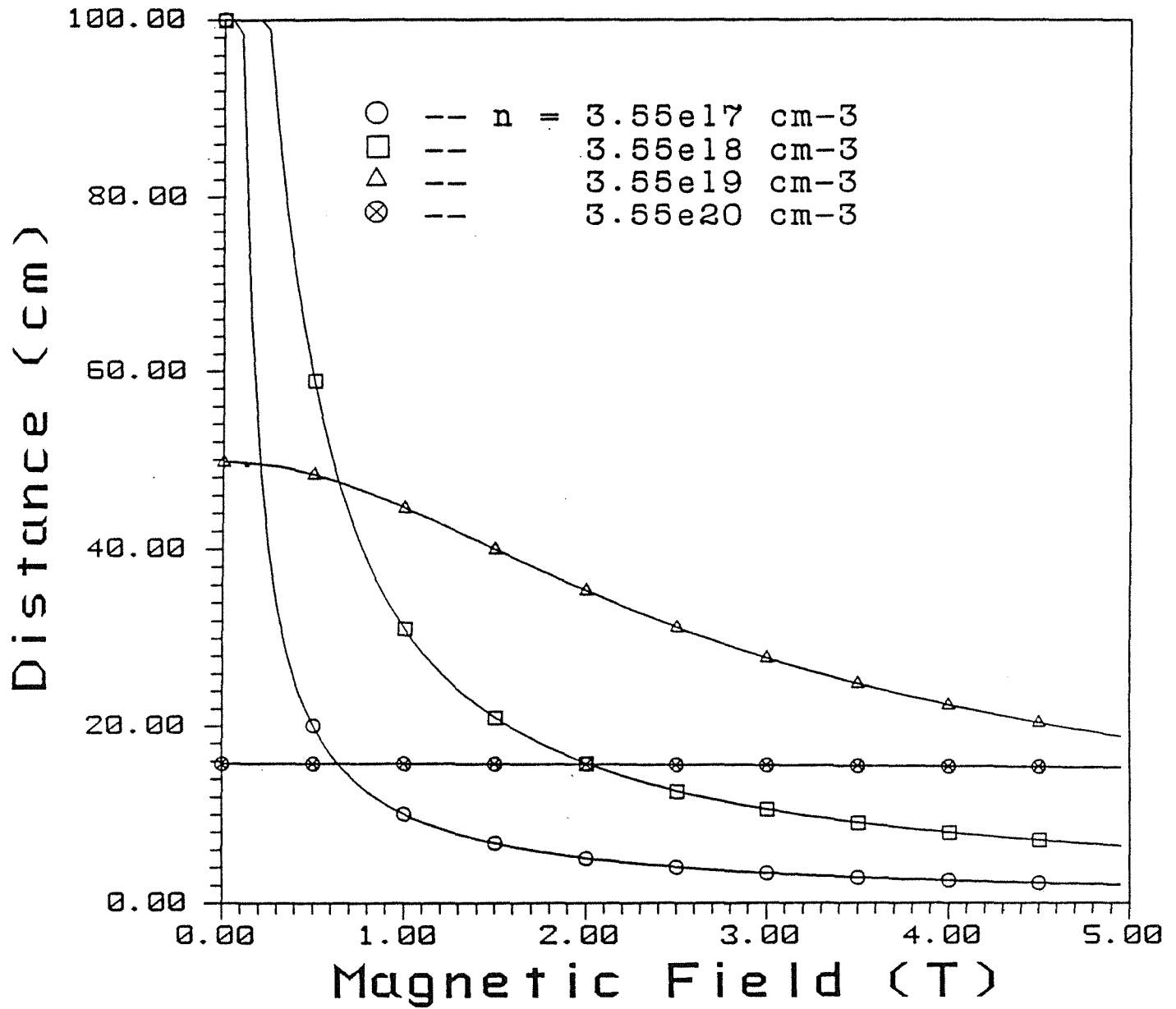
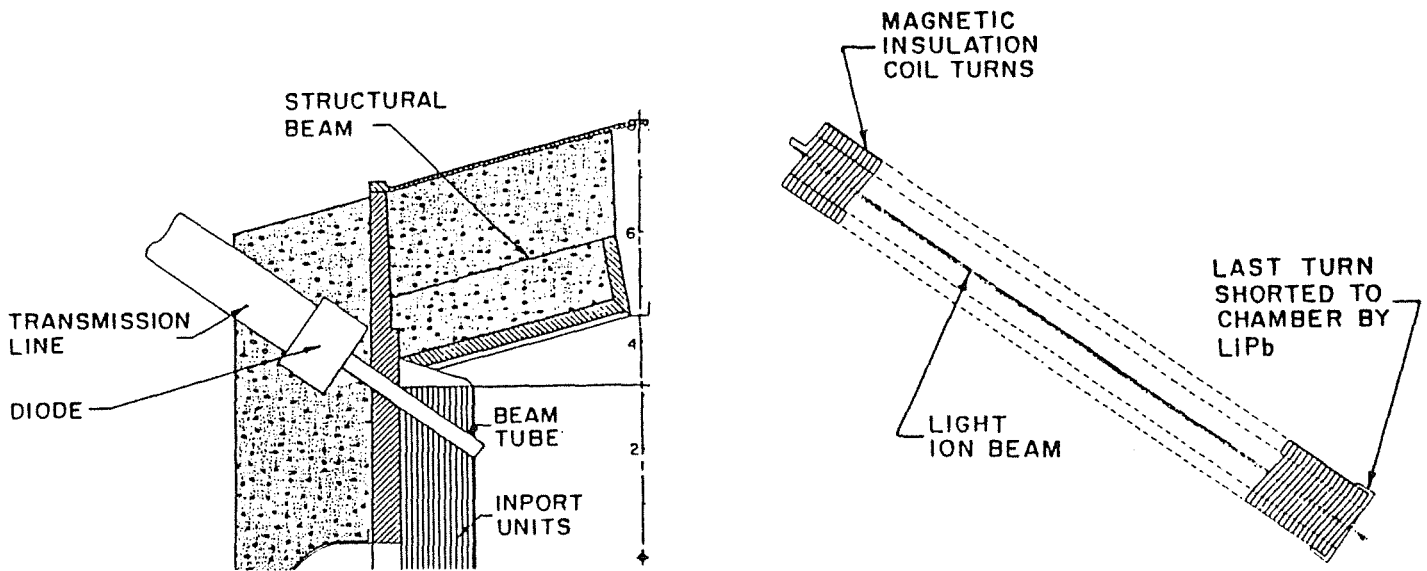


Fig. 4.20. Required channel to wall distance versus applied axial magnetic field and background density.



CONDUCTOR MATERIAL	TZM
MAGNETIC FIELD REQUIRED	3.2 T
VOLTAGE REQUIRED	11.3 kV
TOTAL POWER	26.5 MW

Fig. 4.21. Magnetic insulation system for LIBRA channels.

The magnetic insulation of plasma channels needs to be considered further. Thus far, an analysis assuming Townsend breakdown has been used. The possibility of rapid breakdown due to other physical processes needs investigation. Also, one needs to evaluate the propagation of the ion beam in the presence of the applied magnetic fields.

References for Chapter 4

1. G.A. Moses, et al., "LIBRA -- A Light Ion Beam Fusion Reactor Conceptual Design," University of Wisconsin Fusion Technology Institute Report UWFDM-787 (July 1988).
2. R.R. Peterson, G.W. Cooper, and G.A. Moses, "Cavity Gas Analysis for Light Ion Beam Fusion Reactors," Nucl. Tech./Fusion 1(2), (1981) 377-389.
3. J.J. Watrous, G.A. Moses, and R.R. Peterson, "ZPINCH -- A Multifrequency Radiative Transfer Magnetohydrodynamics Computer Code," University of Wisconsin Fusion Technology Institute Report UWFDM-584 (June 1984).
4. J.J. MacFarlane, "IONMIX -- A Code for Computing the Equation of State and Radiative Properties of LTE and Non-LTE Plasmas," University of Wisconsin Fusion Technology Institute Report UWFDM-750 (December 1987).
5. J.R. Freeman, L. Baker, and D.L. Cook, "Plasma Channels for Intense-Light-Ion-Beam Reactors," Nucl. Fusion, 22, 383 (1982).
6. M. Coppins, "Ideal Magnetohydrodynamic Linear Instabilities in the Zpinch," Plasma Physics and Controlled Fusion, 30, 201 (1988).
7. J.N. Olsen and R.J. Leeper, "Ion Beam Transport in Laser-Initiated Discharge Channels," J. Appl. Phys., 53, 3397 (1982).
8. G.A. Moses, "ION -- A Code to Compute Ion Trajectories in Zpinch Plasma Channels," University of Wisconsin Fusion Technology Institute Report UWFDM-712 (January 1986).
9. P.F. Ottinger, S.A. Goldstein and D. Mosher, "Constraints on Transportable Ion beam Power," Naval Research Laboratory Memorandum Report 4948 (November 1982).
10. R.R. Peterson, "WINDOW -- A Code to Compute Ion Beam Power Constraints," Fusion Power Associates Report FPA-84-6 (December 1984).
11. A.E.D. Heylen, "Electrical Ionization and Breakdown of Gases in a Crossed Magnetic Field," IEEE Proc., Vol. 127, Pt. A, No. 4, May 1980.

5. TARGET

5.1 Target Design

The target design effort for LIBRA is similar in scope to the design effort in the HIBALL study.⁽¹⁾ The initial target concept for LIBRA was published by Bangerter and Meeker⁽²⁾ in 1976. No detailed implosion calculations were done for the LIBRA study. Attention was instead focussed on the dynamics of the target microexplosion, assuming that the target could be imploded to the proper configuration to ignite and burn.

A schematic of the initial target dimensions and those at the instant of ignition are shown in Fig. 5.1. A list of parameters is given in Table 5.1. The target is a single shell with three layers. The outer layer of lead serves as a tamper to enhance the implosion efficiency. The next layer is a deuterated plastic ablator where the majority of the ion energy is deposited. Deuterium is used rather than protium to simplify the separation of tritium from the exhaust of the chamber. The inner layer is frozen DT fuel.

The ion beam pulse shape is shown in Fig. 5.2. The long, 40 ns, low power part is produced by two non-bunched beams while the high power part is produced by overlapping 16 additional bunched beams on the target. The driver design for LIBRA concentrated on the short high power beams. The total energy delivered to the target is therefore $0.4 + 3.6 = 4$ MJ.

At ignition, the DT is compressed to 485 times its solid density to a ρR -value of 2 g/cm^2 . Part of the plastic ablator (14%) has also been compressed around the DT to the same density, but at a ρR -value of 1 g/cm^2 . The remaining ablator and Pb tamper have expanded outward to roughly 10% of their initial density. These conditions are sufficient to produce a 30% burn fraction if the DT fuel ignites. The 3.2 mg of DT fuel will then produce a yield of 320 MJ of fusion energy.

This target design and the ignition conditions assumed for it are meant to be representative of high yield light ion targets. Four MJ of ion energy are assumed to achieve these conditions. This is consistent with published gain curves⁽³⁾ while the peak power of 400 TW is 20% less than published guidelines⁽³⁾ as shown in Fig. 5.3. The gain of 80 is sufficient for economical power production but is also "conservative" in comparison to the gains used in many other reactor design studies. A table of target design parameters is given in Table 5.1.

One important aspect of the target design that has not received substantial attention is illumination symmetry. A direct drive target, like the one used for this analysis, will require very good illumination symmetry--probably better than the axisymmetric

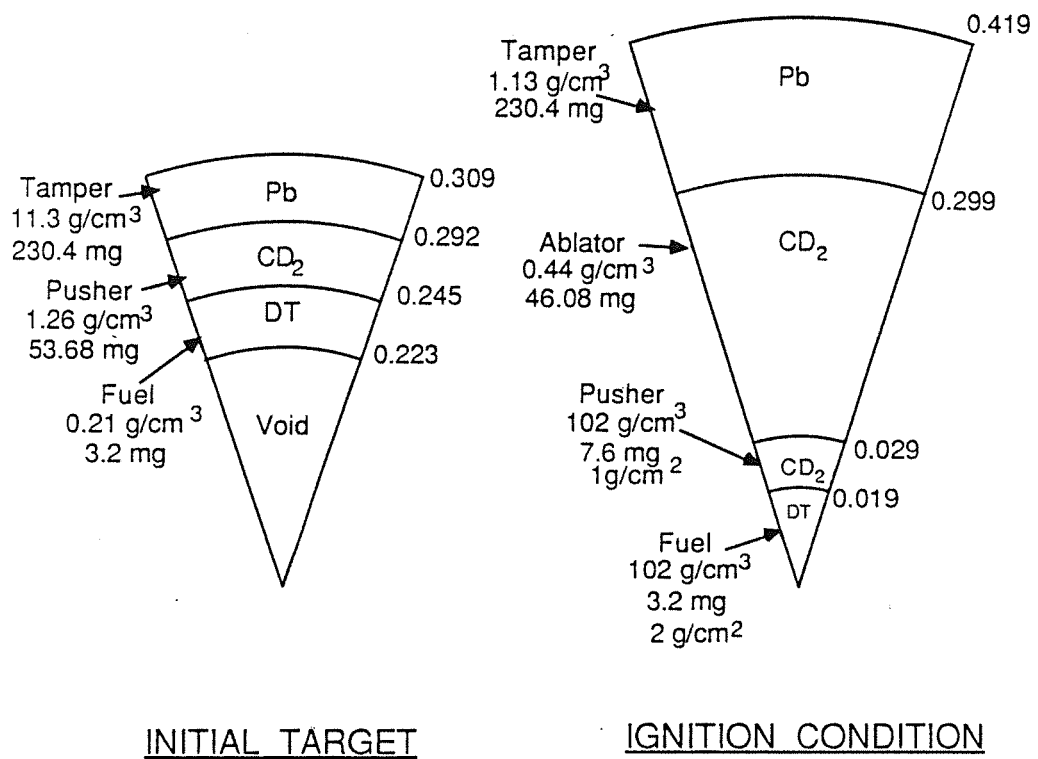


Fig. 5.1. LIBRA target design.

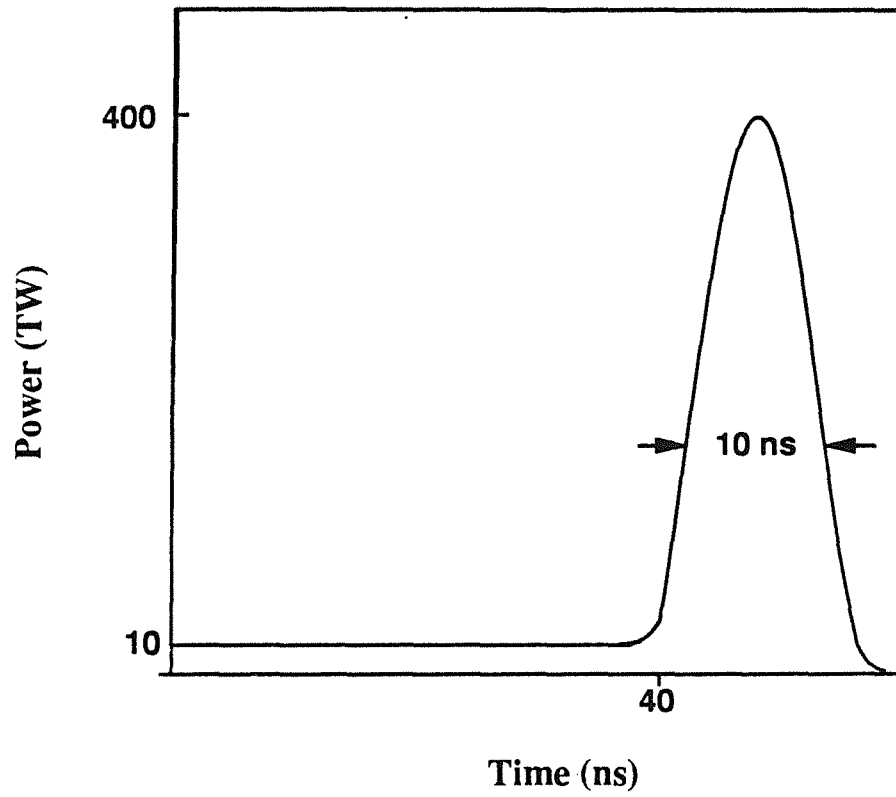


Fig. 5.2. Pulse shape on target.

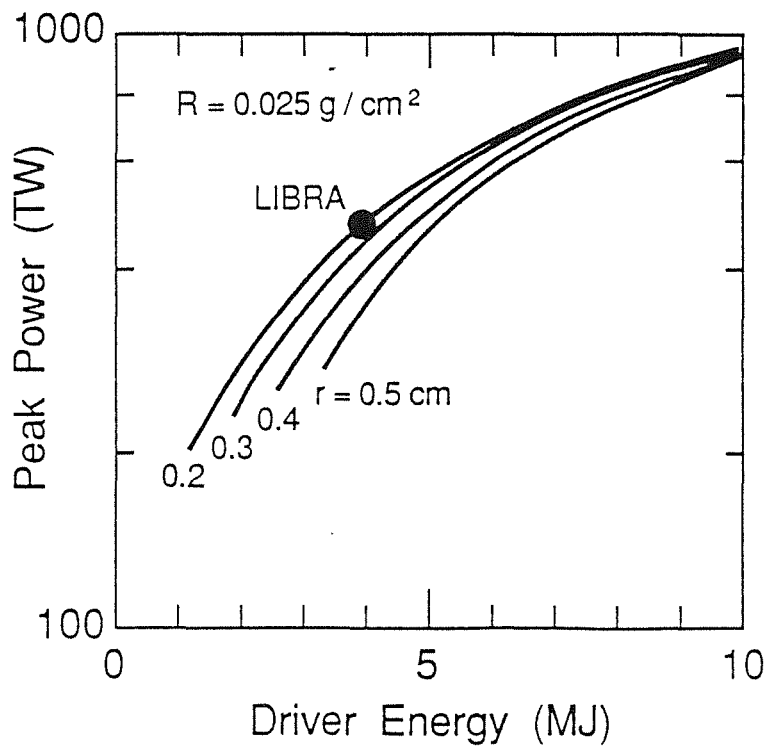
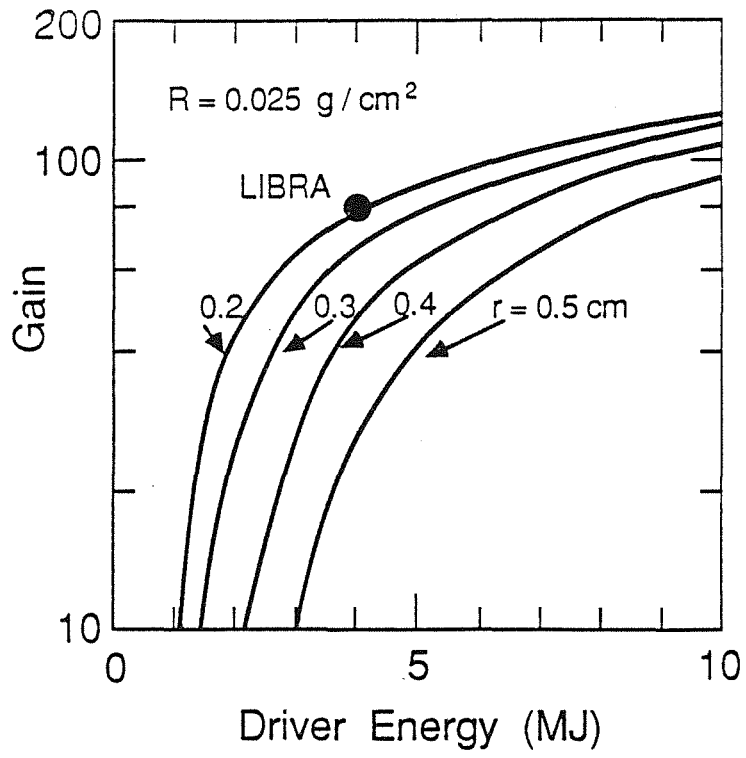


Fig. 5.3. Gain and power relations.
 R = ion range, r = target radius

Table 5.1 Target Parameters

Energy on target	4 MJ
Peak power	400 TW
Ion energy	25-35 MeV
Ion type	Li
Target gain	80
Target fusion yield	320 MJ
Endothermic losses	7 MJ (2.2%)
Neutron yield	216 MJ (67.5%)
Gamma yield	1 MJ (0.3%)
X-ray yield	63 MJ (19.7%)
Ion debris yield	33 MJ (10.3%)
Net target yield	313 MJ
Neutron multiplication	1.025
DT fuel shell mass	3.2 mg
inner radius	0.223 cm
outer radius	0.245 cm
CD ₂ pusher/ablator shell mass	53.7 mg
inner radius	0.245 cm
outer radius	0.292 cm
Pb tamper shell mass	
inner radius	0.292 cm
outer radius	0.309 cm
Initial target temperature	4 K
DT temperature prior to implosion	7 K
Injection velocity	200 m/s
Illumination symmetry	axisymmetric
Number of low power beams	2
Number of high power beams	16
High power pulse width	9 ns
Low power pulse length	40 ns

beams in the LIBRA design. In Section 5.4 we briefly discuss the suitability of the LIBRA target chamber for a hybrid target design. However, we expect that indirect drive target designs with better beam energy smoothing mechanisms might be required for the LIBRA beam placement. This lack of consistency in an otherwise nearly consistent conceptual design is an unfortunate but unavoidable shortcoming.

5.2 Target Microexplosion

Energy is released from the burning target in three forms: neutrons, x-rays, and energetic ion debris. The fraction of total energy in each of these forms and the energy spectrum of each are important inputs to the design of the reactor cavity. The initial split of energy from a DT reaction is of course one 14.1 MeV neutron and one 3.5 MeV alpha particle. However, neutron interactions with the compressed target material significantly soften the neutron spectrum. The energy deposited by the neutrons and alpha particles heats the target and ultimately takes the form of radiated x-rays from the hot plasma or expanding ionic debris.

Neutronics calculations have been performed for the LIBRA target using the one-dimensional discrete ordinates code ONEDANT. The target configuration at ignition used in the calculations is shown in Fig. 5.1. The calculations were performed using spherical geometry and 30 neutron - 12 gamma group cross section data based on the ENDF/B-V evaluation. A uniform 14.1 MeV neutron source was used in the compressed DT fuel zone.

The total energy deposited by neutrons and gamma photons in the target was calculated to be 1.754 MeV per DT fusion. Only 0.11% of this energy is deposited by gamma photons. About 70% of the energy is deposited in the DT fuel zone. Due to (n,2n) and (n,3n) reactions occurring in the target, 1.025 neutrons are emitted from the target for each DT fusion reaction. These neutrons carry an energy of 11.93 MeV implying that the average energy of neutrons emitted from the target is 11.64 MeV. For each DT fusion reaction, 0.013 gamma photons are emitted from the target with an average energy of 3.85 MeV. The energy spectra of neutrons and gamma photons emitted from the LIBRA target are shown in Fig. 5.4. Performing an energy balance for the target indicates that 0.37 MeV of energy is lost in endoergic reactions per DT fusion. For the LIBRA DT fuel yield of 320 MJ, the target yield is calculated to be 313.3 MJ. The neutron and gamma yields are 216.9 and 0.9 MJ, respectively, while the combined x-ray and debris yield is 95.5 MJ. The energy flow for the LIBRA target is given in Fig. 5.5.

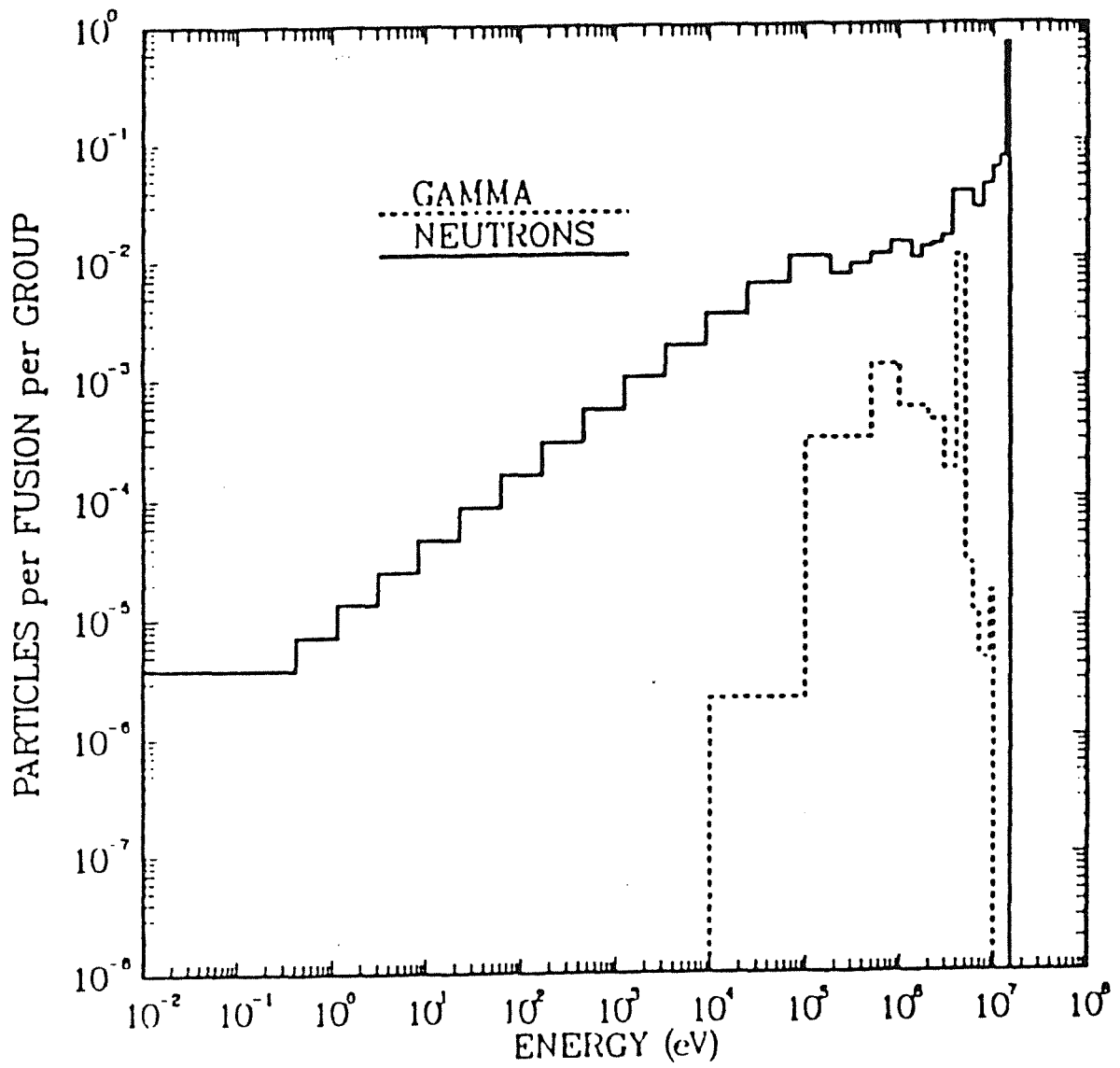


Fig. 5.4. Neutron and gamma spectra.

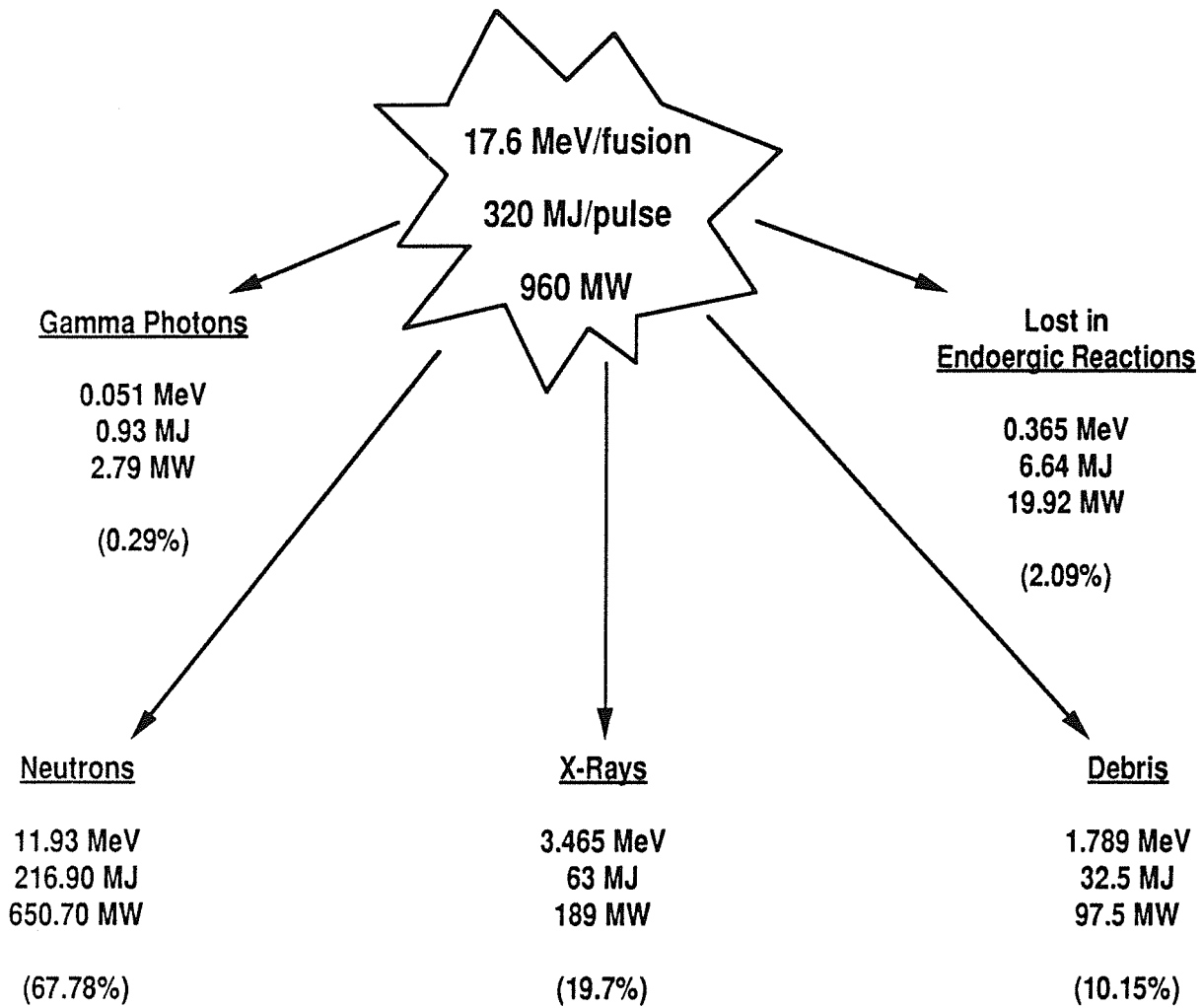


Fig. 5.5. Energy flow for LIBRA target.

The x-ray and ionic debris energy split and spectra were computed by scaling results from PHD-IV⁽⁴⁾ radiation-hydrodynamic, thermonuclear burn simulations. Sesame equations of state and astrophysical library opacities were used in the simulations. The fraction of energy radiated as x-rays is a strong function of the material composition of the target. Bare DT compressed spheres radiate a small fraction of energy as x-rays (~ 5%) and these are in a hard bremsstrahlung spectrum. They originate in the burning fuel. In the LIBRA target, the Pb tamper attenuates the majority of these hard x-rays and re-radiates the energy in a softer blackbody spectrum. The high Z material radiates more efficiently than the DT and thus a larger percentage of energy is in the form of x-rays. This is shown in Fig. 5.5. The x-ray spectrum is shown in Fig. 5.6 and the ion spectrum is given in Table 5.2. No spectral information is available for the ions because their expansion is modelled with a fluid code and only their fluid velocity is computed. As the ions expand they cool to low temperatures by expansion cooling.

These parameters for energy partition and spectra are used as input for the cavity response and blanket response calculations.

Table 5.2 Ion Spectrum

<u>Species</u>	<u>Kinetic Energy/Ion</u>	<u>Total Energy (MJ)</u>
D	1.93	0.08
T	2.89	0.12
He	3.8	0.1
C	11.1	6.2
Pb	198.0	26.5

5.3 Target Heating During Injection

There are three phases of heating that the target experiences. First, there is frictional heating of the sabot that encases the target during the acceleration of the target in the pneumatic gun barrel of the target injector. The pneumatic target injector is the same as the one designed for the HIBALL study, and is shown in Fig. 5.7. The sabot design is from the HIBALL-II⁽⁵⁾ study and is shown in Fig. 5.8. The heat load on the outside of the sabot is estimated to be 51 W/cm². Calculation of the heating of the sabot and target shows that only the sabot is heated during this phase and that the target enters the target chamber at a uniform temperature of 4 K. Secondly, there is heating of the target during its transit from the muzzle of the gun barrel to the focus of the ion

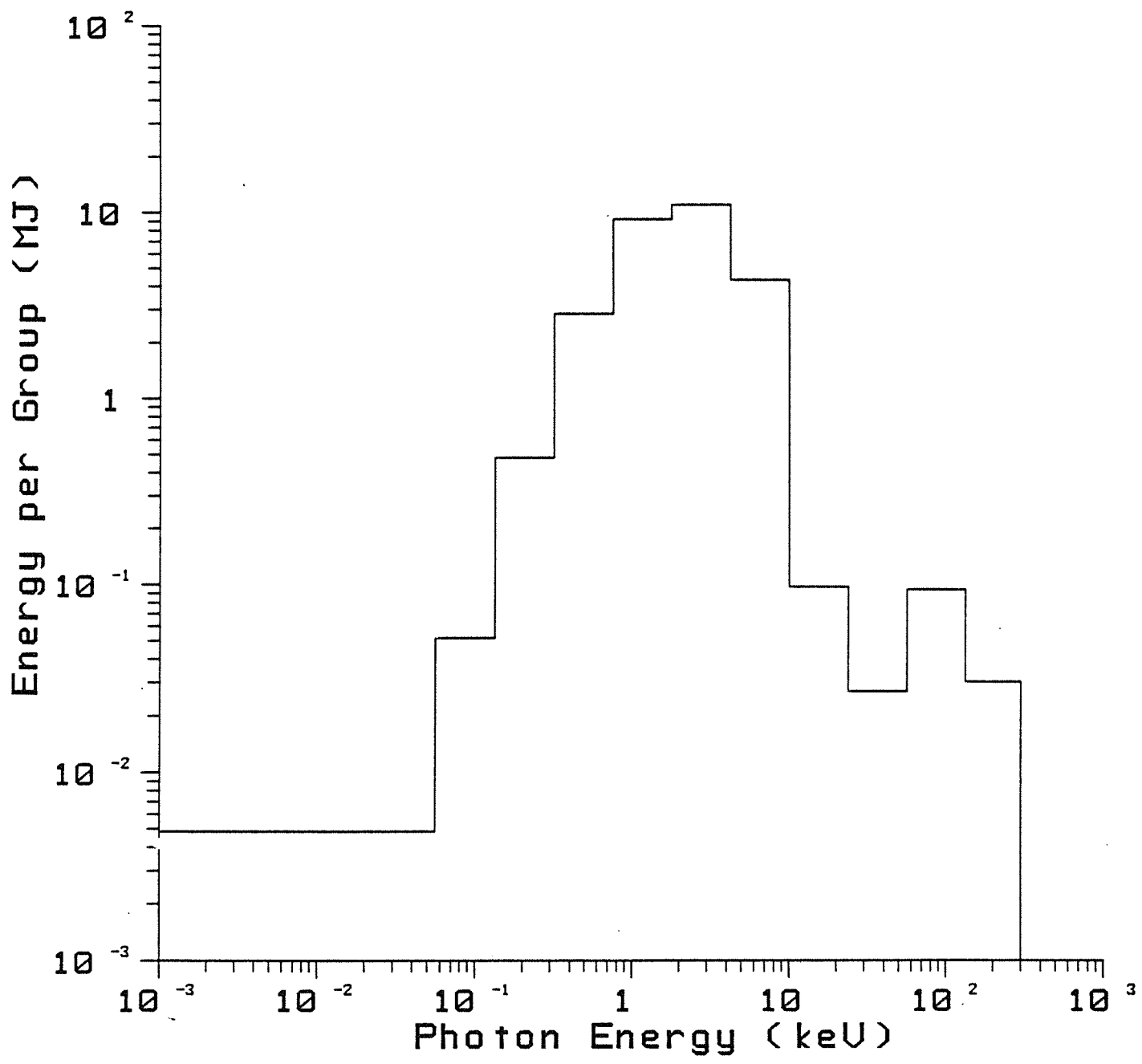


Fig. 5.6. X-ray spectrum.

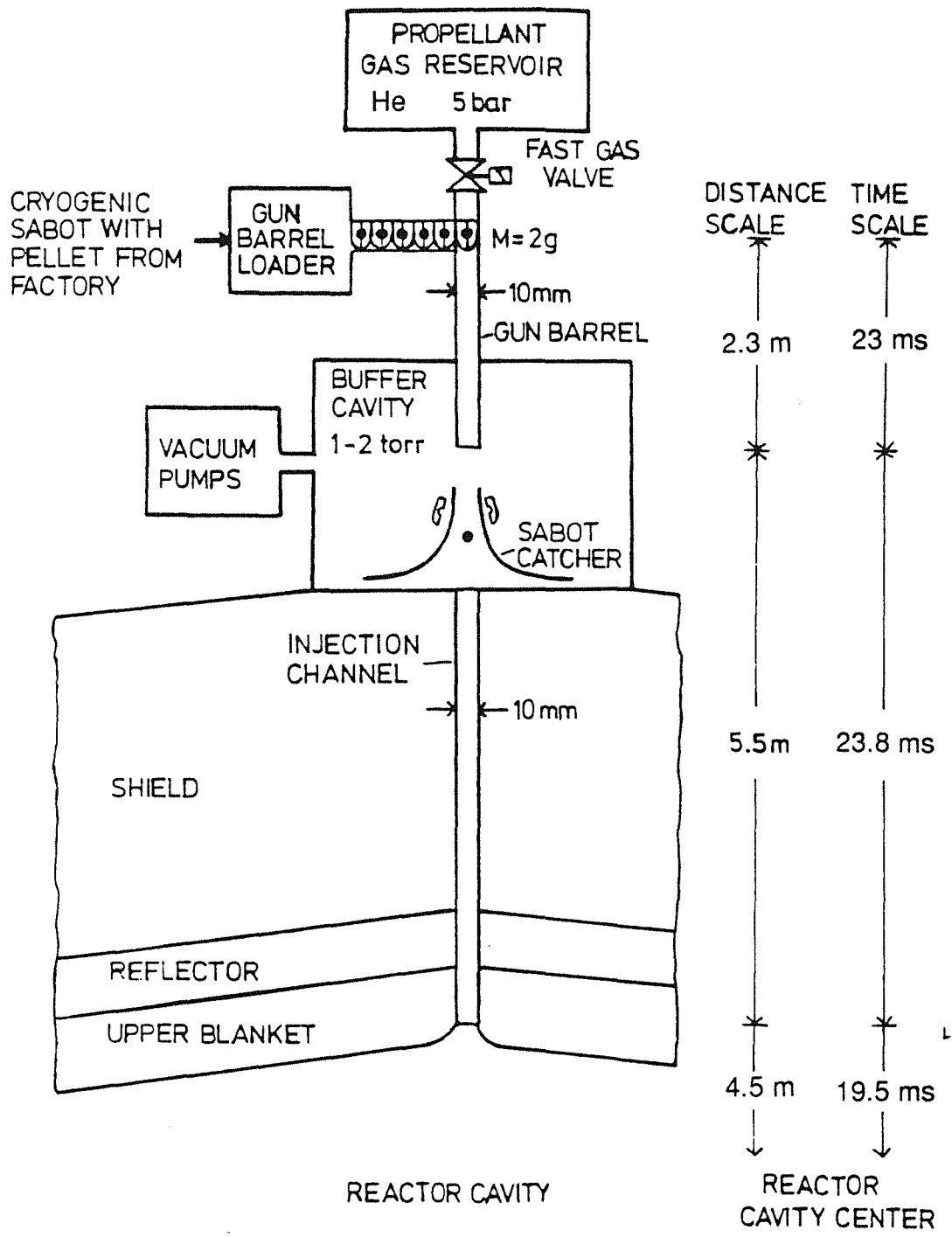


Fig. 5.7. Target injector.

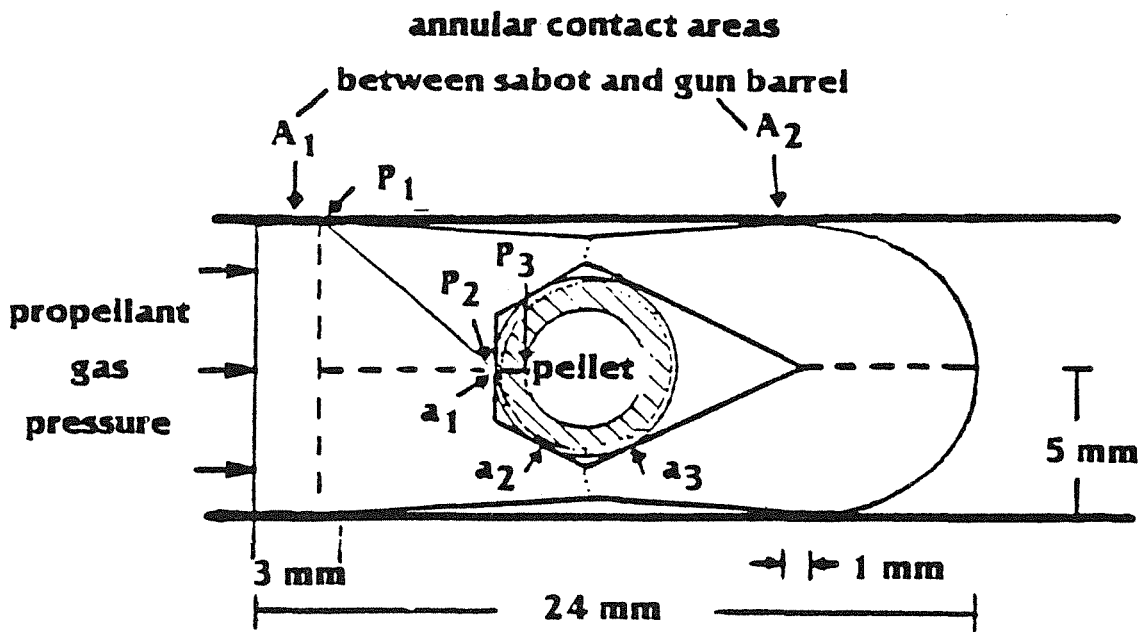


Fig. 5.8. Sabot for LIBRA target.

beams. The target has a speed of 200 m/s and the distance it must travel is 3.9 m, so the time during which this heating occurs is 19.5 ms. The LIBRA target chamber is filled with helium gas at a density of $3.5 \times 10^{18} \text{ cm}^{-3}$ and a temperature of 800 K. Taking the diameter of the target to be 1 cm, the viscosity of helium at 800 K to be $383.6 \times 10^{-6} \text{ g/cm-s}$, and the thermal conductivity of helium under these conditions to be $4.04 \times 10^{-4} \text{ W/cm-K}$, one can easily calculate the convective heating rate of the target to be 8.4 W/cm^2 . Adding this to the radiant heat load from the target chamber, the total heat load during this phase is 10.4 W/cm^2 . The results of the PELLET simulation are shown for this phase in Fig. 5.9. The temperature in the target is shown as a function of position for three times: when the target enters the target chamber ($t = 0$), when the target reaches the ion beam focus ($t = 19.5 \text{ ms}$), and when the ion beams reach the target, that is after the radiant heat from the channel warms the target ($t = 19.502 \text{ ms}$). One sees here that, after injection, the fuel is only heated to about 7 K. The final phase is when the target is near the ion beam focus, after channel formation has begun. Estimates from the channel simulations indicate that the plasma in the channels reaches a temperature of about 20 eV. The channels do not radiate like blackbodies because the helium is fully ionized. The channels overlap about 1 cm from the target and the channel formation simulations indicate the average radiant power density on the target over the roughly $2 \mu\text{s}$ formation time is $2.3 \times 10^4 \text{ W/cm}^2$. This estimate neglects overlapping of radiant heat from adjacent channels and additional heating due to the preionizing laser system. The results, shown in Fig. 5.9, indicate that the target fuel is not heated at all by the channel heat flux because it takes too long to diffuse through the lead and plastic shells. If the heat load on the target during this phase were increased by an order of magnitude, this conclusion would not change.

One can easily understand this result if one considers the thermal conductivity and specific heat times mass density product profiles for the target, shown in Figs. 5.10 and 5.11 respectively. These are the profiles present in the target just as the ion beam strikes the target. In Fig. 5.10, one notices a very low thermal conductivity of plastic. The distance that heat can diffuse into a material in a time Δt is of the order

$$\Delta x = 2\sqrt{\alpha \Delta t} \quad . \quad (5.1)$$

For the lead shell and for $\Delta t = 2 \mu\text{s}$, Δx is 0.0014 cm, which is about what is observed in Fig. 5.9. For a $10 \mu\text{s}$ channel formation time (it is hard to imagine a much longer

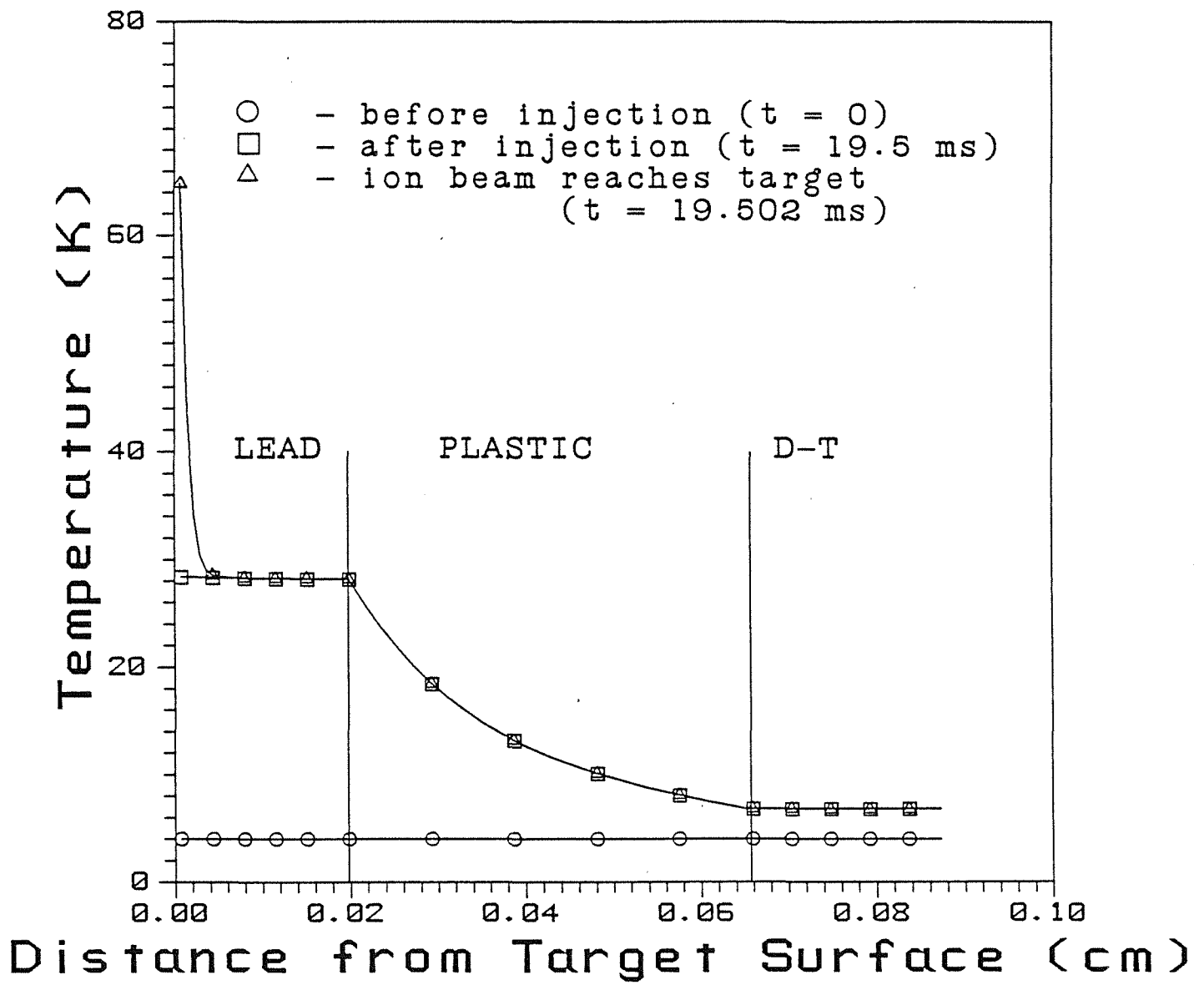


Fig. 5.9. Target heating vs. time.

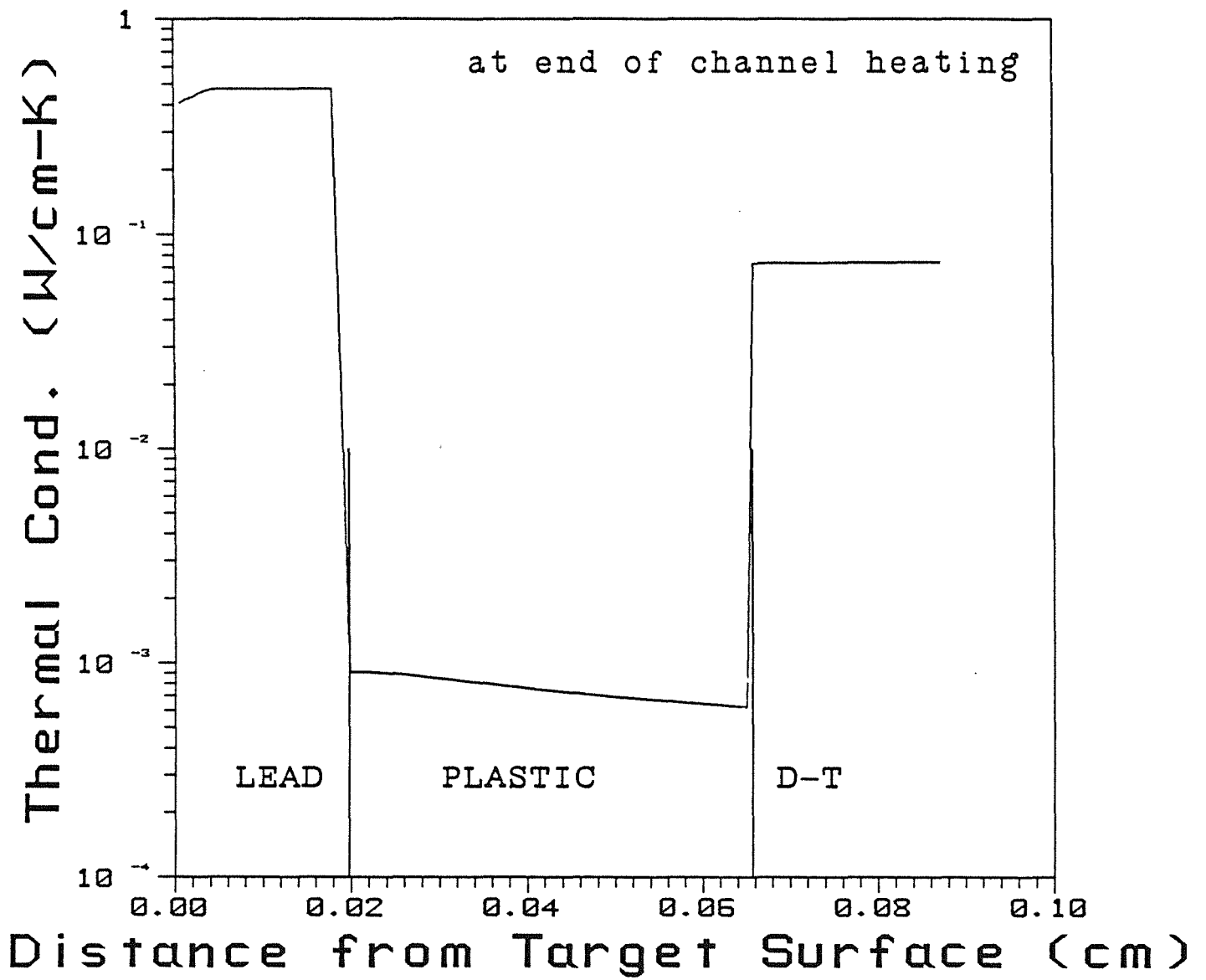


Fig. 5.10. Target thermal conductivity.

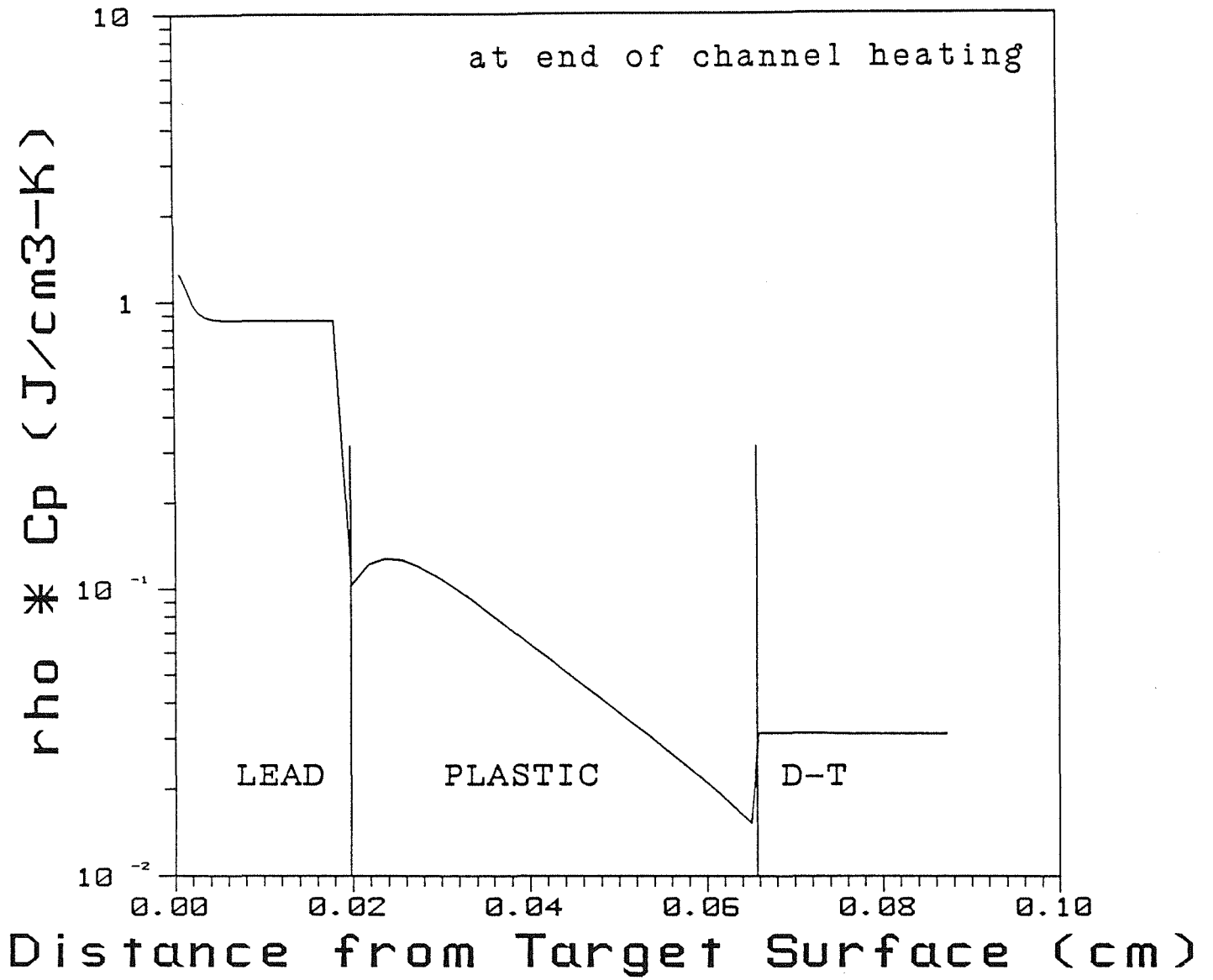


Fig. 5.11. Target specific heat (\times) mass density product.

formation time) the heat would only diffuse 0.0032 cm into the target and would still not have passed the lead shell.

Therefore, a plastic pusher in the target or any other insulating layer solves the problems of DT fuel heating prior to the heating of the target by the ion beam.

5.4 Optional Hybrid Target Design

We have discussed with Mark at Lawrence Livermore National Laboratory the possibilities for a target that combines the positive features of both the direct and indirect drive concepts.⁽⁶⁾ The advantage of such a hybrid design is that the gain-energy relation is improved over that for pure indirect drive, while the beam symmetry requirements are within the range of that which can be achieved within the LIBRA concept. The gain-energy relation for a hybrid drive concept is shown in Fig. 5.12, where one can see the improvement over pure indirect drive. The figure shows two points for hybrid drive, a gain of 90 at an input energy of 2.5 MJ and a gain of 140 at 6.6 MJ input energy. The low energy and gain point was the result of a calculation for a driver beam of 3 GeV Cs at a peak power of 150 TW focused on to a 3.4 mm diameter spot. The $r^{3/2}R$ parameter is 0.004 for this case. The high gain and energy calculation was for 4 GeV Cs on a 5.1 mm diameter spot ($r^{3/2}R = 0.01$) at a peak power of 250 TW. For both cases, the gain is about a factor of two higher than the corresponding curves for pure indirect drive. However, the spot sizes are both significantly less than what we predict for the LIBRA beam propagation scheme, 10 mm. Therefore, only 11% of the beam would be within a 3.4 diameter spot and 89% of the beam would be wasted. This would lead to a much less advantageous gain-energy relation.

The illumination symmetry is improved if one places the beams at nulls of Legendre polynomials.⁽⁷⁾ This approach eliminates long wavelength asymmetries, which are considered to be the most damaging. If one arranges the 18 LIBRA light ion beams in two cones 35° out of the equatorial plane, one can remove some, though not all, of the long wavelength modes. The LIBRA target chamber does in fact have the beams so arranged, though it is not clear if the symmetry is good enough for the hybrid drive scheme. A better scheme would have the beams in cones 50.8° above and below the equatorial plane and also in the equatorial plane, but cones of such high angle are not compatible with the current LIBRA target chamber design.

In summary, the hybrid drive target concept provides a higher gain at lower input energy than does indirect drive, though it is not clear that the LIBRA target chamber

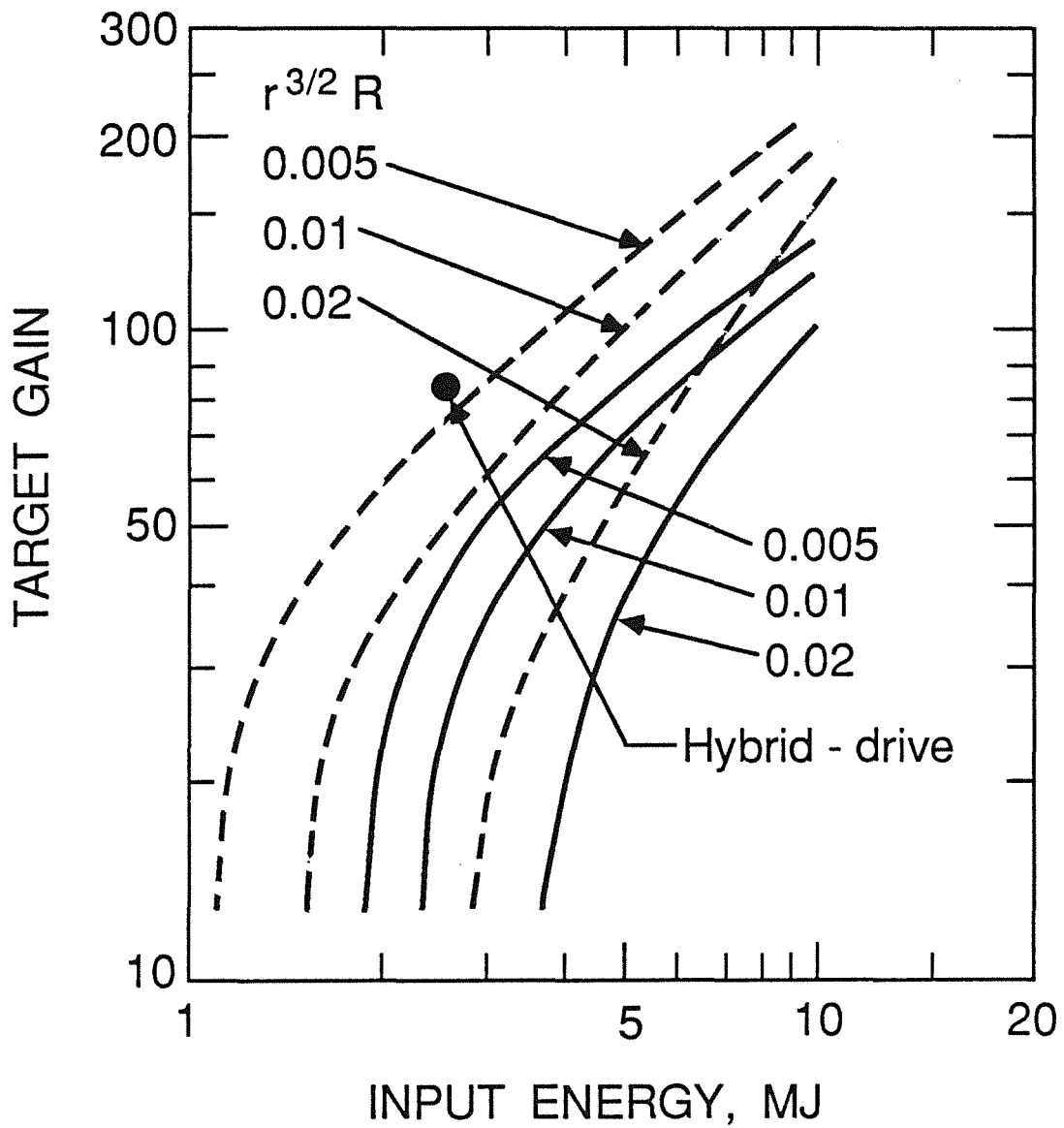


Fig. 5.12. Gain-energy relation for hybrid target.
 R = ion range (g/cm^2), r = radius of target
 Dashed curve is for hybrid-drive, solid curve is for indirect drive

concept will allow adequate beam symmetry. Also, one would need to find a way to focus the light ion beams in LIBRA to a smaller spot or a way to drive the hybrid target with a beam of larger spot size. Therefore, further work on the hybrid concept and modification of target chamber concepts should be considered before the hybrid concept becomes the main line target design for commercial light ion fusion. The advantages of hybrid targets to the economics of power production are quite evident.

References for Chapter 5

1. B. Badger, et al., "HIBALL - A Conceptual Heavy Ion Beam Driven Fusion Reactor Study," University of Wisconsin Fusion Technology Institute Report UWFDM-450.
2. R.O. Bangerter and D. Meeker, "Ion Beam Inertial Fusion Target Designs," Lawrence Livermore Laboratory Report UCRL-78474 (1976).
3. R.O. Bangerter, "Targets for Heavy Ion Fusion," Fusion Tech. 13, 348 (1988).
4. G.A. Moses, et al., "PHD-IV, A Plasma Hydrodynamics-Thermonuclear Burn-Radiative Transfer Computer Code," University of Wisconsin Fusion Technology Institute Report UWFDM-194 (unpublished).
5. B. Badger, et al., "HIBALL-II - An Improved Conceptual Heavy Ion Beam Driven Fusion Reactor Study," University of Wisconsin Fusion Technology Institute Report UWFDM-625 (1984).
6. HIFSA - Heavy Ion Fusion Systems Assessment Project Final Report - Volume II: Technical Analyses, Los Alamos National Laboratory Report, LA-11141-MS, Vol. II (December 1987), pp. 1.3A-1 - 1.3A-15.
7. J. W-K. Mark, "Near Spherical Illumination of Ion-Beam and Laser Targets", Physics Letters 114A, 458 (1986).

6. TARGET CHAMBER DESIGN AND MAINTENANCE

6.1 General Discussion

The LIBRA target chamber is similar to the HIBALL (Heavy Ion Beams and Lithium Lead) reactor design which was completed in 1981.⁽¹⁾ Although the basic configurations of the two reactor systems are similar, there are fundamental differences, some of which are listed below:

1. HIBALL utilized ballistic focusing of heavy ions whereas LIBRA uses a preformed plasma channel for transporting the ions to the target.
2. The ambient gas pressure in HIBALL was 10^{-5} torr, while in LIBRA it is 260 torr (equivalent of 100 torr at 0°C).
3. HIBALL was connected to a steady state vacuum pumping system while LIBRA utilizes a self-pumped feature.
4. In HIBALL the heat exchangers were located in a separate building, whereas in LIBRA they are built into the base of the chamber.
5. The maintenance schemes for the two reactors are substantially different.

These differences are primarily due to the dissimilar process needed for transporting heavy ion beams as opposed to light ion beams. With respect to energy extraction and power cycle considerations, there are no differences.

Location of the heat exchangers in the base of the target chamber in LIBRA was motivated by a single consideration: that of minimizing the total inventory of LiPb. Because of its high density ($\rho \approx 9.6 \text{ g/cm}^3$) transporting LiPb over long distances in pipes is problematic. Further, to avoid any possibility of a water/LiPb interaction, the heat exchangers in the base of the chamber transfer the energy from LiPb to helium gas which then goes to a steam generator and a conventional steam power cycle.

The high pressure in the target chamber needed to form plasma channels has several beneficial aspects. For example, the maximum temperature of the LiPb in the front INPORT units in HIBALL was limited to 500°C because of the low pressure in the chamber (10^{-5} torr). There is no such limitation in LIBRA. But the main benefit is the fact that the chamber can be made to be self-pumping, a feature which would be impossible at the low pressure of HIBALL. The main difficulty of operating at this pressure is the isolation of the beam transmission tubes which have to be at pressures on the order of 10^{-5} torr. Although they have not been designed, it is assumed that some

kind of rotating shutters will be used to isolate the chamber environment from that of the ion diodes.

In LIBRA, as in HIBALL, the breeding/cooling material is $\text{Li}_{17}\text{Pb}_{83}$. The roof, which is designed to be periodically replaced, is cooled with LiPb flowing through wedge shaped modules. After going through the roof this coolant then flows down the vertical sides of the chamber through rear INPORT units. Additional LiPb is routed into the remaining INPORT units. All the coolant then collects in the bottom pool after which it goes through the heat exchangers, giving up its energy to helium gas which is used in a conventional steam cycle.

One of the concerns many people have about this scheme is LiPb dripping from the roof and intersecting the path of a light ion beam. This turns out to be a non-issue. The shortest distance from the roof to a beam outlet is 1.6 m. The distance a droplet travels by gravity in 0.33 s (3 Hz repetition rate) is 0.53 m. Clearly any drop which falls from the roof immediately after a shot will be vaporized and disassembled by the succeeding shot long before it reaches the vicinity of the beam paths. The repetition rate will have to be reduced to 1.75 Hz before this will become a problem.

In the next sections the target chamber and its maintenance are discussed. Target chamber self-pumping, beam line protection and the thermal hydraulics are also described.

6.2 Target Chamber Description

The LIBRA target chamber is an upright cylinder with internal dimensions of 7.7 m height on axis and 6.0 m in diameter as shown in Fig. 6.1. The chamber is characterized by three distinct zones, the blanket, reflector and shield. The blanket in the vertical sides of the chamber consists of a 1.35 m thick zone of flexible porous SiC tubes called INPORT (inhibited flow porous tube) units. Figure 6.2 shows the distribution of the tubes with the first two rows of 3 cm diameter and the following 9 rows of 10 cm diameter tubes respectively. These tubes occupy 33% of the available space and have LiPb breeding/cooling material flowing through them. Since the tubes are porous, there is a wetted film present on the outer surface at all times. This wetted film absorbs the surface heat from x-rays, ion debris and radiant energy coming from the target explosion. The blanket is followed by a 50 cm thick reflector zone made of the ferritic steel HT-9 and also cooled with LiPb. Besides reflecting neutrons, this zone is the primary structural support for the INPORT units and is the vacuum barrier for the chamber.

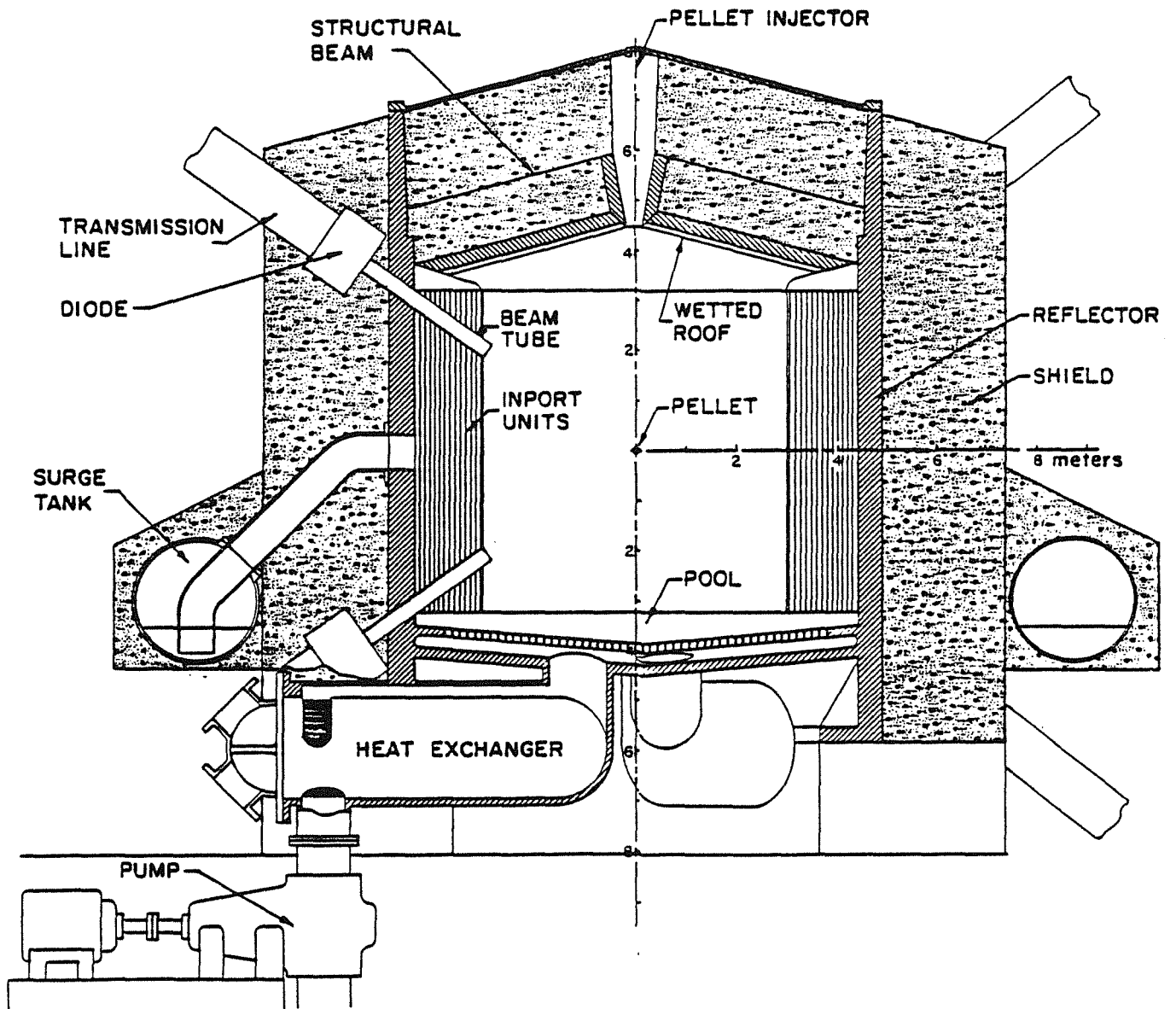
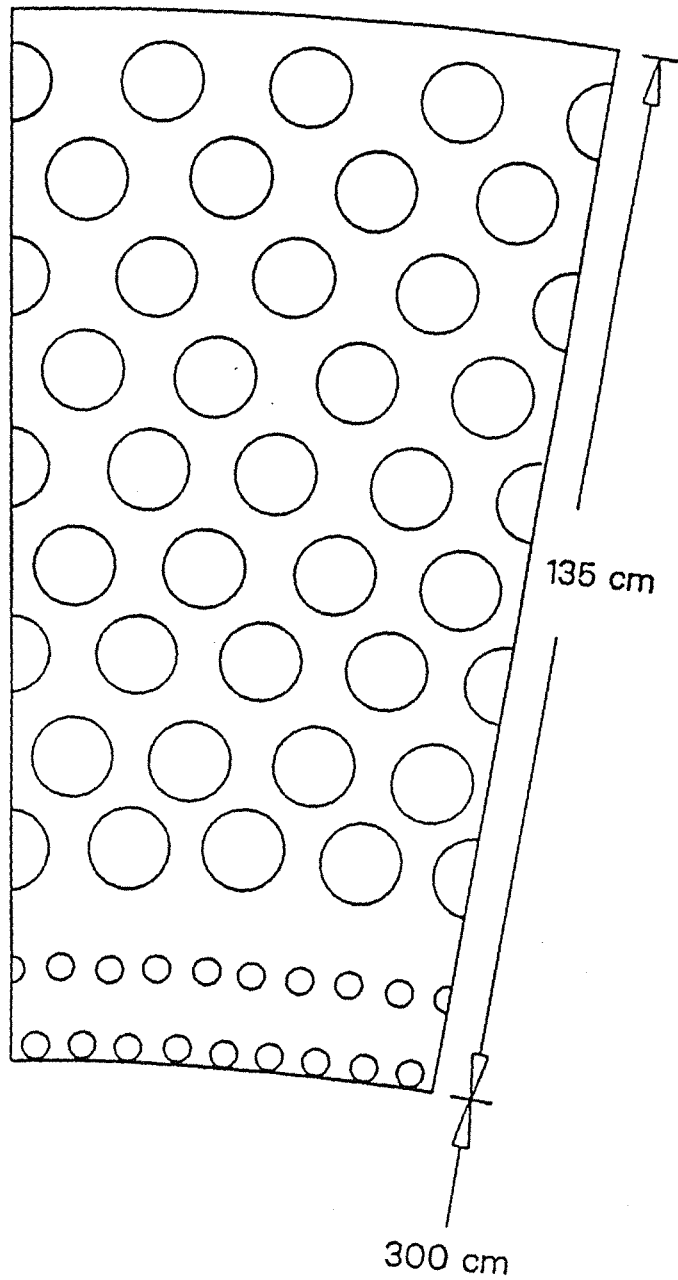


Fig. 6.1. Cross section of the LIBRA reaction chamber.



3 cm INPORTs - 2 rows @ 314 = 628
 10 cm INPORTs - 9 rows @ 140 = 1260
 Packing Fraction = 33 %

Fig. 6.2. Distribution of INPORT units in the LIBRA blanket.

It extends to the top of the chamber where it is sealed to the upper flange of the roof structure. The vertical part of the reflector is penetrated by 18 beam tubes, nine on the top and nine on the bottom, equally distributed, coming in at an angle of 34° to the horizontal, as shown in Fig. 6.1. There are also nine exhaust ducts penetrating the reflector at the midplane connecting the target chamber with the suppression chamber through a LiPb trap. Finally, the reflector is followed by a 2.5 m thick shield made of reinforced concrete. This is cooled by helium gas.

The roof of the chamber is covered with 10 cm thick wedge shaped woven SiC modules which have LiPb flowing through them. These modules are attached to a 25 cm thick HT-9 reflector cooled with LiPb. This reflector is welded to six equally spaced structural beams which are 1.1 m high and 6 cm thick. These beams, along with the integral central hub, constitute the primary support structure for the roof. Six independent shield segments fit between the beams to provide an effective shield thickness of 2.95 m. The last element in the roof is the vacuum flange made of HT-9 which is sealed to the vertical reflector to form the vacuum barrier for the roof. A pellet injector is located in the center of the roof, fitting through the central hub. This pellet injector is sealed to the top vacuum flange and can be removed independently for servicing.

The bottom of the cavity consists of a LiPb pool which is formed by the coolant flowing through the roof modules and the INPORT tubes. It drains through a 15 cm thick perforated plate made of HT-9, which acts as a reflector as well as a shock damper. From there, the LiPb flows down a 20 cm thick splash plate into three ports leading to the three heat exchangers built into the base of the chamber.

A suppression tank is located on the outer perimeter of the target chamber. It is toroidal in shape, 2.30 m in diameter and partially filled with LiPb. The outlet of the exhaust pipes from the target chamber are immersed in this pool of LiPb forming a so-called trap. Gases from the target chamber can exhaust into the suppression tank by bubbling through the LiPb, but they cannot return back, prevented by the column of LiPb. This scheme is part of the self-pumping feature of the target chamber and will be discussed in the next section.

6.3 Target Chamber Evacuation

The LIBRA chamber is designed to be self-pumped by the target explosion generated overpressure which expands into the suppression tank through nine ducts, equally

spaced at the chamber midplane. A He gas equivalent to 100 torr at 300 K is needed for beam propagation.

The gas temperature in the target chamber just prior to a shot is 800 K and the pressure 260 torr. Immediately after the shot the temperature rises to 9000 K and the pressure to 2900 torr. The temperature in the suppression tank LiPb is maintained at 350°C by replenishment and the gas pressure at 260 torr. Right after the shot the gas in the target chamber undergoes an isentropic expansion through the LiPb lock into the suppression chamber. As the gas expands it is also cooled. When the gas pressures in the target and suppression chambers equilibrate, the LiPb trap prevents any further communication between them. The post-expansion gas temperature in the target chamber is higher than it was prior to the shot and the fraction of gas within the INPORT units zone quickly equilibrates with the temperature of the LiPb. Precise determination of the temperature in the LIBRA target chamber upon pressure equilibration is very difficult. In the present calculation we make the following conservative assumptions:

- The gas in the target chamber expands isentropically into the suppression chamber.
- The gas in the INPORT unit zone cools down to the maximum temperature of the LiPb (773 K).
- The gas in the center of the chamber remains at the temperature it cooled down to due to the isentropic expansion.
- The temperature of the gas is then averaged for these two zones and the target chamber pressure is based on this temperature.

As the gas in the target chamber continues to cool down, approaching the initial temperature of 800 K, the pressure falls below the initial pressure of 260 torr. At this point fresh helium gas is injected into the chamber to maintain the pressure at the prescribed pre-shot value. Another simplifying assumption that has been made in this calculation is that the gas entering the suppression chamber is immediately cooled to 350°C. This is not a bad assumption when one considers that the LiPb in the suppression tank can be continuously injected in the form of a mist which falls down to the bottom of the chamber. The LiPb is then pumped out from the bottom of the suppression tank at the same rate it is injected, to maintain the correct level in the tank for proper trap action. In this way, the energy which leaves the target chamber with the evacuated gas is recovered and used in the power cycle.

Table 6.1 gives the results of the calculation as a function of the ratio of the suppression tank volume to the target chamber volume. The first two columns give the average gas temperature and the average gas pressure in the target chamber after equilibration with the gas in the suppression tank. The third column gives the ratio of the pressure after equilibration to the initial pressure in the suppression tank. This is the ratio that the vacuum pumps have to deal with. The fourth column gives the fraction of the target chamber gas evacuated per shot and the last column gives the effective steady state pumping speed needed to pump down the suppression tank to the prescribed initial pressure of 260 torr in 0.33 s.

Figure 6.3 is a plot of the pressure ratio of the equilibrated pressure to the initial pressure and the required effective pumping speed as a function of the volume ratio of the suppression chamber to the target chamber. The only kind of pumps that are capable of operating in such high pressure are mechanical pumps. However, since there will be tritium present in the helium, they must be oil-less pumps, otherwise the oil will be contaminated with tritium. There are mechanical pumps with dry seals, usually made of plastics. It is not recommended that such pumps be used with pressure surges of higher than 30%. Thus it would seem that the cutoff would be at a pressure ratio of 1.3 which occurs at a volume ratio of suppression chamber to target chamber of 0.6. The required pumping speed is 1.67×10^5 ℓ/s for this volume ratio.

Typically, vacuum pumps are more expensive than pressure vessels and a difference of 30% in pumping capacity could be a substantial difference in cost. This would indicate that it would be prudent to choose a larger suppression tank and lower the pumping speed. A word of caution has to be included here. Such high capacity roughing pumps operating in the 250-350 torr regime, especially of the oil-less variety, do not exist today. Such a roughing pump, say of 10^4 ℓ/s capacity, would take a substantial development program to produce.

6.4 Beamline Magnetic Protection

The LIBRA target chamber has 18 beam lines, 9 equally distributed at the top and 9 on the bottom, inclined at 34° to the horizontal. To prevent the beams from shorting to the blanket, they are transported between the INPORT units through magnetically insulated tubes which are shown in Fig. 6.1. Although the scope of this study did not allow a detailed design of how the magnetically insulated tubes protrude through the INPORT units, we assume for the present that the two systems are fully integrated

Table 6.1 Pumping Parameters for LIBRA

Ratio of Suppression Chamber Vol. to Target Chamber Vol.	Gas Avg. Temp. in Target Cham. After Equil. with Suppr. Chamber (K)	Gas Avg. Press. in Target Cham. After Equil. with Suppr. Chamber (torr)	Ratio of Press. After Equil. to Initial Pressure	Fraction of Target Cham. Volume Exhausted per Shot (%)	Steady State Pumping Speed Required (ℓ/s)
1.0	1076	290	1.12	16.4	1.23×10^5
0.9	1118	299	1.15	17.9	1.42×10^5
0.8	1173	308	1.18	19.3	1.53×10^5
0.7	1240	319	1.23	20.7	1.61×10^5
0.6	1317	333	1.28	22.2	1.67×10^5
0.5	1420	353	1.35	23.4	1.71×10^5
0.4	1557	382	1.47	24.4	1.73×10^5

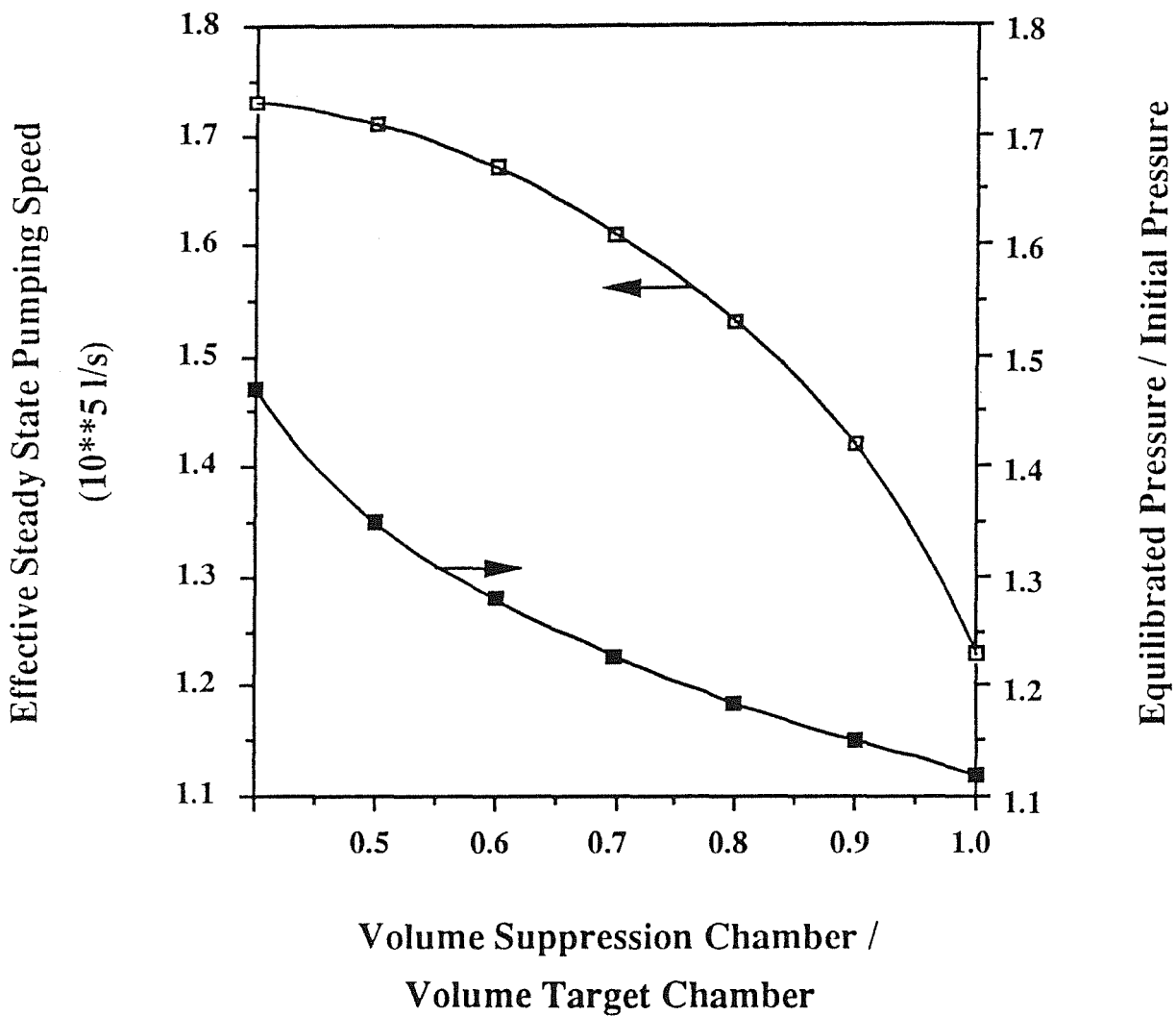


Fig. 6.3. Ratio of equilibrated pressure to initial pressure, and effective pumping speed as a function of the ratio of suppression chamber volume to the reaction chamber volume.

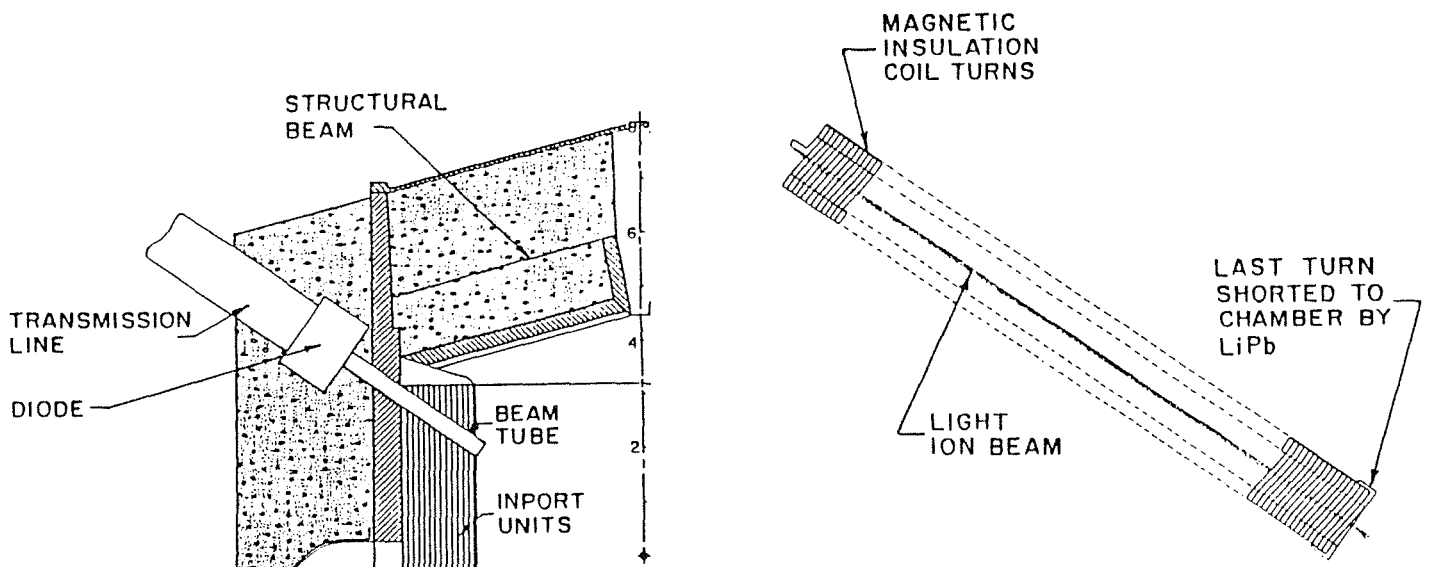
such that there are no unprotected surfaces. Practically, this means that the tubes are concentric with manifolds which carry the LiPb from the upper connecting INPORT units to lower connecting INPORT units.

It has been determined that a magnetic field of 3.2 T is needed within a 20 cm bore beam tube to slow down the electrons sufficiently to allow the channels to form in 1 μ s. To generate this field we have proposed a coil made of the molybdenum alloy TZM, with turn-turn insulation of BeO completely encapsulated in SiC.

Figure 6.4 shows a picture of the coil. It is 2.9 m long with an ID of 20 cm and OD of 34 cm, has 123 turns and requires a current of 60 kA at 11.3 kV. It has a pulse rise time of 5 ms and an L/R decay constant of 22 ms. The power required per beamline is 1.47 MW and the total stored energy in the 18 coils is 8.8 MJ. The coil is fed from the point of attachment to the diode housing and has a current return path through the chamber by virtue of having the last turn shorted to the LiPb. The coil is cooled by the flowing LiPb which surrounds it and the dissipated power is recovered in the LiPb. Table 6.2 gives the parameters of the beamline magnetic insulation coils.

Table 6.2. Parameters of Magnetically Insulated Beam Lines

Number of beamlines	18
Length of beamline (m)	2.9
Conductor material	TZM
Magnetic field generated (T)	3.2
Conductor current (kA)	60
Specific current (MA/m)	2.55
Coil OD/ID (m)	0.34/0.20
Number of turns/coil	123
Voltage required (kV)	11.3
Coil inductance (μ h)	300
Coil resistance (ohms)	0.014
Pulse rise time (ms)	5
L/R time constant (ms)	22
Power/beamline (MW)	1.47
Total stored energy (MJ)	8.8



CONDUCTOR MATERIAL	TZM
MAGNETIC FIELD REQUIRED	3.2 T
VOLTAGE REQUIRED	11.3 kV
TOTAL POWER	26.5 MW

Fig. 6.4. Magnetic insulation beam tube.

The magnetic protection beam lines must be replaced at a frequency consistent with that of the INPORT units, which is every 1.5 (FPY) full power years. It has been estimated that TZM can withstand radiation damage of up to 25-30 dpa,⁽²⁾ before a thermal anneal is required if it operates at $> 500^{\circ}\text{C}$. The maximum neutron wall loading in LIBRA at the midplane is 6 MW/m^2 and thus at the front surface of the coil it is 3.8 MW/m^2 . This produces an average of ~ 40 dpa per FPY. At this rate the TZM would have to be annealed once during its lifetime. Annealing the coils would be trivial by passing a DC current through them during a convenient down time.

It appears that the coil replacement is dictated by radiation damage to the SiC encapsulating material and not the TZM. Maintenance of the target chamber is discussed in Section 6.6.

6.5 Target Chamber Thermal Hydraulics

The target chamber in LIBRA is cooled with LiPb, with the exception of the shield, which is He gas cooled. As a safety feature, no water cooling is used in the target chamber. A single LiPb loop is employed in the reactor. It integrates the cooling of the reflector with the cooling of the roof and the INPORT units, as well as cooling of the exhaust gases in the suppression chamber. The LiPb inventory is minimized by having the heat exchangers built into the base of the target chamber, obviating the need for extensive heavy piping.

There are three separate LiPb circuits within the target chamber all combined into the same coolant loop. The first cools the roof of the chamber. Here the LiPb goes through the reflector flowing toward the center of the chamber and then enters the SiC modules at predetermined radial locations to flow back out. After going through the roof, the heated LiPb flows down the vertical sides of the chamber through rear INPORT units, where the nuclear heating is low, finally joining the bulk of the LiPb in the bottom pool. The second circuit feeds the remaining INPORT units. It enters the tubes at the top and flows down, eventually spilling into the bottom pool. The third circuit is used to cool the exhaust gases in the suppression chamber and to cool the reflector. This LiPb is sprayed into the suppression chamber in the form of a mist to maximize surface area, and falls down to the bottom of the suppression chamber. A constant level has to be maintained in the suppression chamber pool to act as the trap needed to prevent back-flow of gases into the target chamber. From the bottom of the suppression chamber, the LiPb is pumped to the top of the reflector, where it flows down and joins the pool in the bottom of the target chamber.

In all three coolant circuits the inlet temperature is 340°C and the outlet temperature 500°C. An energy balance determines the mass flow rate in each circuit. The total thermal energy in the reactor is 1160.5 MW and the mass flow rate of LiPb is 5.07×10^4 kg/s.

The surface temperature of the front tubes is not critical in LIBRA since the operating pressure needed for channel formation is ~ 260 torr at the operating temperature. The maximum time averaged surface heating at the reactor midplane is ~ 180 W/cm² and when averaged over the whole tube length it is ~ 146 W/cm². In order to maintain an outlet temperature of 500°C from the front tubes, the required LiPb velocity is 2.6 m/s. The maximum surface temperature just prior to a shot is 570°C and the corresponding LiPb vapor pressure is 8×10^{-4} torr. The LiPb vapor will constitute a minute fraction of the gas in the target chamber (~ 3 ppm).

The estimated pressure drop of the LiPb in the whole primary loop is 2 MPa and the pumping power is 10.8 MW. Table 6.3 gives the thermal hydraulic parameters for LIBRA.

Table 6.3. Pertinent LIBRA Thermal Hydraulic Parameters

Gross thermal energy (MW)	1160.5
LiPb inlet temperature (°C)	340
LiPb outlet temperature (°C)	500
LiPb mass flow rate (kg/s)	5.07×10^4
Maximum time averaged surface heat flux (W/cm ²)	180
Maximum steady state surface temperature (°C)	570
Velocity in front row of tubes (m/s)	2.6
LiPb steady state vapor pressure (torr)	8×10^{-4}
Estimated LiPb pressure drop (MPa)	2
LiPb pumping power (MW)	10.8

6.6 Reactor Target Chamber Maintenance

It has been determined that the roof reflector and integral SiC modules, the INPORT units, and the magnetic protection coils are not reactor lifetime components and will have to be replaced periodically.

The maximum dpa/FPY sustained by the SiC in the front row of tubes at the midplane where the maximum time average neutron wall loading is 6.05 MW/m² is

157 dpa/FPY. It has been estimated in HIBALL⁽¹⁾ that up to 1% of the SiC molecules can lose one atom each before any tube strength degradation will occur. The 157 dpa/FPY rate produces a loss of one atom each in 0.67% of the SiC molecules giving the front row of INPORT tubes a lifetime of 1.5 FPY. On the other hand, the roof modules which are exposed to a time average neutron wall loading of 2.83 MW/m^2 will have an expected life of 3.2 FPY.

In Section 6.2 it was decided that the lifetime of the magnetic protection coils based on the damage to their SiC encapsulating cover is 1.5 FPY. Finally, the lifetime of the roof reflector has been estimated to be 4 FPY in Section 8.1.

It appears that a maintenance schedule based on 1.5 FPY cycles is needed. At an availability of 75% this amounts to 24 calendar months. The front row INPORT units and the magnetic protection coils will be replaced every 24 calendar months. The roof SiC modules and the reflector to which they are attached will be replaced every other maintenance cycle, or every 48 calendar months. The remaining INPORT units will be replaced on a schedule consistent with the damage accumulated in them.

Once the LiPb has been drained from the reactor a scheme for dismantling the roof of the chamber to provide access to the interior of the target chamber has been developed. Figure 6.5 shows a picture of the target chamber with a disassembled roof. The first component to be removed is the pellet injector estimated to weigh ~ 14 tonnes. A pellet delivery conveyer system not shown in the drawing will have to be initially removed. The next step is to unbolt and remove the vacuum flange which is the primary vacuum barrier for the roof. This 5 cm thick flange can be sealed with a conventional elastomer seal, since the seal is protected with 3.5 m of shield material, can be changed out each 1.5 FPY and seals against a roughing vacuum of the order 200-300 torr. The mass of the flange is 33 tonnes. Next come the six individual wedge shaped shield segments, each weighing 100 tonnes. Helium gas coolant lines have to be disconnected prior to the removal of the shield segments. Finally, the wagon wheel shaped structural beam assembly with the attached roof reflector and SiC modules is removed as a single unit, also weighing 100 tonnes. There is no need to undo coolant connections since these are made by virtue of aligning supply ports in the reactor target chamber to ports on the roof reflector. The ports will have spring loaded metal seals of the omega bellows type. Furthermore, these seals do not have to be tight since a certain amount of leakage can be tolerated. The leaking LiPb will simply run down the sides of the INPORT units in the back of the reactor.

PELLET INJECTOR
1 ea. M= 14 Tonnes

VACUUM FLANGE
1 ea. M= 33 Tonnes

INDIVIDUAL
SHIELD SEGMENTS
6 ea. M= 100 Tonnes / SEGM.

STRUCTURAL BEAMS
REFLECTOR
WETTED SURFACE PROTECTION
1 ea. M=100 Tonnes

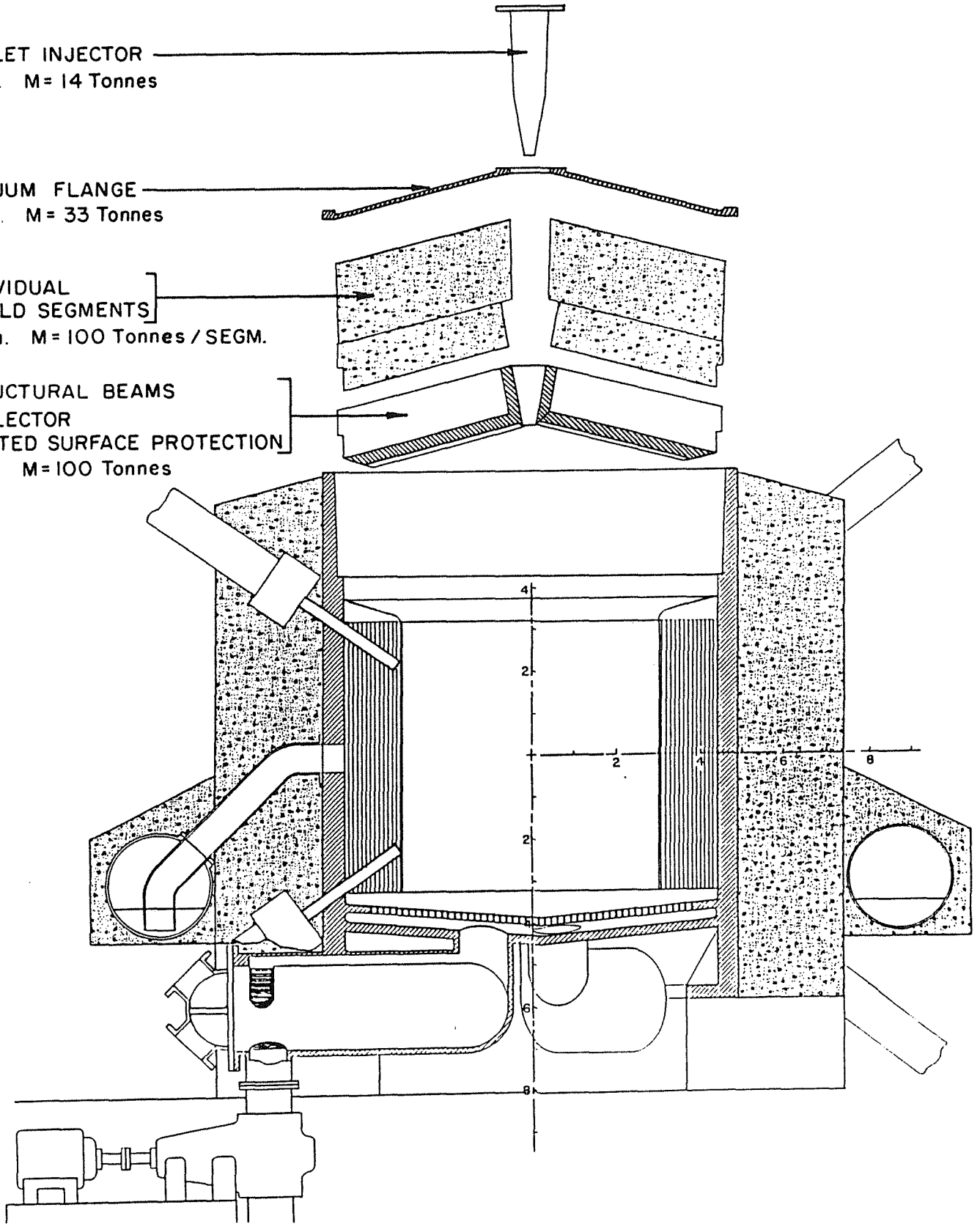


Fig. 6.5. Disassembly sequence for reaction chamber roof.

Once the target chamber roof has been disassembled, free access to the chamber interior is made possible through a 6 m diameter hole. Remote handling machines mounted on the overhead crane can then be lowered into the target chamber to remove and replace the INPORT units and the magnetic protection coils. Afterheat dissipation will not pose a problem since natural convection of air through the reflector coolant passages will be capable of handling it. Containment building air will have to be circulated for cooling and detritiation purposes.

References for Chapter 6

1. "HIBALL, A Conceptual Heavy Ion Beam Driven Fusion Reactor Study," University of Wisconsin Fusion Technology Institute Report UWFDM-450, Kernforschungszentrum Karlsruhe-KfK-3202, June 1981.
2. B. Badger et al., "UWMAK III, A Noncircular Tokamak Power Reactor Design," University of Wisconsin Fusion Technology Report UWFDM-150, July 1976.

7. CAVITY RESPONSE

7.1. Overview

The ablation of LiPb from the surface of the INPORTs and the response of the tubes to the resulting impulse are the major issues discussed in this section. Specifically, the following questions are addressed:

- Where is the target x-ray and debris ion energy deposited?
- How much LiPb is vaporized (ablated) from the INPORTs after each shot?
- What are the conditions (pressure, temperature, radiation flux) at the vapor/liquid LiPb interface as a function of time?
- What is the magnitude of the impulse applied to the INPORTs?
- What effect does varying the cavity size have on the applied impulse and mass of LiPb vaporized?
- What are the general characteristics of the INPORT mechanical response?
- Can INPORT physical parameters be chosen to effect steady state motion which is coplanar with the radial impulsive loading?

Figure 7.1 illustrates the major physical processes occurring in the LIBRA target chamber "cavity". Here, the "cavity" includes the background gas and INPORTs carrying the LiPb. The cavity parameters are listed in Table 1.1. Roughly 20% of the x-ray energy and all of the debris ion energy is deposited in the He gas. This leads to high temperatures and pressures near the center of the cavity, which drive a strong shock wave radially outward. Rapid vaporization of liquid LiPb occurs because roughly 80% of the target x-ray energy is deposited volumetrically in the LiPb. Although other gases (e.g., argon) are better x-ray absorbers than He, the chamber gas composition and density are constrained by beam transport requirements (see Chapter 4). After the target x-rays are absorbed, the high pressures in the LiPb vapor cause it to expand rapidly away from the INPORTs, and creates a "recoil" impulse on the tubes. The expanding LiPb produces a strong inward-moving rarefaction wave, which eventually collides with the outward-moving shock. Calculations indicate that the momentum of the LiPb vapor front strongly dissipates the outward moving shock. Thus the tradeoff associated with the x-ray vaporization of LiPb is this: the inward flowing LiPb vapor front shields the INPORTs from the outward-moving shock, but produces very high instantaneous pressures at the vapor/liquid interface and applies a large recoil impulse to the INPORTs.

The INPORT concept was introduced for the HIBALL conceptual design and has now been adapted for LIBRA. Briefly, each INPORT consists of a tube of braided silicon

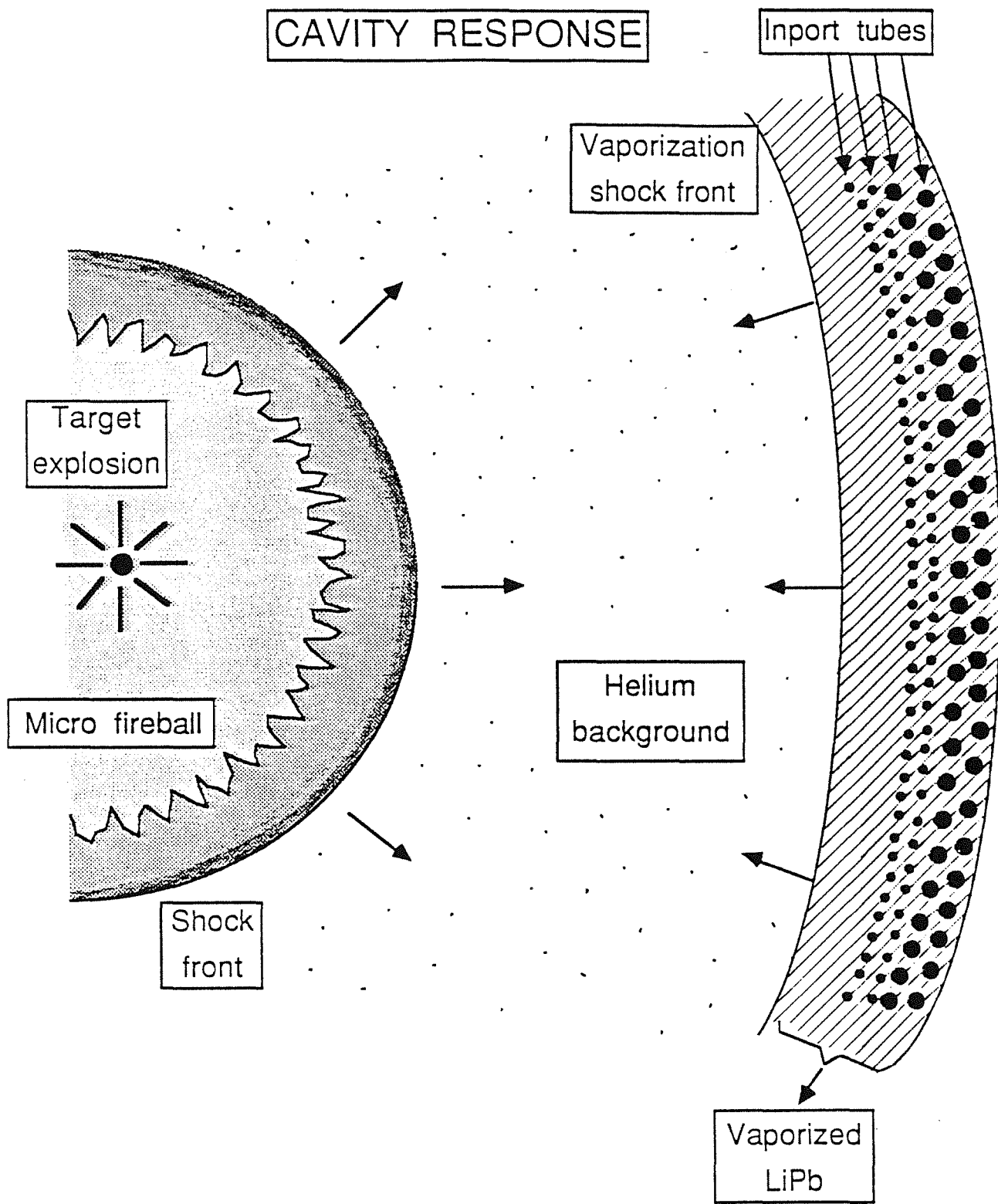


Fig. 7.1. Schematic of physical processes in the LIBRA target chamber following a microexplosion.

carbide, with a porous flexible wall (Fig. 7.2). A fraction of the lithium/lead flowing through the INPORT coats the outer surface and provides protection from x-rays and target debris. Such components have been fabricated and tested for strength at elevated temperatures and fatigue testing of the silicon carbide fibers has also taken place.

The INPORT layout for the first wall and blanket is shown in Fig. 7.3. The first wall consists of 628, 3 cm diameter INPORTs equally divided between the first and second rows. The blanket is made up of 9 rows of 10 cm INPORTs, each row containing 140 units, for a total of 1260. This combination provides a packing fraction of 33%.

7.2. Radiation-Hydrodynamic Calculations for the LIBRA Target Chamber Cavity

7.2.1. Overview of the Radiation-Hydrodynamic Simulations

The post-ignition response of the He background gas and LiPb coating the INPORTs is simulated using the 1-D Lagrangian radiation-hydrodynamics code called CONRAD.⁽¹⁾ CONRAD calculates the energy deposition of target x-rays and debris ions in the cavity gas and first surface material, the vaporization and condensation of first surface material, hydrodynamic flow in the background gas and vaporized material, and energy transport through the vapor and condensed media. In the condensed medium (here, the liquid LiPb), energy is transported by thermal conduction. In the gas, energy is transported by radiation, fluid motion, and electron thermal conduction.

It is emphasized that because CONRAD is a one-dimensional code, it is unable to model the actual geometric configuration of the LIBRA target chamber. This is because the target explodes with spherical symmetry while: (1) the INPORTs constitute a cylindrical first wall for the target chamber cavity, (2) the LiPb surface on each INPORT (i.e., the vapor/liquid interface) is axisymmetric, and (3) the cavity boundary has many holes for beam ports. In our calculations, it is assumed that the cavity boundary is spherically symmetric and located at a distance of 3 meters from the target (i.e., the minimum distance between the target and INPORTs in the LIBRA design). Thus, while the qualitative features of our results should be valid, the numerical values presented in this section must be viewed as approximations.

Energy and momentum transfer in the gas and condensed region are modeled separately. In the condensed region, movement and compression of the fluid are neglected. Energy flow from the vapor/liquid interface toward the SiC weave located 2 mm behind the interface is computed via the conduction equation

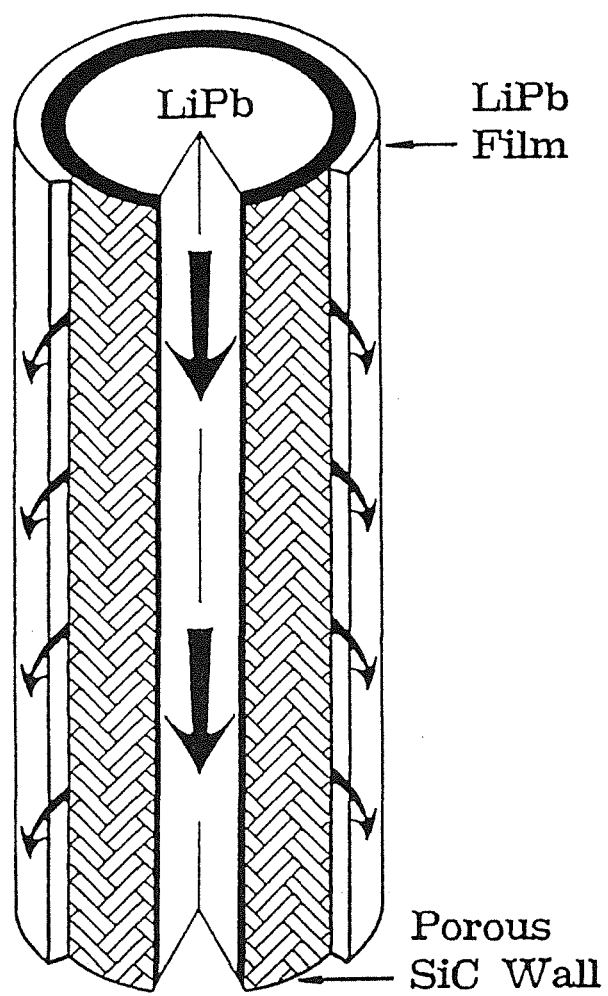
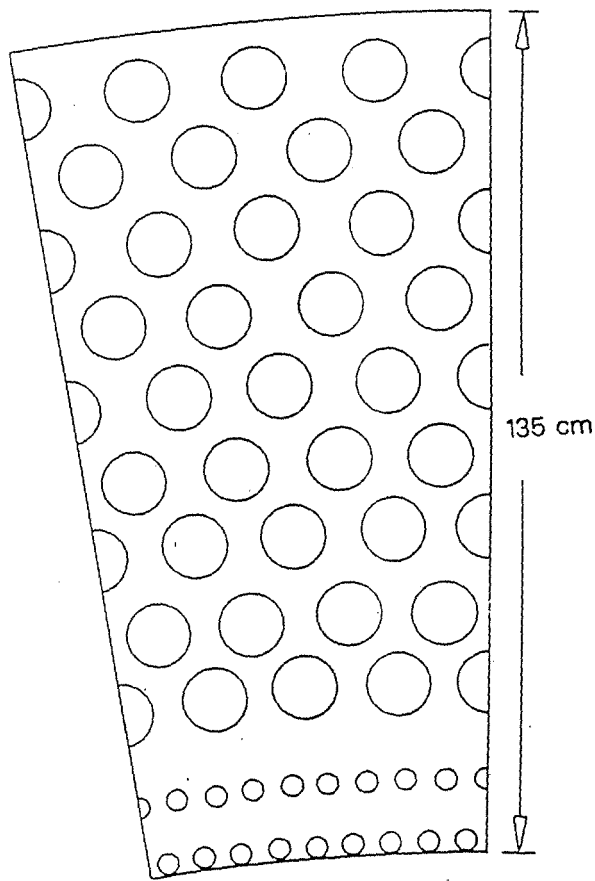


Fig. 7.2. Sectioned INPORT unit.



3 cm INPORTs - 2 rows @ 314
10 cm INPORTs - 9 rows @ 140

Fig. 7.3. LIBRA INPORT layout for first wall and blanket.

$$c_v \frac{\partial T}{\partial t} = \frac{\kappa}{\rho} \frac{\partial^2 T}{\partial x^2} + S \quad (7.1)$$

where T is the temperature of the liquid, c_v is the specific heat, ρ is the mass density, κ is the thermal conductivity, and S is a source term. c_v , ρ and κ are assumed to be constant throughout the liquid. The source term includes energy incident at the vapor/liquid interface due to radiation and debris ions (for LIBRA, the debris ions are stopped in the He near the target). The temperature 2 mm behind the interface (i.e., at the SiC weave) is held fixed at 500°C.

The momentum and energy conservation equations for the plasma have been described in detail elsewhere.⁽²⁾ They will be discussed only briefly here. The momentum conservation equation is given by

$$\frac{\partial u}{\partial t} = -V \frac{\partial}{\partial r} (P + q) - V \frac{\partial p_d}{\partial t} \quad (7.2)$$

where u is the fluid velocity, V is the specific volume, P is the plasma pressure, q is the artificial viscosity and p_d is the debris ion momentum. The first term represents the acceleration due to pressure gradients and the second term represents the contribution from collisions between the background plasma and the debris ions.

The plasma energy equation is

$$c_v \frac{\partial T}{\partial t} = \frac{V}{r^2} \frac{\partial}{\partial r} (r^2 \kappa_p \frac{\partial T}{\partial r}) - \dot{V} (P + q + (\frac{\partial E_p}{\partial V})_T) + A - J + S \quad (7.3)$$

where T is the temperature of both the electrons and ions, κ_p is the plasma thermal conductivity, E_p is the plasma specific internal energy, S is a source function, and A and J are the plasma absorption and emission rates, respectively. Radiation transport is calculated using a multifrequency flux-limited diffusion model. The radiation energy equation for each of the 20 photon energy groups is

$$V \frac{\partial E_R^g}{\partial t} = \frac{V}{r^2} \frac{\partial}{\partial r} (r^2 \kappa_R^g \frac{\partial E_R^g}{\partial r}) - \frac{4}{3} \dot{V} E_R^g - c \sigma_{P,A}^g E_R^g + J^g, \quad g = 1, 20 \quad (7.4)$$

where E_R^g is the radiation energy density of group g , κ_R^g is the radiation conductivity, $\sigma_{P,A}^g$ is the Planck mean opacity for absorption, c is the speed of light and J^g is the plasma emission rate for photons in group g . The radiation absorption, emission and diffusion rates are calculated from the following relations:

$$A = \sum_g c \sigma_{P,A}^g E_R^g \quad (7.5)$$

$$J = \sum_g J^g = \sum_g 4\pi \sigma_{P,E}^g \int_{\nu_g}^{\nu_{g+1}} B_\nu d\nu$$

$$\kappa_R^g = (cV)/(3\alpha_R^g)$$

where the group opacities are defined in Eqns. 7.12 through 7.14.

In practice, the target x-rays are deposited during the initialization procedure. Thus, some of the LiPb is in the vapor phase as the calculation begins. The debris ion energy is deposited through the time-dependent source term in Eqn. 7.3.

For the He and LiPb vapor, momentum and energy transport are governed by Eqns. 7.2 and 7.5. All Lagrangian zones that contain liquid LiPb are not allowed to undergo hydrodynamic motion and energy transport is governed by Eqn. 7.1. As the plasma radiates energy to the INPORTs, the temperature at the vapor/liquid interface rises and some additional LiPb can be vaporized. Thus, the number of Lagrangian zones in the vapor phase can change with time. No mixing occurs between the He and LiPb as no mass is exchanged between zones.

Radiation re-emitted by the cavity gas is effectively deposited at the surface of the interface because of the shorter mean free paths (compared with target x-rays). Vaporization of first surface material in the post-x-ray deposition phase is modeled using the kinetic theory approach of Labuntsov and Kryukov.⁽³⁾ The mass vaporization rate

per unit area is

$$\left(\frac{dm}{dt}\right)_v = \frac{2}{3} \left(\frac{\mu}{RT_v}\right)^{1/2} P_{\text{sat}} \quad (7.6)$$

where T_v is the vapor temperature, P_{sat} is the saturation vapor pressure, μ is the mean atomic weight and R is the gas constant. The rate of condensation of LiPb back onto the INPORTs is

$$\left(\frac{dm}{dt}\right)_c = \frac{2}{3} \left(\frac{\mu}{RT_v}\right)^{1/2} P_v f_s f_{nc} \quad (7.7)$$

where P_v is the vapor pressure, f_s is the sticking coefficient, which represents the fraction of vapor atoms striking the interface that attach to it, and f_{nc} is a parameter which accounts for the presence of noncondensable gases (i.e., He).

Before describing the results of the radiation-hydrodynamic simulations, the details of models used to calculate the equations of state and opacities, target x-ray energy deposition, and debris ion stopping are discussed. Results from the radiation-hydrodynamic calculations are discussed in Section 7.2.5.

7.2.2. Equation of State and Opacity Data

The equations of state and opacities for He and LiPb vapor were calculated using the IONMIX computer code.⁽⁴⁾ IONMIX computes thermodynamic properties and multigroup opacities for multicomponent LTE (local thermodynamic equilibrium) and non-LTE plasmas. The calculations are valid for low-to-moderate density plasmas, where interparticle potentials are unimportant, and at temperatures ≥ 1 eV, where molecular vibrational and rotational effects are unimportant. Thus, the physical and chemical properties of LiPb near the liquid/vapor phase transition are not modeled in detail.

IONMIX computes steady-state ionization populations by balancing the collisional ionization rate with the sum of the collisional, radiative and dielectronic recombination rates for each ion. Similarly, the excitation populations are determined by balancing the collisional excitation rate with the sum of the collisional plus radiative deexcitation rates. Here, "collisions" refer to the electron impact processes, i.e., collisions between ions and free electrons. Rate coefficients are based on the hydrogenic ion

approximation.⁽⁵⁾ Processes which are coupled with the radiation field -- photoionization and photoexcitation -- are not considered in the calculations discussed here. Because of this, the plasma properties are a function of the local plasma density and temperature only, and independent of the radiation field.

After the ionization and excitation populations are determined, the equation of state properties are easily calculated, as interparticle potentials are assumed to be small. Internal energies are computed relative to the ground state energy of the neutral atom of each species. Thus, the specific energy for an arbitrary mixture of ions is

$$E = \frac{n_{\text{tot}}}{\rho} \left\{ \frac{3}{2} (1 + \langle Z \rangle) T + \sum_k f_k \sum_{j=1}^{Z_k} f_{jk} \left[\left(\sum_{\ell=0}^{j-1} \phi_{\ell k} \right) + \left(\sum_{i=n_0+1} f_{ijk} (\Delta E_{i,n_0})_{jk} \right) \right] \right\} \quad (7.8)$$

where ρ is the mass density and n_{tot} is the total number density of nuclei. The relative species, ionization, and excitation fractions are defined by

$$f_k = \frac{n_k}{n_{\text{tot}}}, \quad f_{jk} = \frac{n_{jk}}{n_k}, \quad f_{ijk} = \frac{n_{ijk}}{n_{jk}} \quad (7.9)$$

where n_k , n_{jk} , and n_{ijk} refer to the number density of nuclei of gas species k , the j^{th} ionization state of species k , and the i^{th} excitation state of the j^{th} ionization state of species k , respectively. The $\phi_{\ell k}$ are the ionization potentials, and $\Delta E_{i,n_0}$ the excitation energies with respect to the ground state energy of each ion. The last two terms on the right side of Eqn. 7.8 represent the energy stored in ionization and excitation, respectively. The average charge state and pressure are given by

$$\langle Z \rangle = \sum_k f_k \sum_{i=1}^{Z_k} f_{jk} \cdot j \quad (7.10)$$

and

$$P = (1 + \langle Z \rangle) n_{\text{tot}} kT \quad (7.11)$$

where T represents the temperature of both the electrons and ions, which are assumed to be in equilibrium.

The radiative properties are calculated using hydrogenic ion cross-sections for bound-bound, bound-free, and free-free transitions.⁽⁶⁾ IONMIX computes the absorption coefficient, κ_ν , emission coefficient, η_ν , and scattering coefficient, σ_ν , at a large number ($\sim 10^2$ to 10^3) of specially placed photon frequencies ν . Multigroup Planck mean opacities for absorption and emission are then calculated by integrating over each frequency group:

$$\sigma_{P,A}^g = \frac{1}{\rho} \frac{\int_{\nu_g}^{\nu_{g+1}} \kappa_\nu B_\nu d\nu}{\int_{\nu_g}^{\nu_{g+1}} B_\nu d\nu} \quad (7.12)$$

and

$$\sigma_{P,E}^g = \frac{1}{\rho} \frac{\int_{\nu_g}^{\nu_{g+1}} \eta_\nu d\nu}{\int_{\nu_g}^{\nu_{g+1}} B_\nu d\nu} \quad (7.13)$$

where ν_g and ν_{g+1} are the group boundaries of group g , and B_ν is the Planck function. The Rosseland mean opacity is

$$\sigma_R^g = \frac{1}{\rho} \frac{\int_{\nu_g}^{\nu_{g+1}} \left(\frac{\partial B_\nu}{\partial T}\right) d\nu}{\int_{\nu_g}^{\nu_{g+1}} \frac{1}{\kappa_\nu + \sigma_\nu} \left(\frac{\partial B_\nu}{\partial T}\right) d\nu} \quad (7.14)$$

The Rosseland mean is used to calculate the transport of radiation in the flux-limited diffusion model, while the Planck means are used to calculate the rates of energy exchange between the radiation field and plasma. Note that the Planck means for

emission and absorption must be computed separately because local thermodynamic equilibrium (LTE) is not assumed. At relatively high densities, where collisions dominate all atomic processes, the plasma approaches LTE and the Planck-Kirchhoff relation, $\eta_{\nu} = \kappa_{\nu} B_{\nu}$, becomes valid.

In CONRAD simulations of the LIBRA cavity environment, the He and LiPb vapor are not allowed to mix. Each zone in the hydrodynamic simulation contains either pure He or $\text{Li}_{17}\text{Pb}_{83}$. This allows setting up of two separate equation of state tables using IONMIX. For each density and temperature point in the table, values are tabulated for the specific energy, specific heat capacity, mean charge state, density derivative of the specific energy, and, for each of 20 photon energy groups, the Rosseland mean opacity, and the Planck mean opacities for absorption and emission.

Some results from the IONMIX calculations for He and LiPb are shown in Figs. 7.4 through 7.8. Figs. 7.4 and 7.5 show the internal energy density and mean emission coefficient ($\rho\sigma_{P,E}$ integrated over all photon energies) for He as a function of temperature for 3 different densities: 3×10^{16} , 3×10^{18} and $3 \times 10^{20} \text{ cm}^{-3}$. Recall the cavity initially contains a uniform density He gas of $3.5 \times 10^{18} \text{ cm}^{-3}$. At temperatures $\leq 1 \text{ eV}$, He is essentially an ideal monatomic (neutral) gas. At temperatures $\gg 10 \text{ eV}$, He is fully ionized and the opacity becomes dominated by bremsstrahlung emission. At intermediate temperatures, some structure is evident in both the energy and opacity curves as He is partially ionized. At temperatures $\leq 10 \text{ eV}$, most of the opacity is due to line emission.

In a recent study,⁽⁷⁾ it was shown that radiative recombination and deexcitation rates often exceed the collisional rates at temperatures and densities relevant to high-gain ICF target chambers. Thus, the ionization and excitation populations are not adequately calculated using the Saha equation and Boltzmann statistics, and the plasma is not in LTE. Non-LTE processes tend to reduce the mean ionization state, specific energy, and plasma emission rate relative to LTE. This is shown in Figs. 7.6 and 7.7, where the non-LTE internal energies and emission opacities are compared with the LTE values. At a density of $3 \times 10^{20} \text{ cm}^{-3}$ the non-LTE energies are virtually indistinguishable from the LTE values, as are the emission opacities at temperatures above 2 eV. However, as the density decreases, the ratio of the radiative to collisional recombination rate increases and the plasma deviates more and more from LTE. Thus, in calculations where LTE is assumed, the plasma emission rate -- and thereby the flux at the first wall -- is overestimated.

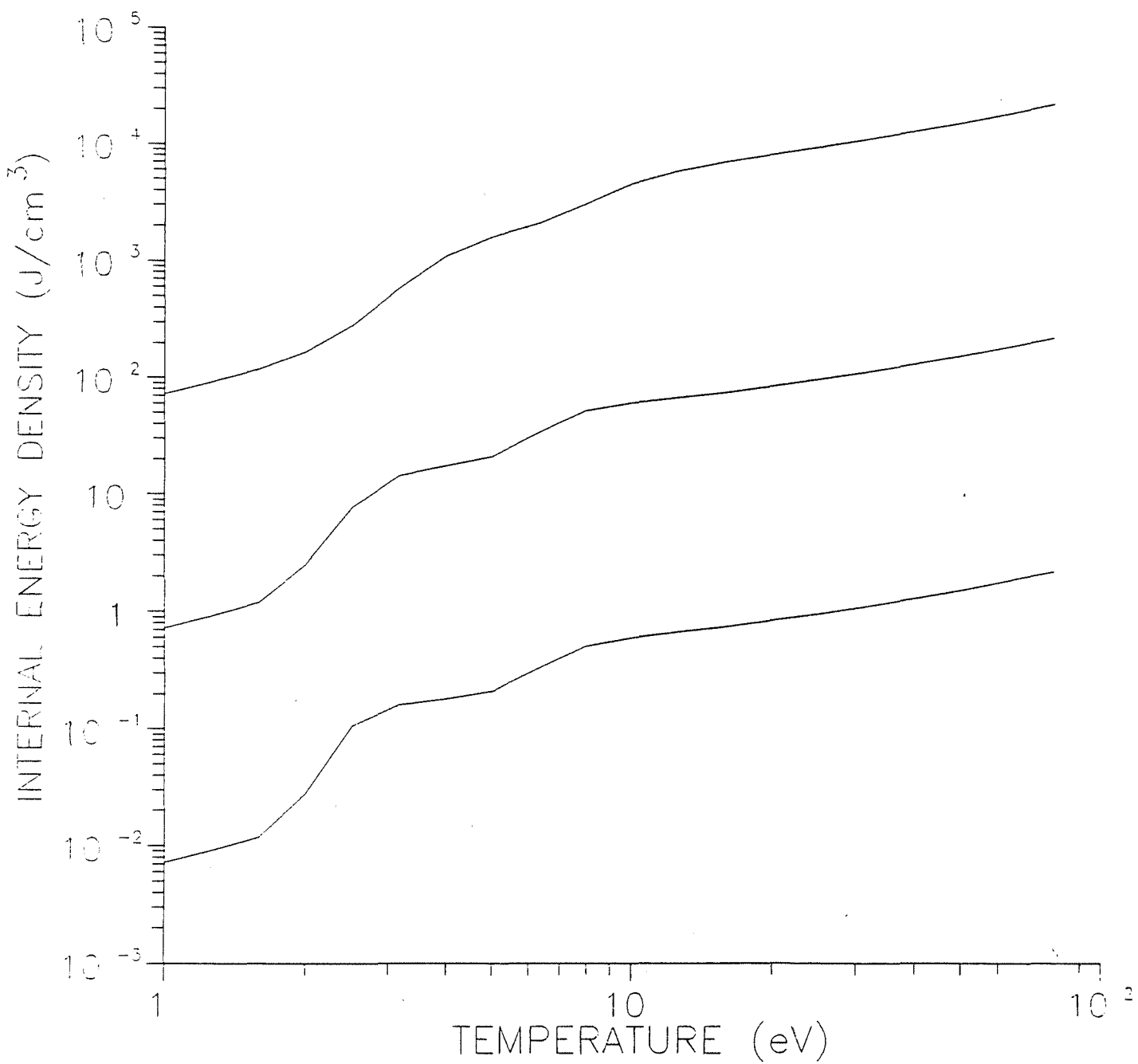


Fig. 7.4. Internal energy for helium vs. temperature at 3 densities: 3×10^{16} (bottom), 3×10^{18} , and $3 \times 10^{20} \text{ cm}^{-3}$ (bottom).

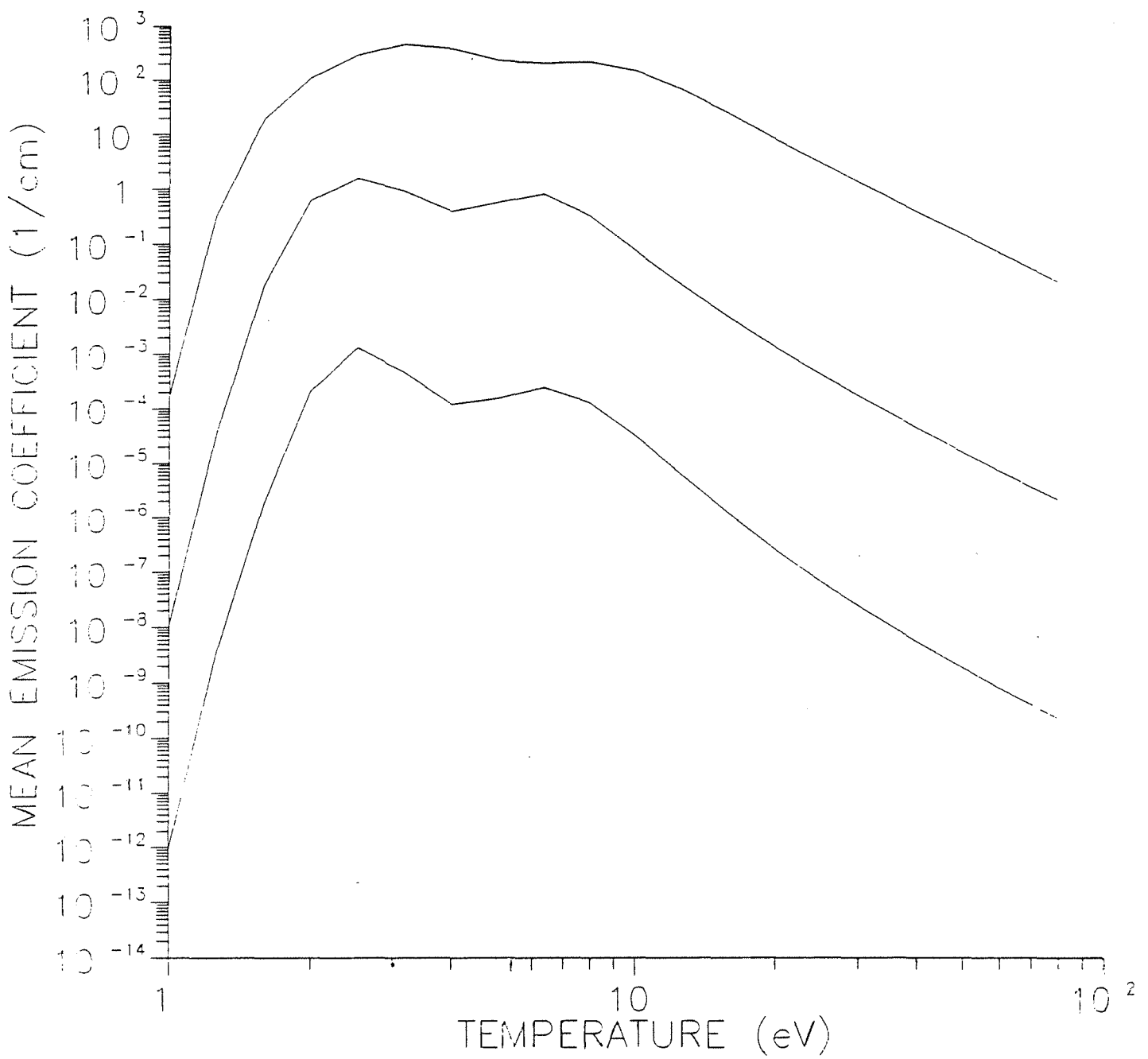


Fig. 7.5. Mean emission coefficient for helium vs. temperature at 3 densities: 3×10^{16} (bottom), 3×10^{18} , and $3 \times 10^{20} \text{ cm}^{-3}$ (top).

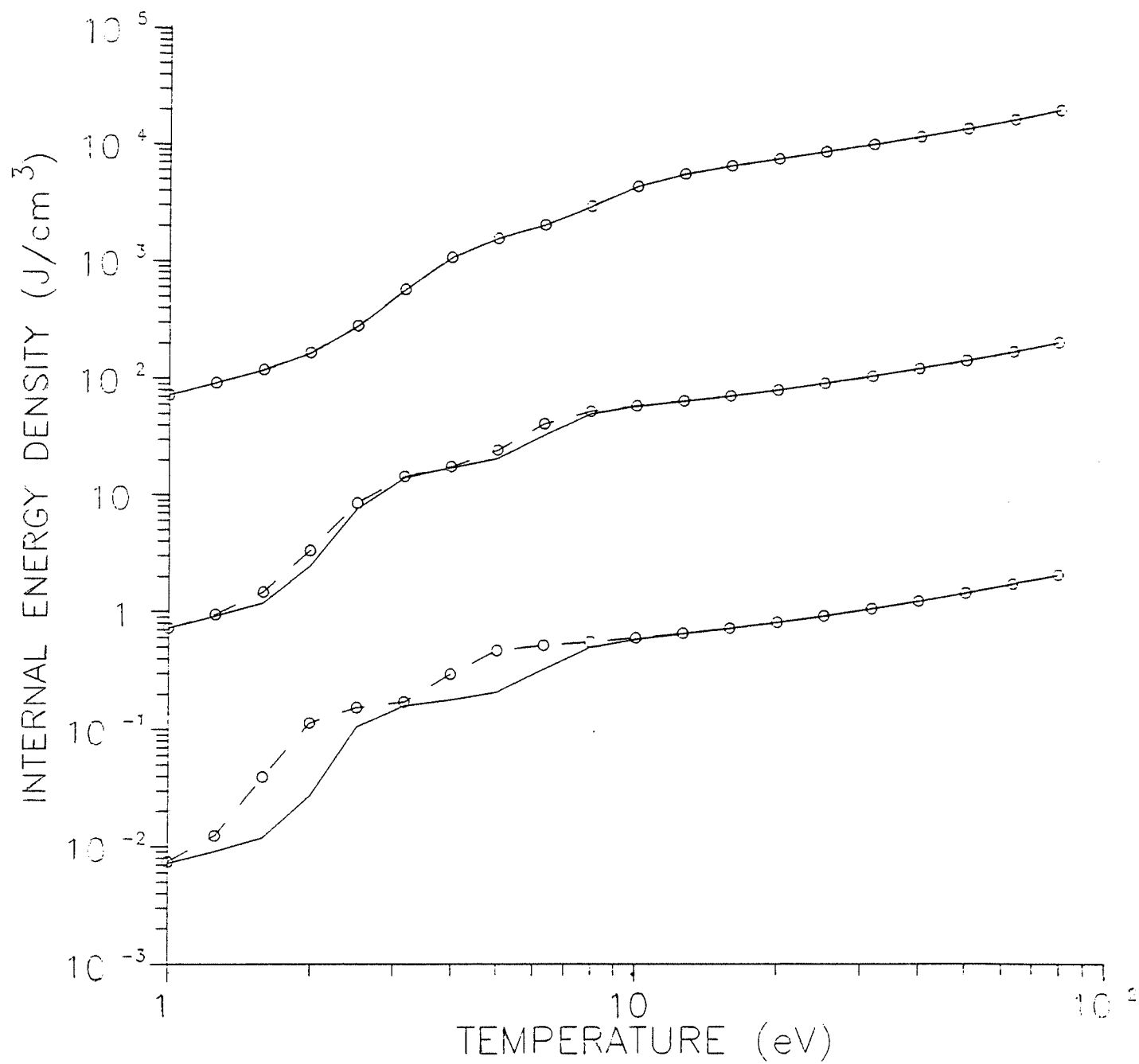


Fig. 7.6. Same as Fig. 7.4, but with LTE results included (dashed lines).

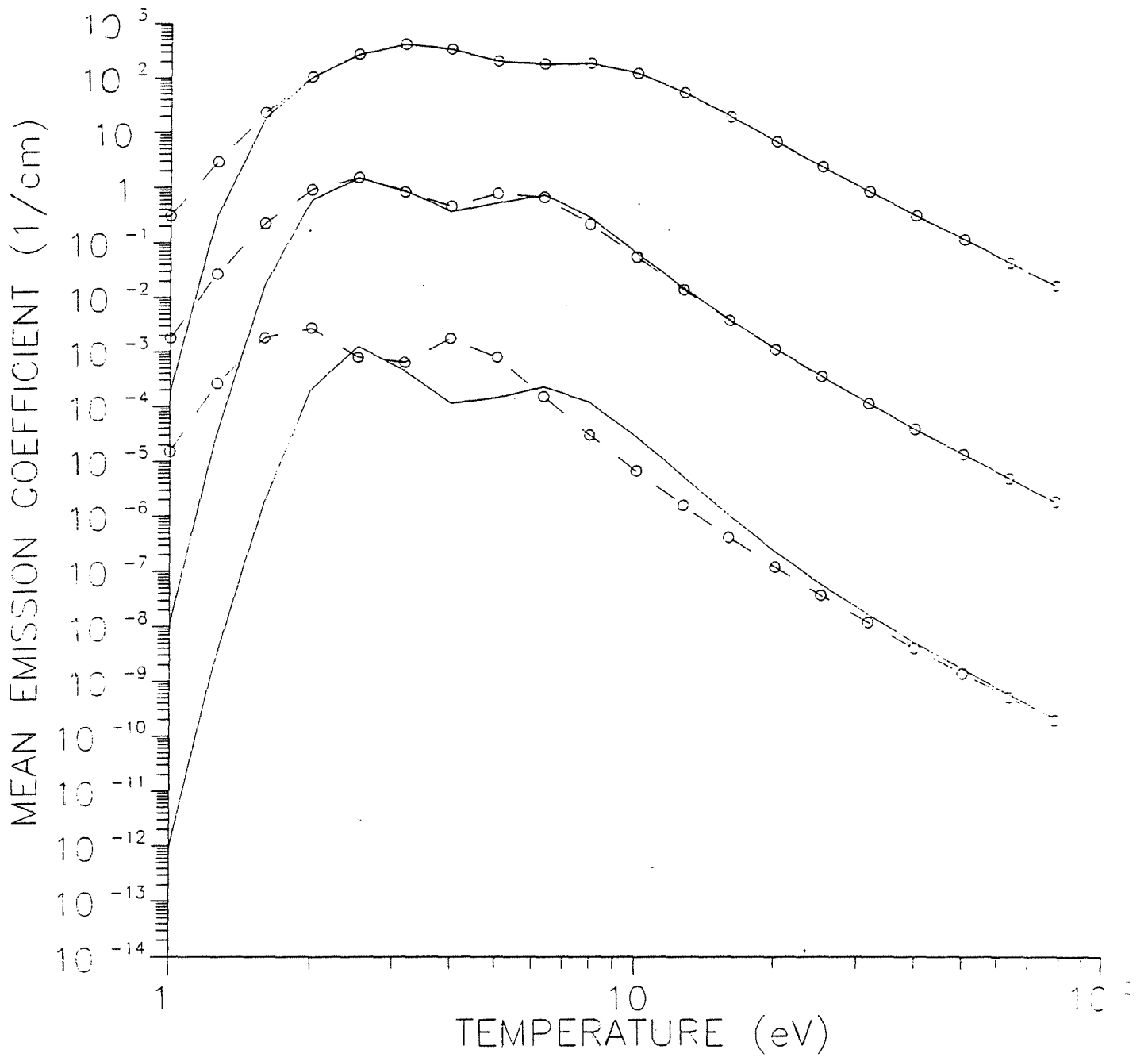


Fig. 7.7. Same as Fig. 7.5, but with LTE results included (dashed lines).

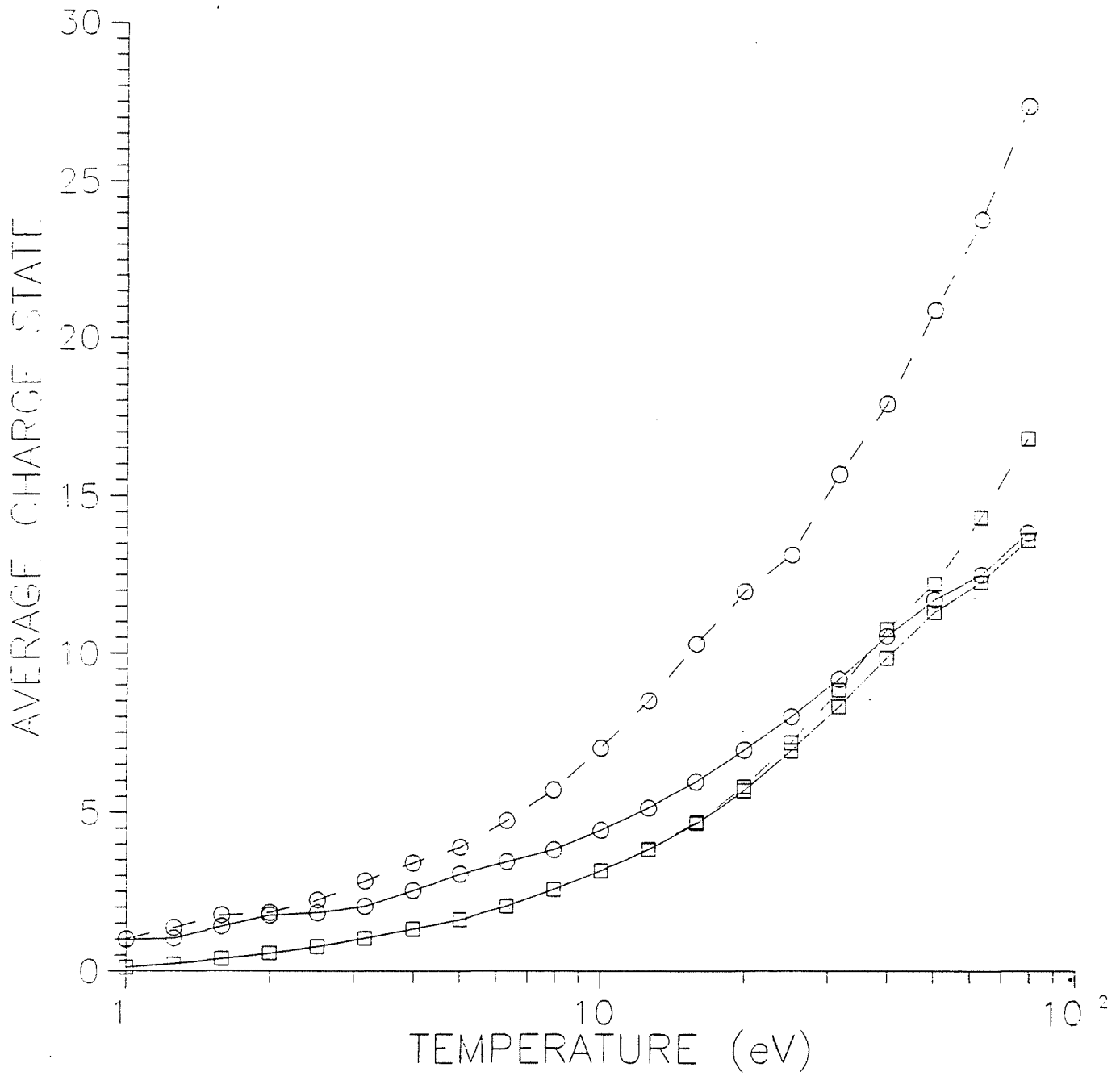


Fig. 7.8. Mean charge state of lithium-lead vs. temperature at 2 densities: 3×10^{16} (circles) and $3 \times 10^{20} \text{ cm}^{-3}$ (squares). The dashed curves represent LTE results.

Figure 7.8 shows the mean charge state of LiPb as a function of temperature at densities of 3×10^{16} (circles) and $3 \times 10^{20} \text{ cm}^{-3}$ (squares). As a reference, the mean density of 10 kg of LiPb vapor -- which is roughly the amount predicted to be vaporized -- spread throughout a 3 m radius spherical cavity is $3 \times 10^{17} \text{ cm}^{-3}$. The solid and dashed curves represent the non-LTE and LTE values, respectively. Again, the disparity between the LTE and non-LTE results becomes greater as the density decreases. In the CONRAD simulations, temperatures in the LiPb vapor range as high as 10 to 20 eV just after the target x-rays are absorbed, and thus some of the LiPb is dissociated and partially ionized.

7.2.3. Target X-ray Energy Deposition and Rapid Vaporization

X-ray energy emitted from the target is deposited throughout the He background gas and in a thin layer of LiPb coating the INPORTs. After the x-rays are absorbed, the energy density within the first few microns of LiPb exposed to the target exceeds the binding energy of the liquid, and a few kilograms of LiPb is ablated from the INPORT tubes after each explosion. The resulting pressures in the LiPb vapor cause it to expand rapidly away from the tubes, providing a strong "recoil" impulse to the INPORTs.

To determine the spatial deposition of the x-ray energy, a multifrequency exponential attenuation model is used. This model assumes the x-rays are deposited instantaneously, and that they originate from a point source. The energy deposited in each zone is given by:

$$\epsilon_{x,g} = \kappa_g F_g \Delta(h\nu)_g e^{-\kappa_g \Delta r} \quad (7.15)$$

where κ_g is the mean absorption coefficient for frequency group g , F_g is the incident flux, Δr is the zone width and $\Delta(h\nu)_g$ is the photon energy group bandwidth. The target x-rays are absorbed by photoionization. In the case where the absorber is a many-electron atom, photoionization of inner shell electrons contributes significantly to the attenuation cross-sections. CONRAD uses the absorption cross-section data of Biggs and Lightfoot.⁽⁸⁾ For each energy group, the x-ray attenuation is calculated for a large number (~ 100) of subgroups to provide sufficient accuracy in frequency regions where the absorption coefficient changes rapidly.

Figure 7.9 shows the target x-ray spectrum used for the LIBRA cavity response calculations. This spectrum is similar to that used in the HIBALL study,⁽⁹⁾ but with the intensities scaled to give a total target x-ray yield of 62.7 MJ.

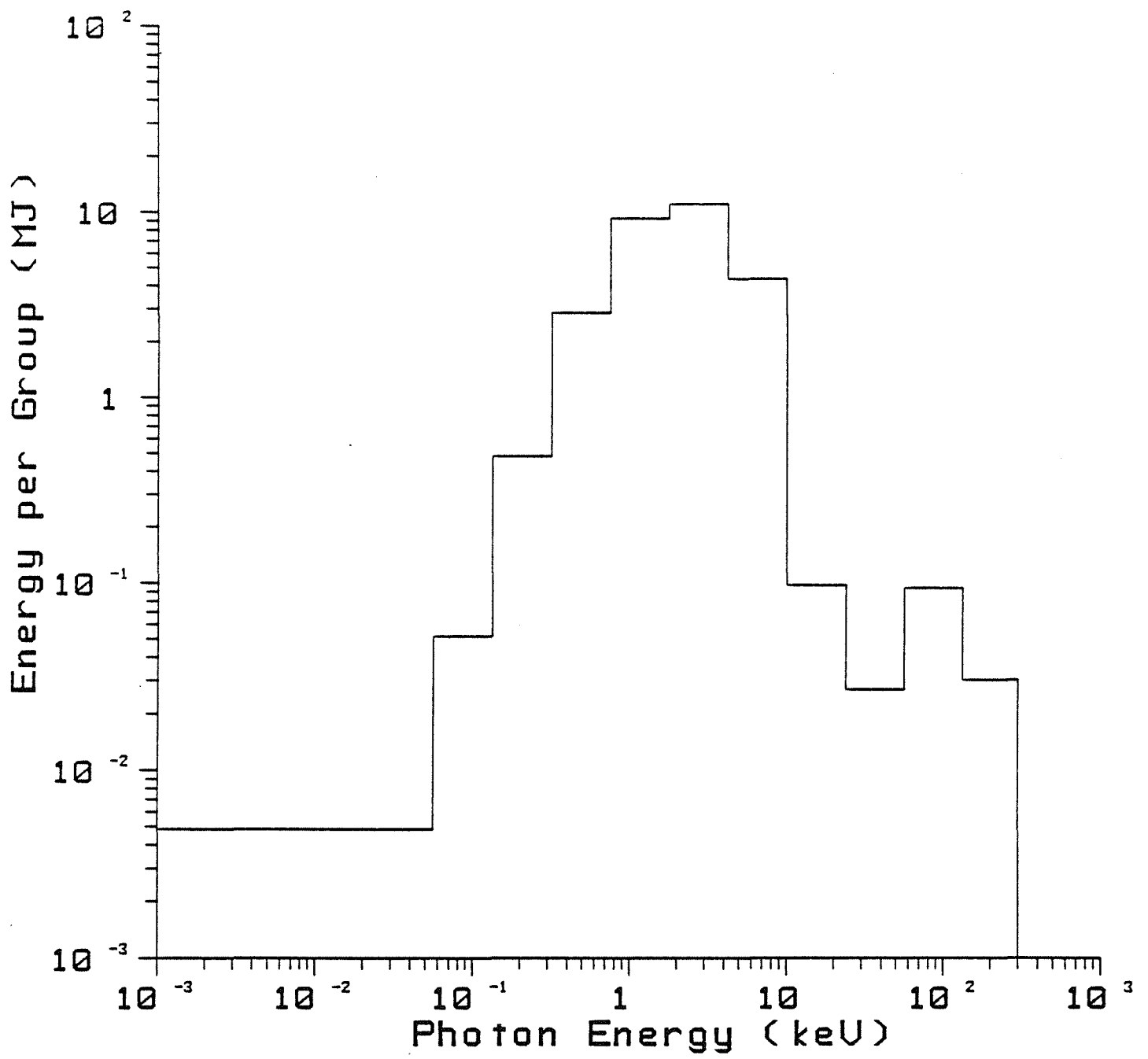


Fig. 7.9. X-ray spectrum from LIBRA target.

The x-ray energy deposition profile in the He gas is shown in Fig. 7.10. Only 12.5 MJ (or 20%) of the x-ray energy is deposited in the He. This is because the absorption cross-section for He is very small at photon energies $\geq 10^2$ eV. The temperature near the center of the cavity just after the x-rays are deposited is about 12 eV. The temperature increases significantly, however, when the target debris ions are stopped near the target. The pressure gradients resulting from this energy deposition profile cause the He near the center of the cavity to rush rapidly outward, forming a strong blast wave.

The remaining 50 MJ of x-ray energy is deposited in a thin region ($\sim 10 \mu\text{m}$) of the LiPb facing the target. Figure 7.11 shows the specific energy deposited in the first $10 \mu\text{m}$ of LiPb behind the liquid LiPb/He gas interface. In this calculation, the photoionization cross-sections for pure lead were used as CONRAD does not presently have the capability to model x-ray attenuation in multi-component materials.

To calculate the amount of LiPb vaporized from the surface of the INPORT tubes, a simple energy balance model is used. The basic features of the model are illustrated in Fig. 7.12. CONRAD divides the condensed material (LiPb) into 3 regions, which are defined by the intersection of the material's specific internal energy profile and the "vaporization energy" and the "sensible heat". The sensible heat is the specific energy of the material at its vaporization temperature. The vaporization energy is the sensible heat plus the heat of vaporization. In region A, the specific energy is higher than the vaporization energy. All material in this region is assumed to become superheated vapor. In region C, the specific energy remains lower than the sensible heat. None of the material in this region is vaporized by the target x-rays. In region B, the specific energy lies between the vaporization and sensible energies, and the temperature is equal to the vaporization temperature. To estimate the amount of material vaporized from region B, CONRAD redistributes the energy within the region so that all material is either at the vaporization energy or the sensible energy, while maintaining energy conservation. The redistributed energy is represented by the dotted line in Fig. 7.12.

In the CONRAD simulations of the LIBRA target chamber, 6.7 kg of LiPb is vaporized immediately by the target x-rays. For a 3 meter spherical target chamber, this corresponds to a layer $6.2 \mu\text{m}$ thick. At later times, "thermal" radiation, i.e., energy absorbed by the He gas and reemitted, heats the LiPb and causes an additional 1 to 2 kg to be vaporized (see below). Again, these results should be viewed as qualitative because the CONRAD calculations are based on a spherical geometry.

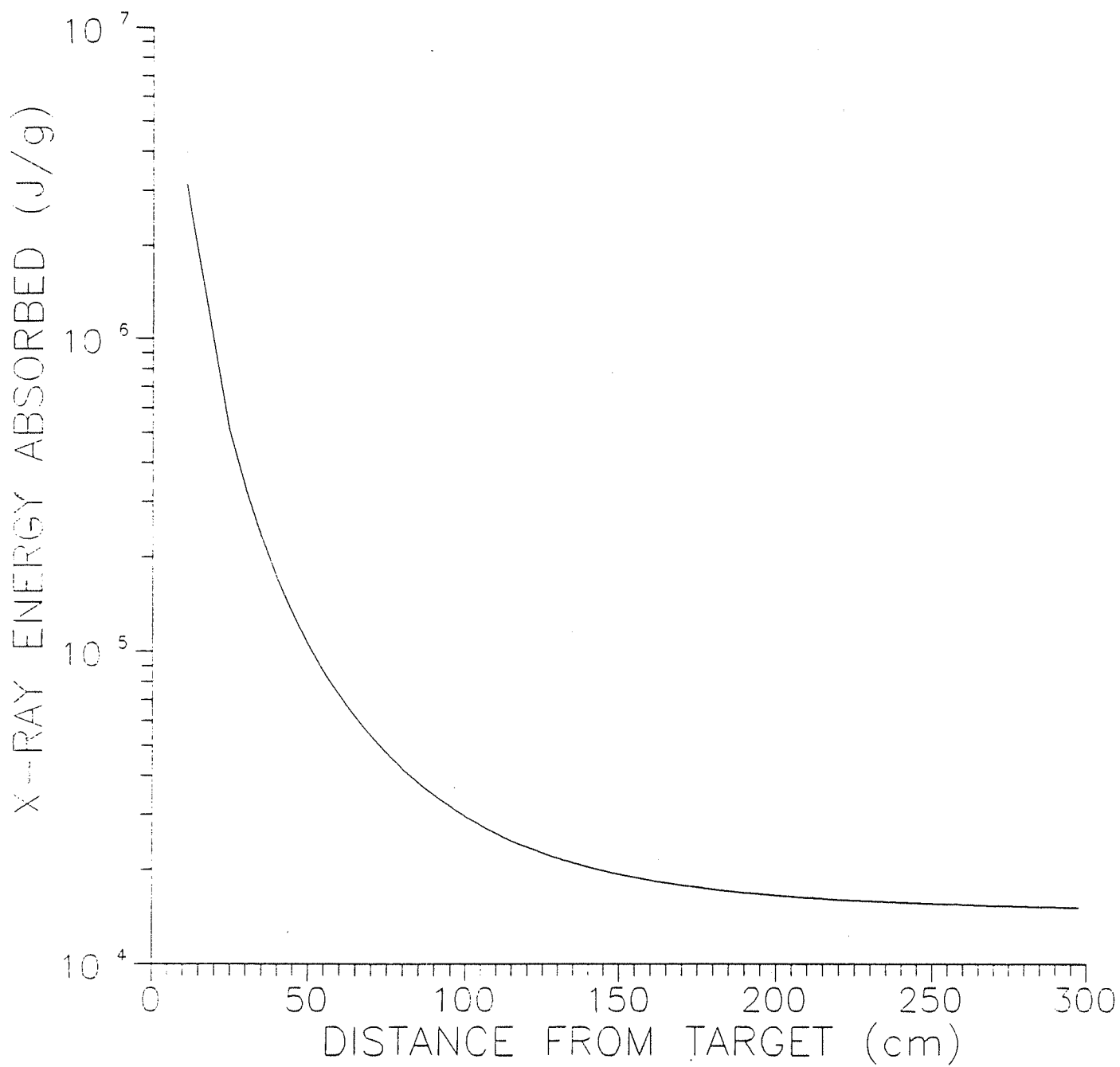


Fig. 7.10. X-ray energy deposition in helium.

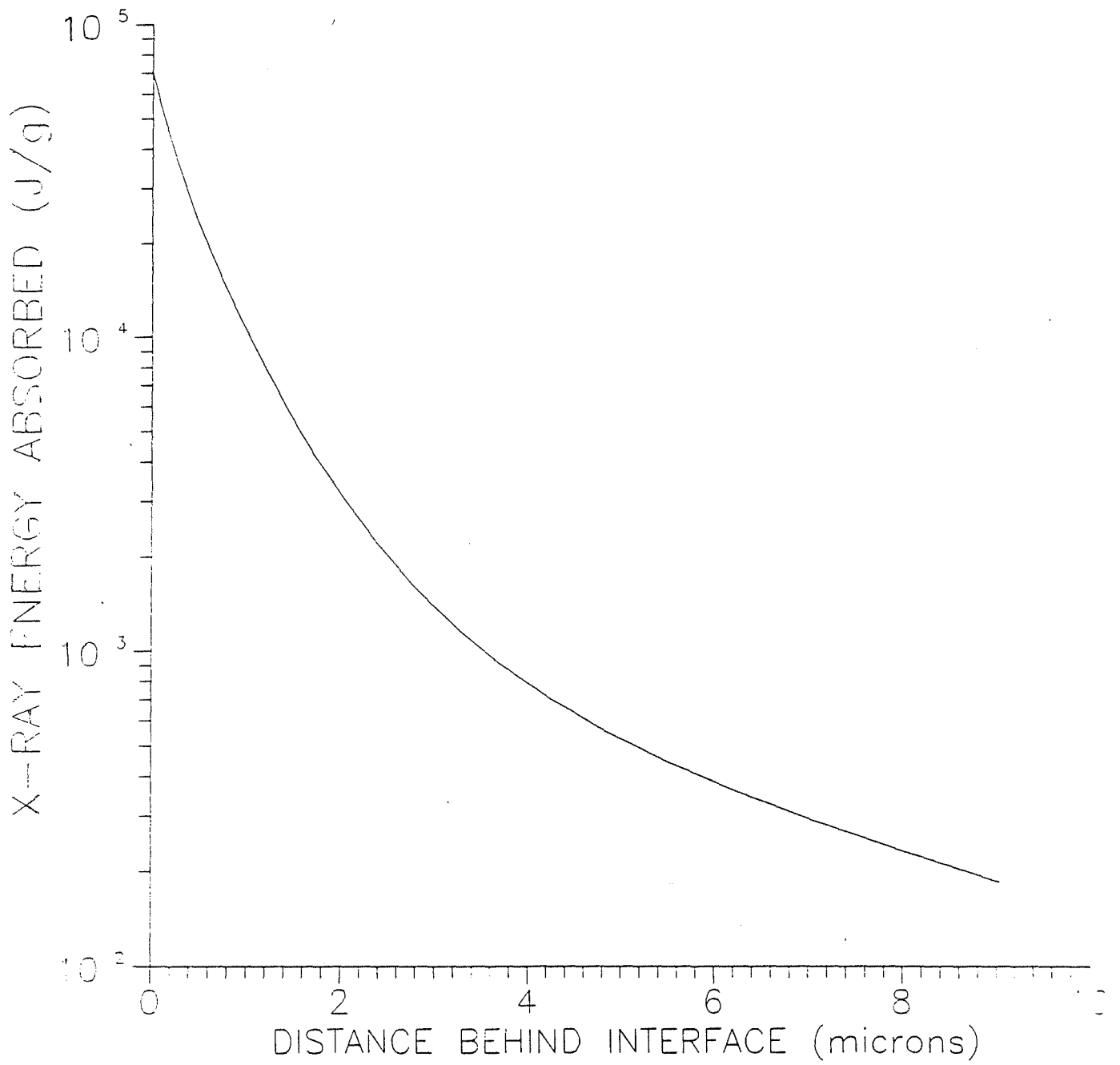


Fig. 7.11. X-ray energy deposition in lithium-lead.

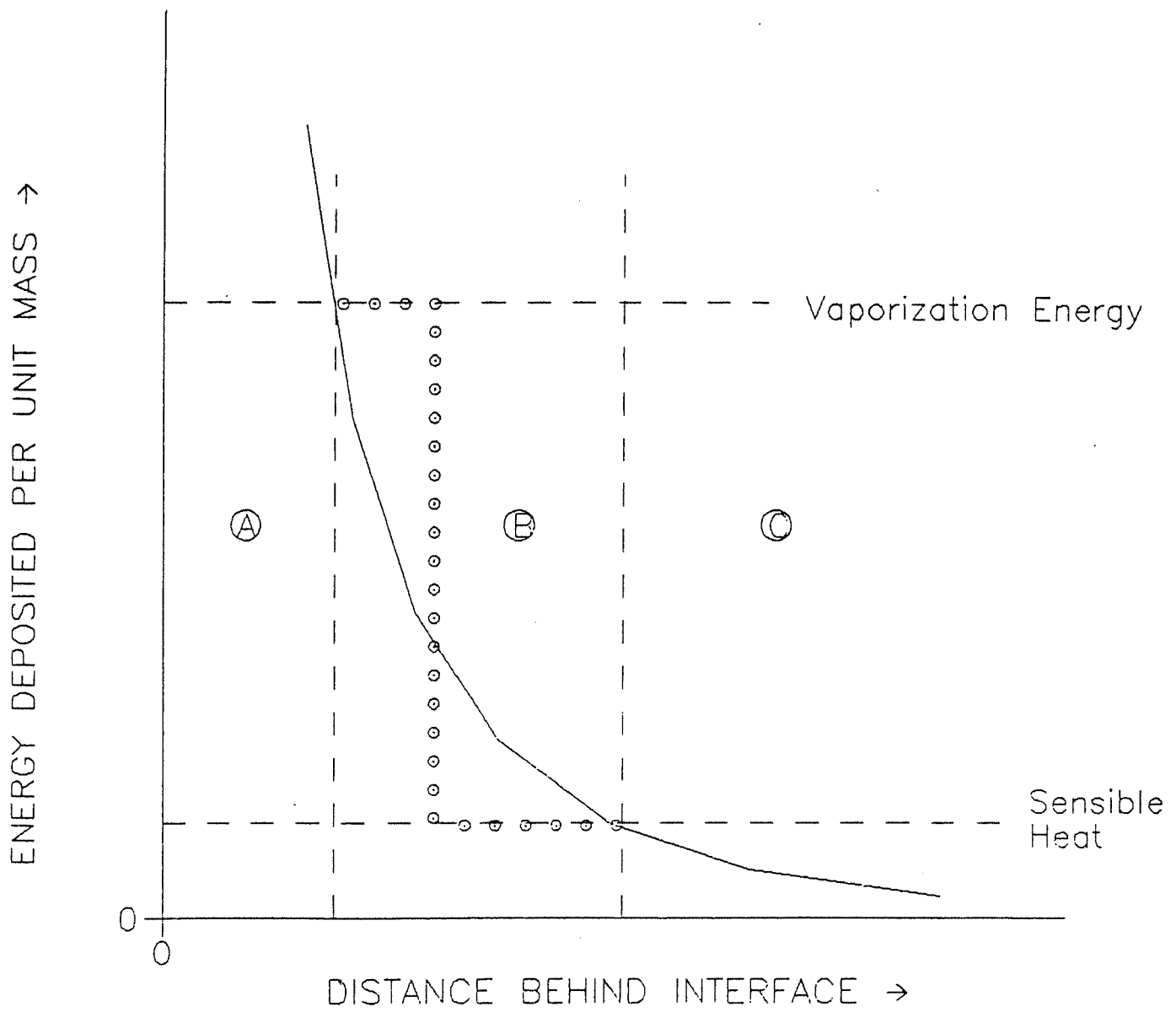


Fig. 7.12. Illustration of x-ray vaporization model.
 Region A: Specific Heat > Vaporization Energy
 Region B: Vaporization Energy > Specific Heat > Sensible Heat
 Region C: Sensible Heat > Specific Heat

When the LiPb is volumetrically heated by the target x-rays, the pressure in the LiPb vapor becomes very high because of the high particle density. This causes the LiPb vapor to flow rapidly away from the INPORTs, and provides a recoil impulse to the tubes. The impulse is calculated by integrating the pressure at the vapor/liquid interface over time. The impulse due to the x-ray vaporization of 6.7 kg in LIBRA is 108 Pa-s. As described below, an additional impulse of about 17 Pa-s is caused by vaporization at later times due to reradiated energy from the cavity gases. Thus, the total impulse applied to the INPORT tubes is about 125 Pa-s. The mechanical response of the tubes to impulses of this magnitude is described in Section 7.3.

The effect of varying the distance to the INPORT tubes has also been studied. Table 7.1 shows the results from calculations in which the minimum tube distance was varied between 2 and 5 meters. Tabulated are the x-ray energy deposited in the LiPb, the mass and thickness of the LiPb region vaporized (due to the target x-rays only), and the resulting recoil impulse on the tubes. Note that the x-ray energy deposited in the LiPb varies little with distance to the tubes. This is because He is effective in attenuating only the lowest energy x-rays, while being essentially transparent to high energy x-rays. This fact, coupled with the greater surface area of LiPb at larger distances, leads to the interesting result that the mass of LiPb vaporized increases with the target-to-tube distance in the 2 to 5 meter range. Both the thickness of the region vaporized and recoil impulse are seen to decrease with increasing distance to the INPORTs.

Table 7.1. Effect of Target-to-Tube Distance on X-ray Vaporization of LiPb

Distance (m)	Energy Deposited in LiPb (MJ)	Mass of LiPb Vaporized (kg)	Thickness of LiPb Layer Vaporized (μm)	Impulse from X-ray Vaporization (Pa-s)
2	52.0	4.51	9.4	208
3	50.2	6.69	6.2	108
4	48.7	8.74	4.6	69
5	47.5	10.88	3.6	47

The pressures in the LiPb vapor immediately after the x-rays are absorbed are extremely high ($\sim 10^4 - 10^5$ MPa). This pressure is applied to the vapor/liquid interface and can generate a shock through the liquid LiPb layer to the SiC weave located 2 mm behind the interface. This could potentially cause two problems. First, the shock could cause structural damage to the SiC weave. Second, a shock reflected from the SiC could cause the ~ 1 mm (or $\sim 10^3$ kg) of LiPb on the outside of the weave to disassemble. In this case, most of the ejected LiPb would be in the form of droplets because the energy required to vaporize 10^3 kg of LiPb is $\sim 10^3$ MJ. Since the time it takes a droplet to fall 6 m to the bottom of the target chamber under the influence of gravity is 1.1 s, it appears that if a large amount of LiPb ($\gg 10$ kg) is ejected from the INPORT tubes after each target explosion, the repetition rate would have to be reduced. This problem should be studied in more detail in the future.

7.2.4. Debris Ion Energy Deposition

Target debris ions are highly charged and have high kinetic energies as they explode into the background gas. The kinetic energy of the debris ions decreases as they undergo ion-electron, ion-neutral, and ion-ion collisions until they eventually reach a state of equilibrium with the surrounding plasma. The rate at which ions transfer their momentum and energy to the background is calculated using a classical stopping power model:⁽¹⁰⁾

$$S = \frac{1}{N_{bg}} \left[\left(\frac{dE}{dx} \right)_{fe} + \left(\frac{dE}{dx} \right)_{be} + \left(\frac{dE}{dx} \right)_{nuc1} \right] \quad (7.16)$$

where (dE/dx) is the kinetic energy lost by a debris ion as it traverses a distance dx through a background medium of density N_{bg} . The three terms on the right hand side of Eqn. 7.16 represent (from left to right) the contributions from collisions with free electrons, bound electrons, and nuclei of the background plasma.

The free electron contribution to the stopping power is given by

$$\left(\frac{dE}{dx} \right)_{fe} = \left(\frac{\omega_p q_1 e}{v_1} \right)^2 G(y^2) \ln \Lambda_{fe} \quad (7.17)$$

where

$$G(y^2) = \text{erf}(y) - \frac{2}{\sqrt{\pi}} e^{-y^2}$$

and

$$\omega_p = \left(\frac{4\pi e^2 n_e}{m_e} \right)^{1/2}$$

is the plasma frequency. Here y is the ratio of the debris ion velocity, v_1 , to the mean electron velocity, $\langle v_e \rangle$; q_1 is the debris ion charge state, e is the electron charge, n_e is the electron density and m_e is the electron mass. The Coulomb logarithm is given by

$$\Lambda_{fe} = (0.764 v_1) / (\omega_p b_{\min})$$

where

$$b_{\min} = a_0 \max \left[q_1 \left(\frac{v_1}{v_0} \right)^2, \frac{v_1}{2v_0} \right],$$

a_0 is the Bohr radius, and v_0 is the Bohr velocity ($= 2.2 \times 10^8$ cm/s). At high temperatures, the background plasma is highly ionized and the stopping power is dominated by the free electron term. Under these conditions, the stopping power is proportional to q_1^2 .

Inelastic scattering with bound electrons and elastic nuclear scattering are important at low temperatures. The nuclear contribution can be written as:

$$\left(\frac{dE}{dx} \right)_{\text{nuc1}} = C_1 \epsilon^{1/2} \exp \{ -45.2 (C_2 \epsilon)^{0.277} \} \quad (7.18)$$

where

$$\epsilon = E/A_1 \text{ (MeV/amu)}$$

$$C_1 = (4.14 \times 10^6 \text{ MeV cm}^2 \text{g}^{-1}) \frac{\rho_2}{A_2^2} \left(\frac{A_1 A_2}{A_1 + A_2} \right)^{3/2} \left(\frac{(Z_1 Z_2)^{1/2}}{Z_1^{2/3} + Z_2^{2/3}} \right)^{3/4}$$

and

$$C_2 = \left(\frac{A_1 A_2}{A_1 + A_2} \right) (Z_1 Z_2)^{-1} (Z_1^{2/3} + Z_2^{2/3})^{-1/2} .$$

The subscripts 1 and 2 refer to the debris ion and background plasma, respectively. A, Z, and ρ refer to the atomic weight, atomic number and mass density, respectively.

The bound electron contribution is calculated using one of two theories, depending on the debris ion velocity. Lindhard-Scharff theory⁽¹¹⁾ is valid when the debris ion velocity is small compared with the orbital velocity of the bound electrons, in which case the bound electrons are treated as a cloud as opposed to point charges. The expression for the Lindhard-Scharff stopping power is:

$$\left(\frac{dE}{dx} \right)_{LS} = (3.84 \times 10^{-18} \text{ keV cm}^{-1}) N_2 \frac{Z_1^{7/6} Z_2^*}{[Z_1^{2/3} + (Z_2^*)^{2/3}]^{3/2}} \left(\frac{E_1}{A_1} \right)^{1/2} \quad (7.19)$$

where E_1 is the debris ion kinetic energy in keV, and Z_2^* is the average number of bound electrons per nucleus. Thus, at low velocities, the rate at which the debris ions lose their energy is proportional to their velocity. When the debris ion velocities are large compared with the electron orbital velocities, the bound electrons can be treated as point charges, and Bethe theory is used to determine the debris ion energy loss rate. The expression for the Bethe stopping power is⁽¹²⁾

$$\left(\frac{dE}{dx} \right)_{\text{Bethe}} = \left(\frac{\omega_p q_1 e}{v_1} \right)^2 \left[\ln \left(\frac{2m_e v_1^2}{\langle \phi_2 \rangle \left(1 - \frac{v_1^2}{c^2} \right)} \right) - \left(\frac{v_1}{c} \right)^2 \right] \quad (7.20)$$

where $\langle \phi_2 \rangle$ is the average ionization potential of the background plasma. To ensure a smooth transition between the two models, we interpolate to get the total bound electron stopping power.

The total debris ion kinetic energy of the LIBRA target is 32.8 MJ. The kinetic energies and charge states for each of the debris ions as they leave the target are listed

in Table 7.2. The ions exploding from the LIBRA target are D, T, He, C, and Pb. All ions are assumed to be singly ionized as they leave the target, and have a velocity of 4.3×10^7 cm/s.

Table 7.2. Target Debris Ion Properties

Species	Kinetic Energy (keV/ion)	Charge State
D	1.90	+1
T	2.86	+1
He	3.80	+1
C	11.1	+1
Pb	198.0	+1

When the stopping ranges of the debris ions are comparable to the size of the cavity, the time-dependence of the debris ions' charge states must be computed to accurately determine the energy deposition profile. This, however, is not the case in the LIBRA simulations because of the high background gas density. In the CONRAD simulations, we find that the debris ions are stopped within a few centimeters of the target when the ions are assumed to be singly ionized. For an actual target explosion, the debris ions would certainly be more highly ionized, and their stopping range would be even shorter. Thus, the time-dependence of the debris ions' charge states is unimportant in the present LIBRA design.

7.2.5. Results of Radiation-Hydrodynamic Simulations

The purpose of the radiation-hydrodynamic calculations is to compute: (1) the time-dependent energy deposition and transport within the target chamber cavity; (2) the vaporization and recondensation of LiPb; and (3) the time-dependent conditions at the INPORTs. In this section, results will first be presented for the vapor region of the cavity, and later for the conditions at the vapor/liquid interface at the tubes.

The fluid motion in the cavity is shown in Fig. 7.13, where the positions of the Lagrangian zone boundaries are plotted as a function of time out to 0.2 ms. For clarity, the position of every third zone is plotted. The dashed line represents the boundary between the He and LiPb vapor. The target explodes at the origin and the initial position of the LiPb is at 3 meters. Figure 7.13 clearly shows the outward moving shock which is

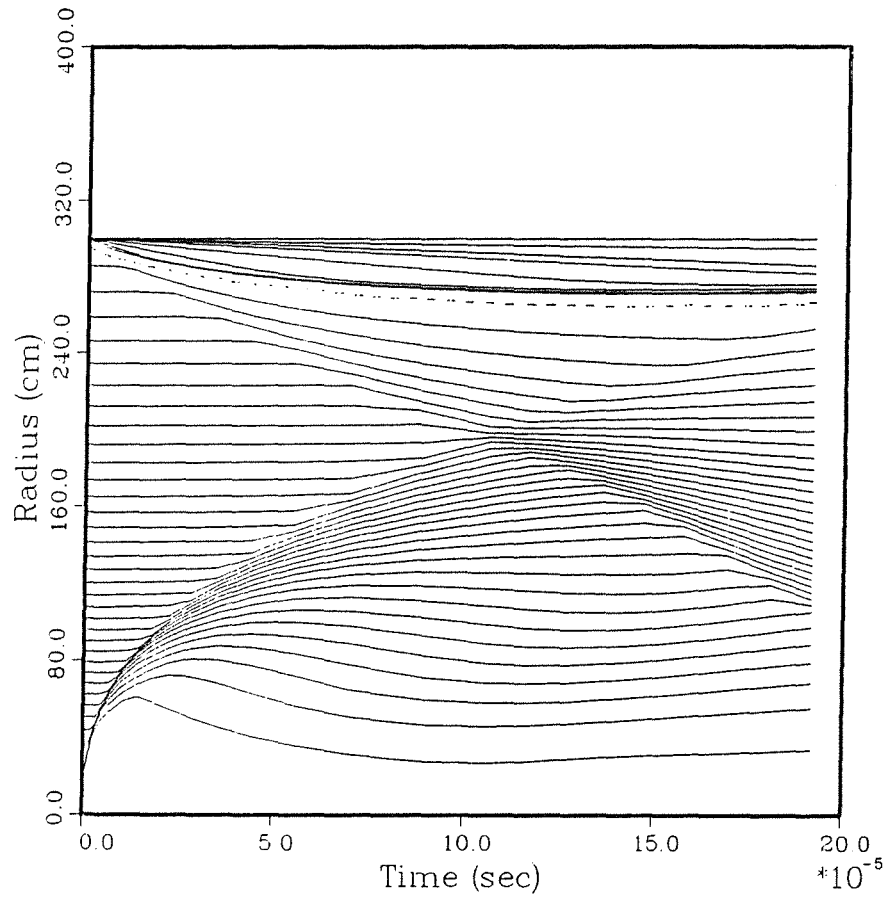


Fig. 7.13. Positions of Lagrangian zone boundaries vs. time.

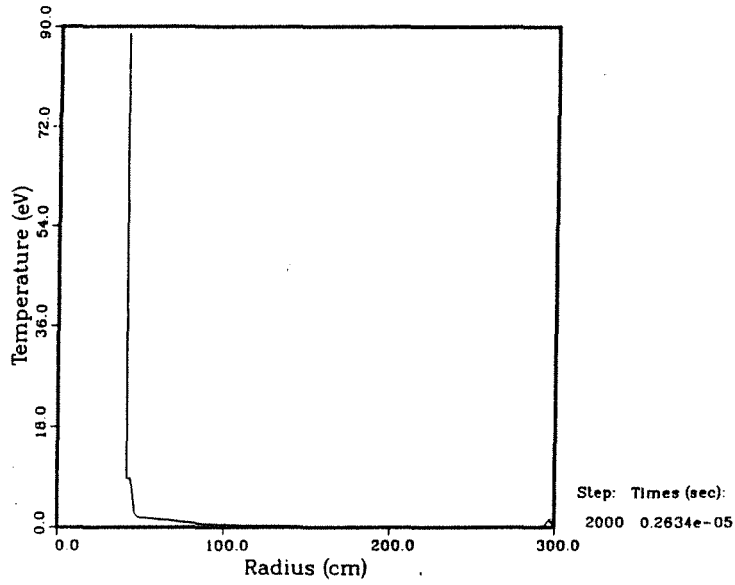
driven by the high-temperature microfireball, and the inward moving flow which is driven by the expansion of LiPb from the INPORTs. The two fronts collide at 0.1 ms at a radius of about 2 meters, and produce reflected shocks that travel in opposite directions.

After the shocks collide, the validity of the CONRAD results are questionable. This is because in the LIBRA cavity, the LiPb expands away from the INPORTs in a direction normal to the tube surfaces, while the shock driven by the microfireball expands spherically. Thus, the interaction between the two fronts will occur later near the top and bottom of the chamber than at the center, where the target-to-tube distance is the smallest. Because of this, concentration on the CONRAD results at times $\leq 10^{-4}$ s is made (the exception to this is the condensation portion of the calculation).

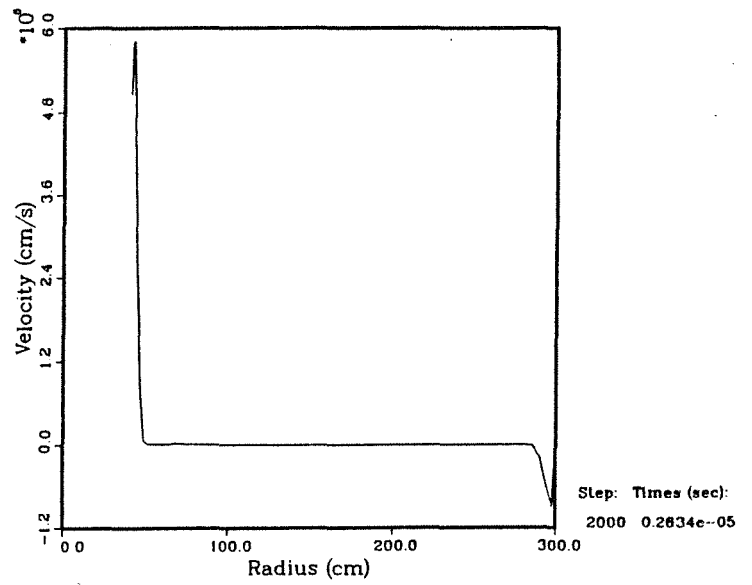
Figures 7.14 through 7.16 show the conditions in the He and LiPb gas at 3 times: 3 μ s (immediately after the debris ions have stopped in the He surrounding the target), 82 μ s (just before the two shock fronts collide), and 200 μ s (after the shocks collide). At each time, the temperature, fluid velocity, pressure and mass density are plotted as a function of distance from the target explosion. At 3 μ s, most of the cavity gas has not had time to respond hydrodynamically. The fluid is stationary except near the target and the INPORTs. The temperature of the microfireball reaches its peak value (~ 90 eV) at this time. The density in the microfireball has dropped by roughly a factor of 10 as mass is pushed ahead of it, forming a shock front. The density of liquid LiPb at the INPORTs is 9.55 g/cm^3 . The velocity plot shows material flowing rapidly in two regions: away from the target explosion and away from the INPORTs (positive velocities indicate material flowing away from the target).

At 82 μ s (Fig. 7.15), the temperature of the microfireball has fallen to below 3 eV. The outward and inward travelling shocks are located at 1.8 and 2.2 m, respectively, and are clearly visible in the pressure plot. The shock fronts are moving toward each other with a speed ~ 10 km/s. The discontinuity near 2.75 m is the He/LiPb (vapor) interface. The results in this region are of questionable validity because CONRAD does not model mixing of the He and LiPb. In addition, the density spike at 2.9 m is artificial, as it is caused by a single Lagrangian cell being vaporized by energy radiated by the microfireball. Note that the temperature in the LiPb close to the INPORTs is very low (< 1000 K). This is simply a result of expansive cooling as the LiPb vapor pushes itself away from the tubes. In this cold region, the Pb becomes supersaturated and it is quite possible that the Pb would homogeneously nucleate and form droplets.

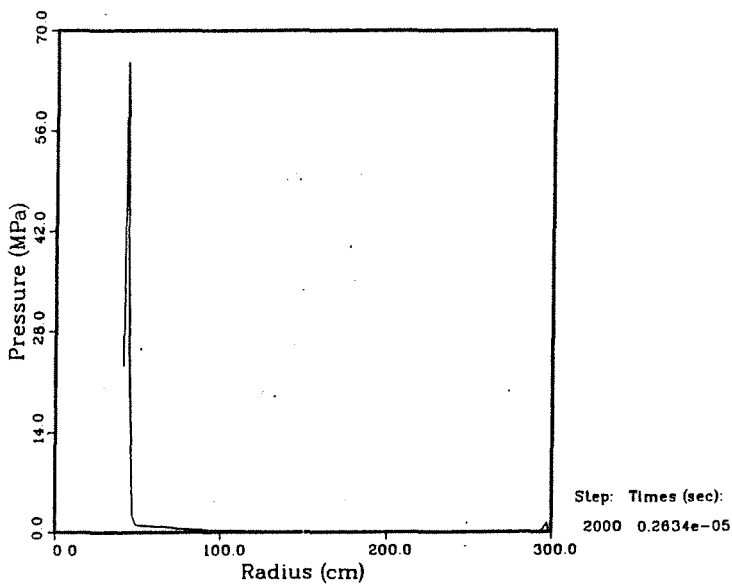
Plasma Temperature vs. Radius



Gas Velocity vs. Radius



Gas Pressure vs. Radius



Mass Density vs. Radius

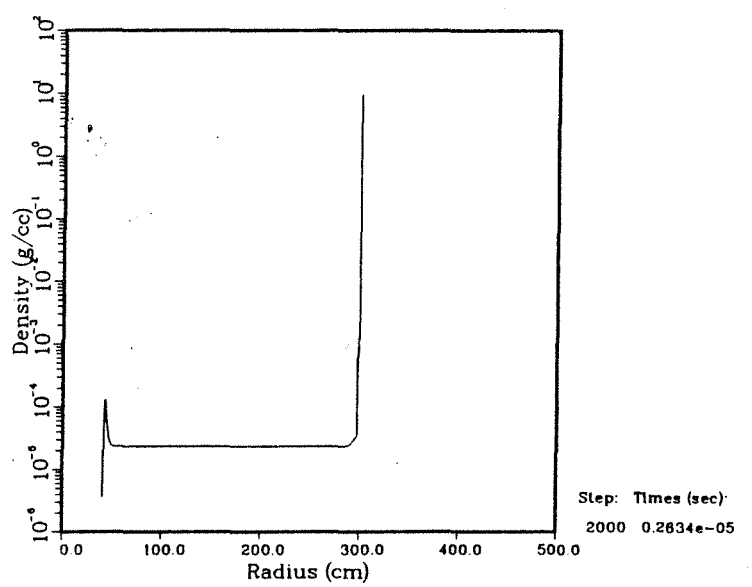
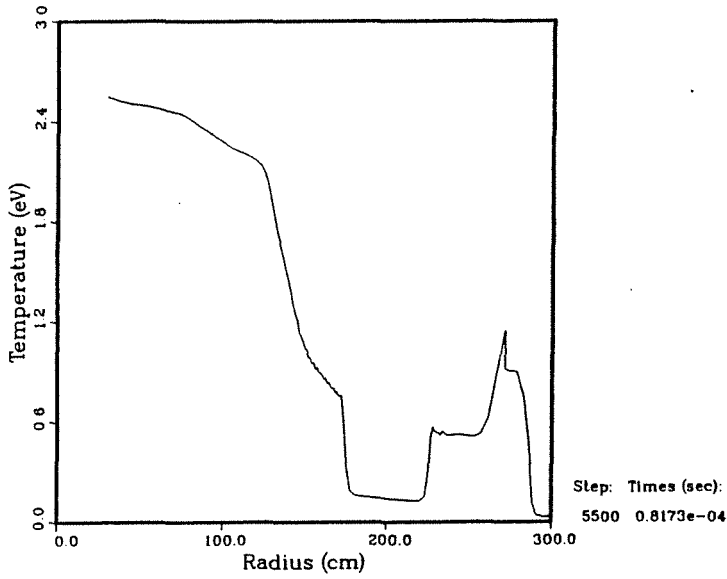
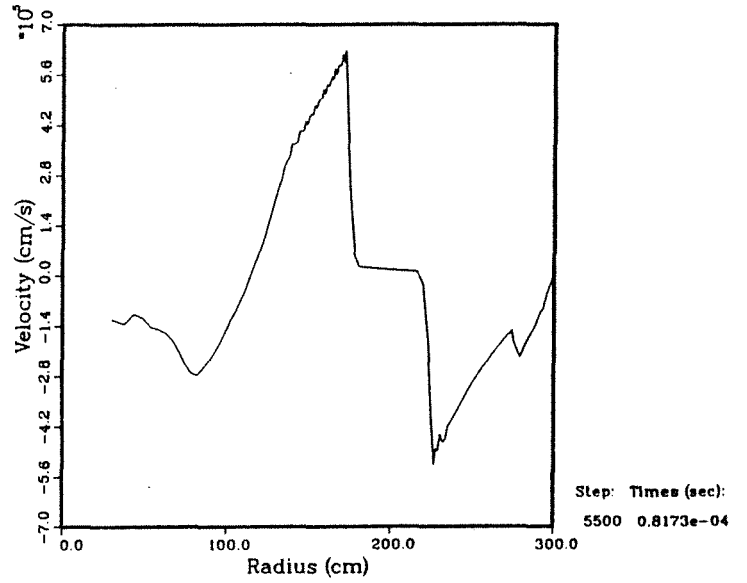


Fig. 7.14. Conditions in cavity at 3 μ s.

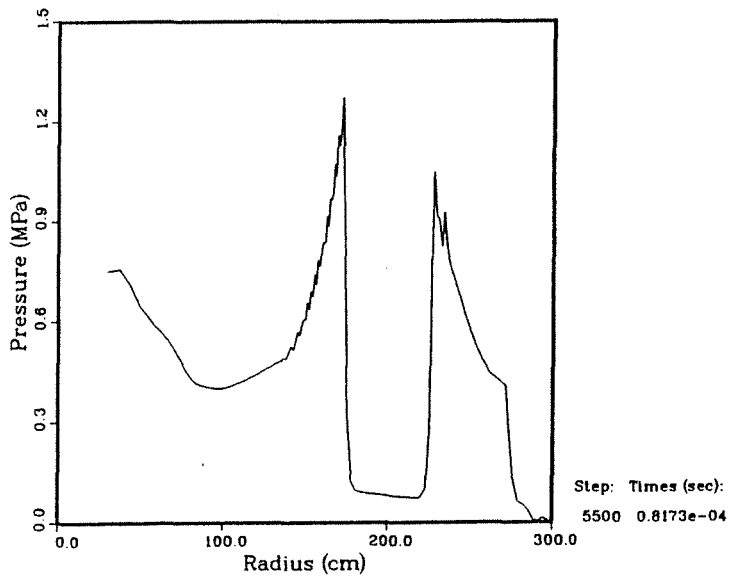
Plasma Temperature vs. Radius



Gas Velocity vs. Radius



Gas Pressure vs. Radius



Mass Density vs. Radius

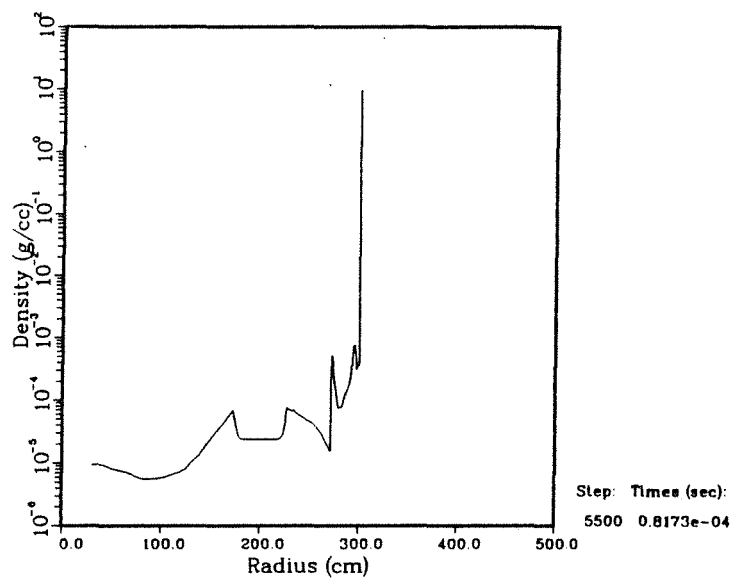


Fig. 7.15. Conditions in cavity at 82 μ s.

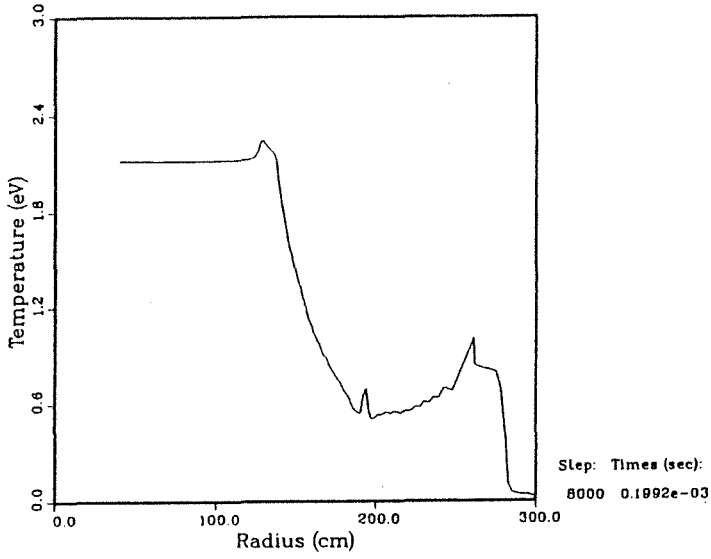
At 200 μs (Fig. 7.16), the reflected shocks are clearly visible at 1.3 m and 2.6 m. Temperatures behind the shocks range from 0.5 eV to 2.1 eV. Thus, if Pb droplets do form in the rarefaction wave near the INPORTs, it seems quite plausible they would revaporize later when the reflected shock travels back through the cold region at $t \sim 0.5$ ms. However, because the cavity is cylindrical, one could also speculate that the droplets in the top and bottom corners of the chamber may not vaporize. Because of these complexities, it is very difficult to predict the physical state of the LiPb at late times.

The physical conditions at the INPORTs are shown in Figs. 7.17 through 7.19. Figs. 7.17 and 7.18 show the radiative flux and time-integrated flux at the vapor/liquid LiPb interface as a function of time after the target x-rays are deposited. A maximum flux of $\sim 1 \times 10^8 \text{ W/cm}^2$ occurs at early times ($< 10^{-8}$ s) and is due to radiation emitted by superheated LiPb. This radiation, however, deposits little energy at the interface because of the short duration of this "pulse". At times $> 10^{-7}$ s, radiation emitted by the microfireball reaches the INPORTs. The peak flux of this radiation is $8 \times 10^5 \text{ W/cm}^2$. Figure 7.18 shows that this radiation deposits ~ 3 MJ (or $\sim 3 \text{ J/cm}^2$) at the tubes by 10 μs . An additional 1 MJ of radiant energy is absorbed by the liquid LiPb between 10 and 200 μs . Thus, of the 95 MJ of x-ray and debris ion energy released by the target, 50 MJ are deposited directly into the LiPb in the form of target x-rays, and an additional 4 MJ are deposited at the vapor/liquid interface by 200 μs .

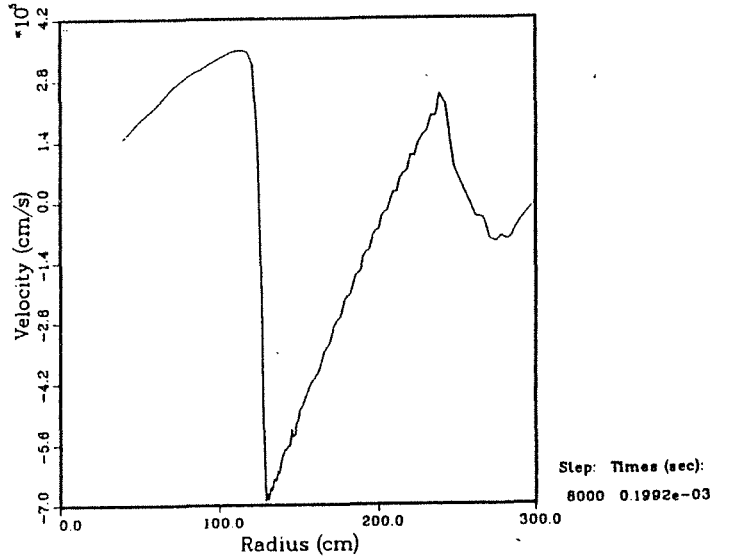
When the energy flux into the LiPb exceeds the rate at which conduction can carry energy through the liquid away from the interface, the temperature at the interface will rise. This is shown in Fig. 7.19, where the temperature of the liquid LiPb at the interface is plotted as a function of time. At times $< 10^{-7}$ s, the temperature falls from its post-x-ray absorption value. As the radiation emitted by the microfireball arrives at the INPORTs, the temperature at the interface rises, and more LiPb is vaporized. At later times, conduction carries energy away from the interface and the temperature falls.

Figure 7.20 shows the mass of LiPb in the vapor phase as a function of time. Approximately 6.7 kg of LiPb is vaporized immediately by the target x-rays (see Section 7.2.3). As the temperature of the liquid at the interface rises, an additional 1.3 kg of LiPb is vaporized. Thus, our 1-D simulations predict the total amount of LiPb vaporized per shot is about 8 kg. This corresponds to a layer with a thickness of 7 μm .

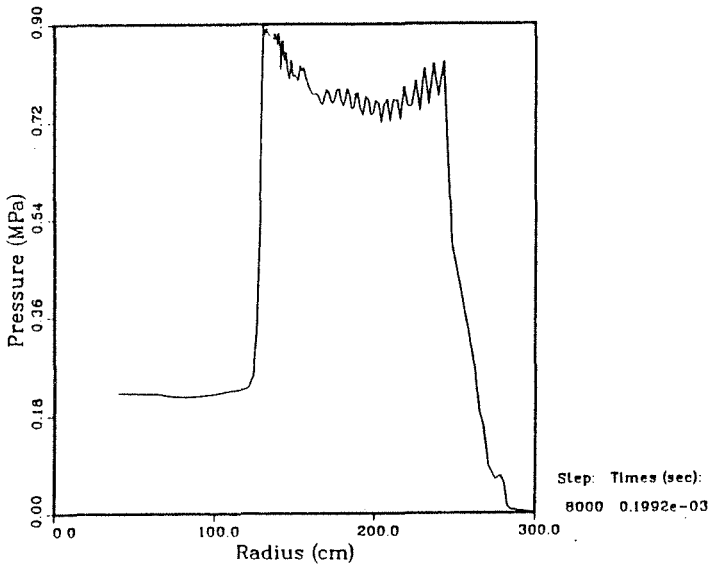
Plasma Temperature vs. Radius



Gas Velocity vs. Radius



Gas Pressure vs. Radius



Mass Density vs. Radius

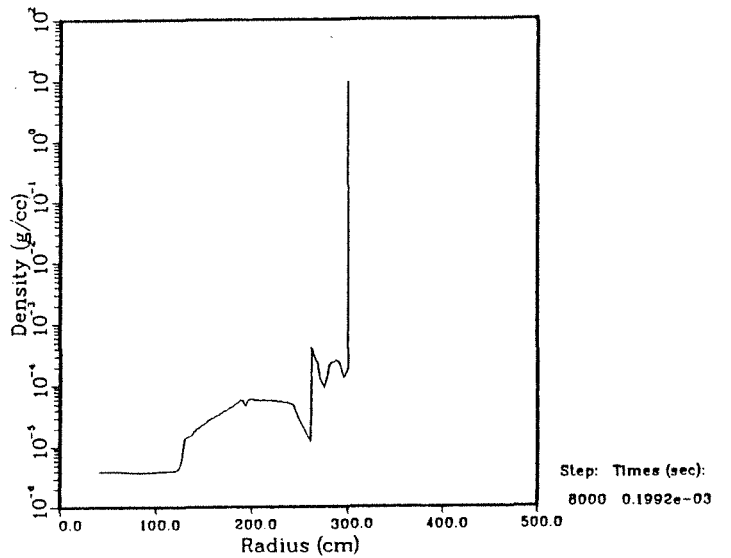


Fig. 7.16. Conditions in cavity at 200 μ s.

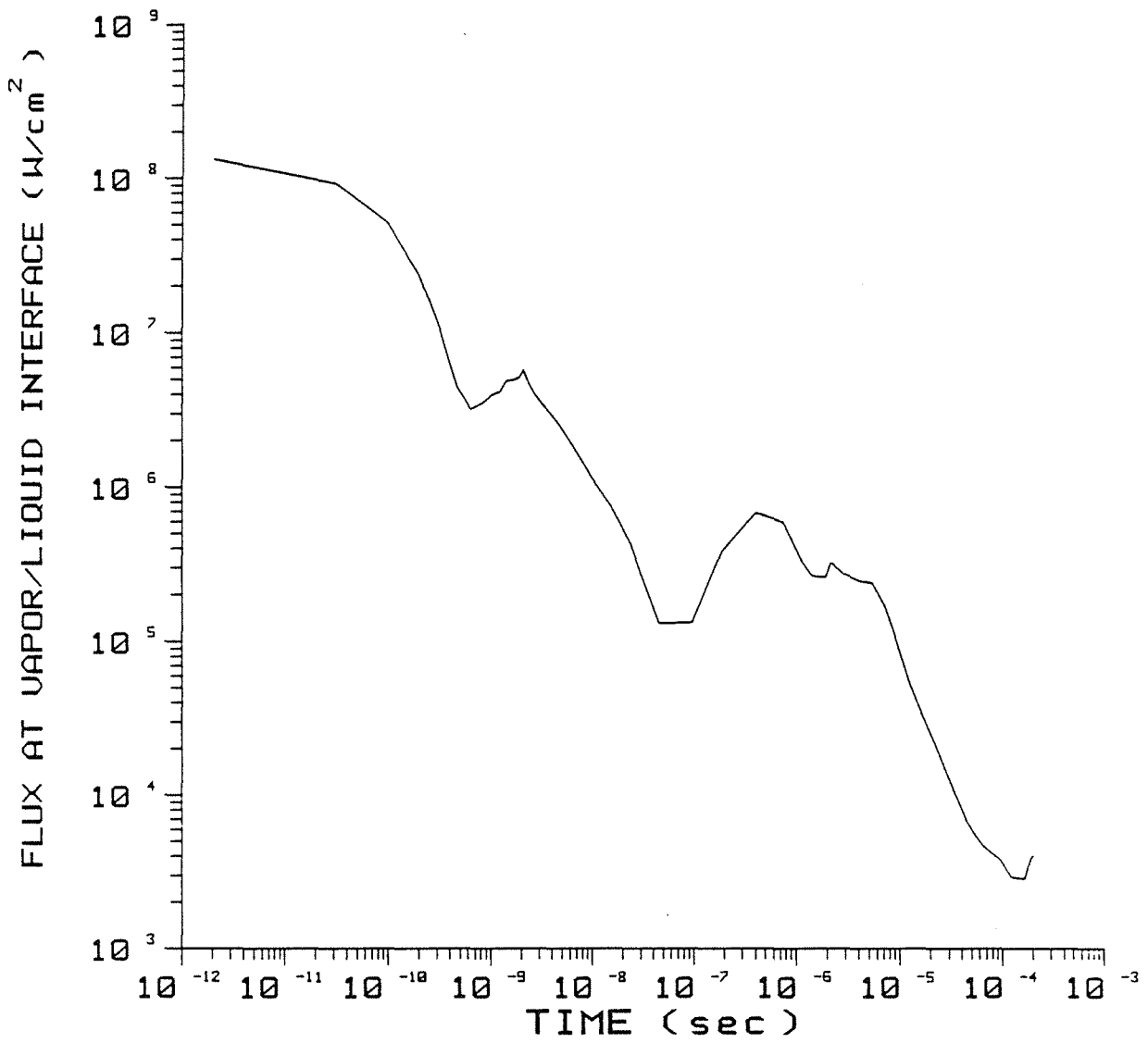


Fig. 7.17. Radiative flux at the vapor/liquid interface vs. time.

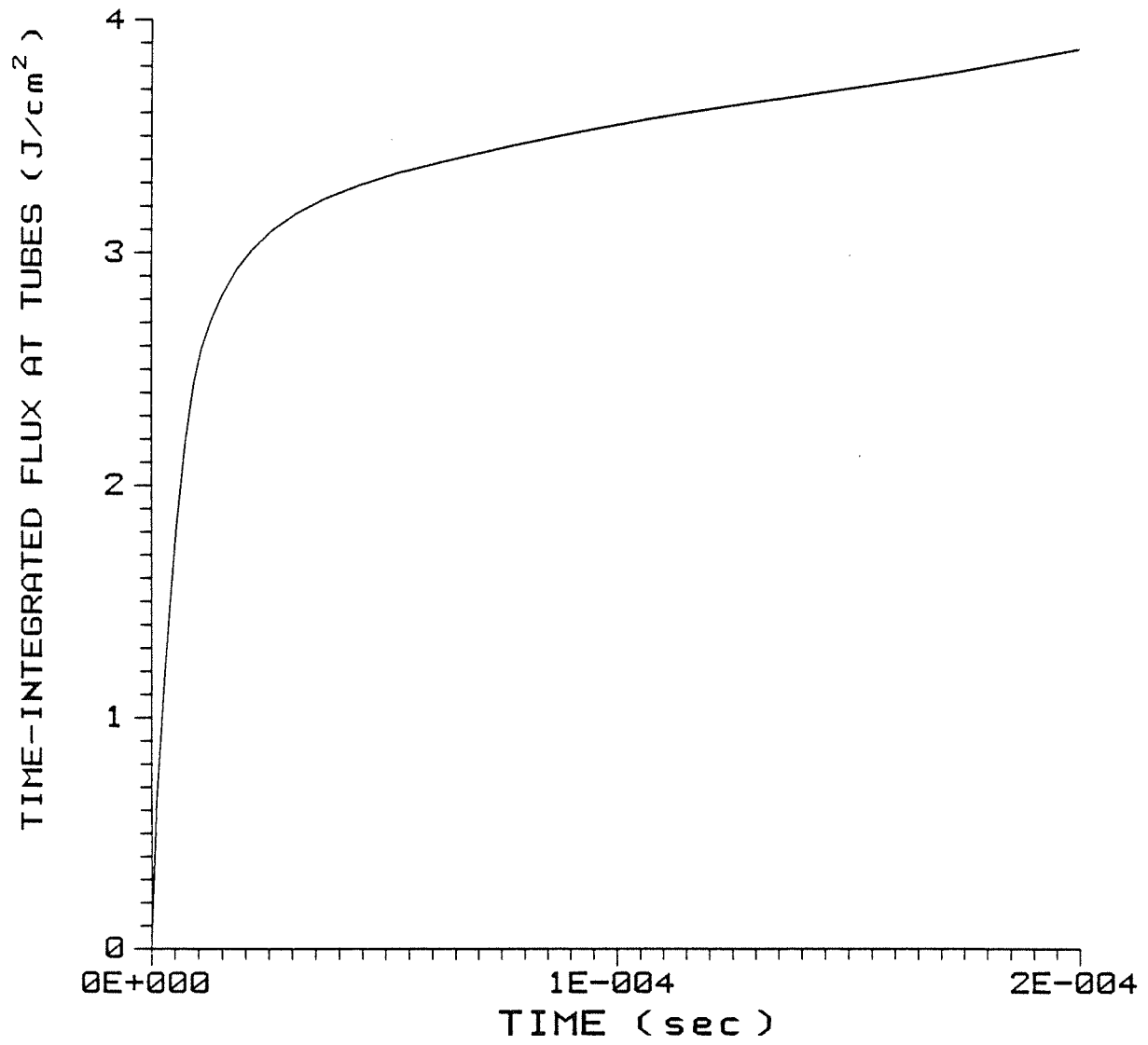


Fig. 7.18. Deposited radiative energy at the vapor/liquid interface vs. time.

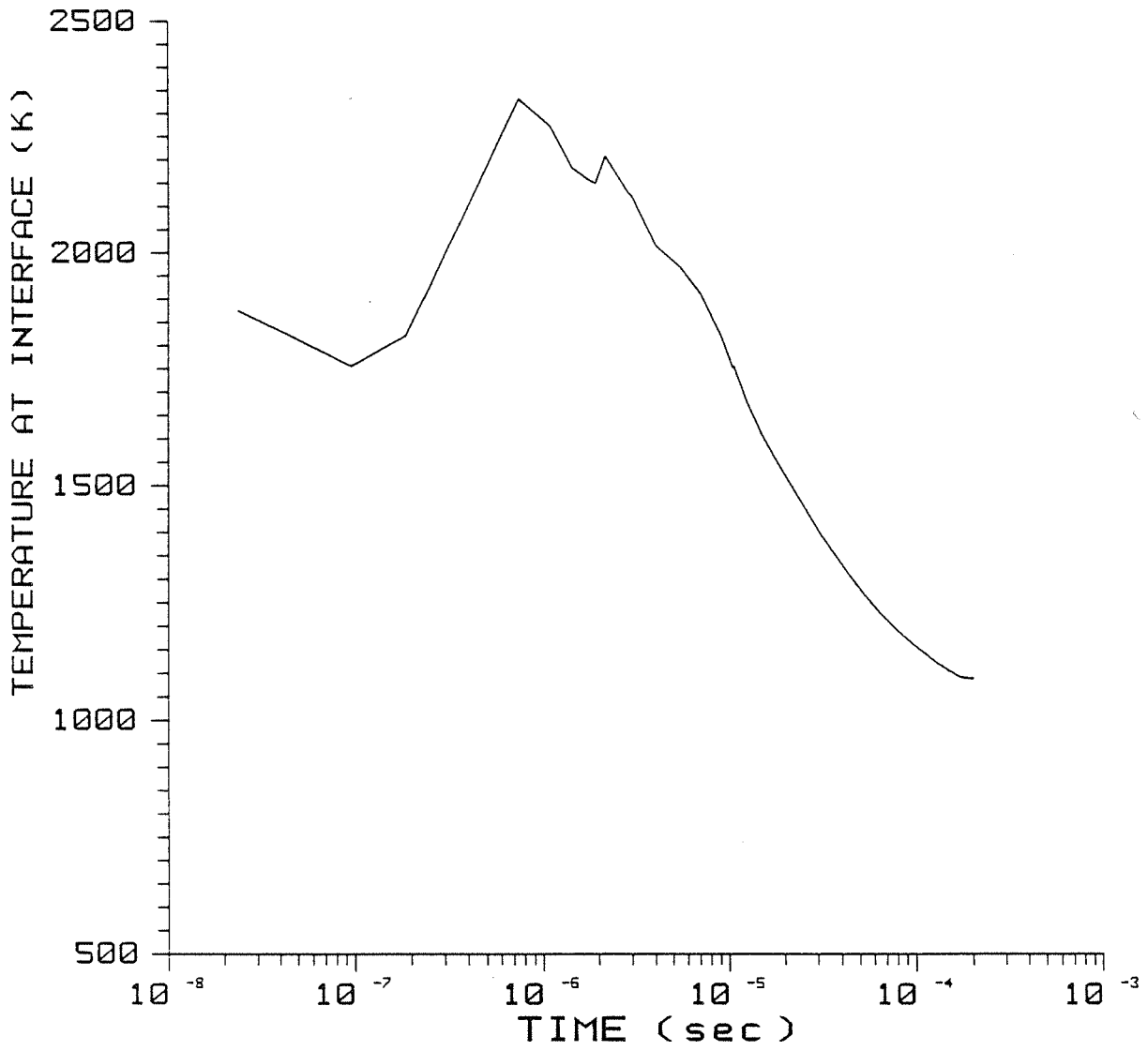


Fig. 7.19. Temperature of liquid LiPb at the interface vs. time.

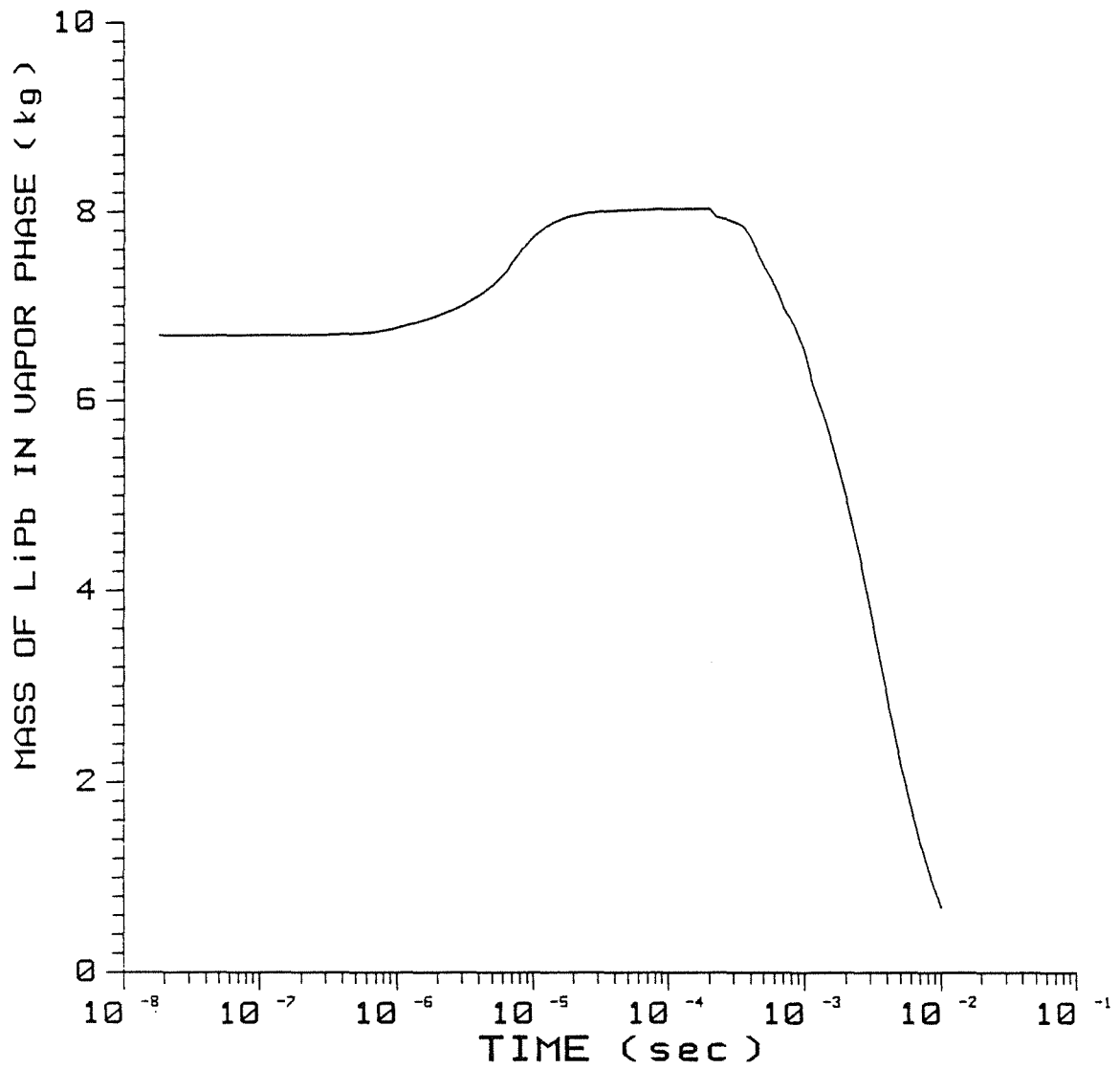


Fig. 7.20. Lithium-lead mass vaporized vs. time.

CONRAD has also been used to calculate the condensation of LiPb back onto the INPORTs. In practice, the simulation is restarted at $t \sim 10^{-4}$ s, with uniform temperatures and pressures throughout the cavity, using the mass of LiPb vapor and total energy from the explosion/vaporization calculation. In this calculation, noncondensable gas effects are neglected, as are chemical bonding effects. $\text{Li}_{17}\text{Pb}_{83}$ is treated as a single atom. Figure 7.20 shows that roughly 90% of the LiPb has recondensed back onto the INPORT tubes by 10^{-2} seconds. At this time, the LiPb/He number ratio is 0.007. Thus, according to these calculations, the LiPb condensation time would not be expected to limit the reactor shot rate of 3 Hz. However, the presence of a noncondensable gas may significantly slow the condensation rate. This is because the fractional abundance of noncondensable gas atoms increases in the Knudson layer, effectively "blocking" the flow of LiPb atoms to the interface. Recent calculations⁽¹³⁾ indicate that the presence of He may dramatically slow the LiPb condensation rate. Because of the uncertainties associated with the condensation times, a pumping system has been devised to evacuate the post-shot gases from the target chamber (see Chapter 6).

7.2.6. Summary of Radiation-Hydrodynamic Calculations

Our results indicate that roughly 80% of the target x-ray energy is deposited in the LiPb coating the INPORTs, and that about 8 kg of LiPb is vaporized after each target explosion. The LiPb vapor expands away from the INPORTs and provides a recoil impulse of 125 Pa-s. The shock driven by the high temperature microfireball contributes little to the total impulse because it is overwhelmed by the inward moving LiPb front. The peak pressures in the LiPb vapor immediately after the target x-rays are absorbed are very high ($\sim 10^5$ MPa). This could potentially cause problems for the structural integrity of the SiC weave of the INPORTs, or perhaps restrict the reactor repetition rate if a significant amount of LiPb were to disassemble from the INPORTs as droplets. The condensation rate of LiPb was not found to limit the reactor shot rate. But because of the uncertainties in this part of the calculation (e.g., noncondensable gas effects, droplet formation), a pumping system is used to clear the cavity of post-shot gases.

7.3. INPORT Mechanical Response

7.3.1 Dynamic Modelling Background

The credibility of the INPORT concept for LIBRA depends upon a design which is characterized by an acceptable mechanical response of these components under proposed

operating conditions. The basis of the response simulation is modal analysis rather than lumped parameter modelling. Also, there are no known finite element programs which contain the features necessary to represent this specialized problem, such as variable tension, sequential shock loading, high damping, nonlinear strain-displacement effects and three dimensional motion. The basic theoretical developments have been presented earlier.⁽¹⁴⁾ Results for the linearized eigenvalue problem⁽¹⁵⁾ included precise natural frequencies and mode shapes, which are important to preclude resonance from synchronization with the drivers. It was shown that the tension gradient due to gravity will become insignificant if the tensile preload force is relatively large compared with the weight. Also, it was determined that the error in neglecting gravity gradients could be reduced if the effective tension includes one half of the weight. These modifications are made for the equations of motion which follow.

7.3.2 Analytical Outline

The governing equations are presented in final form, omitting details of the derivations. The two equations represent dynamic equilibrium in the axial (x) and radial (y) directions, with respect to the cylindrical chamber. The equation of motion for the circumferential (z) direction is identical in form to the second of these equations and can be obtained by replacing the radial component, v, by the circumferential component, w.

Notation

A_t	cross sectional area of tube (INPORT)
c	velocity of internal fluid (LiPb)
E	elastic modulus of INPORT (SiC)
g	gravitational constant
l	length of INPORT
m_f	mass per length of fluid (LiPb)
m_t	mass per length of tube (INPORT)
p	internal pressure
t	time
T_0	static pretension force
u	displacement in axial direction
v	displacement in radial direction
w	displacement in circumferential direction
x	axial coordinate

- κ_0 damping coefficient
 ν Poisson's ratio for INPORT (SiC)

$$(m_f + m_t) \frac{\partial^2 u}{\partial t^2} + m_f \frac{\partial c}{\partial t} + \kappa_0 \frac{\partial u}{\partial t} - EA_t \frac{\partial^2 u}{\partial x^2} - \frac{\partial}{\partial x} \left\{ (EA_t - T^{**}) \left[\frac{1}{2} \left(\frac{\partial v}{\partial x} \right)^2 + \frac{1}{2} \left(\frac{\partial w}{\partial x} \right)^2 - \left(\frac{\partial u}{\partial x} \right) \left(\frac{\partial v}{\partial x} \right)^2 - \left(\frac{\partial u}{\partial x} \right) \left(\frac{\partial w}{\partial x} \right)^2 \right] \right\} = 0 \quad (7.21)$$

$$(m_f + m_t) \frac{\partial^2 v}{\partial t^2} + 2m_f c \frac{\partial^2 v}{\partial x \partial t} + m_f c^2 \frac{\partial^2 v}{\partial x^2} + m_f \frac{\partial c}{\partial t} \frac{\partial v}{\partial x} + \kappa_0 \frac{\partial v}{\partial t} - \frac{\partial}{\partial x} \left\{ T^{**} \frac{\partial v}{\partial x} + (EA_t - T^{**}) \left[\frac{\partial u}{\partial x} - \left(\frac{\partial u}{\partial x} \right)^2 + \frac{1}{2} \left(\frac{\partial v}{\partial x} \right)^2 + \frac{1}{2} \left(\frac{\partial w}{\partial x} \right)^2 \right] \frac{\partial v}{\partial x} \right\} = 0 \quad (7.22)$$

where the effective tension, T^{**} , is given by

$$T^{**} = T_0 - pA_f(1 - 2\nu) + (m_f + m_t)g \ell/2 . \quad (7.23)$$

It can be seen that displacements in all three directions are mutually coupled. However, coupling exists only through nonlinear displacement gradients. Since the longitudinal wave speed terms are much greater than the corresponding transverse wave terms, axial inertia can be neglected. Thus the three principal equations are reduced to two, involving the radial (v) and circumferential (w) components.

These partial differential equations of motion are reduced to a system of coupled ordinary differential equations by Galerkin's method, facilitated by the orthogonal characteristics of the eigenfunctions. For this, the solution components are sums of linear modes:

$$v(x,t) = \sum_{n=1}^{\infty} v_n(t) \phi_n(x) = \sum_{n=1}^{\infty} v_n(t) \sin \frac{n\pi x}{\ell} \quad (7.24)$$

$$w(x,t) = \sum_{n=1}^{\infty} w_n(t) \phi_n(x) = \sum_{n=1}^{\infty} w_n(t) \sin \frac{n\pi x}{\ell} \quad (7.25)$$

where n represents the number of half waves of the particular harmonic. Specific results are obtained by numerically integrating the series of nonlinear equations for $v_n(t)$ and $w_n(t)$ using a high precision Runge-Kutta routine.

7.3.3 Response Characteristics

The maximum steady state motion of the INPORTs is the most important issue for establishing tube placement for the LIBRA cavity design. In determining fundamental characteristics of the response, amplitude-frequency plots have been developed for linear cases, keeping fixed both the impulsive pressure magnitude and the repetition rate. Typical results are shown in Fig. 7.21 for various levels of damping. Dimensionless parameters are used and defined as follows:

$$\begin{aligned} \bar{v} &= \frac{v}{\ell} & \bar{w} &= \frac{w}{\ell} & \bar{t} &= \omega_1 t \\ \bar{a} &= \frac{8m_f c_0}{\ell(m_f + m_t)\omega_1} & \bar{b} &= \frac{\kappa_0}{(m_f + m_t)\omega_1} & \bar{c} &= \frac{EA_t \pi^4}{4\ell^2(m_f + m_t)\omega_1^2} \end{aligned} \quad (7.26)$$

Here \bar{a} and \bar{c} equal to zero imply negligible flow velocity and nonlinear strain effects, respectively. One point on one of these curves corresponds to the steady state response for a particular history. Over 100 data points per curve have been used to accurately display the features. Each data point is obtained by starting the system from rest, then applying sequential impulses at a particular repetition rate until a steady state oscillation persists. Then the maximum steady state displacement is recorded. Typically this may require as many as 1000 shots. From Fig. 7.21, the fundamental period is confirmed to be 2π . A peak also develops for the third harmonic at $\bar{t}_{imp} = 2.09, 2\pi/3$, etc. (Even harmonics, such as the second, are not excited because INPORT motion is symmetric with respect to the midplane of the cavity.)

When nonlinear effects are significant, the modal equations are each similar to that of a Duffing oscillator driven by harmonic excitation. Thus the corresponding nonlinear amplitude-frequency curves will exhibit discontinuous jumps near resonant frequencies. The calculations are essentially the same as the linear cases. To observe the jump effect, the simulation was carried out by gradually increasing or decreasing the

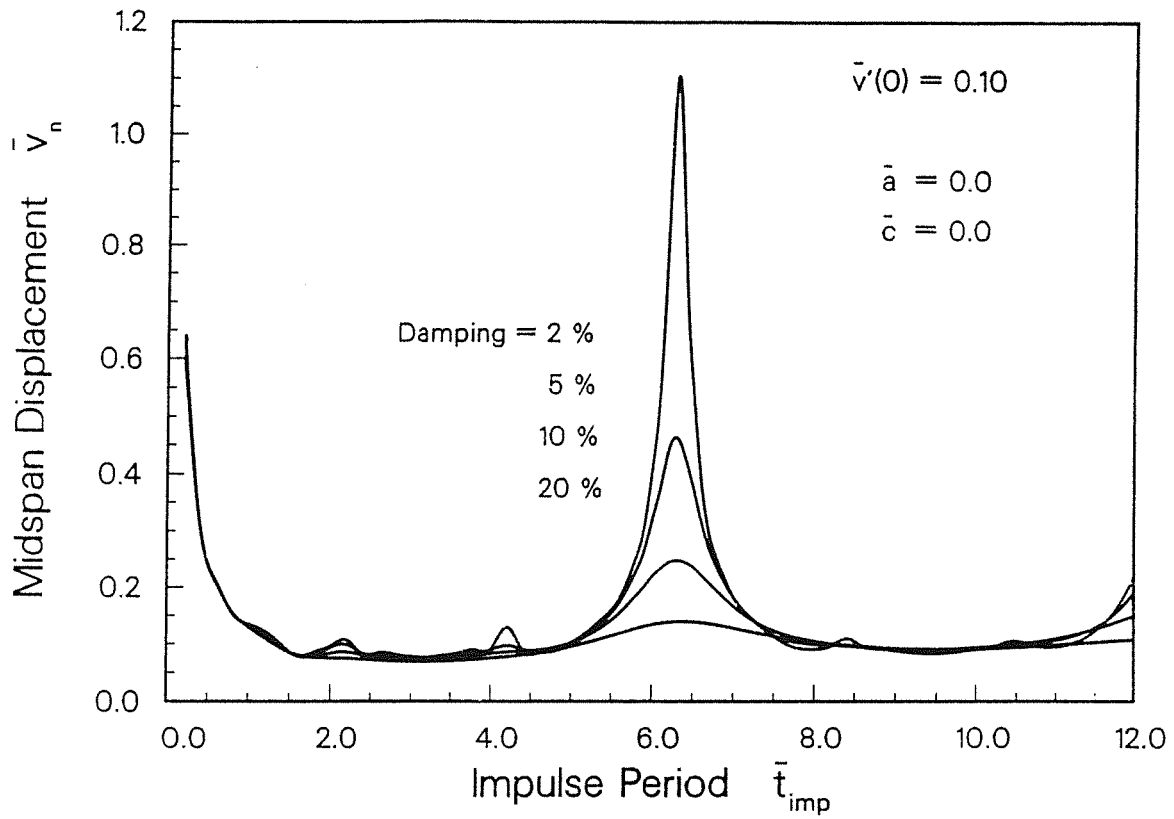


Fig. 7.21. Linear amplitude-frequency response of INPORTs.

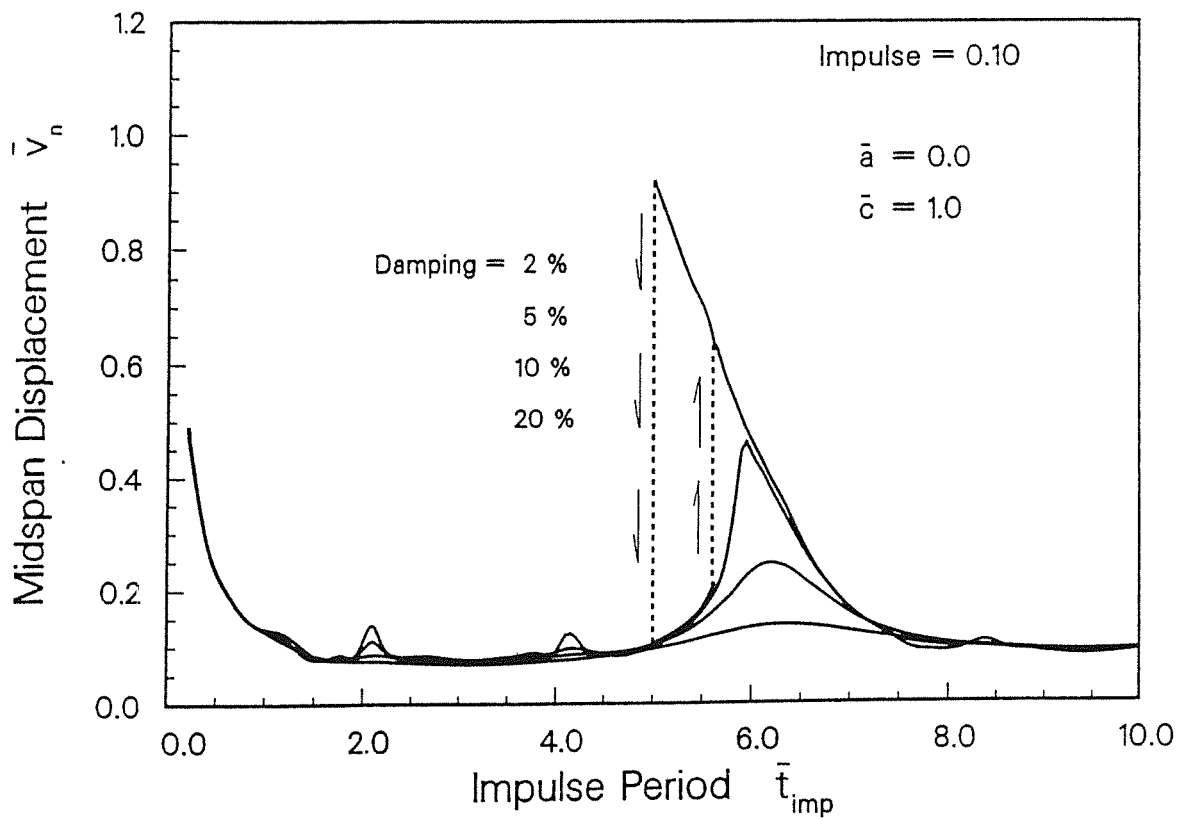


Fig. 7.22. Nonlinear amplitude-frequency response of INPORTs.

repetition rate or $\bar{\tau}_{imp}$, keeping the impulsive pressure amplitude fixed. Results are shown in Fig. 7.22 for $\bar{c} = 1.0$ instead of zero, while all other parameters are the same as Fig. 7.21. For low levels of damping the asymmetries in the curves are not strong enough to develop a vertical tangent. However, at 2% damping, there is a sizable jump associated with the fundamental frequency. As $\bar{\tau}_{imp}$ is decreased from a large value, the steady state amplitude continuously increases as shown by the uppermost curve. At $\bar{\tau}_{imp}$ equal to 5, the response amplitude suddenly drops an order of magnitude (following the dashed curve). In contrast, if $\bar{\tau}_{imp}$ is steadily increased, the steady state amplitude will suddenly jump up to a higher level, at $\bar{\tau}_{imp}$ equal to approximately 5.5. Small changes in the relative repetition rate can produce dramatic changes in the steady-state response, and care must be exercised to avoid operating in such sensitive regimes.

Although the impulsive loading and primary motion of the INPORTs is in the radial direction (v), it is to be expected that imperfections in the system would result in perturbations orthogonal to this (w). This was simulated with the program using 5 modes in both v and w (producing 20 coupled first order equations for Runge-Kutta integration). The strongest influence on three-dimensional vs. two-dimensional motion is the repetition rate value relative to natural frequencies. This is shown in Figs. 7.23, 7.24 and 7.25, in which $\bar{\tau}_{imp}$ has values of 3, 5 and 7 with all other parameters held fixed. In Fig. 7.23, the radial component (v) develops the expected steady state response while the orthogonal (tangential) component (w) diminishes to zero. The orbital plots of v vs. w at midspan show these effects as well, with startup motion ($0 \leq \bar{\tau} < 50$) involving both components but with long term motion ($\bar{\tau} \geq 200$) being planar. However, when $\bar{\tau}_{imp}$ is changed to 5 (Fig. 7.25), the out-of-plane component (w) is initially small but eventually develops into a steady state value comparable to the radial component (v). The orbital plots show initial motion dominated by v but long term response in which the INPORT "whirls", with cross sections following an oval-shaped path. Finally, when $\bar{\tau}_{imp}$ is increased to 7.0 (Fig. 7.25), steady state response for v develops, the tangential component w decays to zero and once again planar displacements characterize the motion. Clearly, for practical purposes, parameters must be prescribed to produce such planar displacements rather than a three dimensional response.

For the proposed LIBRA cavity, some of the INPORT parameters are fixed. However, it is possible to select those remaining to effect an acceptable response, i.e., planar motion with a moderate amplitude. The INPORT length, diameter and wall thickness are 6.4 m, 3 cm and 2 mm, respectively. The mean tension of 3000 N shifts the

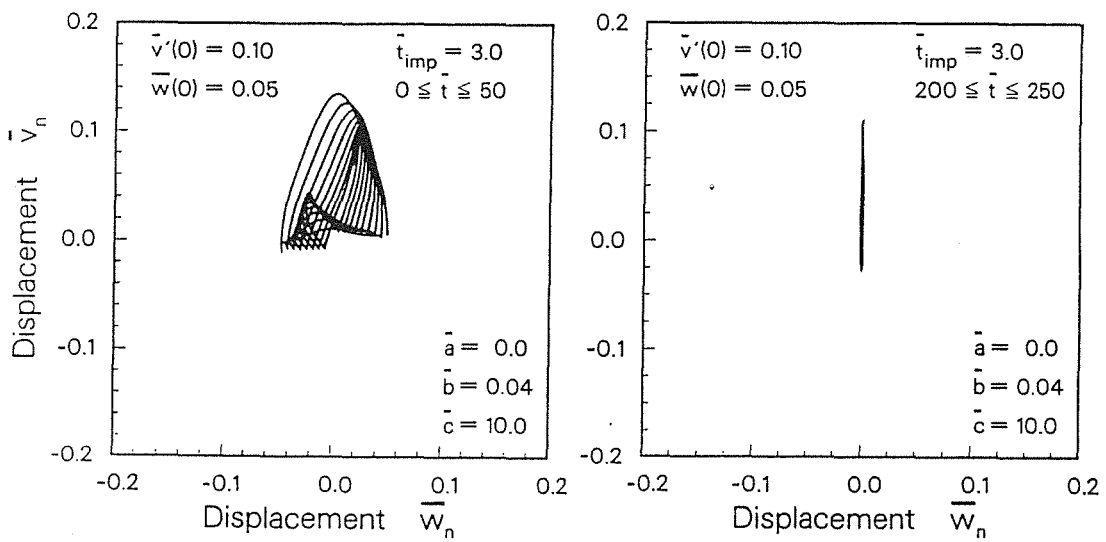
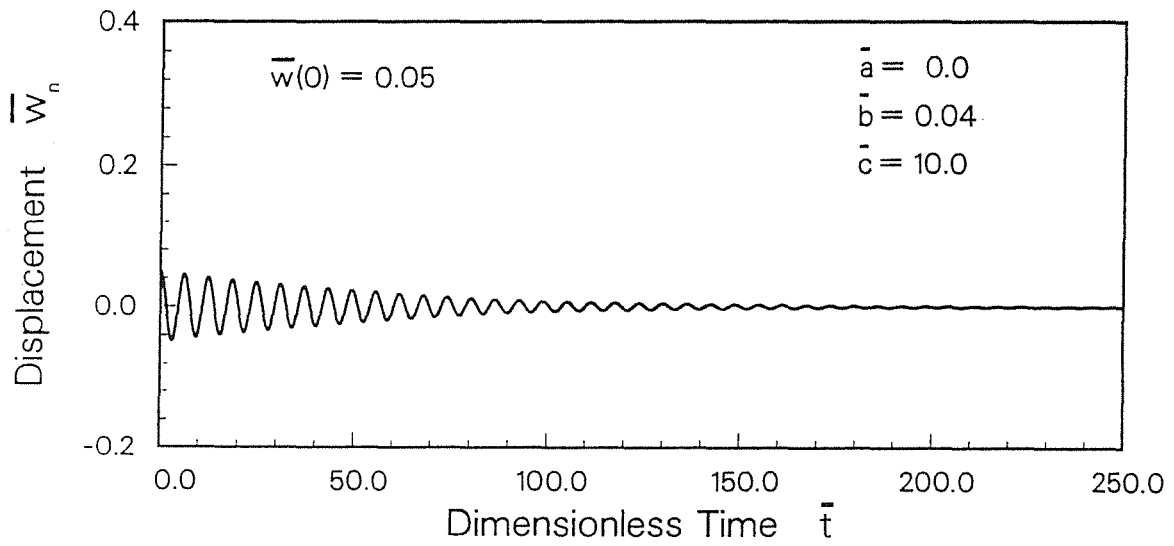
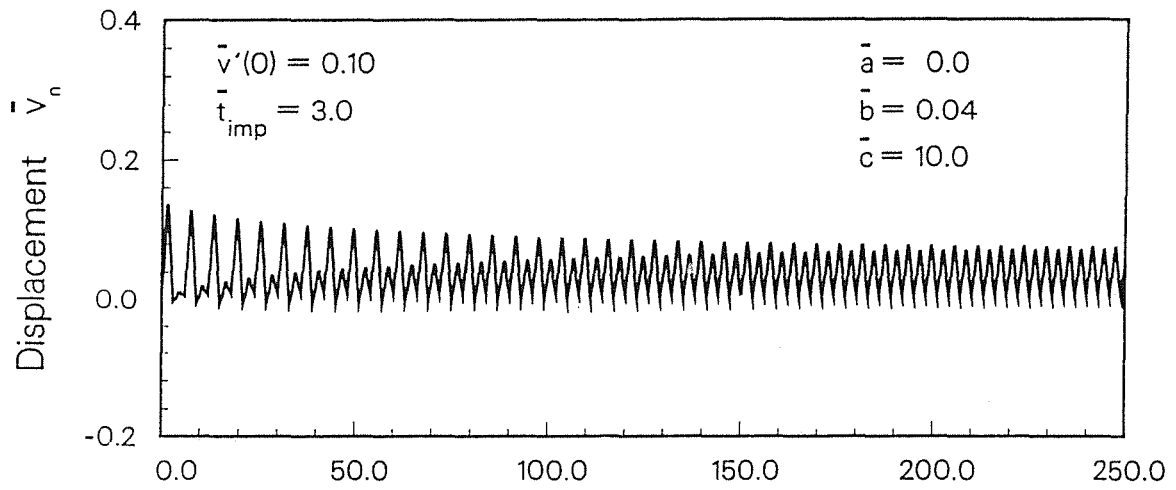


Fig. 7.23. INPORT midspan displacement histories, $\bar{t}_{imp} = 3$.

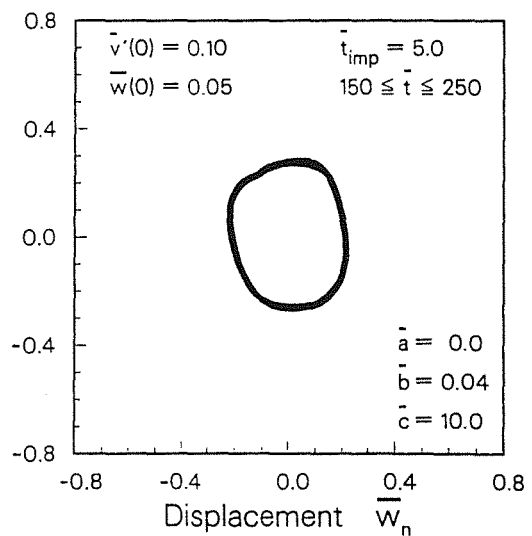
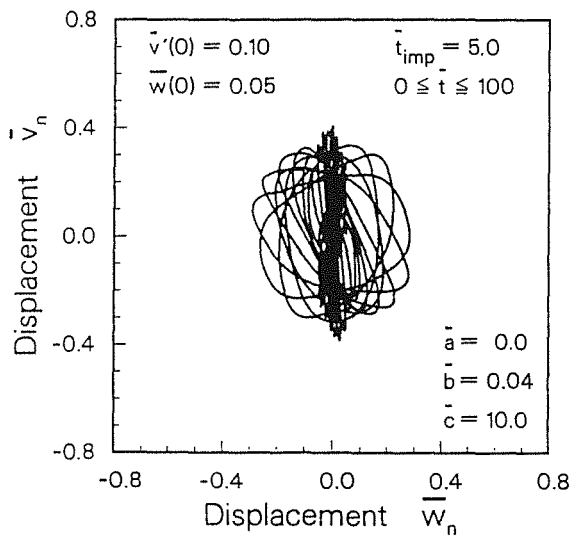
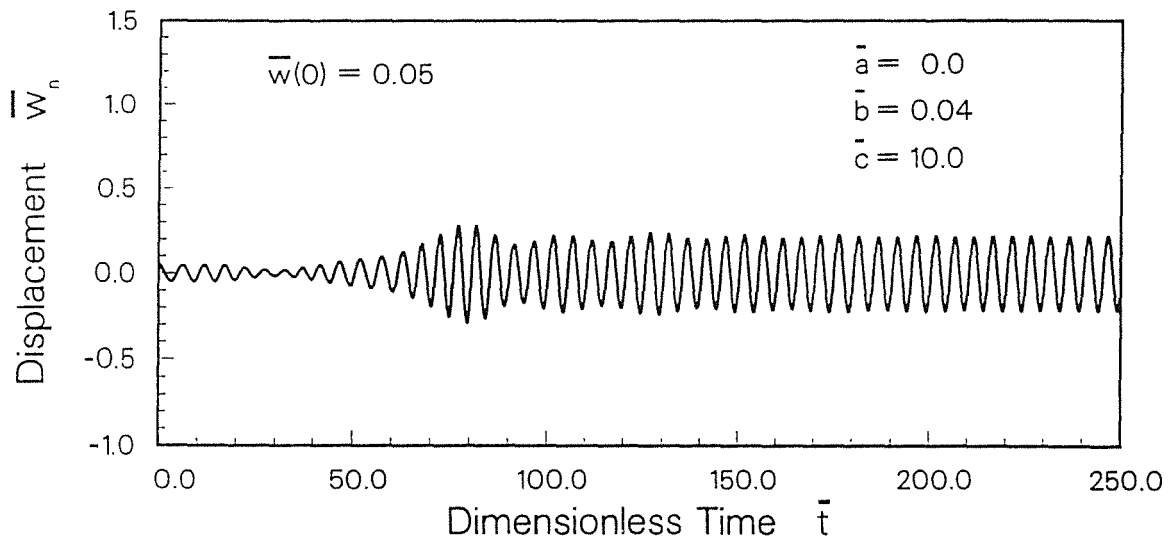
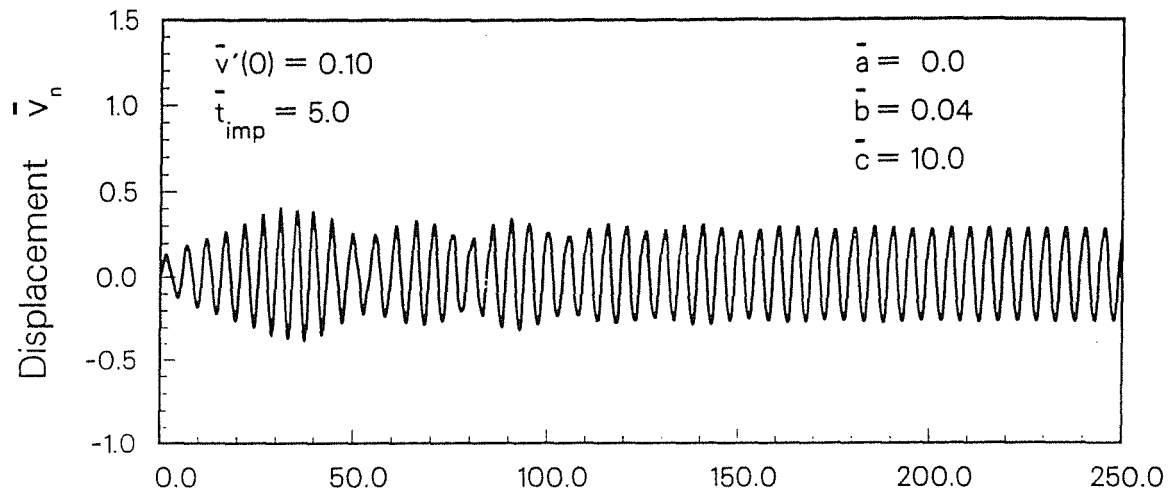


Fig. 7.24. INPORT midspan displacement histories, $\bar{t}_{imp} = 5$.

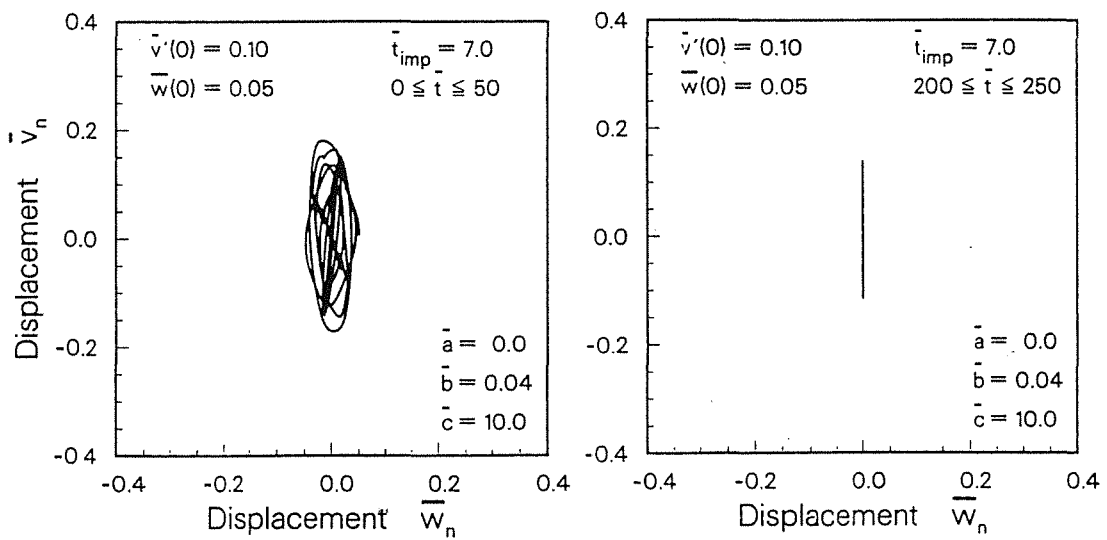
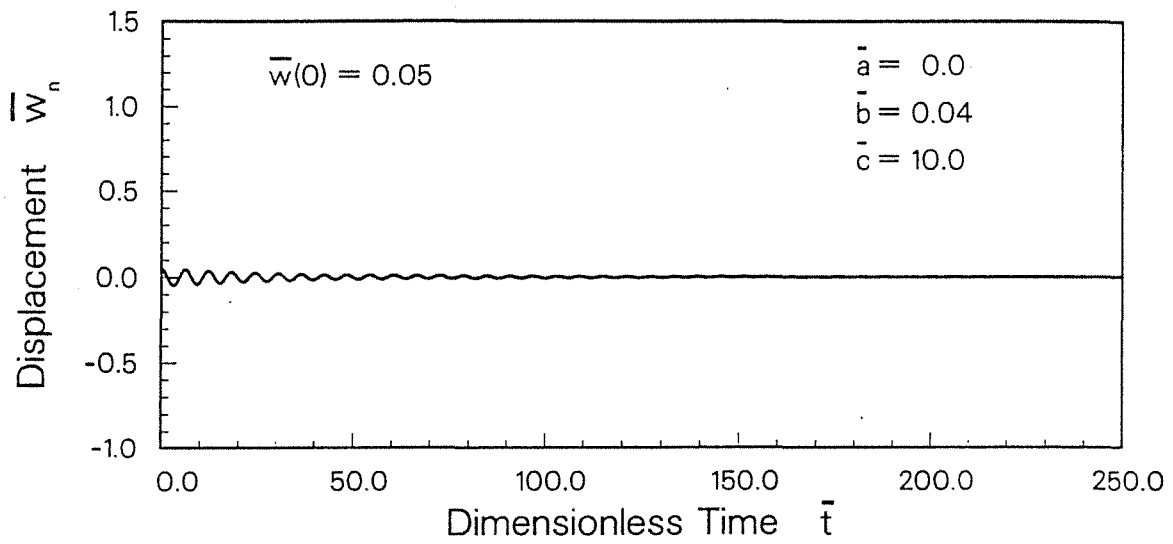
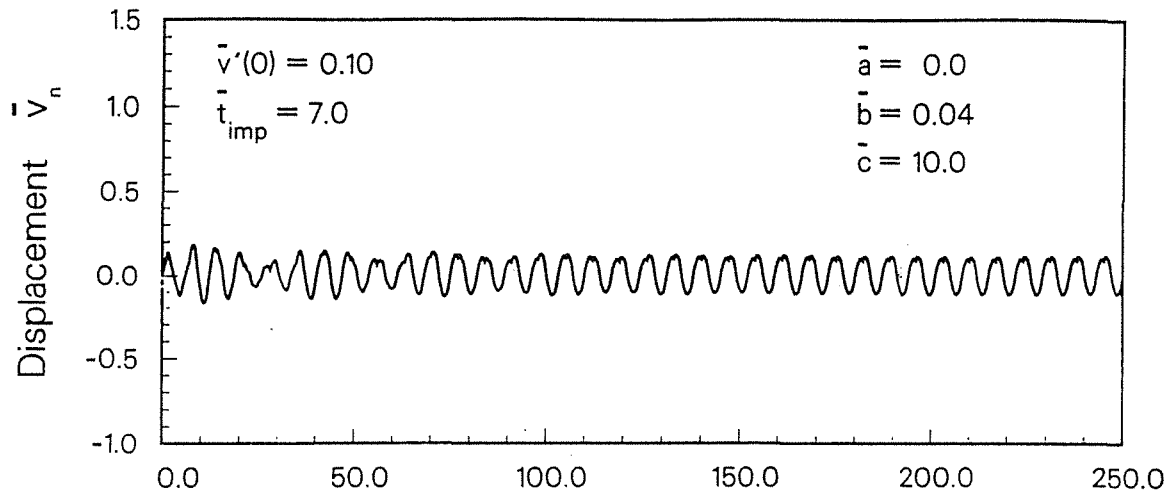


Fig. 7.25. INPORT midspan displacement histories, $\bar{t}_{imp} = 7$.

fundamental frequency away from the impressed repetition rate of 3 Hz but produces axial stresses which are well below current strength levels of silicon carbide fiber. (The wall stresses from hydrostatic pressure are essentially negligible.) Mechanical response results are shown in Fig. 7.26. The impulsive loads of 125 Pa-s intensity produce radial displacements with a maximum startup value of 6 cm and steady-state extremes from 0 to 4 cm, about a mean displacement of 2 cm. The companion circumferential displacement is initially sizable but quickly approaches zero. These features can also be seen in the corresponding total displacement plot of Fig. 7.27. The initial impulse event is labeled 1, second, 2, etc., with the plot limited to the first seven shots for clarity. The long term result would consist of a vertical path, i.e., the desired radial displacement coplanar with the sequential pressure pulses.

Thus, the results show that the initial concern regarding three-dimensional motion of INPORTs was valid. For some designs, it can develop from planar sequential impulsive pressures and would compromise the integrity of the first wall. However, by selectively tuning the system's physical characteristics, the desired planar response can be achieved, legitimizing a circumferentially close-packed double first wall of INPORTs.

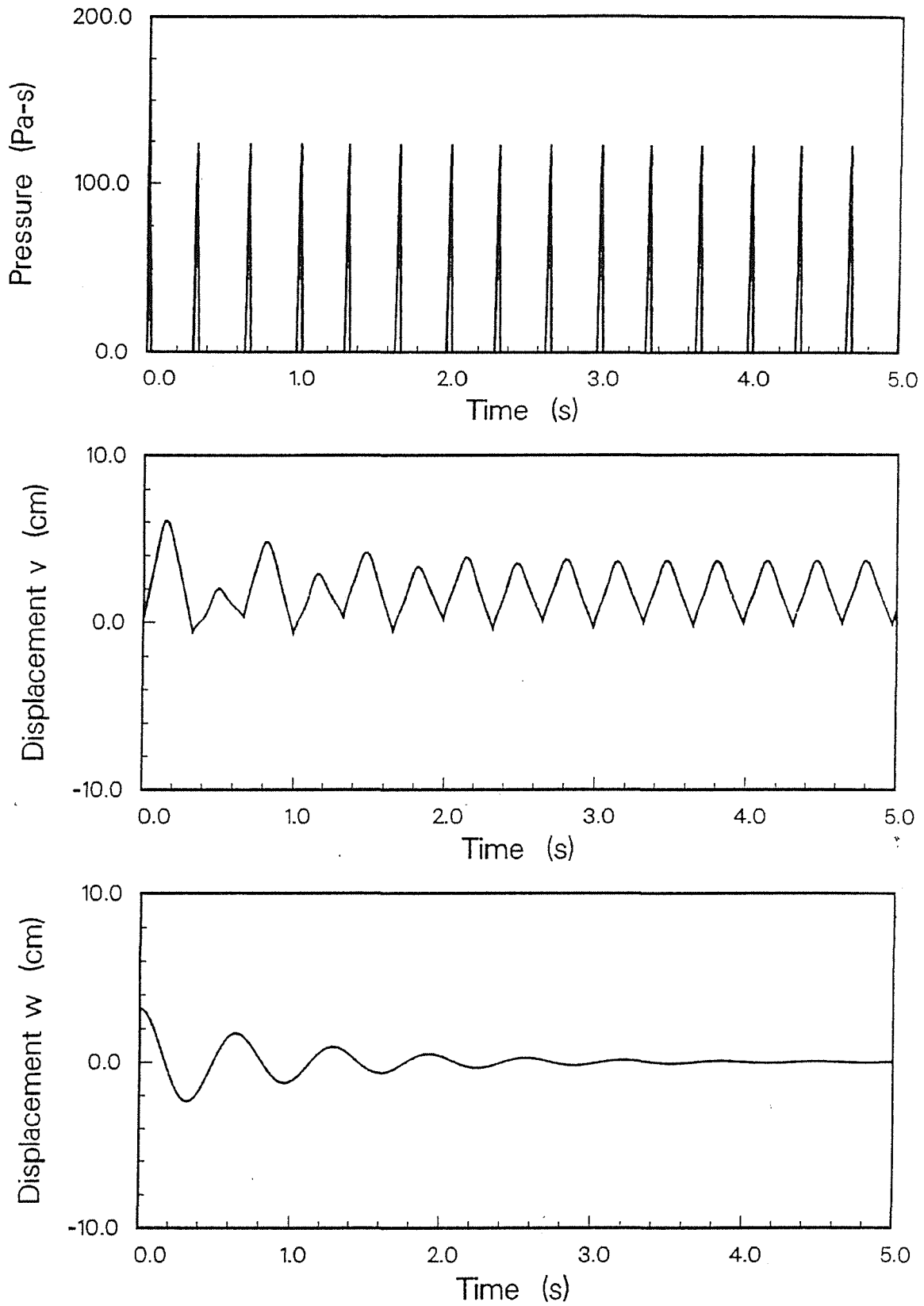


Fig. 7.26. Sequential impulses, radial and circumferential displacement histories.

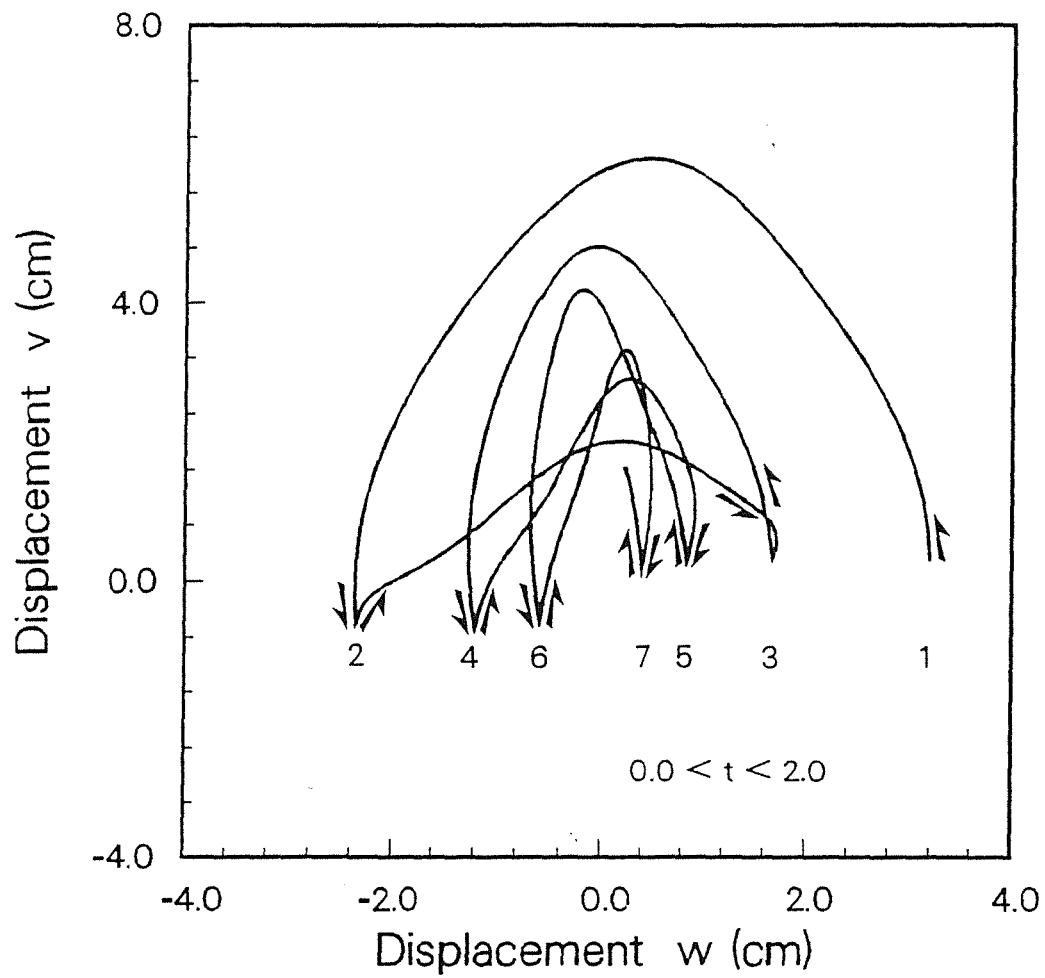


Fig. 7.27. INPORT midspan orbital plots for Fig. 7.26.

References for Chapter 7

1. R. R. Peterson, J. J. MacFarlane, and G. A. Moses, "CONRAD - A Combined Hydrodynamic-Condensation/Vaporization Computer Code", University of Wisconsin Fusion Technology Institute Report UWFD-670, revised July 1988.
2. G. A. Moses, R. R. Peterson, and T. J. McCarville, *Comp. Phys. Comm.* 36, 249 (1985).
3. D. A. Labuntsov and A. P. Kryukov, *Int. J. Heat Mass Transfer* 22, 989 (1979).
4. J. J. MacFarlane, "IONMIX - A Code for Computing the Equation of State and Radiative Properties of LTE and Non-LTE Plasmas", University of Wisconsin Fusion Technology Institute Report UWFD-750, December 1987.
5. D. E. Post, R. V. Jensen, C. B. Tarter, W. H. Grasberger, and W. A. Lokke, *Atomic Data Nucl. Data Tables* 20, 397 (1977).
6. D. Mihalas, Stellar Atmospheres, 2nd Edition (Freeman, New York, 1978).
7. J. J. MacFarlane, G. A. Moses, and R. R. Peterson, "Non-LTE Effects in Inertial Confinement Fusion Target Chambers", *Nucl. Fusion* 29, 27 (1989).
8. K. G. Adams and F. Biggs, "Efficient Computer Access to Sandia Photon Cross Sections", SC-RR-72-0683, Sandia Lab., Dec. 1973.
9. "HIBALL - A Heavy Ion Beam Fusion Reactor Design Study", a Joint FRG & UW Design Effort, University of Wisconsin Fusion Technology Institute Report UWFD-450, June 1981.
10. T. A. Melhorn, *J. Appl. Phys.* 52, 6522 (1981).
11. J. Lindhard and M. Scharff, *Phys. Rev.* 124, 128 (1961).
12. J. D. Jackson, Classical Electrodynamics, 2nd Edition (Wiley, New York, 1975).
13. M. El-Afify and M. Corradini, "Transient Condensation of Vapor Using a Direct Simulation Monte Carlo Method," *Fusion Technology* 15(2), 783 (March 1989).
14. R.L. Engelstad and E.G. Lovell, "Basic Theory for Three-Dimensional Motion of LIBRA INPORT Tubes," Fusion Power Associates Report FPA-84-2, Madison, WI, Oct. 1984.
15. R.L. Engelstad and E.G. Lovell, "Planar Vibrations of LIBRA INPORT Tubes Including Gravity Gradient Effects," Fusion Power Associates Report FPA-84-3, Oct. 1984.

8. CHAMBER NEUTRONICS ANALYSIS

8.1 One-Dimensional Scoping Analysis

A one-dimensional scoping analysis was performed for LIBRA to determine the blanket design options that satisfy the tritium breeding and wall protection requirements. The ONEDANT⁽¹⁾ code was used with the chamber modeled in one-dimensional spherical geometry. Multigroup cross section data based on ENDF/B-V were used in the calculations. A point source emitting neutrons and gamma photons with the spectra calculated for the LIBRA target was used at the center of the 3 m radius cavity. The results were normalized to a DT yield of 320 MJ and a repetition rate of 3 Hz. The blanket is made of banks of INPORT tubes with 0.33 packing fraction. The tubes consist of 2 vol% SiC and 98 vol% $\text{Li}_{17}\text{Pb}_{83}$. A 0.5 m thick reflector consisting of 90 vol% HT-9 and 10 vol% $\text{Li}_{17}\text{Pb}_{83}$ is used behind the blanket.

A minimum tritium breeding ratio (TBR) of 1.1 is required to achieve tritium self-sufficiency. In addition, the INPORT tubes are required to protect the first metallic wall from radiation damage. The peak end-of-life displacements per atom (dpa) in HT-9 is required to not exceed 200 dpa implying that for 30 full power years (FPY) reactor life the peak dpa rate should not exceed 6.6 dpa/FPY. The design should also aim at maximizing the energy multiplication (M) due to its impact on the cost of electricity. In addition, the blanket thickness needs to be minimized to minimize the length of the channel used for beam propagation.

The calculations were performed for 12 cases with different blanket thicknesses (Δ_B) and lithium enrichments (% ^6Li). The results are given in Table 8.1. M_n is the nuclear energy multiplication in the blanket and reflector, while M_o is the overall energy multiplication that gives the ratio between the total energy deposited in the blanket and reflector and the DT yield. For a fixed lithium enrichment, increasing the blanket thickness results in increasing TBR, decreasing M and decreasing damage rate. Increasing the lithium enrichment for a given blanket thickness results in increasing TBR, decreasing M, and decreasing the dpa rate. The TBR and dpa rate values obtained for the different cases analyzed are mapped in Fig. 8.1. In order to satisfy the tritium breeding and wall protection requirements, the design point should be in the box indicated in the upper left corner of the graph. In order to satisfy the other design goals of minimizing the blanket thickness and maximizing M, it is clear that the design point should be at the right or lower boundaries of the box. The intersection of the boundaries of the box with the curves that correspond to different enrichments gives the options that satisfy the design requirements.

Table 8.1. Neutronics Results for the Different Blanket Designs Considered in the Scoping Analysis

Case	% ⁶ Li	Δ_B (cm)	TBR	M_n	M_o	Peak dpa/FPY in HT-9	Peak He appm/FPY in HT-9
1	7.42	50	0.421	1.465	1.313	38.87	75.46
2	7.42	100	0.705	1.450	1.302	18.40	12.91
3	7.42	150	0.944	1.408	1.273	8.51	2.16
4	7.42	200	1.136	1.366	1.243	3.88	0.37
5	30	50	0.791	1.381	1.253	36.00	75.39
6	30	100	1.108	1.357	1.236	16.07	12.89
7	30	150	1.312	1.323	1.212	6.99	2.15
8	30	200	1.445	1.296	1.193	3.00	0.36
9	90	50	1.108	1.311	1.204	31.16	75.18
10	90	100	1.387	1.294	1.192	12.60	13.57
11	90	150	1.528	1.274	1.178	4.95	2.14
12	90	200	1.603	1.260	1.168	1.92	0.36

Table 8.2 gives the nuclear parameters for the different options that satisfy the design requirements. While all options allow the reflector to be a lifetime component, different values of TBR and M are obtained. The high enrichment option yields the thinnest blanket but the energy multiplication is relatively low and excessive tritium breeding is obtained. The largest M is obtained using natural lithium in the $Li_{17}Pb_{83}$ blanket but a relatively long channel is required. To minimize the length of the beam propagation channel, a 1.35 m thick blanket with 90% ⁶Li enrichment is chosen for LIBRA. This yields local (one-dimensional) TBR and energy multiplication values of 1.5 and 1.18, respectively. The peak dpa and helium production rates in HT-9 for this design are 6.6 dpa/FPY and 3.5 He appm/FPY, respectively. Since spherical geometry has been used in the calculations, the damage rates given above represent the worst conditions at the midplane of the cylindrical chamber.

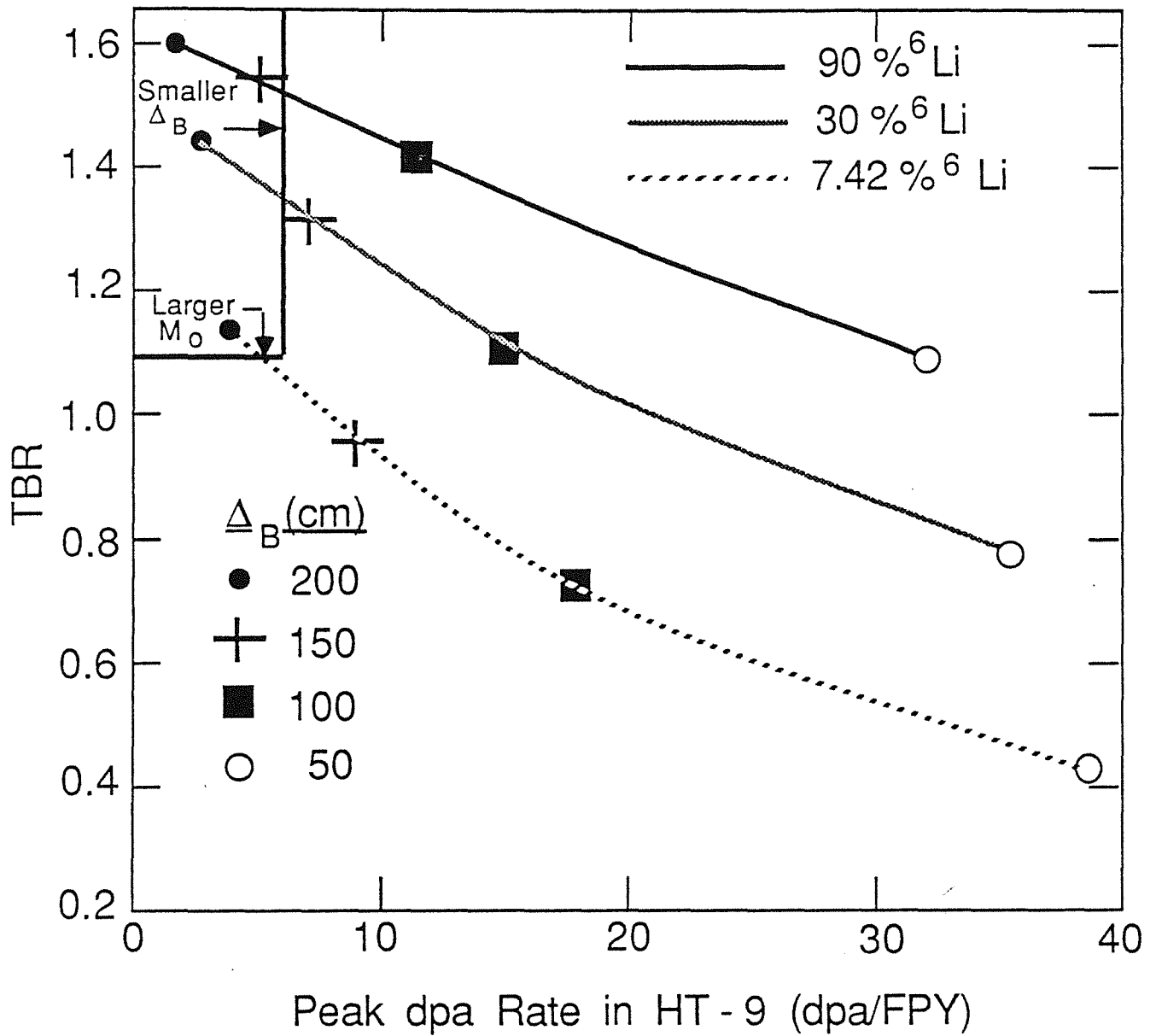


Fig. 8.1. TBR vs. damage rate for the blanket design options considered.

Table 8.2. LIBRA Blanket Design Options Satisfying TBR and Damage Requirements

$\% \text{ } ^6\text{Li}$	Δ_B (cm)	TBR	M_0	dpa/FPY	He appm/FPY
90	135	1.5	1.183	6.6	3.5
30	135	1.32	1.215	6.6	2.0
7.42	190	1.1	1.248	4.4	0.8

Since the baseline blanket design, with a 1.35 m thick zone of INPORT tubes, results in a relatively large TBR in the chamber sides, a smaller local TBR is allowed in the reactor roof. It is estimated that ~ 15% of the neutrons emitted from the target will go directly to the roof. For a local TBR of 1.5 in the side blanket and bottom pool an overall TBR greater than one (~ 1.27) can still be achieved without breeding in the roof. However, a protective layer of $\text{Li}_{17}\text{Pb}_{83}$ is required to protect the structural material in the roof reflector.

A scoping analysis for the roof has led to a 10 cm thick $\text{Li}_{17}\text{Pb}_{83}$ protective layer with 2% SiC fabric followed by a 25 cm thick HT-9 reflector cooled by 10% $\text{Li}_{17}\text{Pb}_{83}$. The local TBR in this zone is 0.8 and the peak dpa rate in HT-9 is 50 dpa/FPY. The roof structure has to be replaced every 4 FPY. Since only ~ 15% of the source neutrons go to the roof, this design will yield an overall TBR that exceeds the minimum requirement by an adequate margin. The impact of neutron streaming on TBR is negligible due to the small solid angle subtended by the penetrations (< 0.5%). Furthermore, no significant radiation damage is expected in the sensitive components of the diodes which are not in direct line of sight of neutrons produced in the target. Detailed three-dimensional neutronics results are given in the next section.

8.2 Three-Dimensional Neutronics Analysis

In this section three dimensional neutronics and photonics blanket and shield calculations for the LIBRA reactor study are presented. A stationary time averaged neutronic and photonic source is used to calculate with the Monte Carlo code MCNP⁽²⁾ scalar flux densities, tritium breeding, and nuclear heating in the different reactor regions. At first, all input data necessary to run the three dimensional Monte Carlo code MCNP 3A will be tabulated; this means especially the input to describe the geometry and the material compositions. This will be followed by a section, which describes the

determination of the complicated LIBRA volumes. The neutronics and photonics source used in the calculations will be explained afterwards.

In the sections presenting the results, first all volumes, masses and gram densities in the different reactor regions are listed, followed by the neutronics and photonics flux densities calculated by MCNP. Afterwards the detailed tritium breeding rates are tabulated. The last section contains the results for the neutronics and photonics nuclear heating.

8.2.1 Reactor Geometrical Model

The main part of work in preparing the code input is to model the geometry for the three-dimensional calculations with MCNP.⁽²⁾ One must define all the surfaces (planes, spheres, cylinders, cones, general quadratic and sometimes also special surfaces of fourth-degree) to be used in the model. In a second step these surfaces are used to define cells by the intersections, unions, and complements of the regions bounded by the surfaces. These cells should be bounded by only a small number of surfaces. The reason for this restriction is explained as follows: because the particle tracks are followed in the system, the intersection of the track with **each** bounding surface of the cell has to be calculated. This is very time consuming if the cell has many surfaces. As a consequence some auxiliary surfaces have been added to the main surfaces defining the LIBRA geometry. One of these surfaces is shown in Fig. 8.2, which subdivides the upper and the lower part of the model. This figure, along with Fig. 8.3 and Fig. 8.4, are graphic output of the program MCNP of the model used in the calculations. This two-dimensional plot, an intersection of the three dimensional x-y-z geometry with a user defined plane, is normally used to control the geometrical input.

When modelling the LIBRA geometry, we have chosen the z-axis to be identical with the axis of the cylindrical vacuum chamber. Because of the 120° symmetry, we have only modelled three of the 9 segments. This can be seen in Fig. 8.3 and Fig. 8.4.

Three segments had to be modelled, because of three holes in the bottom splash plate, which destroys the 40° symmetry of the LIBRA chamber consisting of 9 elements, each containing a beam tube at the top and at the bottom and an exhaust duct in the midplane. One half of two of these holes in the bottom splash plate can be seen in Fig. 8.3. It should be kept in mind that in Fig. 8.3 and Fig. 8.4 the -y-axis starts at the intersection of the two outer bounding planes (shown as straight lines in the figure) and is directed downwards. The -y-axis thus divides the segment in the middle into two identical parts.

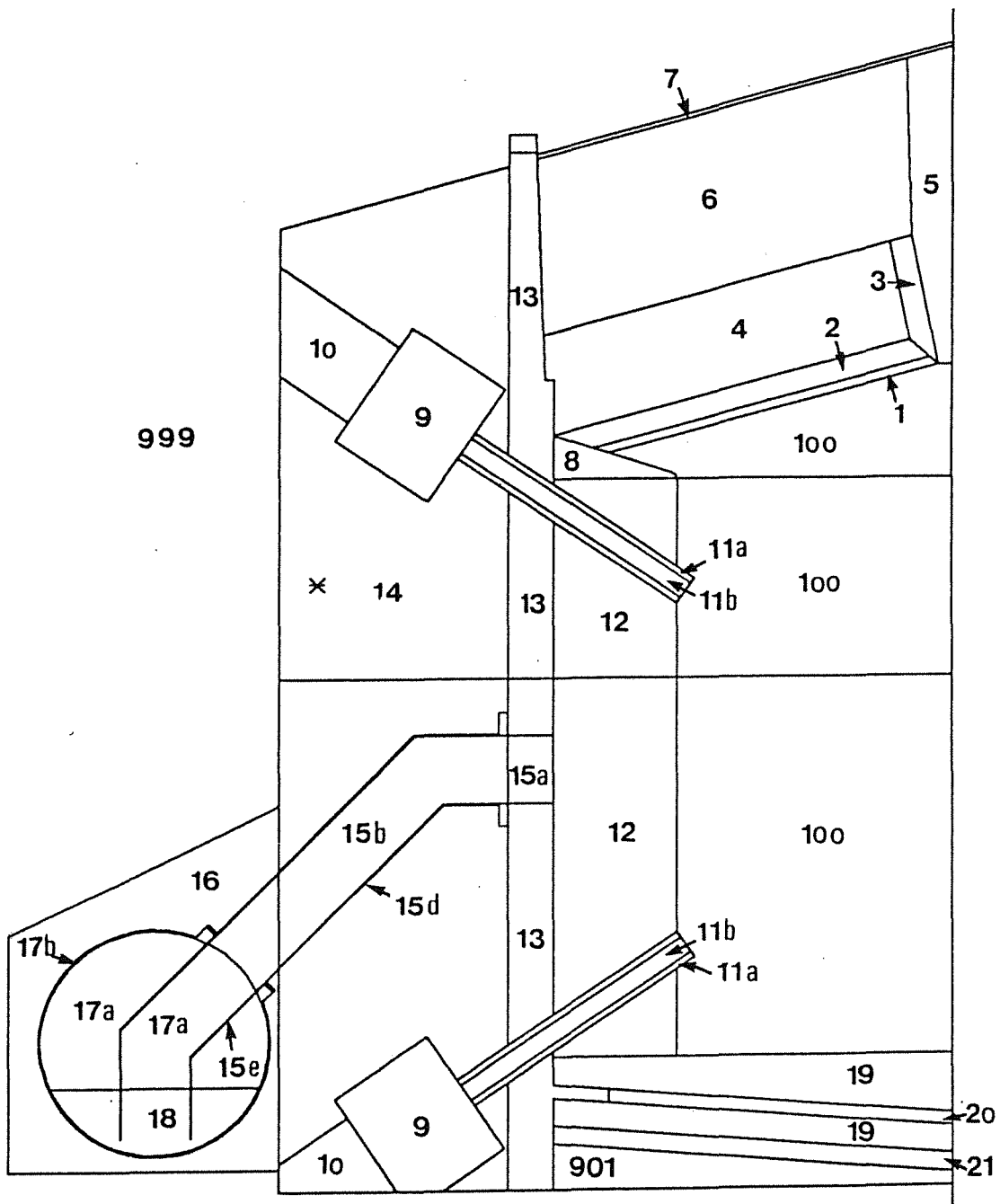


Fig. 8.2. Vertical cut of the geometric model used in the MCNP calculations. The cut-plane is constructed by vectors $e_1 = (0, -1, 0)$ and $e_2 = (0, 0, 1)$; the $-y$ -axis is directed from right to left and the $+z$ -axis from bottom to top.

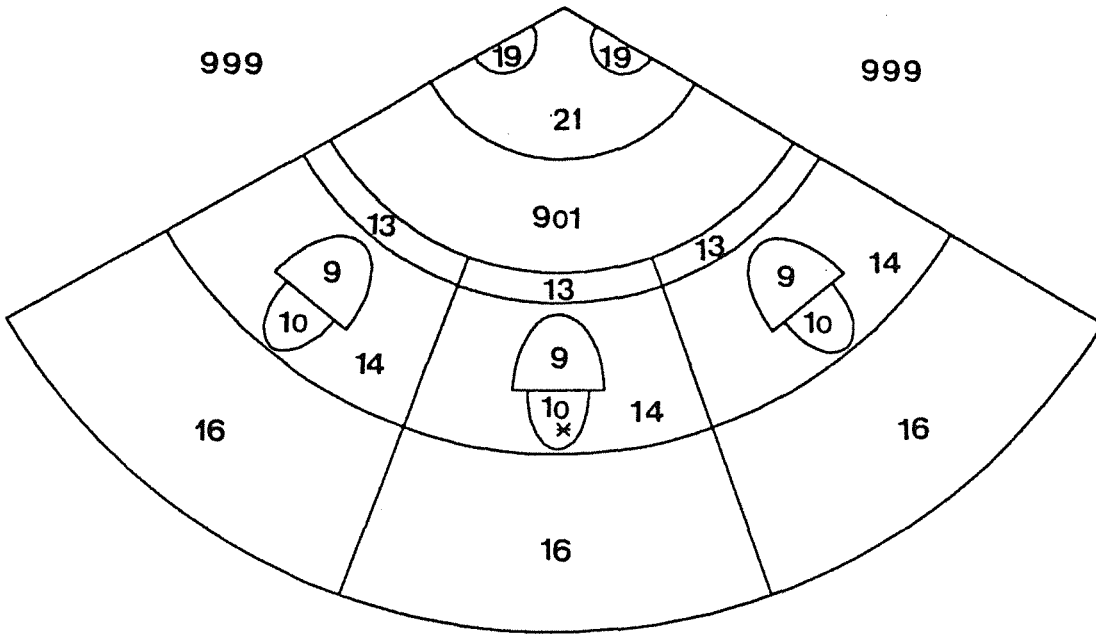


Fig. 8.3. Horizontal cut of the geometric model used in the MCNP calculations. The cut-plane is constructed by vectors $e_1 = (1,0,0)$ and $e_2 = (0,1,0)$ with $z = -430$ cm.

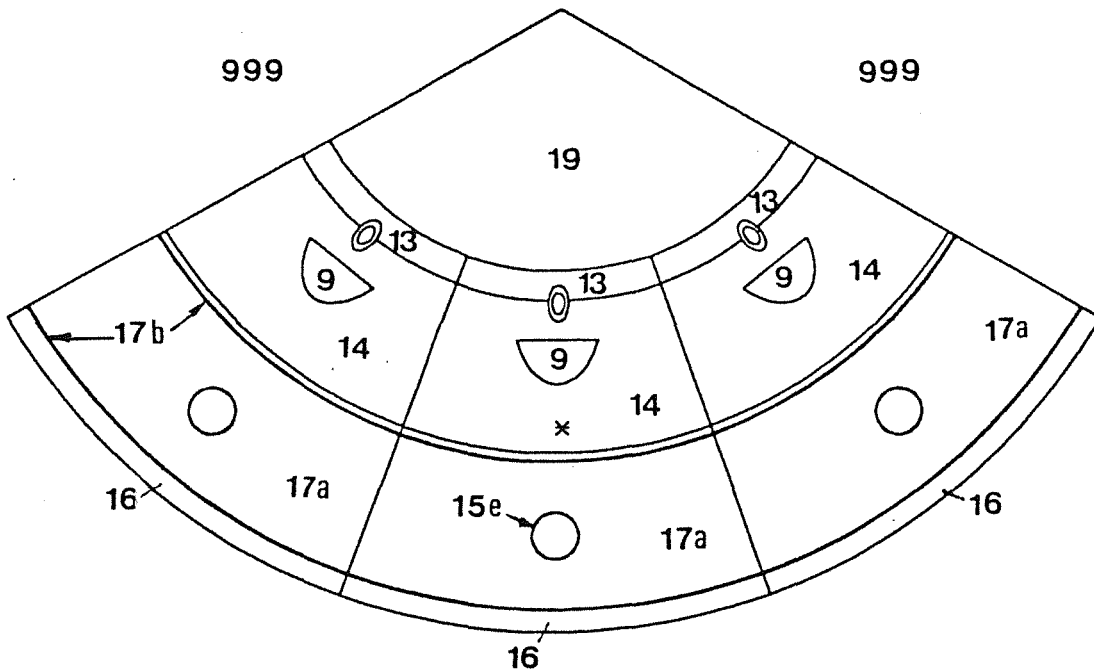


Fig. 8.4. Horizontal cut of the geometric model used in the MCNP calculations. The cut-plane is constructed by vectors $e_1 = (1,0,0)$ and $e_2 = (0,1,0)$ with $z = -330$ cm.

The two outer planes, which are bounding the model, are mirror-reflecting surfaces. The numbers used in the figures are explained in Table 8.3 and Table 8.4. These numbers are also used in following tables.

In comparing our model with the cross section of the LIBRA chamber (Fig. 1.2), one can see that all necessary details for our MCNP calculations have been modelled.

8.2.2 Material Compositions

In this section all material compositions as defined by the University of Wisconsin, Madison, are listed; Table 8.3 and Table 8.4 give the materials for the different reactor zones. The following table (Table 8.5) summarizes the particle densities used in these materials.

The numbers in column 1 of Table 8.3 and Table 8.4 are also used in the preceding figures (Fig. 8.2, Fig. 8.3, and Fig. 8.3) and in the tables, which lists the results of the calculations.

8.2.3 Determination of the Volumes

Only 15 of the 89 volumes of the different cells used in our model are calculated automatically by MCNP; for neutron flux density calculations all volumes must be known. There are two ways to calculate the volumes:

- (1) MCNP itself can be used to obtain the values stochastically as described in (2), p. 160.
- (2) The user himself determines the volumes.

In both cases the volumes not calculated by MCNP itself must be determined before MCNP is used to calculate e.g. the flux densities. These volume values are added to the input of the program.

When MCNP is used, the volumes are calculated by a stochastic estimation using ray tracing. To do this, all cells in the model are voided and particles are started from a sphere surrounding the whole geometry. An inward-directed, biased cosine source with weight equal to πr^2 is used. This will cause a particle flux in the system to statistically approach unity. The cell flux tally (F4) is used to estimate the volume areas: this tally is inversely proportional to the cell volume. In cells whose volumes are known (either calculated automatically by MCNP itself or given in the input), the F4-tally will approach unity, whereas in unknown volumes (with volume initially set to 1.0) the tally

Table 8.3. LIBRA Chamber Component Description (Part 1).

Number	Components	Dimensions	Composition
100	Vacuum Chamber	300cm radius	He gas at 100 torr
1	Roof protective LiPb layer in SiC fabric	10cm effective thickness	95% $\text{Li}_{17}\text{Pb}_{83}$ 5% SiC
2	Steel reflector, cooled with LiPb	25cm	90% steel (IIT-9) 10% $\text{Li}_{17}\text{Pb}_{83}$
3	Roof support structural ring welded to structural beams (4), He cooled	25cm thick 145cm high	95% steel (IIT-9) 5% He coolant
4	Roof support beams welded to ring (3), 6 equally spaced	6cm thick 110cm high	95% steel (IIT-9) 5% He coolant
5	Pellet injector shield module	Scale from drawing	20% steel (C1020) 10% He coolant 70% concrete
6	Roof shield extends into space (4) straddling the structural beams	~ 295cm thick	20% steel (C1020) 10% He coolant 70% concrete
7	Roof vacuum seal flange	5cm thick	100% steel (IIT-9)

Table 8.4. LIBRA Chamber Component Description (Part 2).

Number	Components	Dimensions	Composition
8	Manifold for INPORT units	Scale from drawing	90% $\text{Li}_{17}\text{Pb}_{83}$ 10% SiC
9	Driver diode, 9 on top, 9 on bottom, equally spaced	150cm diameter 100cm thick	30% steel (HT-9) 70% void
10	Beam transmission line	100cm diameter	80% Al 20% void
11	Beam tube (34 degrees angle)		
11a	Beam tube wall (TZM = molybdenum alloy)	7.0cm thick	60.49% TZM 4.78% BeO 34.73% void
11b	Beam tube inner volume	20.0cm diameter	He gas at 100 torr
12	INPORT units	135cm zone thickness	32.34% $\text{Li}_{17}\text{Pb}_{83}$ 0.66% SiC 67.00% void
13	Reflector/vacuum chamber, LiPb cooled	50cm thick	90% steel (HT-9) 10% $\text{Li}_{17}\text{Pb}_{83}$
14	Chamber shield, He cooled	~ 200cm thick	20% steel (C1020) 10% He coolant 70% concrete
15a 15b 15c	Vacuum exhaust tube interior volume	75cm interior diameter	He gas at 100 torr
15d 15e	Vacuum exhaust tube wall	1.0cm thick	100% steel (HT-9)
16	Suppression tank shield	Scale from drawing	10% steel (C1020) 10% He coolant 80% concrete
17a	Suppression tank interior volume	248cm diameter	He gas at 100 torr
17b	Suppression tank wall	2cm thick	100% steel (HT-9)
18	LiPb pool in tank	25% of tank volume	100% $\text{Li}_{17}\text{Pb}_{83}$
19	LiPb pool in reactor chamber	Scale from drawing	100% $\text{Li}_{17}\text{Pb}_{83}$
20	Perforated shock absorbing plate	15cm thick	90% steel (HT-9) 10% $\text{Li}_{17}\text{Pb}_{83}$
21	Bottom splash plate	20cm thick	100% steel (HT-9)
22	LiPb/He heat exchanger, 3 each		N/A
23	LiPb pump		N/A
24	Electric motor		N/A
901	Vacuum region below shock absorbing plate		Vacuum
999	Outside world within surrounding sphere	1200cm sphere radius	Vacuum

Table 8.5. Particle Densities of Materials Used in MCNP Calculations.

Material	Nuclide Names	Particle Densities [10^{24}cm^{-3}]	Remarks
IIT-9	Fe	0.0768	(normally used for neutronic calculations)
	Cr	0.0102	
IIT-9A	Fe	0.07171	(normally used for activation calculations)
	Cr	0.01039	
	Ni	0.00040	
	Mo	0.00049	
	V	0.00028	
	Si	0.00042	
	Mn	0.00043	
	C	0.00078	
	W	0.00013	
$\text{Li}_{17}\text{Pb}_{83}$	${}^7\text{Li}$	0.00500	(90% ${}^7\text{Li}$)
	${}^6\text{Li}$	0.00055	
	Pb	0.02715	
SiC	Si	0.04834	
	Cr	0.04834	
C1020.	Fe	0.0847	(reinforcing steel in concrete)
	Mn	$3.91 \cdot 10^{-4}$	
	Si	$4.25 \cdot 10^{-4}$	
	C	$7.96 \cdot 10^{-4}$	
concrete	H	0.010401	
	C	0.006459	
	O	0.043063	
	Si	0.007814	
	K	0.000268	
	Ca	0.008004	
	Fe	0.000205	
	Na	0.000255	
	Mg	0.000851	
	Al	0.001067	
	N	0.000010	
	S	0.000074	
Ti	0.000015		
Al	Al	0.057	
TZM	Mo	0.06400	
BeO	Be	0.07287	
	O	0.07287	
He	He	$3.55 \cdot 10^{-6}$	(100 Torr. 0 ° Celsius)
He	He	$6.48 \cdot 10^{-4}$	(60 bar. 400 ° Celsius)

estimates the value of the volume. The approach to unity for known volumes can be used to check the volume values given by the user in the input to MCNP.

To achieve small statistical errors in our calculations, about 6,400,000 source particles were started in MCNP using 288 minutes CPU-time on a SIEMENS 7890. The statistical 1- σ -error for most of the volumes then was smaller than 1%.

To check the estimation, nearly all volumes have been calculated analytically or semi-analytically also. In this case the REDUCE system^(4,5) was used to manipulate the algebraic expressions for the different surfaces (REDUCE is very useful to perform coordinate-transformations and analytical integrations). Because analytical integration could only be done in a very few, simple cases, the volumes in nearly all cases were calculated semi-analytically: All expression manipulations were done with REDUCE giving a function, which could be integrated numerically over a one- or two-dimensional region by using the subroutines DCADRE and DBLIN of the IMSL Library.⁽³⁾ In the case of a cylinder bordering the torus, an explicit expression for the integrand was not used, because REDUCE did not solve the equation of the surface $F(x,y,z)=0$ with respect to the variable z . Instead we used the IMSL routine ZREAL2, which uses the Newton iteration method to calculate the zeros of the expression $F(x_{set},y_{set},z)$ by variation of z for values x_{set} and y_{set} given by the integration routine DBLIN.

When comparing the estimated and the calculated values for the various volumes, which was done for 67 cases, we found the following results: For 41 of 67 cases the relative percentage error between estimated and calculated results was smaller than 1- σ , for 64=41+23 cases it was smaller than 2- σ , and for all 67=41+23+3 cases it was smaller than 3- σ . If this is compared to theory, 68% of the results should be within the 1- σ , 95% within the 2- σ , and 99.7% within the 3- σ limits. The calculations give the results: $41/67 \times 100=61\%$, $64/67 \times 100=96\%$, and $67/67 \times 100 = 100\%$, which are close to the theoretical values.

In conclusion one can state: If the volumes have been estimated by MCNP with a statistical error of about one percent (1 σ), and if this accuracy is enough, then it is not necessary to calculate the volumes by an analytical method.

8.2.4 Neutronic and Photonic Source

In Section 5.2 (Target Microexplosion) the neutronics calculations for the LIBRA target are described. A short summary of the results given in Section 5.2 and used in the MCNP calculations will be given here.

The target, for which the geometry and material compositions are given in Fig. 5.1, consists of 3 layers. The outer layer contains lead followed by a layer of deuterated plastic. The inner layer is frozen DT fuel. Per fusion event 1.0248 neutrons and 0.0133 gammas are leaking out of this target. The neutron and gamma spectra shown in Fig. 5.4 are repeated in Fig. 8.5 for the neutrons and in Fig. 8.6 for the photons.

Because MCNP allows only one type of starting particle in a specific calculation, one has - if neutronic and photonic source particles must be considered - always to do one calculation with a neutronic source, where the neutrons and the photons produced by these neutrons are transported, and a second calculation with a photonic source, where only these photons are transported. The results of these two calculations must then be added. Because we have used weight 1 for the neutronic and also the photonic source particles, we had to - for the LIBRA target - multiply the neutronic results by 1.0248 and the photonic results by 0.0133 before adding, in order to get results relating to one fusion event.

8.2.5 Volumes and Masses

In Table 8.6 we have listed the volumes, masses, and gram densities for all LIBRA regions. Volumes and masses are given for the total geometry and not only for parts like 120° sectors. Only if the component can be found more than one time in the LIBRA chamber (as e.g. the beam tubes or vacuum exhaust tubes) the numbers refer to only one of these elements. It should also be noticed, that the values refer to our model shown in Fig. 8.2, where we have introduced an artificial lower plane, which borders the chamber. The units for the different values are always given in the header of each column.

8.2.6 Neutron and Photon Flux Densities

In Table 8.7 the flux densities for neutrons and both type of photons (starting from the source and created by neutrons in the LIBRA chamber) are tabulated. The numbers in left and right parentheses are the statistical errors of the results as calculated by MCNP. This estimated relative error R, which is given by MCNP for each tally, is

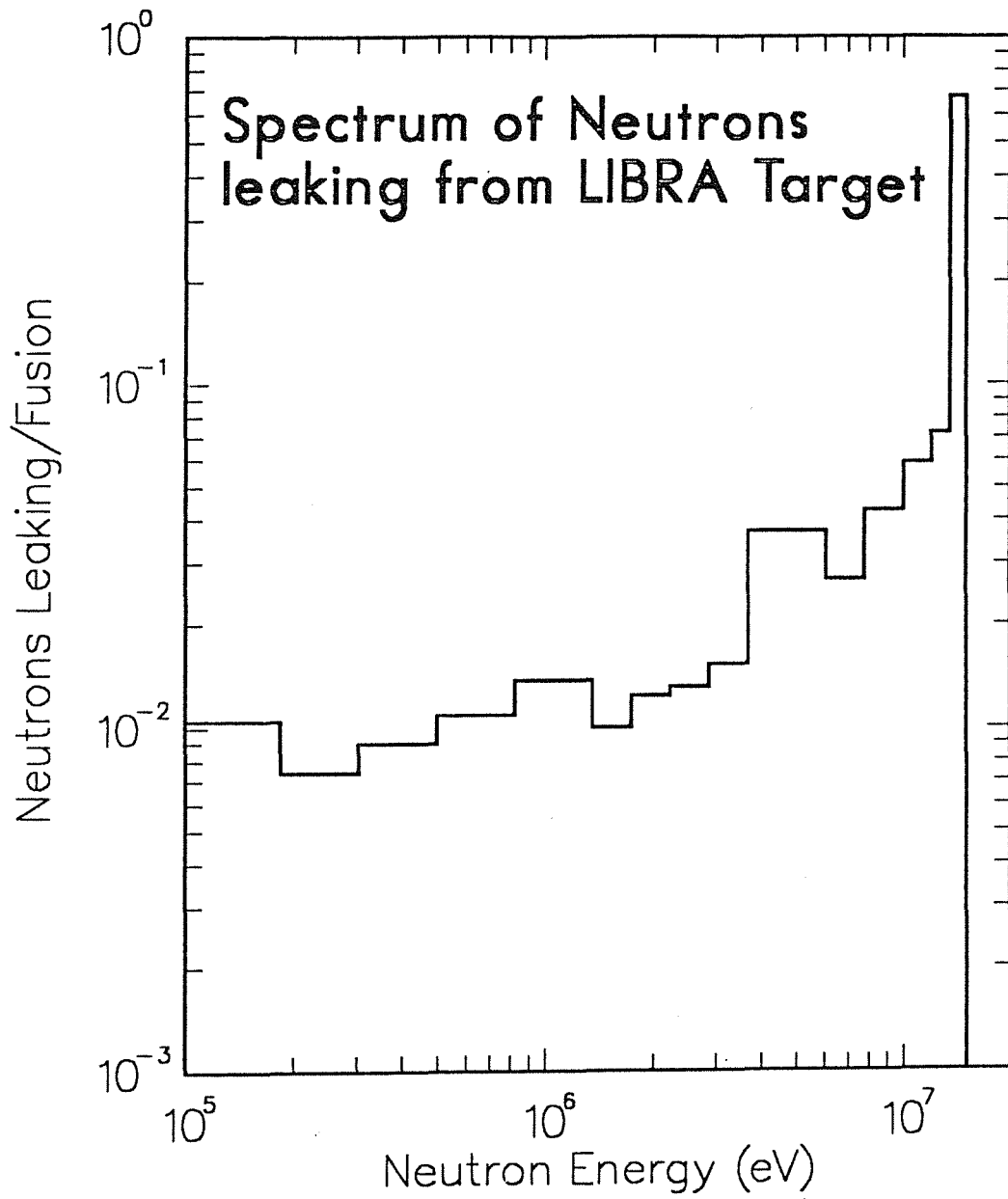


Fig. 8.5. Spectrum of neutrons leaking out of the pellet. The ordinate is the energy integral in each group.

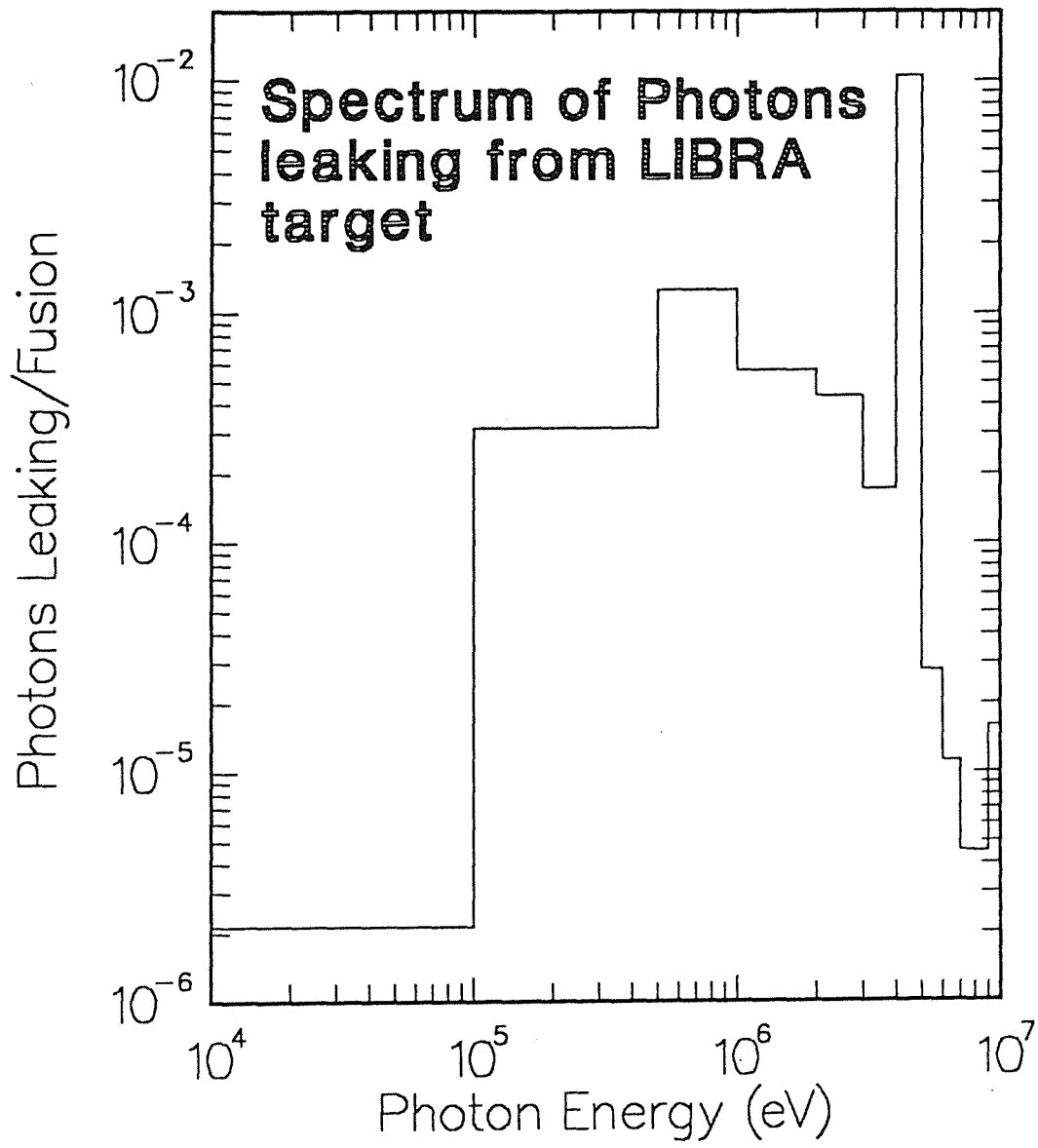


Fig. 8.6. Spectrum of photons leaking out of the pellet. The ordinate is the energy integral in each group.

Table 8.6. LIBRA Volumes and Masses.

Description	Volume [m ³]	Mass [10 ³ kg]	Density [$\frac{g}{cm^3}$]
Vacuum chamber	205.58	0.004851	0.00002
Roof protective layer	4.75	43.171	9.08925
Roof steel reflector	13.79	112.283	8.14220
Roof support structural ring	0.86	6.516	7.60273
Roof support beams	1.57	11.930	7.60273
Pellet injector shield module	1.80	5.791	3.20981
Roof shield	190.03	609.963	3.20981
Roof vacuum seal flange	5.08	40.635	8.00265
Manifold for inport units	8.75	76.807	8.78023
Inport units	196.84	602.463	3.06065
Reflector vacuum chamber	154.47	1257.7	8.14220
Chamber shield	981.60	3150.8	3.20981
Suppression tank shield	254.70	661.729	2.59808
Suppression tank	197.55	0.004661	0.00002
Suppression tank wall	8.77	70.223	8.00265
Li ₁₇ Pb ₈₃ pool in tank	65.89	619.283	9.39828
Li ₁₇ Pb ₈₃ pool in reactor chamber	43.75	411.216	9.39828
Shock absorbing plate	6.63	53.957	8.14220
Bottom splash plate	11.79	94.345	8.00265
Vacuum region below shock absorbing plate	21.74	0.0E+00	0.00000
Upper beam transmission line	0.97	1.991	2.04311
Lower beam transmission line	0.51	1.049	2.04311
Upper driver diode	2.15	12.038	5.60186
Lower driver diode	2.11	11.820	5.60186
Beam tube wall	0.17	1.087	6.31229
Beam tube inner part	0.09	2.1E-06	0.00002
Vacuum exhaust tube inner, volume	1.93	4.6E-05	0.00002
Vacuum exhaust tube wall	0.25	1.979	8.00265

Table 8.7. Neutron and Photon Flux Densities (Part 1). All values in units of $\frac{\text{particles}}{\text{cm}^2 \times \text{fusion}}$

Number	Components	Neutrons	Photons		
			from the pellet	produced in the reactor	total
100	Vacuum chamber	2.47E-05 (0.17 %)	7.59E-08 (0.02 %)	1.02E-06 (0.59 %)	1.10E-06 (0.55 %)
1	Roof protective LiPb layer in SiC fabric	1.56E-05 (0.33 %)	5.05E-09 (0.15 %)	4.98E-07 (0.63 %)	5.03E-07 (0.62 %)
2	Roof steel reflector cooled with LiPb	7.52E-06 (0.43 %)	1.37E-10 (0.73 %)	4.73E-07 (0.65 %)	4.73E-07 (0.65 %)
3	Roof support structural ring	1.13E-06 (3.95 %)	6.21E-11 (4.25 %)	1.51E-07 (5.34 %)	1.51E-07 (5.34 %)
4	Roof support beams	4.17E-07 (2.45 %)	1.51E-13 (48.74 %)	1.22E-07 (3.12 %)	1.22E-07 (3.12 %)
5	Pellet injector shield module	2.63E-07 (4.00 %)	1.91E-10 (3.03 %)	9.90E-08 (6.63 %)	9.92E-08 (6.62 %)
6	Roof shield	1.19E-07 (0.60 %)	7.65E-14 (14.41 %)	5.44E-08 (0.99 %)	5.44E-08 (0.99 %)
7	Roof vacuum seal flange	0.00E+00 (0.00 %)	0.00E+00 (0.00 %)	0.00E+00 (0.00 %)	0.00E+00 (0.00 %)
8	Manifold for INPORT units	4.58E-06 (0.65 %)	1.09E-10 (0.78 %)	5.40E-08 (1.53 %)	5.41E-08 (1.53 %)
9	Driver diode	2.63E-08 (7.24 %)	1.78E-11 (1.67 %)	4.52E-09 (6.72 %)	4.54E-09 (6.69 %)
10	Beam transmission line	5.88E-10 (47.18 %)	0.00E+00 (0.00 %)		
11a	Beam tube wall	6.75E-06 (0.58 %)	1.31E-09 (0.56 %)	1.15E-06 (0.92 %)	1.15E-06 (0.92 %)
11b	Beam tube inner volume	7.88E-06 (0.91 %)	1.59E-08 (0.88 %)	1.25E-06 (1.51 %)	1.27E-06 (1.49 %)
12	INPORT units	1.18E-05 (0.16 %)	1.98E-09 (0.05 %)	2.94E-07 (0.24 %)	2.96E-07 (0.24 %)
13	Reflector vacuum chamber	1.26E-06 (0.41 %)	1.68E-14 (15.94 %)	2.97E-08 (0.70 %)	2.97E-08 (0.70 %)
14	Chamber shield	1.19E-08 (0.80 %)	6.49E-15 (15.76 %)	6.01E-09 (1.31 %)	6.01E-09 (1.31 %)

defined by

$$R = \frac{S_{\bar{x}}}{\bar{x}}$$

with \bar{x} = Monte Carlo (sample) mean and $S_{\bar{x}}$ = standard deviation of the sample. If $E(x)$ is the exact value of the quantity (mean value of x),

$$\bar{x}(1 - R) < E(x) < \bar{x}(1 + R)$$

holds with a probability of 0.68.

In Table 8.7 and Table 8.8 only those flux values are listed where we got statistical errors smaller than 50%, because results with errors greater than 50% are marked as garbage in the MCNP manual. Results with errors between 20% and 50% can be regarded as precise with a factor of a few, whereas results with errors between 10% and 20% are questionable. Nearly all of the tabulated MCNP results have errors smaller than 10% and about one third smaller than 1%. Results with such small errors could be regarded - following the manual - as generally reliable.

Naturally it is possible to improve big statistical errors by increasing the size of the sample. But because the statistical error is inversely proportional to the square root of the number of particles, this would have required much computer time to get questionable results in reactor regions, which are not very important for this type of study. Therefore we also did not try to improve the small number of results not listed by using variance reduction methods. All results given in this and the following tables have been obtained by totally analog Monte Carlo methods.

If there are flux values of zero in the table, this means only that none of the started particles or produced particle has reached this region. For the neutronic source 300,000 particles, using 330 minutes of cpu-time on a Siemens 7890 computer, and for the photonic source 4,485,000 particles, using 248 minutes of cpu-time, have been started.

In column 1 of Table 8.7 and Table 8.8 numbers are given for the different components. These numbers can be found in Fig. 8.2, Fig. 8.3, and Fig. 8.4.

8.2.7 Tritium Breeding Rates

In Table 8.9 the tritium breeding rates for all components of the LIBRA reactor chamber which contain lithium are listed. There is one column for the tritium breeding

Table 8.8. Neutron and Photon Flux Densities (Part 2). All values in units of particles
 $\text{cm}^2 \times \text{fusion}$

N u m b e r	Components	Neutrons	Photons		
			from the pellet	produced in the reactor	total
15a	Vacuum exhaust tube interior volume in steel reflector	3.15E-06 (1.57 %)	0.00E+00 (0.00 %)	1.18E-07 (6.48 %)	1.18E-07 (6.48 %)
15b	Vacuum exhaust tube interior volume in shield	4.50E-07 (2.23 %)	0.00E+00 (0.00 %)	7.13E-08 (4.65 %)	7.13E-08 (4.65 %)
15c	Vacuum exhaust tube interior volume in suppression tank	2.09E-08 (14.55 %)	0.00E+00 (0.00 %)	5.88E-09 (30.31 %)	5.88E-09 (30.31 %)
15d	Vacuum exhaust tube wall in shield	7.27E-07 (2.35 %)	0.00E+00 (0.00 %)	9.26E-08 (3.69 %)	9.26E-08 (3.69 %)
15e	Vacuum exhaust tube wall in suppression tank	6.68E-09 (17.94 %)	0.00E+00 (0.00 %)	1.18E-09 (27.71 %)	1.18E-09 (27.71 %)
16	Suppression tank shield	1.13E-10 (16.90 %)	0.00E+00 (0.00 %)	1.12E-10 (21.28 %)	1.12E-10 (21.28 %)
17a	Suppression tank interior volume	1.07E-09 (20.24 %)	0.00E+00 (0.00 %)	1.39E-10 (35.45 %)	1.39E-10 (35.45 %)
17b	Suppression tank wall	5.74E-10 (22.63 %)	0.00E+00 (0.00 %)	8.84E-11 (32.26 %)	8.84E-11 (32.26 %)
18	Li ₁₇ Pb ₈₃ pool in tank	2.01E-10 (37.97 %)	0.00E+00 (0.00 %)		
19	Li ₁₇ Pb ₈₃ pool in reactor chamber	5.23E-06 (0.36 %)	5.67E-10 (0.16 %)	1.01E-07 (0.57 %)	1.01E-07 (0.57 %)
20	Perforated shock absorbing plate	2.99E-06 (0.93 %)	0.00E+00 (0.00 %)	6.10E-08 (2.04 %)	6.10E-08 (2.04 %)
21	Bottom splash plate	1.76E-07 (2.70 %)	0.00E+00 (0.00 %)	3.89E-09 (7.02 %)	3.89E-09 (7.02 %)
901	Vacuum region below shock absorbing plate	3.50E-08 (3.87 %)	0.00E+00 (0.00 %)	6.23E-10 (28.70 %)	6.23E-10 (28.70 %)
999	Outside world within surrounding sphere	4.89E-10 (2.93 %)	0.00E+00 (0.00 %)	1.36E-11 (25.99 %)	1.36E-11 (25.99 %)

Table 8.9. Tritium Breeding Rates Related to 1 Fusion Neutron. The numbers in () give the estimated (statistical) relative errors at the 1σ -level. See Section 8.2.6 for explanation.

	^6Li	^7Li	Sum
Inport Units	0.865738 (0.24%)	0.001913 (0.32%)	0.867651
$\text{Li}_{17}\text{Pb}_{83}$ -Pool in Reactor Chamber	0.266176 (0.51%)	0.000438 (0.80%)	0.266614
Roof Protective $\text{Li}_{17}\text{Pb}_{83}$ Layer	0.088991 (0.53%)	0.000218 (0.73%)	0.089209
Reflector/Vacuum Chamber	0.071174 (0.95%)	0.000002 (3.52%)	0.071176
Steel Reflector	0.043896 (1.02%)	0.000011 (1.27%)	0.043908
Manifold	0.018528 (0.93%)	0.000013 (2.32%)	0.018542
Shock Absorbing Plate	0.003908 (1.89%)	0.000000 (8.56%)	0.003908
$\text{Li}_{17}\text{Pb}_{83}$ -Pool in Tank	0.000061 (31.93%)	0.000000 (31.93%)	0.000061
Sum	1.358471	0.002596	1.361066

by neutrons reacting with ${}^6_3\text{Li}$ and one column for breeding by neutrons reacting with ${}^7_3\text{Li}$. The last column gives the sum of these two reactions. In the last row of the table the tritium breeding rate for the two nuclides is summed over all components of the reactor chamber. The tritium breeding rate summed over all components and the two nuclides yield the value 1.36 tritium atoms per fusion event.

8.2.8 Neutron and Photon Nuclear Heating

In this section values for neutron and photon nuclear heating for nearly all components of the LIBRA chamber are given. These values have been calculated by MCNP using the F6-Tally (energy deposition averaged over a cell). If no values are given for a specific component, the statistical error in the MCNP calculation was greater than 50% (see Section 8.2.6).

The results produced by MCNP are in units of MeV/gram. The results given in Table 8.10 and Table 8.11 have been produced by multiplication of the MCNP-results with the masses listed in Table 8.6

To renormalize the energy released per fusion event to the planned thermal power, one starts with the target yield of the pellet, which has the value 320 MJ. 80% of this energy (256 MJ) is carried away by the 14.1 MeV neutrons emitted in the fusion process. Thus division of 256 MJ by 14.1 MeV will give the number of neutrons produced in the generation of 256 MJ. This leads to

$$\frac{256 \text{ MJ}}{14.1 \text{ MeV}} = \frac{256 \times 10^6 \text{ J}}{14.1 \times 1.6022 \times 10^{-13} \text{ J}} \text{ fusion events per pellet implosion.}$$

Because in the LIBRA design the fusion targets are imploded at a rate of 3 Hz, this number must be multiplied by 3 yielding

$$\frac{\frac{3}{\text{s}} 256 \times 10^6 \text{ J}}{14.1 \times 1.6022 \times 10^{-13} \text{ J}} = 3.4 \times 10^{20} \text{ fusion events per second.}$$

Table 8.12 and Table 8.13 have been produced by multiplication of the numbers in Table 8.10 and Table 8.11 with this factor and division by the volume values listed in Table 8.6.

Table 8.10. Neutron and Photon Heating (Part 1). The numbers in () give the estimated (statistical) relative errors at the 1 σ -level. See Section 8.2.6 for explanation.

Number	Components	Neutrons [MeV/fusion]	Photons		Total [MeV/fusion]
			from the pellet [MeV/fusion]	produced in the reactor [MeV/fusion]	
100	Vacuum chamber	6.36E-03 (0.17 %)	7.70E-06 (0.01 %)	5.56E-05 (0.75 %)	0.006
1	Roof protective LiPb layer in SiC fabric	5.83E-01 (0.42 %)	6.64E-03 (0.14 %)	4.24E-01 (0.80 %)	1.013
2	Roof steel reflector cooled with LiPb	3.66E-01 (0.70 %)	2.41E-04 (0.73 %)	7.52E-01 (0.86 %)	1.119
3	Roof support structural ring	1.11E-03 (8.21 %)	5.11E-06 (4.36 %)	1.35E-02 (7.23 %)	0.015
4	Roof support beams	3.32E-04 (6.54 %)	1.33E-08 (61.18 %)	2.45E-02 (4.26 %)	0.025
5	Pellet injector shield module	2.71E-03 (7.84 %)	1.63E-05 (3.16 %)	8.31E-03 (8.51 %)	0.011
6	Roof shield	5.90E-02 (1.18 %)	5.02E-07 (14.25 %)	5.32E-01 (1.24 %)	0.591
7	Roof vacuum seal flange	0.00E+00 (0.00 %)	0.00E+00 (0.00 %)	0.00E+00 (0.00 %)	0.00E+00
8	Manifold for INPORT units	2.98E-01 (0.81 %)	2.35E-04 (0.73 %)	7.95E-02 (1.89 %)	0.378
9	Driver diode	2.05E-03 (8.71 %)	5.62E-05 (1.65 %)	1.07E-02 (9.04 %)	0.013
11a	Beam tube wall	1.84E-02 (1.00 %)	4.70E-04 (0.55 %)	2.54E-01 (1.17 %)	0.273
11b	Beam tube inner volume	1.10E-05 (2.21 %)	1.28E-08 (0.83 %)	4.52E-07 (1.99 %)	1.14E-05
12	INPORT units	5.43E+00 (0.20 %)	3.63E-02 (0.05 %)	3.39E+00 (0.29 %)	8.847
13	Reflector vacuum chamber	4.47E-01 (0.66 %)	1.88E-07 (13.78 %)	6.67E-01 (0.96 %)	1.114
14	Chamber shield	2.24E-02 (1.53 %)	1.15E-07 (13.95 %)	3.01E-01 (1.65 %)	0.324

Table 8.11. Neutron and Photon Heating (Part 2). The numbers in () give the estimated (statistical) relative errors at the 1σ -level. See Section 8.2.6 for explanation.

N u m b e r	Components	Neutrons [MeV/fusion]	Photons		Total [MeV/fusion]
			from the pellet [MeV/fusion]	produced in the reactor [MeV/fusion]	
15a	Vacuum exhaust tube interior volume in steel reflector	2.53E-06 (2.84 %)	0.00E+00 (0.00 %)	5.55E-08 (8.25 %)	2.59E-06
15b	Vacuum exhaust tube interior volume in shield	1.58E-06 (4.83 %)	0.00E+00 (0.00 %)	2.82E-07 (5.88 %)	1.86E-06
15d	Vacuum exhaust tube wall in shield	6.50E-04 (5.50 %)	0.00E+00 (0.00 %)	1.81E-02 (5.01 %)	0.019
15e	Vacuum exhaust tube wall in suppression tank	2.16E-06 (24.50 %)	0.00E+00 (0.00 %)	7.49E-05 (29.44 %)	7.71E-05
16	Suppression tank shield	3.52E-05 (25.07 %)	0.00E+00 (0.00 %)	9.75E-04 (27.50 %)	1.01E-03
19	Li ₁₇ Pb ₈₃ pool in reac- tor chamber	1.58E+00 (0.44 %)	7.10E-03 (0.14 %)	7.99E-01 (0.69 %)	2.381
20	Perforated shock absorbing plate	3.12E-02 (1.32 %)	0.00E+00 (0.00 %)	4.94E-02 (2.81 %)	0.081
21	Bottom splash plate	8.10E-04 (3.56 %)	0.00E+00 (0.00 %)	6.17E-03 (9.94 %)	0.007
	System total	8.841	0.051	7.327	16.218

Table 8.12. Neutron and Photon Average Power Density (Part 1). The numbers are based on $3.4 \cdot 10^{20}$ fusions per second. The numbers in () give the estimated (statistical) relative errors at the 1σ -level. See Section 8.2.6 for explanation.

Number	Components	Neutrons [W/cm**3]	Photons		Total [W/cm**3]
			from the pellet [W/cm**3]	produced in the reactor [W/cm**3]	
100	Vacuum chamber	5.06E-03 (0.17 %)	6.12E-06 (0.01 %)	4.42E-05 (0.75 %)	0.005
1	Roof protective LiPb layer in SiC fabric	2.01E+01 (0.42 %)	2.29E-01 (0.14 %)	1.46E+01 (0.80 %)	34.870
2	Roof steel reflector cooled with LiPb	4.34E+00 (0.70 %)	2.85E-03 (0.73 %)	8.92E+00 (0.86 %)	13.261
3	Roof support structural ring	2.12E-01 (8.21 %)	9.74E-04 (4.36 %)	2.57E+00 (7.23 %)	2.786
4	Roof support beams	3.46E-02 (6.54 %)	1.38E-06 (61.18 %)	2.56E+00 (4.26 %)	2.591
5	Pellet injector shield module	2.45E-01 (7.84 %)	1.48E-03 (3.16 %)	7.52E-01 (8.51 %)	0.999
6	Roof shield	5.08E-02 (1.18 %)	4.32E-07 (14.25 %)	4.58E-01 (1.24 %)	0.508
7	Roof vacuum seal flange	0.00E+00 (0.00 %)	0.00E+00 (0.00 %)	0.00E+00 (0.00 %)	0.00E+00
8	Manifold for INPORT units	5.56E+00 (0.81 %)	4.39E-03 (0.73 %)	1.49E+00 (1.89 %)	7.055
9	Driver diode	8.72E-03 (8.71 %)	2.39E-04 (1.65 %)	4.55E-02 (9.04 %)	0.054
11a	Beam tube wall	9.70E-01 (1.00 %)	2.48E-02 (0.55 %)	1.34E+01 (1.17 %)	14.414
11b	Beam tube inner volume	1.09E-03 (2.21 %)	1.28E-06 (0.83 %)	4.50E-05 (1.99 %)	1.14E-03

Table 8.13. Neutron and Photon Average Power Density (Part 2). The numbers are based on $3.4 \cdot 10^{20}$ fusions per second. The numbers in () give the estimated (statistical) relative errors at the 1σ -level. See Section 8.2.6 for explanation.

Number	Components	Neutrons [W/cm**3]	Photons		Total [W/cm**3]
			from the pellet [W/cm**3]	produced in the reactor [W/cm**3]	
12	INPORT units	4.50E+00 (0.20 %)	3.02E-02 (0.05 %)	2.81E+00 (0.29 %)	7.345
13	Reflector vacuum chamber	4.73E-01 (0.66 %)	1.98E-07 (13.78 %)	7.06E-01 (0.96 %)	1.179
14	Chamber shield	3.72E-03 (1.53 %)	1.92E-08 (13.95 %)	5.02E-02 (1.65 %)	0.054
15a	Vacuum exhaust tube interior volume in steel reflector	2.08E-04 (2.84 %)	0.00E+00 (0.00 %)	4.56E-06 (8.25 %)	2.13E-04
15b	Vacuum exhaust tube interior volume in shield	2.05E-05 (4.83 %)	0.00E+00 (0.00 %)	3.64E-06 (5.88 %)	2.41E-05
15d	Vacuum exhaust tube wall in shield	7.26E-02 (5.50 %)	0.00E+00 (0.00 %)	2.02E+00 (5.01 %)	2.092
15e	Vacuum exhaust tube wall in suppression tank	4.64E-04 (24.50 %)	0.00E+00 (0.00 %)	1.61E-02 (29.44 %)	1.65E-02
16	Suppression tank shield	2.26E-05 (25.07 %)	0.00E+00 (0.00 %)	6.25E-04 (27.50 %)	0.001
19	Li ₁₇ Pb ₈₃ pool in reactor chamber	5.88E+00 (0.44 %)	2.65E-02 (0.14 %)	2.98E+00 (0.69 %)	8.894
20	Perforated shock absorbing plate	7.69E-01 (1.32 %)	0.00E+00 (0.00 %)	1.22E+00 (2.81 %)	1.987
21	Bottom splash plate	1.12E-02 (3.56 %)	0.00E+00 (0.00 %)	8.55E-02 (9.94 %)	0.097

In Table 8.14 and Table 8.15 the power values in units of MW for the different reactor components are listed. These values have been produced out of the MCNP results similar to the power densities in units of W/cm^3 given in Table 8.12 and Table 8.13, but suppressing the division by the volume values.

The total thermal power produced by neutrons and photons from the target in the LIBRA reactor chamber adds up (see Table 8.15) to 883.5 MW. If the values, given in Fig. 5.5 for x-rays (189 MW) and the debris (97.5 MW) are added, the result is 1170 MW. This is very close to the design parameter of 1160 MW given in Table 1.1

8.3 Activation Analysis

8.3.1 Calculational Procedure

Neutron transport calculations have been performed for the LIBRA chamber using the one-dimensional discrete ordinates code ONEDANT⁽¹⁾ and the LANL MATXS5⁽⁶⁾ cross section data library processed from the ENDF/B-V files. The standard LANL 30 neutron-12 gamma group structure was used in the calculations. The problem has been modeled in spherical geometry with materials and dimensions consistent with a cut through the midplane of the reactor. A point source was used at the center of the 3 m radius chamber. The LIBRA target neutron spectrum that accounts for neutron-target interactions was used to represent the source spectrum. The source strength was normalized to the DT target yield of 320 MJ and the 3 Hz repetition rate.

The radial build used in the calculations is given in Fig. 8.7. The concrete shield thickness was determined such that the biological dose rate outside the shield during reactor operation does not exceed 2.5 mrem/hr. Figure 8.8 gives the dose rate at the back of the shield as a function of the thickness of the helium cooled steel reinforced concrete shield. Since a spherical geometry was used in the calculations, the results correspond to the conditions at the reactor midplane where the dose rate is expected to be greatest. A shield thickness of 2.6 m, which yields a dose rate of 1.4 mrem/hr during operation, is used in the activation calculations. While the initial LIBRA chamber design uses the ferritic steel alloy HT-9 as chamber structural material, activation calculations have been performed also for a modified HT-9 alloy which would have lower long term activity.⁽⁷⁾ The elemental compositions of these ferritic steel alloys as well as those for the SiC, $Li_{17}Pb_{83}$, concrete and carbon steel C1020 used in the activation calculations are given in Table 8.16.

Table 8.14. Neutron and Photon Power (Part 1). The numbers are based on $3.4 \cdot 10^{20}$ fusions per second. The numbers in () give the estimated (statistical) relative errors at the 1σ -level. See Section 8.2.6 for explanation.

Number	Components	Neutrons [MW]	Photons		Total [MW]
			from the pellet [MW]	produced in the reactor [MW]	
100	Vacuum chamber	3.47E-01 (0.17 %)	4.19E-04 (0.01 %)	3.03E-03 (0.75 %)	0.350
1	Roof protective LiPb layer in SiC fabric	3.18E+01 (0.42 %)	3.62E-01 (0.14 %)	2.31E+01 (0.80 %)	55.206
2	Roof steel reflector cooled with LiPb	2.00E+01 (0.70 %)	1.31E-02 (0.73 %)	4.10E+01 (0.86 %)	60.956
3	Roof support structural ring	6.05E-02 (8.21 %)	2.78E-04 (4.36 %)	7.35E-01 (7.23 %)	0.796
4	Roof support beams	1.81E-02 (6.54 %)	7.23E-07 (61.18 %)	1.34E+00 (4.26 %)	1.355
5	Pellet injector shield module	1.48E-01 (7.84 %)	8.90E-04 (3.16 %)	4.53E-01 (8.51 %)	0.601
6	Roof shield	3.21E+00 (1.18 %)	2.73E-05 (14.25 %)	2.90E+01 (1.24 %)	32.203
7	Roof vacuum seal flange	0.00E+00 (0.00 %)	0.00E+00 (0.00 %)	0.00E+00 (0.00 %)	0.00E+00
8	Manifold for INPORT units	1.62E+01 (0.81 %)	1.28E-02 (0.73 %)	4.33E+00 (1.89 %)	20.571
9	Driver diode	1.11E-01 (8.71 %)	3.06E-03 (1.65 %)	5.81E-01 (9.04 %)	0.696
11a	Beam tube wall	1.00E+00 (1.00 %)	2.56E-02 (0.55 %)	1.39E+01 (1.17 %)	14.892
11b	Beam tube inner volume	5.97E-04 (2.21 %)	6.99E-07 (0.83 %)	2.46E-05 (1.99 %)	6.22E-04
12	INPORT units	2.96E+02 (0.20 %)	1.98E+00 (0.05 %)	1.84E+02 (0.29 %)	481.943
13	Reflector vacuum chamber	2.44E+01 (0.66 %)	1.02E-05 (13.78 %)	3.63E+01 (0.96 %)	60.706

Table 8.15. Neutron and Photon Power (Part 2). The numbers are based on $3.4 \cdot 10^{20}$ fusions per second. The numbers in () give the estimated (statistical) relative errors at the 1σ -level. See Section 8.2.6 for explanation.

N u m b e r	Components	Neutrons [MW]	Photons		Total [MW]
			from the pellet [MW]	produced in the reactor [MW]	
14	Chamber shield	1.22E+00 (1.53 %)	6.28E-06 (13.95 %)	1.64E+01 (1.65 %)	17.634
15a	Vacuum exhaust tube interior volume in steel reflector	1.38E-04 (2.84 %)	0.00E+00 (0.00 %)	3.02E-06 (8.25 %)	1.41E-04
15b	Vacuum exhaust tube interior volume in shield	8.62E-05 (4.83 %)	0.00E+00 (0.00 %)	1.53E-05 (5.88 %)	1.02E-04
15d	Vacuum exhaust tube wall in shield	3.54E-02 (5.50 %)	0.00E+00 (0.00 %)	9.85E-01 (5.01 %)	1.021
15e	Vacuum exhaust tube wall in suppression tank	1.18E-04 (24.50 %)	0.00E+00 (0.00 %)	4.08E-03 (29.44 %)	4.20E-03
16	Suppression tank shield	1.92E-03 (25.07 %)	0.00E+00 (0.00 %)	5.31E-02 (27.50 %)	0.055
19	Li ₁₇ Pb ₈₃ pool in reac- tor chamber	8.58E+01 (0.44 %)	3.87E-01 (0.14 %)	4.35E+01 (0.69 %)	129.717
20	Perforated shock absorbing plate	1.70E+00 (1.32 %)	0.00E+00 (0.00 %)	2.69E+00 (2.81 %)	4.389
21	Bottom splash plate	4.41E-02 (3.56 %)	0.00E+00 (0.00 %)	3.36E-01 (9.94 %)	0.380
	System total	481.589	2.784	399.116	883.489

Table 8.16 Elemental Composition (wt%) Used for LIBRA Activation Analysis

Element	SiC ($\rho=3.21 \text{ g/cm}^3$)	Li ₁₇ Pb ₈₃ ($\rho=9.71 \text{ g/cm}^3$)	C1020 ($\rho=7.93 \text{ g/cm}^3$)	HT-9 ($\rho=7.8 \text{ g/cm}^3$)	Mod. HT-9 ($\rho=7.8 \text{ g/cm}^3$)	Concrete ($\rho=2.32 \text{ g/cm}^3$)
H						0.75
Li		0.62				
B				0.01	0.001	
C	29.35		0.2	0.2	0.15	5.55
N				0.05	0.001	0.01
O				0.01	0.007	49.29
Na		0.00018				0.42
Mg						1.48
Al	0.55			0.01	0.008	2.06
Si	70		0.25	0.35	0.2	15.70
P				0.02	0.013	
S				0.02	0.004	0.17
K		0.00012		0.0003	0.0003	0.75
Ca	0.09	0.00018				22.95
Ti				0.09	0.1	0.05
V				0.3	0.3	
Cr				12.0	11.0	
Mn			0.45	0.55	0.53	
Fe	0.0001		99.1	85.0	85.16	0.82
Co				0.02	0.005	
Ni				0.5	0.006	
Cu		0.0002		0.09	0.003	
Zr				0.001	0.001	
Nb				0.11	0.00011	
Mo				1.0	0.00027	
Ag		0.001		0.0001	0.00009	
Cd				0.0001	0.0001	
Sn				0.003	0.003	
Sb		0.0003		0.001	0.0005	
Ba				0.001	0.0002	
Tb				0.0005	0.0002	
Ta				0.001	0.0004	
W				0.5	2.50	
Tr				0.0005	0.0002	
Pb		99.37		0.001	0.0005	
Bi		0.004		0.001	0.0002	

8-30

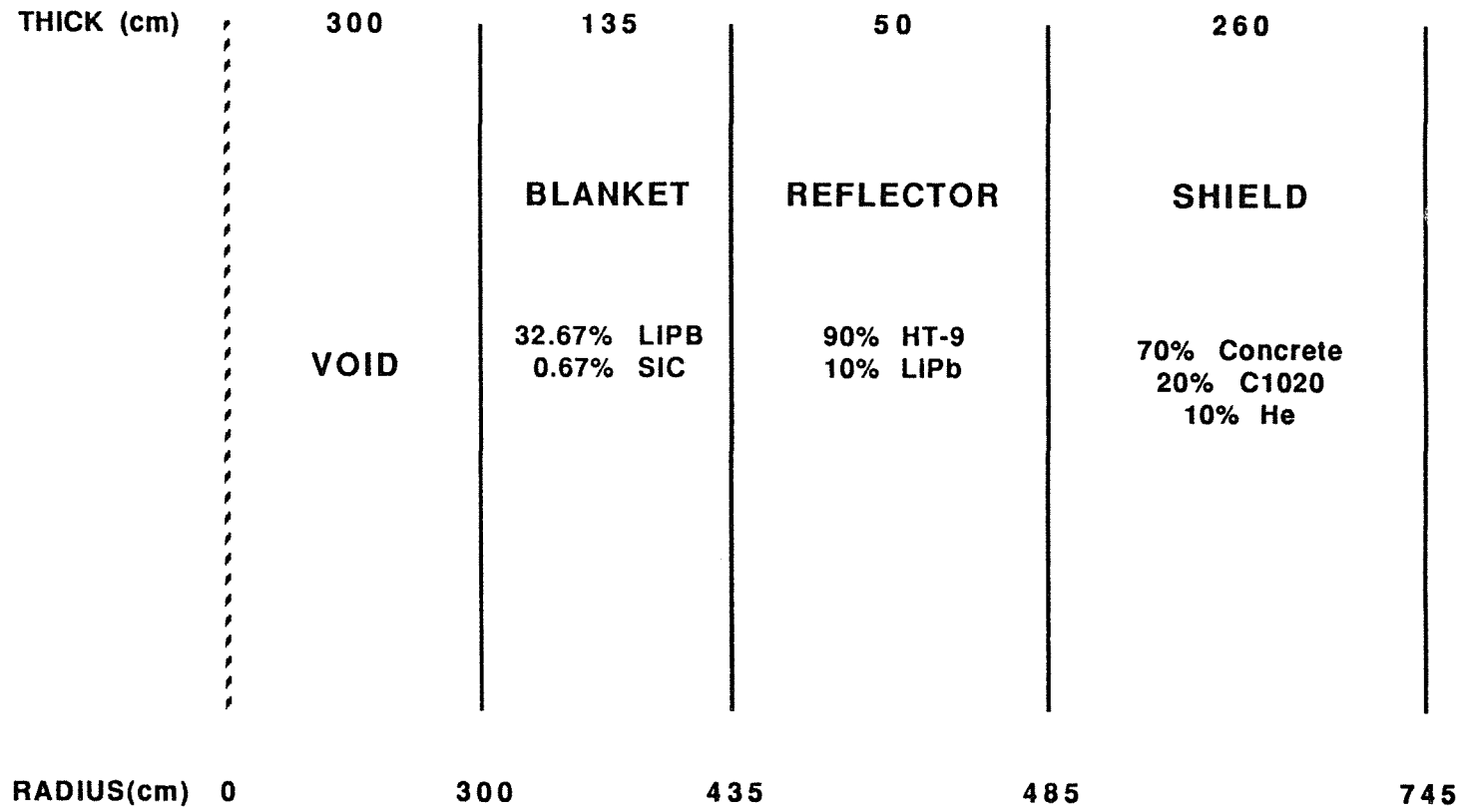


Fig. 8.7. Radial build used in the activation calculations.

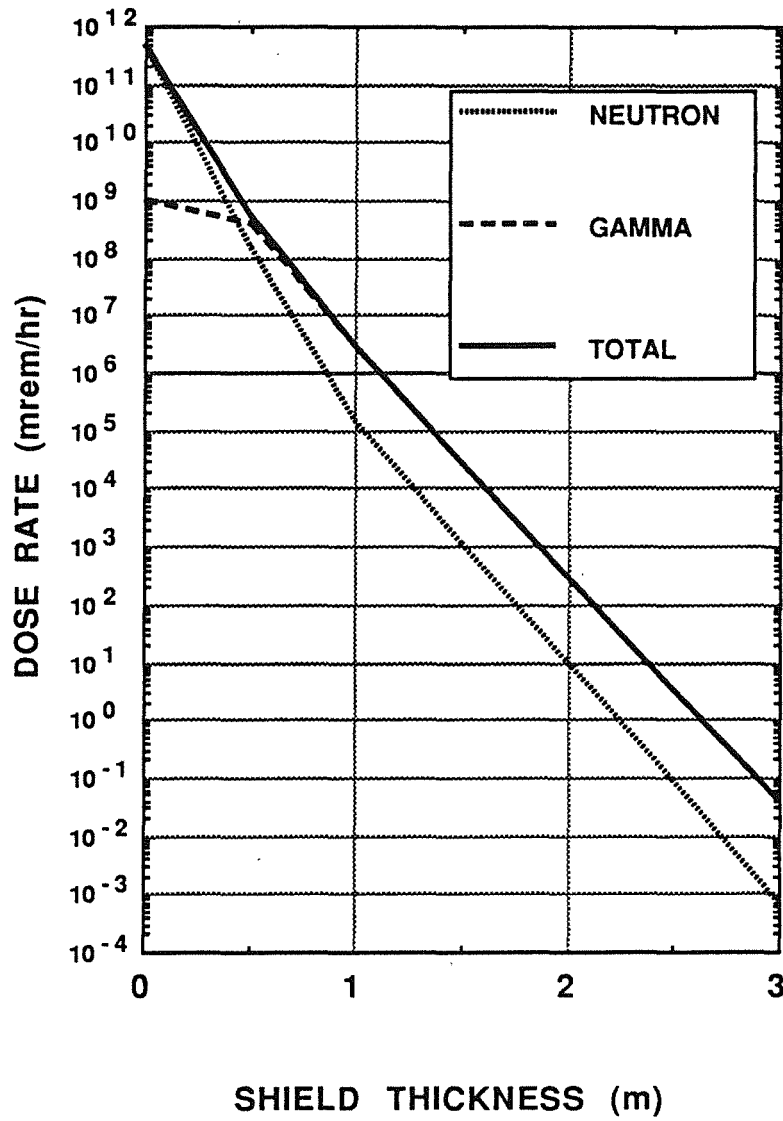


Fig. 8.8. Effect of shield thickness on dose rate during reactor operation.

The neutron flux obtained from the neutron transport calculations has been used in the activation calculations. The radioactivity code DKR-ICF⁽⁸⁾ has been used with the ACTL⁽⁹⁾ neutron transmutation data library. The decay and gamma source data are taken from the Table of Isotopes.⁽¹⁰⁾ The DKR-ICF code allows for appropriate modeling of the pulsing schedule. Using an equivalent steady state operation results in underestimating the produced activity, particularly at short times following shutdown as will be shown in the following section. The pulse sequence used in the activation calculations is shown in Fig. 8.9. The reactor is assumed to be shut down for 5 days every month for routine maintenance and for 40 days every year for extended maintenance. This operational schedule corresponds to a reactor availability of 75%. The activity for the reflector and shield was calculated for the 40 year reactor lifetime while the activity for the SiC INPORT tubes in the blanket was determined for an operating time of 2 years. The coolant activity was calculated separately by modifying the operation schedule to allow for the fact that the coolant spends only half the time exposed to neutrons in the reactor. The coolant residence time in the reactor is assumed to be 10 seconds.

The dose rate at the back of the shield following shutdown was determined by combining the decay gamma source given by DKR-ICF with the adjoint dose field determined by performing a gamma adjoint calculation using ONEDANT with flux-to-dose conversion factors representing the source at the back of the shield. Since the contact dose at the back of the shield is determined mainly by the shield and reflector activation, an operation time of 40 years was used in the dose calculations. Notice that the short term activity and dose activation parameters (within about a year after shutdown) are independent of the operation time while the long term activity (more than ~ 10 years after shutdown) which is important for waste management is approximately proportional to the operation time.

8.3.2 Activity, Biological Hazard Potential (BHP) and Decay Heat in the LIBRA Chamber Structure

The total activity as a function of time after shutdown is given in Fig. 8.10 for the case when HT-9 is used as structural material in the reflector. The results are given in Fig. 8.10 for both cases when the pulse sequence shown in Fig. 8.9 is utilized and when an equivalent steady state operation is considered. It is clear that using the steady state operation results in a factor of two lower activity at shutdown with the difference being

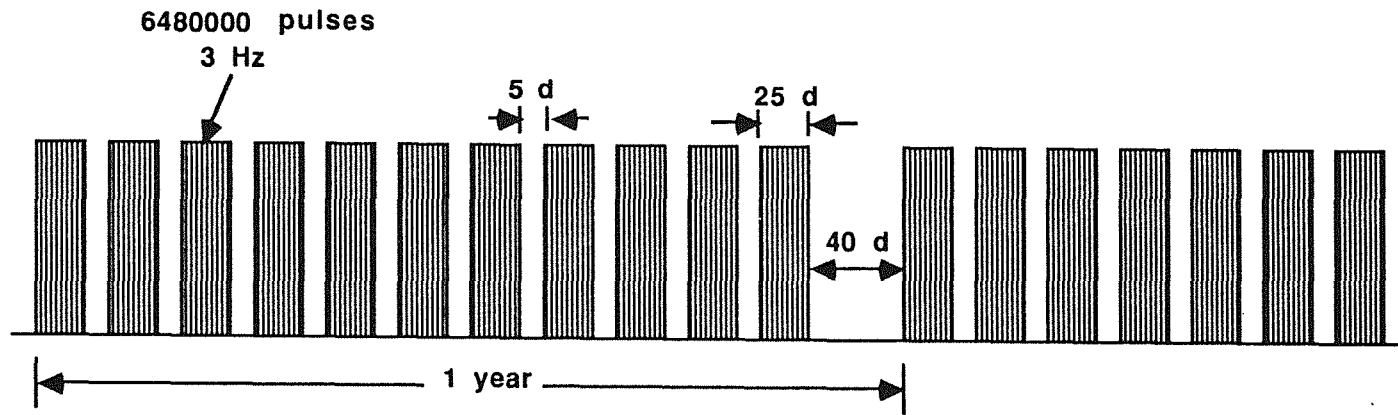


Fig. 8.9. Pulse sequence used in the LIBRA activation calculations.

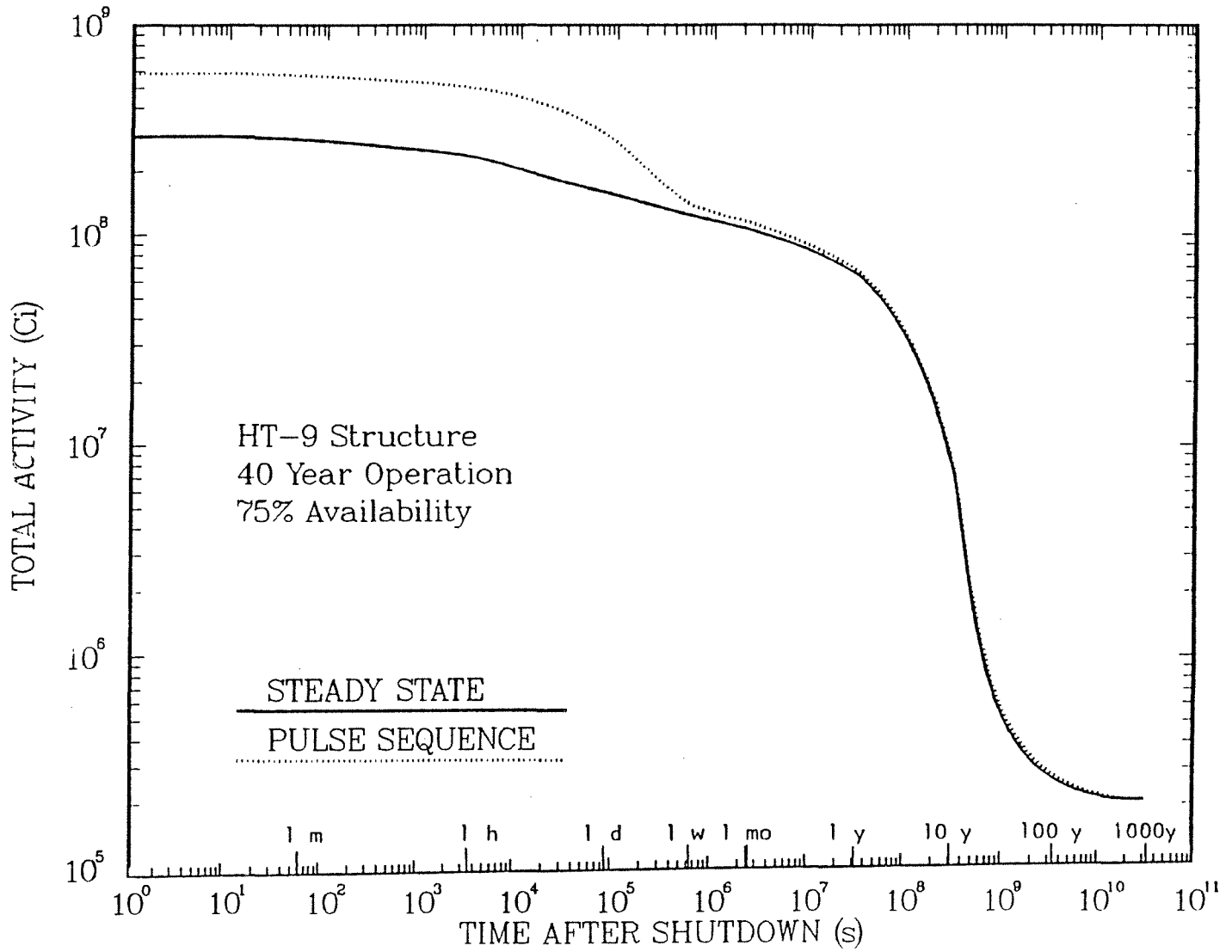


Fig. 8.10. Effect of pulse sequence on total activity in LIBRA chamber.

negligible only after about one month following shutdown. The large difference within a short time following shutdown is due to the fact that the activity is dominated by short lived radionuclides whose activities are sensitive to the operational schedule prior to shutdown due to buildup during the on-time with the subsequent decay between periods of operation. Notice that the average neutron flux used in the equivalent steady state calculation is lower than that during the on-time preceding shutdown. On the other hand, the long term activity is dominated by long lived radionuclides whose activity is determined by the total neutron fluence regardless of the temporal variation of the flux.

The effect of replacing HT-9 by the low activation alloy, modified HT-9; is shown in Fig. 8.11. The total activity at shutdown increases by a factor of ~ 2.5 while the long term activity decreases by a factor of ~ 25. This results from reducing the amount of Mo, Nb and Ni which contribute to the long term activity, while increasing the content of W which contributes to the short term activity. Table 8.17 compares the activity, biological hazard potential (BHP), measured in km³ of air required to dilute the isotopic concentration to the maximum permissible concentration, and the decay heat measured in MW at shutdown for the cases with HT-9 or modified HT-9. The modified HT-9 is recommended for the LIBRA reference design since the long term activity is more of a concern due to its impact on waste management.

Table 8.17 Effect of Reflector Material on Radioactivity Parameters at Shutdown

	Activity (Ci)		BHP (km ³ air)		Decay Heat (MW)	
	HT-9	Mod. HT-9	HT-9	Mod. HT-9	HT-9	Mod. HT-9
Blanket	2.77×10^7	2.77×10^7	9.35×10^5	9.35×10^5	0.47	0.47
Reflector	5.47×10^8	1.536×10^9	8.58×10^7	1.741×10^8	3	6.774
Shield	9.06×10^6	9.06×10^6	6.54×10^5	6.54×10^5	0.064	0.064
Total	5.838×10^8	1.573×10^9	8.74×10^7	1.757×10^8	3.534	7.308

Figure 8.12 gives the activity in the blanket, reflector, and shield as a function of time after shutdown. The total activity per unit of thermal power at shutdown is 1.36 Ci/W and drops to 0.16 Ci/W in one week. Almost all of the total activity results from

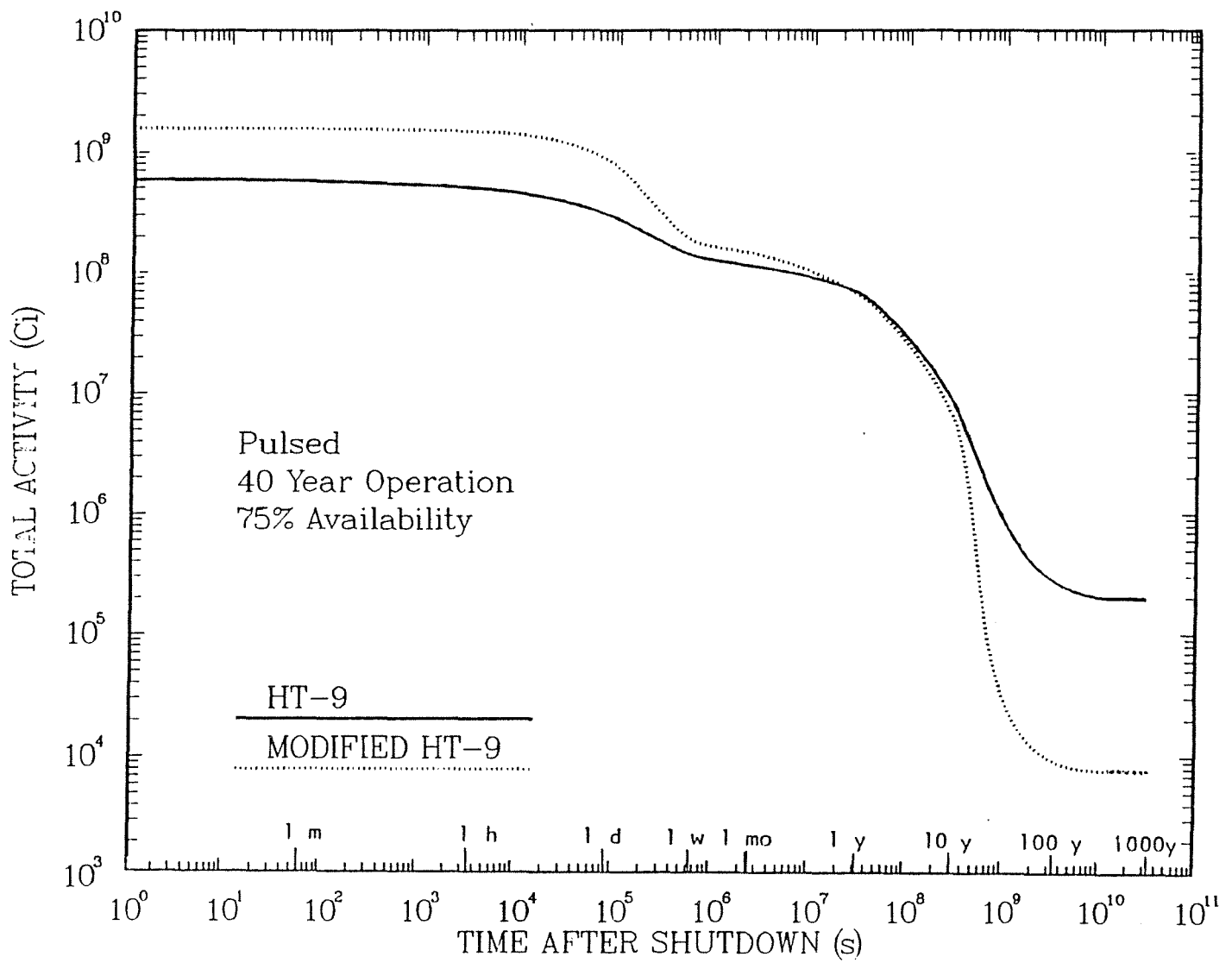


Fig. 8.11. Effect of low activation structure on total activity in LIBRA chamber.

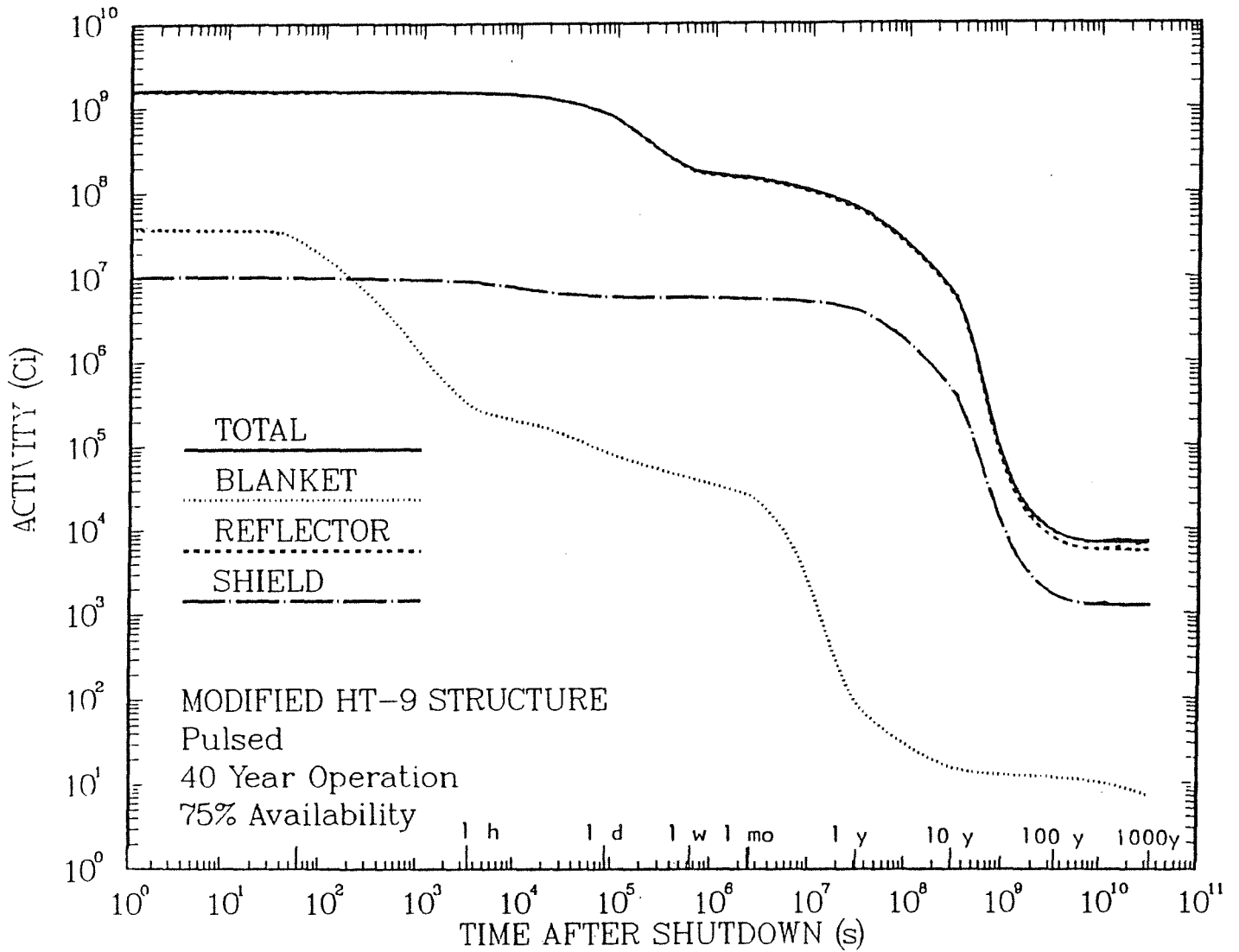


Fig. 8.12. Activity after shutdown in different LIBRA chamber regions.

the activation of the reflector structure. The contribution from the activity of the SiC used in the blanket is very small and drops rapidly after shutdown. Table 8.18 lists the major contributing radionuclides in the different reactor zones at different times following shutdown. The results for the BHP and decay heat are given in Fig. 8.13 and Fig. 8.14, respectively. The variation with time after shutdown is similar to that for the activity. The BHP value per unit thermal power at shutdown is $151 \text{ km}^3/\text{kW}$ and the decay heat is 0.63%. It should be pointed out that although a spherical geometry model was used, the calculated total activity is expected to be close to that obtained in the actual right cylindrical chamber since the same number of neutrons which activate the chamber materials is incident on the blanket in both cases.

8.3.3 Waste Disposal Rating (WDR) of LIBRA Chamber Structure

The specific activities calculated for the different radionuclides have been used with the U.S. waste disposal limits (WDL) to evaluate the radwaste of the LIBRA chamber. The 10CFR61 limits⁽¹¹⁾ (the current U.S. legal limits) were used. Table 8.19 lists the calculated WDR values for Class C low level waste (LLW) for the different reactor regions. An operation time of 2 years is used for the blanket while the reflector and shield have an operation time of 40 years. The WDR is defined as $\sum C_i/WDL_i$, where C_i is the specific activity of the i th nuclide and WDL_i is the waste disposal limit. A WDR value ≤ 1 implies that the radwaste classifies as Class C LLW and qualifies for shallow land burial.

The results are given for both cases with HT-9 and modified HT-9 reflector structure. The non-compacted values are based on averaging over the total volume of the particular region implying that internal voids are to be filled with concrete before disposal. On the other hand, the compacted values correspond to crushing the solid waste before disposal. The WDR values are given also for the case when the reflector and shield are disposed of together. While the WDR values for the blanket and shield are much smaller than unity, the reflector WDR is larger than unity when HT-9 is used implying the need for deep geological burial. Replacing HT-9 by the low activation modified HT-9 results in the reflector being classified as Class C LLW.

^{14}C , generated from the $^{13}\text{C}(n,\gamma)$ reaction, is the only contributing radionuclide to the WDR for the blanket and shield. On the other hand, about 98% of the WDR for the modified HT-9 reflector is contributed by ^{94}Nb which is produced by the $^{93}\text{Nb}(n,\gamma)$ reaction and (n,p), (n,np), (n,d), and (n,t) reactions with the different Mo isotopes. This

Table 8.18 LIBRA Activity Major Contributors

Time After Shutdown	Blanket	Reflector	Shield
0	²⁸ Al, 2.24 m, (a) 91.9% ^(b) ²⁹ Al, 6.56 m, 4.4%	¹⁸⁷ W, 23.85 h, 82.3% ⁵⁵ Fe, 2.68 y, 4.1%	⁵⁵ Fe, 2.68 y, 47.9% ⁵⁶ Mn, 2.58 h, 37%
1 m	²⁸ Al, 2.24 m, 92.3% ²⁹ Al, 6.56 m, 5.4%	¹⁸⁷ W, 23.85 h, 82.4% ⁵⁵ Fe, 2.68 y, 4.1%	⁵⁵ Fe, 2.68 y, 48.7% ⁵⁶ Mn, 2.58 h, 37.5%
10 m	²⁸ Al, 2.24 m, 63.1% ²⁹ Al, 6.56 m, 22.4%	¹⁸⁷ W, 23.85 h, 82.8% ⁵⁵ Fe, 2.68 y, 4.2%	⁵⁵ Fe, 2.68 y, 51.5% ⁵⁶ Mn, 2.58 h, 38%
1 h	²⁴ Na, 15 h, 45% ³¹ Si, 2.62 h, 34.2%	¹⁸⁷ W, 23.85h, 83.5% ⁵⁵ Fe, 2.68 y, 4.3%	⁵⁵ Fe, 2.68 y, 56.2% ⁵⁶ Mn, 2.58 h, 33.1%
6 h	²⁴ Na, 15 h, 57.4% ³⁷ Ar, 35 d, 27.6%	¹⁸⁷ W, 23.85 h, 84.8% ⁵⁵ Fe, 2.68 y, 5%	⁵⁵ Fe, 2.68 y, 75% ⁵⁶ Mn, 2.58 h, 11.5%
1 d	²⁴ Na, 15 h, 47.7% ³⁷ Ar, 35 d, 51.8%	¹⁸⁷ W, 23.85 h, 78.4% ⁵⁵ Fe, 2.68 y, 7.8%	⁵⁵ Fe, 2.68 y, 85% ⁴⁵ Ca, 165 d, 3.8%
1 w	³⁷ Ar, 35 d, 99%	⁵⁵ Fe, 2.68 y, 35.7% ¹⁸⁵ W, 75.1 d, 33.1%	⁵⁵ Fe, 2.68 y, 86% ⁴⁵ Ca, 165 d, 3.7%
1 mo	³⁷ Ar, 35d, 100%	⁵⁵ Fe, 2.68 y, 43.3% ¹⁸⁵ W, 75.1 d, 32.9%	⁵⁵ Fe, 2.68 y, 89.3% ⁴⁵ Ca, 165 d, 3.5%
1 y	³⁷ Ar, 35 d, 41.5% ⁵⁵ Fe, 2.68 y, 25.4%	⁵⁵ Fe, 2.68 y, 80.6% ⁵⁴ Mn, 312.2 d, 11.9%	⁵⁵ Fe, 2.68 y, 98.7% ⁴⁵ Ca, 165 d, 1.2%
10 y	³⁹ Ar, 269 y, 47.1% ¹⁴ C, 5730 y, 13.8%	⁵⁵ Fe, 2.68 y, 89.1%	⁵⁵ Fe, 2.68 y, 99.5%
100 y	³⁹ Ar, 269 y, 48.4% ¹⁴ C, 5730 y, 17.6%	⁴⁰ K, 1.3 x 10 ⁹ y, 86% ⁶³ Ni, 100 y, 6.8%	⁴¹ Ca, 1.03 x 10 ⁵ y, 98.2% ¹⁴ C, 5730 y, 1.6%
1000 y	¹⁴ C, 5730 y, 29.1% ⁴¹ Ca, 1.03 x 10 ⁵ y, 24.2%	⁴⁰ K, 1.3 x 10 ⁹ y, 97.1% ¹⁴ C, 5730 y, 1.6%	⁴¹ Ca, 1.03 x 10 ⁵ y, 98.2% ¹⁴ C, 5730 y, 1.5%

(a) Half life

(b) Percentage contribution

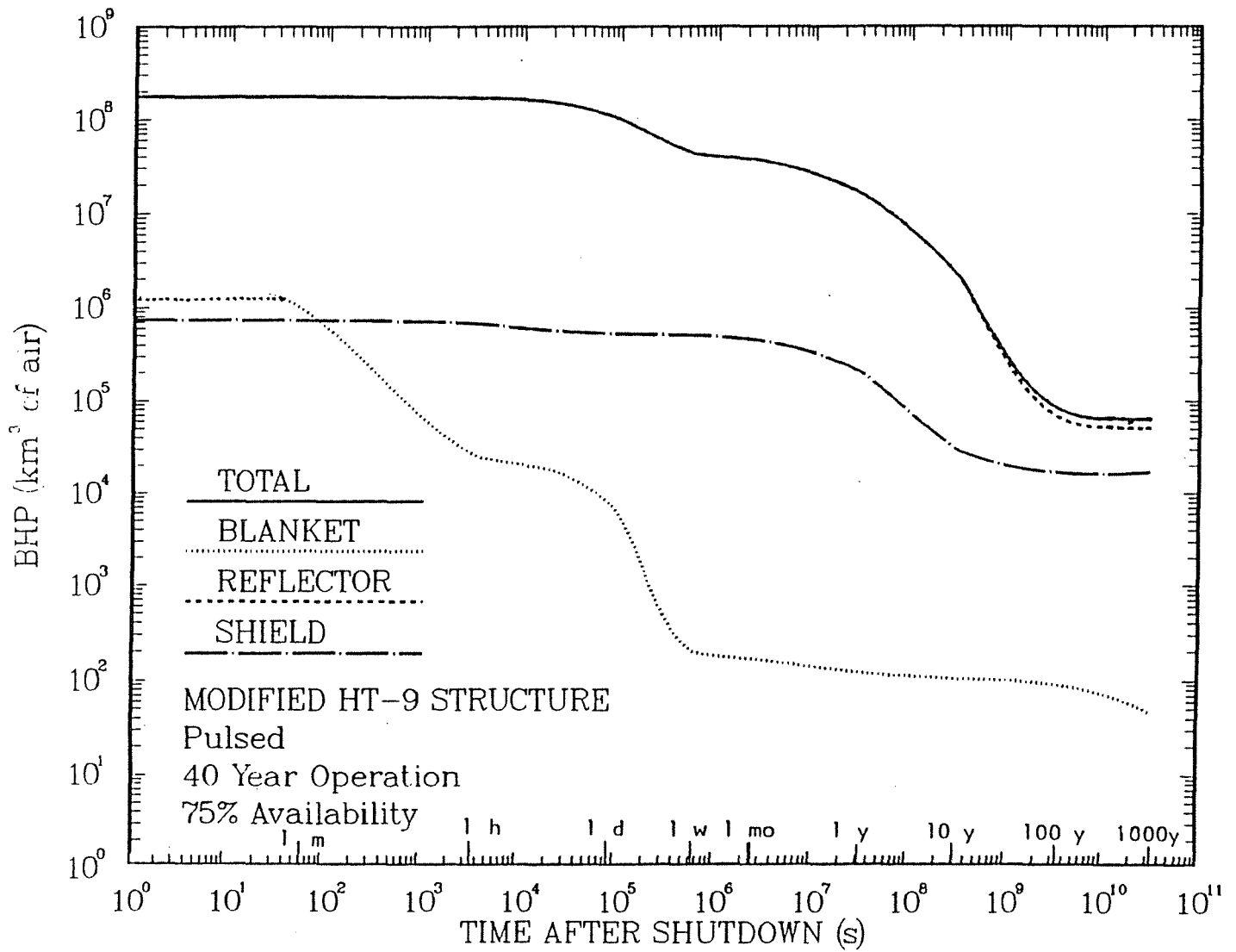


Fig. 8.13. Biological hazard potential in different LIBRA chamber regions.

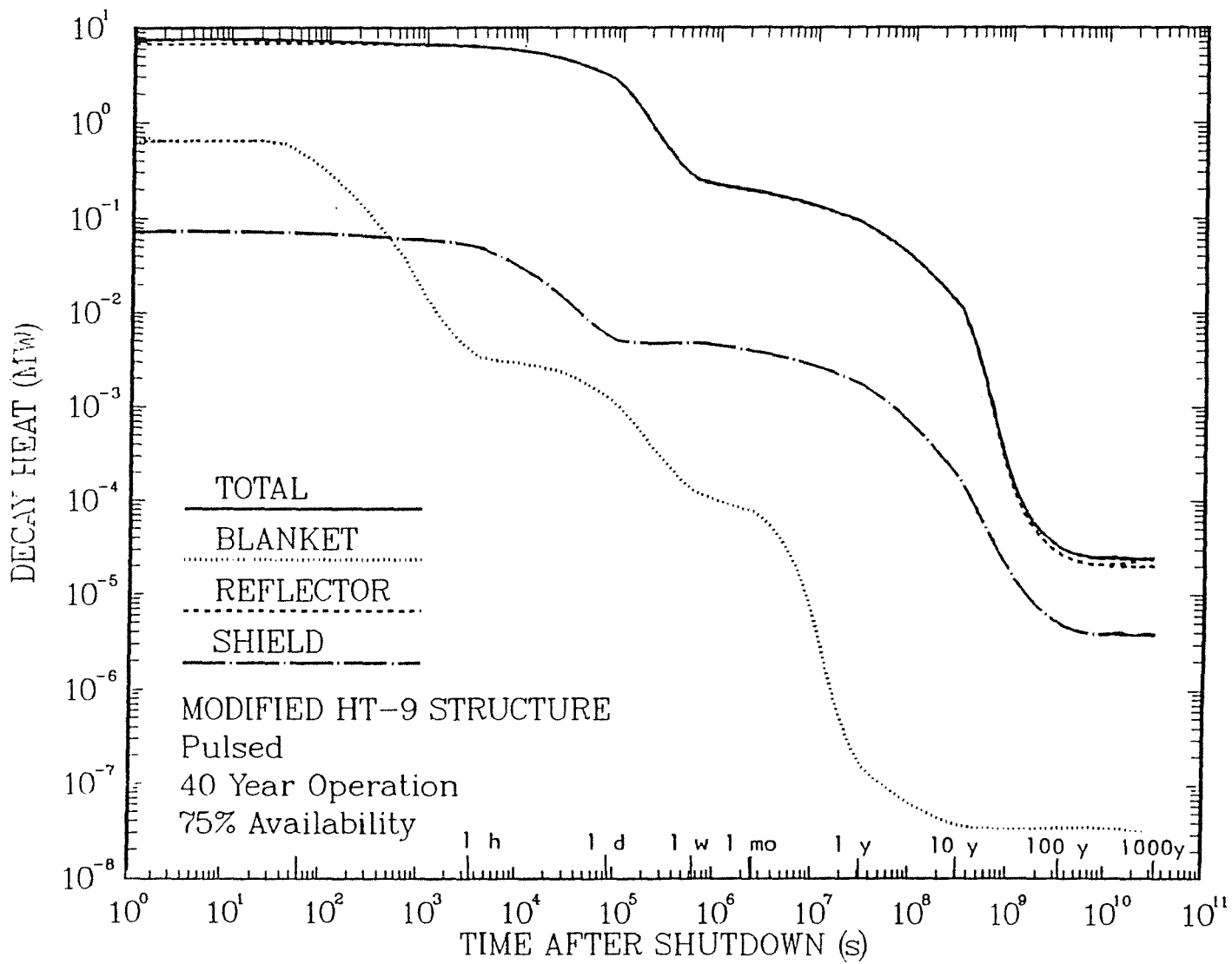


Fig. 8.14. Decay heat in different LIBRA chamber regions.

explains the three order of magnitude reduction in the reflector WDR by replacing HT-9 by modified HT-9. Table 8.20 gives the contribution of the different radionuclides to the reflector WDR.

8.3.4 Coolant Activity

The activity produced in the $\text{Li}_{17}\text{Pb}_{83}$ coolant has been determined. We assumed that the coolant volume in the loop outside the chamber is the same as that in the chamber. The residence time of the coolant in the chamber was taken to be 10 seconds. A total reactor operation time of 40 years is considered. Table 8.21 gives the total coolant activity and BHP at shutdown with the contributions from the different radionuclides. It is clear that at shutdown, the major contributor to the activity and BHP is ^{209}Pb ($T_{1/2} = 3.25$ h). ^{203}Pb is the major activity contributor between 6 hours and a week after shutdown. The long term activity is contributed by $^{108\text{m}}\text{Ag}$, ^{204}Tl , and ^{205}Pb . ^{210}Po , which is produced from the Bi impurities, is an alpha emitter and volatile and represents a particular concern in LiPb systems. ^{210}Po is the major contributor to the coolant BHP between a week and a year after shutdown. During this period the ^{210}Po BHP values change from 7×10^5 to 1.2×10^5 km^3 of air.

8.3.5 Dose After Shutdown

The dose rate at the back of the shield that results from the gamma decay of the activation products in the chamber materials is given in Fig. 8.15 as a function of time after shutdown. The dose rate after shutdown is quite low (1.43×10^{-5} mrem/hr at shutdown). Notice that the decay dose rate value immediately after shutdown is five orders of magnitude lower than the prompt dose rate during reactor operation.

Table 8.19 Class C Waste Disposal Rating for LIBRA Chamber*

	HT-9 Reflector		Modified HT-9 Reflector	
	Non-Compacted	Compacted	Non-Compacted	Compacted
Blanket	6.07×10^{-6}	9.06×10^{-4}	6.07×10^{-6}	9.06×10^{-4}
Reflector	708	789	0.72	0.8
Shield	2.73×10^{-4}	3.03×10^{-4}	2.73×10^{-4}	3.03×10^{-4}
Reflector and Shield	68	75	0.07	0.08

Table 8.20 Isotopic Contribution to Reflector WDR*

Isotope	WDR	
	Mod. HT-9	HT-9
^{14}C	0.012	0.608
^{59}Ni	6.59×10^{-4}	5.5×10^{-2}
^{63}Ni	1.17×10^{-3}	9.03×10^{-2}
^{94}Nb	0.706	706
^{99}Tc	1.2×10^{-4}	0.446
Total	0.72	708

* A WDR value of less than 1 qualifies that material for Class C waste disposal procedures.

Table 8.21 Coolant Activity and BHP at Shutdown

Isotope	$T_{1/2}$	Activity (Ci)	BHP (km ³ air)
He-6	0.808 s	2.01×10^7	6.70×10^5
Li-8	0.844 s	7.21×10^{-4}	2.40×10^4
F-20	11 s	1.04×10^4	2.28×10^2
Ne-23	37.2 s	3.10×10^3	3.04×10^1
Ar-37	34.8 d	1.27×10^4	1.27×10^{-1}
Cu-62	9.74 m	7.02×10^3	2.34
Cu-64	12.7 h	1.86×10^4	4.65×10^2
Ag-106	24 m	2.17×10^4	7.25×10^2
Ag-106 m	8.5 d	1.12×10^4	1.12×10^5
Ag-108	2.42 m	3.46×10^5	1.73×10^2
Ag-108 m	130 y	6.04×10^3	3.19×10^4
Ag-110	24.6 s	2.64×10^5	3.75×10^1
Ag-110 m	250 d	1.04×10^4	1.37×10^4
Tl-204	3.78 y	1.03×10^5	1.13×10^5
Pb-203	2.17 d	8.31×10^7	1.38×10^6
Pb-205	1.5×10^7 y	1.97×10^3	1.96×10^4
Hg-203	46.6 d	2.30×10^5	1.15×10^5
Hg-205	5.2 m	2.17×10^6	7.23×10^4
Pb-209	3.25 h	2.28×10^8	2.28×10^9
Bi-210	5.01 d	5.73×10^3	2.87×10^4
Po-210	138.4 d	4.44×10^3	7.4×10^5
Total		3.34×10^8	2.283×10^9

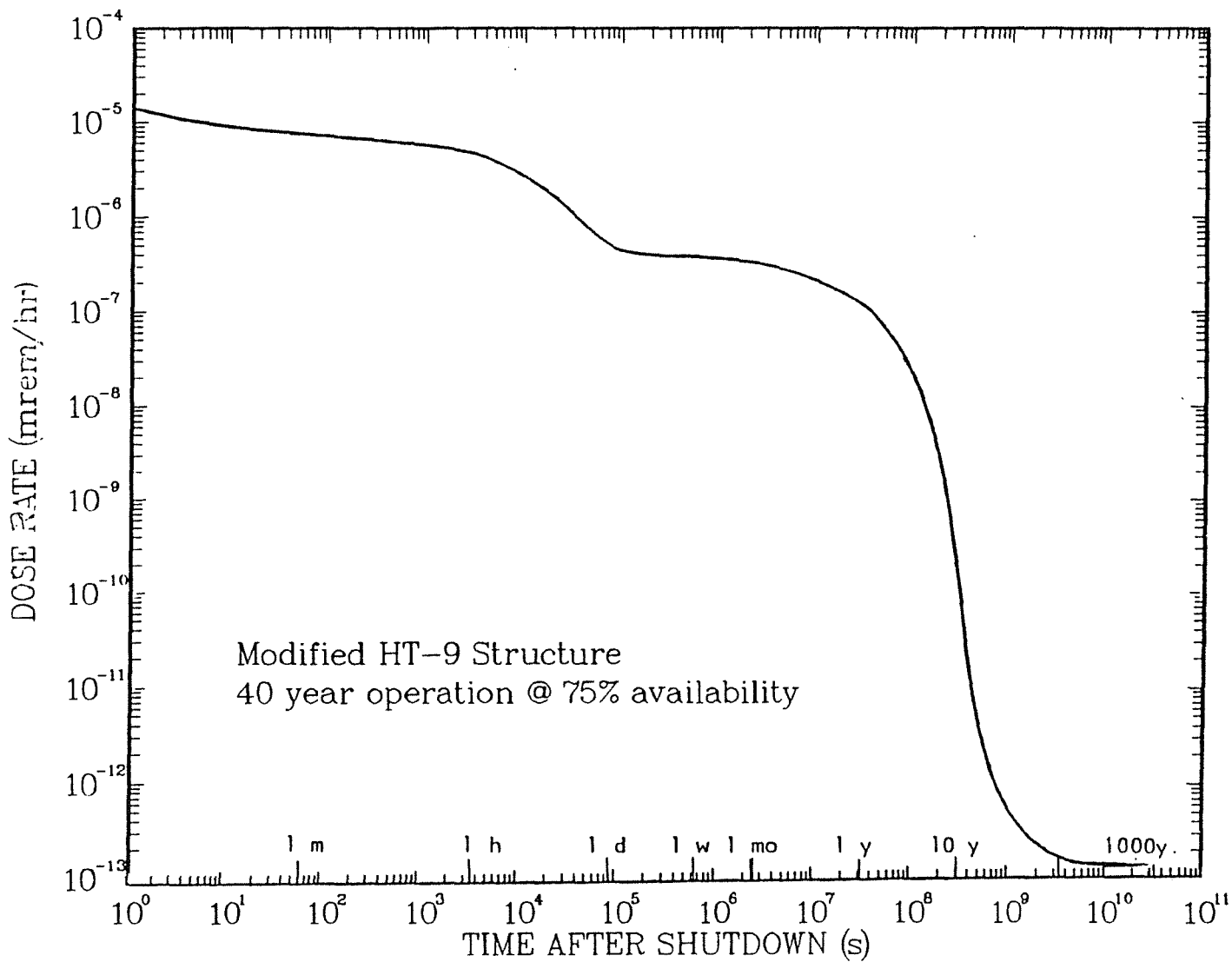


Fig. 8.15. Dose rate at back of shield as a function of time after shutdown.

References for Chapter 8

1. R. O'Dell et al., "User's Manual for ONEDANT: A Code Package for One-Dimensional, Diffusion-Accelerated, Neutral Particle Transport," LA-9184-M, Los Alamos National Laboratory (1982).
2. Judith F. Briesemeister, "MCNP-A General Monte Carlo Code for Neutron and Photon Transport Version 3A," LA-7396-M, Rev. 2, Los Alamos, September 1986.
3. "IMSL Library, Problem-Solving Software System for Mathematical and Statistical Fortran Programming, Edition 9," Revised June 1982, IMSL LIB-0009, Houston, Texas.
4. Gerhard Reyna, "REDUCE, Software for Algebraic Computation," Springer-Verlag, 1987.
5. Anthony C. Hearn, "REDUCE User's Manual," The Rand Corporation, Santa Monica, CA, July 1987.
6. R. MacFarlane, "Nuclear Data Libraries from Los Alamos for Fusion Neutronics Calculations," Trans. Am. Nucl. Soc., 46, 271 (1984).
7. D. Smith et al., "Blanket Comparison and Selection Study - Final Report," ANL/FPP-84-1, Argonne National Laboratory (1984).
8. D. Henderson and O. Yasar, "DKR-ICF: A Radioactivity and Dose Rate Calculation Code Package," University of Wisconsin Fusion Technology Institute Report UWFD-714 (1986).
9. M. Gordinier and R. Howerton, "ACTL: Evaluated Neutron Activation Cross Section Library Evaluation Techniques and Reaction Index," UCRL-50400, Vol. 18 (1978).
10. C.M. Lederer et al., Table of Isotopes, 6th and 7th Editions, Wiley (1967 and 1978).
11. Nuclear Regulatory Commission, 10CFR Part 61, "Licensing Requirements for Land Disposal of Radioactive Waste," Federal Register FR47, 57446 (1982).

9. TRITIUM SYSTEMS

The principal tritium systems considered in LIBRA are the fueling and breeding circuits. In addition, the tritium inventories in the reactor subsystems are identified. Such inventories and locations are required in order to evaluate the potential radiological hazards to the plant personnel and the surrounding environment during routine and off-normal releases of tritium.

9.1 Tritium Fuel Preparation

The fuel targets are prepared in a Target Fabrication Facility which is separated from the reactor hall. The proposed fuel targets consist of a three-layer structure of spherical shells, Fig. 9.1, in which a uniform shell of solid, molecular DT coats the interior surface of a polymeric shell, possibly composed of deuterated methylmethacrylate, which in turn is overcoated with a Pb shell. At the proposed fueling rate of 3 Hz nearly 270,000 targets will need to be fabricated and injected into the reactor cavity per full power day. The mass production of acceptable targets will require the development of relatively simple target fabrication procedures together with many advanced, automated manufacturing processes. On-line quality assurance instrumentation must be developed to assure that the targets meet specification and, also, to detect off-normal operations so that the percentage of rejects is low. Additionally, the quantity of tritium involved in the manufacturing process should be kept as low as possible so that the total on-site tritium inventory is small.

A conceptualized procedure is presented for target fabrication which appears to be amenable to mass production and requires a minimal excess of tritium during the manufacturing process. The process begins with the pre-selection of uniform polymeric shells which have a small entrance hole in each shell. These shells are positioned on trays which are placed into a pass-box which is subsequently evacuated. The trays of shells are then conveyed into a high pressure box containing molecular DT at 23 MPa, Fig. 9.2(a). This pressure is sufficient to fill the cavity of each sphere with 3.2 mg of gaseous DT, 1.28 mg D and 1.92 mg T. A plug of the same polymer as the shell is inserted into each shell, sealing the required fuel inside. The filled shells are transferred to a small box, Fig. 9.2b, in which the atmospheric DT is diluted and replaced with helium at the same pressure and temperature. The transfer box cannot be evacuated at this stage because the plug in the shell is not sufficiently robust to withstand a large differential pressure. The exterior of the shells is relatively free of DT at this stage so

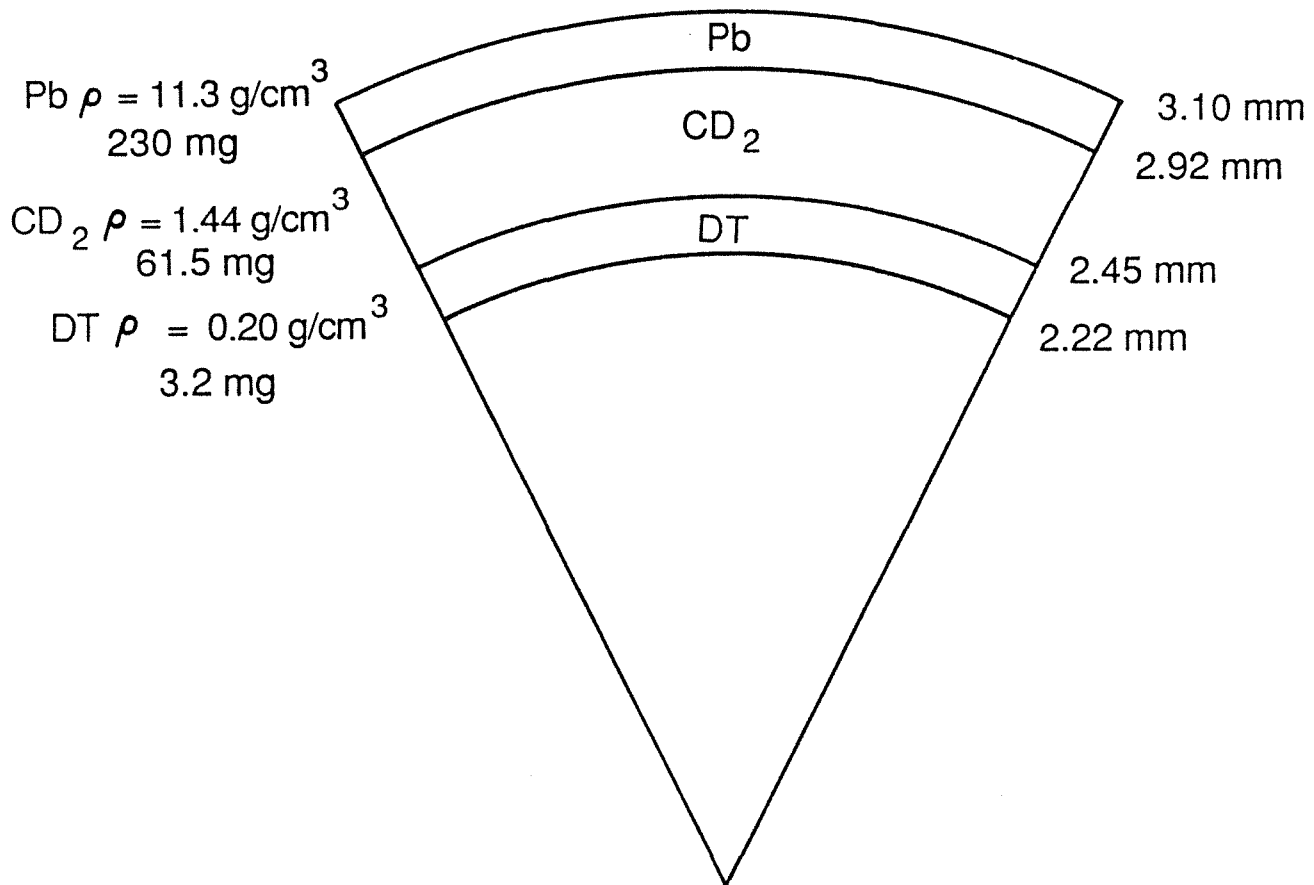


Fig. 9.1. Cross-section of a fabricated target.

Automated Target Production

9-3

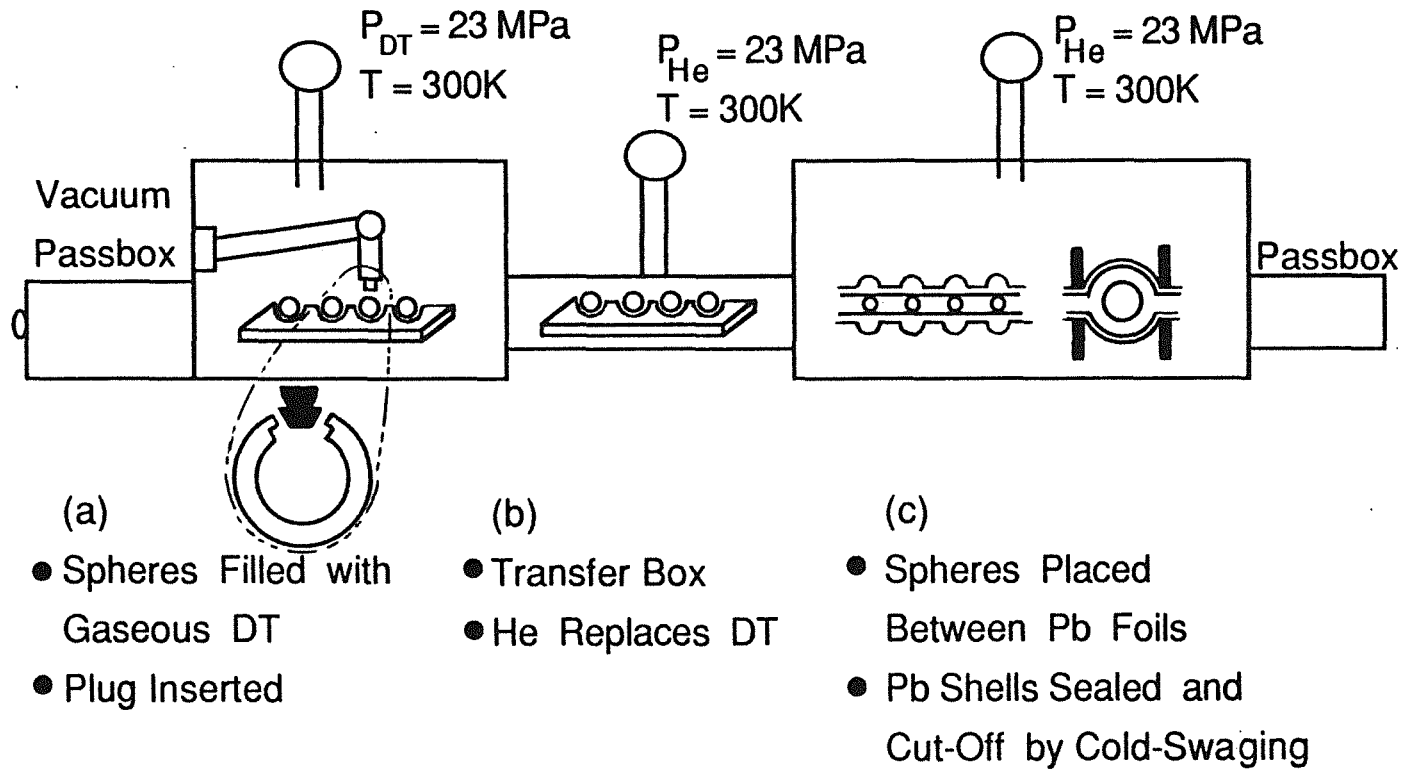
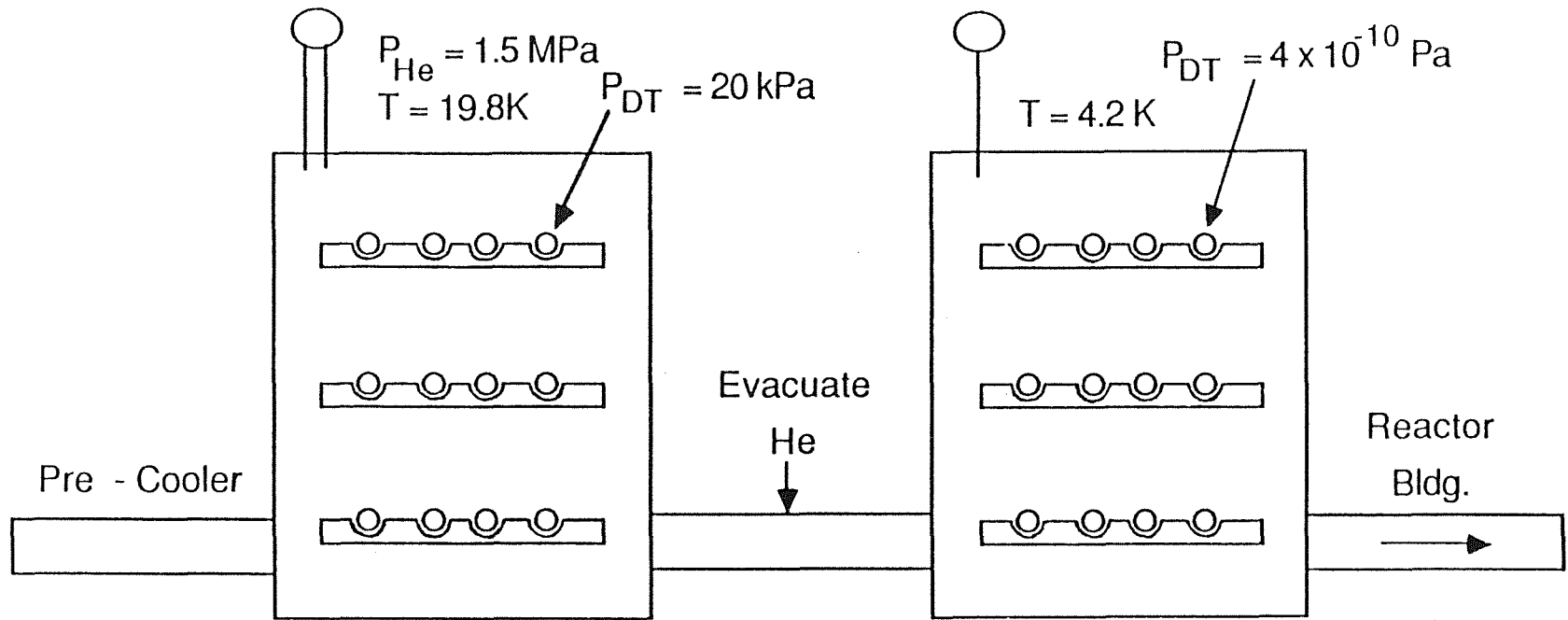


Fig. 9.2. Automated production facility for loading of targets.



(d) He Refrigerator

(e) Target Storage

- 2 Hr. Hold
- Radiation Induced Sublimation of DT Forms Uniform Coating

- One Day Reserve

Fig. 9.2. (Continued) Automated production facility for loading of targets.

that the spheres can be placed on sheets of lead foil, containing a dimple for each sphere, Fig. 9.2(c). A similar Pb foil sheet is placed on top of the spheres. An automated tool is utilized here which cuts off and cold-swages a Pb foil sphere around each polymer shell.

The fabricated shells are next transferred to a helium refrigerator in which the temperature is reduced to the triple point of DT, 19.8 K at 20 kPa. The targets remain at this temperature for ~ 2 hr while a uniform thickness of solid DT forms on the interior of the polymer shell. The uniformity of the fuel coating is caused by the radioactively induced sublimation of the DT.⁽¹⁾ Subsequently, the prepared targets are stored at 4.2 K where the internal pressure of DT is only 4×10^{-10} Pa so that the helium overpressure can be removed before the targets are delivered to the reactor delivery injector. A one-day's supply of fuel targets is maintained, containing ~ 500 g of tritium, which can be utilized in the event of a malfunction in the target factory. Storage of targets for longer than one day is not recommended at this time because the inventory of tritium is increased.

The procedure outlined above requires ~ 2 hr per batch of targets and an inventory of only ~ 134 g of tritium (41 g in the targets and 93 g in the high pressure box). This tritium inventory is much smaller than that required by an alternative scheme, such as gaseous DT permeation through the polymer shell. For such a procedure it is necessary to consider the time required for the permeation of 6.4×10^{-4} moles of DT through the polymer shell and the allowable differential pressure which can be applied to the hollow sphere. Literature values⁽²⁾ indicate that the methylmethacrylate polymer at ~ 25°C has a permeation rate of 1.1×10^{-15} moles $H_2/s \cdot Pa \cdot m$ and a compressive tensile strength of 70 MPa. These values, combined with the dimensions of the shell, Fig. 9.1, indicate that the differential pressure must be < 21 MPa of DT in order to avoid compressive failure. Because of the relatively thick walls of the polymer, buckling-mode failure of the sphere requires a much higher pressure.⁽³⁾ When the DT pressure for permeation is limited to < 21 MPa, the time required to fill each shell with the required amount of DT is ~ 33 hr. The batch size of targets for this process is increased to ~ 360,000 targets and would require an inventory of ~ 775 g of tritium, nearly 6 times larger than the initially described procedure; consequently, the former method would be preferred.

An experimental program will be needed to develop the automated, mass production of targets as described, and will make use of techniques presently being developed for the handling of high pressure tritium gas.⁽⁴⁾ In order to increase target performance, gold foil has been suggested as a replacement for the Pb. If such a substitution were

made, then nearly 102 kg of Au would be required per full power day, representing an investment of \$1.4 million (U.S.). Because of such a large investment, techniques would need to be developed to recover the Au from the liquid LiPb alloy within the reactor cavity.

9.2 Tritium Breeding and Recovery

During full power operations frozen fuel targets, containing 1.28 mg of deuterium and 1.92 mg of tritium, are delivered into the reactor cavity at the rate of 3 Hz. Inside the reactor cavity the liquid alloy, $\text{Li}_{17}\text{Pb}_{83}$, provides both sensible heat removal and tritium breeding. The debris from the target explosion is essentially deposited in the films of the liquid alloy existing on the outer surfaces of the INPORT tubes and on the pool at the bottom of the reactor. The neutrons from the fusion reaction are chiefly deposited in the alloy contained within the INPORT tubes. The fate of the unburned fuel within the cavity and the location of the tritium produced by neutronic reactions must be considered in order to devise a tritium recovery scheme.

During the fusion burn, ~30% of the fuel is consumed; consequently, 70% of the unburned fuel is propelled throughout the cavity with the target debris. Quickly following the fusion burn, the liquid films of the LiPb alloy are heated, initially by x-ray photons, and later by fast particles so that these films vaporize ~7 kg of LiPb. During this rapid heating phase, the helium gas within the cavity expands and approximately 22% of the gas is expelled through the suppression tank. If the unburned fuel is homogeneously distributed, then ~22% of the D+T is also expelled. The majority of the unburned fuel, 78%, remains in the vapor phase during the time in which the LiPb vapor begins to condense. The chemical composition of the condensing vapor is unknown, but it will probably not be the alloy $\text{Li}_{17}\text{Pb}_{83}$. Most likely, the Li atoms will favor the very stable compound Li_7Pb_2 which has a high melting point. Liquid alloys near this composition, Li_7Pb_2 , are known to dissolve significant amounts of hydrogen. The Li atom concentration formed by the vaporization of one kg of $\text{Li}_{17}\text{Pb}_{83}$ is 10^3 times greater than the atomic concentration of D+T from the unburned fuel; therefore, nearly all of the unburned fuel will be scavenged from the reactor cavity by the condensing LiPb droplets and eventually deposited in the pool at the bottom of the cavity. The pool will also contain all of the tritium bred within the cavity. In addition, the D+T expelled from the cavity to the suppression tank should also dissolve in the liquid $\text{Li}_{17}\text{Pb}_{83}$ alloy in this tank. Because this alloy eventually feeds the reactor cavity, tritium recovery of both

the unburned fuel and the bred fuel will be accomplished principally by tritium extraction from the LiPb alloy in the pool, where tritium will accumulate at the rate of 6.45 mg/s. The Tritium Removal System (TRS) is located external to the reactor cavity. The TRS must process sufficient LiPb that it recovers tritium at the rate at which it forms within the reactor cavity, i.e. 6.45 mg/s. The quantity of LiPb that must be processed in the TRS is dependent upon the tritium concentration, which should be as low as reasonably practical in order to keep a small total tritium inventory. Previous studies have indicated that the achievable minimum tritium partial pressure in the alloy is $\sim 1.3 \times 10^{-2}$ Pa, giving a tritium concentration of approximately 1.4×10^{-4} wppm based upon the experimentally determined Sievert's constant.⁽⁵⁾ At this tritium partial pressure, however, the tritium permeation at the steam generator is $\sim 10^5$ times too large to meet acceptable environmental release practices. For this reason, a tritium removal system is also placed in the helium intermediate transfer circuit, Fig. 9.3.

The TRS must process 6.5 Mg/s of the LiPb alloy, approximately the same flow as to the heat exchanger. Vacuum degassing of tritium⁽⁶⁾ is accomplished from small droplets, 240 μm diameter formed by a spray nozzle at the top of an evacuated vessel which is 6 m high by 10 m diameter. The droplets, which fall by gravity after an initial velocity impulse of 1 m/s, require one second to transit the chamber. During this time $\sim 70\%$ of the tritium effuses from the droplets into the evacuated chamber, which is maintained at a pressure of 1.3×10^{-3} Pa so that the tritium concentration of the degassed alloy is ~ 0.4 wppm. The parameters of the two TRS's are given in Table 9.1.

The TRS for the helium heat transfer circuit utilizes oxidation of the tritium and collection of the tritiated oxide on a desiccant. The intermediate heat exchanger will probably be fabricated from a ferritic steel, HT-9, with the LiPb alloy containing tritium on one side. The helium side of the tubes, approximately 1.5 mm thick, will be coated with a thin Pd catalyst layer $\sim 16 \mu\text{m}$ thick.⁽⁷⁾ An oxygen partial pressure is maintained in the He in the range of 10^{-3} to 10 Pa so that the palladium surface is continuously saturated with oxygen atoms. As a result, the tritium atoms are oxidized as they permeate the heat exchanger tubes and are released as tritiated water into the helium. This water is eventually adsorbed on a desiccant. Approximately 1×10^{-4} g/s of tritium permeates the IHX; however, the catalyst is capable of oxidizing a much greater amount, ~ 0.8 g/s of tritium. In the tritium oxide form tritium should not permeate the steam generator and be lost to the environment. The catalyst has been conservatively estimated to be 99.9% efficient so that 0.1% of the tritium may exist as T_2 (or HT). This

TRITIUM REMOVAL SYSTEMS IN LIQUID BREEDER AND HELIUM COOLANT CIRCUITS

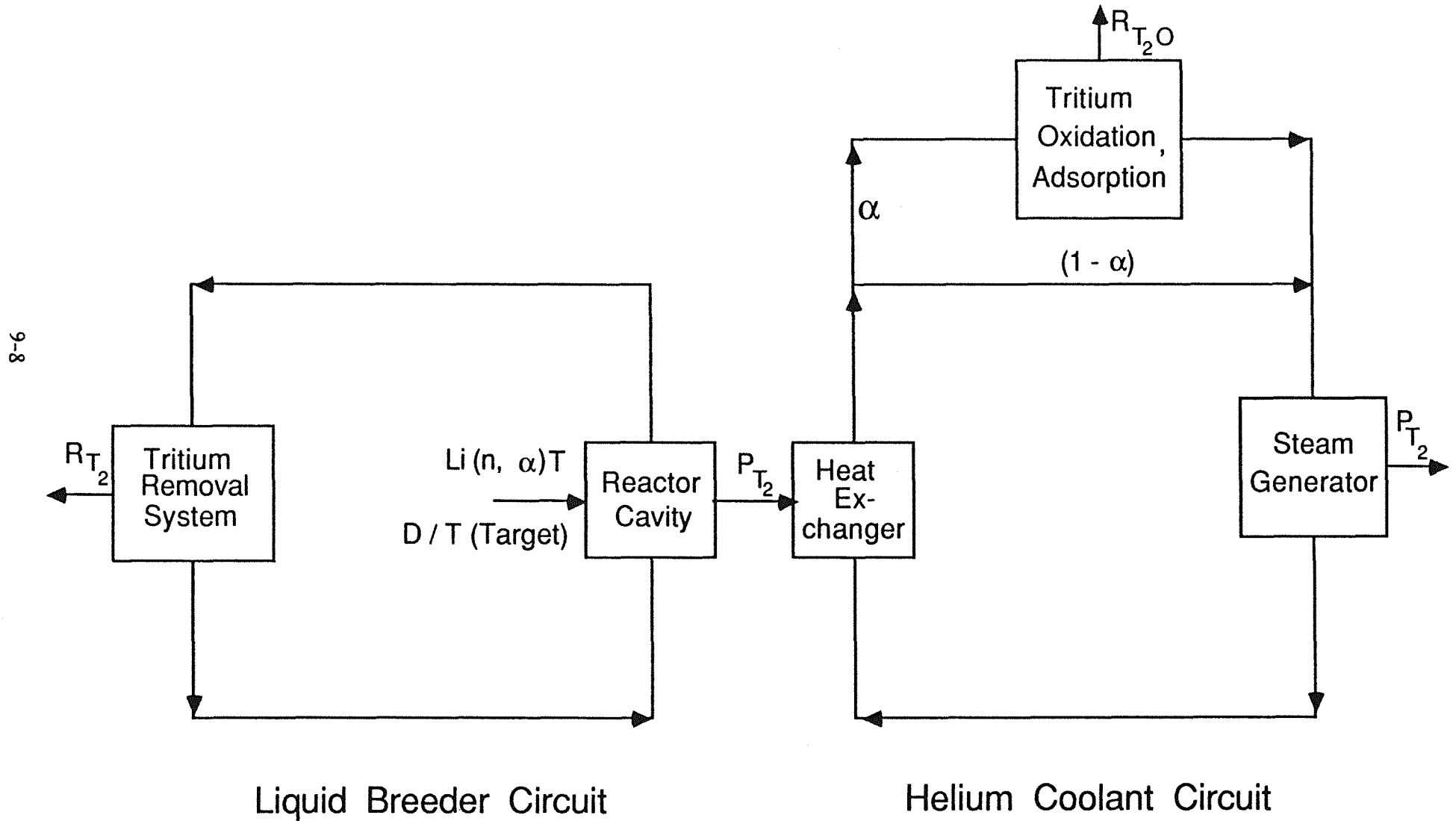


Fig. 9.3. Tritium removal systems for liquid and helium circuits.

Table 9.1 Tritium Removal Systems

Liquid Breeder Alloy

Recovery Technique: Vacuum Degassing of Liquid Droplets

Breeder flow to TRS, m ³ /s	6.5
Tritium pressure at inlet, Pa	1.3 x 10 ⁻²
Tritium conc. at inlet, wppm	1.4 x 10 ⁻⁴
Tritium pressure at outlet, Pa	1.3 x 10 ⁻³
Tritium conc. at outlet, wppm	0.4 x 10 ⁻⁴
Tritium recovery in TRS, g/s	6.45 x 10 ⁻³
Droplet diameter, μm	240
Time of fall, s	1
TRS size, m	10 dia. x 6 ht.
Vacuum port area, m ²	5

Helium Heat Transfer Circuit

Recovery Technique: Catalyzed Oxidation of T₂,
Followed by Adsorption on a Desiccant

Helium flow rate to TRS, kg/s	9 (1% of He flow)
T ₂ O/He, mole fraction	8 x 10 ⁻⁹
T ₂ O pressure, Pa	4 x 10 ⁻²
T ₂ /He, mole fraction	8 x 10 ⁻¹²
T ₂ pressure, Pa	4 x 10 ⁻⁵
Tritium recovery, g/s	1.05 x 10 ⁻⁴

T₂ is oxidized and absorbed on a desiccant when 1% of the He flow is diverted to the TRS. In such a case, T₂ (at a pressure of 4×10^{-5} Pa) will permeate through the SG; however, the SG has an oxide barrier layer on the steam side which is conservatively estimated to decrease the T permeation by a factor of 100. Using these two estimates, we calculate that ~ 18 Ci/d of HTO will accumulate in the steam generator water and be released into the environment. The tritium inventory in the He circuit, existing chiefly as tritiated water, is small, ~ 0.22 g (2200 Ci).

The tritium (containing some H and D impurities) from the TRS's in the Li and the He circuits is sent to a fuel reprocessing building where chemical impurities are removed and the hydrogen isotopes are separated. Only freshly prepared molecular DT (containing little ³He) is then sent to the Target Fabrication Facility.

In addition to the tritium absorbed in the breeder alloy, some tritium dissolves in the SiC fibers of the INPORT tubes. The solubility of tritium in these fibers as a function of the tritium concentration in the alloy has not been determined. The solubility of D₂ gas has been measured in both the alpha and beta forms of SiC powders.⁽⁸⁾ The solubility of D₂ in the beta form increases rapidly below ~ 1000°C while the temperature effect is much smaller for the alpha phase. Examination of the SiC fibers, such as those used in the INPORT tubes, indicates that they contain excess carbon and especially oxygen around the periphery of the fibers.⁽⁹⁾ These observations are consistent with the mode of fabrication of the fibers, e.g. partial oxidation of organosilane polymer fibers. This oxide formation on the fibers should retard the permeation of tritium into the fibers and, by analogy, cause them to behave similarly to the alpha-phase SiC powders. Based upon this analogy, the solubility of tritium in the fibers was estimated to be 9 wppm at 500°C, yielding a total inventory of 150 g of tritium dissolved in the fibers.

9.3 Environmental and Safety Concerns

9.3.1 Tritium Inventory and Pathways

The tritium flow diagram for the complete fuel system is shown schematically in Fig. 9.4 together with the estimated tritium inventories in each of the major subsystems. Because tritium is the most difficult to contain of the radioactive species, its release to either the atmosphere or waterways under routine and accidental conditions must be evaluated, as shown in Table 9.2.

11-6

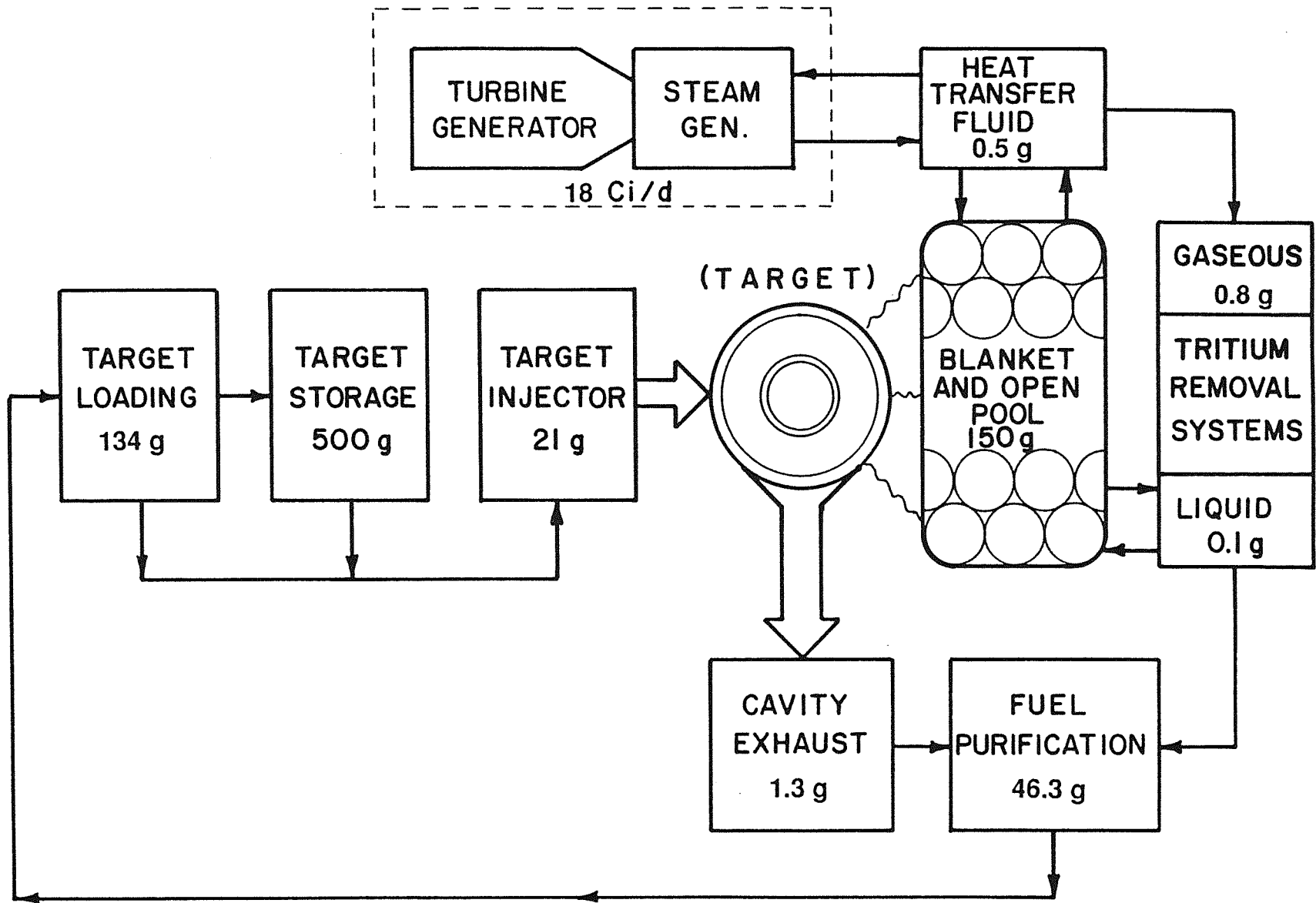


Fig. 9.4. Tritium flow diagram with component tritium inventories.

Table 9.2 Tritium Inventory and Location

<u>Location</u>	<u>System</u>	<u>Tritium</u> g	<u>Routine</u> Ci/d	<u>Accidental</u> T,g
Target Fab. Facility	In-Process	134	5	93
	Storage	500	0	0
Reactor Hall	Fuel Targets	21	0	21
	Breeder Alloy	0.3	2	0.1
	Breeder-TRS	0.1	2	0.1
	INPORT Tubes	150	0	15
	Helium Circuit	0.2	0	0.2
	He-TRS	0.8	1	0.8
	Exhaust	1.3	1	0.6
Fuel Processing	Purification	1.3	1	1.3
	Isotope Separation	45	2	45
Storage (inactive)	Vault	2000	0	0
Steam Generator	Water	0	18	0.2
Total		2854	14 (air) 18 (water)	177.3

Not shown in Fig. 9.4 is the inactive storage, up to several kg of T_2 , absorbed on uranium beds at sub-atmospheric pressure or in shipping containers at near atmospheric pressure. This tritium will be stored in a vault type structure in which water, air and combustible materials must be excluded. This is necessary in order to prevent the generation of heat in the tritium storage containers which would lead to an increase of T_2 pressure and possible leakage of the containers. This vault would contain a dedicated tritium gas waste treatment (TWT) system in which the tritium would be oxidized and the T_2O captured on large desiccant beds for later recycle.

The largest tritium inventory among the active tritium processes, Fig. 9.4, is located in the Target Fabrication Facility, nearly 634 g. Most of this tritium exists in the form of fabricated targets stored at < 19 K. If the refrigeration system failed, then large quantities of gaseous DT would result; consequently, the storage containers for these targets would be connected to large, evacuated tanks by means of a rupture disk so that the overpressure in these storage vessels could be quickly relieved. Additional tanks containing hydrogen getters, such as Zr (Al) or uranium would also be used to adsorb the vented DT. Such procedures have been tested and found to be reliable at TSTA.⁽¹⁰⁾ All the off-gases from the Target Fabrication Facility would flow through a TWT before being released to the atmosphere.

Small quantities of fabricated targets sufficient for one hour of fuel, ~ 21 g of tritium, would be transferred to the fuel injection system which would be located above the roof of the reactor in an isolated compartment in case of tritiated gas release if one or more of the targets would rupture.

The main reactor hall, located within a containment building, would include the reactor cavity and the intermediate heat exchanger for the liquid LiPb/helium. Also within the containment building would be the Tritium Removal Systems for both the liquid metal and the helium heat transfer circuits. Each of these subsystems has a tritium inventory and a routine tritium release. In order to prevent tritium accumulation in the atmosphere within the containment building, each of the process systems will be enclosed within a secondary enclosure containing an inert gas which is routinely circulated to a Tritium Waste Treatment facility for oxidation of the tritium and collection of the tritiated water. Because the exhaust gases of the TWT can be held, monitored and recirculated for further processing, the amount of tritium finally released to the atmosphere can be < 10 Ci/d, as demonstrated by TSTA.⁽¹⁰⁾

In the event of a large release of tritium in the containment building, emergency TWT systems would be activated to circulate the atmosphere and recover the tritium. If the containment structure were not damaged, the exhaust from these TWT's could be recirculated until the tritium concentration was low before being exhausted through a stack. The amount of tritium released will be an economic consideration as well as a radiological health issue based upon the installed and operational costs of the TWT units. The atmosphere chosen for the containment building must also be considered. The use of air is preferred if human maintenance workers are permitted within the building and also, air is a convenient gas for the oxidation of tritium. During operation, however, this atmosphere will be subjected to a significant neutron dose which produces argon-41 and activates the nitrogen to form carbon-14. Both nitrogen and carbon dioxide have been suggested for atmospheres within fusion reactor facilities.⁽¹¹⁾

A major breach of the reactor cavity should be a very unlikely event. More likely would be a rupture of one of the ion beam power feed lines or a leak in the intermediate heat exchanger. The LiPb breeder alloy reacts very slowly with water to release any dissolved tritium. Of greater concern is the rapid heating which would occur if water were mixed with the hot breeder alloy, forming large quantities of steam. In order to prevent such a reaction, helium has been used as the intermediate heat transfer fluid so that the liquid metal cannot come in contact with water in the steam generator. On the other hand, water is used as an insulator for the high voltage lines leading to the ion beam ports. Such ports will need to be examined and modified so as to assure that water cannot enter the beam ports during an accident.

If the accidental ingress of water is excluded from the reactor cavity, then the other accidental possibility is the ingress of air. In such an event the liquid LiPb alloy would form a solid oxide coating which would protect the alloy as it solidifies; consequently, only a small portion of the tritium would be released. Also, the SiC INPORT tubes contain ~ 150 g of tritium which could be oxidized by air; however, SiC reacts very slowly with air and then only at high temperatures. As a result, only a small amount of the tritium dissolved in the fibers should be released.

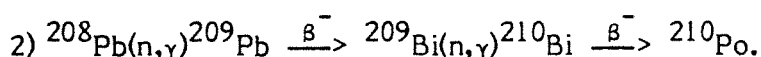
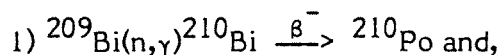
The other major tritium system is the fuel reprocessing system in which the hydrogen isotopes coming from the liquid metal TRS are chemically purified and isotopically separated. This stream should not contain significant impurities because impurities like carbon, nitrogen, oxygen and corrosion products will remain in the liquid metal, which will require routine, on-line removal. The fuel stream will probably be

passed through cryogenic traps to remove any suspended liquid particles and then sent to the cryogenic distillation apparatus which will contain ~ 45 g of tritium in the boiler. The distillation columns with high T₂ concentration will be in a high pressure box. In the event of the loss of refrigeration, these gases will be diverted through a rupture disk to a large evacuated tank which is capable of storing all the gas at atmospheric pressure. These tanks may contain a hydrogen getter material to absorb the tritium and maintain a sub-atmospheric pressure.

9.3.2 Additional Radioactive Products in the Liquid Breeder Alloy

In addition to tritium dissolved in the LiPb alloy other radioactive constituents will be present due to neutron irradiation of the alloy as it transits the reactor. For instance, radioactive isotopes of nickel, iron and chromium, which are corrosion products from the steel piping, will exist in the alloy. These radioactive species will need to be scavenged continuously when a fraction of the flowing heat transfer fluid is diverted to an alloy purification system. Also, a system will be needed to remove the non-metallic impurities such as oxygen, nitrogen and radioactive carbon and silicon dissolved from the INPORT tubes.

A significant quantity of ²¹⁰Po (an alpha-emitter with a 138-day half-life) will be formed from the breeder alloy, ⁽¹²⁾ initially from the impurity ²⁰⁹Bi, and more slowly by the irradiation of ²⁰⁸Pb, as shown by the two reactions,



The ²¹⁰Po production rate has been assessed for the LIBRA study, in Section 8.3.4 and found to be ~ 1 g initially. The vapor pressure of elemental Po is fairly high, ~ 266 Pa at 500°C; consequently, some of it will evaporate from the small droplets formed in the Tritium Removal System. The quantity of Po which effuses from the TRS has been qualitatively assessed in order to determine its impact on the tritium off-gas system and to determine its steady-state concentration in the alloy.

In this assessment, the Po loss rate (radioactive decay plus evaporation) equals the production rate at steady-state, as expressed by the relationship,

$$dm/dt + vnA/RT = P_o \text{ (production) ,} \quad (9.1)$$

where m = mass of Po in the alloy, t = time, v = velocity of Po vapor, n = the gas phase density of Po, $R = 8.3 \text{ m}^3 \cdot \text{Pa/mol} \cdot \text{K}$, and $T = \text{°K}$. The area, A , in this case is the cross-sectional area of the TRS evacuation port, 5 m^2 , which was sized for the tritium gas flow. The Po gas-phase density, n , is a function of the Po partial pressure, P_{Po} , which is determined by the relationship,

$$P_{Po} = (P_{Po}^0)(\gamma)(x) \quad (9.2)$$

where P_{Po}^0 = the vapor pressure of elemental Po (233 Pa at 500°C)

x = the mole fraction Po in the liquid alloy, and

γ = the activity coefficient of Po in the liquid alloy.

By combining Eqns. (9.1) and (9.2) one can determine a value for m , the mass of Po in the liquid alloy, if a value for γ is available. Because the value of γ for Po dissolved in this liquid alloy has not been determined, two extreme values were considered. In one case, an ideal solution ($\gamma = 1$) was assumed which indicated that a steady-state concentration of 0.48 g of Po (~ 2200 Ci) would exist in the alloy after ~ 2 yrs of irradiation and would increase to ~ 2.0 g (8800 Ci) in ~ 30 yrs. An alternative case made use of the fact that the activity coefficient for Po in liquid bismuth had been measured yielding a value of 4×10^{-3} at 500°C. If the Pb alloy, containing a significant Bi impurity, behaved similarly, then the retention of Po in the liquid alloy increases to ~ 8.0 g in two years. This Po retention can be decreased when the size of the vacuum port is increased to its maximum physical size (~ 75 m²), so that the Po concentration is decreased ~ 50%, yielding approximately 4.2 g (18,500 Ci) after 2 yrs and 17 g (74,000 Ci) after ~ 30 yrs.

Because of its short half-life ²¹⁰Po does not pose a long-term waste disposal hazard; however, its prompt release during an accident does pose an airborne radiological concern. The pathways by which Po could be released from the alloy during an accident must be evaluated as well as the fractional release of the Po inventories given above. In addition, the Po hazard to plant personnel tending the TRS systems must be considered. Because of the volatile nature of Po it would probably be collected on cryogenic filters installed in the TRS off-gas ducts. Such filters would collect between 7 and 15 g (32,500 to 75,000 Ci) of ²¹⁰Po per year, depending on the value of the activity coefficient. These filters would need to be safely removed and stored.

9.4 Environmental Analysis

9.4.1 Tritium Release During Normal Operation

Release rates of tritium estimated for normal operation of the LIBRA plant are given in Table 9.2. On the basis of the calculational procedure described in the national German guidelines,⁽¹³⁾ the committed effective dose equivalents due to airborne and liquid effluents have been calculated for the most exposed individual (about 100 m distance from the site).⁽¹⁴⁾ For the dose assessments of discharges to the atmosphere, meteorological data measured at Karlsruhe, FRG, have been used; in the case of liquid effluents, an average flow rate for the river water of $1000 \text{ m}^3/\text{s}$ was assumed. Because of the predominant contribution of the wet deposition processes to radiation exposure, releases from 100 m and 200 m stacks give nearly the same dose values. The results are shown in Table 9.3. The estimated doses are well below the present limit of $3 \cdot 10^{-4} \text{ Sv/y}$ * prescribed by the German radiation protection regulations. They decrease with growing distance and are in the range of 10^{-6} Sv/y at about 1 km from the site.

For comparison, radiation doses estimated on a $1 \text{ GWe} \cdot \text{y}$ basis for a typical pressurized water reactor (PWR) and a respective reprocessing plant are quoted.⁽¹⁵⁾ Whereas the LIBRA plant will release tritium only, additional radionuclides, e.g. radioactive noble gases (Kr, Xe) and aerosols (fission and activation products) must be accounted for in the case of the PWR and the reprocessing plant. For a 100 m stack, the committed effective dose equivalent due to gaseous and liquid effluents during normal operation of a PWR at 1 km distance is about $1.5 \cdot 10^{-6} \text{ Sv}/(\text{GWe} \cdot \text{y})$; the corresponding value for a reprocessing plant (200 m stack) is about $2.5 \cdot 10^{-7} \text{ Sv}/(\text{GWe} \cdot \text{y})$. It should be recalled that the results for the PWR and its respective reprocessing plant are based on realistic (measured) data, whereas the estimates for the LIBRA plant depend upon the assumptions made in the source term calculations.

9.4.2 Accidental Releases of Radioactivity

Licensing regulations will require the consequence analysis of radioactivity release from the reactor plant to the environment. This analysis will have to be performed following through all possible accident sequences which can lead to major radioactivity releases from the plant.

* $1 \text{ Sv/y} = 11.4 \text{ mRem/hr}$

Potential accidental releases of tritium from the LIBRA plant are listed in Table 9.2. However, not all T-releases listed in this table are considered to occur at the same time. Therefore, as an example for the consequence analysis a puff release (2 h) of 100 g tritium in the form of HTO ($\hat{=} 10^6$ Ci) is assumed. The radiation dose an individual receives from a puff release at a certain distance from the plant depends on its position relative to the radioactive plume, the release height and the meteorological conditions (e.g. wind speed v , wind direction, diffusion category DC). The committed effective dose equivalents have been calculated for the activity release mentioned above at a height of 50 m during the day for two different weather conditions (DC = D, $v = 5$ m/s, no rain; DC = F, $v = 2$ m/s, no rain). The new computer program UFOTRI for assessing the offsite consequences from accidental tritium releases has been applied.⁽¹⁶⁾ The exposure pathways considered are internal exposure via inhalation (including reemission and skin absorption) and ingestion of contaminated foodstuffs. In Figures 9.5 and 9.6, the dose estimates under the centerline of the plume are presented as a function of distance from the plant and for each exposure pathway separately. In both cases, the ingestion dose is a factor of 3-4 higher than the inhalation dose. Dependent on the dispersion conditions, the maximum dose values are calculated at about 300 m and 2 km from the site, respectively; they do not exceed about $5 \cdot 10^{-3}$ Sv. If the same activity release is assumed in the form of HT, the corresponding dose values are a factor of about 10 smaller.⁽¹⁷⁾

Table 9.3 Tritium Release During Normal Operation of the LIBRA Plant and Resulting Doses of the Most Exposed Individual

	Release Rate [Ci/d]	Committed Effective Dose Equivalent [Sv]
Airborne*	14	10^{-5}
Liquid*	18	$5 \cdot 10^{-7}$

*Tritium release in the form of HTO

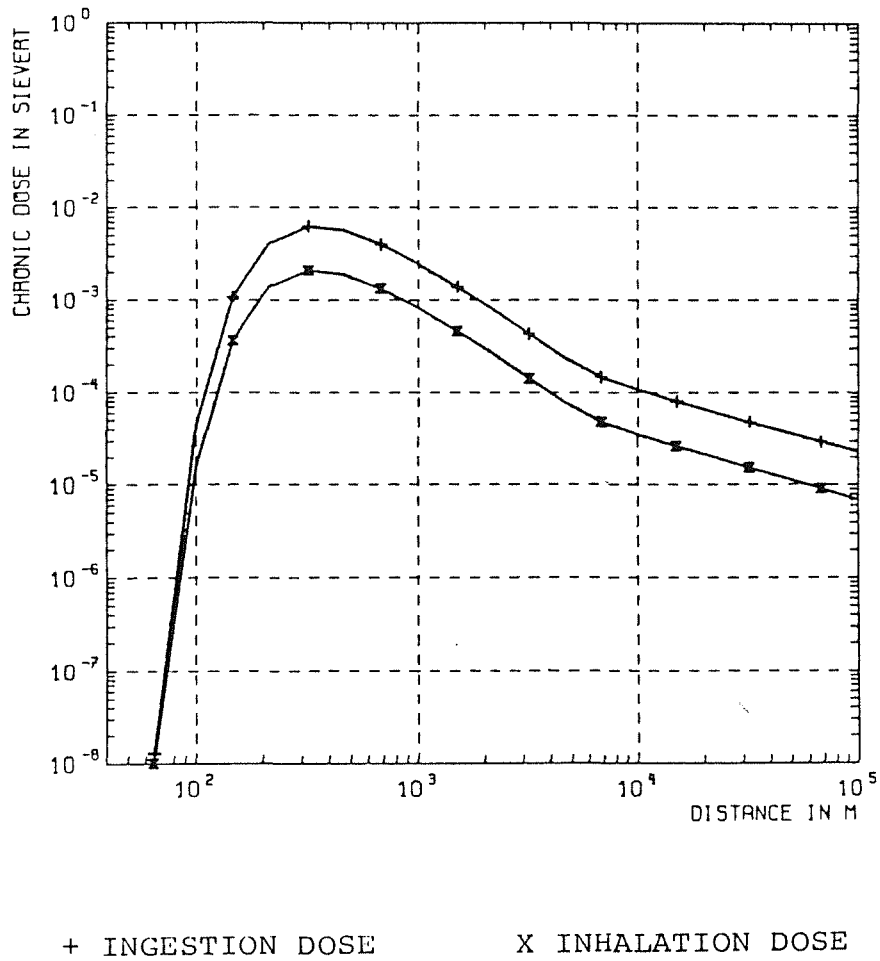


Fig. 9.5. Committed effective dose equivalent under plume centerline (100 g HTO, diffusion category D, wind velocity 5 m/s).

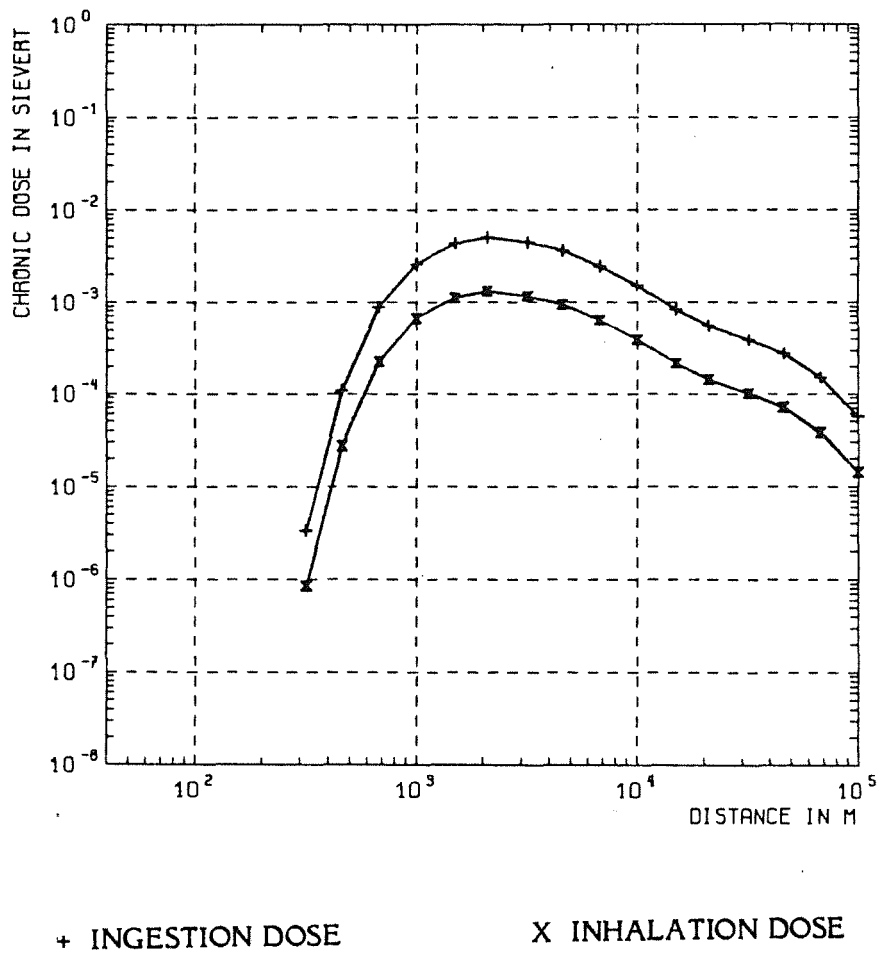


Fig. 9.6. Committed effective dose equivalent under plume centerline (100 g HTO, diffusion category F, wind velocity 2 m/s).

References for Chapter 9

1. J.K. Hoffer and L.R. Foreman, "Radioactively Induced Sublimation in Solid Tritium," *Phys. Rev. Letters*, 60, 1310 (1988).
2. W.J. Roff, J.R. Scott and J. Pacette, Handbook of Common Polymers, CRC Press, Cleveland, 1971.
3. J.H. Campbell, J.Z. Grens, J.F. Poco and B.H. Ives, "Preparation and Properties of Polyvinyl Alcohol Microspheres," Lawrence Livermore National Lab, UCRL-53750 (1986).
4. S.W. Wilson, et al., "A New Glove-Box System for a High Pressure Tritium Pump," *Fusion Tech.*, 14, 1005 (1988).
5. Y.C. Chan and E. Veleckis, "A Thermodynamic Investigation of Dilute Solutions of Hydrogen in Liquid LiPb Alloys," *J.Nuclear Materials*, 122 & 123, 935 (1984).
6. K.E. Plute, E.M. Larsen and L.J. Wittenberg, "Tritium Recovery from Liquid Lithium-Lead by Vacuum Degassing," *Nuclear Tech./Fusion*, 4, 407 (1983).
7. C. Hsu and R.E. Buxbaum, "Palladium-Catalyzed Oxidative Diffusion for Tritium Extraction from Breeder-Blanket Fluids at Low Concentrations," *J. Nuclear Materials*, 141-143, 238 (1986).
8. R.A. Causey, J.D. Fowler, C. Ravanbakht, T.S. Elleman, and K. Verghese, "Hydrogen Diffusion and Solubility in SiC," *J.Amer. Ceramic Soc.*, 61, 221 (1978).
9. Y-W. Chang, A. Zangvil and J. Lipowitz, "Characterization of Si, C, N, O Fibers by Analytical STEM and Scanning Auger Techniques", *Silicon Carbide Symposium 1987, Proceedings American Ceramic Society, Columbus, Ohio*, pp. 435-443 (1989).
10. J.L. Anderson, et al., "Experience of TSTA Milestone Runs with 100 Gram-Level of Tritium", *Fusion Technology* 14, 2, Part 2A, pp. 438-443 (Sept. 1988).
11. J.B. Cannon (ed.), "Background Information and Technical Assessment of Environmental Implications of Magnetic Fusion Energy", Chapter 6: Occupational Health and Safety, United States Department of Energy, Office of Fusion Energy Report DOE/ER-0170 (Aug. 1983).
12. N.J. Hoffman, K.A. Murray, J.A. Blink, W.R. Meir, and W.F. Vogelsang, "Polonium Aspects Associated With the Use of Lead-Lithium Blankets in Fusion Applications," *Fusion Tech.*, 8, 1376 (1985).
13. Bundesministerium des Inneren, *Allgemeine Berechnungsgrundlagen für die Strahlenexposition bei radioaktiven Ableitungen mit der Abluft oder in Oberflächengewässer vom 1.7.1988.*
14. P. Handge, Gesellschaft für Reaktorsicherheit (GRS) mbH, Köln, personal communication, 15 April 1989.
15. G. Kessler, *Nuclear Fission Reactors*, Chapter 8, Springer-Verlag, Wien, 1983, ISBN 3-211-81713-1.

16. W. Raskob, "UFOTRI: Program for Assessing the Offsite Consequences from Accidental Tritium Releases", KfK 4605, Kernforschungszentrum Karlsruhe (1990).
17. J. Ehrhardt and W. Raskob, Private Communication, Kernforschungszentrum Karlsruhe, April 1989.

10. POWER CONVERSION AND BALANCE OF PLANT

10.1 LIBRA Power Cycle

The power cycle in LIBRA utilizes a He gas intermediate loop to transfer the energy from the LiPb to the steam. There are several advantages for this kind of an arrangement. Two of the most obvious are:

1. Eliminates the possibility of a LiPb/water interaction
2. Eliminates tritium diffusion into the steam.

There are three LiPb/He heat exchangers built into the base of the target chamber. As the LiPb flows down from the bottom pool through the perforated plate, it enters into three separate parts, each leading to a heat exchanger. Once in the heat exchanger enclosure, it flows radially outward along the upper tube bundle shroud, then enters the tube bundle zone through an oblong orifice as shown in Fig. 10.1. From here the LiPb flows between the tubes radially inward, then makes a U turn and flows radially outward to exit the heat exchanger at the bottom. The He gas at 8 MPa is confined to the tubes in the heat exchanger. It enters the heat exchanger through the bottom inlet orifice, flows radially inward, makes a U bend and flows radially outward exiting through the upper outlet orifice. In this configuration a true counterflow heat exchange is achieved between the LiPb and the He gas. Each heat exchanger has a tube bundle which is 2 m in diameter and has a heat transfer area of 2210 m². The average He gas velocity is 80 m/s. The He gas enters at 300°C and exits at 470°C giving a log mean temperature difference with the LiPb of 35°C.

The three heat exchangers in the base of the target chamber are designed for easy removal of the tube bundle for maintenance. Figure 10.1 shows the cross section of one heat exchanger and the perspective of another. The cross-sectional view shows how the tube bundle can be slid out from the base of the chamber. It should be mentioned here that some leakage of He gas from the heat exchangers is tolerable. Gas would be swept out of the chamber by the flowing LiPb ending up at a free surface. Gas that diffuses into the chamber would have no adverse effect on the operation of the reactor, since it is already filled with He gas.

A single reheat stage superheated steam power cycle is proposed, with the steam temperature of 430°C and steam pressure 11 MPa. The steam mass flow rate is 2.3×10^6 kg/hr and the steam generator surface area is 6×10^3 m². At these conditions the gross thermal efficiency is 38%.

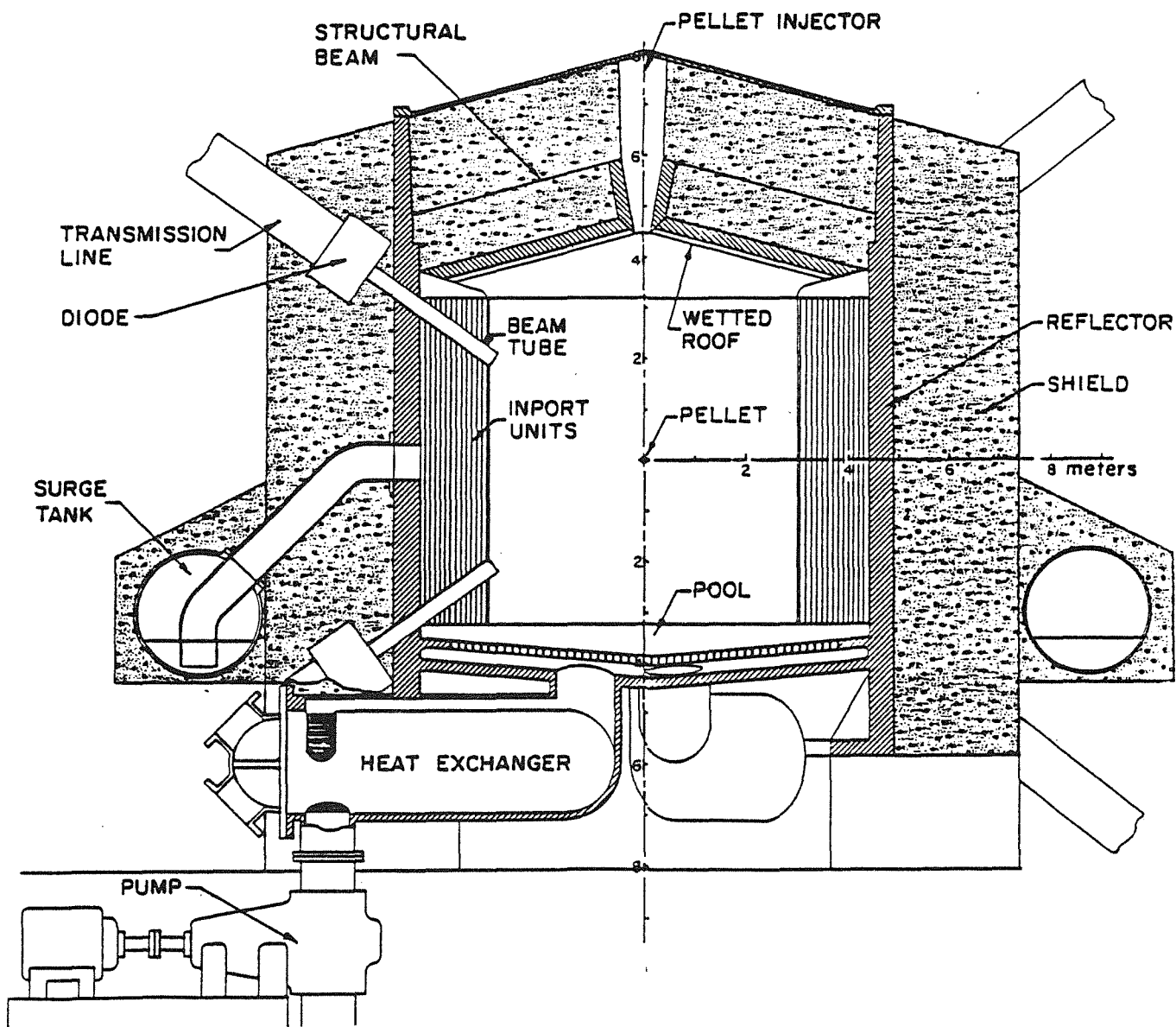


Fig. 10.1. LIBRA reaction chamber.

Figure 10.2 is a power flow diagram for LIBRA. The figure shows that a total of 960 MW of energy is released from the target, of which 19.9 MW is lost in endoergic losses. The amount in x-rays and ion debris is 286.6 MW leaving a total of 653.5 MW from gammas and neutrons. A blanket energy multiplication of 1.28 is applied to the gamma and neutron fraction. The total thermal energy, including LiPb pump heating and magnetic beam insulation losses (37.4 MW), is equal to 1160.5 MW_{th}. The total electric power generated at a 38% gross efficiency is 441 MWe, of which 110 MWe are needed for operating the plant. A total of 331 MWe is available for sale and distribution giving an overall net plant efficiency of 28.5%. Table 10.1 gives the power cycle parameters for LIBRA.

Table 10.1 Power Cycle Parameters

Type of steam cycle	Superheated steam
Steam temperature (°C)	430
Steam pressure (MPa)	11
Steam mass flow rate (kg/hr)	2.3×10^6
Feedwater temperature (°C)	300
Reheat temperature (°C)	430
Steam generator surface area (m ²)	6×10^3
Gross thermal conversion efficiency (%)	38
Gross electric power generation (MWe)	441
Net plant efficiency (%)	28.5
Net electric power generation (MWe)	331

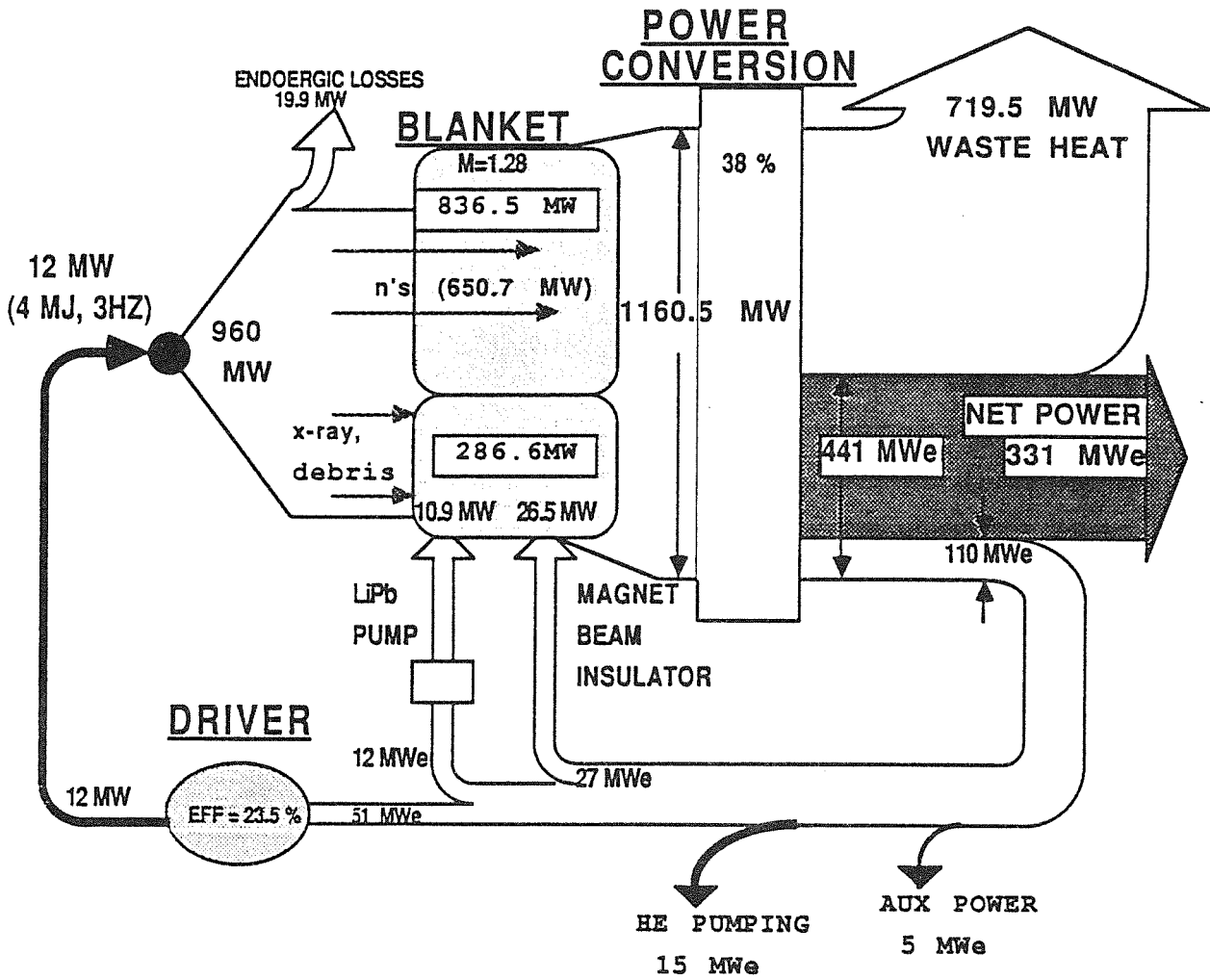


Fig. 10.2. Power flow diagram for LIBRA.

11. COST ESTIMATE

A preliminary costing analysis for the LIBRA reactor has been performed using the FUSCOST code,⁽¹⁾ a PC-based menu driven program for economic analysis of fusion facilities. The scaling laws used in this code are taken from the latest available up-to-date information from both MFE and ICF sources.^(2,3,4,5) The scaling laws calculate the direct cost of the plant equipment, given the reactor parameters. The economic model then calculates all the other components of the cost such as total direct costs, indirect costs, total capital cost, operating costs and the cost of electricity. Inputs to the economic model such as inflation and escalation rates, interest rates, construction time etc. are provided by the user of the code.

11.1 Scaling Laws

As in most ICF reactor systems, the reactor direct costs are dominated by the cost of the driver. The LIBRA driver cost was estimated in Section 2.11. For a 4 MJ driver utilizing ignitron switches, the cost for 3 Hz rep. rate system is 443.3 M\$ (1989) or 426.3 M\$ (1988). For 12 Hz it is 470 M\$ (1988). Following this weak dependence on repetition rate and using a 0.8 power dependence for scaling energy on target, we derive the following expression for the driver cost:

$$C_d = (410.8 + 5.1724 \text{ CRR}) \left(\frac{E_d}{4} \right)^{0.8} \quad (1989 \text{ M\$})$$

where CRR is the rep. rate and E_d is the driver energy on target. It is useful to compare this estimate with that recommended for use in SAFIRE, a Systems Analysis Code for ICF Reactor Economics.⁽⁵⁾ The recommended scaling law in 1987\$ is:

$$C_d = 75 \left(\frac{E_d}{1 - 0.075R} \right)^{0.8} \quad (1987 \text{ M\$})$$

where R is the distance from the diode to the target. If this scaling law is inflated to 1988, using the Consumer Price Index, the above estimate becomes:

$$C_d = 78.1 \left(\frac{E_d}{1 - 0.075R} \right)^{0.8} \quad (1988 \text{ M\$})$$

The driver cost estimated for LIBRA by Pulse Sciences Inc. is 443.3 M\$ (1989) and by the SAFIRE code 382 M\$. We will use the PSI driver costs, since they are more firmly grounded in present day technology (HERMES-III), and use SAFIRE for obtaining all the other costs.

Table 11.1 gives the scaling laws used in calculating some of the other major cost items.

Table 11.1. Some Pertinent Scaling Laws (1987\$)*

Turbine plant equipment	$\$0.35\text{M} (P_{th})^{0.8}$
Electric plant equipment	$\$5.7\text{M} (P_g)^{0.2}(P_{in})^{0.3}$
Miscellaneous plant equipment	$\$5.05\text{M} (P_g)^{0.3}$
Liquid metal pumps	$\$27.45\text{M} (m/3.2)^{0.8}$
Liquid metal heat exchanger	$\$81.2\text{M} (P_{th}/2081)$
Maintenance equipment	$\$4.1\text{M} (P_{th})^{0.3}$
Instrumentation and control	$\$2.52\text{M} (P_{th})^{0.3}$
Heat rejection	$\$145\text{k} (P_g)^{0.8}$
Reactor building	$\$3.8\text{k}(V)^{0.8}$
Tritium building	$\$4.96\text{k}(V)^{0.8}$
Maintenance building	$\$1.8\text{k} (V)^{0.7}$
Radwaste building	$\$4.96\text{k} (V)^{0.8}$

*Scaled to 1988\$ by Consumer Price Index factor, 1.041

The units used are:

- P_{th} - total thermal power (MW)
- P_g - total gross electric power (MW)
- P_{in} - driver input power (MW)
- m - mass flow rate (kg/hr)
- V - volume in m³
- M - million
- k - thousand

11.2 Unit Costs

The most relevant unit costs of materials are given in Table 11.2:

Table 11.2 Relevant Material Unit Costs (1987\$)*

Fabricated SiC tubes	$\$950/\text{kg}$
Fabricated SiC roof modules	$\$1900/\text{kg}$
20% ⁶ Li enriched Li ₁₇ Pb ₈₃	$\$12/\text{kg}$
Fabricated steel	$\$30/\text{kg}$
Concrete for shield	$\$1000/\text{m}^3$

*Scaled to 1988\$ by Consumer Price Index factor, 1.041

11.3 Target Costs

For the reference design we have assumed a target cost of 18¢/target based on reference [7]. In this report Pendergrass et al. estimate the cost of a single shell direct drive target as ranging from 27¢/target for a pulse rep-rate of 3 Hz to 18¢/target for a rep-rate of 20 Hz. In a mature fusion economy where the target factory will not be a captive unit of a power plant, it is reasonable to assume that a factory with many assembly lines will produce targets consistent with a rep-rate of 20 Hz, thus providing targets for several ICF power plants simultaneously.

11.4 Economic Model

Once the total direct costs (TDC) are determined, the economic model then computes the remaining quantities of interest.^(8,9) These are the total overnight costs, total capital costs, the levelized annual operating cost, the annual operation and maintenance cost, the annual fuel cost and the cost of electricity. These quantities are computed in both constant and current dollar modes. For LIBRA we will report only the constant dollar values to be able to compare them with other reactor studies which also use the constant dollar mode.

The total overnight cost is the sum of the direct and indirect costs, thus the interest on the capital as well as inflation and escalation are not included. Total indirect costs are obtained by multiplying the total direct costs by the home office factor, field office factor, and owner's cost factor.

The levelized annual financial outlay includes the cost of capital, the cost of fuel (target costs) and operation and maintenance costs. The cost of capital is the product of the fixed charge rate and the total capital cost. The fixed charge rate is a function of many factors.⁽⁹⁾ Of course the main factor is the interest rate, but it also includes the salvage fraction at end of life, income tax rate, property tax rate, investment tax credit, annual interim replacement fraction, total plant life, construction time, escalation and inflation rates and finally, depreciation time. The cost of fuel is simply the target cost. Finally, operation and maintenance is taken as 3% of the total overnight cost, a value which is fairly representative of current nuclear power plants.

The cost of electricity is then simply the levelized annual cost divided by the net power generated which in the case of LIBRA at an availability of 75% is 2.138×10^9 kWh. Table 11.3 gives the parameters used in the economic model.

11.5 Capital Costs and Cost of Electricity

Table 11.4 gives the total direct costs in 1988 dollars, broken into the major accounts. As might be expected, the driver cost dominates, accounting for 46% of the total. The reactor cavity and some of the balance of plant accounts, such as the turbine plant, buildings, heat transfer and electric plant are also large cost items. Figure 11.1 is a bar chart of the total direct costs.

Table 11.3. Parameters Used in Economic Model

Plant availability (%)	75
Years of accelerated tax depreciation	10
General inflation rate (%)	6
Cost escalation rate, average (%)	6
Construction time in years	6
Plant life in years	30
Construction factor (%)	10
Home office factor (%)	10
Field office factor (%)	10
Owner's cost factor (%)	5
Rate of return on common stock (%)	14
Fraction of capital from common stock (%)	40
Rate of return on preferred stock (%)	11
Fraction of capital from preferred stock (%)	10
Interest rate on capital borrowed (%)	10
Fraction of capital borrowed (%)	50
Investment tax credit rate (%)	8
Property tax rate (%)	2
Levelized interim replacement cost fraction (%)	1

Table 11.4. LIBRA Total Direct Costs (\$M 1988)

	<u>Costs From (SAFIRE) Code</u>
Driver (PSI Based)	426
Turbine plant	97
Reactor chamber	82
Buildings	78
Heat transfer equipment	75
Electric plant	57
Maintenance equipment	34
Miscellaneous plant	31
Instrumentation and control	20
Fuel handling equipment	20
Heat rejection	16
Cost of land acquisition	<u>5</u>
Total Direct Costs	941

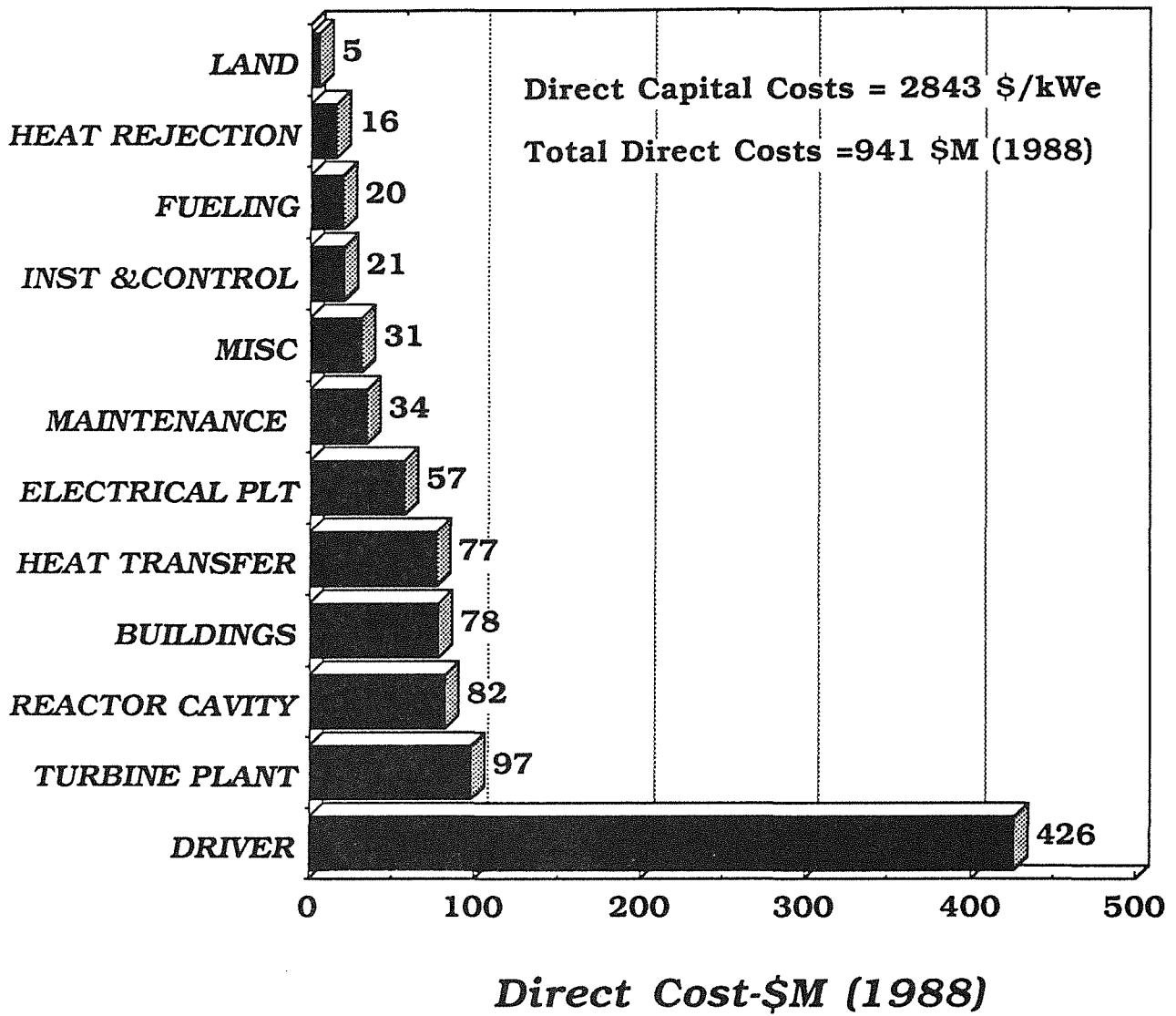


Figure 11.1. Total direct capital costs for LIBRA.

The total direct unit cost for LIBRA is \$2894/kWe as estimated by PSI and \$2779/kWe as estimated by SAFIRE. It is interesting to compare the LIBRA direct unit cost with those calculated for other fusion reactor designs performed over the past 15 years and normalized to 1988 dollars. Figure 11.2 shows the LIBRA cost along with two heavy ion beam systems, HIBALL-I and HIBALL-II as well as five tokamak confinement devices. The heavy ion beam systems were 4000 MWe and in general the tokamak systems were in the 1000 MWe or higher range. The point to be made is that the LIBRA costs are slightly higher than the others in spite of the fact that it is only producing 331 MWe of electricity. Economy of scale will reduce the LIBRA direct unit cost if the reactor is designed to be of the 1000 MWe range (see Section 11.6).

Table 11.5 gives the remaining costs described in the economic mode.

Table 11.5 Summary of Cost Parameters for LIBRA (331 MWe)

	(1988\$)	
	<u>\$M</u>	<u>\$/kWe</u>
Total Direct Capital Cost	941	2843
Total Indirect Capital Cost	329	-
Total Overnight Costs	1270	3837
Time Related Costs	384	-
Total Capital Cost	1654	4997
	<u>\$M/y</u>	<u>mills/kWh</u>
Annualized Fuel Costs	13	-
Annualized O&M Costs	39	-
Annualized Cost of Capital	141	-
Total Annualized Costs	193	-
Total Cost of Electricity	-	88.7

The cost of electricity (COE) is calculated from the levelized annual cost:

$$\text{COE} = \frac{193 \times 10^9 \text{ mills}}{(331 \times 10)^3 \text{ kWe} \frac{8760 \text{ hours}}{\text{year}} (0.75)}$$

$$= 88.7 \text{ mills/kWh.}$$

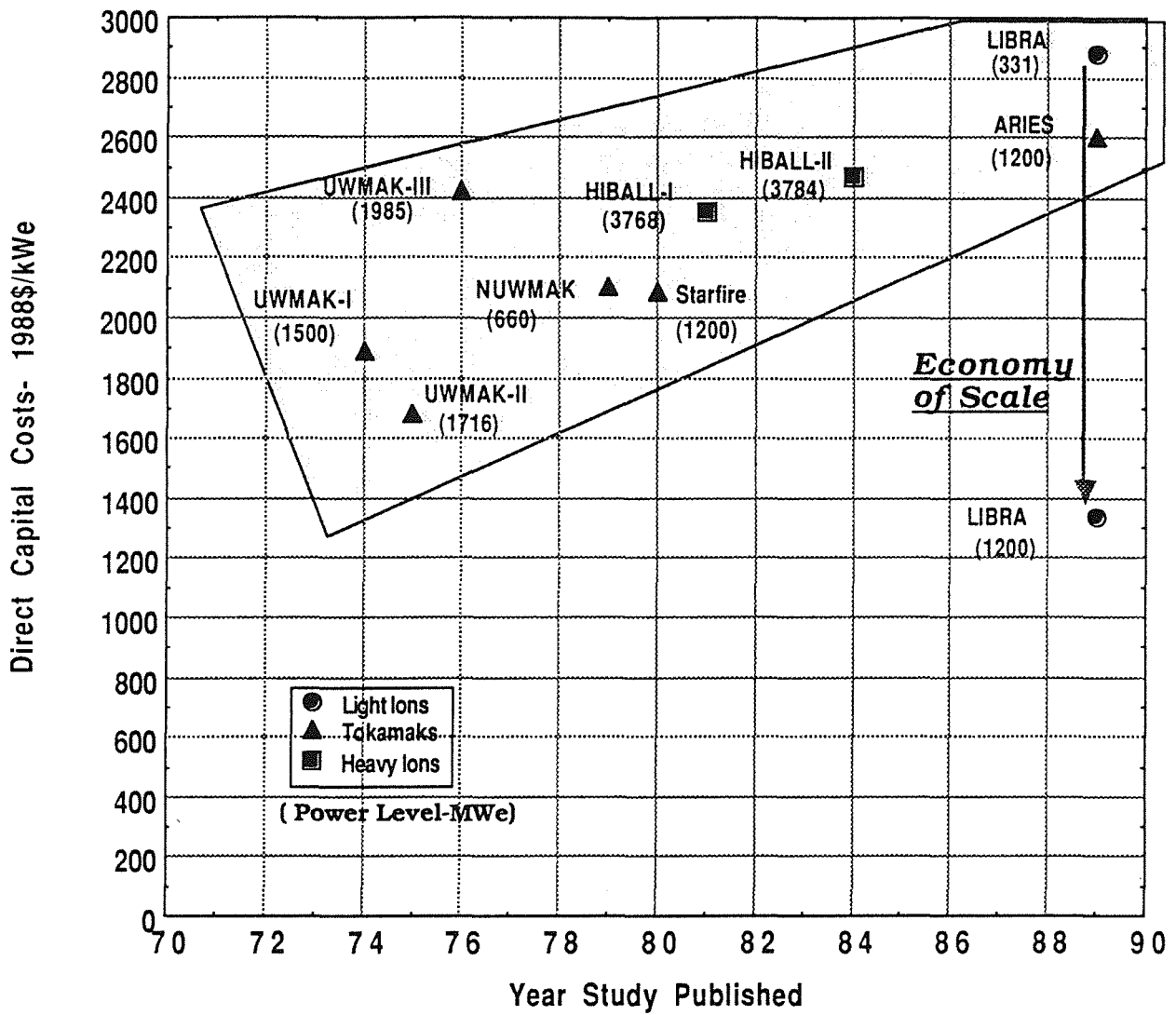


Figure 11.2. Direct capital costs of recent full scale commercial fusion reactors.

It is interesting to determine the COE sensitivity to the cost of targets. For example, if the cost of targets doubles to 36¢/target, the COE rises from 88.7 to 96 mills/kWh, an increase of only 8%.

11.6 Economic Implications of Scaling LIBRA from 330-1200 MWe

It is well known that economy of scale will reduce the cost of electricity (COE) as the power output is increased. One of the problems with fusion, both magnetic and inertial, is the inability to produce low power systems with good economics, at least in the presently envisioned embodiments. Among the inertial confinement concepts, the light ion beams have a definite edge over lasers and heavy ion beams to produce power at power levels of < 1000 MWe while maintaining some economic competitiveness. At 331 MWe, the net power output of LIBRA, the COE is 88.7 mills/kWh and the unit direct cost is 2843 \$/kW when costed in constant 1988 dollars. In this section we have scaled LIBRA up from 331 MWe to a nominal 1200 MWe level by invoking several scaleup scenarios. We have selected five scenarios for presentation and these will be discussed in the next several paragraphs, as well as modifications to accommodate the increased power load on the reactor chamber.

11.6.1 Reactor Chamber Modifications

A scaleup in the power output by a factor of 3.6 requires concomitant modifications in the chamber design. These changes fall into two categories:

1. Increased fluence necessitates more protection for the permanent reflector wall.
2. Higher power requires increased LiPb flow within the cavity.

In order for the permanent reflector wall to survive the added fluence of a factor of 3.6 by the reactor end of life, the effective thickness of the LiPb in the INPORT unit zone must be increased by 10 cm. However, since the distance from the target to the driver diodes cannot be increased beyond the nominal 6 m, the distance from the target to the first row of tubes and from the target to the surface of the reflector cannot be increased. This fixes the number of 2 cm diameter INPORT units at the same value as for the 330 MWe case. The number of 10 cm diameter tubes must be increased to provide the added protection. This is accomplished by spacing the 10 cm diameter tubes closer together, increasing their number from 1260 to 1550, an increase in mass of associated components by 23.5%. The solid fraction goes up from 33% to 40%.

The LiPb velocity in the front row of tubes is increased from 1 m/s to 3.6 m/s thus maintaining the same temperature rise in the front row. This is still well within credible parameters since the flow in the HIBALL front row of tubes was 5 m/s. The flow in the rear tubes is increased by a factor of 2.9 and in all cases remain < 2 m/s. Flow in the tubes closer to the target is higher than in tubes in the rear of the breeding zone.

For costing purposes the chamber materials have been increased by 25%. For consistency, the volumes of all the buildings were also increased the same amount.

11.6.2 Scaleup Scenarios

Five scaleup scenarios have been envisaged. They are:

- I. Increasing the rep-rate from 3 Hz to 11 Hz while keeping the same driver energy (4 MJ) and the same target gain. The thermal power is 4257 MW_{th} and the net electric power 1218 MWe. Beam insulating, LiPb pumping, He gas pumping, auxiliary power and driver electric requirements are increased by a factor of 3.6. Target cost is held at 18¢/target.
- II. Repetition rate is increased from 3 Hz to 6 Hz and target gain from 80-144. Driver energy is unchanged. Beam insulating and driver electric requirements are doubled, while the systems associated with increased power handling by 3.6 as above. The thermal power is 4214 MW_{th} and the net electric 1330 MWe. Because of the higher target gain we have used a target cost of both 18¢/target and 36¢/target.
- III. Driver energy and repetition rate is unchanged but target gain is increased from 80 to 285. The gross thermal power is 4187 MW_{th} and the net electric 1398 MWe. Target costs are 18¢ and 36¢/target.
- IV. Driver energy increased from 4 to 6 MJ, repetition rate from 3 Hz to 6 Hz and target gain from 80-100. The gross thermal power is 4214 MW_{th} and net electric 1279 MWe. The target cost is taken as 18¢/target.
- V. In this scenario we assume that a single driver is used to drive two identical chambers. The driver energy is 6 MJ, each chamber repetition rate is 3 Hz and target gain is 100. Again the target cost is 18¢/target. Gross thermal power is 4214 MW_{th} and net electric is 1279 MWe.

11.6.3 Scaling Laws

The same scaling laws outlined in Section 11.1 are used to perform the economics analysis.

11.6.4 Results and Conclusions

Table 11.6 gives the results of the economic analysis for the five scenarios. The first four lines give the parameters used and the cost of the target. The gross thermal power and net electric power are listed next. The next eleven lines give the costs of the various reactor components. The driver cost was obtained using the PSI scaling law. The last four lines give the total direct costs in million of dollars, the unit direct costs in \$/kWe, the total capital costs in millions of dollars and the COE in mills/kWh.

Table 11.6 Libra Scaling Comparisons*

	I	II(a)	II(b)	III(a)	III(b)	IV Primary Reference	V Backup Reference
Driver Energy, MJ	4	4		4		6	6
Rep. Rate, Hz	11	6		3		6	3+3
Target Gain	80	144		285		100	100
Target Cost, ¢	18	18	36	18	36	18	18
Thermal Power, MW _{th}	4257	4214		4187		4214	4214
Net Electric, MWe	1218	1330		1398		1279	1279
Driver Cost, M\$	468	442		426		611	611
Miscel. Plant, M\$	46	46		46		46	46
Turbine Plant, M\$	280	278		276		278	278
Electric Plant, M\$	144	120		97		135	135
Heat Rej., M\$	49	47		46		48	48
Maint. Equip., M\$	50	50		50		50	50
Inst. & Contr., M\$	31	31		31		31	31
Fuel Handl., M\$	26	26		26		26	26
Heat Trans., M\$	252	249		247		249	259
Reactor Chamb., M\$	102	102		102		102	188
Land & Buldings, M\$	94	94		94		94	125
Tot. Dir. Costs, M\$	1543	1485	1485	1441		1671	1798
Unit Dir. Cost, \$/kWe	1267	1117	1117	1031		1306	1406
Tot. Cap. Costs, M\$	2711	2609	2609	2531		2936	3159
Cost of Elect., mills/kWh	42.8	35.6	38.4	31.6	33.0	41.3	44.2

*Where costs are quoted they are in 1988\$M

The COE ranges from a low of 31.6 mills/kWh for case IIIa to a high of 44.2 mills/kWh for case V. From the standpoint of overall technical credibility, we have selected case IV as our primary reference and case V as the backup reference. Thus, it appears that the COE can be reduced from 88.7 to 41.3 mills/kWh, more than 50%, by increasing the power output from 330 MWe to a nominal value of 1200 MWe while using entirely credible scaling laws. Likewise the unit direct costs go down from 2843 to 1306 \$/kWe.

Figure 11.3 shows the comparison of the unit direct costs and the COE for the LIBRA reference design point of 330 MWe and the nominal 1200 MWe case IV selected as the primary reference. Although the points are joined by a straight line, in the actual case, they would fall on a curve with some scaling function.

Two interesting points can be made with the 330 and 1200 MWe LIBRA design costs in Figure 11.2. First of all, the cost of even a low power light ion reactor like LIBRA is very competitive with larger (1200-3400 MWe) DT tokamak and heavy ion beam reactors. Secondly, when we take advantage of the economy of scale by increasing the power level of LIBRA up to 1200 MWe, it becomes clearly one of the most economical DT reactors designed in the last decade.

This point is emphasized even more in Fig. 11.4 where we have compared the direct capital costs versus reactor power level for heavy ions (HIBALL-I and II), a laser reactor (SOLASE) and several recent DT tokamaks. This figure shows that the eventual commercialization of light ion beams could be favored over heavy ion beams if the cost of RF or induction linacs cannot be reduced. This favorable position can also be claimed against the recent large and difficult to maintain tokamaks.

In summary, it is clear that the economic potential of light ion beam fusion is promising if technical difficulties relating to beam transport and focussing can be overcome. It is not easy at this time to see if these problems are any more difficult than confinement in tokamaks. If the two problems can be solved on the same time scale, then the low reactor driver cost of light ion beams may present society with its most economical form of electricity.

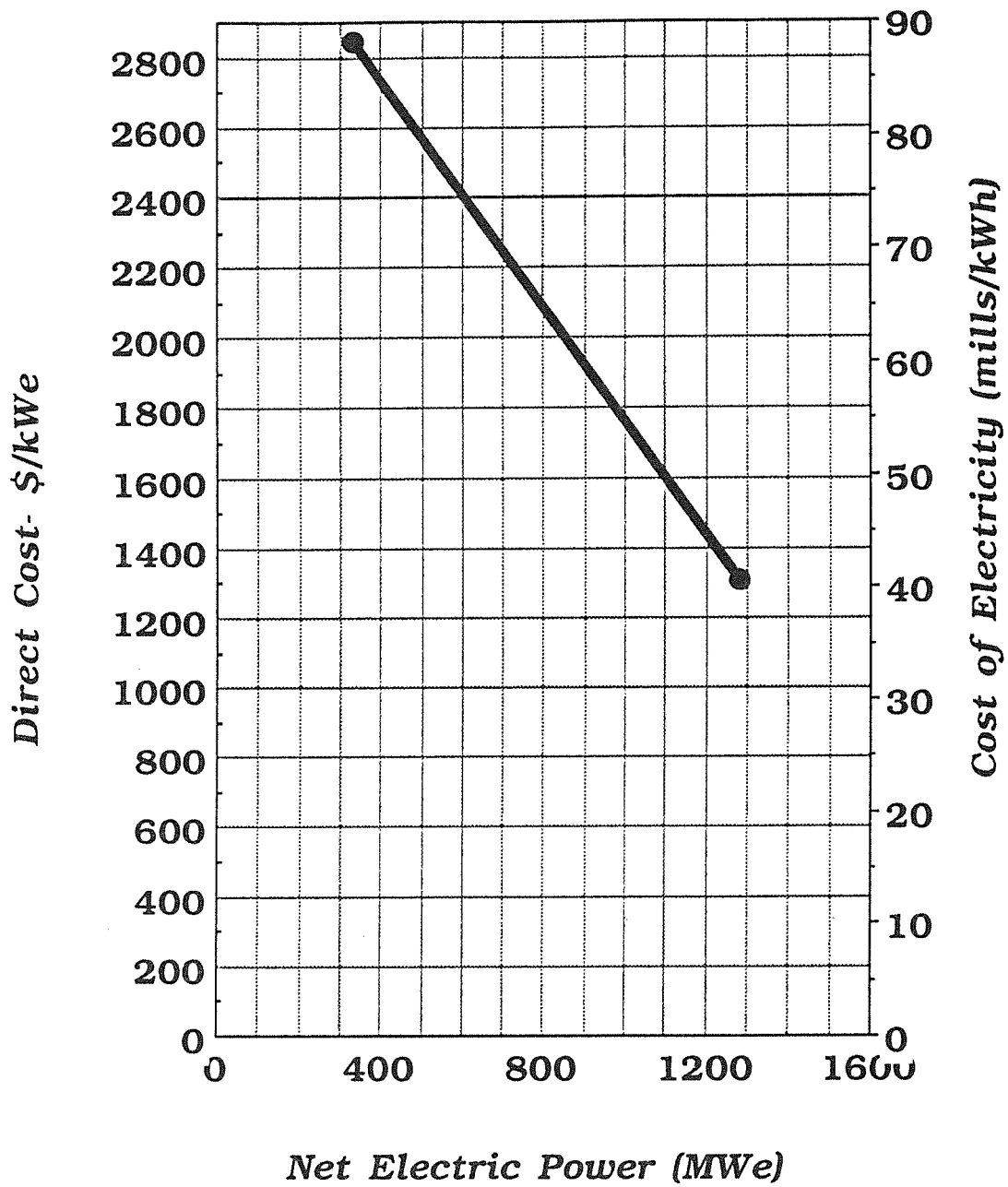


Figure 11.3. Comparison of LIBRA scaling from 330 MWe to 1200 MWe.

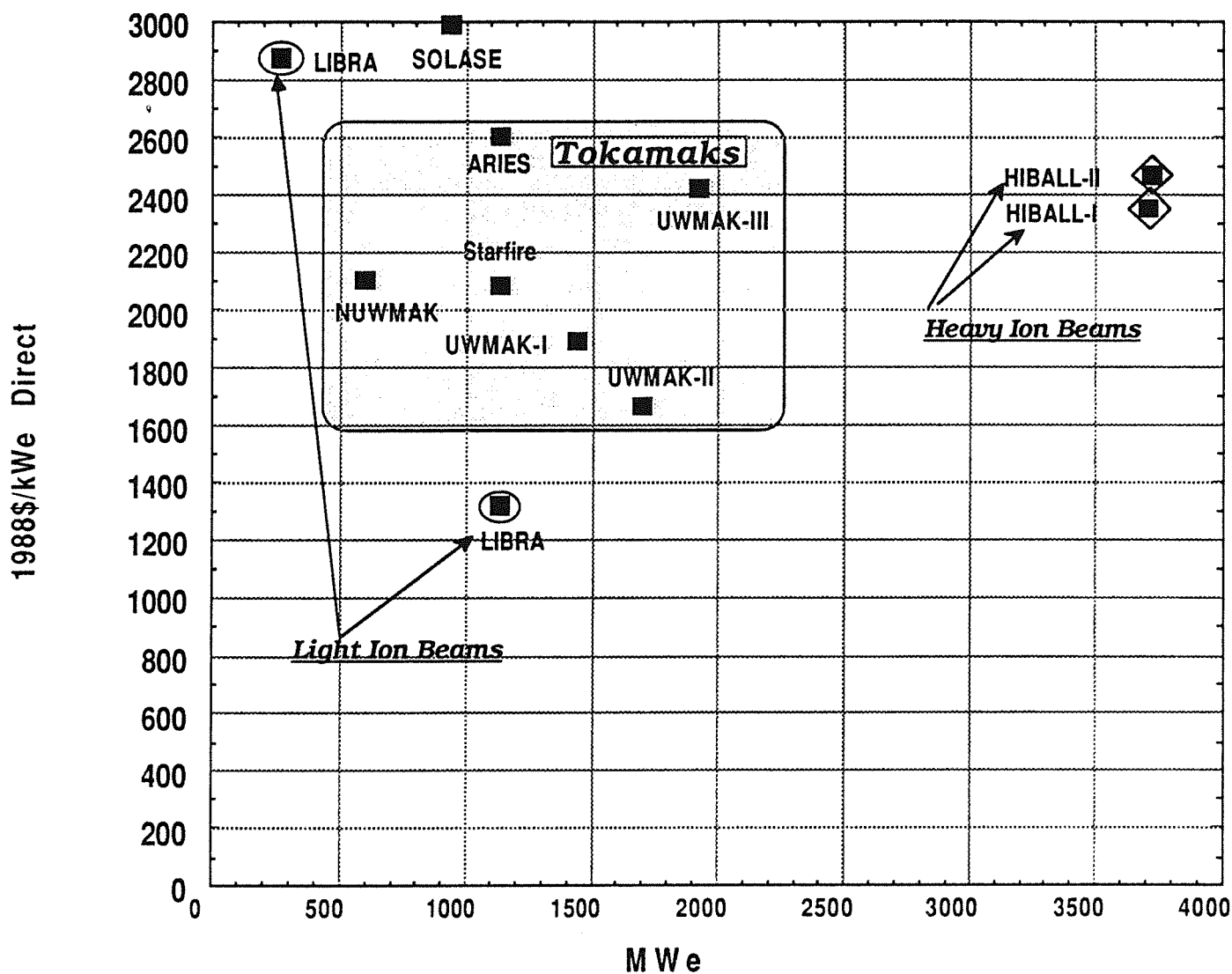


Figure 11.4. Relationship between size and cost of recent DT tokamak, laser, and ion beam fusion reactor designs.

References for Chapter 11

1. Zoran Musicki, "FUSCOST: A PC-Based Menu Driven Program for Economic Analysis of Fusion Facilities," 12th Symposium on Fusion Engineering, Monterey, CA, Oct. 1987, University of Wisconsin Fusion Technology Institute Report UWFD-743.
2. Scott Thompson, "Reference Cost Data for Fusion Studies," Fusion Engineering Design Center, Sept. 1986.
3. Z. Musicki, "The Economic Analysis of SIRIUS-M, A Symmetrically Illuminated, ICF Engineering Test Reactor," University of Wisconsin Fusion Technology Institute Report UWFD-708, Sept. 1986
4. Z. Musicki, "Continuation of Economic Analysis of SIRIUS-M," University of Wisconsin Fusion Technology Institute Report UWFD-746, Sept. 1987.
5. T.J. McCarville, W.R. Meier, C.F. Carson, B.B. Glasgow, "SAFIRE - A Systems Analysis Code for ICF Reactor Economics," LLNL UCRL-15872, Vol. 1, January 12, 1987.
6. E.K. Cleveland et al., "Preliminary Scoping Study for the Target Development Facility," Los Alamos Technical Associates Inc. Report SAND 83-7005.
7. J.H. Pendergrass, et al., "Heavy-Ion Fusion Target Cost Model", Fusion Technology, Vol. 13, 2, pp.375-395 (Feb. 1988).
8. Wayne R. Meier, "A Standard Method for Economic Analyses of ICF Power Plants", 7th Topical Meeting on the Technology of Fusion Energy, Reno, NV, June 1986.
9. J. Sheffield, et al., "Cost Assessment of a Generic Magnetic Fusion Reactor", Fusion Technology, Vol. 9, 2, pp. 199-249 (March 1986).

LIBRA PARAMETER LISTING

Contents	Page
1. General Parameters	A-1
2. Target Parameters	A-2
3. Target Manufacture and Delivery Parameters	A-4
4. Driver Parameters	A-6
5. Diode Parameters	A-9
6. Preformed Plasma Channel Parameters	A-12
7. Ion Beam Parameters	A-14
8. Cavity and Blanket Parameters	A-16
9. Chamber, Reflector and Shield Parameters	A-20
A. Reflector	A-20
B. Shield	A-22
10. Power Conversion and Balance of Plant	A-23
11. System Parameters	A-24
12. Tritium Parameters (for 30% Burnup)	A-25
13. LIBRA Costing	A-27

1. GENERAL PARAMETERS*

Average DT power - 17.6 MeV/fusion (MW)	960
Target power (MW)	940.08
Target energy multiplication	0.9792
Target yield (MJ)	<u>313.36</u>
Ion type	Li ⁺
Ion energy (MeV)	25-35
Ion beam pulse energy (MJ)	4
Target gain	<u>80</u>
Overall driver efficiency (%)	23.6
Fusion gain η_G	16
Overall energy multiplication	1.17
Nuclear energy multiplication	<u>1.20</u>
Gross thermal power	1161
Net thermal efficiency (%)	38
Gross electrical output (MW)	441
Recirculating power fraction (%)	<u>25</u>
Net electrical output (MW)	331
Chamber repetition rate (Hz)	3
Chamber geometry	cyl
Chamber diameter (m)	<u>8.7</u>
Chamber height (m) (at vacuum wall)	6.4
Chamber material	HT-9
# of beam ports	36
ion diodes	16+2
return paths	<u>16+2</u>
Breeding material	Pb ₈₃ Li ₁₇
Tritium breeding ratio	1.4
Chamber gas	He
Chamber gas pressure at 0°C (torr)	100
Neutron wall loading (MW/m ²)	<u>6</u>

*TBD = To Be Determined

2. TARGET PARAMETERS

Composition	
D (mg)	1.28
T (mg)	1.92
DT load (mg)	<u>3.2</u>
Pusher/Absorber (mg)	53.68
Tamper (mg)	230.4
Burnup (%)	30
Total mass (mg)	<u>287.28</u>
Configuration (# of shells)	1
Initial DT shell diameter (cm)	0.6
Absorbed ion energy (MJ)	4
DT yield (MJ)	<u>320</u>
Target yield (MJ)	313.36
Target energy multiplication	0.9792
Target gain	80
Average DT power (MW)	<u>960</u>
Target power (MW)	940.08
Neutron yield (MJ)	216.9
Ave. neutron energy (MeV)	11.64
Neutron multiplication	<u>1.0248</u>
Fraction of yield in neutrons	0.692
Gamma yield (MJ)	0.93
Ave. gamma energy (MeV)	3.85
Fraction of yield in gammas	<u>0.003</u>
X-ray yield (MJ)	62.672
X-ray spectrum - blackbody (keV)	1
Fraction of yield in X-rays	0.2
Debris yield (MJ)	<u>32.858</u>
Debris spectrum (keV/amu)	0.6
Fraction of yield in debris	0.1048
Radioactivity production (Ci/target @ t = 0)	TBD
Target injection velocity (m/s)	<u>200</u>

Max. DT temperature after injection (K)	6.7
Max. DT temperature after channel heating (K)	6.8
Target injector type	<u>gas gun</u>

Acceleration (m/s ²)	10 ⁴
Acceleration time (ms)	23
Travel distance in buffer gas (m)	2.0
Injector tube length (m)	3.5
Target travel time in buffer gas and injector tube (ms)	23.8
Target travel time in target chamber gas (ms)	19.5
Tolerance on total travel time (ms)	<u>3.0 x 10⁻³</u>
Distance injector tube to focus (m)	4.5
Initial DT temperature (K)	4
Max. DT temperature after injection (K)	6.7
Tracking:	
Lateral tracking	<u>none</u>
Longitudinal tracking, type	light beam interception
Tracking position 1, distance from focus (m)	<u>TBD</u>
Tracking position 2, distance from focus (m)	TBD
Light beam diameter (mm)	0.2
Precision of arrival time prediction (μs)	± 1
Duration of processing tracking results (ms)	<u>1</u>

4. DRIVER PARAMETERS

Ion

Type	Li ⁺
Charge state	+1
Energy (MeV)	26-35
Velocity (m/s)	2.86×10^7
Beta, $\beta = v/c$.095
Gamma, $\gamma = (1 - \beta^2)^{-1/2}$	1.0046
Mass number (amu)	7

Accelerator - general

Type	Helia
Efficiency	47
Number of modules	16
Number of stores/module	26
Number of return current paths/module	26
Outer radius of inductive voltage adder (m)	20.4
Inner radius of inductive voltage adder (m)	6.0
Outer radius of MITL (m)	6.0
Inner radius of MITL (m)	6.0
Radius of water-vacuum interface (m)	TBD
Radius of diodes (m)	6.0
Energy in primary store (MJ)	15.4
Energy at diodes (EM) (MJ)	7.2
Power at diodes (EM) (TW)	184
Voltage across diodes (MV)	26-35
Impedance (ohms)	3

Type Prime Storage

Type	(rotating
Number/module	machine
Volume/module (m ³)	+ step up
Energy density (MJ/m ³)	transformer)
Charge time (s)	TBD
Discharge time (s)	TBD
Charging voltage (MV)	TBD
Discharging voltage (MV)	TBD

Dielectric	TBD
Efficiency	72
Charging Pulse Line (CPL)	
Number/module	<u>26</u>
Length (m)	180
Diameter (m)	.95
Gap (m)	.22
Material	<u>water</u>
Charging time (μ s)	TBD
Discharging time (μ s)	TBD
Switch type	magnetic
Dielectric	metglas
Voltage (MV)	<u>TBD</u>
Pulse Forming Lines (PFL)	
Number/module	26
Length (m)	1.0
Radius (m)	<u>.95</u>
Gap width (m)	.13-.20
Geometry	conical
Material	TBD
Switch type	<u>magnetic</u>
Dielectric	metglas
Charging time (ns)	TBD
Discharging time (ns)	TBD
Voltage (MV)	<u>1.15</u>
Inductive Voltage Adder (IVA)	
Number of cells/module	26
Material	metglas
Bore (m)	<u>1.0</u>
Vacuum insulator diameter (m)	1.70
Cell diameter (m)	1.80
Cell length (m)	<u>.554</u>

Average cell voltage (MV)	1.15
Average module voltage (MV)	30.0
Module pulse width (ns)	40.0
Magnetic insulated transmission lines (MITL)	
Number	0*
Length (m)	TBD
Vacuum gap (cm)	TBD
Height (cm)	TBD
Width (cm)	TBD
Material	TBD
Voltage (MV)	TBD
Efficiency of CPL + PFL + IVA + MITL	65%

*Not included in present design but may be included in future.

5. DIODE PARAMETERS

General Parameters

Diode type	single gap applied-B
Source type	EHD-liquid Li
Number of main diodes	16
Number of prepulse diodes	2
Diode efficiency (%)	80
Efficiency from diode to target (%)	60

Main Diode Parameters

Energy output per diode (MJ)	0.360
Energy on target per diode (MJ)	0.225
Nominal voltage (MV)	30
Minimum voltage (MV)	26.1
Maximum voltage (MV)	33.9
Bunching factor	4.33
Channel length (cm)	600
Nominal voltage pulse width @ diode (ns)	39
Nominal voltage pulse width @ target (ns)	9.0
Nominal output current per diode (kA)	308
Nominal output power per diode (TW)	9.23
Ion microdivergence (mrad)	5
Maximum anode current density (kA/cm ²)	5
Maximum power brightness (TW/cm ² /rad ²)	6 x 10 ³
Nominal impedance (ohms)	76
Nominal A-K gap (cm)	2.4
Dynamic gap (cm)	1.94
Applied magnetic field (T)	8.6
Critical magnetic field (T) @ 30 MV	4.3
Anode surface area (cm ²)	79
Critical insulation voltage (MV)	50
Actual anode current density (kA/cm ²)	3.90
Actual diode power brightness (TW/cm ² /rad ²)	4.67 x 10 ³
Anode outer radius (cm)	5.19

Anode inner radius (cm)	1.31
Focal length (cm)	51.9
Macrodivergence R/F (rad)	0.10
Focal spot radius (cm)	<u>0.35</u>
Focal spot area (cm ²)	0.38
Prepulse Diode Parameters	
Energy output per diode (MJ)	0.36
Energy on target per diode (MJ)	<u>0.20</u>
Nominal voltage (MV)	30
Minimum voltage (MV)	30
Maximum voltage (MV)	30
Bunching factor	<u>1</u>
Channel length (cm)	600
Nominal voltage pulse width @ diode (ns)	39
Nominal voltage pulse width @ target (ns)	<u>39</u>
Nominal output current per diode (kA)	278
Nominal output power per diode (TW)	8.33
Ion microdivergence (mrad)	5
Maximum anode current density (kA/cm ²)	<u>5</u>
Power brightness (TW/cm ² /rad ²)	6 x 10 ³
Nominal impedance (ohms)	76
Nominal A-K gap (cm)	2.4
Dynamic gap (cm)	1.94
Critical insulation voltage (MV)	<u>50</u>
Actual anode current density (kA/cm ²)	3.52
Actual diode power brightness (TW/cm ² /rad ²)	4218
Applied magnetic field (T)	8.6
Critical magnetic field (T)	<u>4.3</u>
Anode surface area (cm ²)	79
Anode outer radius (cm)	5.19
Anode inner radius (cm)	1.31
Focal length (cm)	51.9
Macrodivergence R/F (rad)	<u>0.10</u>

Focal spot radius (cm)	0.35
Focal spot area (cm ²)	0.38
Ion Source Parameters	
Enhanced field at anode surface (MV/cm)	100
Gap field near anode (MV/cm)	<u>5</u>
Anode enhancement factor	20
Critical or "turn on" voltage (MV)	10
Diode Vacuum Parameters	
Minimum gas density (atoms/cm ³)	<u>TBD</u>
Diode chamber volume (cm ³)	TBD
Gas type	TBD
Puff gas mass (g)	TBD
Gas leakage from cavity per shot (g)	<u>TBD</u>
Total gas mass	TBD
Maximum gas density (atoms/cm ³)	TBD
Gas pumping port radius (cm)	TBD
Gas pumping pipe length (cm)	<u>TBD</u>
Gas pumping conductance	TBD
Gas pumping rate (1/s)	TBD
Diode Protection Parameters	
Type	<u>Rotating vane shutters</u>
Number of disks	TBD
Shutter speed (rev/s)	TBD
Aperture diameter (cm)	20
Shutter thickness (cm)	<u>TBD</u>
Impulse on shutters (MPa-s)	TBD
Diode Heat Rejection	
Average rejection power per diode (kW)	290
Heat rejection method	lithium coolant
Diode Radioactivity	
Activity after 1 FPY from fusion neutrons (Ci)	TBD
Activity after 1 FPY from from 30 Mev Bremss (Ci)	TBD

6. PREFORMED PLASMA CHANNEL PARAMETERS

Number of ion channels	16+2
Number of return current channels	16+2
Channel length (m)	5.4
Channel diameter (cm)	1.0
Cavity gas density before discharge (cm ⁻³)	3.55 x 10 ¹⁸
Cavity gas temperature before discharge (eV)	0.67
Channel density	
g/cm ³	6.64 x 10 ⁻⁶
#/cm ³	1 x 10 ¹⁸
Channel temperature (eV)	
Before ion beam	20
After ion beam	35
Discharge current (kA)	100
Discharge current density (kA/cm ²)	127
Discharge rise time (μs)	1
Total energy in capacitor banks (MJ)	0.44
Circuit inductance (μH)	12
Circuit capacitance (μF)	0.34
Discharge voltage (kV)	1200
Maximum azimuthal magnetic field strength (T)	2.8
Position of maximum B-field (cm)	0.5
Ion cyclotron freq. (s ⁻¹)	1.3 x 10 ⁸
Laser type	TBD
Wavelength (μm)	TBD
Laser beam diameter (cm)	0.4
Intensity (W/cm ²)	TBD
Pulse energy/channel (J)	TBD
Total energy in laser beams (J)	TBD
Laser efficiency	TBD
Energy to drive lasers (J)	TBD
Ionization/excitation mechanism	LIBORS
Energy hitting target (J)	TBD
Magnetic insulation of channels	
Number of beamlines	18

Length of each (m)	2.9
Specific current (MA/m)	2.55
Magnetic field (T)	3.2
Conductor current (kA)	<u>60</u>
Current density (kA/cm ²)	4
Conductor x-section (cm x cm)	2.25 x 6.7
Number of turns	123
Inductance of coil (μH)	<u>300</u>
Coil resistance (ohms)	.0137
Inductive resistance (ohms)	0.188
Voltage pulse magnitude (kV)	11.3
L/R time constant (ms)	<u>22</u>
Voltage rise time (ms)	5
Power dissipated/beamline (MW)	1.47
Total power (MW)	26.5
Stored energy/beamline (MJ)	<u>0.54</u>

7. ION BEAM PARAMETERS

Ion type	Li
Ion charge state	3
Nominal ion energy (MeV)	
At channel entrance	30
At channel exit	<u>22.5</u>
Energy/channel (MJ)	
At channel entrance	0.36
At channel exit	0.29
On target	<u>0.225</u>
Average power/channel (TW)	
At channel entrance	9.23
At channel exit	32.2
On target	<u>25</u>
Beam current/channel (MA)	
At channel entrance	0.308
At channel exit	1.43
On target	<u>1.11</u>
Pulse bunching factor	4.33
Energy loss in channel (MJ)	0.65
Total beam energy (MJ)	
At channel entrance	<u>5.76</u>
At channel exit	4.64
On target	3.60
Total average beam power (TW)	
At channel entrance	<u>148</u>
At channel exit	515.2
On target	400
Total beam current (MA)	
At channel entrance	<u>4.93</u>
At channel exit	22.9
On target	17.8
Beam overlap radius (cm)	1.3
Overlap efficiency (%)	<u>80</u>

Energy on target (MJ)	3.6
Average power on target (TW)	400
Peak power on target (TW)	400
Beam divergence half-angle (radians)	
At channel entrance	0.10
At channel exit	0.10
Beam brightness $B=IV/\pi r^2 \theta^2$ (TW/cm ² /rad ²)	
At channel entrance	1175
At channel exit	4100
Focal spot size (cm)	
At channel entrance	0.35
At channel exit	0.35
Total # of ions (cm ⁻³)	8.3×10^{17}
Total mass of ions (g)	9.7×10^{-6}

8. CAVITY AND BLANKET PARAMETERS

Coolant	Li ₁₇ Pb ₈₃
Breeding Material	Li ₁₇ Pb ₈₃
Li-6 enrichment, %	90
Tube Region	
Inport structural material (v/o)	SiC (2)
Inport coolant (v/o)	Li ₁₇ Pb ₈₃ (98)
First surface radius (m)	3
Tube bank thickness (m)	1.35
Tube bank packing fraction	0.33
Effective coolant thickness at first wall (cm)	50
Mass of coolant in tubes (tonnes)	627
Front tubes	
Length (m)	6.4
Diameter (cm)	3
Thickness (mm)	3
Number	628
Secondary tubes	
Length (m)	6.4
Diameter (cm)	10
Thickness (mm)	10
Number	1260
Number of beam ports	18
Diameter of beam port (cm)	20
Cavity gas	
Type	He
Pressure @ 0°C (torr)	100
Density (g/cm ³)	2.36 x 10 ⁻⁵
(#/cm ³)	3.55 x 10 ¹⁸
Temperature (eV)	0.07
(K)	800
Pressure at op. temp. (torr)	300
Flow rate (kg/s)	TBD
(torr-ℓ /s)	TBD

Speed (m/s)	
Outlet	TBD
At channel	TBD
Eqm. radioactivity (Ci)	
Cavity Gas	TBD
Target	TBD
Fireball	
Initial size (cm)	40
Initial temperature (eV)	100
Initial energy (MJ)	45
Max. heat flux on first surface (W/cm ²)	10 ⁶
Total energy flux on first surface (J/cm ²)	12.5
Arrival time of max. heat flux (s)	2 x 10 ⁻⁸
Max. overpressure on first surface (MPa)	10 ⁵
Arrival time of max. overpressure (s)	2 x 10 ⁻⁹
Duration of pressure pulse (s)	10 ⁻⁸
Cooldown time of cavity gas (s)	0.33
Time between shots (s)	0.33
Total impulse (Pa-s)	125
Chamber top	
Structural material and (v/o)	SiC (5)
Coolant (v/o)	Li ₁₇ Pb ₈₃ (95)
Height from chamber center (m)	4.45
Region thickness (cm)	10
Mass of coolant in cavity top (tonnes)	40.5
Number of penetrations in top region	1
Total area of penetrations at chamber inner surface (cm ²)	3.1
Chamber pool	
Structural material and (v/o)	0
Coolant (v/o)	Li ₁₇ Pb ₈₃ (100)
Ave. depth (cm)	45
Distance, chamber center to surface (m)	3.2
Mass of coolant in pool (tonnes)	238

Maximum 1st surface neutron energy current - at chamber midplane (MW/m ²)	6
Uncollided neutrons streaming through each beam line penetration per shot	3.24 x 10 ¹⁶
DT power (MW)	960
Total nuclear power in cavity (MW)	TBD
Tube region	TBD
Cavity top	TBD
Cavity bottom	TBD
Total power in cavity, including x-rays and debris (MW)	TBD
Average power density (W/cm ³)	TBD
Tube region	TBD
Top region	TBD
Bottom region	TBD
Peak/average spatial power density in tube region	TBD
Impulse on first wall tubes (Pa-s)	125
Amount of coolant blown off per shot (kg)	9
Maximum dpa/FPY	
Tube region	TBD
Top region	TBD
Bottom region	TBD
Maximum He production (appm/FPY)	TBD
Tube region	TBD
Top region	TBD
Bottom region	TBD
Maximum SiC burnup (appm/FPY)	TBD
Tube region	TBD
Top region	TBD
Tritium breeding per DT fusion	TBD
⁶ Li	TBD
Tube region	TBD
Top region	TBD
Bottom region	TBD

⁷ Li	TBD
Tube region	TBD
Top region	TBD
Bottom region	<u>TBD</u>
Coolant	
Inlet temp., first wall tubes (°C)	338
Outlet temp., first wall tubes (°C)	500
Flow rate, first wall tubes (kg/s)	4.26 x 10 ³
Flow velocity, first wall tubes (m/s)	1.0
Avg. flow velocity, secondary tubes (m/s)	<u>0.5</u>
Total mass flow rate (kg/s)	5.12 x 10 ⁴
Pressure (MPa)	2.3
ΔP for entire loop (MPa)	2.0
Pumping power delivered to coolant (MW)	<u>10.9</u>

9. CHAMBER, REFLECTOR AND SHIELD PARAMETERS

A. Reflector

Structural material	HT-9
Coolant	<u>Li₁₇Pb₈₃</u>
Side reflector	
Inside diameter (m)	8.7
Thickness (m)	0.5
Mass of structure (tonnes)	1068
Mass of coolant (tonnes)	146
v/o of structure	90
v/o of coolant	<u>10</u>
Top reflector	
Thickness (m)	0.25
Mass of structure (tonnes)	86
Mass of coolant (tonnes)	11.8
v/o of structure	90
v/o of coolant	<u>10</u>
Bottom of reflector (splash plate)	
Thickness (m)	0.35
Mass of structure (tonnes)	143
Mass of coolant (tonnes)	11.2
v/o of structure	94
v/o of coolant	<u>6</u>
Total mass of structural material in reflector (tonnes)	1297
Total mass of coolant in reflector (tonnes)	169
Average power density (W/cm ³)	
Side reflector	TBD
Top reflector	TBD
Bottom reflector (splash plate)	<u>TBD</u>
Peak/average spatial power density - in side reflector	TBD
Power deposited in reflector (MW)	TBD
Side	TBD
Top	TBD
Bottom	<u>TBD</u>

Maximum dpa/FPY	TBD
Side reflector	TBD
Top reflector	TBD
Bottom reflector	TBD
Maximum He production in structural material (appm/FPY)	TBD
Side reflector	TBD
Top reflector	TBD
Bottom reflector	TBD
Tritium breeding per DT fusion	TBD
⁶ Li	TBD
Side	TBD
Top	TBD
Bottom	TBD
⁷ Li	TBD
Side	TBD
Top	TBD
Bottom	TBD
Coolant	
Mass of coolant within reflector (tonnes)	163.4
Flow rate (kg/hr)	2.85 x 10 ⁷
Inlet temperature (°C)	338
Outlet temperature (°C)	450
Maximum coolant velocity (m/s)	0.5
Pressure (MPa)	2.3
ΔP for entire loop (MPa)	2
Pumping power delivered to coolant (MW)	1.68
Maximum structure temperature (°C)	490

B. Shield

Structural material and (v/o)	SS (20)
Shield material (v/o)	Concrete (70)
Coolant and (v/o)	<u>He (10)</u>
Side shield	
Inside diameter (m)	9.7
Thickness (m)	TBD
Top shield	
Height above midplane at centerline (m)	4.8
Thickness (m)	<u>TBD</u>
Bottom shield	
Height below midplane (m)	TBD
Thickness (m)	
Maximum power density at midplane (W/cm ³)	TBD
Average power density (W/cm ³)	TBD
Power deposited in shield (MW)	<u>TBD</u>
Dose rate during operation at outer surface	TBD
of shield at midplane (mrem/hr)	
neutron	TBD
gamma	<u>TBD</u>
Coolant	He
Inlet temperature (°C)	200
Outlet temperature (°C)	380
Flow rate (kg/hr)	<u>2 x 10⁵</u>
Maximum velocity (m/s)	40
Pressure (MPa)	8
ΔP in entire loop (MPa)	0.3
Pumping power delivered to coolant (MW)	2.64
Peak structure temperature (°C)	<u>400</u>

10. POWER CONVERSION AND BALANCE OF PLANT

Intermediate heat exchange	Li ₁₇ Pb ₈₃ /He
Li ₁₇ Pb ₈₃ mass flow rate (kg/s)	5.12 x 10 ⁴
Li ₁₇ Pb ₈₃ inlet temperature (°C)	500
Li ₁₇ Pb ₈₃ outlet temperature (°C)	338
Surface area (m ²)	6630
He gas pressure (MPa)	8
Average He gas velocity (m/s)	80
He gas inlet temperature (°C)	300
He gas outlet temperature (°C)	470
Steam generator	
Type of steam cycle	Superheated
Steam temperature (°C)	430
Steam pressure (MPa)	11
Steam mass flow rate (kg/hr)	2.3 x 10 ⁶
Feedwater temperature (°C)	300
Reheat temperature (°C)	430
Steam generator surface area (m ²)	6 x 10 ³
Gross thermal conversion efficiency (%)	38
Gross electric power generation (MWe)	441
Net plant efficiency (%)	28.5
Net electric power generation (MWe)	331

12. TRITIUM PARAMETERS (FOR 30% BURNUP)

Material inserted per shot	
D - target (mg)/(# of atoms)	1.28/3.84 x 10 ²⁰
T - target (mg)/(# of atoms)	1.92/3.84 x 10 ²⁰
CD ₂ - target (mg)/(# of atoms)	61.5 mg/2.30 x 10 ²¹ (C)
	<u>4.61 x 10²¹(D)</u>
Pb - target (mg)/(# of atoms)	230.4/6.69 x 10 ²⁰
Li - ion beam (mg)/(# of atoms)	9.7 x 10 ⁻³ /8.3 x 10 ¹⁷
Li - INPORT (g)/(# of atoms)	52.3/5.3 x 10 ²⁴
Pb - INPORT (g)/(# of atoms)	8940/2.6 x 10 ²⁵
D ₂ (target injector) mg/shot/# of atoms	1.6/4.8 x 10 ²⁰
Total D, T, D ₂ (mg)/(# of atoms)	<u>4.8/1.25 x 10²¹</u>
Fractional burnup, f _b = T _b /(T _b + T _p)	0.30
# of shots per second	3
Cavity pressure (torr @ 0°C)	100
Coolant breeding region	(liquid)
Breeding material	Li ₁₇ Pb ₈₃
Flow rate (kg/hr)	<u>1.84 x 10⁸</u>
Breeder mass (kg)	2 x 10 ⁶
Inlet temperature (°C)	338
Outlet temperature (°C)	500
Breeding ratio	1.4
Steady state tritium concentration (wppm)	1.4 x 10 ⁻⁴
Tritium pressure (torr @ 500°C)	<u>10⁻⁴</u>
Extractor	
Mass flow rate (kg/s)	6.5 x 10 ³
Inlet temperature (°C)	500
Outlet temperature (°C)	500
Inlet concentration (wppm)	1.4 x 10 ⁻⁴
Outlet concentration (wppm)	<u>0.4 x 10⁻⁴</u>
Extraction method	Droplet Degassing
Size of extractor	6 m hi x 10 m dia.
Mass of breeding material within extractor (kg)	6.3 x 10 ⁴
% of total breeding material within extractor	<u>3.2</u>

Steam generator

Material composition	TBD
Wall thickness (mm)	TBD
Primary inlet temperature (°C)	TBD
Primary outlet temperature (°C)	TBD
Secondary inlet temperature (°C)	TBD
Secondary outlet temperature (°C)	TBD
Secondary pressure (MPa)	TBD
Surface area (m ²)	TBD
Tritium permeation rate to H ₂ O (Ci/d)	18

Tritium inventory - steady state

Breeding material

Reactor chamber (g)	0.2
Reflector (g)	0.1
Silicon carbide (g)	150
Cavity exhaust pumps (g)	1.3
Cryogenic distillation columns (g)	45
Fuel cleanup (g)	1.3
Structural material and piping	
Target manufacture/delivery (g)	155
Steam generator piping (g)	0.5
Storage - one day fuel supply (kg)	0.5
Total (kg)	0.854
Total (Ci)	1 x 10 ⁷

Containment

Total building volume (m ³)	TBD
Volume of reactor & auxiliaries (m ³)	TBD
Cleanup volume (m ³)	TBD
Containment pressure (torr @ 0°C)	TBD
Time for tritium cleanup (hr)	TBD

13. LIBRA COSTING

Main Account	\$M ('86)
Land and Land Rights	5
Site and Buildings	78
Reactor Cavity	<u>82</u>
Heat Transfer System	71
Fuel Handling, Radwaste, Injector	20
I & C	21
Maintenance Equipment	<u>34</u>
Heat Rejection	16
Electrical Plant	57
Turbine Plant	97
Accelerator	426
Target Factory	<u>-</u>
 TOTAL	 941